NANOZYMES: FROM RATIONAL DESIGN TO BIOMEDICAL APPLICATIONS

EDITED BY: Kelong Fan, Youhui Lin and Vipul Bansal
PUBLISHED IN: Frontiers in Chemistry

frontiers Research Topics

ISSN 1664-8714
ISBN 978-2-88966-821-2
DOI 10.3389/978-2-88966-821-2

About Frontiers

Frontiers is more than just an open-access publisher of scholarly articles: it is a pioneering approach to the world of academia, radically improving the way scholarly research is managed. The grand vision of Frontiers is a world where all people have an equal opportunity to seek, share and generate knowledge. Frontiers provides immediate and permanent online open access to all its publications, but this alone is not enough to realize our grand goals.

Frontiers Journal Series

The Frontiers Journal Series is a multi-tier and interdisciplinary set of open-access, online journals, promising a paradigm shift from the current review, selection and dissemination processes in academic publishing. All Frontiers journals are driven by researchers for researchers; therefore, they constitute a service to the scholarly community. At the same time, the Frontiers Journal Series operates on a revolutionary invention, the tiered publishing system, initially addressing specific communities of scholars, and gradually climbing up to broader public understanding, thus serving the interests of the lay society, too.

Dedication to Quality

Each Frontiers article is a landmark of the highest quality, thanks to genuinely collaborative interactions between authors and review editors, who include some of the world's best academicians. Research must be certified by peers before entering a stream of knowledge that may eventually reach the public - and shape society; therefore, Frontiers only applies the most rigorous and unbiased reviews.
Frontiers revolutionizes research publishing by freely delivering the most outstanding research, evaluated with no bias from both the academic and social point of view.
By applying the most advanced information technologies, Frontiers is catapulting scholarly publishing into a new generation.

What are Frontiers Research Topics?

Frontiers Research Topics are very popular trademarks of the Frontiers Journals Series: they are collections of at least ten articles, all centered on a particular subject. With their unique mix of varied contributions from Original Research to Review Articles, Frontiers Research Topics unify the most influential researchers, the latest key findings and historical advances in a hot research area! Find out more on how to host your own Frontiers Research Topic or contribute to one as an author by contacting the Frontiers Editorial Office: frontiersin.org/about/contact

NANOZYMES: FROM RATIONAL DESIGN TO BIOMEDICAL APPLICATIONS

Topic Editors:
Kelong Fan, Institute of Biophysics, Chinese Academy of Sciences (CAS), China
Youhui Lin, Xiamen University, China
Vipul Bansal, RMIT University, Australia

Citation: Fan, K., Lin, Y., Bansal, V., eds. (2021). Nanozymes: From Rational Design to Biomedical Applications Lausanne: Frontiers Media SA.
doi: 10.3389/978-2-88966-821-2

Table of Contents

frontiers in Chemistry

EDITORIAL
published: 30 March 2021
doi: 10.3389/fchem.2021.670767

Editorial: Nanozymes: From Rational Design to Biomedical Applications

Kelong Fan[1,2]*, *Youhui Lin*[3]* and *Vipul Bansal*[4]*

[1] Chinese Academy of Sciences (CAS) Engineering Laboratory for Nanozyme, Key Laboratory of Protein and Peptide Pharmaceutical, Institute of Biophysics, Chinese Academy of Sciences, Beijing, China, [2] Nanozyme Medical Center, School of Basic Medical Sciences, Zhengzhou University, Zhengzhou, China, [3] Fujian Provincial Key Laboratory for Soft Functional Materials Research, Department of Physics, Research Institute for Biomimetics and Soft Matter, Xiamen University, Xiamen, China, [4] Ian Potter NanoBioSensing Facility, NanoBiotechnology Research Laboratory, School of Science, Royal Melbourne Institute of Technology (RMIT) University, Melbourne, VIC, Australia

Keywords: nanozyme, enzymatic activities, biosensor, antioxidant, catalytic therapy

Editorial on the Research Topic

Nanozymes: From Rational Design to Biomedical Applications

As the next generation of artificial enzymes, nanozymes are functional nanomaterials that are able to mimic the catalytic function of enzymes. Like natural enzymes, nanozymes can effectively catalyze the conversion of enzyme substrates under mild conditions and exhibit similar catalytic efficiencies and reaction kinetics. Moreover, in certain applications, compared with natural enzymes, nanozymes show several advantages, including multifunctionality, tunability of catalytic activities, low cost, scalable production, and high stability. So far, more than 900 nanozymes have been reported from 350 laboratories in 30 countries, and their applications have been extended to the fields of biology, medicine, agriculture, and environmental governance. In this special issue, we compiled 13 papers from 72 authors on the latest advances in nanozymes and their applications.

As an important advance in the field, the development of nanozyme-based probes for sensing important targets has become one of the hot topics in this research area. For example, the trimetallic PdCuAu nanozyme (Nie et al.) was used as a difunctional probe for temperature monitoring and molecular detection. The thermosensitive property of PdCuAu nanozyme was used for temperature sensing, and the peroxidase-like activity was applied to detect H_2O_2 and glucose. In another work, Long et al. decorated Au@Pt@Mesoporous SiO_2 nanozyme with antigens to detect mumps virus. The core–shell structure with Au@Pt nanozymes and mesoporous SiO_2 guaranteed the interaction of Au@Pt nanozymes and substrates, as well as prevented antigen molecules from blocking the active nanozyme core. In another study, Nguyen et al. designed a nanozyme-based test strip by utilizing the special color change property of cerium oxide nanozymes. The cerium oxide nanozyme and cholesterol oxidase were immobilized on the strips. When cholesterol was introduced, it was catalyzed by cholesterol oxidase to produce H_2O_2, leading to the color change of cerium oxide nanozymes from white to yellow. This work developed a point-of-care testing method for cholesterol without requiring an additional chromogenic substrate. The authors also reported a method to quantify the results of nanozyme-strip by a smartphone.

It has been reported that enzyme-like activities of nanozymes can be selectively regulated by specific molecules. Therefore, many nanozyme-based molecular detection strategies are also developed based on this property. Platinum nanozymes exhibiting robust oxidase-like activity were synthesized and modified using sodium alginate (SA-PtNPs) (He et al.). As an antioxidant, oligomeric proanthocyanidin inhibited the oxidase-like activity of platinum nanozymes, resulting in a reduction of color change intensity. Besides antioxidants, dopamine can suppress the catalytic activities as well. Yang et al. developed a novel method to synthesize Fe_2O_3 nanozyme, which was deposited on the surface of carbon nanotubes obtained by atomic layer deposition. By this way, the

Edited by:
Xiaomin Li,
Fudan University, China

Reviewed by:
Yong Fan,
Fudan University, China

****Correspondence:***
Kelong Fan
fankelong@ibp.ac.cn
Youhui Lin
linyouhui@xmu.edu.cn
Vipul Bansal
vipul.bansal@rmit.edu.au

Specialty section:
This article was submitted to Nanoscience, a section of the journal Frontiers in Chemistry

Received: *22 February 2021*
Accepted: *09 March 2021*
Published: *30 March 2021*

Citation:
Fan K, Lin Y and Bansal V (2021) Editorial: Nanozymes: From Rational Design to Biomedical Applications. Front. Chem. 9:670767. doi: 10.3389/fchem.2021.670767

size of Fe_2O_3 nanozymes was precisely controlled within 1 nm, leading to the excellent peroxidase-like activity. When the hybrid nanozymes were used to detect dopamine, the limit of detection was as low as 0.11 μM.

In spite of multiple applications, it is worth noting that only few investigations have focused on understanding the mechanisms of inhibition on the enzymatic activities of nanozymes. In this context, Liang et al. pointed out that the specific complexation between salicylic acid and Fe^{3+} in the active center of MIL-53(Fe) induced the inhibition effect of the peroxidase-like activity. Then the rapid colorimetric sensing platform was constructed with high selectivity and sensitivity to salicylic acid. Apart from that, Mo et al. carried out a detailed study about the inhibition of iron oxide nanozymes (IONzyme) caused by guanidine chloride (GuHCl), a commonly used protein denaturant. In this research, Guanidine chloride disturbed the peroxidase-like activity of IONzymes and resulted in nanoparticle aggregation, which was found as not the foremost reason for the nanozyme inactivation. The results of electron spin resonance spectroscopy revealed a change in unpaired electrons, based on which, the authors attributed the suppression of activity to the interaction of GuHCl with iron atoms. By analyzing the Michaelis-Menten model, they concluded that the GuHCl competed with the substrate H_2O_2 and bound to IONzymes.

In addition to a number of original research outputs reported in this special issue, several excellent reviews provide us with a comprehensive understanding of recent progress made in different aspects of nanozymes research. For instance, the intrinsic enzyme-like activity of IONzymes has been exploited for decades. Sutrisno et al. has nicely summarized the previous clinical exploitations of IONzymes for cancer therapy while placing special emphasis on major factors impacting upon their catalytic efficiency and therapeutic performance, as well as outlining representative studies to overcome certain limitations. Yuan et al. highlighted the most recent methods of nano iron sulfide synthesis, including modifications and characterizations. Strikingly, nano-sized iron sulfides demonstrate versatile physicochemical properties, enzyme-like catalysis, high stability and biocompatibility, which facilitates their biomedical applications.

Several other kinds of nanozymes have also been gradually developed. Zhang et al. discussed the enzymatic attributes and biomedical applications of gold clusters. Gold cluster nanozymes possess multiple enzyme-like activities, which are affected by different loading materials, or environment. In regard to applications, ion detection is a common utilization of gold cluster nanozymes, on account of their high susceptibility to heavy metal ions and anions. Further, the luminescence of gold cluster nanozymes is in favor of combing imaging and therapy for *in vivo* theranostics. Finally, challenges including biodistribution and reaction mechanisms of gold nanoclusters need further study. Cai and Yang summarized a wider category of nanozymes—two-dimensional nanomaterials (2D NMs). The top-down and bottom-up methodologies are commonly used methods to synthesize layered and non-layered 2D NMs. The multiple enzyme-like properties are affected by the type of material and the synthesis method. As for application, the authors emphasized the importance of toxicology studies, noting that the biocompatibility of these materials may be related to several structural/compositional parameters and physicochemical properties. Modifying these materials with biocompatible molecules may offer a viable solution for their applications. Tian et al. directed our attention to the rational design of antioxidant nanozymes. Nanozymes with SOD- and catalase-like activities were highlighted as appropriate candidates for antioxidant application. Ways to regulate the antioxidant activities of nanozymes were summarized, and the applications of anti-aging study, inflammation treatment, neurological diseases, and other biological applications were introduced. Huang et al. noticed that inorganic nanomaterials play a role in modulating biomimetic catalytic performance, including those of traditional artificial enzymes and nanozymes. For traditional artificial enzymes, inorganic nanomaterials may interact with active molecules, which may enhance their catalytic efficiency and induce special attractive features. When modulating nanozymes, inorganic nanomaterials regulate the stability and activity of nanozymes and influence multiple catalytic systems. Rational design strategies and in-depth investigation of potential applications are likely to bloom the field of this hybrid nanotechnology.

Despite the remarkable progress made in nanozyme research, there are still many challenges that remain to be addressed. The range of catalytic functionalities of nanozymes need to be further expanded to other enzyme classes, and the catalytic activity and specificity of nanozymes need to be improved. In contrast to natural enzymes that are typically highly selective not only for specific reactions but also to a single or selected few substrates; nanozymes tend to show a much wider substrate scope, and in certain cases multiple enzyme-like activities. Deciphering the mechanism of catalytic action of nanozymes will help us to better understand these differences. The nanozyme community needs to query the distinctness of nanozymes that set them apart from catalysts and bring them a step closer to the natural enzymes. Until these aspects are clearly addressed, some in the community are likely to see the rapidly emerging field of nanozymes with an iota of apprehension. Irrespective of these scrutinies and fundamental questions whether "nanozyme" is a true enzyme-mimic, it remains beyond a doubt that these types of materials offer remarkable potential for a variety of applications. In the context of biomedical applications of nanozymes, more efforts are needed to balance the surface modification strategies and optimum enzymatic activity of nanozymes with an emphasis to regulate the multi-enzymatic activities of nanozymes. In addition, the safety concerns of nanozymes for *in vivo* applications also need to be managed, as is a common practice with any foreign material introduced in the body.

We hope that this special issue will be able to share the latest advances in the field, provide current investigators with some food for thought, and inspire researchers with sparkling ideas to further advance the field of nanozymes. Last, but not the least, we would like to thank all the authors, reviewers, and the Frontiers in Chemistry development team for their great efforts in producing this special issue.

AUTHOR CONTRIBUTIONS

KF conceived and drafted the manuscript. YL and VB discussed and commented on the manuscript. All authors contributed to the article and approved the submitted version.

FUNDING

This work was financially supported by CAS Interdisciplinary Innovation Team (JCTD-2020-08) and the National Natural Science Foundation of China (No. 31900981).

Conflict of Interest: The authors declare that the research was conducted in the absence of any commercial or financial relationships that could be construed as a potential conflict of interest.

frontiers in Chemistry

REVIEW
published: 03 April 2020
doi: 10.3389/fchem.2020.00219

Enzyme-Like Properties of Gold Clusters for Biomedical Application

Yunguang Zhang[1], *Shuo Li*[1], *Haile Liu*[2], *Wei Long*[3]* *and Xiao-Dong Zhang*[2]*

[1] *School of Science, Xi'an University of Posts and Telecommunications, Xi'an, China,* [2] *Department of Physics and Tianjin Key Laboratory of Low Dimensional Materials Physics and Preparing Technology, School of Sciences, Tianjin University, Tianjin, China,* [3] *Institute of Radiation Medicine, Chinese Academy of Medical Sciences and Peking Union Medical College, Tianjin, China*

In recent years, the rapid development of nanoscience and technology has provided a new opportunity for the development and preparation of new inorganic enzymes. Nanozyme is a new generation of artificial mimetic enzyme, which like natural enzymes, can efficiently catalyze the substrate of enzyme under mild conditions, exhibiting catalytic efficiency, and enzymatic reaction kinetics similar to natural enzymes. However, nanozymes exist better stability than native enzymes, it can still maintain 85 % catalytic activity in strong acid and alkali (pH 2∼10) or large temperature range (4∼90°C). This provides conditions for designing complex catalytic systems. In this review, we discussed the enzymatic attributes and biomedical applications of gold nanoclusters, including peroxidase-like, catalase-like, detection of heavy metal ions, and therapy of brain and cancer etc. This review can help us understand the current research status nanozymes.

Keywords: gold nanoclusters, nanozyme, enzyme-like properties, cancer therapy, bio-detection

Edited by:
Kelong Fan,
Institute of Biophysics (CAS), China

Reviewed by:
Rong Yang,
National Center for Nanoscience and Technology (CAS), China
Xiangheng Niu,
Jiangsu University, China
Lizeng Gao,
Institute of Biophysics (CAS), China

***Correspondence:**
Wei Long
longway@irm-cams.ac.cn
Xiao-Dong Zhang
xiaodongzhang@tju.edu.cn

Specialty section:
This article was submitted to Nanoscience, a section of the journal Frontiers in Chemistry

Received: *03 January 2020*
Accepted: *09 March 2020*
Published: *03 April 2020*

Citation:
Zhang Y, Li S, Liu H, Long W and Zhang X-D (2020) Enzyme-Like Properties of Gold Clusters for Biomedical Application. Front. Chem. 8:219. doi: 10.3389/fchem.2020.00219

INTRODUCTION

The natural enzyme is a kind of biocatalyst that is closely related to many life activities (Arnold et al., 2001). Similar to other catalysts, the presence of natural enzymes can greatly speed up the reaction and sometimes participate in the reaction, but the enzyme itself does not change before or after the reactions (Wilhelmová, 1996). In addition, it exhibits high catalytic efficiency, mild reaction conditions and high specificity (Sheldon, 2007). However, lots of natural enzymes are proteins, which are susceptible to high temperature, acidic or alkaline, causing loss of catalytic activity (Chang, 2013). In addition, natural enzymes presented in living organisms are difficult to purify, relatively expensive, and not easily transported and stored (Scopes, 2013). To overcome the limitations of instability and high cost for natural enzymes, researchers are looking for different ways to prepare mimetic enzymes to replace natural enzymes (Chen et al., 2010; Yang et al., 2016). Until now, different types of mimic enzymes have been designed and used in many biological fields, such as immunoassay (Lequin, 2005), glucose detection (Song et al., 2010), heavy metal ion detection (Kim et al., 2001), free radical protection (Barzegar and Moosavi-Movahedi, 2011), and tissue engineering (Griffith and Naughton, 2002). Host-guest chemistry (Wan et al., 2006) and supramolecular chemistry (Steed and Atwood, 2013) lay an important theoretical foundation for mimic enzyme. In essence, the basic meaning of host-guest chemistry comes from the interaction between enzyme and substrate, which is embodied in the complementary spatial and electronic arrangement of the binding site between the subject and the guest (Spichiger-Keller, 2008). This host-guest complementarity is similar to the combination of the nanozymes and the substrate. Based on non-covalent bond interactions, such as electrostatic interactions, hydrogen bonding and van der Waals forces (Pasternack et al., 1998; Wei and Wang, 2013), supramolecules are produced by the combination of substrate and receptor (Geim and Grigorieva, 2013). When receptors combine with complex ions or molecules, a supramolecule with stable structure and properties is formed, which has the functions of molecular recognition, catalytic and selective output. Host-guest chemistry and supramolecules chemistry are important theoretical weapons for the simulation of artificial enzymes.

At present, the ideal traditional enzyme systems include cyclodextrin (Del Valle, 2004), cyclophane (Gleiter and Hopf, 2006) and cyclic aromatic hydrocarbons (Tsipis and Tsipis, 2003). The chemical composition of traditional mimic *peroxidase-like activation* enzyme is non-protein, but these enzymes have similar catalytic performance to natural enzymes (Meeuwissen and Reek, 2010). These traditional mimetic enzymes are superior to natural enzymes in thermal stability and acid-base resistance, but their shortcomings, such as too-complex structure, difficulties in separation, single catalytic active sites, and low catalytic efficiency, still stunt their development progress (Liu Q. et al., 2017). With the development of nanomaterials, the researches on the catalysis of nanomaterials have also achieved many new results (Yin and Talapin, 2013). Nanozymes have the dual identities of enzymes and nanomaterials (Roduner, 2006). Unlike natural enzymes or traditional artificial enzymes, nanozymes (Wang et al., 2013; Li et al., 2015; Zhou et al., 2017; Fan et al., 2018; Qu et al., 2018; Chen et al., 2019; Huang et al., 2019a,b; Jiang et al., 2019; Liang and Yan, 2019; Liu et al., 2019; Mu et al., 2019a,b; Wu et al., 2019; Xu et al., 2019; Yan et al., 2019) have many physical and chemical properties, besides their catalytic functions (Senanayake et al., 2013). For example, Fe_3O_4 and CdS nanoparticles not only have the catalytic functions of peroxidase and superparamagnetic activities, but also have the property of luminescence (Liu et al., 2011). The enzymatic activity of nanozymes is not only related to its composition, crystal form and structure, but also to its surface properties (Lin et al., 2014a). Take gold nanoclusters (Au NCs) as an example, the combination of certain small molecules with Au NCs can change the surface microenvironment, resulting in changes in the catalytic activities of Au NCs (Jin, 2010). Wang et al. found that the surface modification of Au NCs can affect its catalytic activity (Yuwen et al., 2014). The Au NCs were modified with amino and citric acid respectively to make positive and negative charges on the surface, and then catalytically oxidize ABTS (Erel, 2004) (negatively charged) and TMB (Ding et al., 2018) (positively charged) to detect its catalytic activity. The amino and citric acid modified Au NCs were found to have high affinity to the substrates ABTS and TMB. Not only small molecules can be combined with Au NCs, inorganic nanoparticles, metal ions and biomacromolecules (such as DNA, RNA) can also be combined with it to change the surface microenvironment of Au NCs, thereby changing its catalytic activity. Compared with other nanomaterials with simulating peroxidase, gold nanoclusters have the advantages of small size, good stability, good biocompatibility, and are more prominent in the application of biological analysis. However, the potential of Au NCs as enzyme mimics is easily limited by the low catalytic activity at neutral environment. In addition, since the surface atom is the key catalytic sites for gold clusters, modification of nanozymes with various coating molecules may block their active sites, reducing or inhibiting their enzymatic activity. This review details the enzymatic properties of gold nanoclusters and their applications in biomedicine in recent years.

ENZYME-LIKE ACTIVITY OF GOLD CLUSTERS

Peroxidase-Like Property of Gold Clusters

Peroxidase (Gao et al., 2007) is a kind of natural enzyme that have catalytic oxidation effects on hydrogen peroxide. The establishment of an analytical method involving H_2O_2 is of great significance in analytical chemistry and clinical medicine. In recent years, Au NCs have been reported to have peroxidase-like properties and are used in the fields of bionics, biosensing, and biomedicine (Feng et al., 2017; Liao et al., 2017). First, H_2O_2 can be adsorbed on the surface of gold nanomaterials, and the O–O bonds of H_2O_2 may be decomposed into dihydroxy radicals; at the same time, the generated hydroxyl radicals may be stabilized by gold nanomaterials through partial electron exchange interactions. This may contribute to their catalytic capabilities. **Figure 1** shows the adsorption and decomposition of H_2O_2 on Au(111) under different pH conditions (Li et al., 2015). Under neutral conditions, H_2O_2 adsorbed on the surface of Au (111) can undergo acid decomposition and alkali decomposition. According to the principle of lowest energy, alkaline decomposition is more inclined under neutral conditions (**Figure 1A**) (He et al., 2012). It is worth noting that under these conditions, the adsorbed O^* cannot generate O_2 under the high energy barrier of 1.42 eV (Wu et al., 2019). Under acidic conditions, the decomposition pathway of H_2O_2 is similar to the decomposition of alkalis under neutral conditions. First, OH^* is generated and then O^* and H_2O^* are generated. The generated O^* can extract H from the substrate. Therefore, under acidic and neutral conditions, Au (111) has peroxidase activity (**Figure 1B**). Ding et al. used 3, 3′, 5,5′-tetramethylbenzidine (TMB) as a substrate and found that histidine-modified gold clusters (His-Au NCs) have peroxidase-like activity. When H_2O_2 is present, peroxidase can catalyze the oxidation of TMB. Reaction, when His-Au NCs is mixed with H_2O_2 and TMB, the solution rapidly changes from colorless to blue, and the maximum absorption wavelength of the mixture is 652 nm. This is due to the TMB is oxidized to oxTMB and the solution is blue. These results indicated that His-Au NCs are capable of oxidizing TMB to develop color and have peroxidase-like properties (Liu Y. et al., 2017). Lin et al. compared the catalytic activity of unmodified Au NCs and studied the effect of amino-modified gold clusters (NH_2-Au NCs) and citric acid-modified gold clusters (itrate-Au NCs) on the substrates ABTS and TMB. It was found that the surface unmodified Au NCs has the highest peroxidase activity. NH_2-Au NCs have higher catalytic activities for ABTS than citrate-Au NCs, while NH_2-Au NCs have lower catalytic activity for TMB than itrate-Au NCs. For the surface modified by Au NCs has different charges, it exhibits different variation, and the ability to adsorb the oxidized substrate is different, thus showing the difference in catalytic activity. The biocompatibility of Au

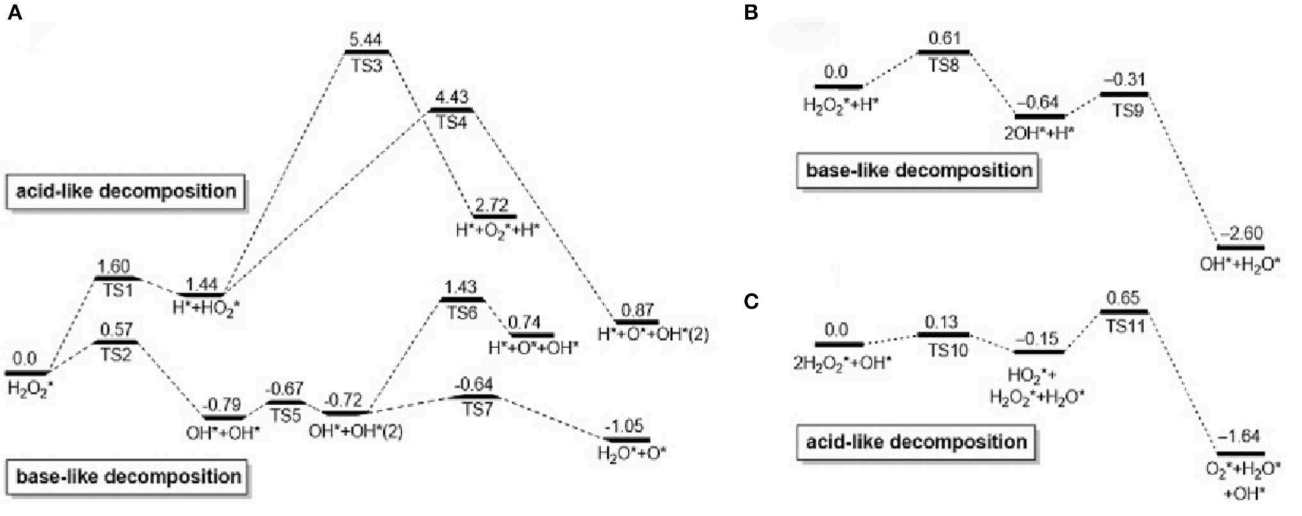

FIGURE 1 | Calculated reaction spectrum (unit: eV) of H_2O_2 decomposition on Au surface: **(A)** neutral, **(B)** acidic, **(C)** basic [reproduced from Li et al. (2015) with permission from The Elsevier].

NCs was adjusted by selecting different ligands (Liu et al., 2016). *Wang's team* prepared bovine serum albumin (BSA) modified Au NCs. In order to improve the peroxidase- like activity of Au NCs (Wang et al., 2011). Wen et al. used the horseradish peroxidase properties of gold nanoclusters to detect H_2O_2 (Wen et al., 2011). Jiang et al. discovered and applied precious metal nanoclusters. They report that gold chains of ferritin iron (Au-Ft) can produce a blue reaction by catalyzing the oxidation of TMB by H_2O_2. Compared to the native enzyme, Au-Ft exhibits higher activity and pH, temperature range, and the catalyzed reaction follows typical Mie kinetics. The lower K_m value ($0.097\,\mu M$) was exhibited by the Au-Ft kinetic parameters, and the specific activity for TMB oxidation exceeded HRP. According to these findings, Au-Ft was used as a peroxide mimic enzyme to perform glucose spectrometry. Photometric analysis the system exhibited acceptable repeatability and high specificity (Liu J. et al., 2017).

Catalase-Like Property of Gold Clusters

Catalase is an important enzyme that prevents oxidative damage of cells by reactive oxygen species (Glorieux and Calderon, 2017). For Au NCs, Au^{2+} is first reduced by a H_2O_2 to form Au^+, which is accompanied by the production of protons and O_2. After that, another H_2O_2 can be combined with oxygen vacancies to oxidize Au^+ to Au^{2+} and release H_2O. This completes the simulation of hydrogen peroxide. Most nanomaterial-based peroxidase mimetics typically exhibit enzymatic activity under alkaline conditions rather than under physiological conditions (Góth et al., 2004; Glorieux and Calderon, 2017). Under the basic conditions of OH pre-adsorption, H_2O_2 first transfers one H^* to the pre-adsorbed OH to form HO_2^* and H_2O^*; then, HO_2^* gives one H to the other H_2O_2 and finally produces H_2O * and O_2 * (**Figure 1C**). Therefore, hydrogen peroxide-based activity can be observed under alkaline conditions (Li et al., 2015). He et al. (2013) demonstrated the intrinsic catalase activity of Au NCs using electron spin resonance spectroscopy combined with spin trapping and spin labeling. Under normal and basic conditions, Au NCs exhibit inherent catalase catalytic activity because Au NCs can convert H_2O_2 to H_2O and O_2. However, under acidic conditions, the catalase-like activity of Au NCs is significantly reduced, and once trapped in organelles, such as endosomes (pH≈5.5) and lysosomes (pH≈4.8), hydroxyl groups are produced. Free radicals (•OH) can easily induce apoptosis. Therefore, the catalase-like activity of Au NCs is limited (He et al., 2013). To change this situation, Liu et al. studied amine-terminated macromolecularly encapsulated gold nanoclusters (Au NCs-NH_2). Au NCs-NH_2 exhibits good catalase activity at physiologically acidic pH values (Liu C. P. et al., 2017). **Figure 2A** is a schematic diagram showing the enzymatic activity of Au NCs-NH_2, which can catalyze the production of O_2 by H_2O_2 by catalase activity. They changed the different groups of dendrimers, added Au NCs-OH and Au NCs-COOH, and studied the relative H_2O_2 consumption of Au NCs-NH_2, Au NCs-OH and Au NCs-COOH under different solution pH values. A comparison of the amounts, they still have significant catalase-like activity at pH 4.8-7.4 (**Figure 2B**). By comparing the catalytic activities of Au NCs-NH_2, Au NCs-OH and Au NCs-COOH at various concentrations of H_2O_2 at pH 4.8 and pH 7.4, the effect of Au NCs-NH_2 was significantly better (**Figure 2C**). Fan et al. synthesized a derivative protein (apoFt) as a nanoreactor to obtain Au-apoFt with adjustable size and uniform dispersion. The catalytic activity of both was observed at pH and temperature compared to natural catalase. As the pH and temperature increase, the enzyme activity of Au-apoFt increases. The increase in pH may be due to the presence of OH- which promotes the dehydrogenation step of water in the catalytic reaction, showing an increase in enzyme activity. With rising of temperature, the increase in the enzyme activity of Au-apoFt may be due to an increase in the rate of molecular motion, which allows more H_2O_2 to adsorb to the surface of the Au nanoclusters, showing an increase in catalytic activity. Liu et al.

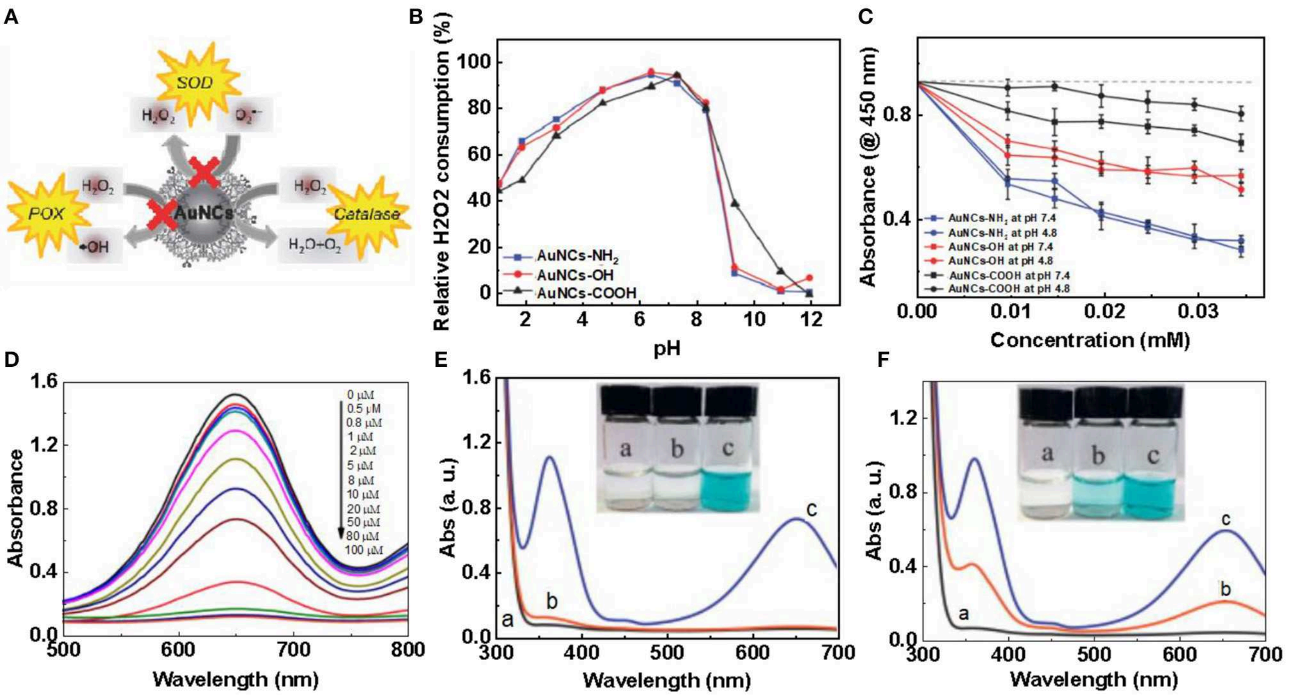

FIGURE 2 | Catalase-like of gold clusters **(A)** Au NCs-NH$_2$ can catalyze H_2O_2 to produce H_2O and O_2 through catalase-like activity. **(B)** Consumption of H_2O_2 by Au NCs-NH$_2$, Au NCs-OH and Au NCs-COOH at the same concentration (0.02×10^{-3} M). **(C)** The catalytic activities of different concentrations of Au NCs-NH$_2$, Au NCs-OH and Au NCs-COOH on H_2O_2 (0.1×10^{-3} M) at pH 4.8 and 7.4 [reproduced from Liu C. P. et al. (2017) with permission from The Small]. **(D)** Effects of different concentrations of Ag^+ on catalase activity of BSA-Au NCs. Red BSA-Au NCs [reproduced from Chang et al. (2016) with permission from The Elsevier]. **(E)** And blue BSA-Au NCs. **(F)** Catalyze TMB under different conditions: (a) under visible light, (b) in the presence of Au NCs, (c) in the presence of Au NCs under visible light [reproduced from Wang et al. (2015) with permission from The Elsevier].

found that bovine serum albumin-protected gold nanoclusters (BSA-Au NCs) can sensitively measure H_2O_2 concentration (**Figure 2D**). Red BSA-Au NCs have no catalytic activity for TMB in the presence of oxygen but no light, and have catalytic activity in the presence of oxygen and light (**Figure 2E**); blue BSA-Au NCs have a slight catalytic activity for TMB in the presence of oxygen but no light, and have strong catalytic activity when oxygen and light coexist (**Figure 2F**). The experiment shows that light can stimulate the catalytic activity of Au NCs (Wang et al., 2015).

Glucose Oxidase-Like Property and Superoxide Dismutase-Like Property of Gold Clusters

Glucose oxidase (GOD) is widely distributed in animals and plants and microorganisms, and can specifically catalyze the production of glucose into gluconic acid and hydrogen peroxide under aerobic conditions (Gibson et al., 1964; Wilson and Turner, 1992; Bankar et al., 2009; Luo et al., 2010). At present, the application fields of GOD are constantly expanding, and the demand in domestic and foreign markets has increased dramatically. Low yield, low enzyme activity, and complex detection methods are the limiting factors for GOD industrialization. A lot of work has been done at home and abroad and significant progress has been made. Recent studies have proved that gold clusters have excellent GOD-like enzyme activity. Luo et al. reported an interesting autocatalytic, self-limiting system that controls the controlled growth of Au NCs with GOD-like (Luo et al., 2010). In this system, Au NCs can serve as both seeds and catalyst, that is, the Au NCs catalyzed glucose oxidation *in situ* produced H_2O_2, and induced the Au NCs seeds in the presence of gold chloride ions. More importantly, the growth of Au NCs is internally regulated by two negative feedback factors, the reduced size-dependent activity of Au NCs and the glucose-induced surface passivation of the products, leading to rapid self-limiting systems. Pandey et al. (2007) used chemical synthesis to covalently combine GOD with the surface of gold nanoclusters to form a GOD-Au NCs complex, which improves the catalytic activity of GOD, improves stability, and enhances the enzyme response temperature and pH durability (Xia et al., 2013). However, this method only improves the performance of the enzyme and does not fundamentally solve the problem. The activity of the enzyme is still restricted by a series of factors, and other substances are introduced into the reaction system, which makes the entire system more complicated. Rossi et al. found that in the presence of O_2, glucose can be catalyzed by "bare" gold nanoclusters to produce gluconic acid and H_2O_2 (Pina et al., 2011). Based on the promotion of alkali and the production of H_2O_2, they proposed the mechanism

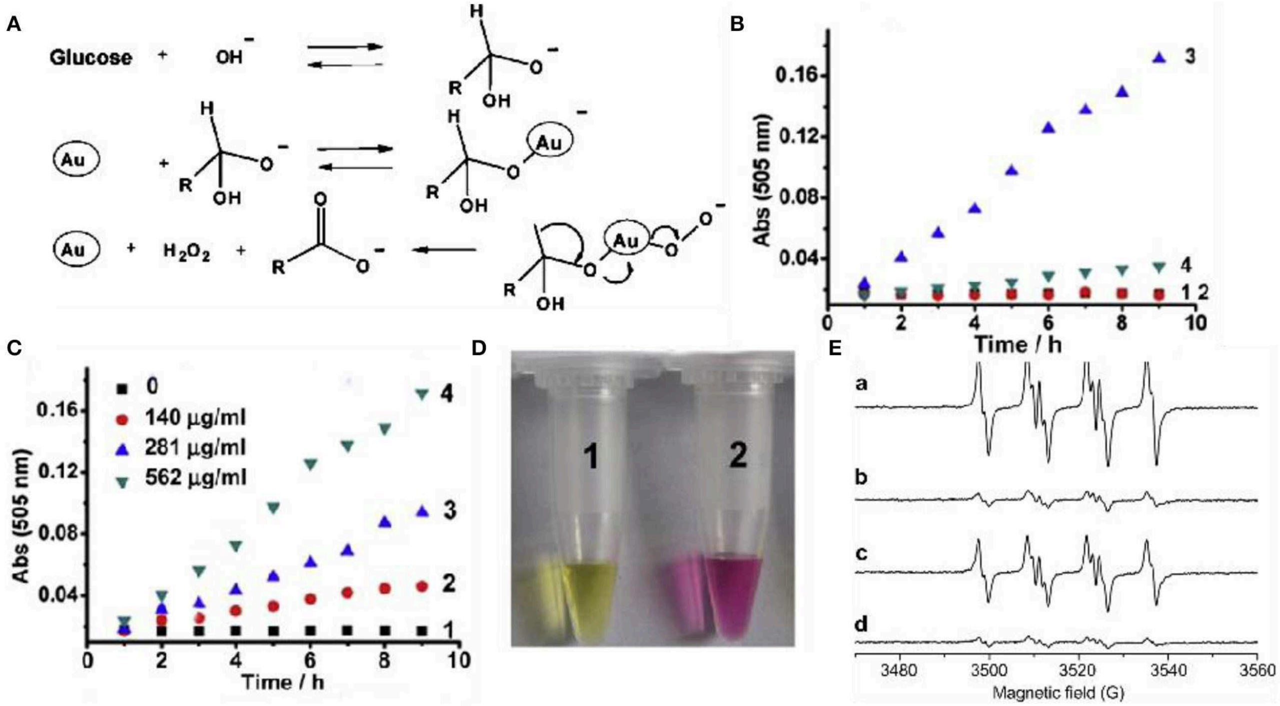

FIGURE 3 | Glucose oxidase-like and superoxide dismutase-like of gold clusters **(A)** Catalytic mechanism of GOD-like enzymes of Au nanoparticles [reproduced from Lin et al. (2014a) with permission from The Wiley-VCH]. **(B)** The oxidative decomposition of glucose into gluconic acid, absorbance at 505 nm. (1) Glucose only (2) EMSN-Au NPs alone (3) Glucose and EMSN-Au NPs (4) Glucose and EMSN-Au NPs. **(C)** In the presence of different concentrations of EMSN-Au NPs, glucose is oxidative decomposed into gluconic acid, the absorbance at 505 nm. **(D)** Typical photo of methyl red solution of glucose and EMSN-Au NPs [reproduced from Lin et al. (2014a) with permission from The Elsevier]. **(E)** Au NPs scavenge SOD-like activity of superoxide [reproduced from He et al. (2013) with permission from The Elsevier].

of molecular activated gold catalysis (**Figure 3A**). The surface of the gold atom interacts with the hydrated glucose anion to form electron-rich gold, which effectively activates molecular oxygen through nucleophilic attack. O_2 and gold intermediates $Au^{2+} + \text{-}O_2^{2-}$ or $Au + \text{-}O_2^-$ can act as a bridge for the conversion of electrons from glucose to hydrogen peroxide. Thereby the final reaction product is formed. Lin et al. studied mesoporous silica-encapsulated gold nanoclusters (EMSN-Au NPs) with GOD properties through UV-Vis (**Figures 3B,C**) (Lin et al., 2014a). First, the GOD mimicking activity of EMSN-Au NPs in solution was evaluated. Glucose is catalyzed by them in the presence of O_2 to produce gluconic acid. During the experiment, they used methyl red to detect the change in pH of the solution, as shown in **Figure 3D**. The results further confirmed that gluconic acid was indeed produced in the reaction catalyzed by EMSN-Au NPs. Superoxide dismutase (SOD) is a kind of antioxidant metal enzyme *in vivo*. It can catalyze superoxide anion free radical disproportionation to generate hydrogen peroxide and oxygen, which is very important in anti-oxidation. Gold nanoclusters decompose O^{2-} into molecular oxygen (O_2) and hydrogen peroxide (H_2O_2) through a cyclic redox electron transfer mechanism, thereby eliminating O_2^- activity. Weiwei et al. verified the SOD activity of Au NPs through ESR experiments (**Figure 3E**) (He et al., 2013).

Effect of Support and Particle Size on Gold Cluster Activity

The enzymatic activities of nanomaterials are related to size (Mavrikakis et al., 2000; Lopez et al., 2004; Molina and Hammer, 2005; Miller et al., 2006; Zhou et al., 2010; Brodersen et al., 2011). It is possible to regulate the activity of nanomaterials by controlling their size, which has been confirmed in many studies. For gold nanomaterials as an example; the enzyme-like activity of gold nanoclusters is stronger than that of gold nanoparticles. Li et al. compared the enzyme-like activities of gold nanozymes with different structures and morphologies, including Au nanoclusters, Au nanoparticles, and Au nanotubes. At the same specific surface area, the Au nanoclusters had the strongest enzyme-like activity, while the Au nanotubes had the weakest enzyme-like activity. Through the study and analysis, they concluded that the differences in the enzyme-like activity of materials may be related to the differences in the crystal planes (Li et al., 2015). Corma et al. supported gold atoms on functionalized carbon nanotubes and explored their catalytic properties for phenol. They have catalytic activity equivalent to that of thiol oxidase. The catalytic activity also decreases with the increase of the size of the gold cluster, until it almost disappeared. According to theoretical calculations, smaller gold clusters can activate thiophenol and O_2 and are therefore active, while larger nanoparticles are inactivated by alkoxides and

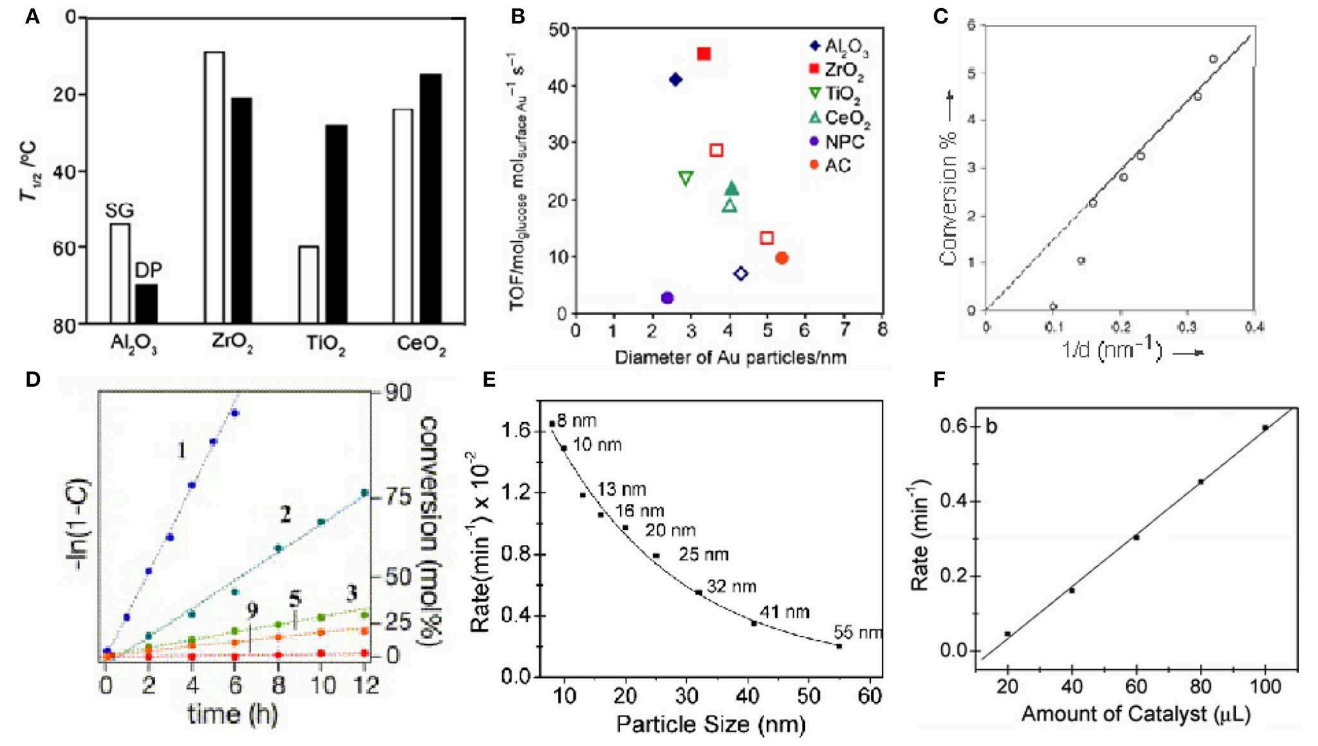

FIGURE 4 | Effect of support and particle size on gold cluster activity **(A)** Catalytic performance of different supported gold nanoclusters for CO. **(B)** Turnover frequency of glucose oxidation [reproduced from Ishida et al., 2008 with permission from The Wiley-VCH]. **(C)** Relationship between conversion rate and particle size [reproduced from Comotti et al. (2010) with permission from The Wiley-VCH]. **(D)** Relationship between the catalytic activities of Au: PVP clusters for the aerobic oxidation of hydroxybenzyl alcohol and the nuclear size [reproduced from Tsunoyama et al. (2006) with permission from The Elsevier]. **(E)** Graph of reduction rate as a function of R-Au particle size. **(F)** Relationship between different volumes and reaction rates [reproduced from Panigrahi et al. (2007) with permission from The American Chemical Society].

lose their activity (Corma et al., 2013). Tamao et al. tested the catalytic performance of gold nanoparticles on CO under different loads (**Figure 4A**). Compared with ZrO_2, TiO_2 and CeO_2, Al_2O_3 has a lower catalytic activity (Ishida et al., 2008). Oxygen vacancies can be formed at the peripheral interface of the Au particles. When gold nanoclusters are deposited on carbon materials and polymers, they lose their catalytic activity at temperatures above 120°C In the CO oxidation reaction, the catalytic activity of glucose oxidation observed on Au catalysts is more affected by Au particle size than by carrier properties, and is related to the turnover frequency (TOF) of Au atoms on the surface (**Figure 4B**). Rossi et al. studied the effect of particle size on the catalytic activity by using gold clusters (3–10nm) dispersed in water (Comotti et al., 2010). According to their research, the catalytic activity of glucose oxidase increases with decreasing particle size (**Figure 4C**). They first showed that gold nanoclusters (Au NCs) can catalyze the oxidation of glucose in the presence of O_2 to produce gluconic acid and H_2O_2. In contrast, other metal nanomaterials tested, such as Cu, Ag, Pd, and Pt, did not show significant oxidase-like activity under similar conditions (Comotti et al., 2010; Quan et al., 2015). Lin et al. compared the CAT activity of several clusters experimentally, and the results showed that the CAT activity of Pt and Pd was better than that of Au and Ag. Otherwise, the SOD-like and CAT-like activity of Au and Pt nanozymes increased under alkaline conditions and decreased under acidic conditions (Lin et al., 2014b). Tsunoyama et al. prepared a group of monodisperse gold clusters (Au: PVP) through seed-mediated growth in the presence of polyvinylpyrrolidone (PVP) (Tsunoyama et al., 2006). The catalytic activity of Au: PVP clusters on hydroxybenzyl alcohol decreases with increasing core size (**Figure 4D**). Panigrahi et al. studied a core-shell Nano composite (R-Au) (**Figure 4E**) and derived the relationship between reduction rate and gold nanoclusters size (Panigrahi et al., 2007). The reaction rate decreases with increasing particle size. When the particle size is increased to 32 nm, as the particle size increases, the decline rate tends to be gentle. They believe that as the particle size increases, the decrease in catalytic performance is due to the increase in particle surface roughness. Therefore, the smaller the particle size, the higher the catalytic activity (**Figure 4F**).

APPLICATION OF GOLD CLUSTERS

Detection of Heavy Metal Ions

At present, heavy-metal contamination has caused great threats to the human health and our living environment. It is of great significance for the detection of heavy metals, with high selectivity of heavy metals (Bhan and Sarkar, 2005; Gallardo et al., 2014; Martin and Griswold, 2018). It is well-known

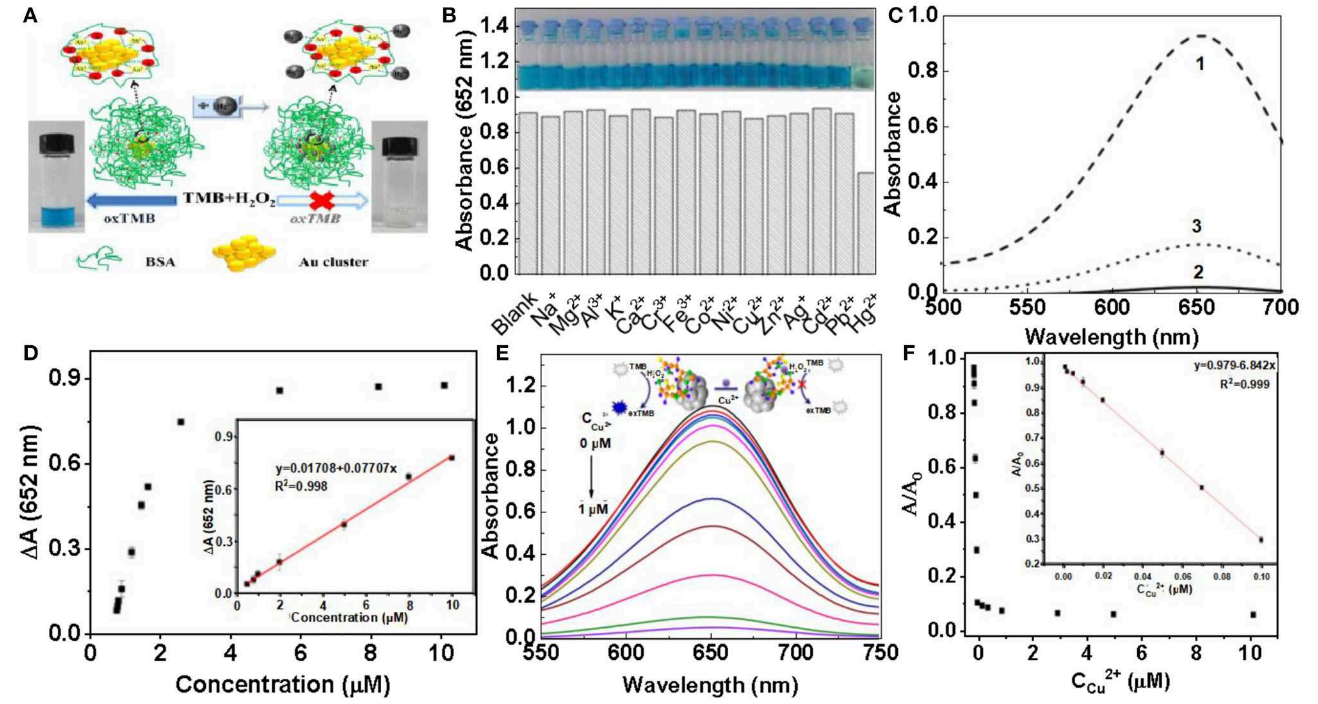

FIGURE 5 | Detection of heavy metal ions **(A)** Schematic diagram of Hg^{2+} detection principle. **(B)** The effect of different metal ions on the peroxidase like activity of BSA-Au NCs. **(C)** The inhibition of Hg^{2+} on the activity of BSA-Au NCS peroxidase under different conditions [reproduced from Zhu et al. (2013) with permission from The Elsevier]. **(D)** Hg^{2+} can specifically interact with Au^+ and inhibit enzyme activity [reproduced from Chang et al. (2016) with permission from The Elsevier]. **(E)** Effect of different concentrations of copper ions on the absorption strength of solution. **(F)** A/A_0 plot plotted at the concentration of Cu^{2+}. A and A_0 are absorbance at 652 nm with and without copper ions [reproduced from Liu Y. et al. (2017) with permission from The Elsevier].

that mercury is a toxic heavy metal and widely found in the environment (Ercal et al., 2001). Mercury ion (Hg^{2+}) is the most common heavy metal ions. Even at very low concentrations, its destructive properties can affect the brain, god system and kidney (Bhan and Sarkar, 2005). Therefore, it is necessary to establish a fast, simple and sensitive method to detect Hg^{2+} in the environment. Zhu et al. found that Hg^{2+} has a selective inhibitory effect on the peroxidase activity of BSA-Au clusters (Zhu et al., 2013). The effect of common metal ions on the catalytic activity of BSA-Au was investigated using fluorescence quenching (**Figure 5A**). At the same concentration, Na^+, Fe^{3+}, Co^{2+}, Ag^+, Mg^{2+}, Al^{3+}, K^+, Ca^{2+}, Cr^{3+}, Ni^{2+}, Cu^{2+}, Zn^{2+}, Cd^{2+}, Pb^{2+} to BSA-Au NCs have no effect on peroxidase-like activity. Hg^{2+} can inhibit the peroxidase-like activity of BSA-Au NCs and hardly catalyze the color reaction of TMB and H_2O_2 (**Figure 5B**). Similarly, the absorption spectrum of the reaction solution at 652 nm can also indicate that Hg^{2+} can inhibit the catalytic activity of BSA-Au NCs (**Figure 5C**, curve 2). Chelation of EDTA with Hg^{2+} can reduce the inhibitory effect of Hg^{2+} on the catalytic activity of BSA-Au NCs (**Figure 5C**, curve 3). Because mercury is easily complexed with sulfur, mercury ions (Hg^{2+}) can combine with cysteine through Hg-S bond to form Hg-Cys complex. The affinity of cysteine to Hg^{2+} was significantly higher than that of other metal ions. Based on this mechanism, Ding et al. constructed fluorescence quenching of citrate-modified Au NCs to detect Hg^{2+} in tap water (Ding et al., 2012). Then, Qi et al. reported a probe that can paper-based visualization of Hg^{2+} based on conjugates of Tb^{3+}/BSA-Au NCs. The probe can be highly complexed with Hg^{2+} via Hg-S bonds, and therefore has excellent selectivity. The method is simple and easy to operate, with only a ultraviolet lamp needed, which can be greatly promoted in practical applications (Qi et al., 2015). Using similar sensing mechanism, Lin et al. constructed a method to detect Hg^{2+} and methylmercury in seawater based on Lys protected Au NCs probe, and Xu et al. also used lysozyme-modified Au NCs to visually detect Hg^{2+} in water by visual and fluorescent colorimetry (Xu et al., 2015). The Zhu working group provided us with a colorimetric method that can detect Hg with high sensitivity and selectivity. They also detected of different working fluids and the influence of common metal ions on the catalytic activity. Finally, Hg^{2+} can specifically interact with Au^+ to inhibit enzyme activity (**Figure 5D**) (Zhu et al., 2013). Liu et al. combined the peroxidase-like nanozymes activity of gold nanoclusters with the double-stranded nature of amino acids, and proposed a simple, sensitive and selective method for the detection of Cu^{2+} and histidine (His). The addition of different concentrations of Cu^{2+} can inhibit the peroxidation of histidine-gold nanoclusters (His-Au NCs) to varying degrees (**Figure 5E**). The absorbance of the solution at 652 nm gradually decreases with increasing Cu^{2+} concentration, so this method can be used to detect the concentration of Cu^{2+} in the solution. According to this calibration curve, Cu^{2+} can be measured with high sensitivity (**Figure 5F**) (Liu Y. et al., 2017). Although gold nanocluster probes with enzyme activity have been widely developed in recent years, many problems still need to be solved. First, most of the probes with enzyme activity controlled by metal ions are POD activity, while few probes are available for other types of enzyme activities. In addition, the sensor mechanism of the probes is relatively single, and more types of mechanisms need to be developed to design the probes. Finally, there is little research on the application in biological matrix or *in vivo*, which is very important for the biological application of enzyme activity.

Anion Detection

Inorganic anions are widely present in ecosystems, but it should be noted that most inorganic anions have two-sided effects on the ecological environment and human health (Velizarov et al., 2004). Shojaeifard et al. tested environmental water and CN in human serum based on a combination of Au NCs and copper (II)-phthalocyanine complexes. Under the condition of CN^-, the binding of Au NCs to the copper (II)-phthalocyanine complex is destroyed, so the fluorescence of the copper (II)- phthalocyanine complex quenched by Au NCs is restored, thus forming a stable $[Au\ (CN)_2]^-$. The method has good selectivity, high sensitivity and is suitable for popularization (Shojaeifard et al., 2016). Liu et al. also constructed a method based on Au NCs to detect CN^- in environmental water samples, and successfully used to detect CN^- in food sand samples and biological samples (Liu et al., 2010). Xiong et al. synthesized BSA-Au NCs and successfully detected Cl^- in tap water with a detection limit of 0.50 μmol/L (Xiong et al., 2015). Wang et al. used glutathione-coated Au NCs as probes to construct a method for detecting I^- in water with a detection limit of 400 nmol/L. This method can selectively identify I^- from 12 common anions such as F^-, Cl^-, Br^- (Yang et al., 2014). At the same time, Chang group used DNA as template to synthesize gold/silver nanozymes. Clusters were used to detect S^{2-} in hot spring and seawater samples. This method specifically recognized S^{2-} from Au^{3+}, Ag^+ and DNA in the presence of $NaBH_4$. The quenching mechanism is that S can interact with gold and silver atoms, thus resulting in changes in the conformation of the template DNA (Chen et al., 2011). At present, gold clusters have been used to detect anions *in vitro* more thoroughly and sensitively, but few studies have been done in combination with organisms. The biological environment is more complex, so anion detection *in vivo* will be a challenge. In addition, the role of gold clusters in organisms should not only be a function of detection, but also require us to develop more properties of gold clusters for the diagnosis and treatment of organisms.

Biological Application of Gold Clusters

Tumor Treatment

Nanoprobe with enzymatic properties have been attracting increasing attention in early screening and diagnosis of cancer (Schaller and Graf, 2004; Spichiger-Keller, 2008; He et al., 2010; Chi et al., 2012; Li and Xiaogang, 2015). In order to achieve the specificity and high accuracy of tumor detection, it was necessary to design and prepare an enzyme-simulated nanoprobe with tumor targeting, high enzyme activity and containing luminescent properties. Hu et al. described the folate receptor based gold nanoclusters (NCs-FA), which are novel luciferase mimic nanoprobes with high stability, low cytotoxicity and high enzyme activity. O-Phenylenediamine (OPD), 3-amino-9-ethylcarbazole (AEC), 5-aminosalicylic acid (5ASA) and 3,3,5,5-tetramethylbenzidine (TMB) can be used NCs-FA catalyzes to produce red, brown, brown, and blue. Experiments prove that NCs-FA nanoprobe has peroxidase activity (**Figure 6A**). To visualize the uptake of NCS-FA nanoprobes by cells, MCF-7 and HepG2 cells were stained with NCs-FA nanoprobes (NC) and observed under a focused laser microscope (**Figure 6B**) (Hu et al., 2014). The probes (NC) stained MCF-7 and HepG2 tumor tissues and observed them by fluorescence microscopy (**Figure 6C**). It confirmed that NCs-FA nanoprobes target tumor cells *via* FR. Au NPs have low anticancer activity and are widely used in drug carriers, biological imaging, and other fields. The new selenium-containing molecule (EGSE-TME) has low anticancer activity, but the combination of NCs-FA and EGSE-TME has produced a system with good anticancer activity. Li et al. synthesized Au NP/Se. In order to explore its cytotoxicity, tumor mice were injected with PBS, Au NP/citrate, EGSe-tMe, and Au NP/Se on day 0 and 8, respectively. Compared with the tumor volume of the control group, mice treated with Au NP/ citrate, EGSe-tMe had less obvious tumor growth inhibition effect, and however, mice treated with Au NP/Se showed tumor growth strong inhibitory effect (**Figure 6D**). There was no significant cha of mice treated with Au NP/Se (**Figure 6E**). And photographs of mice after administration of different drugs on day 10 were observed, which showed that the systemic toxicity of Au NP/Se was low (Li et al., 2016). However, there are still some problems in the development of nanoprobe for tumor microenvironment. Further binding to ligands may help to reduce toxicity and guide targeting, but can affect the catalytic activity and subsequent metabolism of the nanozymes, as well as the microenvironment of the organisms. Although nanoprobes have achieved good results in animal experiments, the differences between animals and humans are huge, and their clinical applications need to be further developed and utilized.

Brain Therapy

The toxicity of nanozymes has caused widespread concern (Zhang et al., 2018). Liu et al. found that amino-terminated gold nanoclusters (Au $NCs-NH_2$) have low cytotoxicity and can protect primary neurons from oxidative damage (Liu et al., 2016). The peroxidase-like activity of Au $NCs-NH_2$ is inhibited by the polymerized 3-amines, and thus exhibits catalase-like activity, which decomposes H_2O_2, thereby providing neurons with protection against oxidative damage (**Figure 7A**) (Mukherjee et al., 2010). Compared to the control, H_2O_2 excitation resulted in significant cell death and less red fluorescence. Neuronal cells were pre-treated with Au $NCs-NH_2$ and showed red fluorescence similar to that of the control group after challenge with H_2O_2. The same is true for neurons treated with Au $NCs-NH_2$ alone, further demonstrating the low cytotoxicity of Au $NCs-NH_2$ (**Figure 7B**) (Wang et al., 2013). Cell viability in different treatment groups was determined by MTT assay and treatment with H_2O_2 alone (100×10^{-6} or 200×10^{-6} M) resulted in a significant decrease in neuronal cell viability. Pretreatment with Au $NCs-NH_2$ followed by challenge with H_2O_2, the cells remained viable and the results were similar to the untreated

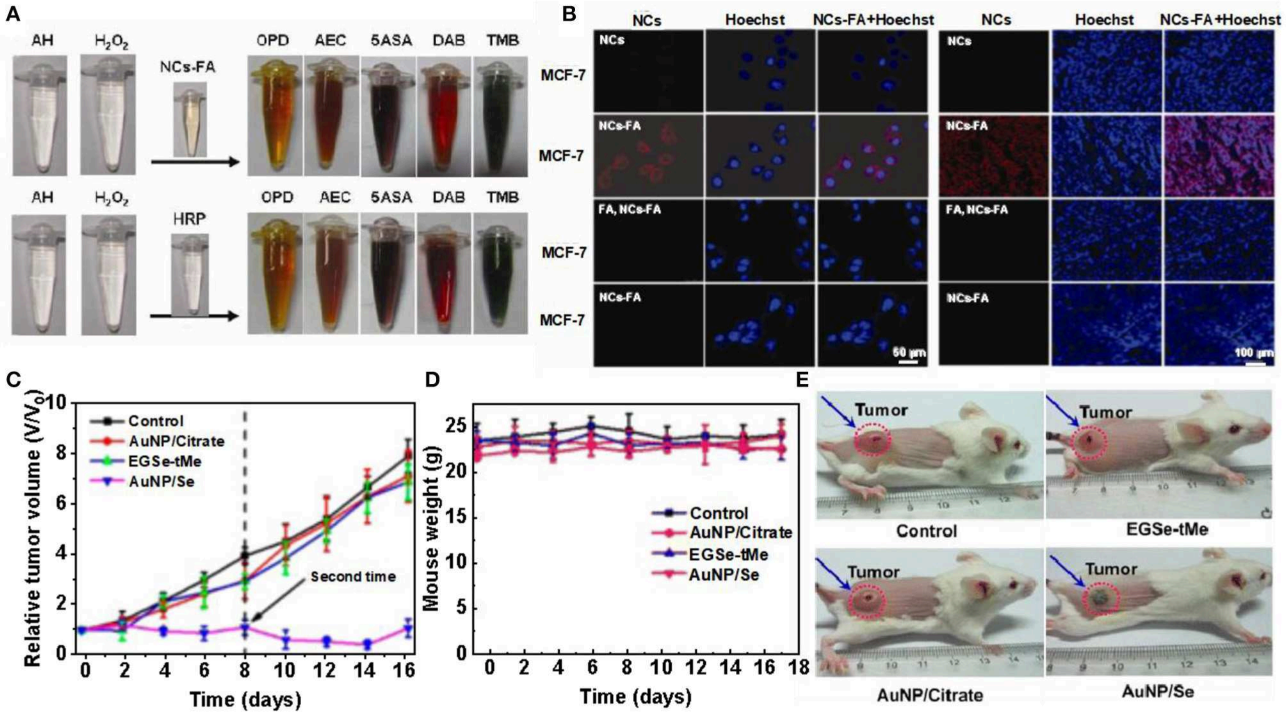

FIGURE 6 | Gold clusters for tumor treatment. **(A)** NCs-FA and HRP catalyze the color contrast of OPD, AEC, 5ASA, DAB, and TMB. **(B)** MCF-7 cells and HepG2 cells were stained with NCs-FA under a confocal laser microscope [reproduced from Hu et al. (2014) with permission from The Ivy Publisher]. **(C)** Fluorescence imaging of NCs-FA stained MCF-7 and HepG2 tumor tissues. **(D)** Relative tumor volume of mice after different drug treatments. **(E)** Body weight changes in mice after different drug treatments [reproduced from Li et al. (2016) with permission from The American Chemical Society].

controls. This indicates that pretreatment of primary neuronal cells with Au NCs-NH_2 have resistance to H_2O_2 induced toxicity (**Figure 7C**) (Huang et al., 2004). The catalase-like activities of Au NCs-NH_2 and Au NCs-OH prepared from different end groups of dendrimers were not affected at different pH, but the catalytic performance of Au NCs-NH_2 for H_2O_2 was significantly better than that of Au NCs-OH (**Figure 7D**) (Jao et al., 2010). The level of H_2O_2 in cells after H2DCFDA staining was quantified by flow cytometry, and the protective effect of NCs-NH_2 in H_2O_2 treated neurons was obtained (**Figures 7E,F**). The fluorescence intensity of neurons pretreated with Au NCs-NH_2 was significantly increased compared to the control (Graf et al., 2004). Although the catalytic activity of nanozymes is closely related to their surface properties, the mechanism of enzymelike activity of its surface coating is poorly understood. Once the nano-enzyme loses its surface accessibility, its catalytic performance will be inhibited, thus affecting its application in brain therapy and other aspects. Currently, biomedical research on gold nanoclusters without surface coating is limited due to concerns about their toxicity and stability.

CONCLUSION

In this article, we attempt to give a comprehensive overview based on gold nanoclusters. We have summarized the characteristics of enzymes such as glucose oxidase, peroxidase, catalase, superoxide dismutase, etc. The applications of gold nanoclusters in ion detection, tumor treatment and brain treatment were analyzed. This enzymatic property of gold clusters is derived from the functional groups present on the gold itself or on the surrounding monolayer. Although the development of gold clusters catalysts has made encouraging progress, the overall performance of these artificial catalytic systems is often not comparable to natural catalysts. To this end, the following aspects are awaiting implementation:

(1) In recent years, with the development of nanotechnology, we can control the size and shape of nanoparticles by including hydrogen reduction, self-assembly, porous support matrix and surfactant assisted methods to adjust their catalytic activity. Because of the size dependence of gold nanomaterials, this allows us to conduct directional manipulation of surface properties. Because the surface charge and other parameters have great influence on the cell adhesion behavior, the preparation of gold nanoclusters enzyme with atomic precision is a promising method to affect the biological activity. In addition, catalysts with atomic precision are more conducive to revealing the relationship between electronic structure and properties. At the same time, the sources of catalytic activity of functional groups, and the future work may continue to focus on

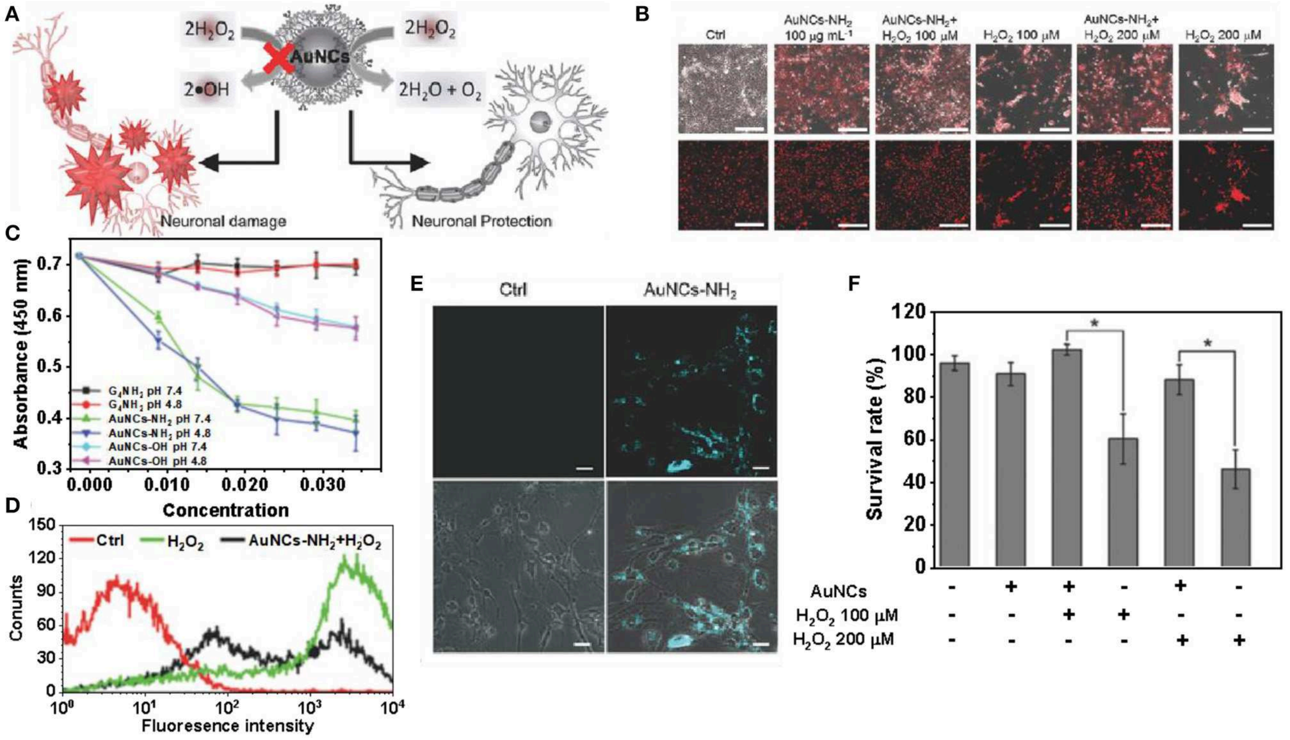

FIGURE 7 | Gold clusters for brain disease treatment. **(A)** Au NCs coated with dendrimers have the effect of detoxifying H_2O_2 to protect neurons from oxidative damage. **(B)** The H_2O_2 challenge resulted in significant cell death, with less red fluorescence than the control. **(C)** Cell viability of neurons pretreated with AuNCs-NH_2 under H_2O_2. **(D)** The catalytic activities of G_4NH_2, Au NCs-OH and Au NCs-NH_2 on H_2O_2 were compared at pH 4.8 and 7.4, respectively. **(E)** Changes in DCF fluorescence intensity in neurons pretreated with Au NCs-NH_2. **(F)** Confocal fluorescence images of neuronal cells treated with Au NCs-NH_2 for 24 h [reproduced from Liu et al. (2016) with permission from The Small].

changes in functional groups present at catalytic sites, resulting in highly active catalysts. More importantly, we hope to open up new strategies to significantly improve catalytic performance and biosafety through the regulation of three changes in atomic accuracy, catalytic sites and functional groups.

(2) Although rapid progress has been made in the development of nanomaterials with enzyme mimicking activity, it is unclear how widely these materials are used *in vivo* and clinically. So far, it is uncertain whether gold nanoclusters with enzyme-like activity can significantly replace many naturally occurring enzymes. All endogenous enzymes in our bodies are as a whole system and work interdependently. Any artificial substitutes, including nanoclusters, may not be suitable for the system and may cause serious side effects. During the expression of enzyme-like functions, nanoclusters can generate free radicals, causing toxicological effects. Therefore, it is worthy of further study to make full use of the beneficial effect of the enzyme-like activity of the nanoclusters and explore their application *in vivo*.

(3) Although many researchers have demonstrated the therapeutic effects of nanozymes systems through cell and animal experiments, it is still difficult to explain the mechanism of nanozymes systems *in vivo* through these biological experiments. For example, quantifying reaction kinetics *in vivo* is not an easy task, although the available evidence supports the ultimate therapeutic outcome of these nanozymes. We can only know the results, but not the processes in the body. In recent years, multifunctional optical probes have been widely developed to detect the concentration and distribution of specific biochemical substances in the biological environment. Therefore, we may need to develop multifunctional nanometer enzyme probes, such as using the luminescence of gold clusters for imaging or sensing (Such as detecting markers of neurological disease), and then combining its enzyme-like properties for treatment, which can achieve the purpose of combining diagnosis with treatment, providing powerful help for the study of the distribution and mechanism of action of nanomaterials in living organisms. These diagnostic reagents are expected to help accurately characterize the catalytic process *in vivo*, and ultimately comprehensively clarify the relationship between the composition, structure, and *in vivo* properties of nanozymes drugs.

AUTHOR CONTRIBUTIONS

SL wrote the first draft. HL and X-DZ modified the manuscript content and format. YZ and WL modified the syntax.

FUNDING

This work was financially supported by the National Natural Science Foundation of China (Grant No. 91859101, 81971744, U1932107, 81673106, and 81471786), CAMS Innovation Fund for Medical Science (2017-12M-1-012) and National Natural Science Foundation of Tianjin (No. 19JCZDJC34000), the Innovation Foundation of Tianjin University.

REFERENCES

Arnold, F. H., Wintrode, P. L., Miyazaki, K., and Gershenson, A. (2001). How enzymes adapt: lessons from directed evolution. *Trends Biochem. Sci.* 26, 100–106. doi: 10.1016/S0968-0004(00)01755-2

Bankar, S. B., Bule, M. V., Singhal, R. S., and Ananthanarayan, L. (2009). Glucose oxidase–an overview. *Biotechnol. Adv.* 27, 489–501. doi: 10.1016/j.biotechadv.2009.04.003

Barzegar, A., and Moosavi-Movahedi, A. A. (2011). Intracellular ROS protection efficiency and free radical-scavenging activity of curcumin. *PLoS ONE* 6:26012. doi: 10.1371/journal.pone.0026012

Bhan, A., and Sarkar, N. (2005). Mercury in the environment: effect on health and reproduction. *Rev. Environ. Health.* 20, 39–56. doi: 10.1515/REVEH.2005.20.1.39

Brodersen, S. H., Grønbjerg, U., Hvolbæk, B., and Schiøtz, J. (2011). Understanding the catalytic activity of gold nanoparticles through multi-scale simulations. *J. Catal.* 284, 34–41. doi: 10.1016/j.jcat.2011.08.016

Chang, H. T., Chen, P. C., Periasamy, A. P., Harroun, S. G., and Wu, W. P. (2016). Photoluminescence sensing systems based on copper, gold and silver nanomaterials. *Coordin. Chem. Rev.* 320, 129–138. doi: 10.1016/j.ccr.2015.12.002

Chang, T. M. S. (2013). *Biomedical Applications of Immobilized Enzymes and Proteins*. Quebec City, QC: Springer.

Chen, J., Huang, L., Wang, Q., Wu, W., Zhang, H., Fang, Y., et al. (2019). Bio-inspired nanozyme: a hydratase mimic in a zeolitic imidazolate framework. *Nanoscale.* 11, 5960–5966. doi: 10.1039/C9NR01093A

Chen, W.-Y., Lan, G.-Y., and Chang, H.-T. (2011). Use of fluorescent DNA-templated gold/silver nanoclusters for the detection of sulfide ions. *Anal. chem.* 83, 9450–9455. doi: 10.1021/ac202162u

Chen, Z., Xu, L., Liang, Y., and Zhao, M. (2010). pH-sensitive water-soluble nanospheric imprinted hydrogels prepared as horseradish peroxidase mimetic enzymes. *Adv. Mater.* 22, 1488–1492. doi: 10.1002/adma.200903122

Chi, X., Huang, D., Zhao, Z., Zhou, Z., Yin, Z., and Gao, J. (2012). Nanoprobes for *in vitro* diagnostics of cancer and infectious diseases. *Biomaterials* 33, 189–206. doi: 10.1016/j.biomaterials.2011.09.032

Comotti, M., Pina, C. D., Matarrese, R., and Rossi, M. (2010). The catalytic activity of "naked" gold particles. *Angew. Chem. Int. Edit.* 116, 5936–5939. doi: 10.1002/ange.200460446

Corma, A., Concepción, P., Boronat, M., Sabater, M. J., Navas, J., and Yacaman, MJ. (2013). Exceptional oxidation activity with size-controlled supported gold clusters of low atomicity. *Nat. Chem.* 5, 775–81. doi: 10.1038/nchem.1721

Del Valle, E. M. (2004). Cyclodextrins and their uses: a review. *Process Biochem.* 39, 1033–1046. doi: 10.1016/S0032-9592(03)00258-9

Ding, N., Zhao, H., Peng, W., He, Y., Zhou, Y., Yuan, L., et al. (2012). A simple colorimetric sensor based on anti-aggregation of gold nanoparticles for Hg^{2+} detection. *Colloid. Surface. A.* 395, 161–167. doi: 10.1016/j.colsurfa.2011.12.024

Ding, Y., Zhao, J., Li, B., Zhao, X., Wang, C., Guo, M., et al. (2018). The CoOOH-TMB oxidative system for use in colorimetric and test strip based determination of ascorbic acid. *Microchim. Acta.* 185:131. doi: 10.1007/s00604-018-2675-z

Ercal, N., Gurer-Orhan, H., and Aykin-Burns, N. (2001). Toxic metals and oxidative stress part I: mechanisms involved in metal-induced oxidative damage. *Curr. Top. Med. Chem.* 1, 529–539. doi: 10.2174/1568026013394831

Erel, O. (2004). A novel automated direct measurement method for total antioxidant capacity using a new generation, more stable ABTS radical cation. *Clin. Biochem.* 37, 277–285. doi: 10.1016/j.clinbiochem.2003.11.015

Fan, K., Xi, J., Fan, L., Wang, P., Zhu, C., Tang, Y., et al. (2018). *In vivo* guiding nitrogen-doped carbon nanozyme for tumor catalytic therapy. *Nat. Commun.* 9:1440. doi: 10.1038/s41467-018-03903-8

Feng, J., Huang, P., Shi, S., Deng, K.-Y., and Wu, F.-Y. (2017). Colorimetric detection of glutathione in cells based on peroxidase-like activity of gold nanoclusters: a promising powerful tool for identifying cancer cells. *Anal. Chim. Acta.* 967, 64–69. doi: 10.1016/j.aca.2017.02.025

Gallardo, C., Monrás, J., Plaza, D., Collao, B., Saona, L., Durán-Toro, V., et al. (2014). Low-temperature biosynthesis of fluorescent semiconductor nanoparticles (CdS) by oxidative stress resistant Antarctic bacteria. *J. Biotechnol.* 187, 108–115. doi: 10.1016/j.jbiotec.2014.07.017

Gao, L., Zhuang, J., Nie, L., Zhang, J., Zhang, Y., Gu, N., et al. (2007). Intrinsic peroxidase-like activity of ferromagnetic nanoparticles. *Nat. Nanotechnol.* 2, 577–83. doi: 10.1038/nnano.2007.260

Geim, A. K., and Grigorieva, I. V. (2013). Van der Waals heterostructures. *Nature* 499, 419–425. doi: 10.1038/nature12385

Gibson, Q. H., Swoboda, B. E., and Massey, V. (1964). Kinetics and mechanism of action of glucose oxidase. *J. Biol. Chem.* 239, 3927–3934.

Gleiter, R., and Hopf, H. (2006). *Modern Cyclophane Chemistry*. Heidelberg; Braunschweig: John Wiley Sons.

Glorieux, C., and Calderon, P. B. (2017). Catalase, a remarkable enzyme: targeting the oldest antioxidant enzyme to find a new cancer treatment approach. *Biol. Chem.* 398, 1095–1108. doi: 10.1515/hsz-2017-0131

Góth, L., Rass, P., and Páy, A. (2004). Catalase enzyme mutations and their association with diseases. *Mol. Diagn.* 8, 141–149. doi: 10.1007/BF03260057

Graf, E. R., Zhang, X. Z., Jin, S. X., Linhoff, M. W., and Craig, A. M. (2004). Neurexins induce differentiation of GABA and glutamate postsynaptic specializations via neuroligins. *Cell*, 119, 1013–1026. doi: 10.1016/j.cell.2004.11.035

Griffith, L. G., and Naughton, G. (2002). Tissue engineering–current challenges and expanding opportunities. *Science* 295, 1009–1014. doi: 10.1126/science.1069210

He, W., Wamer, W. G., Hu, X., and Wu, X. (2013). Intrinsic catalytic activity of Au nanoparticles with respect to hydrogen peroxide decomposition and superoxide scavenging. *Biomaterials* 34, 765–773. doi: 10.1016/j.biomaterials.2012.10.010

He, W., Zhou, Y.-T., Wamer, W. G., Boudreau, M. D., and Yin, J.-J. (2012). Mechanisms of the pH dependent generation of hydroxyl radicals and oxygen induced by Ag nanoparticles. *Biomaterials* 33, 7547–7555. doi: 10.1016/j.biomaterials.2012.06.076

He, X., Gao, J., Gambhir, S. S., and Cheng, Z. (2010). Near-infrared fluorescent nanoprobes for cancer molecular imaging: status and challenges. *Trends Mol. Med.* 16, 574–583. doi: 10.1016/j.molmed.2010.08.006

Hu, D., Sheng, Z., Fang, S., Wang, Y., Gao, D., Zhang, P., et al. (2014). Folate receptor-targeting gold nanoclusters as fluorescence enzyme mimetic nanoprobes for tumor molecular colocalization diagnosis. *Theranostics* 4, 142–153. doi: 10.7150/thno.7266

Huang, H., Starodub, O., McIntosh, A., Atshaves, B. P., Woldegiorgis, G., Kier, A. B., et al. (2004). Liver fatty acid-binding protein colocalizes with peroxisome proliferator activated receptor α and enhances ligand distribution to nuclei of living cells. *Biochemistry* 43, 2484–2500. doi: 10.1021/bi0352318

Huang, L., Chen, J., Gan, L., Wang, J., and Dong, S. (2019a). Single-atom nanozymes. *Sci. Adv.* 5:eaa5490. doi: 10.1126/sciadv.aav5490

Huang, Y., Ren, J., and Qu, X. (2019b). Nanozymes: classification, catalytic mechanisms, activity regulation, and, applications. *Chem. Rev.* 119, 4357–4412. doi: 10.1021/acs.chemrev.8b00672

Ishida, T., Kinoshita, N., Okatsu, H., Akita, T., Takei, T., and Haruta, M. (2008). Influence of the support and the size of gold clusters on catalytic activity for glucose oxidation. *Angew. Chem.* 47, 9265–9268. doi: 10.1002/anie.200802845

Jao, Y.-C., Chen, M.-K., and Lin, S.-Y. (2010). Enhanced quantum yield of dendrimer-entrapped gold nanodots by a specific ion-pair association and microwave irradiation for bioimaging. *Chem. Commun.* 46, 2626–2628. doi: 10.1039/b926364k

Jiang, D., Ni, D., Rosenkrans, Z. T., Huang, P., Yan, X., and Cai, W. (2019). Nanozyme: new horizons for responsive biomedical applications. *Chem. Soc. Rev.* 48, 3683–3704. doi: 10.1039/C8CS00718G

Jin, R. (2010). Quantum sized, thiolate-protected gold nanoclusters. *Nanoscale* 2, 343–362. doi: 10.1039/B9NR00160C

Kim, Y., Johnson, R. C., and Hupp, J. T. (2001). Gold nanoparticle-based sensing of "spectroscopically silent" heavy metal ions. *Nano Lett.* 1, 165–167. doi: 10.1021/nl0100116

Lequin, R. M. (2005). Enzyme immunoassay (EIA)/enzyme-linked immunosorbent assay (ELISA). *Clin. Chem.* 51, 2415–2418. doi: 10.1373/clinchem.2005.051532

Li, J., Liu, W., Wu, X., and Gao, X. (2015). Mechanism of pH-switchable peroxidase and catalase-like activities of gold, silver, platinum and palladium. *Biomaterials* 48, 37–44. doi: 10.1016/j.biomaterials.2015.01.012

Li, T., Li, F., Xiang, W., Yi, Y., Chen, Y., Cheng, L., et al. (2016). Selenium-containing amphiphiles reduced and stabilized gold nanoparticles: kill cancer cells via reactive oxygen species. *ACS Appl. Mater. Inter.* 8, 22106–22112. doi: 10.1021/acsami.6b08282

Li, W., and Xiaogang, Q. (2015). Cancer biomarker detection: recent achievements and challenges. *Chem. Soc. Rev.* 44, 2963–2997. doi: 10.1039/C4CS00370E

Liang, M., and Yan, X. (2019). Nanozymes: from new concepts, mechanisms, and standards to applications. *Acc. Chem. Res.* 52, 2190–2200. doi: 10.1021/acs.accounts.9b00140

Liao, H., Liu, G., Liu, Y., Li, R., Fu, W., and Hu, L. (2017). Aggregation-induced accelerating peroxidase-like activity of gold nanoclusters and their applications for colorimetric Pb^{2+} detection. *Chem. Commun.* 53, 10160–10163. doi: 10.1039/C7CC05409B

Lin, Y., Ren, J., and Qu, X. (2014a). Nano-gold as artificial enzymes: hidden talents. *Adv. Mater.* 26, 4200–4217. doi: 10.1002/adma.201400238

Lin, Y., Ren, J., and Qu, X. (2014b). Catalytically active nanomaterials: a promising candidate for artificial enzymes. *Accounts Chem. Res.* 47, 1097–1105. doi: 10.1021/ar400250z

Liu, C. P., Wu, T. H., Lin, Y. L., Liu, C. Y., Wang, S., and Lin, S. Y. (2016). Tailoring enzyme-like activities of gold nanoclusters by polymeric tertiary amines for protecting neurons against oxidative stress. *Small* 12, 4127–4135. doi: 10.1002/smll.201503919

Liu, C. P., Wu, T. H., Liu, C. Y., Chen, K. C., Chen, Y. X., Chen, G. S., et al. (2017). Self-supplying O_2 through the catalase-like activity of gold nanoclusters for photodynamic therapy against hypoxic cancer cells. *Small* 13:1700278. doi: 10.1002/smll.201700278

Liu, H., Hong, G., Luo, Z., Chen, J., Chang, J., Gong, M., et al. (2019). Atomic-precision gold clusters for NIR-II imaging. *Adv. Mater.* 31:1901015. doi: 10.1002/adma.201901015

Liu, J., Wang, Z., Yan, X., and Jian, P. (2017). Metallic cobalt nanoparticles imbedded into ordered mesoporous carbon: a non-precious metal catalyst with excellent hydrogenation performance. *J. Colloid Interf. Sci.* 505, 789–795. doi: 10.1016/j.jcis.2017.06.081

Liu, Q., Yang, Y., Lv, X., Ding, Y., Zhang, Y., Jing, J., et al. (2017). One-step synthesis of uniform nanoparticles of porphyrin functionalized ceria with promising peroxidase mimetics for H_2O_2 and glucose colorimetric detection. *Sensor. Actuat B-Chem.* 240, 726–734. doi: 10.1016/j.snb.2016.09.049

Liu, S., Lu, F., Xing, R., and Zhu, J. J. (2011). Structural effects of Fe_3O_4 nanocrystals on peroxidase-like activity. *Chem. Eur. J.* 17, 620–625. doi: 10.1002/chem.201001789

Liu, Y., Ai, K., Cheng, X., Huo, L., and Lu, L. (2010). Gold-nanocluster-based fluorescent sensors for highly sensitive and selective detection of cyanide in water. *Adv. Funct. Mater.* 20, 951–956. doi: 10.1002/adfm.200902062

Liu, Y., Ding, D., Zhen, Y., and Guo, R. (2017). Amino acid-mediated 'turn-off/turn-on' nanozyme activity of gold nanoclusters for sensitive and selective detection of copper ions and histidine. *Biosens. Bioelectron.* 92, 140–146. doi: 10.1016/j.bios.2017.01.036

Lopez, N., Janssens, T., Clausen, B., Xu, Y., Mavrikakis, M., Bligaard, T., et al. (2004). On the origin of the catalytic activity of gold nanoparticles for low-temperature CO oxidation. *J. Catal.* 223, 232–235. doi: 10.1016/j.jcat.2004.01.001

Luo, W., Zhu, C., Su, S., Li, D., He, Y., Huang, Q., et al. (2010). Self-catalyzed, self-limiting growth of glucose oxidase-mimicking gold nanoparticles. *ACS Nano.* 4, 7451–7458. doi: 10.1021/nn102592h

Martin, S., and Griswold, W. (2018). Human health effects of heavy metals. *Internation. J.* 15, 1–6. doi: 10.14445/23939133/IJAC-V5I1P102

Mavrikakis, M., Stoltze, P., and Nørskov, J. K. (2000). Making gold less noble. *Catal. Lett.* 64, 101–106. doi: 10.1023/A:1019028229377

Meeuwissen, J., and Reek, J. N. (2010). Supramolecular catalysis beyond enzyme mimics. *Nat. Chem.* 2, 615–21. doi: 10.1038/nchem.744

Miller, J., Kropf, A., Zha, Y., Regalbuto, J., Delannoy, L., Louis, C., et al. (2006). The effect of gold particle size on AuAu bond length and reactivity toward oxygen in supported catalysts. *J. Catal.* 240, 222–234. doi: 10.1016/j.jcat.2006.04.004

Molina, L., and Hammer, B. (2005). Some recent theoretical advances in the understanding of the catalytic activity of Au. *Appl. Catal. A-Gen.* 291, 21–31. doi: 10.1016/j.apcata.2005.01.050

Mu, X., He, H., Wang, J., Long, W., Li, Q., Liu, H., et al. (2019a). Carbogenic nanozyme with ultrahigh reactive nitrogen species selectivity for traumatic brain injury. *Nano Lett.* 19, 4527–4534. doi: 10.1021/acs.nanolett.9b01333

Mu, X., Wang, J., Li, Y., Xu, F., and Long, W. (2019b). Redox trimetallic nanozyme with neutral environment preference for brain injury. *ACS Nano.* 13, 1870–1884. doi: 10.1021/acsnano.8b08045

Mukherjee, S. P., Davoren, M., and Byrne, H. J. (2010). *In vitro* mammalian cytotoxicological study of PAMAM dendrimers–towards quantitative structure activity relationships. *Toxicol. in vitro* 24, 169–177. doi: 10.1016/j.tiv.2009.09.014

Pandey, P., Singh, S. P., Arya, S. K., Gupta, V., Datta, M., Singh, S. et al. (2007). Application of thiolated gold nanoparticles for the enhancement of glucose oxidase activity. *Langmuir.* 23, 3333–3337. doi: 10.1021/la062901c

Panigrahi, S., Basu, S., Praharaj, S., Pande, S., Jana, S., Pal, A., et al. (2007). Synthesis and size-selective catalysis by supported gold nanoparticles: study on heterogeneous and homogeneous catalytic process. *J. Phys. Chem. C.* 111, 4596–4605. doi: 10.1021/jp067554u

Pasternack, R. F., Gibbs, E. J., Collings, P. J., dePaula, J. C., Turzo, L. C., and Terracina, A. (1998). A non-conventional approach to supramolecular formation dynamics. *J. Am. Chem. Soc.* 120, 5873–5878. doi: 10.1021/ja980186q

Pina, C. D., Falletta, E., and Rossi, M. (2011). Update on selective oxidation using gold. *Chem. Soc. Rev.* 41, 350–369. doi: 10.1039/C1CS15089H

Qi, Y.-X., Zhang, M., Zhu, A., and Shi, G. (2015). Terbium (iii)/gold nanocluster conjugates: the development of a novel ratiometric fluorescent probe for mercury (ii) and a paper-based visual sensor. *Analyst* 140, 5656–5661. doi: 10.1039/C5AN00802F

Qu, X., Sun, H., Zhou, Y., and Ren, J. (2018). Carbon nanozymes: enzymatic properties, catalytic mechanism and applications. *Angew. Chem.* 57, 9224–9237. doi: 10.1002/anie.201712469

Quan, H., Zuo, C., Li, T., Liu, Y., Li, M., Zhong, M., et al. (2015). Electrochemical detection of carcinoembryonic antigen based on silver nanocluster/horseradish peroxidase nanocomposite as signal probe. *Electrochim. Acta.* 176, 893–897. doi: 10.1016/j.electacta.2015.07.086

Roduner, E. (2006). Size matters: why nanomaterials are different. *Chem. Soc. Rev.* 35, 583–592. doi: 10.1039/b502142c

Schaller, B., and Graf, R. (2004). Cerebral is chemia and reperfusion: the pathophysiologic concept as a basis for clinical therapy. *J. Cerebr. Blood. F. Met.* 24, 351–371. doi: 10.1097/00004647-200404000-00001

Scopes, R. K. (2013). *Protein Purification: Principles and Practice*. LaTrobe, VIC: Spring Science Business Media.

Senanayake, S. D., Stacchiola, D., and Rodriguez, J. A. (2013). Unique properties of ceria nanoparticles supported on metals: novel inverse ceria/copper catalysts for CO oxidation and the water-gas shift reaction. *Accounts. Chem. Res.* 46, 1702–1711. doi: 10.1021/ar300231p

Sheldon, R. A. (2007). Enzyme immobilization: the quest for optimum performance. *Adv. Synth. Catal.* 349, 1289–1307. doi: 10.1002/adsc.200700082

Shojaeifard, Z., Hemmateenejad, B., and Shamsipur, M. (2016). Efficient on–off ratiometric fluorescence probe for cyanide ion based on perturbation of the interaction between gold nanoclusters and a copper (II)-phthalocyanine complex. *ACS Appl. Mater. Inter.* 8, 15177–15186. doi: 10.1021/acsami.6b01566

Song, Y., Qu, K., Zhao, C., Ren, J., and Qu, X. (2010). Graphene oxide: intrinsic peroxidase catalytic activity and its application to glucose detection. *Adv. Mater.* 22, 2206–2210. doi: 10.1002/adma.200903783

Spichiger-Keller, U. E. (2008). *Chemical Sensors and Biosensors for Medical and Biological Applications*. New York, NY: John Wiley and Sons.

Steed, J. W., and Atwood, J. L. (2013). *Supramolecular Chemistry*. Durham: John Wiley and Sons.

Tsipis, A. C., and Tsipis, C. A. (2003). Hydrometal analogues of aromatic hydrocarbons: a new class of cyclic hydrocoppers (I). *J. Am. Chem. Soc.* 125, 1136–1137. doi: 10.1021/ja028786j

Tsunoyama, H., Sakurai, H., and Tsukuda, T. (2006). Size effect on the catalysis of gold clusters dispersed in water for aerobic oxidation of alcohol. *Chem. Phys. Lett.* 429, 528–532. doi: 10.1016/j.cplett.2006.08.066

Velizarov, S., Crespo, J. G., and Reis, M. A. (2004). Removal of inorganic anions from drinking water supplies by membrane bio/processes. *Rev. Environ. Sci. Bio.* 3, 361–380. doi: 10.1007/s11157-004-4627-9

Wan, Y., Yang, H., and Zhao, D. (2006). "Host– Guest" chemistry in the synthesis of ordered non-siliceous mesoporous materials. *Accounts Chem. Rev.* 39, 423–432. doi: 10.1021/ar050091a

Wang, G.-L., Jin, L.-Y., Dong, Y.-M., Wu, X.-M., and Li, Z.-J. (2015). Intrinsic enzyme mimicking activity of gold nanoclusters upon visible light triggering and its application for colorimetric trypsin detection. *Biosens. Bioelectron.* 64, 523–529. doi: 10.1016/j.bios.2014.09.071

Wang, X., Wu, P., Lv, Y., and Hou, X. (2011). Ultrasensitive fluorescence detection of glutaraldehyde in water samples with bovine serum albumin-Au nanoclusters. *Microchem. J.* 99, 327–331. doi: 10.1016/j.microc.2011.06.004

Wang, X., Zhang, Y., Li, T., Tian, W., Zhang, Q., and Cheng, Y. (2013). Generation 9 polyamidoamine dendrimer encapsulated platinum nanoparticle mimics catalase size, shape, and catalytic activity. *Langmuir* 29, 5262–5270. doi: 10.1021/la3046077

Wei, H., and Wang, E. (2013). Nanomaterials with enzyme-like characteristics (nanozymes): next-generation artificial enzymes. *Chem. Soc. Rev.* 42, 6060–6093. doi: 10.1039/c3cs35486e

Wen, F., Dong, Y., Feng, L., Wang, S., and Zhang, S. (2011). Horseradish peroxidase functionalized fluorescent gold nanoclusters for hydrogen peroxide sensing. *Anal. Chem.* 83, 1193–1196. doi: 10.1021/ac1031447

Wilhelmová, N. (1996). Cornish-bowden, a.: fundamentals of enzyme kinetics. *Biol. Planrraum.* 38, 430–430. doi: 10.1007/BF02896674

Wilson, R., and Turner, A.P.F. (1992). Glucose oxidase: an ideal enzyme. *Biosens. Bioelectron.* 7, 165–185. doi: 10.1016/0956-5663(92)87013-F

Wu, J., Wang, X., Wang, Q., Lou, Z., Li, S., Zhu, Y., et al. (2019). Nanomaterials with enzyme-like characteristics (nanozymes): next-generation artificial enzymes (II). *Chem. Soc. Rev.* 48, 1004–1076. doi: 10.1039/C8CS00457A

Xia, X., Long, Y., and Wang, J. (2013). Glucose oxidase-functionalized fluorescent gold nanoclusters as probes for glucose. *Anal. Chim. Acta.* 772, 81–86. doi: 10.1016/j.aca.2013.02.025

Xiong, X., Tang, Y., Zhang, L., and Zhao, S. (2015). A label-free fluorescent assay for free chlorine in drinking water based on protein-stabilized gold nanoclusters. *Talanta* 132, 790–795. doi: 10.1016/j.talanta.2014.10.022

Xu, B., Wang, H., Wang, W., Gao, L., Li, S., Pan, X., et al. (2019). A single-atom nanozyme for wound disinfection applications. *Angew. Chem. Int. Edit.* 58, 4911–4916. doi: 10.1002/anie.201813994

Xu, X., Li, Y.-F., Zhao, J., Li, Y., Lin, J., Li, B., et al. (2015). Nanomaterial-based approaches for the detection and speciation of mercury. *Analyst.* 140, 7841–7853. doi: 10.1039/C5AN01519G

Yan, R., Sun, S., Yang, J., Long, W., Wang, J., Mu, X., et al. (2019). A nanozyme-based bandage with single-atom catalysis for brain trauma. *ACS Nano.* 13, 11552–11560. doi: 10.1021/acsnano.9b05075

Yang, B., Li, J., Deng, H., and Zhang, L. (2016). Progress of mimetic enzymes and their applications in chemical sensors. *Crit. Rev. Anal. Chem.* 46, 469–481. doi: 10.1080/10408347.2016.1151767

Yang, X., Wang, J., Su, D., Xia, Q., Chai, F., Wang, C., et al. (2014). Fluorescent detection of TNT and 4-nitrophenol by BSA Au nanoclusters. *Dalton T* 43, 10057–10063. doi: 10.1039/C4DT00490F

Yin, Y., and Talapin, D. (2013). The chemistry of functional nanomaterials. *Chem. Soc. Rev.* 42, 2484–2487. doi: 10.1039/c3cs90011h

Yuwen, L., Xu, F., Xue, B., Luo, Z., Zhang, Q., Bao, B., et al. (2014). General synthesis of noble metal (Au, Ag, Pd, Pt) nanocrystal modified MoS2 nanosheets and the enhanced catalytic activity of Pd–MoS_2 for methanol oxidation. *Nanoscale* 6, 5762–5769. doi: 10.1039/C3NR06084E

Zhang, Y., Wang, F., Liu, C., Wang, Z., Kang, L., Huang, Y., et al. (2018). Nanozyme decorated metal–organic frameworks for enhanced photodynamic therapy. *ACS Nano.* 12, 651–661. doi: 10.1021/acsnano.7b07746

Zhou, X., Xu, W., Liu, G., Panda, D., and Chen, P. (2010). Size-dependent catalytic activity and dynamics of gold nanoparticles at the single-molecule level. *J. Am. Chem. Soc.* 132, 138–146. doi: 10.1021/ja904307n

Zhou, Y., Liu, B., Yang, R., and Liu, J. (2017). Filling in the gaps between nanozymes and enzymes: challenges and opportunities. *Bioconjugate Chem.* 28, 2903–2909. doi: 10.1021/acs.bioconjchem.7b00673

Zhu, R., Zhou, Y., Wang, X.-L., Liang, L.-P., Long, Y.-J., Wang, Q.-L., et al. (2013). Detection of Hg2+ based on the selective inhibition of peroxidase mimetic activity of BSA-Au clusters. *Talanta* 117, 127–132. doi: 10.1016/j.talanta.2013.08.053

Conflict of Interest: The authors declare that the research was conducted in the absence of any commercial or financial relationships that could be construed as a potential conflict of interest.

ORIGINAL RESEARCH
published: 07 April 2020
doi: 10.3389/fchem.2020.00244

Trimetallic PdCuAu Nanoparticles for Temperature Sensing and Fluorescence Detection of H_2O_2 and Glucose

Furong Nie[1]†, Lu Ga[2]†, Jun Ai[1]* and Yong Wang[3]*

[1] College of Chemistry and Enviromental Science, Inner Mongolia Normal University, Hohhot, China, [2] College of Pharmacy, Inner Mongolia Medical University, Hohhot, China, [3] College of Geographical Science, Inner Mongolia Normal University, Hohhot, China

The design of palladium-based nanostructures has good prospects in various applications. This paper reports a simple one-step synthesis method of PdCuAu nanoparticles (PdCuAu NPs) prepared directly in aqueous solution. PdCuAu NPs have attracted much attention owing to their unique synergistic electronic effect, optical and catalytic performance. As temperature sensor, PdCuAu NPs are sensitive to the fluorescence intensity change in the temperature range of 4–95°C, which is due to its unique optical properties. The prepared PdCuAu NPs have excellent catalytic performance for peroxidase-like enzymes. It can catalyze TMB rapidly in the presence of hydrogen peroxide and oxidize it to visible blue product (oxTMB). Based on its unique peroxidase-like properties, this study used PdCuAu NPs colorimetric platform detection of hydrogen peroxide and glucose. The linear ranges of hydrogen peroxide and glucose were 0.1–300 μM and 0.5–500 μM, respectively, and the detection limits (LOD) were 5 and 25 nM, respectively. This simple and rapid method provides a good prospect for the detection of H_2O_2 and glucose in practical applications.

Keywords: trimetallic alloyed nanoparticles, temperature-sensitive, sensor, peroxidase-like activity, colorimetric system

Edited by:
Youhui Lin,
Xiamen University, China

Reviewed by:
Wei Luo,
Donghua University, China
Yan Yan Huang,
Nanjing Forestry University, China

***Correspondence:**
Jun Ai
imacaj01@163.com
Yong Wang
wangyonglsx@163.com

†These authors have contributed equally to this work

Specialty section:
This article was submitted to Nanoscience, a section of the journal Frontiers in Chemistry

Received: *05 February 2020*
Accepted: *16 March 2020*
Published: *07 April 2020*

Citation:
Nie F, Ga L, Ai J and Wang Y (2020) Trimetallic PdCuAu Nanoparticles for Temperature Sensing and Fluorescence Detection of H_2O_2 and Glucose. Front. Chem. 8:244. doi: 10.3389/fchem.2020.00244

In recent years, the research on the preparation and application of nano-device mainly focuses on the preparation and application of polymetallic nanomaterials (Dubau et al., 2015; Xia et al., 2015; Luo and Shen, 2017; Yang et al., 2017; Tang et al., 2018). Because of their unique physical and chemical properties, polymetallic nanomaterials have been widely used in optics, chemical reactions, fuel cells, sensors and catalysts (Huang et al., 2014; Khan et al., 2015; Tang et al., 2018; Wang et al., 2018). At present, Pt-based nanomaterials are the most widely used catalysts because of their high catalytic activity in cathodic and anodic reactions (Khan et al., 2015; Wang et al., 2018). Consequently, tri-metallic Pt-based alloys for instance Pt-Ni-Cu (Tang et al., 2018), Pt-Ni-Co (Huang et al., 2014; Sriphathoorat et al., 2016), Pt-Pd-Cu (Yin et al., 2012; Tian et al., 2017), Pt-Pd-Co (Cho et al., 2014; Song et al., 2015), Pt-Fe-Ni (Li and Chan, 2013), Pt-Fe-Co (Hwang et al., 2011), and Pt-Pd-Au (Li et al., 2018) aroused the attention of many studies. However, due to the low cost and high catalytic activity of Pd-based catalysts, there are few studies on Pd-based catalysts (Guo et al., 2014; Jiang et al., 2015; Xu et al., 2015; Yousaf et al., 2017a), therefore, Pd-based catalysts are the most promising substitute for Pt-based catalysts (Xu et al., 2015; Yousaf et al., 2017a; Wang et al., 2018). Many researchers have done a lot of work on Pd-based catalysts to improve the catalytic performance of palladium catalysts (Wang X. et al., 2015; Xue et al., 2017; Yousaf et al., 2017b). Wang et al. reported a very simple method to synthesize trimetal PdCuAu nanoparticles (NPs) with branched structure, so the PdCuAu NPs have excellent catalytic performance, durability and methanol oxidation resistance (Wang et al., 2018). Huang et al. proposed to prepare an ordered PdCu-based NPs (PdCuCo, and PdCuNi) by colloidal chemistry. PdCuCo NPs have excellent stability and activity in redox reaction because of their intermetallic phase and composition advantages (Jiang et al., 2016). Yang's group reported that the CuPd alloy with controllable shape was preparation of oleylamine by electric substitution reaction. Put Cu in Pd could reduce the bond intensity among the intermediate and palladium, cause the enhancement of lattice shrinkage, thus improving the electrocatalytic performance of redox reaction (Chen D. et al., 2017). Consequently, the Pd-based alloy nanomaterials are considered as a promising catalyst with enhanced catalytic performance. However, Pd-based alloy nanomaterials are seldom used in the field of sensors. In this paper, the application of Pd-based alloy nanomaterials in sensors is studied.

In recent years, thermosensitive materials have shown significant activity due to their possible applications in nanoscale temperature measurement (Zhou et al., 2018). Though, many temperature sensitive materials have a single signal response, and the fluorescence stability and contrast are poor. Dong group studied a novel dual fluorescence temperature sensor based on DNA- template Ag NCs. It has two fluorescence peaks and can be used for sensitive detection of temperature changes from 15 to 45°C (Zhou et al., 2018). Oemrawsingh studied that the single emitter fluorescence of Ag NCs increased 5-fold when the temperature dropped from 295 to 1.7 K (Oemrawsingh et al., 2012). Chen et al. reported a hairpin-like Ag NCs with DNA template. The Ag NCs exhibited reversible fluorescence properties between 25 and 66°C due to the loosening and compacting of the four-stranded template structure (Zhao et al., 2015). A one-step synthesis method for prepared high fluorescence bimetallic Cu-Au nanoclusters (Cu/Au BNCs) was proposed by Ai group. The fluorescence signals of Cu/Au BNCs exhibited reversible response and good sensitivity in the temperature range of 20–70°C (Nie et al., 2018). The Pd-based alloy nanomaterials have been successfully applied to temperature sensing in this paper.

Peroxidases are an important biocatalyst in organism, which can catalyze many kinds of biochemical reactions effectively, for example, they can deactivate toxic substances, oxidize fatty acids, regulate oxygen concentration and so on. Because of their incredible efficiency and high substrate specificity, they are of great importance in diagnosis and analysis (Guo et al., 2018). In recent years, nanozymes have attracted much attention due to their endogenous mimic enzymes similar to natural enzymes, it can catalyze substrate reaction (Yan et al., 2018). Compared with natural enzymes, nano-enzyme production process is simple and economical, and it has excellent robustness and stability. In the past, researchers have found that various nanomaterials possess catalytic properties of peroxidase-like enzymes. Among many nanomaterials, inorganic nanomaterials have also attracted attention, including metal oxides V_2O_3 (Han et al., 2015), NiO (Liu et al., 2015), CuO (Wang et al., 2013; Chen M. et al., 2017), CeO_2 (Liu et al., 2017a; Sun et al., 2017; Ge et al., 2019; Yang et al., 2019), and sulfides ZnS

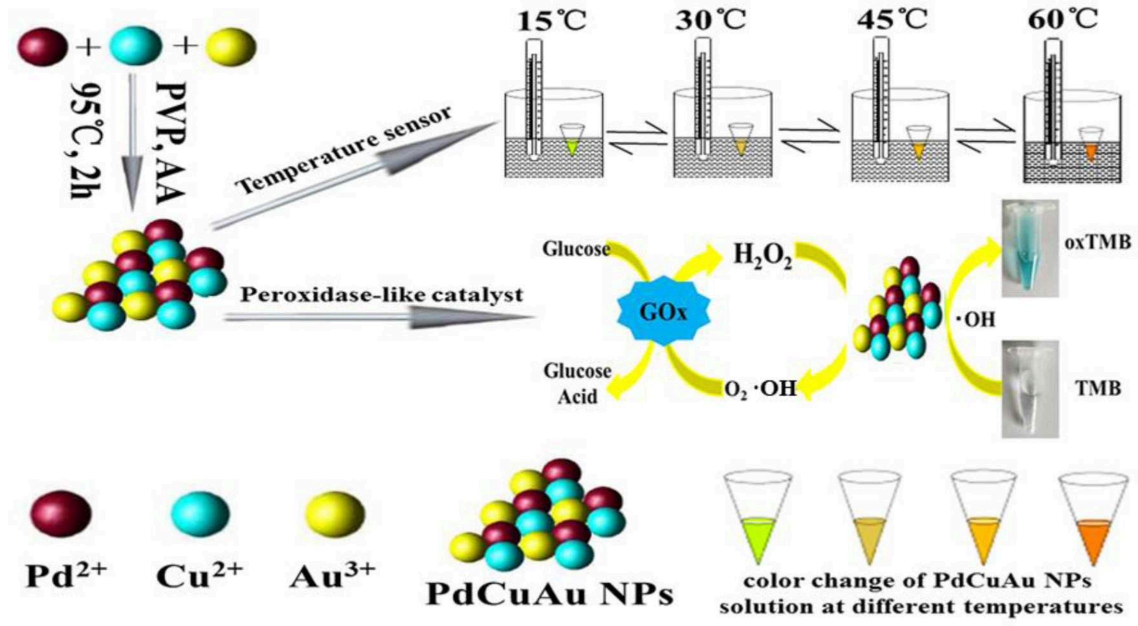

SCHEME 1 | Synthesis of PdCuAu NPs and their application as temperature sensors and colorimetric detection of H_2O_2 and glucose with enzyme mimic.

(Liu et al., 2017b), CdS (Liu et al., 2014), CuS (Zhang et al., 2017a) etc. Compared to the analytical methods including electrochemistry (Niu et al., 2013), fluorescence (Hu et al., 2014; Shan et al., 2014), chemiluminescence (Luo et al., 2015), mass spectroscopy (Chen et al., 2012), colorimetric detection method has the advantages of low cost, high selectivity and strong practicability, and is favored by researchers. In addition, because the color change of the substrate does not require any complicated instrument, it is easy to observe with the naked eye, so it has a wide range of applications in many fields (Ding et al., 2017).

Herein, we report a one-step synthesis of trimetallic PdCuAu nanoparticles (NPs) in aqueous phase without any intermediates. The sensitive fluorescence signals of PdCuAu NPs are reversible and recyclable in the range of 4–95°C. The prepared PdCuAu NPs show superior catalytic activity and sensitive in answer to the chromogenic substrate TMB, it can catalyze TMB in the presence of H_2O_2. So, the flow chart for the preparation of PdCuAu NPs and the application of PdCuAu NPs as temperature sensors and peroxidase-like enzymatic reactions are described in **Scheme 1**.

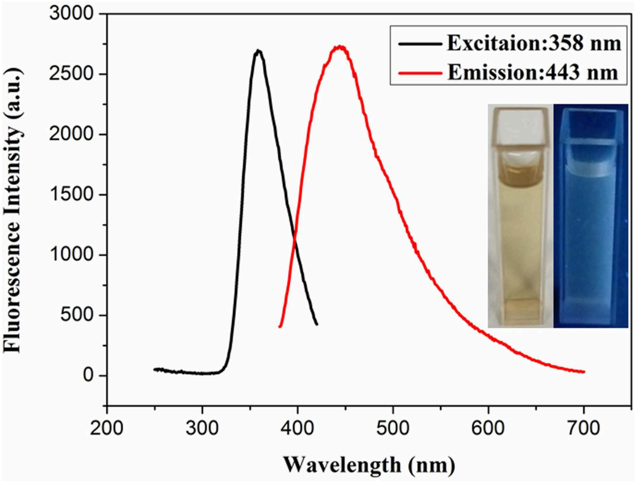

FIGURE 1 | Fluorescence spectra of PdCuAu NPs. [Insets, the left panel was shown in visible light, and the right was viewed under UV radiation (365 nm)].

RESULTS AND DISCUSSION

Optimization and Characterization of the Synthesis Conditions of PdCuAu NPs

This is a very simple and easy to operate synthesis process: take 355 μ L H_2PdCl_4 solution (56.4 mm), 1 ml Cu $(NO_3)_2$ solution (0.1 M), and 412 μ L $HAuCl_4$ solution (48.6 mM) and mix them evenly, and then add 500 μ L HCl (10%), 100 mg KBr and 50 mg PVP into them after ultrasonic degradation, and then add 2 ml ascorbic acid (AA) (0.1 M) After heating the mixed solution in a water bath at 95°C and stirring for 2 h, the primary product PdCuAu NPs is obtained after natural cooling. The primary product PdCuAu NPs is centrifuged at a centrifugal rate of 5,000 rpm for 15 min, and then the supernatant and sediment are centrifuged. The purified final product is stored in 4 In the environment of °C, it is used for the following analysis and characterization experiments, i.e., ultraviolet spectrum analysis, fluorescence spectrum analysis, transmission electron microscopy test, infrared spectrum test, XRD and XPS test.

The reaction mixture was heated for 2 h by simple heat treatment at 95°C in a water bath. The obtained tri-metallic PdCuAu NPs were canary yellow in water phase (see **Figure 1**, inset, left). The pale blue fluorescence was observed in the PdCuAu NPs solution under UV illumination at 365 nm (see **Figure 1**, inset, right), and the PdCuAu NPs are excited at 358 nm and emit at 443 nm. Typical magnification transmission electron microscopy (TEM) and high-resolution TEM (HRTEM) images of the as-prepared product are shown in **Figure 2**. Their particles are distributed between 10 and 25 nm, with an average particle size of 13 nm (see **Figures 2a,b**). Since the measured lattice distance of PdCuAu NPs are 0.2106 nm, the lattice fringes of PdCuAu NPs are assigned to the (111) plane of the Fourier filtering image (see **Figures 2c,d**).

The crystal structure of PdCuAu NPs is measured by XRD. As shown in **Figure 3A**, the representative diffraction peaks at 38.18, 40.12, 44.39, 64.58, and 77.55° are assigned to the (111), (111), (200), (220), and (311) planes of PdCuAu NPs, respectively. The peak positions of PdCuAu NPs are all situated between the homologous peaks of pure Au (JCPDS card no. 04-0784) and Pd (JCPDS card no. 46-1043), which confirm the formation of PdCuAu alloy. Both the HRTEM pattern (see **Figures 2c,d**) and from the XRD analysis (see **Figure 3A**), we can see that PdCuAu NPs show good crystallinity. The surface properties of PVP and CuAu, PdAu, PdCu, and PdCuAu NPs were characterized by FT-IR spectrometer. Exactly as shown in **Figure 3B**, the peak at 3,445 and 1,075 cm^{-1} were the characteristic absorption peak of the N-H stretching vibration of PVP, 2,955 cm^{-1} for the C-H stretching vibration of aromatic ring, 2,141 cm^{-1} for the stretching vibration of C-H outside the surface, 1,660 and 1,441 cm^{-1} for the C-C stretching vibration of aromatic ring skeleton, 1,294 cm^{-1} for the C-N stretching vibration of aromatic hydrocarbons. By comparison, the peak at 2,955 and 2,141 cm^{-1} disappeared in PdCuAu NPs, it indicates the breakup of C-H bond and the formation of new copper compounds. As determined by the TEM-EDS analysis, the atomic percentage of Pd in these nanocrystals is 42.14% and Au in these nanocrystals is 55.62%, the atomic ratio of Pd/Au in the as-prepared sample is ∼1:1 (see **Figure S1**). Among the TEM-EDS pattern (see **Figure S1**), FT-IR pattern (see **Figure 3B**) and XPS pattern (see **Figure 3C**) show that the formation of copper compounds. The surface chemical composition and valence state of PdCuAu NPs were further studied by X-ray photoelectron spectroscopy (XPS). As shown in **Figure 3C**, the Pd 3d region of the sample can be divided into two pairs of doublets. Two Pd 3d peaks are located at 335.6 and 340.9 eV, corresponding to the Pd $3d_{5/2}$ and Pd $3d_{3/2}$ states of metallic Pd, respectively. The binding energies at 932.4 and 952.3 eV correspond to Cu $2p_{3/2}$ and Cu $2p_{1/2}$ by fitting these peaks, which are assigned to Cu^+ and

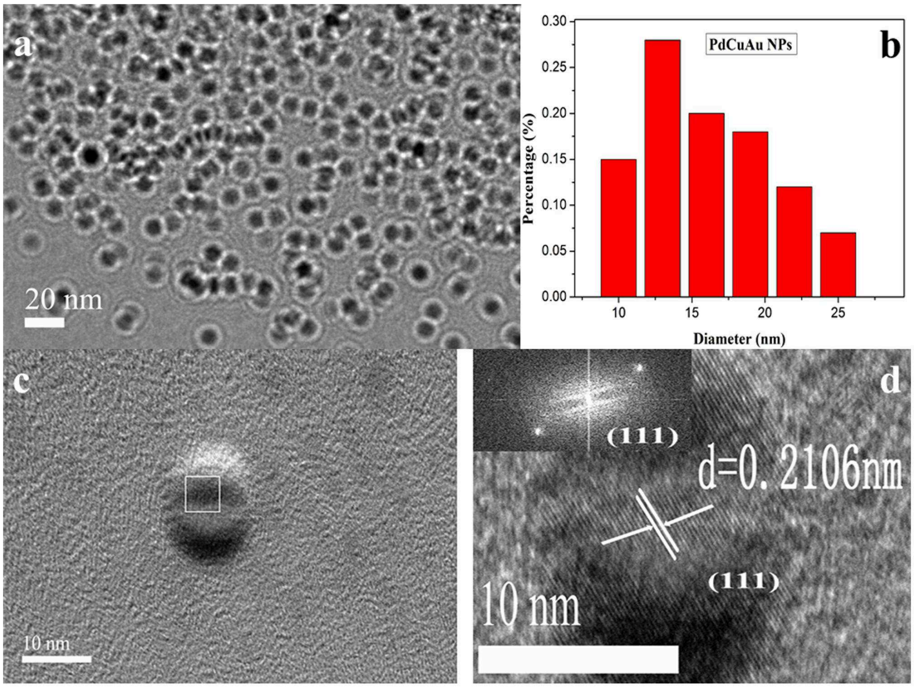

FIGURE 2 | (a) TEM images of the PdCuAu NPs. **(b)** The size distribution of PdCuAu NPs. **(c)** HRTEM image of the PdCuAu NPs. **(d)** The lattice fringes in the square area in **(c)** and the inset displays the corresponding FFT pattern.

Cu^{2+}, respectively. Similarly, the peaks at 83.8 and 87.5 eV are attributed to Au $4f_{7/2}$ and Au $4f_{5/2}$ by fitting these peaks, it is proved that Au^{3+} is reduced to Au^0. Therefore, Pd and Au are the main species of PdCuAu NPs, so PdCuAu NPs have the potential to be effective catalysts.

Some controlled contrast experiments were carried out to explore the influencing factors in the process of synthesizing PdCuAu NPs. Pd/Cu/Au molar ratio, (Pd/Cu/Au = 1:1:1, 1:2:1, 1:1:2 mol/mol) were researched and the corresponding fluorescence spectra were shown in **Figure S2A**. The optimal Pd/Cu/Au molar ratio is 1:5:1, the fluorescence intensity of PdCuAu NPs (1:5:1) are the strongest (see **Figure S2B**) and it can also be obtained from the TEM image that the dispersion of PdCuAu NPs (1:5:1) are the best and the particle size is uniformity (see **Figure S3**). **Figure S4** showed that the PdCuAu NPs exhibited the maximum fluorescence intensity under a water bath at 95°C for 2 h. If the time is too short, the temperature is too low, and the reaction may not be complete, resulting in agglomeration of PdCuAu NPs (see **Figures S5**, **S6**). By comparison, the fluorescence intensity of CuAu, PdAu, PdCu NPs are weak and the products tended to aggregate (see **Figures S7A**, **S8**). If there is no Br^- in the reaction, irregular and agglomerated PdCuAu NPs can be obtained, which fully shows that Br- plays a key role in the formation of PdCuAu NPs (see **Figures S7B**, **S9**). In addition, Cu^{2+} plays a very important role in controlling the morphology and fluorescence of PdCuAu NPs. For bimetallic PdAu, if Cu^{2+} is not added, the resulting nanoparticles are irregular, and these nanoparticles were exhibited weak fluorescence intensity (see **Figures S7B**, **S9**). When PVP is not added in the preparation process, many large particles will be obtained and serious agglomeration will occur. Copolymer PVP as a template can effectively improve the dispersion of nucleated nanoparticles and reduce the possibility of agglomeration (see **Figures S6B**, **S8**). Moreover, we also found that HCl has a significant effect on the morphology and fluorescence of PdCuAu NPs. In the absence of HCl, agglomerated and irregular nanoparticles were formed due to their rapid reduction kinetics (see **Figures S7B,C**, **S10**). Because HCl can reduce the reduction ability of ascorbic acid, the reduction rate of metal salt precursors in the reactants will be reduced when HCl is added to the reaction system. According to the above control experiments, we synthesized the PdCuAu NPs in a water bath at 95°C for 2 h with a molar ratio of Pd/Cu/Au equal to 1:5:1. The optical stability of PdCuAu NPs was further studied by fluorescence spectroscopy, as shown in **Figure S11**. With the passage of time, the fluorescence intensity of PdCuAu NPs was monitored periodically by fluorescence characterization. The results showed that the fluorescence intensity of PdCuAu NPs changed little within 45 days. Therefore, PdCuAu NPs have good stability.

Fluorescence Detection for Temperature Sensor

In recent years, there is little research on temperature sensors, and the PdCuAu NPs prepared in this paper have a good response by fluorescence detection in a wide temperature

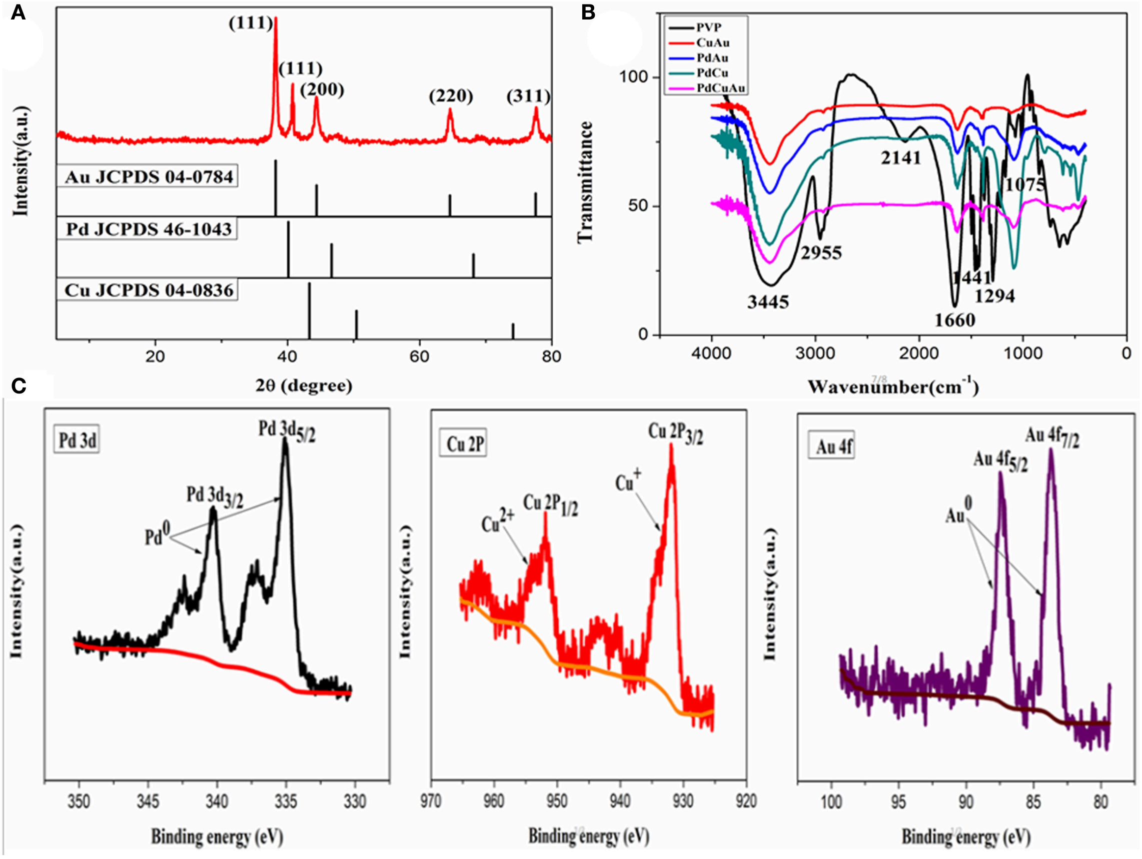

FIGURE 3 | (A) XRD pattern of PdCuAu NPs, the standard patterns of pure Au (JCPDS card no. 04-0784), Pd (JCPDS card no. 46-1043) and Cu (JCPDS card no. 04-0836) are shown for comparison. **(B)** FT-IR spectra of pure PVP, CuAu, PdAu, PdCu, and PdCuAu NPs. **(C)** X-ray photoelectron spectroscopy spectra of Pd 3d, Cu 2p, and Au 4f of the as-prepared PdCuAu NPs.

range of 4–95°C. Therefore, PdCuAu NPs has potential application as a temperature sensor. As shown in **Figure 4A**. The fluorescence intensity of PdCuAu NPs decreased with the increase of temperature, but the emission peak position of PdCuAu NPs did not shift in the temperature range studied. The reason for this phenomenon may be due to the thermal motion of the non-radiative process, that is to say, the frequency of collision and the rate of non-radiative transition of the molecule will increase at high temperature, thus reducing the emission intensity of the excited state (Wang C. et al., 2015; Wang et al., 2016; Jiang et al., 2017). In the temperature range of 4–95°C, the linear relationship between fluorescence intensity and temperature is illustrated in **Figure 4B**, the linear equation was $F = -29.03T + 3{,}204$ ($R = 0.9988$). Furthermore, the recyclability and reversibility of resultant PdCuAu NPs based on a fluorescent thermometer were also investigated. As revealed in **Figure 4C**, the response of PdCuAu NPs to temperature is reversible. After heating and cooling, the reversible process can repeat at least eight cycles without obvious change of fluorescence signal. The results show that PdCuAu NPs have excellent reutilization in response to temperature changes.

Peroxidase-Like Catalytic Activity of PdCuAu NPs

In order to explore the catalytic activity of PdCuAu NPs, the peroxidase activity of PdCuAu NPs was studied with TMB as chromogenic substrate. The top of **Figure 5B** point out the color changes in different environments. When there is H_2O_2 in the reaction system, PdCuAu NPs can catalyze the oxidation of TMB to produce typical blue products visible to the naked eye, indicating that PdCuAu NPs have the peroxidase activity. Like natural peroxidase HRP, temperature and pH are important factors affecting the catalytic activity of PdCuAu NPs. The peroxidase-like activity of PdCuAu NPs at different pH environments (3.5–6.0) and temperatures (25–60°C) was studied (see **Figure S12**). The catalytic activity of PdCuAu NPs increases with the increase of pH. When the pH is equal to 5.0, the catalytic activity of PdCuAu NPs reaches the maximum. If the pH < 5.0, the catalytic activity of PdCuAu NPs decreases, this

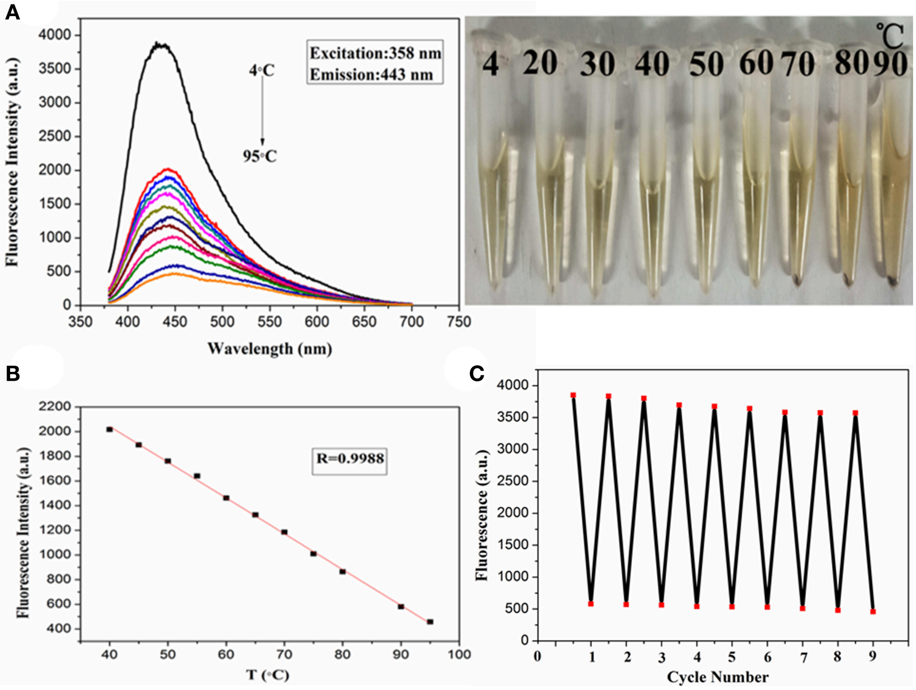

FIGURE 4 | (A) Fluorescence spectra of PdCuAu NPs with temperature ranging from 4 to 95°C. **(B)** The linear relationship between changes of temperature and fluorescence intensity. **(C)** The fluorescence response of eight cycles at 4–95°C.

is because pH < 2 easily produces yellow diimine, and pH > 5 will accelerate the decomposition of hydrogen peroxide (see **Figure S12A**). Besides, the effect of temperature on PdCuAu NPs also discussed, because temperature can accelerate enzymatic reaction, but too high temperature will lead to inactivation of enzymatic reaction, so there is an optimum temperature for enzymatic reaction. The optimum temperature for enzymatic reaction in this study is 40°C (see **Figure S12B**). For the comparative experiment of catalytic activity of PdCuAu NPs, the steady-state kinetics method was used in this experiment. A typical Michaelis-Menten curve was obtained by controlling the concentration of one peroxidase substrate unchanged and then changing the concentration of another peroxidase substrate (see **Figures S13A–D**). In **Table S1**, we can see the kinetic parameters of enzymes derived from Lineweaver-Burk. As everyone knows that K_m can express the affinity of specific enzymes to substrates. When the K_m value is small, the affinity between enzyme and substrate is strong, whereas a weaker affinity. It can be drawn from **Table S1**, the K_m value of PdCuAu NPs with H_2O_2 as the substrate was low. On the one hand, the K_m value of PdCuAu NPs with TMB as substrate was low, which indicates that PdCuAu NPs have strong affinity with TMB. In addition, the K_m of PdCuAu NPs as shown in **Table S1** is lower than that of other reported materials. Therefore, in subsequent experiments, we chose pH $= 5.0$ and temperature was 40°C as the best reaction conditions. Because PdCuAu NPs have excellent catalytic performance, we designed a convenient, rapid and direct colorimetric method for the detection of H_2O_2. **Figures 5A,B** showed that the absorbance of TMB is positively correlated with the concentration of H_2O_2 at 652 nm with the $R = 0.9975$. The linear regression equation obtained was $A = 6.95 \times 10^{-3}$ $[H_2O_2] + 0.04713$ with a linear range of 0.1–300 µM. When the signal-to-noise ratio (S/N) is 3, the calculated LOD = 5 nM, which is much lower than the detection limit of other reported nanomaterials, for instance Co_3O_4 NPs (Ding et al., 2017) GQDs/CuO nanocomposites (Zhang et al., 2017b). GOx can catalyze the oxidation of glucose to produce H_2O_2, that is to say, PdCuAu NPs as a peroxidase coupled with GOx to simulate the above-mentioned TMB-H_2O_2 system to indirectly detect glucose (see **Scheme 1**). As shown in **Figure 6A**, when the maximum absorption wavelength is 652 nm, the absorbance increases with the increase of glucose concentration. The linear range of the standard curve of absorbance changes with glucose concentration is 0.5–500 µM with the $R = 0.9928$ and the linear regression equation obtained was $A = 6.512 \times 10^{-4}$ [glucose] $+ 0.04484$. When the signal-to-noise ratio (S/N) is 3, the LOD of this method is as low as 25 nM, which is much lower than the LOD reported in the previous literature, such as Pt nanoclusters (Jin et al., 2017), $NiCo_2O_4$/3DGF (Wu et al., 2015). The color change of different concentration of glucose solution can be observed with eyes very clearly (top of **Figure 6B**). PdCuAu NPs detection system shows a wide linear range and it has excellent sensitivity to glucose. The selectivity of glucose/GOx/PdCuAu NPs/TMB system was also studied. under the same conditions, we selected several other sugars (fructose, sucrose, lactose and maltose) for the comparative

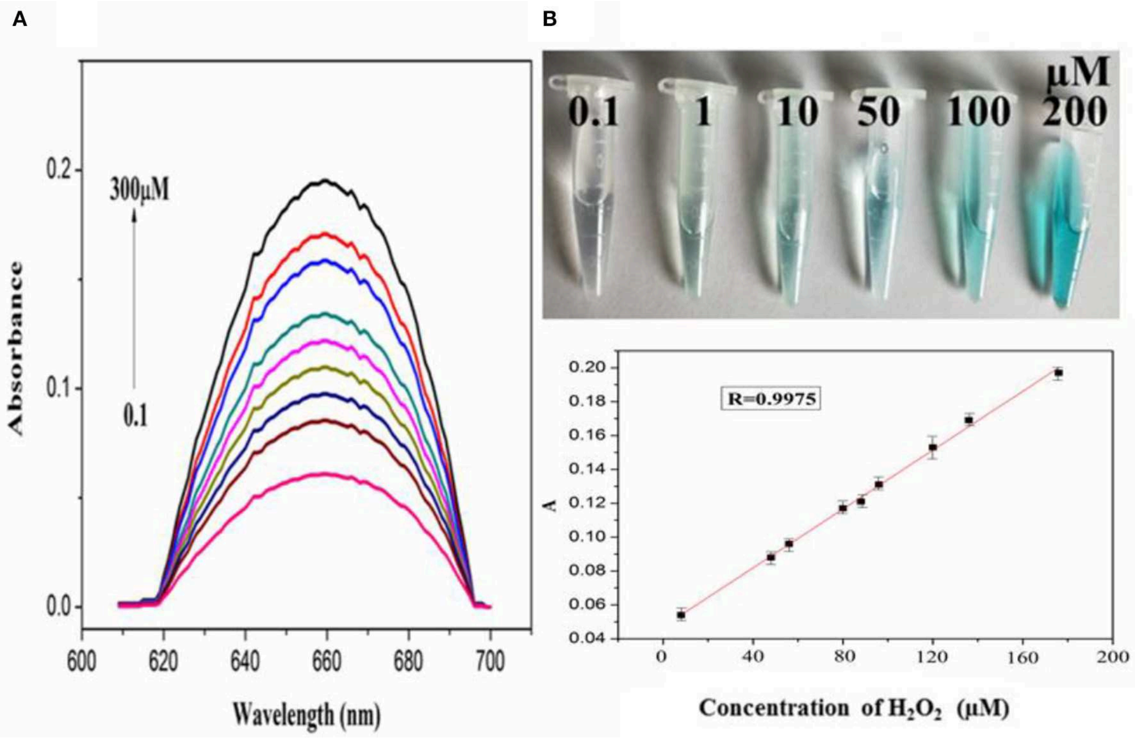

FIGURE 5 | (A) The absorption spectra of PdCuAu NPs and TMB system upon adding different concentrations of H_2O_2 (0.1–300 μM, from bottom to top). **(B)** The corresponding linear calibration plots for H_2O_2, top: the corresponding color changes.

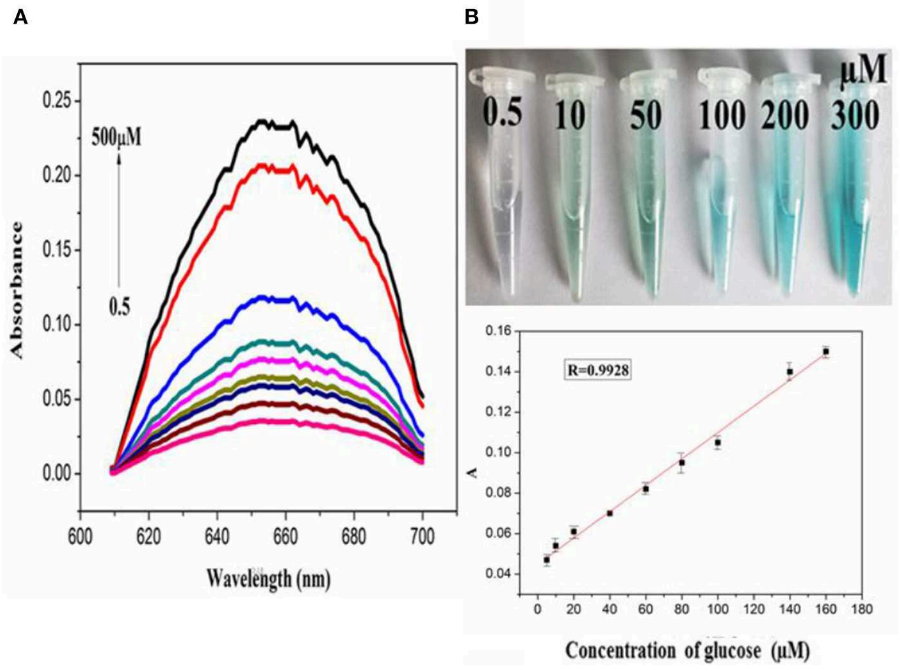

FIGURE 6 | (A) The absorption spectra of PdCuAu NPs and TMB system upon adding different concentrations of glucose (0.5–500 μM, from bottom to top). **(B)** The corresponding linear calibration plots for glucose, top: the corresponding color changes.

experiment. We can get it from **Figure S14**, glucose analogs had little interference in the detection of glucose. This indicates that the system of glucose/GOx/PdCuAu NPs/TMB has high selectivity for the detection of glucose due to the specificity of GOx. Therefore, glucose sensor based on PdCuAu NPs can be established successfully.

CONCLUSIONS

In conclusion, the synthesis of polymetallic nanomaterials requires very stringent conditions. This is because it is difficult to control the reduction and nucleation process of metal salt precursors in the reactants, so we successfully prepared PdCuAu NPs by a very simple one-pot synthesis method in this experiment. The method is simple in operation, mild in reaction conditions and does not require multi-step synthesis. Moreover, the growth mechanism of PdCuAu NPs was also studied through a series of control experiments. The resultant PdCuAu NPs show remarkable features including fluorescence properties and superior catalytic activity. The research shows that it has good sensitivity to temperature change and good linear relationship, so it can be used in thermal imaging of biological environment. Additionally, the prepared PdCuAu NPs have peroxidase-like catalytic properties. It can catalyze TMB in the presence of H_2O_2 to produce color reaction, and the whole experimental process only takes 10 min. Therefore, we constructed a colorimetric sensor with high selectivity and rapid response using PdCuAu NPs as mimetic enzymes, and applied it to the detection of H_2O_2 and glucose. The synthesized PdCuAu NPs have excellent temperature sensors and catalytic performance for peroxidase-like enzymes. The PdCuAu NPs have good stability. However, It is not clear which metal of the three metal system has peroxidase properties. According to these studies, this kind of PdCuAu NPs-based sensor has a promising prospect in the biological chemistry.

DATA AVAILABILITY STATEMENT

All datasets generated for this study are included in the article/**Supplementary Material**.

AUTHOR CONTRIBUTIONS

FN, LG, JA, and YW conceived and carried out experiments, analyzed data, and wrote the paper. All authors read and approved the final manuscript.

FUNDING

This work was supported by the National Natural Science Foundation of China (Grant no. 21864020), the Natural Science Foundation of Inner Mongolia (Grant no. 2018MS02012), Collaborative Innovation Center for Water Environmental Security of Inner Mongolia Autonomous Region, China, (Grant no. XTCX003), Young Science and Technology Talents Program (Leading Person) in Inner Mongolia Autonomous Region Colleges and Universities (Grant no. NJYT-19-A04).

SUPPLEMENTARY MATERIAL

The Supplementary Material for this article can be found online at: https://www.frontiersin.org/articles/10.3389/fchem.2020.00244/full#supplementary-material

REFERENCES

Chen, D., Sun, P., Liu, H., and Yang, J. (2017). Bimetallic Cu–Pd alloy multipods and their highly electrocatalytic performance for formic acid oxidation and oxygen reduction. *J. Mater. Chem. A* 5, 4421–4429. doi: 10.1039/C6TA10476B

Chen, M., Ding, Y., Gao, Y., Zhu, X., Wang, P., Shi, Z., et al. (2017). N, N′-di-caboxy methyl perylene diimides (PDI) functionalized CuO nanocomposites with enhanced peroxidase-like activity and their application in visual biosensing of H_2O_2 and glucose. *RSC Adv.* 7, 25220–25228. doi: 10.1039/C7RA04463A

Chen, R., Xu, W., Xiong, C., Zhou, X., Xiong, S., Nie, Z., et al. (2012). High-salt-tolerance matrix for facile detection of glucose in rat brain Microdialysates by MALDI mass spectrometry. *Anal. Chem.* 84, 465–469. doi: 10.1021/ac202438a

Cho, Y.-H., Kim, O.-H., Chung, D. Y., Choe, H., Cho, Y.-H., and Sung, Y.-E. (2014). PtPdCo ternary electrocatalyst for methanol tolerant oxygen reduction reaction in direct methanol fuel cell. *Appl. Catal. B Environ.* 154–155, 309–315. doi: 10.1016/j.apcatb.2014.02.016

Ding, Y., Chen, M., Wu, K., Chen, M., Sun, L., Liu, Z., et al. (2017). High-performance peroxidase mimics for rapid colorimetric detection of H_2O_2 and glucose derived from perylene diimides functionalized Co_3O_4 nanoparticles. *Mater. Sci. Eng. C* 80, 558–565. doi: 10.1016/j.msec.2017.06.020

Dubau, L., Asset, T., Chattot, R., Bonnaud, C., Vanpeene, V., Nelayah, J., et al. (2015). Tuning the performance and the stability of porous hollow PtNi/C nanostructures for the oxygen reduction reaction. *ACS Catal.* 5, 5333–5341. doi: 10.1021/acscatal.5b01248

Ge, J., Yang, X., Luo, J., Ma, J., Zou, Y., Li, J., et al. (2019). Ordered mesoporous CoO/CeO2 heterostructures with highly crystallized walls and enhanced peroxidase-like bioactivity. *Appl. Mater. Today* 15, 482–493. doi: 10.1016/j.apmt.2019.03.009

Guo, J., Wang, Y., and Zhao, M. (2018). 3D flower-like ferrous(II) phosphate nanostructures as peroxidase mimetics for sensitive colorimetric detection of hydrogen peroxide and glucose at nanomolar level. *Talanta* 182, 230–240. doi: 10.1016/j.talanta.2018.01.080

Guo, S., Zhang, X., Zhu, W., He, K., Su, D., Mendoza-Garcia, A., et al. (2014). Nanocatalyst superior to Pt for oxygen reduction reactions: the case of core/shell Ag(Au)/CuPd nanoparticles. *J. Am. Chem. Soc.* 136, 15026–15033. doi: 10.1021/ja508256g

Han, L., Zeng, L., Wei, M., Li, C., and Liu, A. (2015). Mesoporous carbon composite with novel per-oxidase-like activity towards glucose colorimetric assay. *Nano* 7, 11678–11685. doi: 10.1039/C5NR02694F

Hu, A. L., Liu, Y. H., Deng, H. H., Hong, G. L., Liu, A. L., Lin, X. H., et al. (2014). Fluorescent hydrogen peroxide sensor based on cupric oxide nanoparticles and its application for glucose and L-lactate detection. *Biosens. Bioelectron.* 61, 374–378. doi: 10.1016/j.bios.2014.05.048

Huang, X. Q., Zhao, Z. P., Chen, Y., Zhu, E. B., Li, M. F., Duan, X. F., et al. (2014). A rational design of carbon-supported dispersive Pt-based octahedra as efficient oxygen reduction reaction catalysts. *Energy Environ. Sci.* 7, 2957–2962. doi: 10.1039/C4EE01082E

Hwang, S. J., Yoo, S. J., Jang, S., Lim, T.-H., Hong, S. A., and Kim, S.-K. (2011). Ternary Pt–Fe–Co alloy electrocatalysts prepared by electrodeposition:

elucidating the roles of Fe and Co in the oxygen reduction reaction. *J. Phys. Chem. C* 115, 2483–2488. doi: 10.1021/jp106947q

Jiang, G., Zhu, H., Zhang, X., Shen, B., Wu, L., Zhang, S., et al. (2015). Core/Shell face-centered tetragonal FePd/Pd nanoparticles as an efficient non-Pt catalyst for the oxygen reduction reaction. *ACS Nano* 9, 11014–11022. doi: 10.1021/acsnano.5b04361

Jiang, K., Wang, P., Guo, S., Zhang, X., Shen, X., Lu, G., et al. (2016). Ordered PdCu-based nanoparticles as bifunctional oxygen-reduction and ethanol-oxidation electrocatalysts. *Angew. Chem. Int. Ed.* 55, 9030–9035. doi: 10.1002/anie.201603022

Jiang, K., Wu, J., Wu, Q., Wang, X., Wang, C., and Li, Y. (2017). Stable fluorescence of green-emitting carbon nanodots as a potential nanothermometer in biological media. *Part. Part. Syst. Charact.* 34:1600197. doi: 10.1002/ppsc.201600197

Jin, L., Meng, Z., Zhang, Y., Cai, S., Zhang, Z., Li, C., et al. (2017). Ultrasmall Pt nanoclusters as robust peroxidase mimics for colorimetric detection of glucose in human serum. *ACS Appl. Mater. Interfaces* 9, 10027–10033. doi: 10.1021/acsami.7b01616

Khan, M., Yousaf, A. B., Chen, M. M., Wei, C. S., Wu, X. B., Huang, N. D., et al. (2015). Mixed-phase Pd–Pt bimetallic alloy on graphene oxide with high activity for electrocatalytic applications. *J. Power Sources* 282, 520–528. doi: 10.1016/j.jpowsour.2015.02.090

Li C., Wang H., Li Y., Yu H., Yin S., Xue H. et al. (2018). Tri-metallic PtPdAu mesoporous nanoelectrocatalysts. *Nanotechnology* 29, 255404–255413. doi: 10.1088/1361-6528/aabb47

Li, B. S., and Chan, S. H. (2013). PtFeNi tri-metallic alloy nanoparticles as electrocatalyst for oxygen reduction reaction in proton exchange membrane fuel cells with ultra-low Pt loading. *Int. J. Hydrog. Energ.* 38, 3338–3345. doi: 10.1016/j.ijhydene.2013.01.049

Liu, Q., Chen, P., Xu, Z., Chen, M., Ding, Y., Yue, K., et al. (2017b). A facile strategy to prepare porphyrin functionalized ZnS nanoparticles and their peroxidase-like catalyty for colorimetric sensor of hydrogen peroxide and glucose. *Sens. Actuat. B Chem.* 251, 339–348. doi: 10.1016/j.snb.2017.05.069

Liu, Q., Jia, Q., Zhu, R., Shao, Q., Wang, D., Cui, P., et al. (2014). 5,10,15,20-Tetrakis(4-carboxylphenyl)porphyrin–CdS nanocomposites with intrinsic peroxidase-like activity for glucose colorimetric detection. *Mater. Sci. Eng. C* 42, 177–184. doi: 10.1016/j.msec.2014.05.019

Liu, Q., Yang, Y., Lv, X., Ding, Y., Zhang, Y., Jing, J., et al. (2017a). One-step synthesis of uniform nanoparticles of porphyrin functionalized ceria with promising peroxidase mimetics for H_2O_2 and glucose colorimetric detection. *Sens. Actuat. B Chem.* 240, 726–734. doi: 10.1016/j.snb.2016.09.049

Liu, Q. Y., Yang, Y. T., Li, H., Zhu, R. R., Shao, Q., Yang, S. G., et al. (2015). NiO nanoparticles modified with 5, 10, 15, 20-tetrakis (4-carboxylpheyl)-porphyrin: promising peroxidase mimetics for H_2O_2 and glucose detection. *Biosens. Bioelectron.* 64, 147–153. doi: 10.1016/j.bios.2014.08.062

Luo, F., Lin, Y., Zheng, L., Lin, X., and Chi, Y. (2015). Encapsulation of hemin in metal–organic frameworks for catalyzing the chemiluminescence reaction of the H_2O_2-Luminol system and detecting glucose in the neutral condition. *ACS Appl. Mater. Interfaces* 7, 11322–11329. doi: 10.1021/acsami.5b01706

Luo, S., and Shen, P. K. (2017). Concave platinum–copper octopod nanoframes bounded with multiple high-index facets for efficient electrooxidation catalysis. *ACS Nano* 11, 11946–11953. doi: 10.1021/acsnano.6b04458

Nie, F. R., Ga, L., Ai, J., and Wang, Y. (2018). Synthesis of highly fluorescent Cu/Au bimetallic nanoclusters and their application in a temperature sensor and fluorescent probe for chromium(III) ions. *RSC Adv.* 8, 13708–13713. doi: 10.1039/C8RA02118J

Niu, X., Lan, M., Zhao, H., and Chen, C. (2013). Highly sensitive and selective Nonenzymatic detection of glucose using three-dimensional porous nickel nanostructures. *Anal. Chem.* 85, 3561–3569. doi: 10.1021/ac3030976

Oemrawsingh, S. S. R., Markešević, N., Gwinn, E. G., Eliel, E. R., and Bouwmeester, D. (2012). Spectral properties of individual DNA-hosted silver nanoclusters at low temperatures. *J. Phys. Chem. C* 116, 25568–25575. doi: 10.1021/jp307848t

Shan, X. Y., Chai, L. J., Ma, J. J., Qian, Z. S., Chen, J. R., and Feng, H. (2014). B-doped carbon quantum dots as a sensitive fluorescence probefor hydrogenperoxide andglucose detection. *Analyst* 139, 2322–2325. doi: 10.1039/C3AN02222F

Song, P., Liu, L., Wang, A.-J., Zhang, X., Zhou, S.-Y., and Feng, J.-J. (2015). One-pot synthesis of platinum–palladium–cobalt alloyed nanoflowers with enhanced electrocatalytic activity for ethylene glycol oxidation. *Electrochim. Acta*. 164, 323–329. doi: 10.1016/j.electacta.2015.02.229

Sriphathoorat, R., Wang, K., Luo, S. P., Tang, M., Du, H. Y., Du, X. W., et al. (2016). Well-defined PtNiCo core–shell nanodendrites with enhanced catalytic performance for methanol oxidation. *J. Mater. Chem. A* 4, 18015–18021. doi: 10.1039/C6TA07370K

Sun, L., Ding, Y., Jiang, Y., and Liu, Q. (2017). Montmorillonite-loaded ceria nanocomposites with superior peroxidase-like activity for rapid colorimetric detection of H_2O_2. *Sensor. Actuat. B Chem*. 239, 848–856. doi: 10.1016/j.snb.2016.08.094

Tang, M., Luo, S. P., Wang, K., Du, H. Y., Rinrada, S., and Shen, P. K. (2018). Simultaneous formation of trimetallic Pt-Ni-Cu excavated rhombic dodecahedrons with enhanced catalytic performance for the methanol oxidation reaction. *Nano Res.* 11, 4786–4795. doi: 10.1007/s12274-018-2063-3

Tian, L. L., Chen, Y. L., Wu, S. P., Cai, Y. H., Liu, H. D., Zhang, J., et al. (2017). One-pot synthesis of cubic PtPdCu nanocages with enhanced electrocatalytic activity for reduction of H_2O_2. *RSC Adv.* 7, 34071–34076. doi: 10.1039/C7RA03220J

Wang, C., Lin, H., Xu, Z., Huang, Y., Humphrey, M. G., and Zhang, C. (2016). Tunable carbon-dot-based dual-emission fluorescent nanohybrids for ratiometric optical thermometry in living cells. *ACS Appl. Mater. Interfaces* 8, 6621–6628. doi: 10.1021/acsami.5b11317

Wang, C., Ling, L., Yao, Y., and Song, Q. (2015). One-step synthesis of fluorescent smart thermo-responsive copper clusters: a potential nanothermometer in living cells. *Nano Res.* 8, 1975–1986. doi: 10.1007/s12274-015-0707-0

Wang, H. J., Yin, S. L., Li, Y. H., Yu, H. J., Li, C. J., Deng, K., et al. (2018). One-step fabrication of tri-metallic PdCuAu nanothorn assemblies as an efficient catalyst for oxygen reduction reaction. *J. Mater. Chem. A*. 6, 3642–3648. doi: 10.1039/C7TA10342E

Wang, X., Choi, S. I., Roling, L. T., Luo, M., Ma, C., Zhang, L. et al. (2015). Palladium-platinum core-shell icosahedra with substantially enhanced activity and durability towards oxygen reduction. *Nat. Commun.* 6:7594. doi: 10.1038/ncomms8594

Wang, Z., von dem Bussche, A., Kabadi, P. K., Kane, A. B., and Hurt, R. H. (2013). Biological and environmental transformations of copper-based nanomaterials. *ACS Nano* 7, 8715–8727. doi: 10.1021/nn403080y

Wu, M., Meng, S., Wang, Q., Si, W., Huang, W., and Dong, X. (2015). Nickel–cobalt oxide decorated three-dimensional graphene as an enzyme mimic for glucose and calcium detection. *ACS Appl. Mater. Interfaces* 7, 21089–21094. doi: 10.1021/acsami.5b06299

Xia, B. Y., Wu, H. B., Li, N., Yan, Y., Lou, X. W., Wang, X. (2015). One-pot synthesis of Pt-Co alloy nanowire assemblies with tunable composition and enhanced electrocatalytic properties. *Angew. Chem., Int. Ed*. 54, 3797–3801. doi: 10.1002/anie.201411544

Xu, G.-R., Liu, F.-Y., Liua, Z.-H., and Chen, Y. (2015). Ethanol-tolerant polyethyleneimine functionalized palladium nanowires in alkaline media: the "molecular window gauze" induced the selectivity for the oxygen reduction reaction. *J. Mater. Chem. A* 3, 21083–21089. doi: 10.1039/C5TA06644A

Xue, Q., Xu, G. R., Mao, R. D., Liu, H. M., Zeng, J. H., Jiang, J. X., et al. (2017). Polyethyleneimine modified AuPd@PdAu alloy nanocrystals as advanced electrocatalysts towards the oxygen reduction reaction. *J. Energy Chem*. 26, 1153–1159. doi: 10.1016/j.jechem.2017.06.007

Yan, G., Zhang, Y., and Di, W. (2018). An enzymatic reaction mediated glucose sensor activated by MnO_2 nanosheets acting as an oxidant and catalyst. *Analyst* 143, 2915–2922. doi: 10.1039/C8AN00657A

Yang, L., Zhang, Q., Cui, Z., Gerboth, M., Zhao, Y., Xu, T. T., et al. (2017). Ballistic phonon penetration depth in amorphous silicon dioxide. *Nano Lett.* 17, 7218–7225. doi: 10.1021/acs.nanolett.7b02380

Yang, X., Cheng, X., Ma, J., Zou, Y., Luo, W., and Deng, Y. (2019). Large-pore mesoporous CeO2–ZrO2 solid solutions with in-pore confined Pt nanoparticles for enhanced CO oxidation. *Small* 15:1903058. doi: 10.1002/smll.201903058

Yin, A. X., Min, X. Q., Zhu, W., Liu, W. C., Zhang, Y. W., and Yan, C. H. (2012). Pt-Cu and Pt-Pd-Cu concave nanocubes with high-index facets and superior electrocatalytic activity. *Chem. Eur. J.* 18, 777–782. doi: 10.1002/chem.201102632

Yousaf, A. B., Imran, M., Uwitonze, N., Zeb, A., Zaidi, S. J., Ansari, T. M., et al. (2017a). High-temperature and high-pressure pyrolysis of hexadecane: molecular dynamic simulation based on reactive force field (ReaxFF). *J. Phys. Chem. C* 121, 2069–2078. doi: 10.1021/acs.jpca.612367

Yousaf, A. B., Imran, M., Zaidi, S. J., Kasak, P., Ansari, T. M., Manzoor, S., et al. (2017b). Synergistic effect of interfacial phenomenon on enhancing catalytic performance of Pd loaded MnOx–CeO_2-C hetero-nanostructure for hydrogenation and electrochemical reactions. *J. Mater. Chem. A* 5, 10704–10712. doi: 10.1039/C7TA02122D

Zhang, L., Chen, M., Jiang, Y., Chen, M., Ding, Y., and Liu, Q. (2017a). A facile preparation of montmo rillonite supported copper sulfide nanocomposites and their application in the detection of H_2O_2. *Sens. Actuat. B Chem*. 239, 28–35. doi: 10.1016/j.snb.2016.07.168

Zhang, L., Hai, X., Xia, C., Chen, X. W., and Wang, J. H. (2017b). Growth of CuO nanoneedles on graphene quantum dots as peroxidase mimics for sensitive colorimetric detection of hydrogen peroxide and glucose. *Sens. Actuat. B Chem*. 248, 374–384. doi: 10.1016/j.snb.2017.04.011

Zhao, T. T., Chen, Q. Y., and Yang, H. (2015). Spectroscopic study on the formation of DNA-Ag clusters and its application in temperature sensitive vehicles of DOX. *Spectrochim. Spectrochim. Acta A Mol. Biomol. Spectrosc*. 137, 66–69. doi: 10.1016/j.saa.2014.08.025

Zhou, W. J., Zhu, J. B., Teng, Y., Du, B. J., Han, X., and Dong, S. J. (2018). Novel dual fluorescence temperature-sensitive chameleon DNA-templated silver nanocluster pair for intracellular thermometry. *Nano Res*. 11, 2012–2023. doi: 10.1007/s12274-017-1817-7

Conflict of Interest: The authors declare that the research was conducted in the absence of any commercial or financial relationships that could be construed as a potential conflict of interest.

frontiers in Chemistry

ORIGINAL RESEARCH
published: 05 June 2020
doi: 10.3389/fchem.2020.00463

A Novel Nanoprobe Based on Core–Shell Au@Pt@Mesoporous SiO_2 Nanozyme With Enhanced Activity and Stability for Mumps Virus Diagnosis

Lin Long[1,2†], *Rui Cai*[3,4†], *Jianbo Liu*[1*] *and Xiaochun Wu*[3,4*]

[1] *College of Opto-electronic Engineering, Zaozhuang University, Zaozhuang, China,* [2] *Zaozhuang Municipal Center for Disease Control and Prevention, Zaozhuang, China,* [3] *CAS Key Laboratory of Standardization and Measurement for Nanotechnology, CAS Center for Excellence in Nanoscience, National Center for Nanoscience and Technology, Beijing, China,* [4] *University of Chinese Academy of Sciences, Beijing, China*

Edited by:
Kelong Fan,
Institute of Biophysics (CAS), China

Reviewed by:
Hui Wei,
Nanjing University, China
Aiguo Wu,
Ningbo Institute of Materials Technology & Engineering (CAS), China

***Correspondence:**
Jianbo Liu
linyibm@163.com
Xiaochun Wu
wuxc@nanoctr.cn

†*These authors have contributed equally to this work*

Specialty section:
This article was submitted to Nanoscience,
a section of the journal Frontiers in Chemistry

Received: *17 February 2020*
Accepted: *04 May 2020*
Published: *05 June 2020*

Citation:
Long L, Cai R, Liu J and Wu X (2020) A Novel Nanoprobe Based on Core–Shell Au@Pt@Mesoporous SiO_2 Nanozyme With Enhanced Activity and Stability for Mumps Virus Diagnosis. Front. Chem. 8:463.
doi: 10.3389/fchem.2020.00463

Nanoporous materials with core-shell structure have received lots of attention owing to the great versatility of the functional cores and shells and their potential application in catalysis and biological applications. In this work, a facile method has been developed to synthesize uniform Au@Pt@mesoporous SiO_2 nanostructures with high peroxidase-like activity, which had a well-defined core–shell structure with Au nanorods@Pt nanodots as a core and mesoporous SiO_2 as a shell. The mesoporous SiO_2 shell can not only provide convenient transmission channels but offer a substantial location for accommodation of large biomolecules, such as antibodies and antigens. Here a novel nanoprobe based on Au@Pt@mesoporous SiO_2 nanozyme modified with mumps antigens was reported. Notably, the encapsulation of Au@Pt nanorod in mesoporous SiO_2 shell was able to hinder the interaction between catalytical nanoparticles and recognition antigens, retaining the catalytic activity of the inner active nanoparticle core. Furthermore, this nanoprobe exhibited an extraordinarily stability and showed excellent activity. As a result, we presented an enzyme linked immunosorbant assay (ELISA) for the diagnosis of mumps virus; this proposed method exhibited good sensitivity to mumps-specific IgM antibodies. The limit of detection can be as low as 10 ng/mL, which was more sensitive compared to the conventional immunoassay. Our results indicated that this nanoprobe hold great promise with opportunities for applications of biosensors, catalysis and biotechnology.

Keywords: Au nanorods, platinum, mesoporous SiO_2, core–shell, nanozyme, enhanced activity, virus diagnosis

INTRODUCTION

Mumps is a common childhood infectious disease caused by a the mumps virus. Although most cases of infection lead to a mild disease, orchitis, permanent deafness, and disability are some untoward effects of mumps (Galazka et al., 1999). A laboratory diagnosis of mumps is based on detection of viral nucleic acid using polymerase chain reaction (PCR), isolation of the virus from saliva or spinal fluid, or serological confirmation (Maillet et al., 2015). In the absence of successful virus isolation in cell-culture or reverse transcription-PCR (RT-PCR) detection, serological markers can provide a simple, and useful diagnosis (Hviid et al., 2008). A commonly used serological confirmation for the rapid diagnosis of mumps infection is demonstration of specific immunoglobulin M (IgM) class antibody (Krause et al., 2007). However, mumps-specific IgM antibodies might be low or undetectable if serum are collected before 4 days of clinical presentation, thus giving false-negative results (Warrener and Samuel, 2006). For this reason, a simple and sensitive laboratory diagnosis of mumps virus is needed. Among various efficient bioassays for diagnosing infectious diseases, natural enzyme labels have shown great potential in various bioassays, as they can catalyze various colorimetric reactions with good sensitivity and selectivity toward the target molecules (Gut et al., 1985). However, methods based on enzyme labels also have several limitations including the natural instability of proteins during long-term operation or storage (Rashidian et al., 2013). Nanozyme with catalytical-like activity have been emerging alternatives to natural enzymes in bioassays (Gao et al., 2007). The replacement of natural enzymes by catalytical nanomaterials in immunoassay may have advantages in several aspects, such as their shape- (structure-, size-, composition-) tunable catalytic activities, large surface area for bioconjugation and modification, greater resistance to extremes of pH and temperature, and so on (Wu et al., 2019).

Recently Pt nanoparticles have been found to exhibit catalase-like, superoxide dismutase (SOD)-like, peroxidase-like, and oxidase-like activities (Ma et al., 2011). Considering the size- and shape-dependent properties, nanosized Pt nanoparticles of 2∼4 nm diameter are found to have the excellent catalytic activity. However, small nanoparticles are unstable and tend to agglomerate to larger clusters, resulting in the loss of their original catalytic activity (Narayanan and El-Sayed, 2004). Various efforts have been made to fabricate novel nanostructures with higher activity and lower cost for catalytic applications (Zhang et al., 2007). In particular, gold nanoparticle has been regarded as a well-known bio-materials for their excellent biocompatibility and large specific surface area; thus, Pt covering Au or Au-Pt core–shell nanoparticle structure have been reported for a wide range of applications (Wu et al., 2018). Previously, our group found Au@Pt core/shell nanostructures exhibit peroxidase activity and such a structure was highly desirable for catalysis, since the large surface area of gold nanorod (NR) provided numerous adhesion sites for the small Pt nanodots (Liu et al., 2012). With this in mind, herein, we developed a facile method to fabricate a new nanozyme by encapsulating Au@Pt NR in mesoporous SiO_2 shell (**Figure 1A**). The obvious advantages of mesoporous SiO_2 shell are the high surface area, open mesoporous channel and easy modified properties (Lin et al., 2013). On the basis of these characteristics, mesoporous SiO_2-coated nanoparticles are proposed as an ideal carrier for loading biomolecules (Zhang et al., 2012). Thus, in this study, a novel nanoprobe for mumps virus serodiagnosis was developed by modifying the Au@Pt@mesoporous SiO_2 nanozyme (APMSN) with mumps antigens. Using captured-type ELISA, we demonstrated the applicability of this antigens-conjugated APMSN (Ags-APMSN) for the reliable, simple, and sensitive detection of mumps-specific IgM antibodies (**Figure 1B**).

MATERIALS AND METHODS

Materials, Reagents, and Instruments

Cetylmethylammonium bromide (CTAB), sodium borohydride ($NaBH_4$), chloroauric acid ($HAuCl_4{\cdot}3H_2O$), silver nitrate ($AgNO_3$), potassium tetrachloroplatinate (II) (K_2PtCl_4), L-ascorbic acid (AA), tetraethyl orthosilicate (TEOS), Sodium hydroxide (NaOH), sulfuric acid (H_2SO_4), hydrogen peroxide (H_2O_2), 2,2′-azino-bis(3-ethylbenzo-thiazoline-6-sulfonic acid) diammonium salt (ABTS), 3,3′,5,5′-tetramethylbenzidine (TMB) and o-phenylenediamine (OPD) were purchased from Alfa Aesar (USA). Mumps antigen was purchased from Beijing Cy-tech Biotech Co., Ltd. (China). Mumps antigen coated plate, mumps virus IgM ELISA kit were purchased from IBL International GmbH (Germany). Transmission electron microscopy (TEM) images were acquired with Tecnai G2 T20 S-TWIN microscope. Energy dispersive X-ray analysis (EDX) and scanning transmission electron microscopy (STEM) element mappings were performed on Tecnai G2 F20 U-Twin microscope. The effective diameter and zeta potential were obtained from Zetasizer Nano ZS. UV-vis-NIR absorption spectra were obtained from Perkine-Elmer Lambda 950 and Varian Cary 50. The ELISA test was performed on Infinite^{TM} M200.

Preparation of Au NRs and Au@Pt NRs

A seed-mediated growth method was used to synthesize Au NRs. First, Au seeds were synthesized by reduction of $HAuCl_4$ with $NaBH_4$. 100 μL of 24 mM $HAuCl_4$ was mixed with 7.5 mL of 0.1 M CTAB and 9.4 mL water. 600 μL of 0.01 M $NaBH_4$ was then added. Vigorous stirring of the seed solution was continued for 3 min, the seed solution was kept undisturbed at 30°C for 30 min prior to any further experimentation. Growth solution consisted of 2.04 mL of 24 mM $HAuCl_4$, 1.05 mL of 10 mM $AgNO_3$, 100 mL of 0.1 M CTAB, and 2 mL of 0.5 M H_2SO_4. 120 μL seed solution was added to the growth solution and 800 μL of 0.1 M AA to initiate the growth of Au NRs. After 12 h, the nanorods can be concentrated by centrifugation at 12000 rpm for 5 min twice.

Au NR colloids (0.1 mL) were added into the mixture of K_2PtCl_4 (75 μL, 2 mM) and freshly prepared ascorbic acid (15 μL, 0.1 M AA). After stirring for 30 min, the obtained Au@Pt NRs can be concentrated by centrifuging at 12,000 rpm for 5 min twice.

Preparation of APMSNs and Ags-APMSNs

Au@Pt NR solutions (10 mL) were added into the mixture of CTAB (75 μL, 0.1 M) and NaOH (50 μL, 0.2 M) with stirring. Three 30 μL TEOS (20%) were added at 30 min intervals. The mixture was stirring for 24 h in a 30°C water bath. The obtained APMSNs can be concentrated by centrifuging at 12,000 rpm for 5 min twice. To remove the CTAB template, the precipitate was collected and re-dispersed into 60 mL ethanol/NH_4NO_3 solution (6 g/L) for 24 h at 50°C, and then centrifuged at 12,000 rpm for 5 min twice with ethanol.

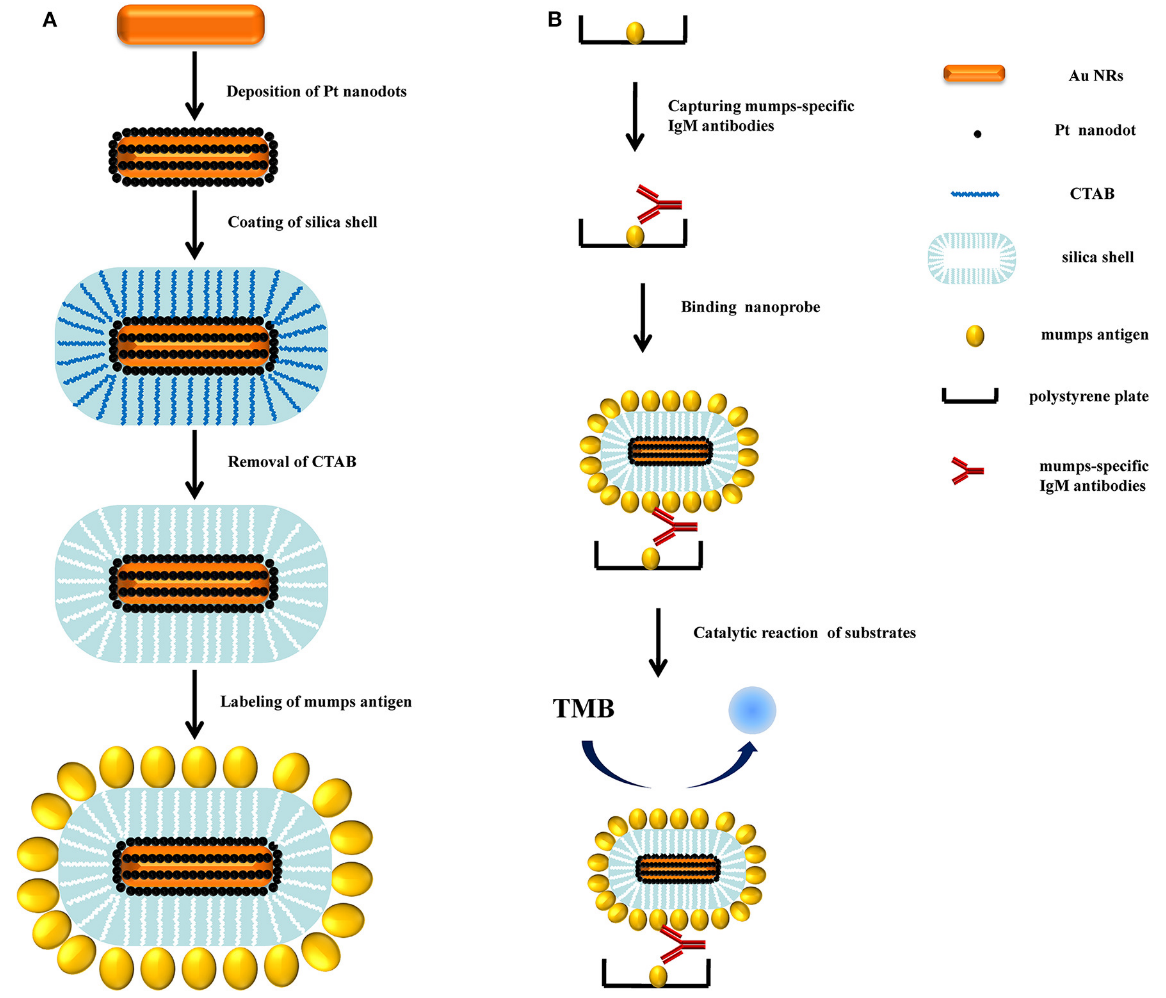

FIGURE 1 | (A) Schematic diagram of the fabrication procedure for the Ags-APMSN. **(B)** Schematic illustration of the immunoassay of Ags-APMSN based ELISA system.

APMSNs solution (50 µL 5 nM) were added into the mixture of PBS buffer (900 µL, 0.1 M, pH 7.4) and mumps antigen (50 µL, 10 mg/mL) and incubated for 96 h at 4°C. The obtained Ags-APMSNs were can be concentrated by centrifuging at 12,000 rpm for 5 min twice. The precipitate was re-dispersed in PBS buffer (100 µL, 0.1 M, pH 7.4).

Measurement of Peroxidase-Like Activity of Ags-APMSNs

Experiments on the TMB-H_2O_2 catalytic reaction were carried out with 0.4 mM TMB, 100 mM H_2O_2, and 0.05 nM Ags-APMSNs in a reaction volume of 3 mL. Unless otherwise stated, the reaction was carried out at 30°C in PBS buffer (0.1 M, pH 5) and used for absorption spectroscopic measurements at 650 nm.

Detection of Mumps-Specific IgM Antibodies by ELISA

Firstly, 100 µL per well of mumps antigen was loaded into the wells of a 96-well microtiter plate for 12 h at 4°C. The plates were then washed three times with PBST buffer. After that, 200 µL of 5% BSA in PBS was added to the each wells and incubated for 3 h at 30°C. After the wells were washed with PBST buffer three times, 100 µl of diluted samples were added to the each wells and incubated at 37°C for 0.5 h. After the wells were washed with PBST buffer three times, 100 µl Ags-APMSNs were added to wells and incubated at 37°C for 0.5 h. After the wells were washed with PBST buffer three times, 100 µL PBS buffer (pH 5) of substrate solution containing 0.4 mM TMB and 100 mM H_2O_2 was added into each well. After incubating at 30°C for 10 min, the absorbance of each well was measured at 650 nm by a microplate reader.

RESULTS AND DISCUSSION

Characterization of APMSNs and Ags-APMSNs

The working principle of the rationally designed APMSNs was schematically represented in **Figure 1A**. Au NRs (**Figure 2A**) were used as seeds to for subsequent overgrowth of Pt nanodots. Pt nanodots with sizes of 2–3 nm formed a nanoisland shell on Au NRs from the transmission electron microscopy (TEM) image (**Figure 2B**). Obviously, the Au NRs provided a well-dispersed surface distribution of Pt nanodots. The surfaces of Au@Pt NRs are stabilized by the CTAB surfactants. The CTAB molecules, can also serve as template for the formation of the mesoporous silica shell. The average thickness of the mesoporous SiO_2 layer surrounding the Au@Pt NR was around 25 nm (**Figure 2C**). **Figure 2D** showed STEM images and EDX element mappings of Au, Pt, and Si for one selected nanoparticle. Pt are found in the shell outside the Au core, and Si are in the outer shell. Furthermore, after the removal of the CTAB by NH_4NO_3/ethanol solution, the channel-like mesopores were all open and gave good mass transport and accessibility to their internal surfaces.

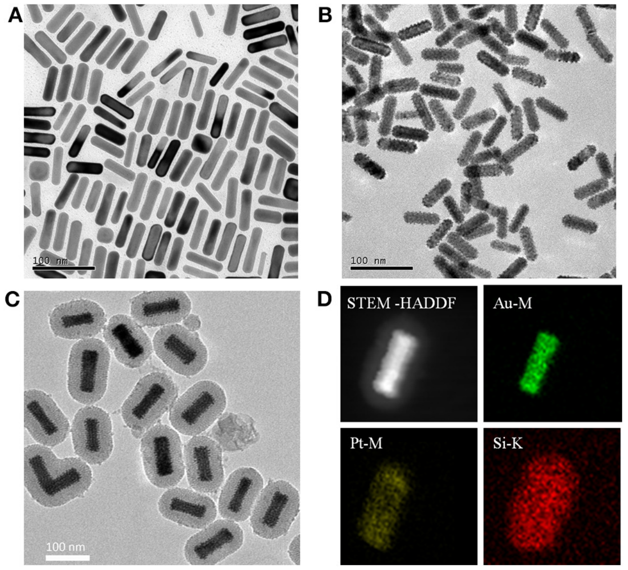

FIGURE 2 | Typical TEM images of **(A)** Au NRs, **(B)** Au@Pt NRs, and **(C)** APMSNs. **(D)** STEM-HAADF image and STEM-EDX maps of Au, Pt, and Si, respectively.

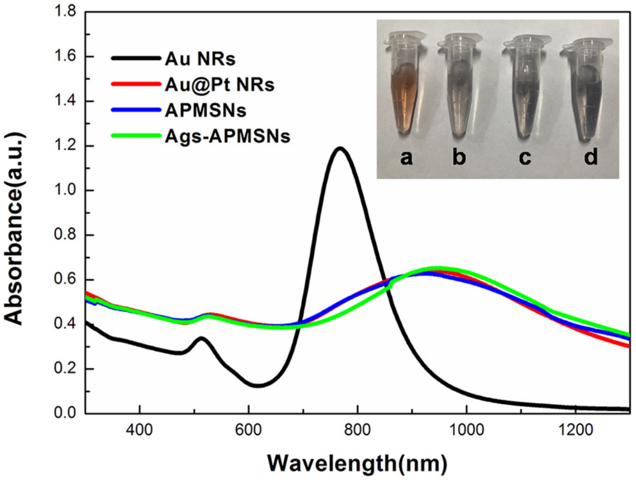

FIGURE 3 | UV-vis absorption spectra of Au NRs, Au@Pt NRs, APMSNs and Ags-APMSNs. Insets are the corresponding photographs of the **(a)** Au NRs, **(b)** Au@Pt NRs, **(c)** APMSNs, and **(d)** Ags-APMSNs solutions.

TABLE 1 | Different characterization of five kinds of nanoparticles.

Material	LSPR peak (nm)	Effective diameter (nm)	Zeta potential (mV)
AuNRs	768	17.1 ± 0.6	20.9 ± 0.4
Au@Pt NRs	892	46.0 ± 0.5	20.8 ± 0.6
Au@Pt@ mesoporous SiO_2 NRs with CTAB template	916	100.6 ± 0.7	−25.2 ± 0.6
APMSNs	926	92.1 ± 0.6	−19.1 ± 0.6
Ags-APMSNs	950	126.9 ± 1.5	−14.3 ± 0.5

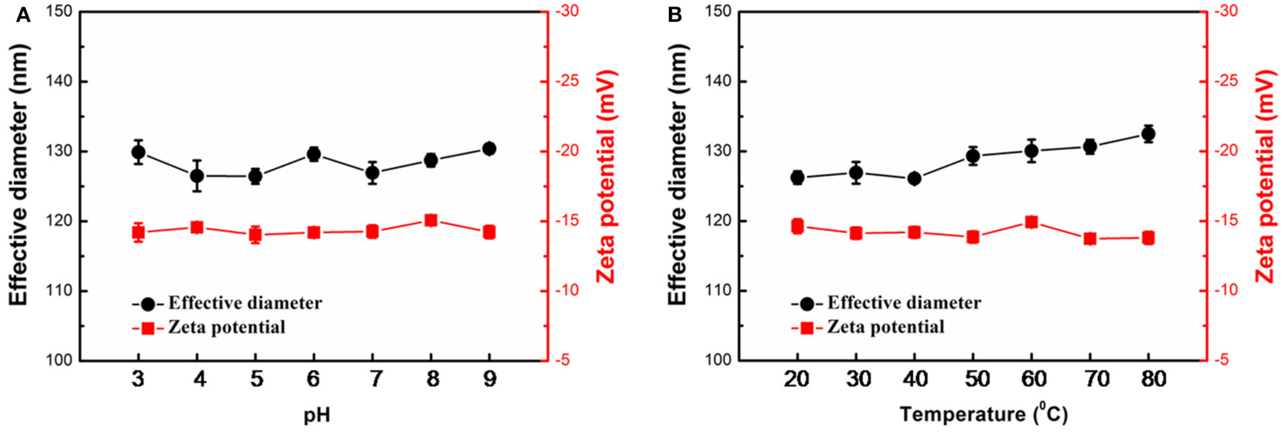

FIGURE 4 | Stability of the Ags-APMSNs against pH **(A)** and temperature **(B)** variations from the viewpoints of effective diameter and Zeta potential. The samples were treated with 0.1 M PBS buffers (0.1 M) with different pH values for 3 h or incubated at different temperatures for 3 h before characterizations.

Due to the phenomenon of surface plasmon resonance (SPR), the Au NRs exhibit striking optical properties. The SPR properties of Au NRs depend on the aspect ratio and the dielectric constant of gold and surrounding medium. In our experiment, Au NRs exhibited a longitudinal SPR (LSPR) peak at 768 nm (**Figure 3**), and the LSPR peak of the Au@Pt NRs shifted toward the red direction (892 nm) when Pt nanodots were formed on the surface of Au NRs. The quite large red-shift and intensity damping here mainly came from the dielectric constant of the Pt and the porous shell structure of the Pt nanodots. **Figure 3** also showed that upon surface modification by mesoporous SiO_2 layer and antigen molecular, the position or width of the Au@Pt NRs remained almost unchanged.

In this study, we used dynamic light scattering (DLS) measurements to determine the surface potential of the nanoparticles (**Table 1**). The positive charge ($\zeta = +20$ mV) developed in Au NRs and Au@Pt NRs were assumed to CTAB bilayer at the NR surface. As shown in **Table 1**, mesoporous SiO_2 coating reversed the surface charge of the Au@Pt NRs to negative. After removal of the CTAB template there is a small loss of charge. **Table 1** also illustrated that the surface potential become less negative after antigen conjugation process, due to the electrostatic interaction between the positively charged antigen and the negatively charged nanorod surface.

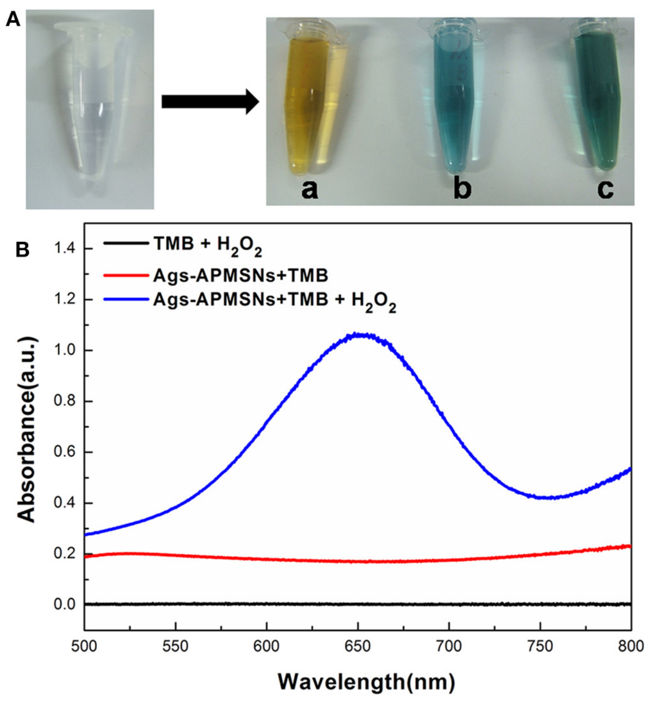

FIGURE 5 | (A) Photographs of the reaction solutions in the absence and presence of Ags-APMSNs [**(a)** OPD, **(b)** TMB and **(c)** ABTS]. **(B)** UV-vis absorption spectra of the TMB-H_2O_2 (black line), TMB-Ags-APMSNs (red line), and TMB-H_2O_2-Ags-APMSNs (blue line) solution. The concentration of TMB was 0.4 mM, the concentration of H_2O_2 was 100 mM, the concentration of Ags-APMSNs was 0.05 nM and the reaction time was 10 min.

Additionally, DLS measurements were used to monitor the effective diameter of the nanoparticles. It is worth notioning that the DLS measurements only provides an average spherical diameter; hence, due to the rod shape, the effective sizes determined by DLS measurements here cannot be taken literally. The effective sizes in our case was used to demonstrate the relative size upon the variation of coatings. The DLS results revealed that the effective diameter of Au NRs, Au@Pt NRs, and APMSNs with CTAB template were 17.1 ± 0.6, 46.0 ± 0.5, and 100.6 ± 0.7 nm, respectively. **Table 1** further showed that the effective diameter of the APMSNs increased evidently from 92.1 to 126.9 nm after antigen conjugation process. These results demonstrated the successful preparation of the Ags-APMSN based on the chemical modification that can be used in the following immunoassay.

The stability of Ags-APMSNs upon pH and temperature changes were determined using DLS analysis as well. Previous studies suggested that the CTAB-stabilized Au@Pt NRs showed low dispersion stability in PBS buffers (Liu et al., 2012), whereas mesoporous shell could keep these active Au@Pt NRs catalysts robust to harsh environments (**Figure 4**). The results indicated that no obvious change was observed for the effective diameter and Zeta potential of the Ags-APMSNs over a wide range of pH from 3 to 9 and temperatures from 20 to 80°C.

Peroxidase-Like Activity of Ags-APMSNs

Previously, we found that Au@Pt NRs have intrinsic peroxidase-like activities, and the experimental and calculated results suggest the peroxidase-like activities of Au@Pt NRs can be ascribed to the larger surface exposure of the Pt island shell (Shen et al., 2015). **Figure 5A** showed the comparison of Ags-APMSN catalyzed oxidation reaction and color changes

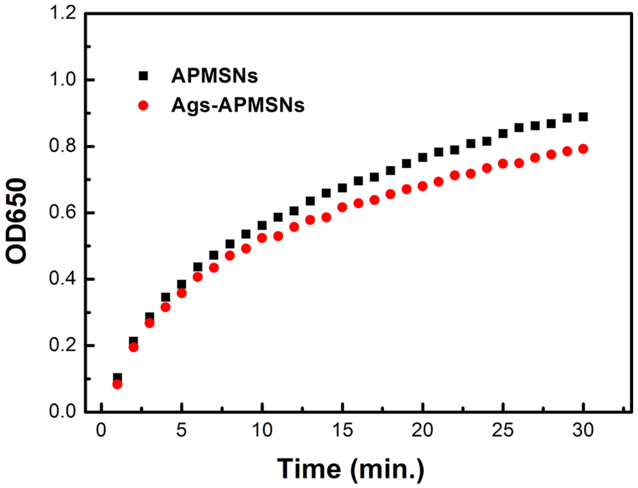

FIGURE 6 | Absorbance evolution at 650 nm as a function over time for TMB oxidation in the presence of H_2O_2 catalyzed by APMSNs and Ags-APMSNs. The concentration of TMB was 0.4 mM, the concentration of H_2O_2 was 100 mM and the concentration of APMSNs or Ags-APMSNs was 0.025 nM.

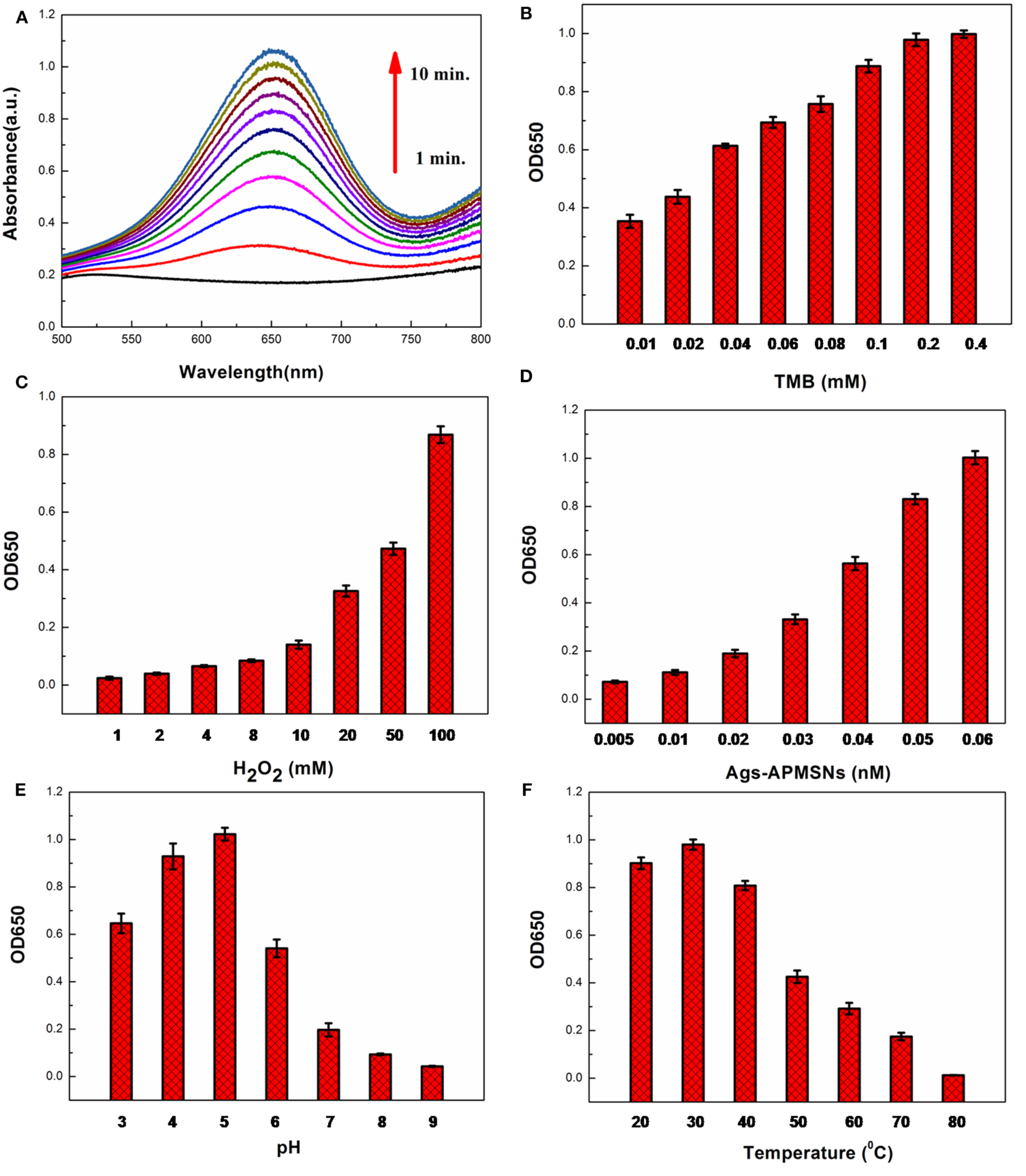

FIGURE 7 | (A) Time-dependent absorbance changes of oxidation of TMB in the presence of H_2O_2. Effects of TMB concentration **(B)**, H_2O_2concentration **(C)**, Ags-APMSNs concentration **(D)**, pH **(E)**, and temperature **(F)** on catalytic activity of the Ags-APMSNs. Reaction conditions: **(A)** 0.4 mM TMB, 100 mM H_2O_2, and 0.05 nM APMSNs; **(B)** 100 mM H_2O_2, 0.05 nM APMSNs and 10 min; **(C)** 0.4 mM TMB, 0.05 nM APMSNs and 10 min; **(D)** 0.4 mM TMB, 100 mM H_2O_2 and 10 min; **(E)** 0.4 mM TMB, 100 mM H_2O_2, 0.05 nM APMSNs and 10 min at different pH; **(F)** 0.4 mM TMB, 100 mM H_2O_2, 0.05 nM APMSNs and 10 min at different temperatures.

occurring with horseradish peroxidase (HRP) labels with different chromogens, such as TMB, OPD, and ABTS in the presence of substrate (H_2O_2), suggesting that the functionalized nanoprobe, Ags-APMSNs, had the peroxidase-like activity of Au@Pt NRs, consistent with the previous study (Liu et al., 2012).

Furthermore, we selected TMB as the colorimetric substrate to demonstrate this clearly. It has been well-established that TMB can be oxidized by hydrogen peroxide to form a blue color product, as judged by the appearance of the characteristic absorption peak at 650 nm. As shown in **Figure 5B**, in the absence of Ags-APMSNs, the TMB–H_2O_2 solution presented a negligible absorption in the range from 500 to 800 nm. In contrast, after addition of Ags-APMSNs, the solutions exhibited adsorption peaks centered at 650 nm. The significant increase in absorbance at 650 nm suggests that Ags-APMSNs catalyzes the oxidation of TMB by H_2O_2. All these observations confirmed the intrinsic peroxidase-like activity of the Ags-APMSNs, similar to that found in Au@Pt NRs previously (Liu et al., 2012).

On the other hand, for most nanozyme, the catalytic sites and recognition sites are not spatially separated. Hence, antigens-occupied catalytic sites should influence the catalytic activity of Au@Pt NRs and cause extra waste of catalysts. The encapsulation of Au@Pt NR in mesoporous SiO_2 shell was able to hinder the interaction between nanoparticles and antigen moleculars, and the reacting substrates can directly access the Au@Pt NR cores through the mesopores within the SiO_2 shells and the product can readily exit through these mesopores.

As shown in **Figure 6**, the Ags-APMSNs exhibited an catalytic activity toward TMB in the presence of H_2O_2 similar to the case of APMSNs (the Ags-APMSNs maintained 90% activity of APMSNs). Since antigens conjugation had negligible influence on the catalytic activity of the APMSNs, this designed nanozyme have realized spatial separation of recognition sites and catalytic sites.

Effect of Substrate and Ags-APMSNs Concentrations, pH, and Temperature

It has been reported that the peroxidise-like activities activity of nanozyme is dependent on the substrate concentrations, pH of the reaction buffer and incubation temperature. The color reaction of TMB by H_2O_2 was employed to optimize the catalytic condition (**Figure 7A**). **Figure 7B** showed the dependence of absorbance at 650 nm on the concentration of TMB. The results indicated that the catalytic activity of Ags-APMSNs was rapidly increased initially with the increase of TMB concentration and then tended to saturate beyond 0.2 mM. Only slight changes in light intensity were observed when TMB concentration was above 0.2 mM. The influence of H_2O_2 concentration was investigated and the results were shown in **Figure 7C**. It can be seen that the activity of Ags-APMSNs increased with increased H_2O_2 concentration from 1 to 100 mM. As shown in **Figure 7D**, the catalytic activity of Ags-APMSNs increased gradually with the concentration of Ags-APMSNs from 0.005 to 0.06 nM. To know whether the catalytic activity of the Ags-APMSNs was dependent on pH of the reaction buffer and incubation temperature, the experiments were performed by varying the pH from 3 to 9 and temperatures from 20 to 80°C. The result suggested that the optimal pH is 5 and the optimal temperature is 30°C (**Figures 7E,F**), which was consistent with the feature of HRP labels.

Based on abovementioned results, the optimum conditions selected for the following biomedical assay were as follows: 0.4 mM TMB, 100 mM H_2O_2, pH 5, and 30°C.

Application of Immunoassay

Figure 1B is a schematic of the whole assay steps used in this work, which the Ags-APMSNs were utilized as a nanoprobe instead of HRP labels for the determination of

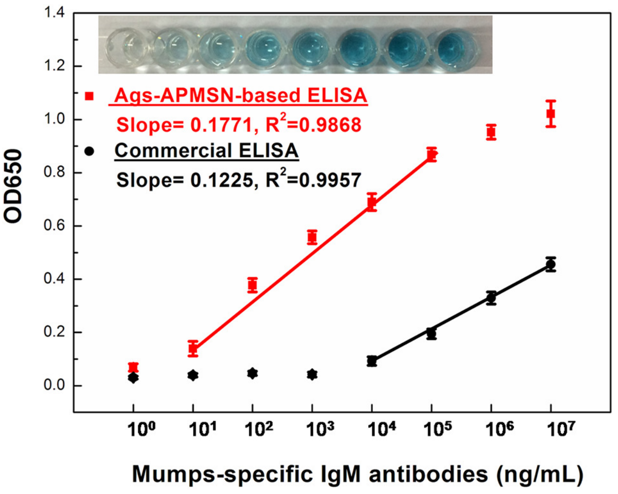

FIGURE 8 | Calibration plot of absorption values at 650 nm vs. mumps-specific IgM antibodies at different concentration. The insets are the typical photograph of the wells of the Ags-APMSN-based ELISA.

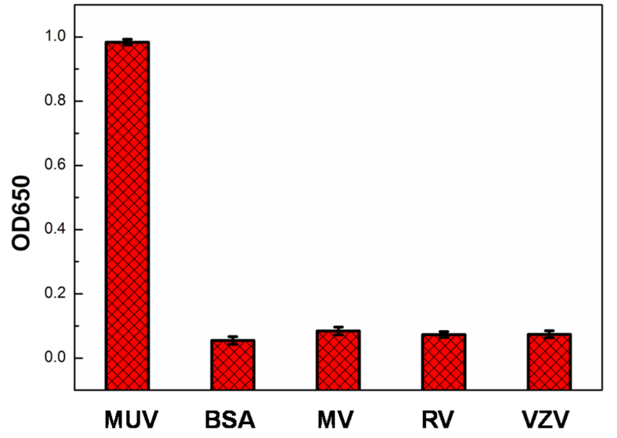

FIGURE 9 | Specificity of mumps virus, BSA, measles virus (MV), rubella virus (RV), and varicella-zoster virus (VZV) positive serum using Ags-APMSN-based ELISA.

TABLE 2 | Comparison of assay performance of Ags-APMSN-based ELISA and commercial ELISA for real blood serum samples.

Assay	Total	Positive	Negative
Ags-APMSN-based ELISA	40	20	20
Commercial ELISA	40	20	20

mumps-specific IgM antibodies. The assay was performed in mumps antigen-immobilized microplate wells. First, the samples were added and mumps-specific IgM antibodies present in the sera would bind to the antigens. After washing, bound IgM antibodies were detected using Ags-APMSNs, following which a detector system with chromogen substrate revealed the presence or absence of mumps-specific IgM antibodies in the test samples.

Figure 8 showed the typical curve for different concentrations of mumps-specific IgM antibodies standard solutions. Owing to the high catalysis activity of Ags-APMSN, this proposed ELISA generated higher absorbance at 650 nm than the commercial ELISA and was able to quantify the target antigen faster. Significantly, compared to the commercial ELISA or captured-ELISA method (Glikmann et al., 1986), greatly amplified sensitivity was achieved as this proposed method has a limit of detection for mumps-specific IgM antibodies of 10 ng/mL in the linear range from 10 to 10^5 ng/mL. Moreover, as the SiO_2 shell have less interaction with plate surface, the unbound Ags-APMSN could be removed when the plates were washed. Thus, this proposed ELISA could reduce the high background signal or false-positive reactions as well.

For testing if the detection of mumps-specific IgM antibodies was specific, control experiments were taken using BSA, measles virus, rubella virus and varicella-zoster virus positive serum. The selectivity of this proposed method was shown in **Figure 9**. In comparison to the mumps virus positive serum, there were no remarkable response in the other samples, indicating this proposed ELISA exhibited high selectivity toward mumps-specific IgM antibodies (**Figure 9**).

Also, the proposed ELISA based on Ags-APMSN catalyzed colorimetric immunoassay was tested in real blood serum for the diagnosis of mumps. The serum sample was obtained from Zaozhuang Municipal Center for Disease Control and Prevention and diluted 100 times in dilution buffer before assay (**Figure S1** and **Table S1**). The results were compared with those obtained by the commercial ELISA (**Table 2**). As can be seen, the results obtained from this proposed ELISA agreed well with those obtained from the commercial ELISA. Therefore, the proposed method is suitable and satisfactory for diagnosis of mumps of real samples in clinical application.

CONCLUSION

In conclusion, a novel nanoprobe was designed and synthesized. The results have shown that this functionalized nanoprobe, Ags-APMSNs, had intrinsic peroxidase-like activity, which can also serve as a medical diagnosis regent. In contrast to the natural enzyme labels, the obtained Ags-APMSNs are readily prepared, robust in harsh chemical environment, and cost-effective. Notably, the mesoporous SiO_2 shell was able to hinder the interaction between catalytical nanoparticles and recognition antigens, retaining the catalytic activity of the inner active nanoparticle core. To facilitate further applications of this nanoprobe, an immunoassay was performed based on their enhanced catalytic activity. The nanoprobes were successfully utilized to detect the mumps-specific IgM antibodies in sera sensitively with the limit of detection as low as 10 ng/mL. The present work confirmed that the Ags-APMSNs were expected as a novel immunological probe for a wide range of practical applications in various areas, ranging from biosensing to clinical virus diagnosis.

DATA AVAILABILITY STATEMENT

The original contributions presented in the study are included in the article/**Supplementary Material**, further inquiries can be directed to the corresponding authors.

AUTHOR CONTRIBUTIONS

LL participated in the experiment and drew the scheme and figures. RC performed the experiments. JL wrote the paper with support from XW.

FUNDING

This work was financially supported by the National Key Basic Research Program of China (2016YFA0200903 and 2017YFF0204706), the Strategic Priority Research Program of the Chinese Academy of Sciences (Y9F9XD01ZX), the National Natural Science Foundation of China (91127013 and 61704149), the Project Special Funding of Taishan Scholar and the funding by Qingchuang Science and Technology plan of Shandong Universities (2020KJA010 and 2019KJN001).

SUPPLEMENTARY MATERIAL

The Supplementary Material for this article can be found online at: https://www.frontiersin.org/articles/10.3389/fchem.2020.00463/full#supplementary-material

REFERENCES

Galazka, A. M., Robertson, S. E., and Kraigher, A. (1999). Mumps and mumps vaccine: a global review. *Bull. World Helth Organ.* 77, 3–14.

Gao, L., Zhuang, J., Nie, L., Zhang, J., Zhang, Y., Gu, N., et al. (2007). Intrinsic peroxidase-like activity of ferromagnetic nanoparticles. *Nat. Nanotechnol.* 2, 577–583. doi: 10.1038/nnano.2007.260

Glikmann, G., Pedersen, M., and Mordhorst, C. (1986). Detection of specific immunoglobulin m to mumps virus in serum and cerebrospinal fluid samples from patients with acute mumps infection, using an antibody-capture enzyme immunoassay. *Acta Pathol. Microbiol. Immunol. Scand. C* 94, 145–156. doi: 10.1111/j.1699-0463.1986.tb02104.x

Gut, J. P., Spiess, C., Schmitt, S., and Kirn, A. (1985). Rapid diagnosis of acute mumps infection by a direct immunoglobulin M antibody capture enzyme immunoassay with labeled antigen. *J. Clin. Microbiol.* 21, 346–352.

Hviid, A., Rubin, S., and Mühlemann, K. (2008). Mumps. *Lancet* 371, 932–944. doi: 10.1016/s0140-6736(08)60419-5

Krause, C. H., Molyneaux, P. J., Ho-Yen, D. O., Mcintyre, P., Carman, W. F., and Templeton, K. E. (2007). Comparison of mumps-IgM ELISAs in acute infection. *J. Clin. Virol.* 38, 153–156. doi: 10.1016/j.jcv.2006.10.010

Lin, Y., Li, Z., Chen, Z., Ren, J., and Qu, X. (2013). Mesoporous silica-encapsulated gold nanoparticles as artificial enzymes for self-activated cascade catalysis. *Biomaterials* 34, 2600–2610. doi: 10.1016/j.biomaterials.2013.01.007

Liu, J., Hu, X., Hou, S., Wen, T., Liu, W., Zhu, X., et al. (2012). Au@Pt core/shell nanorods with peroxidase-and ascorbate oxidase-like activities for improved detection of glucose. *Sens. Actuators B* 166, 708–714. doi: 10.1016/j.snb.2012.03.045

Ma, M., Zhang, Y., and Gu, N. (2011). Peroxidase-like catalytic activity of cubic Pt nanocrystals. *Colloids Surf. A* 373, 6–10. doi: 10.1016/j.colsurfa.2010.08.007

Maillet, M., Bouvat, E., Robert, N., Baccard-Longère, M., Morel-Baccard, C., Morand, P., et al. (2015). Mumps outbreak and laboratory diagnosis. *J. Clin. Virol.* 62, 14–19. doi: 10.1016/j.jcv.2014.11.004

Narayanan, R., and El-Sayed, M. A. (2004). Shape-dependent catalytic activity of platinum nanoparticles in colloidal solution. *Nano Lett.* 4, 1343–1348. doi: 10.1021/nl0495256

Rashidian, M., Dozier, J. K., and Distefano, M. D. (2013). Enzymatic labeling of proteins: techniques and approaches. *Bioconjugate Chem.* 24, 1277–1294. doi: 10.1021/bc400102w

Shen, X., Liu, W., Gao, X., Lu, Z., Wu, X., and Gao, X. (2015). Mechanisms of oxidase and superoxide dismutation-like activities of gold, silver, platinum, and palladium, and their alloys: a general way to the activation of molecular oxygen. *J. Am. Chem. Soc.* 137, 15882–15891. doi: 10.1021/jacs.5b10346

Warrener, L., and Samuel, D. (2006). Evaluation of a commercial assay for the detection of mumps specific IgM antibodies in oral fluid and serum specimens. *J. Clin. Virol.* 35, 130–134. doi: 10.1016/j.jcv.2005.10.008

Wu, J., Qin, K., Yuan, D., Tan, J., Qin, L., Zhang, X., et al. (2018). Rational design of Au@ Pt multibranched nanostructures as bifunctional nanozymes. *ACS Appl. Mater. Interfaces* 10, 12954–12959. doi: 10.1021/acsami.7b17945

Wu, J., Wang, X., Wang, Q., Lou, Z., Li, S., Zhu, Y., et al. (2019). Nanomaterials with enzyme-like characteristics (nanozymes): next-generation artificial enzymes (II). *Chem. Soc. Rev.* 48, 1004–1076. doi: 10.1039/c8cs00457a

Zhang, J., Sasaki, K., Sutter, E., and Adzic, R. (2007). Stabilization of platinum oxygen-reduction electrocatalysts using gold clusters. *Science* 315, 220–222. doi: 10.1126/science.1134569

Zhang, Z., Wang, L., Wang, J., Jiang, X., Li, X., Hu, Z., et al. (2012). Mesoporous silica-coated gold nanorods as a light-mediated multifunctional theranostic platform for cancer treatment. *Adv. Mater.* 24, 1418–1423. doi: 10.1002/adma.201104714

Conflict of Interest: The authors declare that the research was conducted in the absence of any commercial or financial relationships that could be construed as a potential conflict of interest.

frontiers in Chemistry

ORIGINAL RESEARCH
published: 11 June 2020
doi: 10.3389/fchem.2020.00491

Reversible Inhibition of Iron Oxide Nanozyme by Guanidine Chloride

Wei-chuan Mo[1†], Jia Yu[1†], Li-zeng Gao[5], Ying Liu[1,3*], Yan Wei[1,2] and Rong-qiao He[1,4*]

[1] State Key Laboratory of Brain and Cognitive Sciences, Institute of Biophysics, University of the Chinese Academy of Sciences, CAS, Beijing, China, [2] CAS Key Laboratory of Mental Health Laboratory, Institute of Psychology, Beijing, China, [3] School of Life Sciences, Beijing University of Chinese Medicine, Beijing, China, [4] Southwest Medical University, Luzhou, China, [5] CAS Engineering Laboratory for Nanozyme, Institute of Biophysics Key Laboratory of Protein and Peptide Drugs, Institute of Biophysics, CAS, Yangzhou, China

Nanozymes have been widely applied in bio-assays in the field of biotechnology and biomedicines. However, the physicochemical basis of nanozyme catalytic activity remains elusive. To test whether nanozymes exhibit an inactivation effect similar to that of natural enzymes, we used guanidine chloride (GuHCl) to disturb the iron oxide nanozyme (IONzyme) and observed that GuHCl induced IONzyme aggregation and that the peroxidase-like activity of IONzyme significantly decreased in the presence of GuHCl. However, the aggregation appeared to be unrelated to the quick process of inactivation, as GuHCl acted as a reversible inhibitor of IONzyme instead of a solo denaturant. Inhibition kinetic analysis showed that GuHCl binds to IONzyme competitively with H_2O_2 but non-competitively with tetramethylbenzidine. In addition, electron spin resonance spectroscopy showed that increasing GuHCl level of GuHCl induced a correlated pattern of changes in the activity and the state of the unpaired electrons of the IONzymes. This result indicates that GuHCl probably directly interacts with the iron atoms of IONzyme and affects the electron density of iron, which may then induce IONzyme inactivation. These findings not only contribute to understanding the essence of nanozyme catalytic activity but also suggest a practically feasible method to regulate the catalytic activity of IONzyme.

Keywords: nanozyme, peroxidase, guanidine chloride, activity inhibition, electron spin resonance, g-factor, aggregation

Edited by:
Youhui Lin,
Xiamen University, China

Reviewed by:
Juewen Liu,
University of Waterloo, Canada
Xiaogang Qu,
Chinese Academy of Sciences, China
Zhen Liu,
Beijing University of Chemical Technology, China

***Correspondence:**
Rong-qiao He
herq@ibp.ac.cn
Ying Liu
yingliu@bucm.edu.cn

†These authors have contributed equally to this work

Specialty section:
This article was submitted to Nanoscience, a section of the journal Frontiers in Chemistry

Received: 27 December 2019
Accepted: 12 May 2020
Published: 11 June 2020

Citation:
Mo W, Yu J, Gao L, Liu Y, Wei Y and He R (2020) Reversible Inhibition of Iron Oxide Nanozyme by Guanidine Chloride. Front. Chem. 8:491. doi: 10.3389/fchem.2020.00491

INTRODUCTION

Since the discovery of the peroxidase-like activity of iron oxide nanoparticles in 2007 (Gao et al., 2007), the application of nanozymes has rapidly emerged as a novel field. Nanozymes have been widely used in the field of biotechnology and biomedicine, e.g., hydrogen peroxide (H_2O_2) detection (Wei and Wang, 2008), DNA detection (Park et al., 2011), and immunohistochemical staining (Wu et al., 2011). To date, nanozymes have been described as nanomaterials with intrinsic enzyme-like activities, which are of broad interest for clinical use (Quick et al., 2008; Kelong et al., 2012; Zhang et al., 2016).

Many researchers believe that the nanoscale effect is a decisive factor in the nanozyme's catalytic activity. Nanomaterials can simulate the function of proteins by modifying their size, surface charge and groups (Kotov, 2010). In particular, the surface charge properties of the nanomaterials are considered to play a key role in the nanoscale effect (Sen and Barisik, 2018). However, it is still lacking direct evidence to support this hypothesis. Given that ferrous ions are capable of catalyzing the degradation of H_2O_2 in the Fenton reaction (Fenton, 1894), many researchers believe that the iron atom at the surface of iron oxide nanozymes (IONzyme) probably participates in the Fenton mechanism (Wang et al., 2010; Niu et al., 2011) and contributes to the catalytic capacity. However, the peroxidase-like activity of the non-metal nanozymes (e.g., carbon-based nanozymes) (Song et al., 2010) could not be explained by the Fenton mechanism (Wei and Wang, 2013). Therefore, in addition to the Fenton reaction, other nanozyme mechanisms must be elucidated by further theoretical and experimental studies.

Fan and colleagues simulated the catalytic microenvironment of horseradish peroxidase (HRP) on the surface of IONzyme by histidine residue modification and successfully boosted the catalytic efficiency of IONzyme up to 20.8 times (Fan et al., 2017). This result illuminates another aspect of nanozyme's catalytic activity and showed that protein-based enzymology theory and methodology could facilitate uncovering the underlying mechanism of the enzyme-like activity of nanomaterials. "Enzyme inactivation," e.g., by site-specific mutation, protein truncation, inhibition, and denaturation to reduce the enzyme activity, is a standard strategy for studying the active site and catalytic mechanism of a protein enzyme by comparing the enzymatic properties of the inactivated protein with those of its native form. Therefore, a controllable method of nanozyme inactivation would add to our understanding of the essence of its catalytic mechanism.

Recently, Zhang and colleagues recorded IONzyme inactivation concurrent with IONzyme aggregation when the IONzymes were suspended in cell culture medium (DMEM with 10% fetal bovine serum). They ascribed the decrease in activity to the medium-induced aggregation of nanoparticles (Zhang et al., 2016). Meanwhile, Liu and colleagues observed that halide ions (Xs) can affect the activity of gold nanozyme. The enzymatic-inhibition effect of Xs did not show time dependence, although the size of the gold nanozymes varied over time (Liu et al., 2017). Although these studies did not reach an agreement on the explanation of nanozyme inactivation, they implied that ion-rich conditions can reduce the enzymatic activity of nanozymes, which further revealed that nanozymes can exhibit inactivation properties analogous to those of protein enzymes. However, an in-depth investigation is still needed to uncover the underlying details.

In this study, we analyzed the effects of GuHCl, a commonly used denaturant for natural enzymes, on the representative peroxidase-like activity of IONzyme in the presence of hydrogen peroxide (H_2O_2) and tetramethylbenzidine (TMB). We found that GuHCl induced both aggregation and inactivation of IONzyme and bound to the iron atom on the surface of IONzyme, resulting in inactivation. The substrate H_2O_2 may bind to the iron atom because of its competition with GuHCl in binding to IONzyme, and TMB is associated with oxygen atoms because of its non-competition with GuHCl.

MATERIALS AND METHODS

Reagents

Iron-based nanozyme Fe_3O_4 magnetic nanoparticles (IONzymes; Diameter, 90 nm) were synthesized according to the solvothermal method (Fan et al., 2017; see the brief description in the materials and methods section in the supporting information). The nanozyme suspensions were ultra-sonicated (250 W, 15 s; SCIENTZ, Zhejiang, China) before use if not stated otherwise. Tetramethylbenzidine chromogen solution (TMB, $\varepsilon = 3.9 \times 10^4$ $M^{-1}cm^{-1}$ at 652 nm) was purchased from Wantai Co. Beijing (China). Guanidine hydrochloride (GuHCl) was purchased from Amresco (Solon, OH, USA). Hydrogen peroxide (H_2O_2) and sodium acetate buffer (NaAc, pH = 4.5) were purchased from Sinopharm Chemical Reagent (Shanghai, China). Distilled water was retreated and collected on a Thermo Scientific Barnstead Nanopure water purifier (18.2 MΩ; Dubuque, IO, USA).

Assay of Peroxidase-Like Activity

The peroxidase-like activities of IONzyme were measured in TMB chromogen solution. IONzyme suspension with or without GuHCl was loaded into a 96-well plate and incubated at room temperature (usually ∼2 min unless otherwise stated), followed by the addition of the working solution, and the absorbance (652 nm, see the UV/Vis absorption spectra of reaction solutions containing TMB with or without GuHCl in **Figure S3**) was recorded at 37°C on a Microplate spectrophotometer (Molecular Devices, Sunnyvale, CA, USA). The working solution containing TMB chromogen solution mixed with NaAc buffer at 1:1 (v/v) with the addition of H_2O_2. Given the Nanozyme aggregation probably disturbed the absorption reading (**Figure 1A**), the initial reaction velocity (V_0) was calculated by the software using 0–300 s reads (Softmax pro 6, Molecular Devices, Sunnyvale, CA, USA) and used to evaluate the peroxidase-like activity of IONzyme. Note that the 100 μL reaction mixture contained concentrations of TMB, H_2O_2 and IONzyme of 0.4, 600 mM, and 5 mg/L, respectively, unless otherwise stated. The pH of all the reaction mixtures are 4.5. For the computation of IC_{50}, the curves were fit to

$$y = 100\%/[1 + (I/\mathrm{IC}_{50})] \tag{1}$$

where I is the inhibitor concentration, and y is the percentage of activity.

For recycling IONzymes, GuHCl was removed from the reaction mixture by centrifugation (16,000 × g, 25°C, 30 min). After the GuHCl supernatant was discarded, the precipitated IONzyme was washed with H_2O twice. Then, the washed IONzymes were resuspended in H_2O or GuHCl to the same volume for the activity assays.

Inhibition Kinetics Analysis

The inhibition kinetics assays were carried out under the conditions described above, except for measurements of IONzyme activities using different concentrations of TMB at a fixed concentration of H_2O_2 (2.7 M) or using different concentrations of H_2O_2 at a fixed concentration of TMB

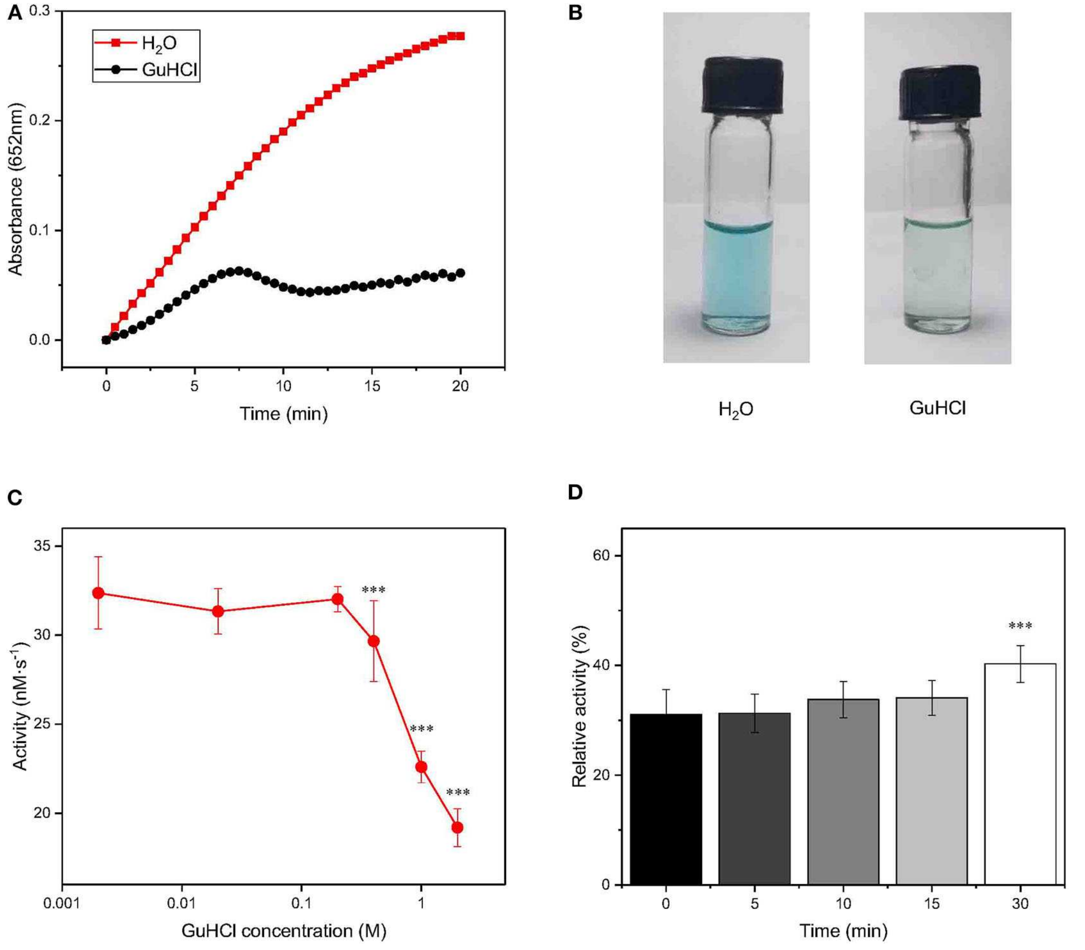

FIGURE 1 | Changes in the activity of IONzyme at different concentrations of GuHCl. IONzyme (final concentration, 0.5 μg/100 μl) was mixed with 2.0 M GuHCl in water at room temperature. H_2O_2 (0.6 M) and TMB (0.4 mM) suspended in 200 mM sodium acetate buffer (pH 4.5) were added to the reaction mixture, followed by measurements of the absorbance at 652 nm (pH 4.5, 37°C) **(A)**. Changes in the absorbance between 0 and 150 s were used to calculate the peroxidase-like activity of IONzymes (nM·s^{-1}). Aliquots (blue, oxidized TMB) were taken in Eppendorf tubes from the reaction at 2 min, compared with H_2O as a control **(B)**. IONzyme was mixed with different concentrations of GuHCl, and aliquots were taken for activity measurement ($n = 12$) **(C)**. The data on the relative changes in the peroxidase activity of IONzyme incubated with 2.0 M GuHCl for different times were normalized to those of the untreated control ($n = 6$) **(D)**. Data are the mean ± SD. ***$P < 0.001$.

(0.4 mM). The apparent kinetic parameters were calculated based on the function

$$V_0 = V_{max} \times \frac{[S]}{K_m + [S]} \tag{2}$$

where V_0 is the initial reaction velocity, V_{max} is the maximal reaction velocity, $[S]$ is the concentration of substrate and K_m is the Michaelis constant.

Dynamic Light Scattering (DLS)

The IONzyme was incubated with GuHCl, and the intensities of light scattering were recorded at different time points on a DynaPro NanoStar DLS instrument (Wyatt technology, Santa Barbara, CA, USA). The resulting hydrodynamic radii were calculated according to the manufacturer's instructions.

Electron Spin Resonance (ESR) Spectroscopy

IONzymes were mixed with NaAC buffer (pH = 4.5) and GuHCl as mentioned above. Then, the mixtures were transferred into a glass capillary and placed in the ESR cavity. All ESR measurements were carried out at room temperature on an ESR spectroscope (Bruker A300-10/12, Billerica, USA) with 20 mW microwave power. The modulation field was 1 G, and the scan range was 6,000 G.

Statistical Methods

Data are shown as the means ± SD. Data were obtained from at least three independent experiments. One-way ANOVA was applied for mean comparison. Significance was accepted at $p < 0.05$.

RESULTS

IONzyme Is Inactivated by GuHCl in a Concentration- and Treatment Time-Dependent Manner

To test whether IONzyme could be inhibited by GuHCl as a natural enzyme could, we mixed IONzyme ($\phi = 90$ nm) with GuHCl (2.0 M) and tested the peroxidase activity using a H_2O_2-3,3′,5,5′-tetramethylbenzidine (TMB) colorimetric system (Fan et al., 2017). A deeper blue color indicates more oxidized TMB produced. As shown in **Figure 1A**, the activity of IONzyme, represented by absorbance detection, decreased dramatically in the presence of GuHCl compared with the control group in the absence of GuHCl. The product in the GuHCl-containing system was a shallower blue than that generated in the control, indicating that the enzyme-like activity of IONzymes declined after mixing with GuHCl (**Figure 1B**).

To reveal the character of IONzyme inactivation by GuHCl, we analyzed the effects with a concentration gradient of GuHCl solution. As shown in **Figure 1C**, the activity of IONzyme (initial reaction velocity, V_0) significantly decreased at GuHCl concentrations higher than 0.4 M. Higher concentrations gave a stronger effect. The IC_{50} for the decrease in IONzyme activity was ∼2.6 M GuHCl. The activity of IONzyme was not markedly affected by GuHCl concentrations no greater than 0.2 M (**Figure 1C**). When the incubation time of IONzyme with GuHCl increased to 24 h, the GuHCl-induced IONzyme inactivation became stronger within the effective concentrations, and the complete repression of IONzyme was detected in 1 M GuHCl (**Figure S1**). These data indicated that IONzyme activity can be inhibited by GuHCl in a concentration- and time-dependent manner.

To further investigate the IONzyme-GuHCl interaction, we incubated IONzyme with GuHCl for different lengths of time (0, 5, 10, 15, and 30 min) and measured its activity. As shown in **Figure 1D**, ∼70% decreases in activity could be immediately detected upon the addition of GuHCl. The level of residual activity in the presence of GuHCl did not change when the incubation time was prolonged for no more than 15 min, and the activity fluctuated slightly upon incubation for 30 min. These results indicated that the interaction between GuHCl and IONzyme rapidly approaches equilibrium in the initial stage. The suppression of IONzyme activity may identify GuHCl as an inhibitor of IONzyme.

GuHCl-Induced Inhibition of IONzyme Is Reversible

To clarify whether the inhibitory effect of GuHCl on IONzyme peroxidase-like activity is reversible, we tested the peroxidase-like activity of IONzyme recycled from the IONzyme-2 M GuHCl mixture using centrifugation. Upon the addition of GuHCl, As shown in **Figure 2**, the IONzyme in 2 M GuHCl retained 33% of the activity of the control ($p < 0.001$), and the recycled IONzyme (de-GuHCl sample) exhibited 86% activity. Furthermore, when we re-added 2 M GuHCl to the de-GuHCl sample and tested the activity again, the same level of inhibition compared with the control (∼67%) of IONzyme occurred again. The remaining activity showed no significant difference from that of the GuHCl sample before recycling ($P = 0.9557$), and the dynamics curve of the reaction maintained the same pattern (**Figure 2B**). These data indicate that the inhibitory effect of GuHCl on IONzyme is reversible.

GuHCl Acts as an IONzyme Inhibitor by Competition With the Substrate H_2O_2

To investigate the mechanism of the interaction between GuHCl and IONzyme, we performed inhibition kinetic analysis. First, H_2O_2 was titrated at several fixed concentrations (1, 1.5, and 2 M) of GuHCl and at a fixed concentration of TMB.

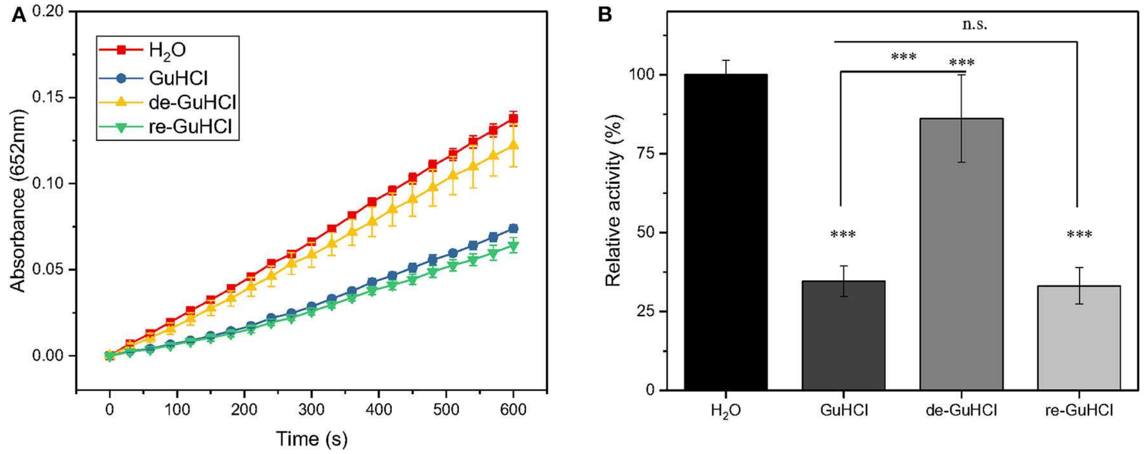

FIGURE 2 | GuHCl is a reversible inhibitor of IONzyme. The peroxidase activity of recycled IONzyme was analyzed and shown by the dynamic changes in the absorbance **(A)** and the relative activity **(B)**. Conditions are shown in **Figure 1**. Samples included the untreated IONzyme control (H_2O), IONzyme mixed with GuHCl (GuHCl), recycled IONzyme after the removal of GuHCl (de-GuHCl), and the de-GuHCl sample with GuHCl re-added (re-GuHCl) ($n \geq 12$). Data are the mean ± SD. $^{***}P < 0.001$, No significance (N.S.), $P > 0.5$.

The results showed that the GuHCl-IONzyme interaction fit the Michaelis–Menten model. As shown in **Figures 3A,B**, the lines for GuHCl-treated samples intersected on the Y axis, suggesting that GuHCl is a competitive inhibitor of IONzyme against the substrate H_2O_2. Second, similar experiments were carried out with different concentrations of TMB and fixed concentrations of H_2O_2. During this time, the lines for GuHCl-treated groups intersected on the X axis, indicating that GuHCl is a non-competitive inhibitor of IONzyme with TMB as a substrate (**Figures 3C,D**). For both experiments, the lines of the control samples (without the addition of GuHCl) deviated somewhat from the intersection point compared to other lines.

The data were fitted to the Michaelis–Menten model to obtain the parameters, which are presented in **Table 1**. When using H_2O_2 as a substrate, Vmax is stable with increasing inhibitor concentration; that is, the effect of GuHCl can be eliminated by increasing the concentration of H_2O_2 in the reaction system. However, the value of Km gradually increased, i.e., with increasing inhibitor concentration, the affinity between IONzyme and H_2O_2 decreased, and these changes were consistent with the characteristics of competitive inhibitors. When TMB is used as a substrate, with increasing inhibitor concentration, Vmax decreases while Km remains unchanged, which is consistent with the characteristics of non-competitive inhibition. After the addition of 1 M GuHCl, the catalytic efficiency of IONzyme on TMB and H_2O_2 decreased by 46 and 56%, respectively, and both decreased further as the concentration of GuHCl was increased.

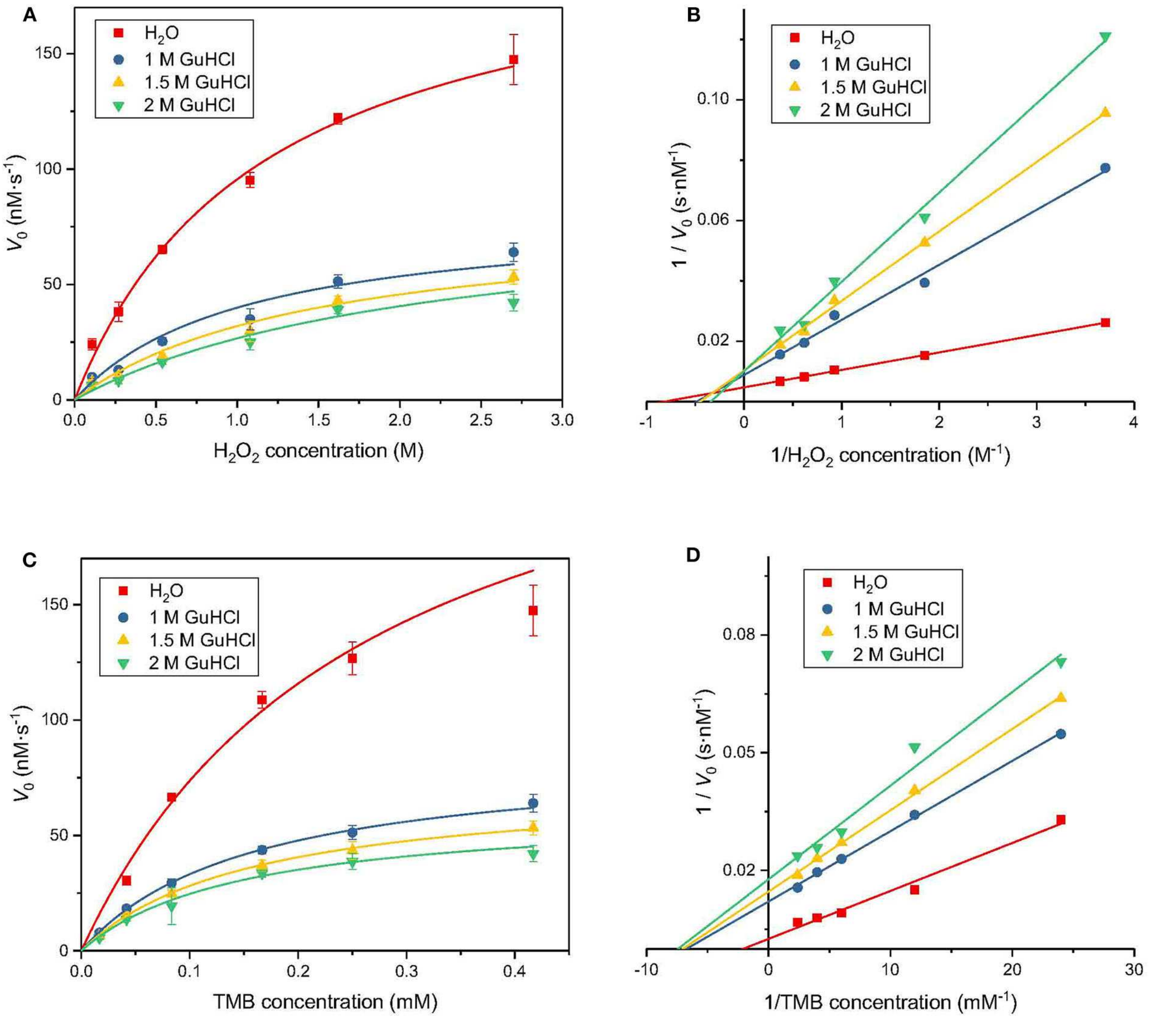

FIGURE 3 | Inhibition kinetics analysis of IONzyme at different GuHCl concentrations. Conditions are shown in **Figure 1**, except that K_m, V_{max}, k_{cat}, and k_{cat}/K_m were analyzed at different H_2O_2 concentrations **(A)**. The Lineweaver-Burk plot of the data from **(A)** is shown in **(B)**. The data for different concentrations of TMB are shown in **(C)** and the Lineweaver-Burk plot of the data from **(C)** are in **(D)**. Data from 3 separate experiments ($n \geq 8$). Data are the mean ± SD.

TABLE 1 | Comparison of the kinetic parameters of Fe_3O_4 IONzymes in H_2O or GuHCl.

	[E] (M)	Substrate	K_m (mM)	V_{max} (M s^{-1})	k_{cat} (s^{-1})	k_{cat}/K_m (s^{-1} M^{-1})
IONzyme (in water)	4.2×10^{-12}	TMB	0.267	2.70×10^{-7}	6.43×10^{4}	2.41×10^{8}
	4.2×10^{-12}	H_2O_2	1,165	2.07×10^{-7}	4.93×10^{4}	4.23×10^{4}
IONzyme (GuHCl- 1 M)	4.2×10^{-12}	TMB	0.157	8.52×10^{-8}	2.03×10^{4}	1.29×10^{8}
	4.2×10^{-12}	H_2O_2	1,033	8.12×10^{-8}	1.93×10^{4}	1.87×10^{4}
IONzyme (GuHCl- 1.5 M)	4.2×10^{-12}	TMB	0.158	7.26×10^{-8}	1.73×10^{4}	1.09×10^{8}
	4.2×10^{-12}	H_2O_2	1,496	7.98×10^{-8}	1.90×10^{4}	1.27×10^{4}
IONzyme (GuHCl- 2 M)	4.2×10^{-12}	TMB	0.148	6.12×10^{-8}	1.46×10^{4}	9.86×10^{7}
	4.2×10^{-12}	H_2O_2	2,200	8.52×10^{-8}	2.03×10^{4}	9.23×10^{3}

K_m, the apparent affinity; [E] is the IONzyme concentration, K_m is the Michaelis constant, V_{max} is the maximal reaction velocity and k_{cat} is the catalytic constant, where $k_{cat} = V_{max}/[E]$. k_{cat}/K_m reflects the catalytic efficiency.

Inactivation May Not Depend on GuHCl-Induced IONzyme Aggregation

To determine whether the reported IONzyme aggregation was involved in the GuHCl-induced inactivation of IONzyme, in addition to the competitive interaction of GuHCl with substrate H_2O_2, the progressive aggregation of IONzymes was recorded during incubation with 2 M GuHCl for 30 min by dynamic light scattering. The size was represented by the hydrodynamic radius. As shown in **Figure 4A**, the size of IONzymes with water as a control did not significantly change during the incubation. However, the IONzymes with GuHCl were markedly larger than the control at 0 h and continued to increase with time, indicating that aggregates appear immediately upon the addition of GuHCl and continue growing. On the other hand, the activity of IONzymes, as mentioned previously, dropped immediately after IONzymes were mixed with GuHCl and remained stable at an inhibited level (35–55% of control) during the 30 min incubation (**Figure 1D**). Thus, the growth of aggregates did not enhance the inactivation. Since the activity of IONzymes was not changed at GuHCl concentrations >0.4 M, we determined whether IONzyme aggregation was induced at a low concentration of GuHCl (0.2 M) The results distinctly showed aggregation of IONzyme in 0.2 M GuHCl after 24 h, even using a μm-scale microscope (**Figure 4B**).

To demonstrate that aggregation did not affect the function of IONzyme, we employed 1 M $(NH_4)_2SO_4$, another commonly applied inducer for protein aggregation, to determine whether it could mimic the effects of GuHCl. As shown in **Figures 4C,D**, the size of particles did not significantly change after 1 h of incubation in water (with radii of 54.18 ± 0.86 nm at 0 h and 53.02 ± 3.29 nm at 1 h) but was distinctly enlarged in $(NH_4)_2SO_4$ with either no or 1 h pre-incubation, and longer pre-incubation times gave larger aggregates (with radii of 114.80 ± 9.37 nm at 0 h and 388.87 ± 27.56 nm at 1 h). Moreover, the aggregated samples with different sizes show similar activities. These data indicate that IONzyme aggregation, which was also induced by 1 M $(NH_4)_2SO_4$,, does not affect the activity of IONzymes. Therefore, the GuHCl-IONzyme interaction definitely induces incidental IONzyme aggregation, but the aggregation may not contribute to GuHCl-induced IONzyme inactivation under our experimental conditions.

Interaction Between GuHCl and Iron Atom Correlates With the Inactivation of IONzymes

To check whether GuHCl binds to the iron atom in the interaction between GuHCl and IONzyme, we applied ESR spectroscopy to analyse the unpaired electrons in the IONzymes, which could reflect the character of the iron atom (Hagen, 2008). We mixed IONzyme with GuHCl in NaAC buffer (pH = 4.5) and measured the ESR spectrum at room temperature (**Figure S2**). As shown in **Figure 5A**, the g-factor value could be observed. The value of the g-factor was approximately 2.4 in the control and did not show a significant change in GuHCl at concentrations lower than 0.2 M. Then, it decreased quickly until the concentration of GuHCl reached 2 M and remained slightly >2.2. The change in the g-factor value with increasing GuHCl level shows a similar pattern to the inactivation of IONzymes under the same experimental conditions (**Figure 1C**, **Figure S1**). These results suggest that the activity changes in IONzyme are due to the interaction of IONzyme with GuHCl. GuHCl binds to the iron atom and affects the electron density of iron, inducing IONzyme inactivation. In addition, the inactivation level could be adjusted by GuHCl at concentrations between 0.4 and 2 M.

Based on the above experimental results, we established a model for IONzyme catalyzed reaction (**Figure 5B**). Since GuHCl binds to the iron atom on the IONzyme, and is a competitive inhibitor for H_2O_2, we conclude that H_2O_2 also binds the iron atom on the IONzyme during the reaction. GuHCl binds to the IONzyme non-competitively with TMB, so TMB binds to the oxygen atoms on the IONzyme.

DISCUSSION

In the current study, we employed GuHCl to investigate whether IONzyme has the characteristic inactivation property of a natural enzyme. The results show that GuHCl induces IONzyme aggregation and inhibits the representative peroxidase-like activity of IONzyme in a concentration- and treatment time-dependent manner. However, the aggregation process appears to be unrelated to inactivation; instead, GuHCl acts as a reversible inhibitor showing typical kinetic competition with substrate H_2O_2. ESR spectrum analysis revealed that the interaction of

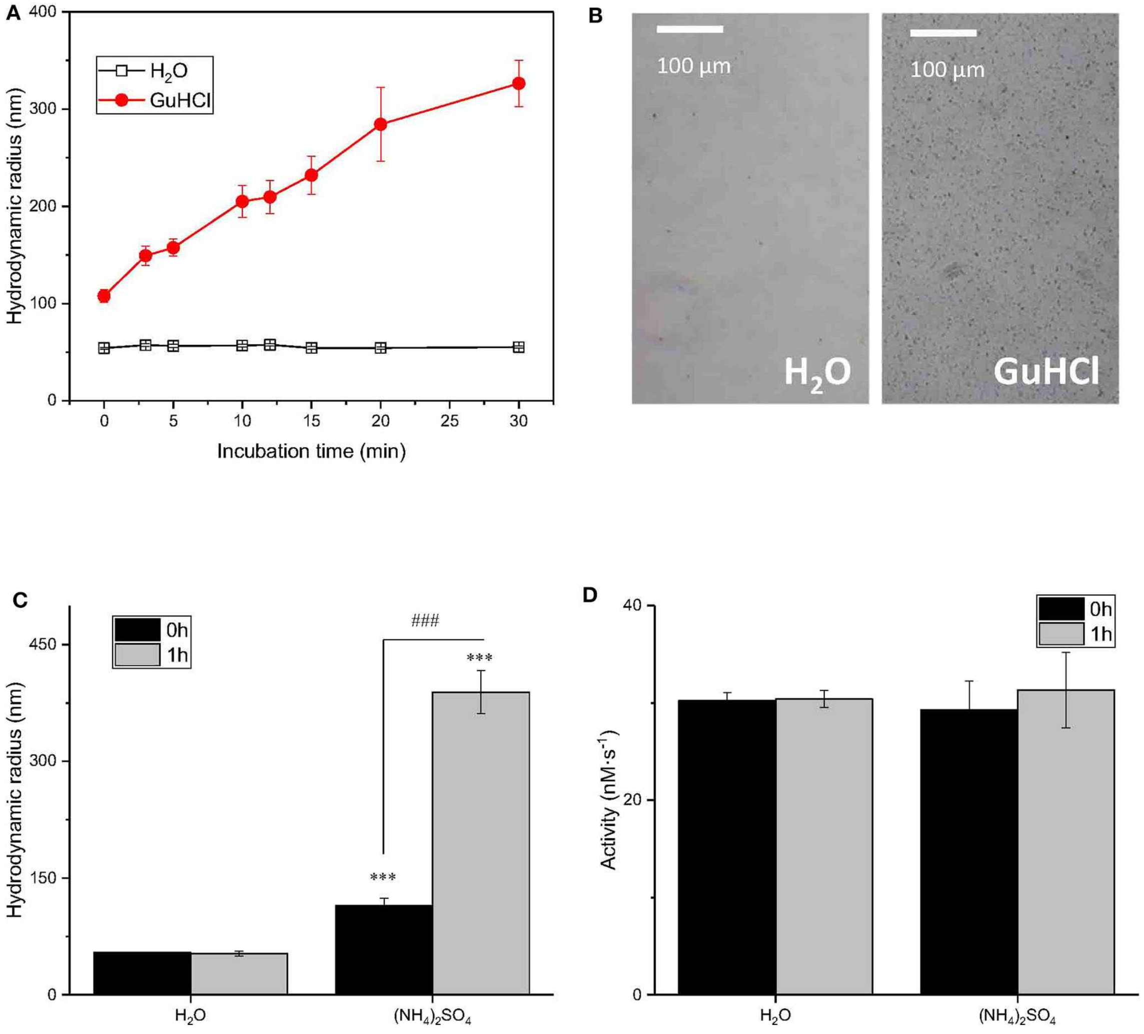

FIGURE 4 | The relationship between the IONzyme peroxidase-like activity and the radius. Dynamic light scattering was employed to measure the hydrodynamic radii of IONzymes. Time course of IONzyme hydrodynamic radii in H_2O or 2 M GuHCl **(A)** IONzyme aggregation was observed under a microscope after incubation the Nanozyme (0.91 μg/100 μl; concentration of Nanozyme in the Nanozyme-GuHCl incubation mixture before adding the reaction buffer) in 0.2 M GuHCl for 24 h **(B)** Comparison of IONzyme hydrodynamic radius **(C)** and peroxidase-like activity **(D)** in H_2O or 0.5 M $(NH_4)_2SO_4$ with 0 or 1 h pre-incubation time. ***$P < 0.001$ (vs. H_2O−0 h). ###$P < 0.001$ (vs, $(NH_4)_2SO_4$−0 h).

GuHCl with IONzyme induces changes in the unpaired electrons in the iron atom correlated with the inactivation of IONzyme. Our study revealed a reversible inhibition property of IONzyme mimicking that of protein enzymes and provided another way to interpret the catalytic mechanism and control nanozyme activity.

Similar to the inactivation and reactivation of a protein enzyme, the reversibility of the inactivation of IONzyme in the presence of GuHCl was also observed under our experimental conditions. To indicate this characteristic inactivation, we applied GuHCl and developed a procedure to affect the peroxidase-like activity of IONzymes. Although proteins undergo denaturation and renaturation, most proteins cannot be completely reactivated after inactivation by GuHCl denaturation; examples include creatine kinase (CK) (Zhou et al., 1993) and D-glyceraldehyde-3-phosphate dehydrogenase (GAPDH) (Liang et al., 1990). Proteins are characterized as "fragile" and are much more vulnerable to denaturants than IONzymes. The easy inactivation and reactivation of IONzyme suggest a convenient way to regulate its function by adjusting the concentration of GuHCl, which may facilitate the application of IONzyme.

GuHCl is widely used as a denaturant of authentic enzymes. As described previously (Zhang et al., 1993), protein inactivation and aggregation feature in "a fast inactivation followed by a slow conformational change:" that is, while the protein conformation undergoes little change, the enzymatic activity will decrease markedly (Xiao et al., 1993). This phenomenon is explained by the concept that the active site is much more flexible than the conformation of the molecule as a whole (Tsou, 1998). Therefore, the active site is vulnerable to disturbance by the denaturant GuHCl, and inactivation occurs before the overall

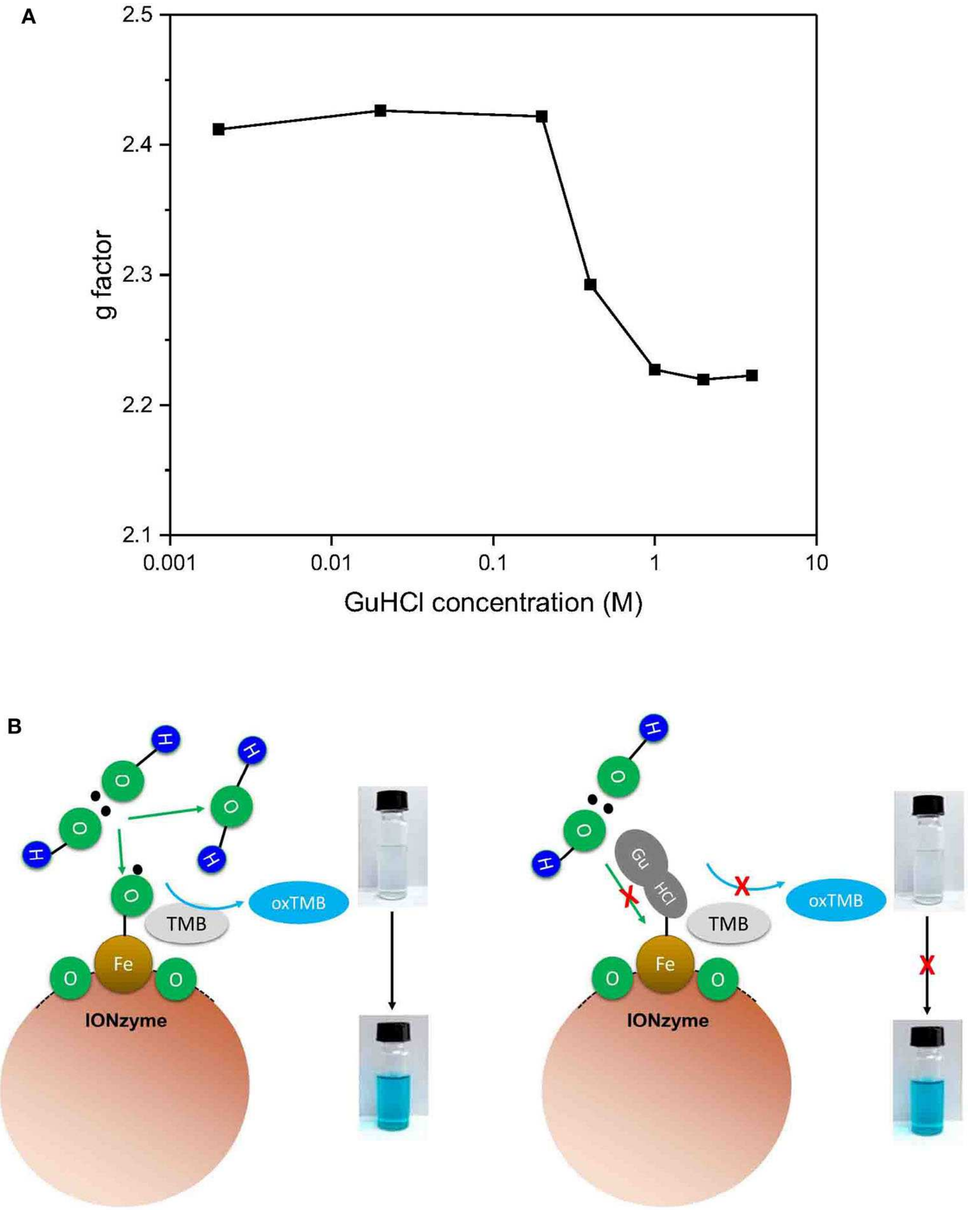

FIGURE 5 | Mechanism of the peroxidase reaction catalyzed by IONzyme. Electron spin resonance spectroscopy was used to analyse the interaction between IONzyme and GuHCl in sodium acetate buffer. The change in the g factors of IONzymes in different concentrations of GuHCl **(A)**. A putative Scheme of IONzyme catalytic reaction **(B)**.

protein molecular conformation changes. The denaturant GuHCl is regarded as a conformational change reagent but does not bind to the essential catalytic groups (Zhou et al., 1993). Now, we can see that GuHCl induces fast inactivation followed by a slow conformational (aggregation) change in IONzyme and acts as an inhibitor in addition to the common role of denaturant. On the other hand, the role of inhibitor was supported by the enzymatic kinetics assay. However, the straight line of the control sample (without the addition of GuHCl) in the reaction of GuHCl-treated IONzyme with different concentrations of H_2O_2 was somewhat decentralized in the double reciprocal plot. We suspect that there might be some other interaction between IONzymes and GuHCl.

In our experiment setup, the inhibition effect can be observed only when the concentration of GuHCl exceed 0.4 M, which is a fairly high concentration. GuHCl-induced aggregation could be observed in low-concentration GuHCl (0.2 M, **Figure 4B**). High-concentration (>0.4 M) GuHCl-induced quick reduction in IONzyme activity occurred before the aggregation is visible. Therefore, the threshold concentration of the GuHCl-induced inhibition cannot be fully explained by aggregation. Given that the activity of IONzyme in 1 M $(NH_4)_2SO_4$ is the same as that in water, thus we can exclude the concern that the observed activity variation is due to the change of ionic strength and further support the conclusion that the effect is aggregation in-dependent. As mentioned above, GuHCl competes with substrate H_2O_2 on binding with the IONzyme. We hypothesized that the competence of GuHCl in competing with H_2O_2 on IONzyme binding is concentration-dependnet. In low GuHCl concentration (<0.2 M), IONzyme prior to bind H_2O_2 rather than GuHCl, which is support by the GuHCl concentration-dependent g-factor changes of the IONzyme in the ESR assay, suggesting a concentration-dependent GuHCl/nanozymes interaction ratio. Our result suggests that a novel interaction of GuHCl with the essential catalytic groups *in situ* at the active site occurred during GuHCl denaturation. Thus, clarification of the nanozyme characteristics helps us to reveal the reaction mechanisms not only of nanozyme but also of natural protein enzymes.

GuHCl, as an inhibitor, contains a guanidyl group and a chloride leading to the inactivation of IONzyme. The competitive manner between GuHCl and H_2O_2 exhibits both of them bind to iron atom in IONzyme. TMB probably binds to the oxygen of Fe_3O_4 because of the non-competitive reaction with GuHCl. Liu and colleagues described the inhibition of the enzymatic-like activity of gold nanoparticles in the presence of halide ions (Liu et al., 2017). They found that halide ions can switch the activity of gold nanozymes by Au-X interactions. Their results indicated that chloride may play an important role in the reaction with IONzyme. However, GuHCl can also be used in the inactivation of other nanozymes, although our work has mainly focused on IONzyme.

In summary, the denaturant GuHCl induces IONzyme aggregation and inhibits its representative peroxidase-like activity. The inactivation results mainly from the role of GuHCl as an inhibitor associated with the iron atom in IONzyme, instead of a denaturant related to conformation changes such as aggregation. This work demonstrates the reversible inhibition of IONzyme, mimicking that of protein enzymes, and provides an additional way to control nanozyme activity. It reveals the catalytic mechanism that H_2O_2 binds to the iron atom and TMB binds to oxygen atom in the IONzyme.

DATA AVAILABILITY STATEMENT

All datasets generated for this study are included in the article/**Supplementary Material**.

AUTHOR CONTRIBUTIONS

JY performed the experiments and wrote the manuscript. WM performed major parts of the experiments and wrote the manuscript. YL provided some ideas, discussed, and wrote the manuscript. YW and LG provided some ideas. RH designed, supervised, and wrote the manuscript.

FUNDING

This project was supported by the National Science Foundation of China (Nos. 31470036, 31870840).

ACKNOWLEDGMENTS

We thank Xiyun Yan, Kelong Fan (Institute of Biophysics, the Chinese Academy of Sciences), Haijun Yang (Tsinghua University), and Weixi Tian (University of Chinese Academy of Sciences) for their helpful discussions. We thank Xiaoxia Yu (IBP, CAS) for the DLS detection and Chong Chen (Yangzhou University) for ESR measurement. We thank Dr. Pingdong Hu (IBP, CAS) for his kind assistance of measuring the UV/Vis adsorption spectrum of the reaction solution.

SUPPLEMENTARY MATERIAL

The Supplementary Material for this article can be found online at: https://www.frontiersin.org/articles/10.3389/fchem.2020.00491/full#supplementary-material

The Supporting Information is available free of charge on the ACS Publications website at doi: 10.3389/fchem.2020.00491, including the long-term effect of GuHCl on the activity of IONzyme and the ESR spectra of IONzymes mixed with different concentrations of GuHCl.

REFERENCES

Fan, K. L., Wang, H., Xi, J. Q., Liu, Q., Meng, X. Q., Duan, D. M., et al. (2017). Optimization of Fe_3O_4 nanozyme activity via single amino acid modification mimicking an enzyme active site. *Chem. Commun.* 53, 424–427. doi: 10.1039/C6CC08542C

Fenton, H. J. H. (1894). LXXIII.-oxidation of tartaric acid in presence of iron. *J. Chem. Soc. Trans.* 65, 899−910. doi: 10.1039/CT8946500899

Gao, L., Zhuang, J., Nie, L., Zhang, J., Zhang, Y., Gu, N., et al. (2007). Intrinsic peroxidase-like activity of ferromagnetic nanoparticles. *Nat. Nanotechnol.* 2, 577–583. doi: 10.1038/nnano.2007.260

Hagen, W. R. (2008). *Biomolecular EPR Spectroscopy*. Boca Raton, FL: CRC Press Inc.

Kelong, F., Changqian, C., Yongxin, P., Di, L., Dongling, Y., Jing, F., et al. (2012). Magnetoferritin nanoparticles for targeting and visualizing tumour tissues. *Nat. Nanotechnol.* 7, 459–464. doi: 10.1038/nnano.2012.90

Kotov, N. A. (2010). Inorganic nanoparticles as protein mimics. *Science* 330, 188–189. doi: 10.1126/science.1190094

Liang, S. J., Lin, Y. Z., Zhou, J. M., Tsou, C. L., Wu, P. Q., and Zhou, Z. K. (1990). Dissociation and aggregation of D-glyceraldehyde-3-phosphate dehydrogenase during denaturation by guanidine-hydrochloride. *Biochim. Biophys. Acta* 1038, 240–246. doi: 10.1016/0167-4838(90)90211-W

Liu, Y., Xiang, Y. P., Zhen, Y. L., and Guo, R. (2017). Halide ion-induced switching of gold nanozyme activity based on au-x interactions. *Langmuir* 33, 6372–6381. doi: 10.1021/acs.langmuir.7b00798

Niu, H., Zhang, D., Zhang, S., Zhang, X., Meng, Z., and Cai, Y. (2011). Humic acid coated Fe_3O_4 magnetic nanoparticles as highly efficient Fenton-like catalyst for complete mineralization of sulfathiazole. *J. Hazardous Mater.* 190, 559–565. doi: 10.1016/j.jhazmat.2011.03.086

Park, K. S., Kim, M. I., Cho, D. Y., and Park, H. G. (2011). Label-free colorimetric detection of nucleic acids based on target-induced shielding against the peroxidase-mimicking activity of magnetic nanoparticles. *Small* 7, 1521–1525. doi: 10.1002/smll.201001886

Quick, K. L., Ali, S. R., Xiong, C., Wozniak, D., and Dugan, L. L. (2008). A carboxyfullerene SOD mimetic improves cognition and extends the lifespan of mice. *Neurobiol. Aging* 29, 117–128. doi: 10.1016/j.neurobiolaging.2006.09.014

Sen, T., and Barisik, M. (2018). Size dependent surface charge properties of silica nano-channels: double layer overlap and inlet/outlet effects. *Phys. Chem. Chem. Phys.* 20, 16719–16728. doi: 10.1039/C8CP01906A

Song, Y., Wang, X., Zhao, C., Qu, K., Ren, J., and Qu, X. (2010). Label-free colorimetric detection of single nucleotide polymorphism by using single-walled carbon nanotube intrinsic peroxidase-like activity. *Chemistry* 16, 3617–3621. doi: 10.1002/chem.200902643

Tsou, C. L. (1998). The role of active site flexibility in enzyme catalysis. *Biochemistry* 63, 253–258.

Wang, N., Zhu, L., Wang, D., Wang, M., Lin, Z., and Tang, H. (2010). Sono-assisted preparation of highly-efficient peroxidase-like Fe_3O_4 magnetic nanoparticles for catalytic removal of organic pollutants with H_2O_2. *Ultrasonics Sonochem.* 17, 526–533. doi: 10.1016/j.ultsonch.2009.11.001

Wei, H., and Wang, E. (2008). Fe_3O_4 magnetic nanoparticles as peroxidase mimetics and their applications in H_2O_2 and glucose detection. *Anal. Chem.* 80, 2250–2254. doi: 10.1021/ac702203f

Wei, H., and Wang, E. K. (2013). Nanomaterials with enzyme-like characteristics (nanozymes): next-generation artificial enzymes. *Chem. Soc. Rev.* 42, 6060–6093. doi: 10.1039/c3cs35486e

Wu, Y. H., Song, M. J., Xin, Z. A., Zhang, X. Q., Zhang, Y., Wang, C. Y., et al. (2011). Ultra-small particles of iron oxide as peroxidase for immunohistochemical detection. *Nanotechnology* 22:225703 doi: 10.1088/0957-4484/22/22/225703

Xiao, J., Liang, S. J., and Tsou, C. L. (1993). Inactivation before significant conformational change during denaturation of papain by guanidine-hydrochloride. *Biochim. Biophys. Acta* 1164, 54–60. doi: 10.1016/0167-4838(93)90111-4

Zhang, Y., Wang, Z., Li, X., Wang, L., Yin, M., Wang, L., et al. (2016). Dietary iron oxide nanoparticles delay aging and ameliorate neurodegeneration in drosophila. *Adv. Mater.* 28, 1387–1393. doi: 10.1002/adma.201503893

Zhang, Y. L., Zhou, J. M., and Tsou, C. L. (1993). Inactivation precedes conformation change during thermal-denaturation of adenylate kinase. *Biochim. Biophys. Acta* 1164, 61–67. doi: 10.1016/0167-4838(93)90112-5

Zhou, H. M., Zhang, X. H., Yin, Y., and Tsou, C. L. (1993). Conformational-changes at the active-site of creatine-kinase at low concentrations of guanidinium chloride. *Biochem. J.* 291, 103–107. doi: 10.1042/bj2910103

Conflict of Interest: The authors declare that the research was conducted in the absence of any commercial or financial relationships that could be construed as a potential conflict of interest.

The reviewer XQ declared a shared affiliation, though no other collaboration, with the authors WM, JY, YL, YW, and RH.

frontiers in Chemistry

ORIGINAL RESEARCH
published: 05 August 2020
doi: 10.3389/fchem.2020.00654

Sodium Alginate Modified Platinum Nanozymes With Highly Efficient and Robust Oxidase-Like Activity for Antioxidant Capacity and Analysis of Proanthocyanidins

Shao-Bin He[1], Liu Yang[1], Xiu-Ling Lin[1], Hua-Ping Peng[1], Zhen Lin[1], Hao-Hua Deng[1]*, Wei Chen[1]* and Guo-Lin Hong[2]*

[1] Fujian Key Laboratory of Drug Target Discovery and Structural and Functional Research, School of Pharmacy, Fujian Medical University, Fuzhou, China, [2] Department of Laboratory Medicine, The First Affiliated Hospital of Xiamen University, Xiamen, China

Platinum nanozymes exhibiting highly efficient and robust oxidase-like activity are successfully synthesized and modified using sodium alginate (SA-PtNPs). According to a steady-state dynamic assay, Michaelis-Menton constant (K_m) is calculated as 11.6 μM, indicating that the affinity of SA-PtNPs toward the substrate, 3, 3′, 5, 5′-tetramethylbenzidine (TMB), is high. It shows in the paper that SA-PtNPs exhibit a significant oxidant effect on substrate-O_2 to produce $O_2^{\bullet -}$ as an oxidase mimic. Moreover, the oxidase-like activity fluctuated slightly under changes in environmental pH and incubation time, implying that SA can increase the dispersibility and stability of PtNPs. A colorimetric assay for oligomeric proanthocyanidins (OPC) was realized given how few explorations of the former there are. We found that the significant inhibitory effect of OPC on the oxidase-like activity is due to the competitive effect between OPC and TMB for binding to the active site of SA-PtNPs, resulting in a color change. Under optimal conditions, the logarithmic value of the chromogenic difference (ΔA_{450nm}) to OPC concentration was linear (4–32.5 μM, $r = 0.999$) with a limit of detection (LOD) of 2.0 μM. The antioxidant capacity of OPC obtained by the Soxhlet extraction method from grape seeds was 2.85 U/mg. The recovery from the experiment in which OPC was added to grape seeds ranged from 97.0 to 98.6% (RSDs of 0.5–3.4%), suggesting a high accuracy in OPC detection. These findings are important because OPC is an internationally recognized antioxidant that eliminates free radicals in the human body and, therefore, may prevent a variety of diseases. Thus, we envisage that this Pt nanozyme-based assay may be prevalent for antioxidant capacity evaluation and analytical applications.

Keywords: sodium alginate, platinum nanozyme, oxidase-like activity, antioxidant capacity, colorimetric, proanthocyanidins

OPEN ACCESS

Edited by:
Kelong Fan,
Institute of Biophysics (CAS), China

Reviewed by:
Ajay Singh Karakoti,
The University of Newcastle, Australia
Yuming Huang,
Southwest University, China
Xiangheng Niu,
Jiangsu University, China
Yan Fu,
Tianjin University, China
Hui Wei,
Nanjing University, China

****Correspondence:***
Hao-Hua Deng
DHH8908@163.com
Wei Chen
chenandhu@163.com
Guo-Lin Hong
18860089899@139.com

Specialty section:
This article was submitted to
Nanoscience,
a section of the journal
Frontiers in Chemistry

Received: *15 February 2020*
Accepted: *23 June 2020*
Published: *05 August 2020*

Citation:
He S-B, Yang L, Lin X-L, Peng H-P, Lin Z, Deng H-H, Chen W and Hong G-L (2020) Sodium Alginate Modified Platinum Nanozymes With Highly Efficient and Robust Oxidase-Like Activity for Antioxidant Capacity and Analysis of Proanthocyanidins.
Front. Chem. 8:654.
doi: 10.3389/fchem.2020.00654

INTRODUCTION

Proanthocyanidin (PC) is a general term for a large class of polyphenolic compounds widely found in plants, red wine, as well as grape seeds (Da Silva et al., 1991; Fracassetti et al., 2013). Its oligomer, oligomeric proanthocyanidin (OPC), is an internationally recognized antioxidant that eliminates free radicals in humans (Weber et al., 2007). Therefore, OPC may provide disease prevention caused by free radicals such as cardiopathy, malignant tumor, and inflammation (Vaid et al., 2012; Coleman and Shaw, 2017; Chen et al., 2019). Thus, OPC is expected to extend its applications in clinical medicine and food health practices. However, owing to the complexity of OPC, there have not been enough studies done on OPC contents and antioxidant capacity. At present, most methods use high-performance liquid chromatography or mass spectrometry technology to analyze PC or OPC and are time-consuming, expensive, and technically demanding (Ortega et al., 2010; Dooren et al., 2018). To this end, it is of fundamental significance to establish a colorimetric method to evaluate antioxidant capacity and analyze PC or OPC; it should have superior visibility, be a time-saver, and be easy to operate.

Since 2007, when Yan's group first discovered that Fe_3O_4 magnetic nanoparticles have catalytic activity like horseradish peroxidase (Gao et al., 2007), researches of nanozymes (nanomaterials with enzyme-like activity) have been continuously deepened, and a series of nanozymes-based analytical assays have subsequently been obtained (Wei and Wang, 2013; Huang et al., 2019). Among the nanomaterials, platinum nanoparticles (PtNPs) have been explored to mimic several kinds of enzyme activities such as peroxidase, catalase, uricase activities, and so on (Dong et al., 2011; Fu et al., 2014; Li et al., 2015; Liu et al., 2015; He et al., 2019a). Meanwhile, the oxidase-like activity of PtNPs has elicited growing attention in recent years (Yu et al., 2014; Deng et al., 2017; He et al., 2019b). Unlike peroxidase, oxidase can catalyze a certain substrate in the absence of H_2O_2, having far-reaching implications for the study of oxidase mimics. Additionally, H_2O_2 is easily decomposed and loses its oxidizing power; this is also disadvantageous for its practical application. Inspired by the above, a new nanozyme with oxidase-like activity is far more propitious to design analytical assays with user-friendly control, stability, and dependability.

During the synthesis of nanomaterials, the role of ligand is also crucial. The protective effect of ligands enables people to successfully obtain a variety of nanomaterials. Moreover, the use of natural products as ligands instead of chemicals to stabilize nanoparticles can greatly improve biocompatibility and broaden their biomedical applications. To this end, efforts have been made to adjust the size and morphology of PtNPs to mimic enzyme-like activity by applying natural products (Deng et al., 2017, 2019; You et al., 2017; He et al., 2019a,b). Sodium alginate (SA) is a natural polysaccharide derived with a certain solubility, stability, and viscosity to form a gel, making them suitable for broad applications (Li et al., 2005; Mokhtari et al., 2017). Given the advantages of SA, the use of SA as a protective agent to modify nanomaterials not only enhances the dispersibility and stability but also provides the possibility of surface modification, nanogel preparation, and potential applications in many fields (Travan et al., 2009).

In this study, SA-PtNPs were prepared by a one-step reduction method using the biocompatible and non-toxic SA as a protective agent. SA-PtNPs have small particle size, good dispersion, and stability (5.9 ± 0.6 nm). Furthermore, SA-PtNPs have intrinsic oxidase activity that can rapidly catalyze the oxidation process of 3, 3′, 5, 5′-tetramethylbenzidine (TMB) leading to a color change. More significantly, the introduction of OPC in SA-PtNPs-catalyzed TMB system results in a competitive inhibition and colorless reaction. Thus, a colorimetric assay for OPC was established based on the excellent oxidase-like activity of SA-PtNPs and the antioxidant capacity of OPC (**Scheme 1**). This study presents a new preparation method for Pt nanozymes and shows a good prospect of application based on SA-PtNPs. On the other hand, this assay also provides a new insight for antioxidant capacity evaluation and opens a new avenue for OPC analysis.

EXPERIMENTAL PART

Synthesis of SA-PtNPs

The synthesis steps are as follows: SA (0.1 g) was added into 50 mL of 1% (v/v) acetic acid solution and completely stirred for about 15 min. Then, 2 mL H_2PtCl_6 (10 mM) was mixed with 47 mL SA solution. The mixture was vortex at ambient temperature for 30 min. One milliliters of newly prepared $NaBH_4$ solution (70 mM) was added to the mixture and was completed within 5 min. The SA-PtNPs (78.03 mg/L) were obtained by stirring in the dark for 90 min. The SA-PtNPs was transferred in a dialysis bag and dialysed against water. The dialysis water was replaced after 1 h followed by frequent changes for 48 h. Finally, the SA-PtNPs were preserved constantly in darkness at 4°C.

OPC Detection

Fifty µL of various concentrations of OPC, 50 µL of TMB (3 mM), and 30 µL of SA-PtNPs (15.61 mg/L) were added into 870 µL of phosphate buffer (pH = 4.5, 50 mM). The mixture was then incubated for 5 min at 37°C. Subsequently, 200 µL of H_2SO_4 (2 M) was introduced to the reaction as a stop buffer. Finally, the solution was transferred to a quartz cell for measurement at 450 nm. Other experimental part can be seen in **Supplementary Material**.

RESULTS AND DISCUSSION

Characterization of SA-PtNPs

SA-PtNPs were prepared by a simple approach with SA as a stabilizing agent and $NaBH_4$ as a reductant. The stabilizing and reducing agents have pivotal effects during the synthesis of SA-PtNPs, thus the concentrations of SA and $NaBH_4$ had to be determined, respectively (**Supplementary Figure 1**). As shown in **Supplementary Figure 1**, the concentrations of SA and $NaBH_4$ on the preparation of SA-PtNPs were optimized to be 2 mg/mL and 1.4 mM. The images in **Figure 1A** display a yellowish-brown

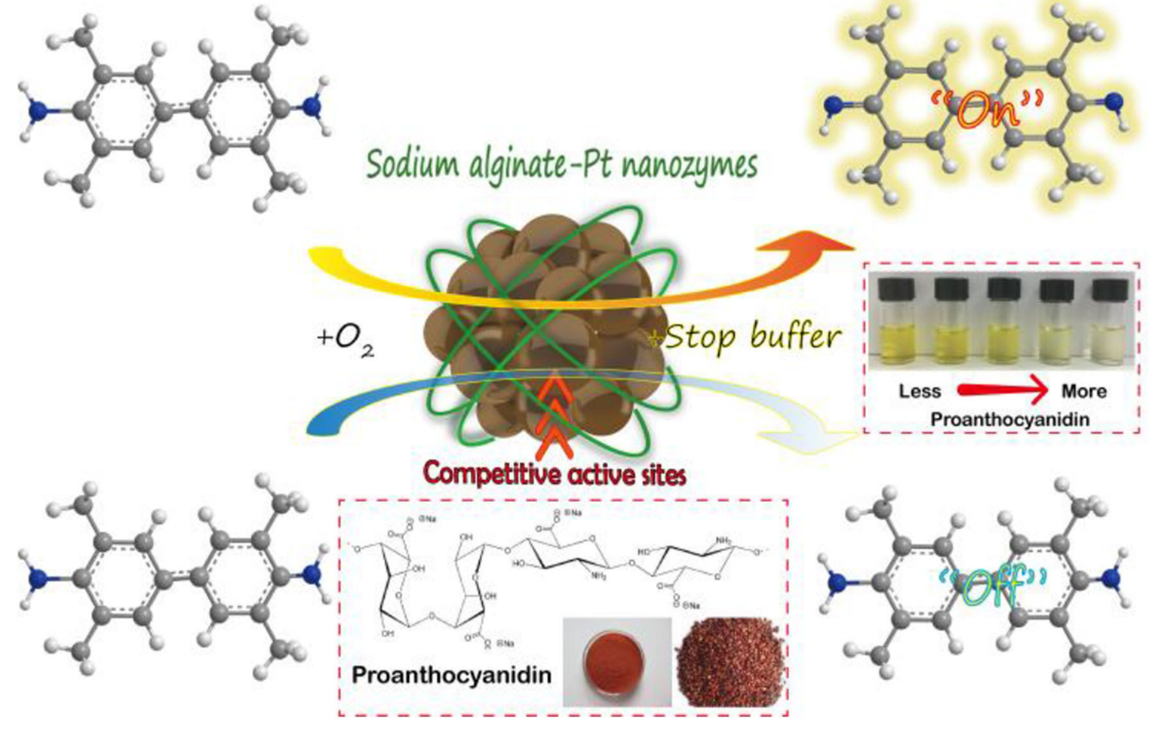

SCHEME 1 | Sodium alginate modified platinum nanozymes with oxidase-like activity for antioxidant capacity and analysis of proanthocyanidins.

product and a state of well-dispersion. Moreover, the high-resolution transmission electron microscope (TEM) image shows that the crystal plane spacing of the SA-PtNPs is 0.19 nm. The size distribution of SA-PtNPs determined from 100 random nanoparticles is shown in **Supplementary Figure 2A** with an average diameter of 5.9 ± 0.6 nm. The energy dispersive X-ray spectroscopy (EDS) characterization results of SA-PtNPs (**Supplementary Figure 2B**) indicate that Pt has a peak at the corresponding elemental feature, indicating the presence of Pt in the material. The infrared spectra of SA and SA-PtNPs are shown in **Figure 1B**. It can be seen that the stretching vibration band of O-H at 3,471 cm^{-1}, the stretching vibration band of C-H at 2,932 cm^{-1}, and the glycoside skeleton absorption peaks of C-O-C at 1,030 and 810 cm^{-1} are invariable. However, the peaks suggesting -COO- in the molecule at 1,613 and 1,412 cm^{-1} shift to higher wavenumbers of 1,634 cm^{-1} and 1,448 cm^{-1}, respectively. These changes probably suggested that the -COO- groups of SA are responsible for interacting with PtNPs.

As shown in **Figure 1C**, X-ray diffraction (XRD) characterization of SA-PtNPs at 39.6°, 46.1°, 67.2°, and 81.2°can be indexed well to the diffraction from (111), (200), (220), and (311) planes of face-centered cubic (fcc) Pt (JCPDS 04-0802), respectively, proving that Pt exists in the crystalline form. Furthermore, the surface elemental analysis of SA-PtNPs was also performed by X-ray photoelectron spectroscopy (XPS). The characteristic spectrum can be mainly decomposed into two pairs of dual states of Pt $4f_{7/2}$ and Pt $4f_{5/2}$. These peaks with the intense distinct peak are concentrated in the binding energies around 71.57 and 75.02 eV, which could be attributed to the existence of metallic platinum (Pt^0). The other peaks at around 75.47 and 78 eV were contributed to the Pt^{4+} (Cho and Ouyang, 2011; Wu et al., 2014), and the relative contents of Pt^0 and Pt^{4+} are 42.7 and 57.3% (**Figure 1D**).

Oxidase-Like Activity of SA-PtNPs

To evaluate the oxidase-like activity of SA-PtNPs, TMB was chosen as the chromogenic substrate in this study. **Figure 2A** shows that SA-PtNPs can quickly catalyze the oxidation of TMB under O_2 to generate a blue outcome with peaks absorption at 370 and 652 nm without of H_2O_2. Since the absorbance at 450 nm after the addition of H_2SO_4 can be stable for a long time with a complete spectrum shift and concomitant hyperchromic effect (Bos et al., 1981; Frey et al., 2000). Therefore, the oxidization reaction in this work was stopped by H_2SO_4, resulting in a yellow substance generated with a maximum absorbance at 450 nm. It's worth mentioning that the oxidase-like activity of SA is so low that their effect on SA-PtNPs can be ignored (**Supplementary Figure 3**).

Some other chromogenic substrates were also tested to demonstrate the versatility of SA-PtNPs, including o-phenylenediamine (OPD), pyrogallol, 2,2′-azino-bis(3-ethylbenzothiazoline-6-sulfonic acid) diammonium salt (ABTS), 4-aminoantipyrine (4-AAP) and N-ethyl-N-(3-sulfopropyl)-3-methylaniline sodium salt (TOPS) (**Supplementary Figure 4**). Thus, these results verified that SA-PtNPs can act as a new

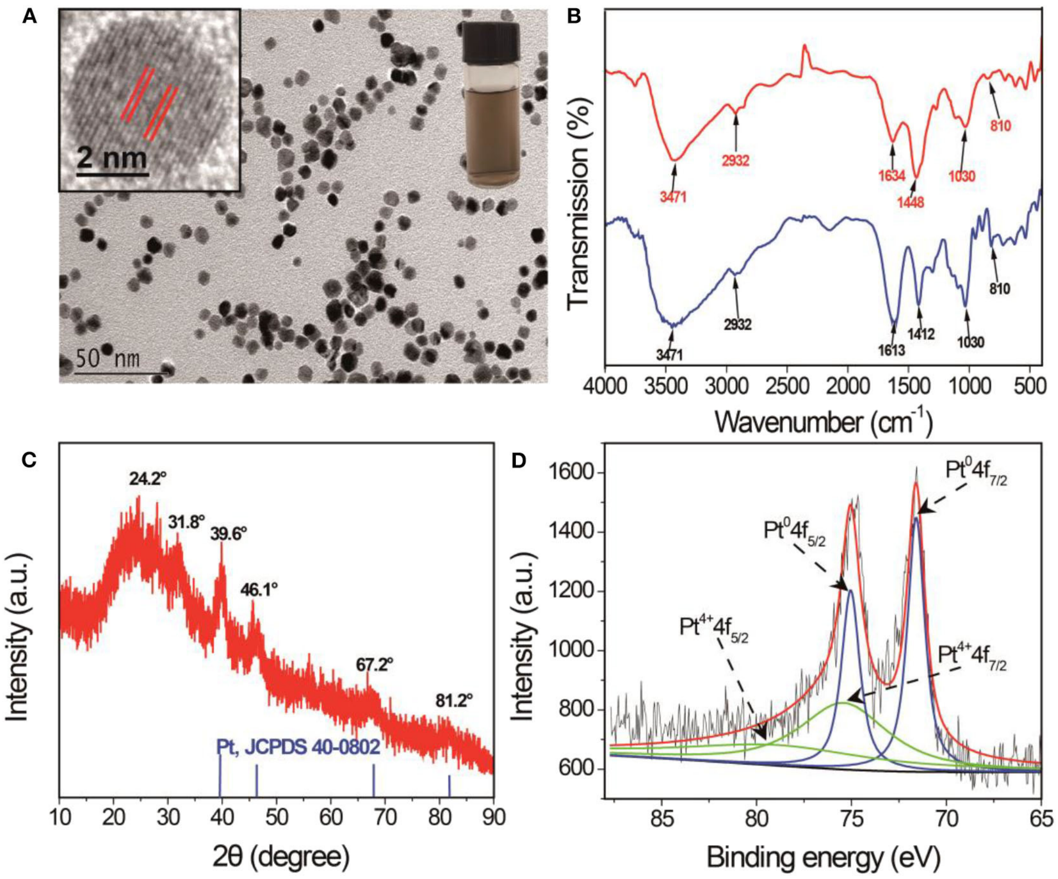

FIGURE 1 | (A) TEM image of SA-PtNPs. Inset: The image and high-resolution TEM image of SA-PtNPs. **(B)** Infrared spectra of SA and SA-PtNPs. **(C)** XRD spectra of SA-PtNPs. **(D)** XPS spectra in the Pt 4f region of SA-PtNPs.

type of oxidase mimic. For further application of the SA-PtNPs-TMB system, pH, temperature, and TMB concentration were optimized to be 4.5, 37°C, and 0.15 mM, respectively (**Supplementary Figure 5**).

The steady-state dynamics assay of the SA-PtNPs-TMB system is depicted in **Figure 2B** with the reaction rate (v) depending on TMB concentration. With the increase of TMB concentration, reaction rate increased quickly at first and then changed slowly. To further study the kinetics, the Michaelis Constant (K_m) value of SA-PtNPs was counted to be 11.6 μM fitting by Michaelis-Menten equation. The K_m is an important parameter used to evaluate the affinity of nanozyme to substrate and to discuss the nanozyme-substrate interaction. **Table 1** also shows the comparison of the K_m value of oxidase mimics and points out that SA-PtNPs have a remarkably high affinity for TMB. As shown in **Supplementary Figure 6**, the specific activity value of SA-PtNP has been evaluated as 2,711 U/g according to the fitted straight line (**Supplementary Figure 6B**) (Jiang et al., 2018).

To determine the mechanism, possible superoxide anions ($O_2^{\bullet-}$) were also studied. First of all, SA-PtNPs-catalyzed TMB oxidation was conducted in air with dissolved oxygen and bubbled with highly pure nitrogen gas, respectively. The reaction rate of SA-PtNPs-catalyzed TMB oxidation was found to decrease rapidly under nitrogen atmosphere, which indicates that dissolved O_2 is involved in the process (**Supplementary Figure 7**). Since ascorbic acid (AA) could eliminate $O_2^{\bullet-}$ (Cai et al., 2018), we performed AA oxidations. As **Figure 2C** shows that AA has an absorption peak at ~250 nm in the wavelength range. A slight variation at 250 nm and oxidation of AA occurred while SA-PtNPs or O_2 was removed. However, when SA-PtNPs and O_2 co-exist, AA was consumed. In this phenomenon, the presence of $O_2^{\bullet-}$ can be ruled out in the SA-PtNPs-TMB system. Furthermore, the oxygen reduction reaction (ORR) assay was carried out to further verify the mechanism. Relevant experiments were carried out with using carbon electrode as electrochemical working electrode which was modified with SA-PtNPs. No peak appear after the mixed solution is filled with nitrogen (**Figure 2D**). It produced a cathode reduction peak at ~-0.34 V in an environment with oxygen. On the basis of these results, the oxidase-like activity of SA-PtNPs originates mainly from the formation of $O_2^{\bullet-}$ during the reaction.

The Contribution of SA in SA-PtNPs

Several experiments have been carried out to investigate the contribution of SA in SA-PtNPs. First of all, we found that bare

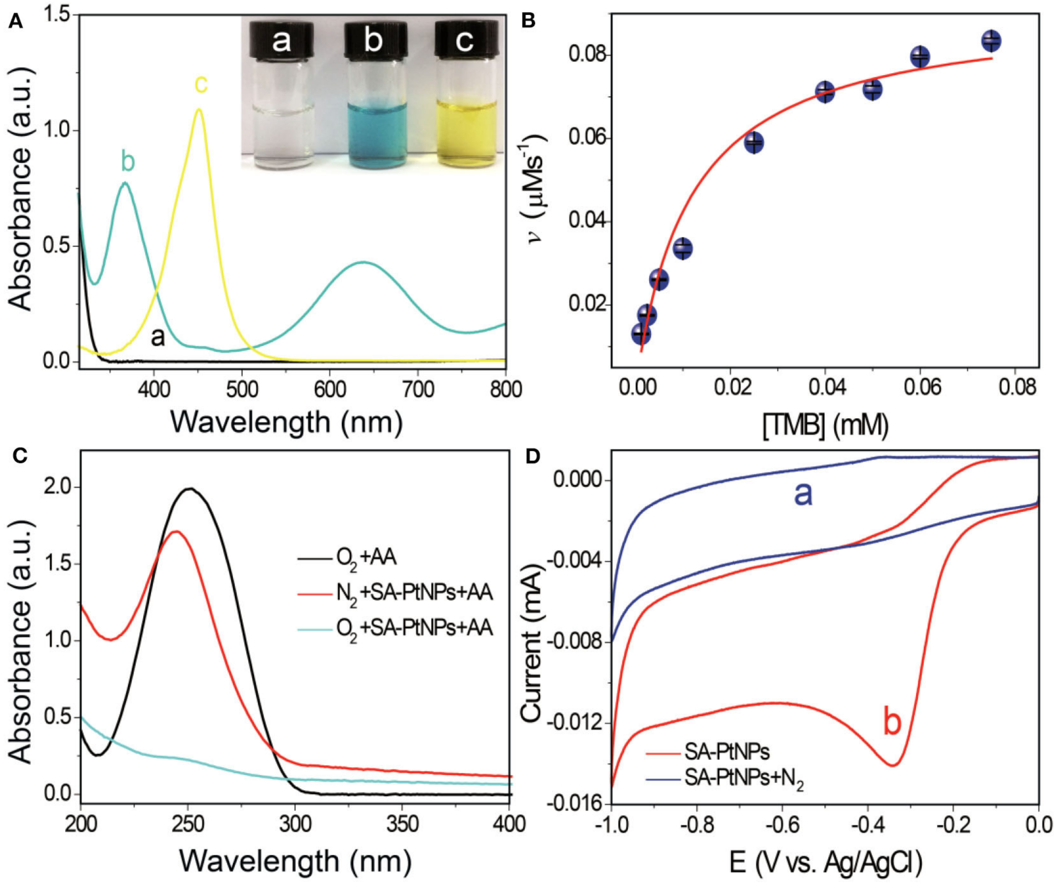

FIGURE 2 | (A) UV-vis absorption spectra of (a) TMB, (b) SA-PtNPs + TMB, (c) SA-PtNPs + TMB + stop buffer (H_2SO_4). The images show the appearance of the relevant reaction liquid. **(B)** Steady-state dynamic assay of SA-PtNPs. **(C)** Absorption spectra of AA after water bathing for 5 min under different conditions. **(D)** ORR assay, cyclic voltammetry of the ORR on an electrode modified with SA-PtNP in (a) N_2 and (b) O_2.

TABLE 1 | Kinetic parameters for nanzoymes as oxidase mimics.

Catalyst	Substrate	K_m (mM)	v_{max} ($\times 10^{-8}$Ms^{-1})	References
CeO_2 NPs	TMB	0.8~3.8	30~70	Asati et al., 2009
MnO_2 NPs		0.04	578	Liu et al., 2012
Ni/Pd hollow NPs		0.11	1.52	Wang et al., 2016
Lysozyme-PtNPs		0.63	270	Yu et al., 2014
Chitosan-PtNPs		0.018	15.7	Deng et al., 2017
Heparin-PtNPs		0.010	4.962	He et al., 2019b
Heparin-OsNPs		0.8	8.45	He et al., 2019c
Citrate-PtNPs		0.1206	6.51	Wu et al., 2014
SA-PtNPs		0.012	9.145	This work

PtNPs show distinct aggregation in solution, while the SA-PtNPs exhibited excellent colloidal stability when SA was introduced into the preparation process (**Supplementary Figure 8**). Compared with bare platinum without any protective agent, SA-PtNPs obtain a much higher oxidase-like activity that implies the improvement effect with the introduction of SA (**Figure 3A**).

As is generally known, the stability of PtNPs against aggregation under different harsh conditions is crucial to the extension of the practical application. To this end, SA-PtNPs were exposed to several pH values (2–12) for 2 h to explore the effect of pH on the oxidase activity. As shown in **Figure 3B**, the oxidase-like activity of SA-PtNPs fluctuated slightly with the change of environment pH, implying excellent pH stability of SA-PtNPs. Furthermore, we found that SA-PtNPs possessed perfect oxidase-like activity even if they have been stored at room temperature for a long time (**Figure 3C**). The above results confirm that the contribution of SA in PtNPs preparation increases the oxidase-like activity and stability of PtNPs.

Antioxidant Capacity Evaluation and Colorimetric Assay for OPC

The phenolic hydroxyl groups in the OPC structure make it a good hydrogen donor and therefore, it has a strong antioxidant capacity (Shao et al., 2018). Owing to the scavenging ability of OPC to $O_2^{\bullet -}$ and the formation of $O_2^{\bullet -}$ in the SA-PtNPs-TMB system, it is speculated that OPC could inhibit the catalytic

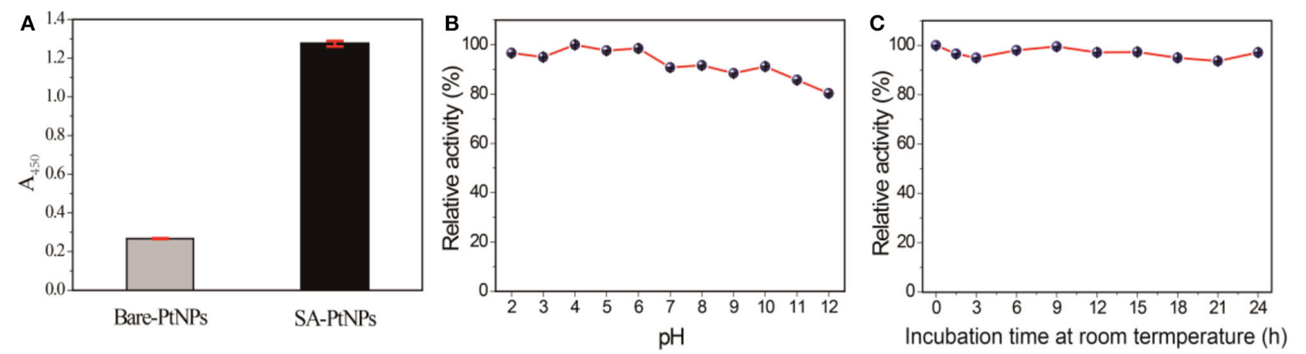

FIGURE 3 | **(A)** Comparison of oxidase activity between SA-PtNPs and bare PtNPs. Relative activity of SA-PtNPs under different **(B)** pH values and **(C)** incubation time. (The maximum value was defined as 100% relative activity).

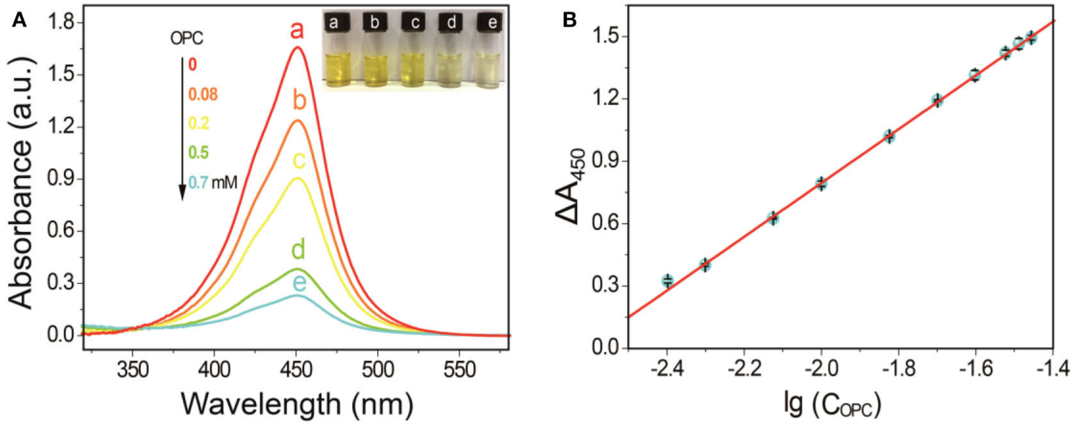

FIGURE 4 | **(A)** Inhibitory effect of OPC at different concentrations on simulated enzyme activity. **(B)** The linearity between ΔA_{450nm} and the logarithmic value of OPC concentration.

process. Thus, a colorimetric assay for OPC was established (**Scheme 1**).

Experimental results in **Figure 4A** indicated the A_{450nm} of the SA-PtNPs-TMB system gradually decreased as the concentration of OPC increases. When the concentration of OPC in the reaction system reached 1 mM, the oxidation of TMB by SA-PtNPs was drastically inhibited. These phenomena fully illustrate that OPC could distinctly inhibit the color response of the SA-PtNPs-TMB system, namely inhibiting the oxidase-like activity of SA-PtNPs. Linearity was obtained by plotting the value of ΔA_{450nm} and the logarithmic value of OPC concentration (**Figure 4B**). ($\Delta A_{450nm} = A_0 - A_t$, where A_0 and A_t are the absorbance of the reaction product at 450 nm in the inexistence and existence of OPC, respectively.) The range of linearity was from 4 to 32.5 µM, the relative standard deviation (RSD) is 0.6% for measuring 10 µM, and limit of detection (LOD) for OPC was 2.0 µM ($\Delta A_{450nm} = 1.1791\ \lg C_{OPC} + 3.1941$, $r = 0.999$). As shown in **Supplementary Table 1**, most reported methods use high-performance liquid chromatography or mass spectrometry technology to analyze PC or OPC and are time-consuming, expensive, and technically demanding. What's more, the proposed method showed a comparable sensitivity and LOD to those of the reported methods.

TABLE 2 | Recovery of standard addition of OPC in grape seeds.

Sample	Measured before addition (µM)	Added (µM)	Found (µM)	Recovery (%)	RSD (%, *n* = 3)
Grape seeds	11.1	10	9.9	98.6	2.4
		15	14.8	98.4	0.5
		20	19.4	97.0	3.4

Based on this linear equation, the antioxidant capacity of OPC was also assessed. Before measurements, OPC extracted from grape seeds was centrifuged to remove any solid residue (Soxhlet extraction method, **Supplementary Material**). AA is a well-recognized substance with antioxidant capacity. In this study, the inhibitory effect of 1 mM AA on the SA-PtNPs-TMB system is defined as 1 U. Therefore, the antioxidant capacity of pure OPC was calculated to be 2.85 U/mg (**Supplementary Material**). More significantly, as shown in **Table 2**, the recoveries of the standard addition experiment in grape seeds ranged from 97.0 to 98.6%

with RSD values of 0.5–3.4%. These results provide a new insight for antioxidant capacity and indicate the accuracy of this assay for OPC analysis.

CONCLUSIONS

A facile one-step synthesis method was successfully introduced to prepare SA-PtNPs (5.9 ± 0.6 nm) using SA as a surface modification agent and $NaBH_4$ as the reducing agent. SA-PtNPs can catalyze the oxidation of the chromogenic substrate TMB by dissolved oxygen and has oxidation simulation enzyme activity. These phenomena demonstrate that SA-PtNPs can perform as a highly efficient and robust oxidase mimic for the catalyzing substract-O_2 reaction. The steady-state kinetic assay has shown that SA-PtNPs have a stronger affinity to TMB than those of most nanozymes. Additionally, the specific activity of SA-PtNPs has been calculated to be 2,711 U/g. The wide pH value and incubation time of the reaction environment have little effect on the oxidase-like activity of SA-PtNPs. Therefore, SA not only increases the dispersibility and stability of PtNPs but also improves the catalytic activity of PtNPs as oxidase mimics. More significantly, results have shown that OPC can effectively prevent oxidation of TMB and have an inhibitory effect on the color development system. The colorimetric assay for OPC in grape seeds established by this phenomenon has good linearity, reproducibility, low limit of detection, and is easy to perform. The antioxidant capacity of pure OPC obtained by the Soxhlet extraction method was 2.85 U/mg. This assay addresses the shortage of OPC methods and extends the potential application of platinum nanozymes.

DATA AVAILABILITY STATEMENT

All datasets generated for this study are included in the article/**Supplementary Material**.

AUTHOR CONTRIBUTIONS

Conceptualization: WC, H-HD, and G-LH. Methodology: G-LH, H-PP, and ZL. Investigation: S-BH, LY, and X-LL. Writing—original draft preparation: S-BH. Writing—review and editing: WC and H-HD. Funding acquisition: WC. All authors have read and agreed to the published version of the manuscript. All authors contributed to the article and approved the submitted version.

FUNDING

This research was funded by the National Natural Science Foundation of China, grant number 21675024; the Program for Innovative Leading Talents in Fujian Province, grant number 2016B016; the Program for Innovative Research Team in Science and Technology in Fujian Province University, grant number 2018B033; and the Science and Technology Project of Fujian Province, grant number 2018L3008.

SUPPLEMENTARY MATERIAL

The Supplementary Material for this article can be found online at: https://www.frontiersin.org/articles/10.3389/fchem.2020.00654/full#supplementary-material

REFERENCES

Asati, A., Santra, S., Kaittanis, C., Nath, S., and Perez, J. M. (2009). Oxidase-like activity of polymer-coated cerium oxide nanoparticles. *Angew. Chem. Int. Edit.* 48, 2308–2312. doi: 10.1002/anie.200805279

Bos, E. S., van der Doelen, A. A., van Rooy, N., and Schuurs, A. H. W. M. (1981). 3,3′,5,5′-Tetramethylbenzidine as an Ames test negative chromogen for horse-radish peroxidase in enzyme-immunoassay. *J. Immunoass. Immunoch.* 2, 187–204. doi: 10.1080/15321818108056977

Cai, S., Xiao, W., Duan, H., Liang, X., Wang, C., Yang, R., et al. (2018). Single-layer Rh nanosheets with ultrahigh peroxidase-like activity for colorimetric biosensing. *Nano Res.* 11, 6304–6315. doi: 10.1007/s12274-018-2154-1

Chen, F., Wang, H., Zhao, J., Yan, J., Meng, H., Zhan, H., et al. (2019). Grape seed proanthocyanidin inhibits monocrotaline-induced pulmonary arterial hypertension via attenuating inflammation: *in vivo* and *in vitro* studies. *J. Nurt. Biochem.* 67, 72–77. doi: 10.1016/j.jnutbio.2019.01.013

Cho, S. J., and Ouyang, J. (2011). Attachment of platinum nanoparticles to substrates by coating and polyol reduction of a platinum precursor. *J. Phys. Chem. C* 115 8519–8526. doi: 10.1021/jp2001699

Coleman, S. L., and Shaw, O. M. (2017). Progress in the understanding of the pathology of allergic asthma and the potential of fruit proanthocyanidins as modulators of airway inflammation. *Food Funct.* 8, 4315–4324. doi: 10.1039/C7FO00789B

Da Silva, J. M. R., Darmon, N., Fernandez, Y., and Mitjavila, S. (1991). Oxygen free radical scavenger capacity in aqueous models of different procyanidins from grape seeds. *J. Agric. Food Chem.* 39, 1549–1552. doi: 10.1021/jf00009a002

Deng, H. H., Lin, X. L., He, S. B., Wu, G. W., Wu, W. H., Yang, Y., et al. (2019). Colorimetric tyrosinase assay based on catechol inhibition of the oxidase-mimicking activity of chitosan-stabilized platinum nanoparticles. *Microchim. Acta* 186:301. doi: 10.1007/s00604-019-3451-4

Deng, H. H., Lin, X. L., Liu, Y. H., Li, K. L., Zhuang, Q. Q., Peng, H. P., et al. (2017). Chitosan-stabilized platinum nanoparticles as effective oxidase mimics for colorimetric detection of acid phosphatase. *Nanoscale* 9, 10292–10300. doi: 10.1039/C7NR03399K

Dong, Y., Chi, Y., Lin, X., Zheng, L., Chen, L., and Chen, G. (2011). Nano-sized platinum as a mimic of uricase catalyzing the oxidative degradation of uric acid. *Phys. Chem. Chem. Phys.* 13, 6319–6324. doi: 10.1039/c0cp01759k

Dooren, I., van, Foubert, K., Theunis, M., Naessens, T., Pieters, L., and Apers, S. (2018). Advantages of a validated UPLC-MS/MS standard addition method for the quantification of A-type dimeric and trimeric proanthocyanidins in cranberry extracts in comparison with well-known quantification methods. *J. Pharmaceut. Biomed.* 148, 32–41. doi: 10.1016/j.jpba.2017.09.002

Fracassetti, D., Costa, C., Moulay, L., and Tomás-Barberán, F. A. (2013). Ellagic acid derivatives, ellagitannins, proanthocyanidins and other phenolics, vitamin C and antioxidant capacity of two powder products from camu-camu fruit (*Myrciaria dubia*). *Food Chem.* 139, 578–588. doi: 10.1016/j.foodchem.2013.01.121

Frey, A., Meckelein, B., Externest, D., and Schmidt, M. A. (2000). A stable and highly sensitive 3, 3′, 5, 5′-tetramethylbenzidine-based substrate reagent for enzyme-linked immunosorbent assays. *J. Immunol. Methods* 233, 47–56. doi: 10.1016/S0022-1759(99)00166-0

Fu, Y., Zhao, X., Zhang, J., and Li, W. (2014). DNA-based platinum nanozymes for peroxidase mimetics. *J. Phys. Chem. C* 118, 18116–18125. doi: 10.1021/jp503242e

Gao, L., Zhuang, J., Nie, L., Zhang, J., Zhang, Y., Gu, N., et al. (2007). Intrinsic peroxidase-like activity of ferromagnetic nanoparticles. *Nat. Nanotechnol.* 2, 577–583. doi: 10.1038/nnano.2007.260

He, S. B., Chen, R. T., Wu, Y. Y., Wu, G. W., Peng, H. P., Liu, A. L., et al. (2019a). Improved enzymatic assay for hydrogen peroxide and glucose by exploiting the enzyme-mimicking properties of BSA-coated platinum nanoparticles. *Microchim. Acta* 186:778. doi: 10.1007/s00604-019-3939-y

He, S. B., Yang, L., Lin, X. L., Chen, L. M., Peng, H. P., Deng, H. H., et al. (2019b). Heparin-platinum nanozymes with enhanced oxidase-like activity for the colorimetric sensing of isoniazid. *Talanta* 211:120707. doi: 10.1016/j.talanta.2019.120707

He, S. B., Zhuang, Q. Q., Yang, L., Lin, M. Y., Kuang, Y., Peng, H. P., et al. (2019c). A Heparinase sensor based on a ternary system of Hg2+-heparin-osmium nanoparticles. *Anal. Chem*. 92, 1635–1642. doi: 10.1021/acs.analchem.9b05222

Huang, Y., Ren, J., and Qu, X. (2019). Nanozymes: classification, catalytic mechanisms, activity regulation, and applications. *Chem. Rev*. 119, 4357–4412. doi: 10.1021/acs.chemrev.8b00672

Jiang, B., Duan, D., Gao, L., Zhou, M., Fan, K., Tang, Y., et al. (2018). Standardized assays for determining the catalytic activity and kinetics of peroxidase-like nanozymes. *Nat. Protoc*. 13, 1506–1520. doi: 10.1038/s41596-018-0001-1

Li, W., Chen, B., Zhang, H., Sun, Y., Wang, J., Zhang, J., et al. (2015). BSA-stabilize d Pt nanozyme for peroxidase mimetics and its application on colorimetric detection of mercury (II) ions. *Biosens. Bioelectron*. 66, 251–258. doi: 10.1016/j.bios.2014.11.032

Li, Z., Ramay, H. R., Hauch, K. D., Xiao, D., and Zhang, M. (2005). Chitosan-alginate hybrid scaffolds for bone tissue engineering. *Biomaterials* 26, 3919–3928. doi: 10.1016/j.biomaterials.2004.09.062

Liu, X., Wang, Q., Zhao, H., Zhang, L., Su, Y., and Lv, Y. (2012). BSA-templated MnO2 nanoparticles as both peroxidase and oxidase mimics. *Analyst* 137, 4552–4558. doi: 10.1039/c2an35700c

Liu, Y., Wu, H., Chong, Y., Wamer, W. G., Xia, Q., Cai, L., et al. (2015). Platinum nanoparticles: efficient and stable catechol oxidase mimetics. *ACS Appl. Mater. Inter*. 7, 19709–19717. doi: 10.1021/acsami.5b05180

Mokhtari, S., Jafari, S. M., and Assadpour, E. (2017). Development of a nutraceutical nano-delivery system through emulsification/internal gelation of alginate. *Food Chem*. 229, 286–295. doi: 10.1016/j.foodchem.2017.02.071

Ortega, N., Romero, M. P., Macià, A., Reguant, J., Anglès, N., Morelló, J. R., et al. (2010). Comparative study of UPLC-MS/MS and HPLC–MS/MS to determine procyanidins and alkaloids in cocoa samples. *J. Food Compos. Anal.* 23, 298–305. doi: 10.1016/j.jfca.2009.10.005

Shao, Y., Hu, Z., Yu, Y., Mou, R., Zhu, Z., and Beta, T. (2018). Phenolic acids, anthocyanins, proanthocyanidins, antioxidant activity, minerals and their correlations in non-pigmented, red, and black rice. *Food Chem*. 239, 733–741. doi: 10.1016/j.foodchem.2017.07.009

Travan, A., Pelillo, C., Donati, I., Marsich, E., Benincasa, M., Scarpa, T., et al. (2009). Non-cytotoxic silver nanoparticle-polysaccharide nanocomposites with antimicrobial activity. *Biomacromolecules* 10, 1429–1435. doi: 10.1021/bm900039x

Vaid, M., Prasad, R., Singh, T., Jones, V., and Katiyar, S. K. (2012). Grape seed proanthocyanidins reactivate silenced tumor suppressor genes in human skin cancer cells by targeting epigenetic regulators. *Toxicol. Appl. Pharm*. 263, 122–130. doi: 10.1016/j.taap.2012.06.013

Wang, Q., Zhang, L., Shang, C., Zhang, Z., and Dong, S. (2016). Triple-enzyme mimetic activity of nicke-palladium hollow nanoparticles and their application in colorimetric biosensing of glucose. *Chem. Commun*. 52, 5410–5413. doi: 10.1039/C6CC00194G

Weber, H. A., Hodges, A. E., Guthrie, J. R., O'Brien, B. M., Robaugh, D., Clark, A. P., et al. (2007). Comparison of proanthocyanidins in commercial antioxidants: grape seed and pine bark extracts. *J. Agric. Food Chem*. 55, 148–156. doi: 10.1021/jf063150n

Wei, H., and Wang, E. (2013). Nanomaterials with enzyme-like characteristics (nanozymes): next-generation artificial enzymes. *Chem. Soc. Rev*. 42, 6060–6093. doi: 10.1039/c3cs35486e

Wu, G. W., He, S. B., Peng, H. P., Deng, H. H., Liu, A. L., Lin, X. H., et al. (2014). Citrate-capped platinum nanoparticle as a smart probe for ultrasensitive mercury sensing. *Anal. Chem*. 86, 10955–10960. doi: 10.1021/ac503544w

You, J. G., Liu, Y. W., Lu, C. Y., Tseng, W. L., and Yu, C. J. (2017). Colorimetric assay of heparin in plasma based on the inhibition of oxidase-like activity of citrate-capped platinum nanoparticles. *Biosens. Bioelectron*. 92, 442–448. doi: 10.1016/j.bios.2016.10.082

Yu, C. J., Chen, T. H., Jiang, J. Y., and Tseng, W. L. (2014). Lysozyme-directed synthesis of platinum nanoclusters as a mimic oxidase. *Nanoscale* 6, 9618–9624. doi: 10.1039/C3NR06896J

Conflict of Interest: The authors declare that the research was conducted in the absence of any commercial or financial relationships that could be construed as a potential conflict of interest.

frontiers in Chemistry

ORIGINAL RESEARCH
published: 02 September 2020
doi: 10.3389/fchem.2020.00798

Reagent-Free Colorimetric Cholesterol Test Strip Based on Self Color-Changing Property of Nanoceria

Phuong Thy Nguyen†*, Young Im Kim*†*and Moon Il Kim**

Department of BioNano Technology, Gachon University, Seongnam-si, South Korea

Paper-based test strip consisting of cerium oxide nanoparticles (nanoceria) as hydrogen peroxide (H_2O_2)-dependent color-changing nanozymes and cholesterol oxidase (ChOx) has been developed for convenient colorimetric determination of cholesterol without the need for chromogenic substrate. The construction of the cholesterol strip begins with physical adsorption of nanoceria on the paper surface, followed by covalent immobilization of ChOx via silanization, chitosan-mediated activation, and glutaraldehyde treatment of the nanoceria-embedded paper matrices. In the presence of cholesterol, ChOx catalyzes its oxidation to produce H_2O_2, which forms peroxide complex on the nanoceria surface and induces visual color change of the nanoceria-embedded paper from white/light yellow into intense yellow/orange, which was conveniently quantified with an image acquired by a conventional smartphone with the ImageJ software. Using this strategy, target cholesterol was specifically determined down to 40 μM with a dynamic linear concentration range of 0.1–1.5 mM under neutral pH condition, which is suitable to measure the serum cholesterol, with excellent stability during 20 days and reusability by recovering its original color-changing activity for 4 consecutive cycles. Furthermore, the practical utility of this strategy was successfully demonstrated by reliably determining cholesterol in human blood serum samples. This study demonstrates the potential of self color-changing nanozymes for developing colorimetric paper strip sensor, which is particularly useful in instrumentation-free point-of-care environments.

Keywords: reagent-free colorimetric assay, paper strip, cholesterol determination, nanoceria, cholesterol oxidase

OPEN ACCESS

Edited by:
Kelong Fan,
Institute of Biophysics (CAS), China

Reviewed by:
Fanggui Ye,
Guangxi Normal University, China
Juewen Liu,
University of Waterloo, Canada
Sanjay Singh,
Ahmedabad University, India

****Correspondence:***
Moon Il Kim
moonil@gachon.ac.kr

†*These authors have contributed equally to this work*

Specialty section:
This article was submitted to Nanoscience, a section of the journal Frontiers in Chemistry

Received: *17 June 2020*
Accepted: *29 July 2020*
Published: *02 September 2020*

Citation:
Nguyen PT, Kim YI and Kim MI (2020) Reagent-Free Colorimetric Cholesterol Test Strip Based on Self Color-Changing Property of Nanoceria. Front. Chem. 8:798. doi: 10.3389/fchem.2020.00798

INTRODUCTION

Cholesterol is a vital construction unit of animal cell membrane and key biosynthetic precursor of steroid hormone, bile acids, and vitamin D (Ikonen, 2008). It is also one of the most crucial biomarkers to diagnose various severe clinical disorders. A low level of cholesterol in human blood is closely related to hypolipoproteinemia, anemia, and septicemia, while elevated cholesterol level is linked to malnutrition hypertension, arteriosclerosis, brain thrombosis, and lipid metabolism dysfunction (Nauck et al., 1997; MacLachlan et al., 2000; Martin et al., 2003; Arya et al., 2008). Thus, it is crucially required to monitor cholesterol levels in clinical diagnosis for preventing these diseases. Until now, numerous analytical methods have been widely exploited for the sensitive quantification of cholesterol, based on high performance liquid chromatography, electrochemistry, fluorescence, chemiluminescence, and molecular imprinting polymer (MIP) technology (Lin et al., 2007; Zhang et al., 2008, 2012; Li et al., 2011; Matharu et al., 2012). However, these cholesterol detection methods require instrumentations with relatively complicated operating procedures, which limits their utilization in instrumentation-free environments. Hence, to facilitate routine cholesterol monitoring in point-of-care testing (POCT) environments, it is necessary to develop more simple strategy with enough sensitivity, reliability, and cost-effectiveness.

In this regard, colorimetric methods for cholesterol detection have gained considerable attention due to its visual detecting capability. Most of them have relied on natural peroxidase or peroxidase-like nanozyme, which combines with ChOx, and chromogenic substrate including 3,3′,5,5′-tetramethylbenzidine (TMB) or 2,2′-azino-bis(3-ethylbenzo-thiazoline-6-sulfonic acid) diammonium salt (ABTS) (Hayat et al., 2015; Kim et al., 2015; Wu et al., 2017; Chung et al., 2018). In the presence of cholesterol, ChOx oxidized cholesterol to produce H_2O_2, which subsequently activated peroxidase or peroxidase-mimicking material to oxidize TMB or ABTS into blue or green colored product, respectively. These methods enable facile detection with high selectivity and sensitivity; however, multiple components including the colorimetric reagents should be involved in the assay, and furthermore, spectrophotometer should be used for absorbance-based quantification of cholesterol.

Nanoceria have been also considered as one of the promising nanozymes for developing colorimetric assays since they catalyze the fast oxidation of colorimetric substrates to generate colored products even without the need for additional oxidizing agents (e.g., H_2O_2). Additionally, they have unique self-color transition property from white/light yellow into intense yellow/orange by H_2O_2-induced alteration of the oxidation state from Ce^{3+} to Ce^{4+} on the nanoparticle surface. Since the self-color change of nanoceria is induced only by H_2O_2 without any dye and the changed color of nanoceria can be returned to its original color due to the recovery of the ionic valence between Ce^{3+} and Ce^{4+}, several colorimetric assays to detect H_2O_2 and other biomolecules including glucose and cholesterol with the aid of the corresponding oxidases have been reported (Ornatska et al., 2011; Kim et al., 2017). Although these examples demonstrate the potential of nanoceria as novel colorimetric transducers to detect H_2O_2 in the sample, they were still not free from spectrophotometer for quantification. Thus, to facilitate practical on-site cholesterol detection, we have developed a paper-based test strip which incorporates both nanoceria and ChOx for the determination of cholesterol level in human blood. Paper-based strip sensors have been widely exploited for colorimetric POCT applications owing to their unique advantages such as portability, disposability, low production cost, large surface area, easy surface functionalization, and strong background contrast for enhancing color signal intensity; however, until now, paper-based cholesterol strip has rarely been reported (Mahato et al., 2017). Various analytical characteristics of the test strip such as sensitivity, specificity, stability, reusability, and clinical utility in cholesterol detection were investigated with real images captured by a smartphone, which is quite suitable in POCT environments.

EXPERIMENTAL SECTION

Materials

Nanoceria (<5 nm in diameter), cholesterol oxidase from *Streptomyces* sp. (ChOx), cholesterol, glucose, uric acid, urea, cysteine, xanthine, galactose, triton X-100, sodium acetate, chitosan, succinic acid, aminopropyl triethoxysilane (APTES), and human blood serum were purchased from Sigma-Aldrich (Milwaukee, WI). Hydrogen peroxide (35 %) was obtained from Junsei Chemical Co. (Japan). Whatman grade 1 qualitative filter papers were purchased from GE Healthcare Co. (USA). All other chemicals were of analytical grade or higher and all solutions were prepared with distilled (DI) water purified using a Milli-Q Purification System (Millipore, USA).

Preparation of Paper Strip Incorporating Nanoceria or Both Nanoceria and ChOx

Paper strip incorporating nanoceria or both nanoceria and ChOx was prepared according to previously reported procedures with slight modifications (Ornatska et al., 2011). First, nanoceria was fully dissolved in sodium acetate buffer (100 mM, pH 5.3) prior to the immobilization on test strip. Whatman filter paper was cut into rectangular strips, soaked in nanoceria solution (15 mg/mL) for 10 min, and dried for 3 h at 70°C. To stabilize nanoceria on the paper, the nanoceria-embedded strip was incubated in 5% APTES in ethanol for 10 min and dried for 10 min at 100°C, which was then used for colorimetric H_2O_2 detection.

For additional ChOx immobilization on the paper, the silanized nanoceria-embedded paper was soaked in chitosan solution (1% chitosan in 0.5% aqueous succinic acid solution) for 10 min and allowed to dry for 10 min at room temperature (RT). Then, the paper was treated with 5% aqueous glutaraldehyde solution for 20 min, washed five times with DI water, and dried for 10 min at RT. Finally, the paper strip was soaked into ChOx solution (6 mg/mL in sodium acetate buffer (100 mM, pH 5.3). After 20 min, the paper was washed with PBS buffer (10 mM, pH 7.4) three times, dried at RT for 10 min, and then used directly or stored at 4°C for further experiments.

The shape and particle size of the nanoceria was checked by transmission electron microscopy (TEM) analysis. For the TEM, 5 μL of nanoceria solution was applied by drop casting the particle suspensions on a carbon-coated copper TEM grid (Electron Microscopy Sciences, USA) followed by drying at RT. The prepared sample was observed using field emission TEM (Tecnai, FEI) with accelerating voltages up to 200 kV. The morphologies and elemental distributions of the paper strip incorporating both nanoceria and ChOx were analyzed by scanning electron microscopy (SEM, Magellan 400) and energy dispersive X-ray spectroscopy (EDX) imaging modes. For SEM analysis, the paper strips were freeze-dried for 2 days and analyzed on SEM. X-ray photoelectron spectroscopy (XPS) (Thermo Scientific, WI) was performed to examine the surface chemical properties of nanoceria. Atomic force microscopy (AFM) was also conducted in the contact mode with a bio atomic force microscope (JPK NanoWizard II, Germany) to characterize the surface morphology of paper strips.

Colorimetric Detection of H_2O_2 and Cholesterol Using Nanoceria-Embedded Paper Strip

H_2O_2 level was quantified by soaking the nanoceria-embedded paper strip into aqueous sample solutions containing various concentrations of H_2O_2 for 3 min at RT. The images of resultant strip were then acquired using a smartphone (GALAXY S8 NOTE, Samsung), followed by converting to cyan-magenta-yellow-black (CMYK) mode, which was subjected to quantitative image processing with the ImageJ software (NIH). For cholesterol determination, cholesterol stock was first prepared by dissolving it in the mixture of isopropanol and Triton X-100 (1:1, v/v), and subsequently diluted with buffer (PBS, pH 7.4) to obtain cholesterol solutions. The paper strip incorporating both nanoceria and ChOx was soaked into the sample solutions containing various concentrations of cholesterol for 50 min at RT. The reacted paper strip was directly used to obtain images with a smartphone and the other procedures were the same as those described for H_2O_2 determination.

Long-term storage stability of the cholesterol sensing strips was assessed by incubating them at different conditions (RT, 4°C, and −20°C), and their residual activities were determined at predetermined time points by measuring their color intensities toward 10 mM cholesterol as described above. Reusability was also evaluated after cycles involving the typical reaction with 10 mM cholesterol and twice washings with aqueous buffer (100 mM sodium acetate, pH 5.3) to remove unreacted cholesterol on the paper. After recovering initial color of the paper strips by incubating them at RT for 5 days, the strip was reused for the measurement of residual color-changing activity toward cholesterol. The relative color intensity (%) was calculated based on the ratio of the residual color intensity to the original one.

For the determination of the cholesterol level in human serum, the original amount of cholesterol in serum was first determined using cholesterol assay kit (Sigma-Aldrich). Predetermined amount of cholesterol was further added into serum to make spiked samples representing normal, boundary, and high levels of cholesterol in blood serum. The concentration of cholesterol in each spiked sample (5-fold dilution) was measured using the same procedures as described above. The recovery rate [recovery (%) = measured value/actual value×100] and the coefficient of variation [CV (%) = SD/average×100] were assessed to determination the precision and reproducibility of the paper strip assay.

RESULTS AND DISCUSSION

Construction of Reagent-Free Cholesterol Sensing Paper Strip

A cholesterol sensing paper strip incorporating both nanoceria and ChOx was developed for convenient reagent-free identification of cholesterol in human blood serum. It was constructed by physically immobilizing nanoceria on the paper matrices, followed by APTES-mediated stabilization, chitosan and glutaraldehyde-mediated activation, and covalent immobilization of ChOx. APTES would form siloxane bridges with the hydroxyl groups of cellulose fibers of the paper matrices, which facilitates hydrogen bonding with the hydroxylated nanoceria surfaces, consequently yielding strong attachment of nanoceria on the paper matrices. Chitosan and glutaraldehyde treatments would also provide rich amine moieties and active aldehyde groups, respectively, both of which efficiently induce covalent linkages with amine groups of ChOx. We envisioned that the paper strip incorporating both nanoceria and ChOx would serve as an efficient colorimetric cholesterol biosensor capable of being used for determining cholesterol level in human blood. In the presence of cholesterol, ChOx on the strip catalyzes the oxidation of cholesterol to produce H_2O_2, which reacts with nanoceria and induces their vivid color change from white/light yellow into intense yellow/orange without any addition of chromogenic substrate. This color change is owing to the H_2O_2-mediated transition of the oxidation state of nanoceria from Ce^{3+} to Ce^{4+} and the formation of peroxide complex at the nanoceria surface (Scholes et al., 2006; Karakoti et al., 2009; Singh et al., 2011). Through the XPS analysis, we observed a significant decrease in the Ce^{3+}/Ce^{4+} ratio of nanoceria after the addition of H_2O_2 (**Figure S1**), that clearly demonstrates the above color transition mechanism. The images of resulting paper strip were acquired using a smartphone, and quantitative information was obtained by simple image processing with ImageJ software (**Figure 1**).

The morphologies and elemental distributions were analyzed by TEM and SEM with EDX (**Figure S2** and **Figure 2**). TEM image showed the spherical shape of the nanoceria with a size of ∼10 nm. From the SEM images, we could see much more irregular surfaces having particle-like dots in the paper strip incorporating both nanoceria and ChOx, while relatively smooth surfaces were observed from the bare paper strip, indicating the effective loading of nanoceria and ChOx on the paper strip. Elemental mapping images of Ce, N, and C elements also demonstrated that nanoceria and ChOx were homogeneously distributed throughout the paper matrices, which may contribute to an enhanced colorimetric response compared with aggregated cases.

Analytical Capability of Paper Strip for the Determination of H_2O_2 and Cholesterol

The colorimetric responses of nanoceria-embedded paper strip toward H_2O_2 were first assessed by soaking the paper strip into sample solutions containing diverse levels of H_2O_2, followed by acquiring images using smartphone (**Figure 3**). ImageJ software was utilized to convert the real images of paper strips into the CMYK mode for quantifying their color intensity. By simple 3 min reaction at RT, the paper strip showed clear color change from white to intense yellow, proportional to the H_2O_2 levels (**Figure 3A**). The color intensity increased with increasing H_2O_2 concentration in the sample, with a dynamic linear range of 0.1–1.5 mM ($R^2 = 0.9946$), and the limit of detection (LOD) was calculated to be as low as 0.05 mM (**Figure 3B**), which is

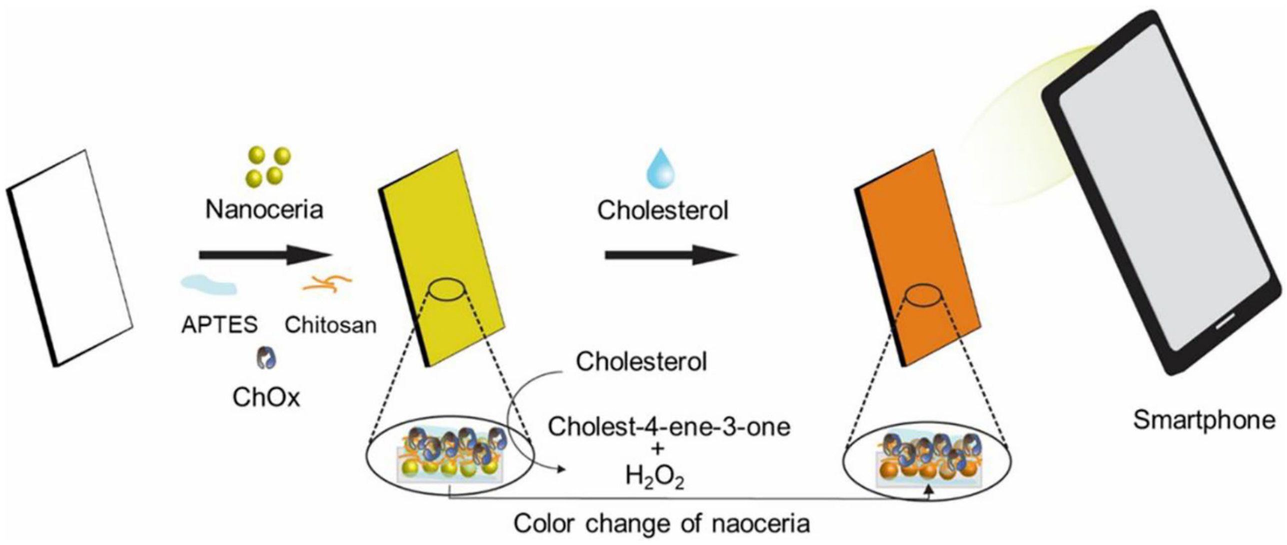

FIGURE 1 | Schematic illustration of the paper strip incorporating nanoceria and ChOx for the smartphone-mediated reagent-free colorimetric determination of cholesterol.

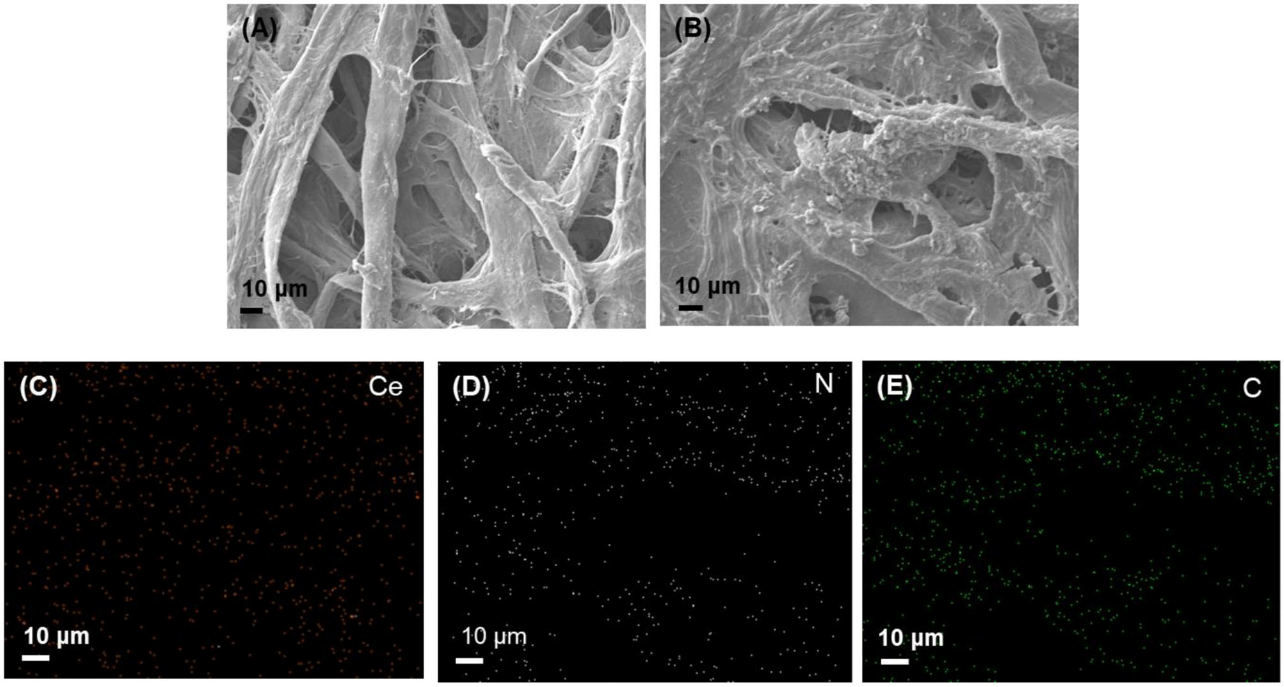

FIGURE 2 | SEM images of **(A)** bare paper strip, **(B)** paper strip incorporating both nanoceria and ChOx, and the corresponding EDS maps of **(C)** Ce, **(D)** N, and **(E)** C elements.

enough for coupling with ChOx to create cholesterol assay system (Kim et al., 2011).

The feasibility of the paper strip incorporating both nanoceria and ChOx was then demonstrated, for colorimetric determination of target cholesterol without involvement of any chromogenic substrate. Although the nanoceria-embedded paper strip incubated with free ChOx without immobilization yielded slightly higher level of color transition toward cholesterol, it is not convenient to use since ChOx was not immobilized on the paper matrices (**Figure S3**). Investigations for the effects of experimental parameters such as temperature, buffer pH, and incubation time on the color intensity of paper strip toward cholesterol showed that 37°C, pH 7, and incubation for 50 min were the ideal assay conditions (**Figure S4**). Although

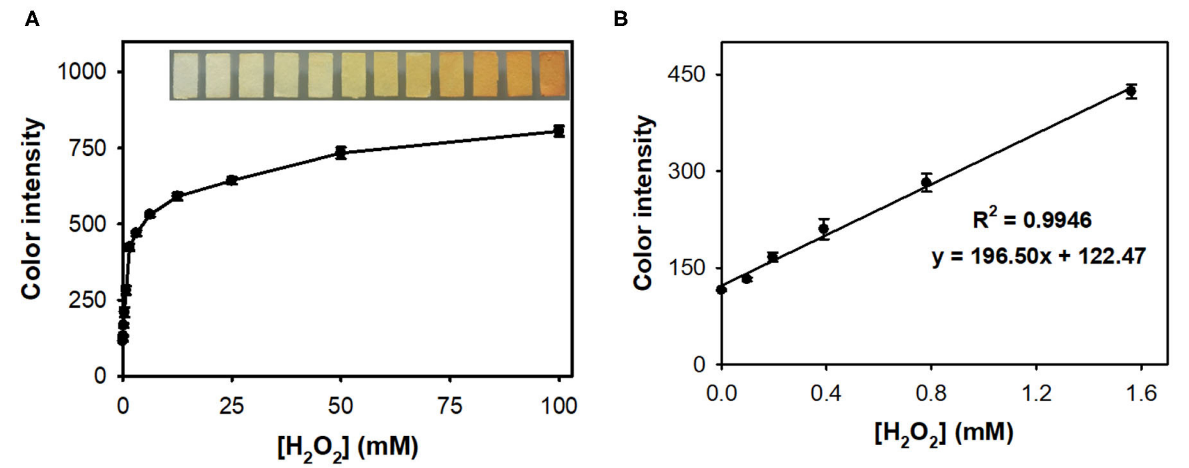

FIGURE 3 | (A) Real images and the corresponding dose-response curve for H_2O_2 determination using nanoceria-embedded paper strip and **(B)** linear calibration plot. The error bars represent the standard deviation of three independent measurements.

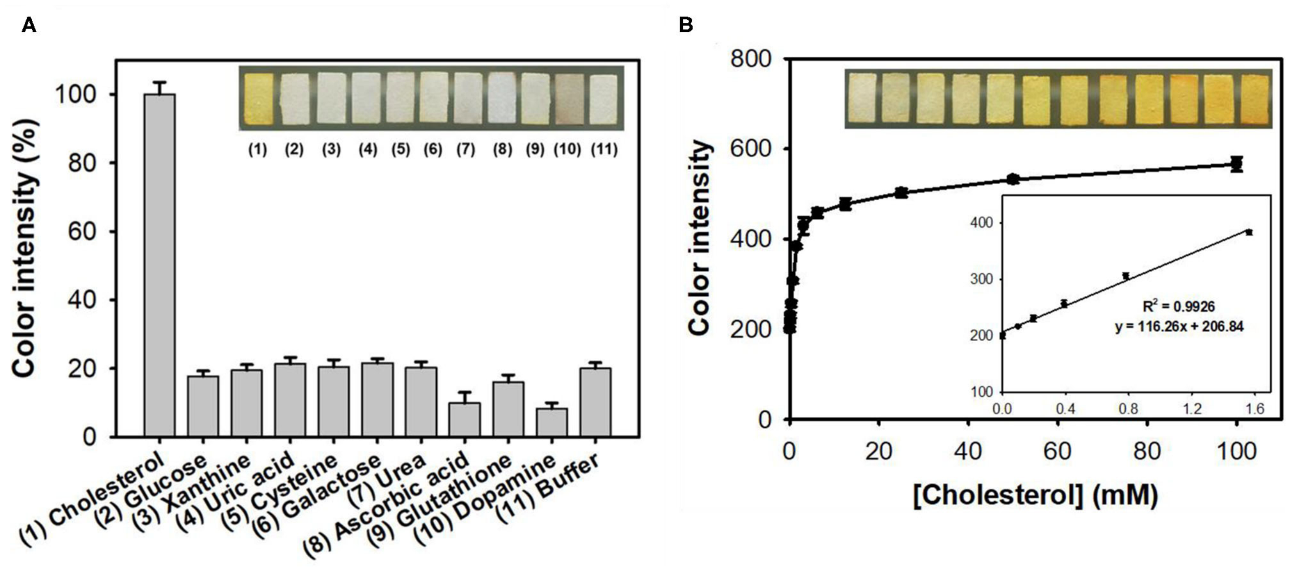

FIGURE 4 | (A) Real images and the corresponding color intensities of the selective colorimetric detection of cholesterol using paper strips incorporating nanoceria and ChOx. A 10 mM concentration of cholesterol was used, while 100 mM of other substrates was used in the experiments. **(B)** Real images, dose-response curve, and the corresponding linear calibration plots for cholesterol determination using paper strips incorporating nanoceria and ChOx. The error bars represent the standard deviation of three independent measurements.

the incubation at 37°C yielded the maximal color intensity, we incubated our paper strip with cholesterol at RT rather than 37°C because of the practical convenience and sufficiently high color intensity at RT (over 90% compared to that from 37°C). Through the simple soaking of the paper strip into the sample solutions, cholesterol was specifically detected by generating intense yellowish color, while no significant color change was observed from the common interfering substances such as glucose, xanthine, uric acid, cysteine, galactose, urea, ascorbic acid, glutathione, and dopamine, which commonly appear in human blood, even at 10-fold higher concentrations to that of cholesterol (**Figure 4A**). Moreover, these interfering compounds did not hinder the color change of the paper strips even when they were co-presented with cholesterol (**Figure S5**). In case of dopamine, although there was a different dark color observed from the paper strip, we could obtain similar yellowish color intensity using the ImageJ software.

Through the analysis of dose-response curve, the LOD for cholesterol was determined to be 0.04 mM, with a dynamic linear range from 0.1 to 1.5 mM (**Figure 4B**). The LOD value of the assay system was calculated based on the formula: LOD $= 3\times\delta/\text{slope}$, where δ is the standard deviation of blank and

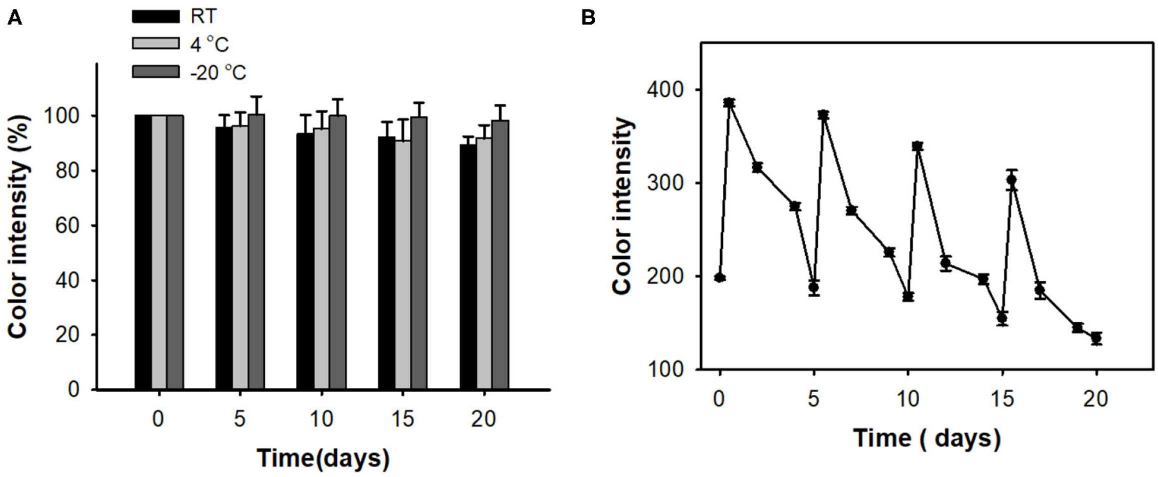

FIGURE 5 | (A) Long-term storage stability and **(B)** reusability of paper strips for cholesterol detection.

TABLE 1 | Detection precision of the paper strip incorporating nanoceria and ChOx for the quantification of cholesterol levels in spiked human serum samples.

	Original amount (mM)	Added (mM)	Expected (mM)	Measured[a] (mM)	SD[b]	CV[c] (%)	Recovery[d] (%)
Normal		1	2.08	2.08	0.08	3.97	99.84
Boundary	1.08	4.5	5.58	5.43	0.31	5.67	97.39
High		6	7.08	7.16	0.33	4.58	101.19

[a] The average value of 5 successive measurement experiments. [b] standard deviation (SD) of 5 measurements. [c] Coefficient of variation = (SD/mean) × 100. [d] Recovery = (Measured value/Expected value) × 100.

slope is the slope of calibration curve (Kim et al., 2018). The LOD and linear range values of our paper strips are among the best describing colorimetric detection of cholesterol (**Table S1**). Furthermore, our system solely enables reagent-free colorimetric determination of cholesterol, which is quite advantageous in practical applications. Considering that the cut-off value of hypercholesterolemia patients is about 6 mM, thus the current cholesterol paper strip is suitable to distinguish patients with hypercholesterolemia and normal persons (Nair et al., 2014). Although the employed nanoceria and ChOx were not uniformly immobilized but aggregated to some extent on paper matrices (**Figure S6**), the detection performances of the developed cholesterol paper strip were enough for practical applications.

We also evaluated long-term storage stability and reusability of the developed cholesterol paper strip. The storage stabilities were examined by measuring the residual color intensities toward cholesterol, during the storages in three conditions at RT, 4°C, and −20°C. The investigations clearly indicated that the paper strip showed excellent storage stability during 20 days (**Figure 5A**). When incubating at RT, our paper strip showed slight decrease in color intensity; however, over 90% of initial activity still remained at 20 days of incubation. The paper strip is also expected to be reused for multiple times owing to the expected decomposition of the adsorbed peroxide species on the surface of embedded nanoceria (Kim et al., 2017). As a result, the paper strip fully regained its original color up to 4 consecutive cycles (**Figure 5B**). However, its maximal color intensity after reaction was gradually decreased, indicating that the immobilized state of nanoceria on the paper matrices would hinder the reversibility of nanoceria.

Determination of Cholesterol Levels in Human Serum Samples

Finally, we examined the diagnostic capability of the paper strip incorporating nanoceria and ChOx, using clinical human serum samples containing representative levels of cholesterol (normal; $\leq$5 mM, boundary; 5–6 mM, and high; $>$6 mM) (Nair et al., 2014). The original amount of cholesterol in the serum samples was first determined using a cholesterol assay kit, and a predetermined amount of cholesterol was added to establish the representative levels. 10-fold dilution was applied to the prepared samples to adjust their cholesterol concentration within our linear range. According to the experimental results, the serum cholesterol levels were quantitatively determined with excellent precision, yielding CVs ranging from 3.97 to 5.67% and recoveries ranging from 97.39 to 101.19% (**Table 1**), validating the excellent reproducibility and reliability of this assay. The precision values were similar to those obtained with commercially-available cholesterol assay kit (**Table S2**). These results demonstrate that the proposed reagent-free colorimetric cholesterol paper strip can be employed as a promising analytical tool for convenient identification and first screening of hypercholesterolemia in POCT environments.

CONCLUSIONS

We herein developed a paper strip sensor incorporating both nanoceria and ChOx, for reagent-free as well as instrumentation-free determination of cholesterol. The paper strip displayed excellent selectivity, sensitivity, and linearity for the determination of target cholesterol by simple processing the real images acquired using a smartphone, with excellent storage stability and reusability. The clinical utility of the strip sensor was successfully demonstrated by reliably determining the cholesterol levels from clinical human serum samples. Since the current nanoceria-embedded paper strip enabled visual detection of the target cholesterol without involvement of any chromogenic dye or detection instrumentation, it should find practical applications in POCT environments.

DATA AVAILABILITY STATEMENT

The original contributions presented in the study are included in the article/**Supplementary Material**, further inquiries can be directed to the corresponding author/s.

AUTHOR CONTRIBUTIONS

PN and YK performed investigation. PN wrote the original draft. MK performed conceptualization, supervision, and reviewing the manuscript. All authors contributed to the article and approved the submitted version.

ACKNOWLEDGMENTS

This work was supported by the National Research Foundation of Korea (NRF) grant funded by the Korea government [Ministry of Science and ICT (NRF- 2019R1A2C1087459)] and by the Gachon University research fund of 2019 (GCU-2019-0362).

SUPPLEMENTARY MATERIAL

The Supplementary Material for this article can be found online at: https://www.frontiersin.org/articles/10.3389/fchem.2020.00798/full#supplementary-material

REFERENCES

Arya, S. K., Datta, M., and Malhotra, B. D. (2008). Recent advances in cholesterol biosensor. *Biosens. Bioelectron*. 23, 1083–1100. doi: 10.1016/j.bios.2007.10.018

Chung, M., Jang, Y. J., and Kim, M. I. (2018). Convenient colorimetric detection of cholesterol using multi-enzyme co-incorporated organic–inorganic hybrid nanoflowers. *J. Nanosci. Nanotechnol*. 18, 6555–6561. doi: 10.1166/jnn.2018.15697

Hayat, A., Haider, W., Raza, Y., and Marty, J. L. (2015). Colorimetric cholesterol sensor based on peroxidase like activity of zinc oxide nanoparticles incorporated carbon nanotubes. *Talanta* 143, 157–161. doi: 10.1016/j.talanta.2015.05.051

Ikonen, E. (2008). Cellular cholesterol trafficking and compartmentalization. *Nat. Rev. Mol. Cell Biol*. 9, 125–138. doi: 10.1038/nrm2336

Karakoti, A. S., Singh, S., Kumar, A., Malinska, M., Kuchibhatla, S. V., Wozniak, K., et al. (2009). PEGylated nanoceria as radical scavenger with tunable redox chemistry. *J. Am. Chem. Soc*. 131, 14144–14145. doi: 10.1021/ja9051087

Kim, D. H., Hur, J., Park, H. G., and Kim, M. I. (2017). Reagentless colorimetric biosensing platform based on nanoceria within an agarose gel matrix. *Biosens. Bioelectron*. 93, 226–233. doi: 10.1016/j.bios.2016.08.113

Kim, H., Lee, J. U., Song, S., Kim, S., and Sim, S. J. (2018). A shape-code nanoplasmonic biosensor for multiplex detection of Alzheimer's disease biomarkers. *Biosens. Bioelectron*. 101, 96–102. doi: 10.1016/j.bios.2017.10.018

Kim, M. I., Cho, D., and Park, H. G. (2015). Colorimetric quantification of glucose and cholesterol in human blood using a nanocomposite entrapping magnetic nanoparticles and oxidases. *J. Nanosci. Nanotechnol*. 15, 7955–7961. doi: 10.1166/jnn.2015.11227

Kim, M. I., Shim, J., Li, T., Lee, J., and Park, H. G. (2011). Fabrication of nanoporous nanocomposites entrapping Fe_3O_4 magnetic nanoparticles and oxidases for colorimetric biosensing. *Chem. Eur. J*. 17, 10700–10707. doi: 10.1002/chem.201101191

Li, J., Zhang, Z., Xu, S., Chen, L., Zhou, N., Xiong, H., et al. (2011). Label-free colorimetric detection of trace cholesterol based on molecularly imprinted photonic hydrogels. *J. Mater. Chem*. 21, 19267–19274. doi: 10.1039/C1JM14230E

Lin, Y.-T., Wu, S.-S., and Wu, H.-L. (2007). Highly sensitive analysis of cholesterol and sitosterol in foods and human biosamples by liquid chromatography with fluorescence detection. *J. Chromatogr. A* 1156, 280–287. doi: 10.1016/j.chroma.2007.01.091

MacLachlan, J., Wotherspoon, A. T. L., Ansell, R. O., and Brooks, C. J. W. (2000). Cholesterol oxidase: sources, physical properties and analytical applications. *J. Steroid Biochem. Mol. Biol*. 72, 169–195. doi: 10.1016/S0960-0760(00)00044-3

Mahato, K., Srivastava, A., and Chandra, P. (2017). Paper based diagnostics for personalized health care: emerging technologies and commercial aspects. *Biosens. Bioelectron*. 96, 246–259. doi: 10.1016/j.bios.2017.05.001

Martin, S. P., Lamb, D. J., Lynch, J. M., and Reddy, S. M. (2003). Enzyme-based determination of cholesterol using the quartz crystal acoustic wave sensor. *Anal. Chim. Acta* 487, 91–100. doi: 10.1016/S0003-2670(03)00504-X

Matharu, Z., Solanki, P. R., Gupta, V., and Malhotra, B. D. (2012). Mediator free cholesterol biosensor based on self-assembled monolayer platform. *Analyst* 137, 747–753. doi: 10.1039/C1AN15196G

Nair, D. R., Sharifi, M., and Al-Rasadi, K. (2014). Familial hypercholesterolaemia. *Curr. Opin. Cardiol*. 29, 381–388. doi: 10.1097/HCO.0000000000000083

Nauck, M., März, W., Jarausch, J., Cobbaert, C., Sägers, A., Bernard, D., et al. (1997). Multicenter evaluation of a homogeneous assay for HDL-cholesterol without sample pretreatment. *Clin. Chem*. 43, 1622–1629. doi: 10.1093/clinchem/43.9.1622

Ornatska, M., Sharpe, E., Andreescu, D., and Andreescu, S. (2011). Paper bioassay based on ceria nanoparticles as colorimetric probes. *Anal. Chem*. 83, 4273–4280. doi: 10.1021/ac200697y

Scholes, F. H., Soste, C., Hughes, A. E., Hardin, S. G., and Curtis, P. R. (2006). The role of hydrogen peroxide in the deposition of cerium-based conversion coatings. *Appl. Surf. Sci*. 253, 1770–1780. doi: 10.1016/j.apsusc.2006.03.010

Singh, S., Dosani, T., Karakoti, A. S., Kumar, A., Seal, S., and Self, W. T. (2011). A phosphate-dependent shift in redox state of cerium oxide nanoparticles and its effects on catalytic properties. *Biomaterials* 32, 6745–6753. doi: 10.1016/j.biomaterials.2011.05.073

Wu, Y., Ma, Y., Xu, G., Wei, F., Ma, Y., Song, Q., et al. (2017). Metal-organic framework coated Fe_3O_4 magnetic nanoparticles with peroxidase-like activity for colorimetric sensing of cholesterol. *Sensor. Actuat. B Chem*. 249, 195–202. doi: 10.1016/j.snb.2017.03.145

Zhang, M., Yuan, R., Chai, Y., Chen, S., Zhong, X., Zhong, H., et al. (2012). A cathodic electrogenerated chemiluminescence biosensor based on luminol and hemin-graphene nanosheets for cholesterol detection. *RSC Adv*. 2, 4639–4641. doi: 10.1039/C2RA20374J

Zhang, N., Liu, Y., Tong, L., Xu, K., Zhuo, L., and Tang, B. (2008). A novel assembly of Au NPs–β-CDs–FL for the fluorescent probing of cholesterol and its application in blood serum. *Analyst*. 133, 1176–1181. doi: 10.1039/B803226B

Conflict of Interest: The authors declare that the research was conducted in the absence of any commercial or financial relationships that could be construed as a potential conflict of interest.

frontiers in Chemistry

REVIEW
published: 10 September 2020
doi: 10.3389/fchem.2020.00818

Nano-Sized Iron Sulfide: Structure, Synthesis, Properties, and Biomedical Applications

Ye Yuan[1,2,3], **Liping Wang**[1,2] **and Lizeng Gao**[3,4*]

[1] Key Laboratory for Molecular Enzymology and Engineering, The Ministry of Education, Jilin University, Changchun, China, [2] School of Life Sciences, Jilin University, Changchun, China, [3] CAS Engineering Laboratory for Nanozyme, Institute of Biophysics, Chinese Academy of Sciences, Beijing, China, [4] Nanozyme Medical Center, School of Basic Medical Sciences, Zhengzhou University, Zhengzhou, China

Nano-sized iron sulfides have attracted intense research interest due to the variety of their types, structures, and physicochemical properties. In particular, nano-sized iron sulfides exhibit enzyme-like activity by mimicking natural enzymes that depend on an iron-sulfur cluster as cofactor, extending their potential for applications in biomedicine. The present review principally summarizes the synthesis, properties and applications in biomedical fields, demonstrating that nano-sized iron sulfides have considerable potential for improving human health and quality of life.

Keywords: nano-sized iron sulfide, structure, synthesis, enzyme-like activities, biomedical applications

Edited by:
Youhui Lin,
Xiamen University, China

Reviewed by:
Xian Chen,
Shenzhen University, China
Amitava Adhikary,
Oakland University, United States

****Correspondence:***
Lizeng Gao
gaolizeng@ibp.ac.cn

Specialty section:
This article was submitted to Nanoscience, a section of the journal Frontiers in Chemistry

Received: *19 May 2020*
Accepted: *04 August 2020*
Published: *10 September 2020*

Citation:
Yuan Y, Wang L and Gao L (2020) Nano-Sized Iron Sulfide: Structure, Synthesis, Properties, and Biomedical Applications. Front. Chem. 8:818. doi: 10.3389/fchem.2020.00818

INTRODUCTION

With the development of nanotechnology (Li et al., 2019), nanomaterials have become a major resource for the development of novel therapeutic medicines and technologies designed to improve human health and the quality of life (Zhang and Webster, 2009; Esmaeili et al., 2020; Wang et al., 2020). In particular, due to their multiple functionality and excellent biocompatibility, iron-based nanomaterials are frequently used in the biomedical field, such as bioseparation, biosensors, magnetic resonance imaging (MRI), tumor hyperthermia, and drug delivery (Chen and Gu, 2017). In addition, recent studies have revealed that these nanomaterials have intrinsic enzyme-like properties (Gao et al., 2007; Xie et al., 2012; Xu et al., 2018), an important form of nanozyme representing a new generation of artificial enzyme (Wei and Wang, 2013; Dong et al., 2019; Liang and Yan, 2019). Currently, the majority of iron-based nanomaterials are iron oxide which possess excellent supraparamagnetic properties, with catalytic activity mimicking that of oxido-reductases, including peroxidase, catalase, superoxide dismutase, and oxidase (Gao et al., 2007; Liang and Yan, 2019). However, iron sulfide nanomaterials have not been comprehensively studied or used in the biomedical fields. Since O and S are congeneric elements, iron sulfide demonstrates similar physiochemical properties as iron oxide (Fu et al., 2019). In addition, the phases of iron sulfide in nature include mackinawite (FeS), pyrrhotite ($Fe_{1-x}S$), pyrite (FeS_2), and greigite (Fe_3S_4), etc., which exhibit more variability than iron oxide containing only Fe_2O_3 and Fe_3O_4. The band gap in iron sulfide is smaller than that of iron oxide, leading to the former having more appropriate electron transfer and conductivity (Wadia et al., 2009; Jin et al., 2017; Zhang et al., 2018). Importantly, iron-sulfur clusters are important cofactors in many enzymes which serve as active centers for electron transfer in catalytic processes and respiratory chain reactions (Qi and Cowan, 2011). Therefore, it is anticipated that iron sulfide nanomaterials will display multiple functionalities and they have great potential in biomedical applications. Herein, we will summarize the types, synthesis and properties of iron sulfide nanomaterials and emphasize their applications in biomedical and medical fields. This will provide a comprehensive understanding of iron sulfide nanomaterials and illustrate their considerable potential as novel multifunctional biomaterials in biomedical applications.

TYPE AND STRUCTURE OF IRON SULFIDE

Solid phases of iron sulfides principally comprise FeS (mackinawite), $Fe_{1-x}S$ (pyrrhotite), FeS_{2p} (pyrite), FeS_{2m} (marcasite), Fe_3S_4 (greigite), and Fe_9S_{11} (smythite). The content of iron within a biomaterial therefore influences its phase, shape, and physical and chemical properties. FeS naturally has a tetragonal structure, with each iron atom coordinated to four sulfurs. For $Fe_{1-x}S$, a monoclinic hexagonal is present. FeS_{2p} forms stable iron (II) disulfides with cubic structures. FeS_{2m} differs from FeS_{2p} as an orthorhombic metastable iron (II) disulfide, whilst Fe_3S_4 is a cubic metastable Fe (II) Fe (III) sulfide. Hexagonal Fe_9S_{11} is related to the $Fe_{1-x}S$ phase (Rickard and Luther, 2007).

Reported crystal structures of iron sulfide are displayed in **Figure 1** (Fleet, 1971; Argueta-Figueroa et al., 2017). FeS possesses a tetragonal layered structure in which the iron atoms are linked through tetrahedral coordination to four equidistant sulfur atoms. A single iron atom is coordinated to four equidistant sulfur atoms. The distance of Fe-Fe is 2.5967 Å. In addition, Fe-Fe bonding is substantial in FeS. To assess the effects of van der Waals forces resulting from the S atoms, sheets including Fe are stacked along the C-axis. The spacing of these layers is 5 Å. The structure of Fe_2S_2 is closed to FeS. The structure of FeS_2 is similar to that of NaCl in which S^{2-} is located at the center of a cube. The cubic structure has a low symmetry. In addition, FeS_2 exhibits chirality through absorbed organic molecules. Fe_3S_4 has an inverse spinel structure in which 8 Fe atoms are located at the tetrahedral A-sites and 16 Fe atoms are located at the B-sites of the octahedron. The unit cell of Fe_3S_4 is 9.876 Å. In addition, the cubic structure of Fe_3S_4 forms a closely packed array of S molecules linked by smaller Fe units (**Figure 1D**). It has been established that the Fe_7S_8 structure is a hexagonal supercell (Fleet, 1971). The viable distribution of vacancy sites ideal for the base structure of NiAs was observed to describe the structure of Fe_9S_{10} (Elliot, 2010).

SYNTHESIS OF NANO-SIZED IRON SULFIDES

Nano-sized iron sulfide encompasses a range of iron and sulfur compounds. Firstly, the range of chemical and biological methods for their production are discussed. In addition, the most reported synthesized methods for creating different phases of iron sulfide are presented in **Table 1**.

Hydrothermal Synthesis

Thermal decomposition is the most commonly-used hydrothermal reaction for iron sulfide production. The typical solvothermal synthesis method of nFeS firstly involves the dissolution of $FeCl_3 \cdot 6H_2O$ in 40 mL of ethylene glycol. NaOAc and organosulfur compounds (allyl methyl sulfide, diallyl sulfide, diallyl trisulfide, diallyl disulfide, cysteine, cystine, glutathione (GSH), or methionine) are then added under continuous and vigorous stirring. The system was then sonicated for 10 min and transferred to a Teflon-lined stainless steel autoclave. The mixture was reacted at 200°C for 12 h and precipitates washed three times with ethanol and water. Finally, the products were dried at 60°C for 3 h (Xu et al., 2018). For FeS_2, the single source molecular precursor Fe^{3+} diethyl dithiophosphate forms an aqueous solution through the reaction of $FeCl_3$ and $(C_2H_5O)_2P(S)SNH_4$, with hexadecyltrimethylammonium bromide (CTAB) added as a surfactant and reacted with a single precursor $[(C_2H_5O)_2P(S)S]_3Fe$ (Wadia et al., 2009). For FeS, $FeCl_3 \cdot 6H_2O$ was dissolved in ultrapure water with ethanolamine and thiourea added to the solution. After stirring for 25 min, the mixture was added to a Teflon lined autoclave and reacted at 180°C for 12 h. The synthesis of Fe_3S_4 differs from that of FeS. $FeCl_3 \cdot 6H_2O$, ethylene glycol, thiourea and H_2O_2 were mixed and reacted at 180°C for 18 h in the presence of the capping agent polyvinyl pyrrolidone (PVP) to prevent excessive growth and aggregation of the nanoparticles (NPs) (Moore et al., 2019). $Fe_{1-x}S$ single crystals were then synthesized through a hydrothermal method by the addition of $K_{0.8}Fe_{1.6}S_2$ crystals, Fe powder, NaOH, and thiourea in deionized water, which was reacted at 120°C for 3–4 days (Guo et al., 2017). Ionic liquids that form extended hydrogen bond systems were then used to form higher structures in the base of the hydrothermal process, as reported by Zheng and colleagues when changing the structure of Fe_3S_4 (Ma et al., 2010). Generally speaking, the product obtained by the hydrothermal method has better dispersibility and controllability, but iron oxide impurities can also appear during the synthesis of iron sulfide. Meanwhile, multiphase iron sulfide appears to occur easily, as assessed by X-ray diffraction (XRD) patterns for hydrothermally-synthesized samples.

Microwave Production

The principal advantages of microwave-assisted methods, compared with conventional heating include its reduced reaction time, smaller particle size distribution, and higher purity. Ethylene glycol is a solvent suitable for microwave-assisted methods owing to its relatively high dipole moment. For FeS_2 microspherolites, $FeSO_4 \cdot 7H_2O$, PVP-K30 and S powder in ethylene glycol can be reacted by microwave in an N_2 atmosphere (Li M. et al., 2011). Although this emerging technique may be more desirable it should be noted that the aggregation phenomenon does not appear to be improved.

Co-precipitation

Chemical co-precipitation does not introduce impurities. The operation is performed under mild conditions and is typically synthesized using Fe_3S_4 methods, in which iron (II) sulfate heptahydrate and sodium sulfide are dissolved in ultrapure deionized water. The solution was then added dropwise to acetic acid to adjust the pH to 3.0, followed by stirring for several minutes. The reaction was prepared under an N_2 atmosphere (Chang et al., 2011). In addition, green synthesis was achieved

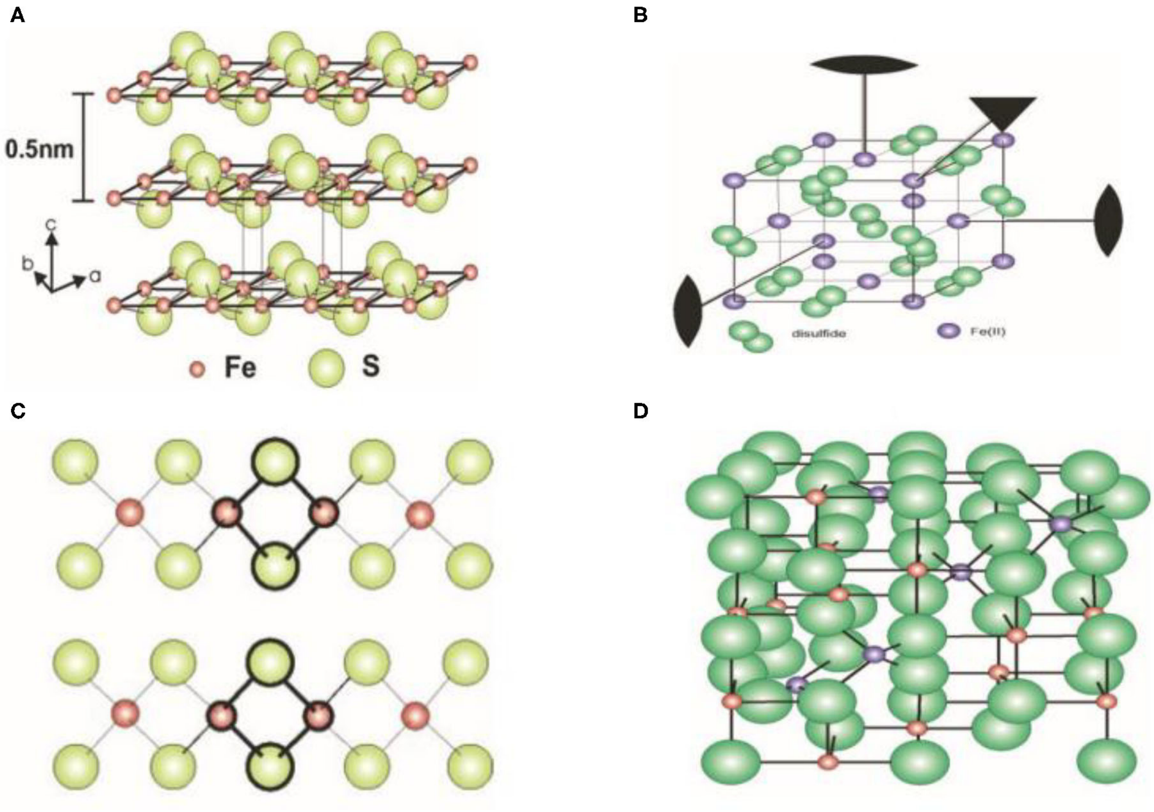

FIGURE 1 | Crystal structure of iron sulfide. **(A)** FeS. **(B)** FeS_2. **(C)** Fe_2S_2. **(D)** Fe_3S_4. Reproduced with permission from Rickard and Luther (2007). Copyright 2007, American Chemical Society.

in a continuous stirred-tank reactor (Simeonidis et al., 2016). As previously reported, the conditions of synthesis required by co-precipitation are harsher than those of other methods, and the products obtained may show poor homogeneity.

High Temperature Chemical Synthesis

Chemical synthesis methods using high temperatures have been reported for FeS_2. Briefly, iron (II) acetylacetonate ($Fe(acac)_2$), trioctylphosphine oxide (TOPO) and oleyamine (OLA) were mixed and degassed at 110°C for 1 h under a vacuum. The mixture was then rapidly heated to 220°C for 1 h under vigorous magnetic stirring in the presence of nitrogen. Sulfur was then quickly injected into the solution, which was heated to 220°C for 1 h. Once the solution cooled, ethanol was added to the precipitate to develop the FeS_2 nanoplates (Bi et al., 2011). Synthesis methods for $Fe_{1-x}S$ and Fe_3S_4 have also been reported. The rapid injection method has been used to reduce the size of Fe_3S_4 (Beal et al., 2012). This method of synthesis is highly sensitive to the experimental conditions.

Sonochemical Synthesis

As a convenient and stable synthetic method, Bala and colleagues described specific FeS' sonochemical synthesis. Firstly, sodium sulfide was dissolved in double distilled water. $FeSO_4 \cdot 7H_2O$ was then independently dissolved in a solution of double distilled water and polyethylene glycol (1:1). The sodium sulfide solution contained a drop of Triton-X surfactant which was added dropwise to the above solution while being continuously sonicated for 30 min. PVP was then added and the system was mixed via ultrasound for a further 30 min (Ahuja et al., 2019).

Other Chemical Methods

Some unusual synthetic chemical methods have been reported. The low temperature synthesis of FeS_2 nanoparticles was described in 2014 (Srivastava et al., 2014a). Briefly, $FeCl_3$ and sodium polysulfide (Na_2S_x) were mixed in pH 5.6 acetate buffer in an anaerobic environment. The black solution then was reacted in a 90–100°C oil bath for 4 h to produce a grayish FeS_2 product. Flux methods were then used to synthesize 1D Fe_7S_8. The reaction was conducted within a furnace at 750–850°C (Kong et al., 2005). FeS can also be created in a biological system (Mei and Ma, 2013).

Biomineralization

The bio-synthesis of iron sulfide using microorganisms is superior for biomedical applications (Li X. et al., 2011). When microorganisms interact with target ions, they are transported into microbial cells to form NPs in the presence of specific enzymes. In addition to the advantages of green synthesis, biological methods improve the biocompatibility of iron sulfide.

TABLE 1 | Appearances, sizes and lattice spaces of iron sulfide.

Phase	Method	Appearances	Size (nm)	Lattice space (nm)	References
FeS	High temperature chemical synthesis	Nanoplates	32–36	0.286	Yang et al., 2015
	Sonochemical synthesis	Spherical	6–20		Ahuja et al., 2019
	Biosystem	Spherical	30–50		Mei and Ma, 2013
	Hydrothermal synthesis	Pomegranate flower-like	3,000		Jin et al., 2017
	Co-precipitation Co-precipitation	Regular spherical Nanoparticles	50 60–80 102 (DLS)		Dai et al., 2009; Agnihotri et al., 2020
	Biomineralization	Spherical	2		Watson et al., 1999
FeS_2	High temperature chemical synthesis	Cubic	60–200		Bi et al., 2011
	Ionic liquid-modulated synthesis	Hexagonal nanoplates	12,000 30 (side length)		Ma et al., 2010
	Hydrothermal synthesis	Quasi-cubic nanocrystal	Over 100		Wadia et al., 2009
	Microwave	Big particles	200		Kim and Batchelor, 2009
	Hydrothermal synthesis	Uniform nanowires	40–60	0.269	Kar and Chaudhuri, 2004
	Hydrothermal synthesis	Nanorods	40–100		Kar and Chaudhuri, 2004
	Hydrothermal synthesis	Nanoribbons	100–250	0.313	Kar and Chaudhuri, 2004
	Microwave	Monodisperse microspherolites	2,400	0.27	Li M. et al., 2011
	Biomineralization	Nanodots	7		Jin et al., 2018
	Low temperature synthesis	Hexagonal	600–700		Srivastava et al., 2014b
Fe_3S_4	Hydrothermal synthesis	Spherical	76 165 (DLS)		Ding et al., 2016
	Hydrothermal synthesis Hydrothermal synthesis	Plates Dispersible nanoparticles	2000–5000 17.7	0.298	Fu et al., 2019; Moore et al., 2019
	Hydrothermal synthesis Hydrothermal synthesis Hydrothermal synthesis	Nanocrystals Hexagonal nanolpates Monodisperse nanocrystals	2.5–4.5 12,000 30 (side length) 100 175 (DLS)		Vanitha and O'Brien, 2008; Ma et al., 2010; He et al., 2013
	Co-precipitation Co-precipitation Co-precipitation	Irregular particles Nanoparticles Platelet-like	50–100 20–35 10–20	0.572	Chang et al., 2011; Paolella et al., 2011; Simeonidis et al., 2016
	High temperature chemical synthesis	Spherical	5	0.25	Beal et al., 2012
Fe_7S_8	Hydrothermal synthesis	Spherical	5.6		Vanitha and O'Brien, 2008
	Flux	hedgehog-like	10,000		Kong et al., 2005
	Flux	Nanorods	200 1500–2000 (length)		Kong et al., 2005
	Flux	Nanosheets	Smaller than 100 (thickness)		Kong et al., 2005
	Hydrothermal synthesis	Nanowires		0.289	Yao et al., 2013
	High temperature chemical synthesis	Nanosheets	5,000 500 (thickness)		Wang et al., 2013

The particles generated have higher catalytic reactivity and a greater surface area. Previous studies have reported that FeS_2, Fe_3S_4, and FeS NPs can be produced by microorganisms. For the biomineralization of Fe_3S_4 and FeS_2, a magnetotactic bacterium has been described (Mann et al., 1990). In 1995, FeS materials were produced by sulfate-reducing bacteria grown on iron containing substrates (Watson et al., 1995). Bazylinski and colleagues also reported the formation of Fe_3S_4 using non-cultured magnetotactic bacteria (Lefèvre et al., 2010). Sulfate-reducing bacteria were able to produce $Fe_{1-x}S$ as reported by Charnock and colleagues (Watson et al., 2000). NPs were subsequently formed at the surface by the microorganisms and as such, the porous structure of the iron sulfide NPs failed to prevent normal metabolism. These studies verified the utility of this method for efficient NP production. Chemical biomineralization methods have also been used to synthesize FeS_2 and FeS Quantum dots (QDs) (Jin et al., 2018; Yang et al., 2020).

Iron Sulfide Modifications

Bare nanocrystal cores have an unstable structure that is prone to photochemical degradation. However, those that are unmodified display higher toxicity. As such, biocompatible moieties are essential as they serve as caps for nanomaterials, including polyethylene glycol (PEG), silica, lactose, citrate, and dextran (Simeonidis et al., 2016; Mofokeng et al., 2017). Previous studies have reported the synthesis, characterization, cytotoxicity and biodistribution of FeS/PEG nanoplates *in vivo* (Yang et al., 2015). An adsorption-reduction method was used to load silver onto the surface of 3-aminopropyltriethoxysilanemodified 3-aminopropyl triethoxysilane (APTES)-modified Fe_3S_4 particles, achieving the preparation of magnetic composite nanoparticles of Fe_3S_4/Ag (He et al., 2013). However, modifications also led to adverse effects. For example, the modification of CTAB inhibited the growth of nano Fe_3S_4 (Simeonidis et al., 2016).

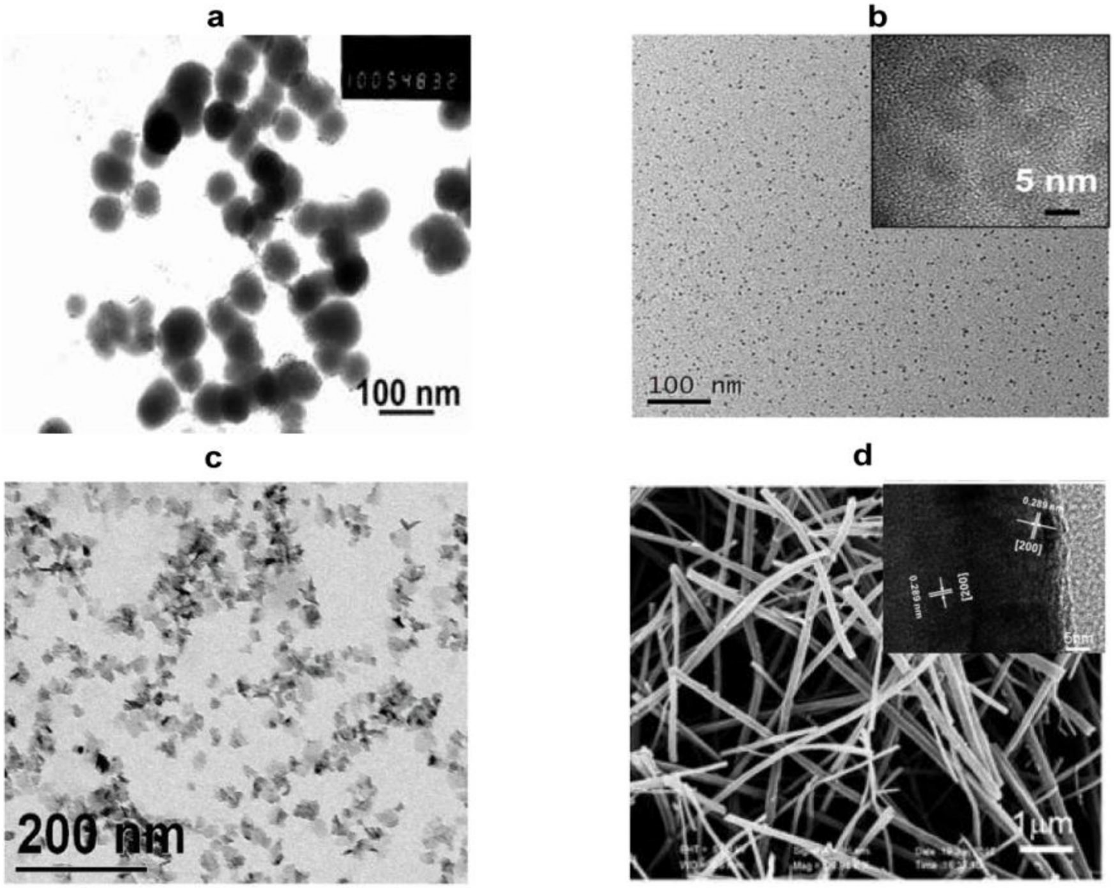

FIGURE 2 | Representative images of nano-sized iron sulfide. **(A)** TEM image of the spherical FeS. Reproduced with permission from Dai et al. (2009). Copyright 2009, Wiley-VCH Verlag GmbH & Co. KGaA, Weinheim. **(B)** TEM and HRTEM of FeS_2 nanodots. Reproduced with permission from Jin et al. (2018). Copyright 2017, American Chemical Society. **(C)** TEM images of platelet-like Fe_3S_4. Reproduced with permission from Paolella et al. (2011). Copyright 2011, American Chemical Society. **(D)** SEM and HRTEM of Fe_7S_8 nanowires. Reproduced with permission from Yao et al. (2013). Copyright 2013, Wiley-VCH Verlag GmbH & Co. KGaA, Weinheim.

Characterization of Iron Sulfide

Detailed characterization is required to confirm the synthesis of iron sulfide. Scanning electron microscopy (SEM) and transmission electron microscopy (TEM) can be used to image surface morphology. These represent the most direct and commonly-used methods to assess the microstructure, size, and dispersion of the materials. Differences in the synthetic methods have presented variations in TEM/SEM imaging, including within the same phase. For FeS, nanoplates, spherical nanoparticles, and pomegranate flower-like shapes have been reported. FeS_2 exists as large particles, cubic nanocrystals, monodisperse microspherolites, spherical and hexagonal nanoribbons, and nanorods. Typical images of iron sulfide are shown in **Figure 2**. **Table 1** reports the most common morphology and size of FeS, FeS_2, Fe_3S_4, and Fe_7S_8. Lattice spaces are measured to judge the crystallinity of the materials. The reported lattice spaces of the iron sulfides are summarized in **Table 1**. The composition, content, and structure of a substance can be analyzed, measured, and inferred using Ultraviolet-visible (UV-Vis) spectrometry and the absorption of UV and visible light. According to previous studies, the UV absorption peaks of FeS are 285 nm and 500 nm (**Table 2**). Information on the composition of the materials and the structure and/or morphology of the atoms or molecules inside the materials can be obtained by XRD analysis. XRD is the most direct indicator of whether a crystal is pure and so represents a convenient system to analyze synthesized materials. JCPDS cards are used to contrast and analyze unknown crystals. JCPDS cards of FeS (JCPDS card No. 15-0037 and 75-0602), FeS_2 (JCPDS card No. 03-065-1211, 89-3057, 65-3321, and 42-130), Fe_3S_4 (JCPDS card No. 16-0713, 89-1998, and 16-0073) and Fe_7S_8 (JCPDS card No. 25-0411 and 76-2308) are listed in **Table 2**. For iron sulfide nanomaterials, the X-ray photoelectron spectroscopy (XPS) of Fe and S are essential. FeS materials are presented in **Table 2** (Fe 2p: $2p_{3/2}$ (711.4 eV), $2p_{1/2}$ (724.9 eV), S 2p: $2p_{3/2}$ (161.1 eV), $2p_{1/2}$ (166.0 eV)), FeS_2 (Fe 2p: $2p_{3/2}$ (707.0 eV), $2p_{1/2}$ (720.0 eV), S 2p $2p_{3/2}$ (162.3 eV), $2p_{1/2}$ (163.5 eV)), Fe_3S_4 (Fe 2p: $2p_{3/2}$ (711.0 eV), S 2p: $2p_{3/2}$ (161.0 eV), $2p_{1/2}$ (162.5 eV)), Fe_7S_8 (Fe

TABLE 2 | UV-VIS, XPS and XRD of iron sulfide.

Phase	UV-Vis peak (nm)	XPS	XRD	References
FeS	500 285 A broad absorption in (400–700 nm)	Fe 2p 2p$_{3/2}$ (711.4 eV) 2p$_{1/2}$ (724.9 eV) S 2p 2p$_{3/2}$ (161.1 eV) 2p$_{1/2}$ (166.0 eV)	JCPDS card No.15-0037 JCPDS card No.75-0602	Guo et al., 2016; Jin et al., 2017; Ahuja et al., 2019; Agnihotri et al., 2020
FeS_2		Fe 2p 2p$_{3/2}$ (707.0 eV) 2p$_{1/2}$ (720.0 eV) S 2p 2p$_{3/2}$ (162.3 eV) 2p$_{1/2}$ (163.5 eV)	JCPDS card No.03-065-1211 JCPDS card No.89-3057 JCPDS card No.65-3321 JCPDS card No.42-1340	Kar and Chaudhuri, 2004; Wadia et al., 2009; Li M. et al., 2011; Gan et al., 2016
Fe_3S_4		Fe 2p 2p$_{3/2}$ (711.0 eV) S 2p 2p$_{3/2}$ (161.0 eV) 2p$_{1/2}$ (162.5 eV)	JCPDS card No.16-0713 JCPDS card No.89-1998 JCPDS card No.16-0073	Ma et al., 2010; Chang et al., 2011; Paolella et al., 2011; Beal et al., 2012; Feng et al., 2013; He et al., 2013; Ding et al., 2016; Moore et al., 2019
Fe_7S_8		Fe 2p 2p3/2 (709.9 eV) (711.6 eV) S 2p 2p$_{3/2}$ (163.5 eV) 2p$_{1/2}$ (164.7 eV)	JCPDS card No. 25-0411 JCPDS card No.76-2308 JCPDS card No.71-0647	Kong et al., 2005; Vanitha and O'Brien, 2008; Wang et al., 2013; Yao et al., 2013; Jin et al., 2019

2p: 2p$_{3/2}$ (709.9 eV), (711.6 eV), S 2p: 2p$_{3/2}$ (163.5 eV), 2p$_{1/2}$ (164.7 eV)). Fourier transform infrared (FTIR) spectroscopy can be used to detect functional groups in a complex mixture and so is therefore essential to the characterization of modified iron sulfide. Previous studies have provided FTIR spectra, showing successful modifications by APTES on the surface of the Fe_3S_4 nanoparticles (He et al., 2013). Fe_7S_8/N-C nanohybrids were prepared for FeMOF and FeMOF-S and analyzed by FTIR (Jin et al., 2019). In addition, energy dispersive spectroscopy (EDS) (Paolella et al., 2011; Ding et al., 2016; Guo et al., 2016), dynamic light scattering (DLS) (He et al., 2013; Ding et al., 2016), Raman spectroscopy (Gan et al., 2016; Guo et al., 2016), selected area electron diffraction (SAED) (Kar and Chaudhuri, 2004), X-ray absorption fine structure (XAFS) (Feng et al., 2013), differential scanning calorimetry (DSC) and thermogravimetric analysis (TGA) (Jin et al., 2019), nitrogen adsorption–desorption isotherms and pore size distribution (Guo et al., 2016) analysis of iron sulfide have been reported as characterization systems.

CHARACTERISTICS OF NANO-SIZED IRON SULFIDES

In addition to both the physical and chemical properties, characteristics include the structure, solubility, stability, reactivity, magnetic properties, and photothermal properties of the products.

Solubility

The major forms of nano-sized iron sulfides are solid precipitates which have poor solubility in water. However, Rickard et al. revealed that sedimental FeS can dissolve at c (S^{2-}) $\leq 10^{-5.7}$ M to form Fe^{2+}. The solubility can be increased in an alkaline as opposed to neutral environment (Rickard, 2006). FeS does not dissolve in HCl, meaning it cannot be removed with HCl (Rickard and Luther, 2007). According to previous studies, the K_{sp} of FeS_2 was $10^{-16.4}$ at 25°C. The solubility products of various iron sulfides were assessed and resulted in consensus values for the pKs (FeS: 3.6 ± 0.2; FeS_2 16.4 ± 1.2; Fe_3S_4 4.4 ± 0.1; Fe_7S_8 5.1 ± 0.1). This improved our understanding of the solubility of iron sulfide in both synthetic and natural water at room temperature (Davison, 1991).

Stability

FeS is stable within the P-T range of the Martian core (Kavner et al., 2001). Understanding the relationship between the stability of iron sulfide and its chemical environment is of key importance. Once iron sulfide is formed, its structure is reversible. Studies have examined the stability of FeS_2 in different temperatures and the concentrations of absorbed water on the surface. Temperature has little effect on the morphology of FeS_2 under low absorbed water concentrations. However, at above 90 K, the conversion from an octahedral structure to a cubic shape is promoted. At higher concentrations of water, the dependence on temperature is more apparent (Barnard and Russo, 2009). The latter study established that functions of the surface ligands affect the stability of FeS_2 (FeS_2 nanorods synthesized in laboratory) (Barand and Russo, 2009). The stability of FeS contributed to low energy excitation from Fe d to S-Sσ*p (Zhang et al., 2018). Fe_3S_4 was observed at 200°C for 30 h then it transformed to FeS_2 over time (Gao et al., 2015).

Reactivity

Iron sulfide is highly reactive to N_2 and H_2S. This reaction occurs at room temperature and the adsorption of N_2 is dependent on the surface FeS and on the electronic state of N_2. A decrease in absorbed N_2 and H_2S could be explained by the formation of ammonia (Kasting, 1993). The reactivity of Fe_7S_8 is similar to FeS (Niño et al., 2018). The presence of both Au^{1+} and Au atoms has been observed on the surface of FeS_2. Au deposition increased at higher pH and temperatures. The reactivity of Au^{1+} sulfides with FeS_2 have also been investigated (Scaini et al., 1998). The reactivity of FeS_2 using gaseous H_2O and O^{2-} was similarly reported. Gaseous H_2O leads to the formation of iron hydroxides on FeS_2. A sequence of different exposures also leads to the formation of a range of products (SO_4^{2-}, $Fe(OH)_3$) (Usher et al., 2005). Recently, FeS_2 was shown to be a potential nanomaterial for prebiotic chemistry due to its highly reactive surface that drives amino acid adsorption (Ganbaatar et al., 2016). Among the most common probes, water molecules have been used to explore

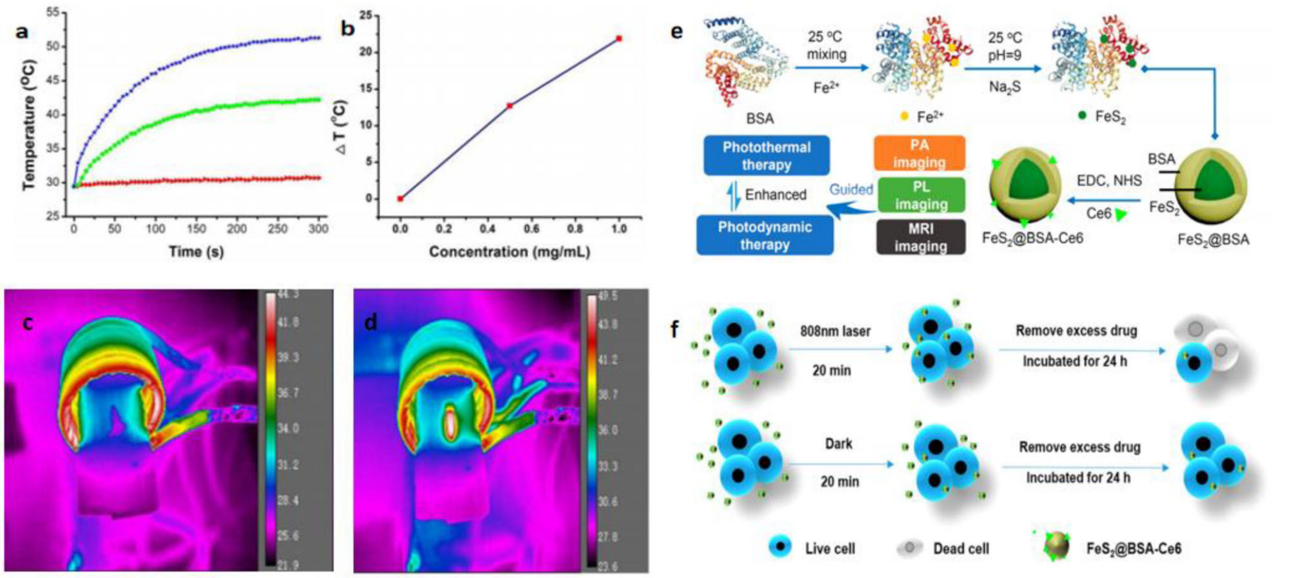

FIGURE 3 | Magnetocaloric conversion performance **(a–d)** and photothermal property of iron sulfides. **(a)** Temperature change of the Fe_3S_4 nanoparticles in water at varied concentrations of Fe^{2+} (i.e., 0, 0.5, and 1.0 mg/mL) as a function of magnetic field action time. **(b)** Plot of temperature change over 300s vs. the concentration of Fe_3S_4 nanoparticles. Thermal imaging of **(c)** pure water and **(d)** Fe_3S_4 nanoparticles (1.0 mg/mL) under the action of an AMF for 5 min. Reproduced with permission from Fu et al. (2019). Copyright 2019, Frontiers in Materials. **(e)** Synthetic route and applications of FeS_2 nanodots in the base of its photothermal activity. **(f)** Scheme showing photothermal enhanced cellular uptake of FeS_2@BSA-Ce6 nanoparticles. Reproduced with permission from Jin et al. (2018). Copyright 2017, American Chemical Society.

the reactivity of FeS_2 (De Leeuw et al., 2000). The different phases of iron sulfide display a wide range of reactivities to chlorinated solvents. Conditions including pH, sulfide concentrations, metal ions, and natural organic matter can affect the reaction kinetics of the degradation of chlorinated solvents (He et al., 2015). The interaction of FeS, Fe_3S_4 and CO_2 have also been reported. The charge transfer on FeS can also effectively activate CO_2, whilst Fe_3S_4 is unreactive to CO_2 (SantosCarballal et al., 2017).

Magnetic Properties

Nanomaterials with magnetic properties have numerous applications, including magnetocaloric therapies, as MRI agents, magnetic separation materials, and magnetic carriers. The discovery of their magnetic properties led to the identification of iron sulfide phases. The ferromagnetism of Fe_7S_8 can be explained by Fe^{3+} ions with excess sulfur (Yosida, 1951). The magnetic susceptibility χ of natural FeS_2 was found to be $64 \times 10^{-6} 68 \times 10^{-6}$ cm^3 /moles between 4.2 and 380 K (Mohindar and Jagadeesh, 1979). Magnetic ordering in FeS was inferred and used to prove strong itinerant spin fluctuations. FeS can also be used as a superconductor (Kwon et al., 2011). Even when the structure of FeS is changed from troilite to the MnP-type under high pressure, the antiferromagnetic properties are preserved until the monoclinic structure is formed (Ono, 2007). The magnetic moment then disappears and yetragonal-phase FeS (Tc: 5K) was observed for the same structure as the superconductor FeSe (Tc: 8 K) (Kuhn et al., 2016). Fe_3S_4 displays high Mrs/χ, (Mrs/χ: the saturation isothermal remnant magnetization: magnetic susceptibility) and its MrsMs (hysteresis ratios) and Bcr/Bc are 0.5 and 1.5 (Ms: saturation magnetization; Bc: the coercive force; Bcr: the coercivity of remanence). Fe_3S_4 also displays unique high-temperature properties, with a clear drop in magnetization from 270 to 350°C (Roberts, 1995). Synthesized Fe_3S_4 contains various crystals from small superparamagnetic grains (non-remanence) to large multi-domain grains (Snowball, 1991). The magnetic hysteresis properties of Fe_7S_8 have also been studied (Menyeh and O'Reilly, 1997). The relationship between structure and magnetic properties has been reported within variable temperatures. Magnetic transitions occurred within the transformation of the structure (Powell et al., 2004). The magnetocaloric conversion ability of Fe_3S_4 nanoparticles has been measured under an alternating magnetic field (AMF). Meanwhile, the excellent physical and chemical properties provide magnetothermal thrombolytic ability in medical applications (Fu et al., 2019; **Figure 3**).

Photothermal Properties

Photothermal therapy (PTT) has attracted considerable attention in recent years. The mechanism of PTT results mainly from photo-absorbing nanomaterials that generate heat through continuous laser irradiation, destroying cancer cells, but causing no damage to healthy tissue. It is therefore necessary to pay attention to the photothermal properties of iron sulfide. PEGylated FeS (FeS-PEG) nanoplates exhibit high near infrared (NIR) absorbance. Using Infrared (IR) thermal imaging, the

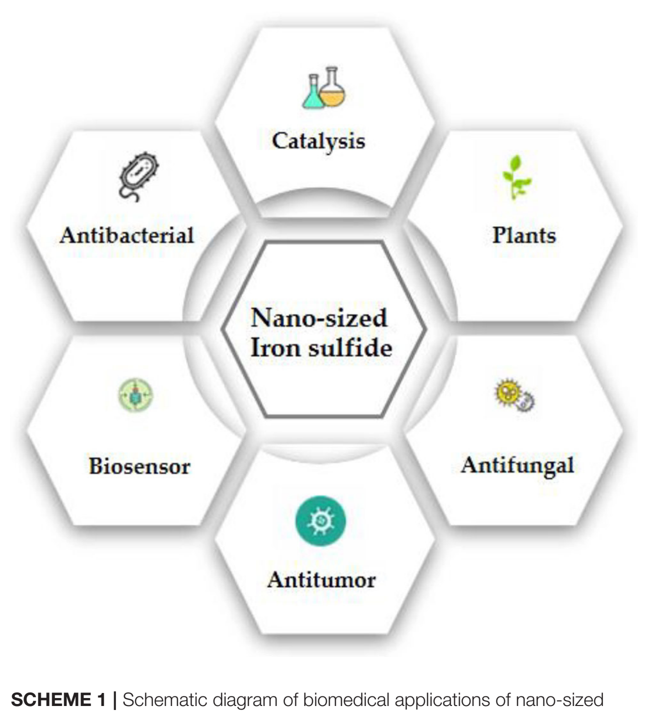

SCHEME 1 | Schematic diagram of biomedical applications of nano-sized iron sulfide.

temperature can reach 70°C within 5 min. Meanwhile, FeS-PEG displays stronger photothermal conversion efficiency than other known iron oxides (Yang et al., 2015). Ultrasmall FeS_2 nanodots have also been synthesized and have been shown to be useful for photodynamic therapy. Chlorin e6 (Ce6) was used to conjugate FeS_2 in the presence of the template bovine serum albumin (BSA). FeS_2@BSA-Ce6 nanodots (7 nm) demonstrated good results in *in vivo* photoacoustic (PA) imaging, MRI and enhanced cellular uptake (Jin et al., 2018; **Figure 3**).

Biomedical Applications

To-date, a variety of biomedical applications of iron sulfide (catalysts, antibacterial agents, cancer therapies, drug delivery systems, thrombolytic agents, biosensors, antifungal agents, seed improvers in phyto-applications) and their functional mechanisms have been summarized (**Scheme 1**).

Enzyme-Like Catalysis

Iron sulfur clusters are critical cofactors in many enzymes and proteins which conduct redox reactions and regulate oxidative stress. Thus, nano-sized iron sulfides are expected to perform similar catalysis and act as nanozymes. Previous studies have shown that iron sulfide can effectively activate persulfate (PS) or peroxymonosulfate (PMS) to generate sulfate radicals (Xiao et al., 2020). Other common reactions involving iron sulfide are shown in section Sonochemical Synthesis. Since iron oxide nanoparticles were shown to possess intrinsic peroxidase activity in 2007 (Gao et al., 2007), it has been speculated that iron sulfide has similar properties. The catalytic processes of iron sulfide are shown in **Figure 4**. High catalytic activity, multi-enzymes activities, harsh environmental resistance, storage stability, and the intrinsic advantages of nanomaterials provide further possibilities for biomedicine development, meaning that good alternatives to natural enzymes exist. The enzymatic activity of iron sulfide has been intensely investigated. In 2010, FeS nanosheets were reported to possess peroxidase-like activity. FeS suspensions were shown to catalyze the oxidation of peroxidase substrates, 3, 3′, 5, 5′-Tetramethylbenzidine (TMB) to produce a blue product in the presence of H_2O_2 (Dai et al., 2009) (**Figure 4**). Fe_7S_8 nanowires' also possessing intrinsic peroxidase activity was also reported in 2013 for which catalytic behavior was observed. The apparent K_M of Fe_7S_8 with TMB as a substrate was 0.548 mM, almost six times lower than that of horseradish peroxidase (HRP). These results demonstrate that Fe_7S_8 has a higher affinity to TMB than to HRP (Yao et al., 2013). In 2015, magnetic Fe_3S_4 NPs was shown to possess peroxidase-like activity. Through investigating steady state kinetics, Fe_3S_4 was shown to possess a higher affinity for H_2O_2 than HRP. The reasons could be that Fe_3S_4 binds to and reacts with H_2O_2, following which nanozyme is released prior to reacting with the second substrate TMB (Ding et al., 2016). nFeS ($Fe_{1-x}S$ and Fe_3S_4) (detailed description in section Hydrothermal Synthesis) have been shown to possess both peroxidase-like and catalase-like activity (**Figure 4**). nFeS is able to decompose H_2O_2 into free radicals and O_2, promoting the release of polysulfanes (Xu et al., 2018). FeS_2 has also been shown to possess amylase-like properties (Srivastava et al., 2014b).

Antibacterial Alternatives

Schoonen et al. reported on the antibacterial action of FeS_2. Its mechanism was shown to be related to the formation of H_2O_2. The same group also reported how minerals can induce the formation of reactive oxygen species (Cohn et al., 2006; Schoonen et al., 2006). The rapid absorption of Fe^{2+} can influence bacterial metabolism. The oxidization of Fe^{2+} to Fe^{3+} leads to reactive oxygen species (ROS) production and biomolecular damage. As a result, iron sulfide can act as antimicrobial agents. Iron sulfides have been reported to be effective in bacterial infections. In 2013, He et al. reported on the bacteriostatic activity of Fe_3S_4/Ag against *E. coli* (86.2%) and *S. aureus* (90.6%). Meanwhile, Fe_3S_4 NPs without Ag have no effect (He et al., 2013). The Arenas-Arrocena group synthesized $Fe_{x-1}S$ NPs and reported their antibacterial and cytotoxic activity in 2018. Antibacterial activity against *S. aureus*, *E. coli* and *E. faecalis* was observed (Argueta-Figueroa et al., 2018). In addition, Gao and coworkers discovered antibacterial inorganic iron polysulfides materials that were converted by organosulfur compounds in 2018. Inorganic nano-sulfides (nFeS, $Fe_{1-x}S$, and Fe_3S_4) have shown inhibition against *Pseudomonas aeruginosa* and *Staphylococcus aureus.* These studies also described new strategies to synthesize iron sulfide nanomaterials. Furthermore, the *S. mutans* biofilm-related infections could be prevented by nFeS (Xu et al., 2018) (**Figure 5**). The antibacterial properties of FeS_2-Bi_2O_3 against the pathogenic microorganisms *Mycobacterium tuberculosis* and *Salmonella* have also been measured (Manafi et al., 2019). Diksha et al. reported that FeS NPs could enhance intrabacterial ROS levels in bacteria by light irradiation in 2020. This was revealed

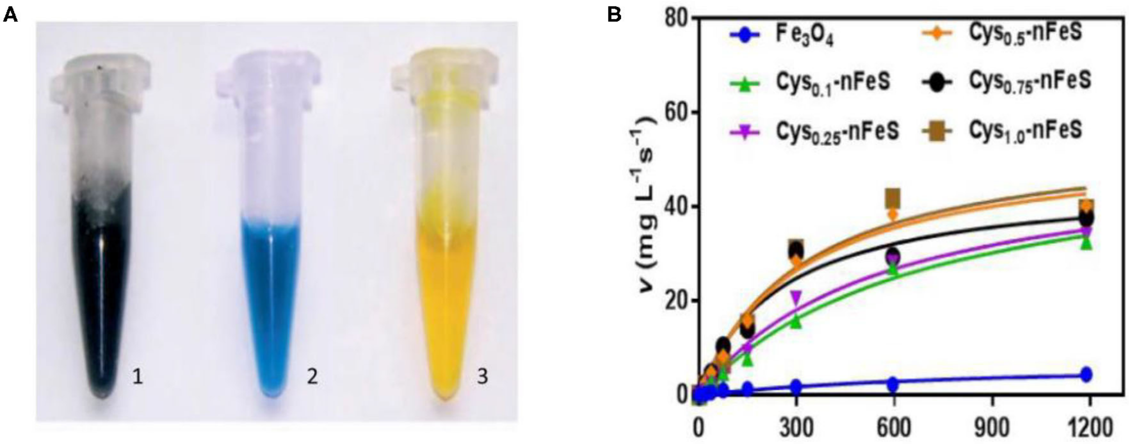

FIGURE 4 | Schematic diagram of catalysis of iron sulfide as a nanozyme. **(A)** The peroxidase-like activity of FeS. Images of the suspension of sheet-like FeS nanostructure (1), mixture of TMB and H_2O_2 after catalytic reaction by sheet-like FeS nanostructure (2), mixture of TMB and H_2O_2 after adding H_2SO_4 to quench the catalytic reaction by sheet-like FeS nanostructure (3). Reproduced with permission from Dai et al. (2009). Copyright 2009, Wiley-VCH Verlag GmbH & Co. KGaA, Weinheim. **(B)** The catalase-like activity of Cys-nFeS. The trend of *KM* and the ratio of *Vmax*/*KM* in the kinetics assay with varied cysteine. Reproduced with permission from Xu et al. (2018). Copyright 2018, Nature Publishing Group.

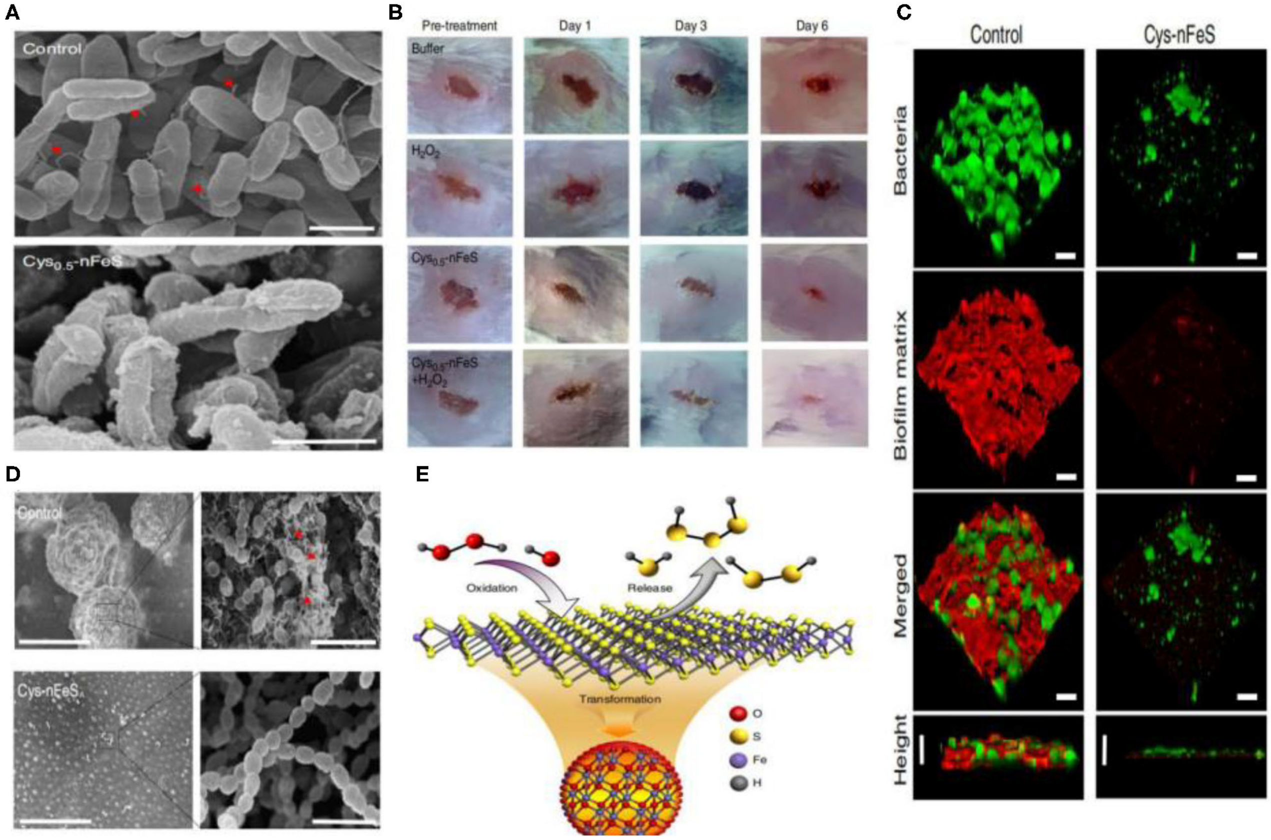

FIGURE 5 | (A) Morphology of *P. aeruginosa* before (control) and after Cys-nFeS treatment. The red triangles indicate flagella. Scale bars: 1 μm. **(B)** Photographs of *P. aeruginosa* infected wounds treated with buffer (control), Cys-nFeS, H_2O_2, and Cys-nFeS + H_2O_2 at different times (five mice in each group). **(C)** Confocal 3D image of a *S. mutans* UA159 biofilm treated by Cys-nFeS. Scale bars: 100 μm. **(D)** SEM image of a *S. mutans* biofilm treated by Cys-nFeS. The red arrows indicate EPS. Left scale bars: 100 μm. Right scale bars: 3 μm. **(E)** Scheme of polysulfane release from nFeS. Reproduced with permission from Xu et al. (2018). Copyright 2018, Nature Publishing Group.

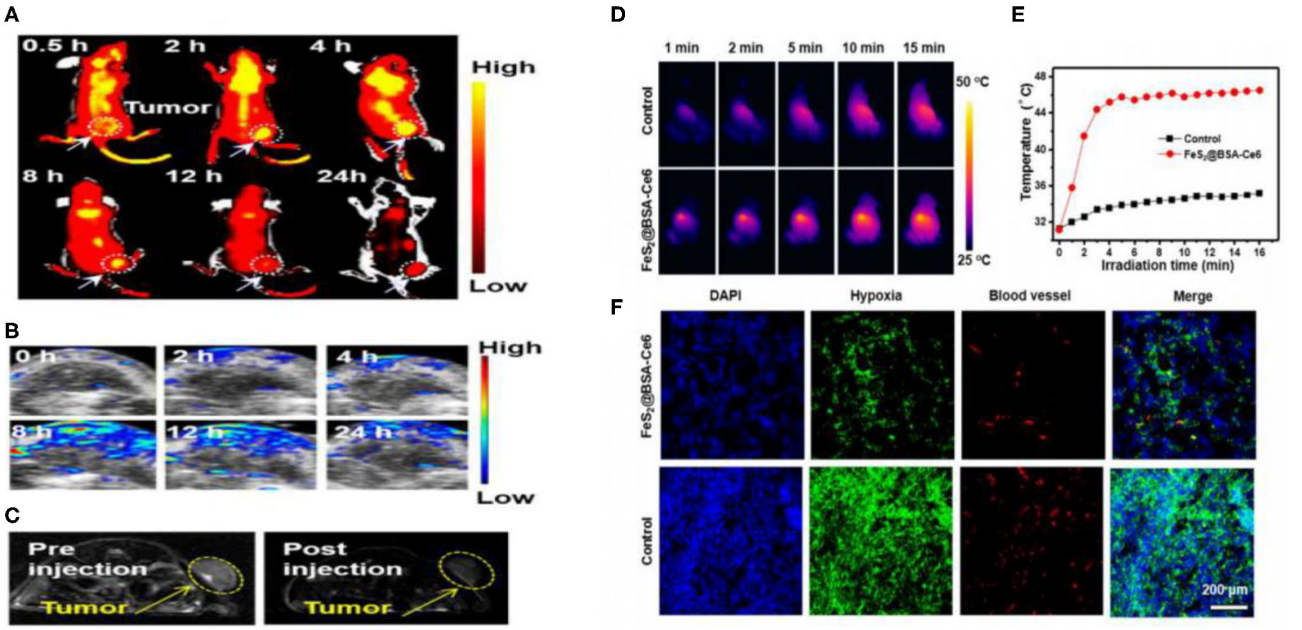

FIGURE 6 | (A) *In vivo* fluorescence images of 4T1 tumor-bearing nude mice taken at different time points post iv injection of FeS_2@BSA-Ce6 nanodots (3.5 mg/kg Ce6 and 12 mg/kg FeS_2). **(B)** Photoacoustic images of tumors in mice taken at different time points post iv injection of FeS_2@BSA-Ce6 nanodots. **(C)** MR images of 4T1 tumor-bearing nude mice before and 8 h after iv injection of FeS_2@BSA-Ce6 nanodots. (3.5 mg/kg Ce6 and 12 mg/kg FeS_2). **(D)** IR thermal images of tumors in mice iv injected with FeS_2@BSA-Ce6 under 808 nm laser irradiation (0.8W/cm^2, 15 min). **(E)** Surface temperature changes of tumors monitored by the IR thermal camera during laser irradiation. **(F)** Representative immunofluorescence images of tumor slices after hypoxia staining. The cell nucleus, hypoxia areas, and blood vessels were stained with DAPI (blue), antipimonidazole antibody (green), and anti-CD31 antibody (red), respectively. Reproduced with permission from Jin et al. (2018). Copyright 2017, American Chemical Society.

as the primary antibacterial mechanism of FeS NPs (Agnihotri et al., 2020).

Cancer Therapy

Chen and colleagues reported that tumors in mice could disturb iron metabolism in the major organs. The chemical form of iron in the tumors was ferrous-sulfide-like iron and ferritin, highlighting the potential of iron sulfide for cancer treatment (Chen and Chen, 2017). Chang et al. synthesized Fe_3S_4 particles with magnetic properties through co-precipitation. The NPs were used for cancer hyperthermia providing a new avenue for multimodal anticancer therapies (Chang et al., 2011). In 2015, Yang et al. concluded that triangle nanoplates (FeS/PEG nanostructures) could be used as nanoagents for *in vivo* MRI-guided photothermal cancer treatment. High doses of FeS nanoplates were shown to be safe and effective in mice. This study highlighted the potential clinical use of FeS, for MRI in addition to PTT (**Figure 6**) (Yang et al., 2015). In 2018, Fe_3S_4 nanosheets were shown to possess high efficiencies for MRI guided photothermal and chemodynamic synergistic therapy, opening up a new direction for the design of inorganic iron sulfide for future clinical applications (Guan et al., 2018). Tiny nano-sized iron sulfide with simple biomineralization method has also been attention owing to its huge potential *in vivo* application especially in cancer therapy combined with its excellent photothermal and magnetic performance. FeS_2@BSA-Ce6 (detailed in section Biomineralization) exhibited good results whether *in vivo* multimodal imaging or *in vivo* combined therapy (Jin et al., 2018). Meanwhile, the latest literature proved 3 nm FeS@BSA QDs could be used as T1-weighted MRI contrast agents. Moreover, the ultrasmall QDs showed good results in photothermal therapy and they could be cleared via glomerular filtration into bladder after treatment (Yang et al., 2020). The use of iron chalcogenides has also been investigated. Cu_5FeS_4-PEG NPs were effective in dual-modal imaging and PTT (Zhao et al., 2016). In 2017, $CuFeS_2$ nanoplates were used for *in vivo* photothermal/photoacoustic imaging and cancer chemotherapy/PTT (Ding et al., 2017).

Drug Delivery

Iron sulfide holds utility as a drug carrier. In previous studies, modified β-cyclodextrin (β-CD) and PEG Fe_3S_4 (GMNCs) were used as drug loading NPs. Both β-CD and PEG have been used to control the shape and size of GMNCs as surfactants. In addition, the biocompatibility of Fe_3S_4 is enhanced, with entrapment efficiencies of 58.7% for the modified delivery of the chemotherapeutic drug doxorubicin. Meanwhile, the enhanced chemotherapeutic treatment of mouse tumors was obtained through the intravenous injection of doxorubicin (Dox) loaded GMNCs (Feng et al., 2013; **Figure 7**).

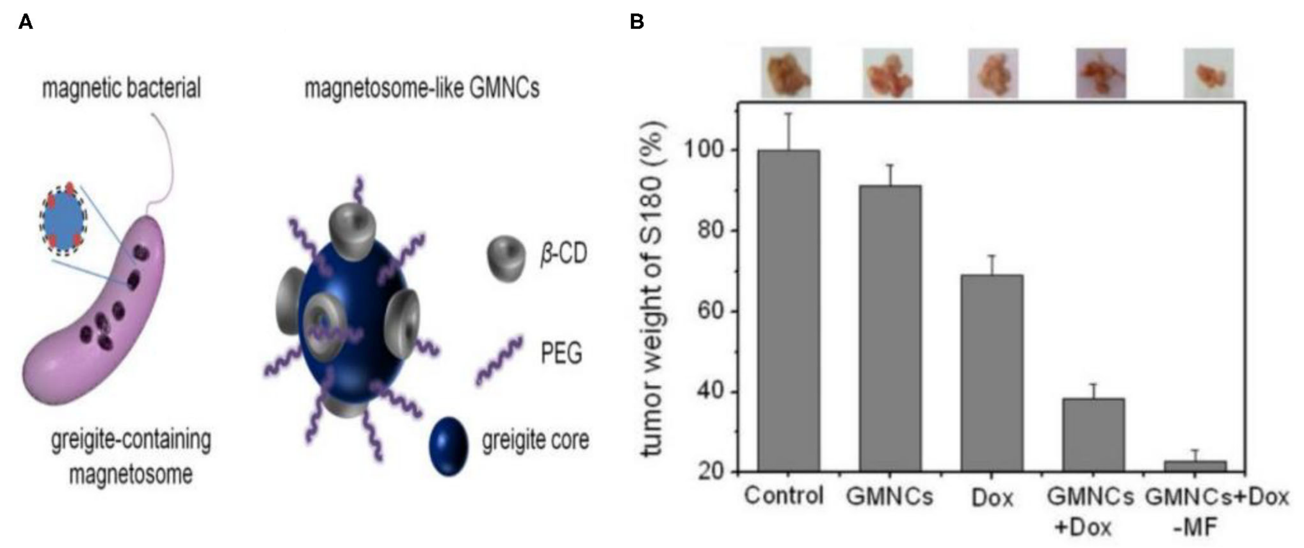

FIGURE 7 | (A) Schematical illustration of the greigite-containing magnetosome and the chemical synthesized magnetosome-like GMNCs. **(B)** Growth inhibition effect in murine S180 sarcoma model of the sample. The photos and weight ratios of tumor tissue from mice treated with normal saline (control group), GMNCs, Dox at low concentration, and GMNCs loading with Dox (without and with the guidance of external magnetic field), respectively. Reproduced with permission from Feng et al. (2013). Copyright 2013, Nature Publishing Group.

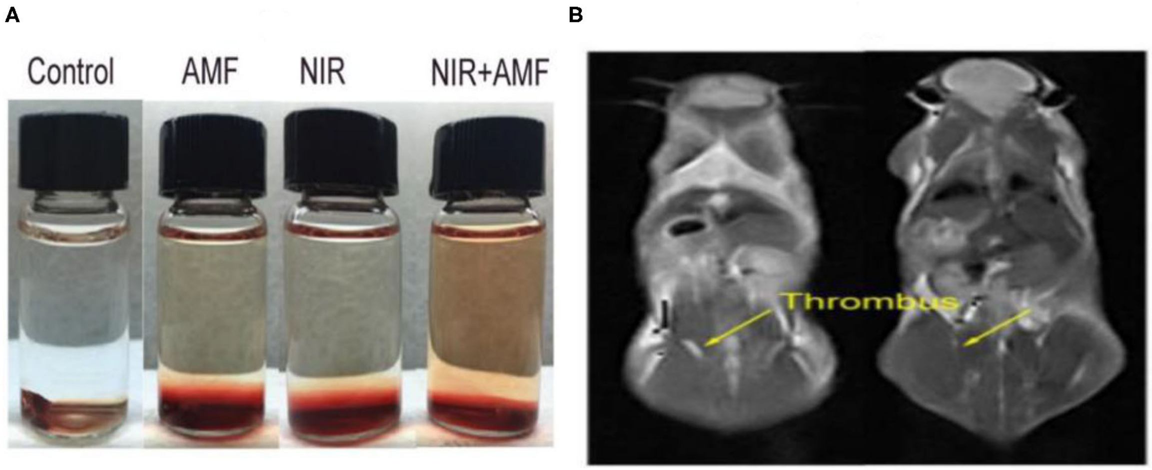

FIGURE 8 | (A) Thrombolytic capacity *in vitro* of Fe_3S_4 nanoparticles under the indicated conditions. Fe_3S_4 nanoparticles: 0.5 mg/mL; NIR: 808 nm, 0.33 W cm^{-2}; AMF: 4.2×10^9 A m^{-1} s^{-1}. **(B)** T2-weighted MR imaging *in vivo* of a mouse with celiac vein thrombosis before (left) and after (right) an intravenous injection of a solution of the Fe_3S_4 nanoparticles followed by the simulation of AMF. Reproduced with permission from Fu et al. (2019). Copyright 2019, Frontiers in Materials.

Thrombolytic Agents

In studies of vascular disease, the removal of thrombosis through non-invasive methods is challenging. However, studies regarding iron sulfide NPs as thrombolytic agents have been reported. Ge et al. first highlighted the utility of Fe_3S_4 NPs as thrombolytic agents with both photothermal and magnetothermal thrombolytic capability. Using Fe_3S_4 nanoparticles, celiac vein thrombosis could be prevented using magnetic hyperthermia combined PTT. Both *in vivo* and *in vitro*, Fe_3S_4 has demonstrated beneficial effects for the removal of thrombi (**Figure 8**), providing a novel hyperthermia strategy for the prevention of thrombosis (Fu et al., 2019).

Biosensors

Iron sulfides have been used as glucose sensors due to their intrinsic peroxidase-like activity (Dai et al., 2009). Glucose sensors can be developed using colorimetric methods in which cascade reactions form the core mechanism of glucose detection. TMB could be oxidized to oxTMB in the presence of glucose, GOx and iron sulfide. H_2O_2 produced by the decomposition

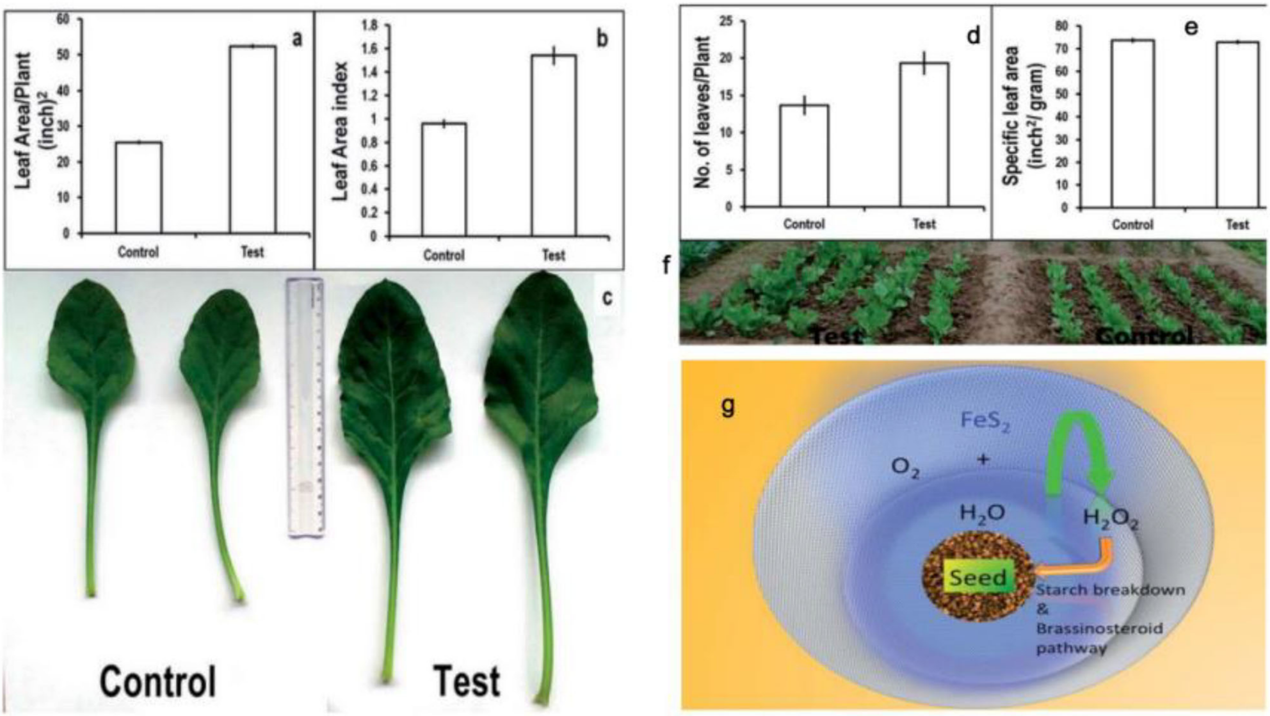

FIGURE 9 | Plant growth parameters: control vs. test (FeS_2). **(a)** Leaf area/Plant, showing significant increase in leaf area/test plants (52.4 ± 0.3) as compared to control (25.6 ± 0.2). **(b)** Leaf area index signifying total photosynthetic area available to plant and high values for test samples (1.5 ± 0.07) can be correlated with high biomass content of pro-fertilized spinach plants in comparison with (0.9 ± 0.02). **(c)** Comparative photograph of leaves showing larger leaf area in test plants as compared to control plants. Plant growth parameters: control vs. test (FeS_2). **(d)** Number of leaves/Plant: control: 13 ± 1.0; test: 19 ± 1.0. **(e)** Specific leaf area signifies leaf thickness and was found similar for both test and control samples. **(f)** Field photograph taken at day 50 (just before harvesting the crop) depicting that the test group plants have comparatively more foliage as compared to the control plants. **(g)** Proposed outline of the mechanism of action of FeS_2 on spinach seed in enhancing germination and plant growth. Reproduced with permission from Srivastava al. (2014). Copyright 2014, The Royal Society of Chemistry.

of glucose in the presence of glucose oxidase can be used as a substrate for iron sulfide. Iron sulfide peroxidase-like mimics can oxidize TMB to oxTMB in the presence of H_2O_2. Fe_7S_8 nanowires also possess peroxidase activity. Using a linear range, glucose concentrations of 5×10^{-6} to 5×10^{-4} M could be detected (Yao et al., 2013). In 2016, Xian and colleagues used Fe_3S_4 magnetic nanoparticles (MNPs) to quantify glucose concentrations in human serum. A linear range was measured from 2 to 100 μM, and the limit of detection (LOD) was 0.16 μM (Ding et al., 2016). These studies highlighted the potential of as-prepared iron sulfide as both glucose sensors and artificial peroxidase nanozymes.

Antifungal Agents

In vitro antifungal FeS NPs exhibited significant anti-fungal activity against *F. verticillioides* at 18 μg ml^{-1}, with a higher efficiency than standard fungicides (carbendazim (median effective dose (ED50): 230 μg ml^{-1}). These were the first reports highlighting the antifungal activity of iron sulfide. The influence of FeS on both seed health and quality parameters of rice was also evaluated based on this antifungal activity. Iron sulfides were shown to be effective in iron deficient soils as an alternative to high dose organic fungicides (Ahuja et al., 2019).

Seed Improvements in Phyto-Applications

FeS_2 represents a photovoltaic material, which increases plant biomass in the seeds of chickpeas (Cicer arietinum). Meanwhile, the mechanism of functional FeS_2 is attributed to its amylase-like activity. In the presence of H_2O and FeS_2, starch in the seeds can be broken down to H_2O_2, which participates in the absorption of CO_2 and improves plant health. Spinach seeds treated with FeS_2 exhibited broader leaf morphologies, larger leaf numbers and an increased biomass (Srivastava et al., 2014b) (**Figure 9**). In later studies, seed priming with FeS_2 was reported as an innovative strategy (Das et al., 2016). FeS_2 also improved both seed yield and growth in the *Brassica juncea* field (Rawat et al., 2017).

CONCLUSIONS

In summary, we have highlighted the most recent methods of nano-iron sulfide synthesis, including nano iron sulfide modifications and characterizations. Strikingly, nano-sized iron sulfides demonstrate versatile physiochemical properties,

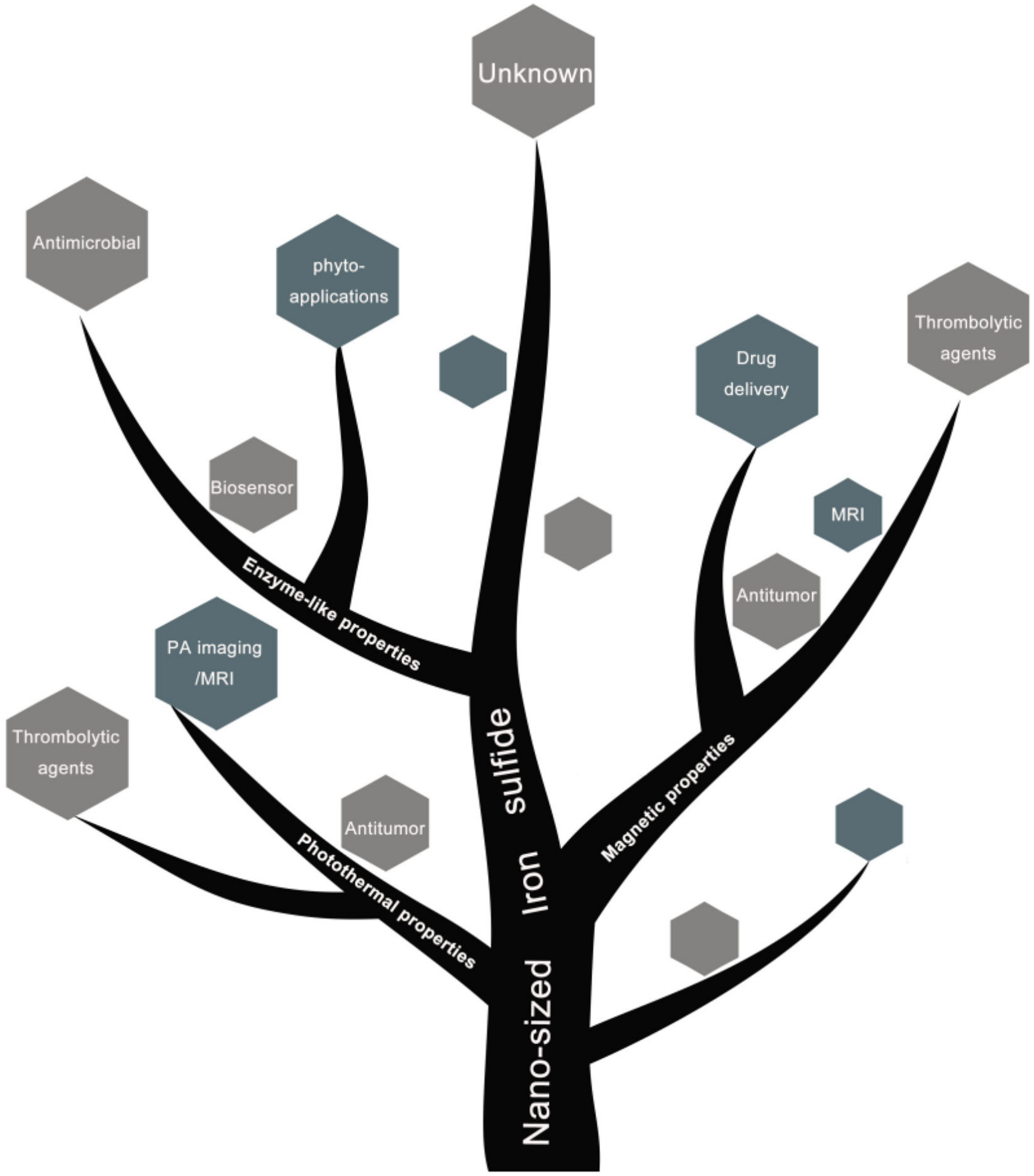

SCHEME 2 | Schematic diagram of biomedical applications based on physiochemical properties of nano-sized iron sulfide.

enzyme-like catalysis, high stability and biocompatibility, which facilitate their biomedical applications. A range of nano-iron sulfides have been assessed in catalysis, tumor therapy, antibacterials and antifungals, drug delivery, biosensors, thrombus removal and in plants. Their advantages include (1) high biocompatibility due to the key role of iron and sulfur in natural life; (2) the photothermal and magnetic properties of nano-sized iron sulfide; (3) their nanostructure and large surface area that can improve drug delivery; and (4) their enzyme-like properties as nanozymes, including their high reactivity to numerous chemical substances that can regulate hydrogen peroxide, ROS and various catalytic reactions to treat related diseases.

Although it has been shown that nano-sized iron sulfides represent great potential in numerous applications in biomedicine (**Scheme 2**), a number of issues remain to be addressed, including the synthesis of iron sulfide that is stable and in a single phase, with modifications to adapt to the biological environment. Studies have found that the modification of molecular CTAB inhibits the preparation of Fe_3S_4 NPs due to competitive inhibition with Na_2S under acidic conditions, resulting in the formation of non-magnetic iron sulfides and other byproducts. Citrate modified nanoparticles have not sufficient particle spacing due to aggregation effects (Simeonidis et al., 2016). In addition, the biomedical assessments of iron sulfides remain sparse, and their mechanisms of action under physiological conditions are poorly understood. The intrinsic enzyme-like properties of iron sulfide as nanozymes may provide a window to understand its biological effects and potential cytotoxicity *in vivo*. Taken together, nano-sized iron sulfides possess versatile physiochemical properties and enzyme-like properties, which describe a form of distinctive nanomaterials with great potential for use in biomedical applications.

AUTHOR CONTRIBUTIONS

All authors listed have made a substantial, direct and intellectual contribution to the work, and approved it for publication.

ACKNOWLEDGMENTS

This work was supported by the National Key R&D Program of China (Grant No. 2018YFC1003500), as well as the National Natural Science Foundation of China (Grant Nos. 81930050, 81671810, and 31701236).

REFERENCES

Agnihotri, S., Mohan, T., Jha, D., Gautam, H., and Roy, I. (2020). Dual Modality FeS Nanoparticles with Reactive Oxygen Species-Induced and Photothermal Toxicity toward Pathogenic Bacteria. *ACS OMEGA* 5, 597–602. doi: 10.1021/acsomega.9b03177

Ahuja, R., Sidhu, A., and Bala, A. (2019). Synthesis and evaluation of iron(ii) sulfide aqua nanoparticles (FeS-NPs) against Fusarium verticillioides causing sheath rot and seed discoloration of rice. *Eur. J. Plant Pathol.* 155, 163–171. doi: 10.1007/s10658-019-01758-3

Argueta-Figueroa, L., Martinez-Alvarez, O., Santos-Cruz, J., Garcia-Contreras, R., Acosta-Torres, L. S., Fuente-Hernández, J., et al. (2017). Nanomaterials made of non-toxic metallic sulfides: a systematic review of their potential biomedical applications. *Mater. Sci. Eng. C* 76, 1305–1315. doi: 10.1016/j.msec.2017.02.120

Argueta-Figueroa, L., Torres-Gómez, N., García-Contreras, R., Vilchis-Nestor, A. R., Martínez-Alvarez, O., Acosta-Torres, L. S., et al. (2018). Hydrothermal synthesis of pyrrhotite ($Fe_{x-1}S$) nanoplates and their antibacterial, cytotoxic activity study. *Progress Nat. Sci.* 28, 447–455. doi: 10.1016/j.pnsc.2018.06.003

Barand, A., and Russo, S. (2009). Modeling the environmental stability of FeS_2 nanorods, using lessons from biomineralization. *Nanotechnology* 20:115702. doi: 10.1088/0957-4484/20/11/115702

Barnard, A., and Russo, S. (2009). Morphological stability of Pyrite FeS_2 nanocrystals in water. *J. Phys. Chem. C* 113, 5376-5380. doi: 10.1021/jp809377s

Beal, J., Etchegoin, P., and Tilley, R. (2012). Synthesis and characterisation of magnetic iron sulfide nanocrystals. *J. Solid State Chem.* 189, 57–62. doi: 10.1016/j.jssc.2012.01.015

Bi, Y., Yuan, Y., Exstrom, C. L., Darveau, S. A., and Huang, J. (2011). Air stable, photosensitive, phase pure iron pyrite nanocrystal thin films for photovoltaic application. *Nano Letter* 11, 4953–4957. doi: 10.1021/nl202902z

Chang, Y., Savitha, S., Sadhasivam, S., Hsu, C., and Lin, F. (2011). Fabrication, characterization, and application of greigite nanoparticles for cancer hyperthermia. *J. Colloid Interface Sci.* 363, 314–319. doi: 10.1016/j.jcis.2010.06.069

Chen, R., and Chen, G. (2017). Tumor-induced disorder of iron metabolism in major organs: a new insight from chemical speciation of iron. *J. Int. Med. Res* 46, 70–78. doi: 10.1177/0300060517718711

Chen, B., and Gu, N. (2017). Current status and development of pharmaceutical iron based nanomaterials. *Mater. China* 36, 211–218.

Cohn, C., Laffers, R., Simon, S., O'Riordan, T., and Schoonen, M. (2006). Role of pyrite in formation of hydroxyl radicals in coal: possible implications for human health. *Part. Fibre Toxicol.* 3:16. doi: 10.1186/1743-8977-3-16

Dai, Z., Liu, S., Bao, J., and Ju, H. (2009). Nanostructured FeS as a mimic peroxidase for biocatalysis and biosensing. *Chem. Eur. J.* 15, 4321–4326. doi: 10.1002/chem.200802158

Das, C., Srivastava, G., Dubey, A., Roy,. M., Jain, S., Sethy, N., et al. (2016). Nano-ironpyrite seed dressing: A sustainable intervention to reduce fertilizer consumption in vegetable (beetroot, carrot), spice (fenugreek), fodder (alfalfa), and oilseed (mustard, sesamum) crops. *Nanotechnol. Environ. Eng.* 1, 1–12. doi: 10.1007/s41204-016-0002-7

Davison, W. (1991). The solubility of iron sulphides in synthetic and natural waters at ambient temperature. *Aquatic Sci.* 53, 309–329. doi: 10.1007/BF00877139

De Leeuw, N., Parker, S., Sithole, H., and Ngoepe, P. E. (2000). Modeling the surface structure and reactivity of pyrite: introducing a potential model for FeS_2. *J. Phys. Chem. B* 104, 7969–7976. doi: 10.1021/jp0009498

Ding, B., Yu, C., Li, C., Deng, X., Ding, J., Cheng, Z., et al. (2017). Cis-platinum pro-drug-attached $CuFeS_2$ nanoplates for *in vivo* photothermal/photoacoustic imaging and chemotherapy/photothermal therapy of cancer. *Nanoscale* 9, 16937–16949. doi: 10.1039/C7NR04166G

Ding, C., Yan, Y., Xiang, D., Zhang, C., and Xian, Y. (2016). Magnetic Fe_3S_4 nanoparticles with peroxidase-like activity, and their use in a photometric enzymatic glucose assay. *Microchim. Acta* 183, 625–631. doi: 10.1007/s00604-015-1690-6

Dong, H., Fan, Y., Zhang, W., Gu, N., and Zhang, Y. (2019). Catalytic mechanisms of nanozymes and their applications in biomedicine. *Bioconjug. Chem.* 30, 1273–1296. doi: 10.1021/acs.bioconjchem.9b00171

Elliot, A. (2010). Structure of pyrrhotite 5c (Fe_9S_{10}). *Acta Crystallogr. Section B* 66, 271–279. doi: 10.1107/S0108768110011845

Esmaeili, E., Eslami-Arshaghi, T., Hosseinzadeh, S., Elahirad, E., Jamalpoor, Z., Hatamie, S., et al. (2020). The biomedical potential of cellulose acetate/polyurethane nanofibrous mats containing reduced graphene oxide/silver nanocomposites and curcumin: antimicrobial performance and cutaneous wound healing. *Int. J. Biol. Macromol.* 152, 418–427. doi: 10.1016/j.ijbiomac.2020.02.295

Feng, M., Lu, Y., Yang, Y., Zhang, M., Xu, Y., Gao, H., et al. (2013). Bioinspired greigite magnetic nanocrystals: chemical synthesis and biomedicine applications. *Sci. Rep.* 3:994. doi: 10.1038/srep02994

Fleet, M. (1971). The crystal structure of a pyrrhotite (Fe_7S_8). *Acta Cryst. B* 27:1864. doi: 10.1107/S0567740871004990

Fu, D., Liu, J., Ren, Q., Ding, J., Ding, H., Chen, X., et al. (2019). magnetic iron sulfide nanoparticles as thrombolytic agents for magnetocaloric therapy and photothermal therapy of thrombosis. *Front. Mater.* 6:316. doi: 10.3389/fmats.2019.00316

Gan, Y., Xu, F., Luo, J., Yuan, H., Jin, C., Zhang, L., et al. (2016). One-pot biotemplate synthesis of FeS_2 decorated sulfur-doped carbon fiber as high capacity anode for lithium-ion batteries. *Electrochim. Acta* 209, 201–209. doi: 10.1016/j.electacta.2016.05.076

Ganbaatar, N., Matsuzaki, N., Nakazawa, Y., Afrin, R., Aono, M., Yano, T., et al. (2016). Surface force analysis of pyrite (FeS_2): its reactivity to amino acid adsorption. *Adv. Mater. Phys. Chem.* 6, 167–176. doi: 10.4236/ampc.2016.67018

Gao, L., Zhuang, J., Nie, L., Zhang, J., Zhang, Y., Gu, N., et al. (2007). Intrinsic peroxidase-like activity of ferromagnetic nanoparticles. Intrinsic peroxidase-like activity of ferromagnetic nanoparticles. *Nat. Nanotechnol.* 2, 577–583. doi: 10.1038/nnano.2007.260

Gao, S., Huang, F., Song, D., Li, G., Liu, Q., Feng, T., et al. (2015). "Growth mechanism and stability study on the Fe_3S_4 nanocrystals synthesized under thermal and humid conditions," in *Proceedings of the 11th International Congress for Applied Mineralogy*. doi: 10.1007/978-3-319-13948-7_13

Guan, G., Wang, X., Li, B., Zhang, W., Cui, Z., Lu, X., et al. (2018). "Transformed" Fe_3S_4 tetragonal nanosheets: a high-efficiency and body-clearable agent for magnetic resonance imaging guided photothermal and chemodynamic synergistic therapy. *Nanoscale* 10, 17902–17911. doi: 10.1039/C8NR06507A

Guo, S., Li, J., Ma, Z., Chi, Y., and Xue, H. (2016). A facile method to prepare FeS/porous carbon composite as advanced anode material for lithium-ion batteries. *J. Mater. Sci.* 52, 2345–2355. doi: 10.1007/s10853-016-0527-y

Guo, Z., Sun, F., Han, B., Lin, K., Zhou, L., and Yuan, W. (2017). Iron vacancy in tetragonal $Fe_{1-x}S$ crystals and its effect on the structure and superconductivity. *Phys. Chem. Chem. Phys.* 19, 9000–9006. doi: 10.1039/C7CP00068E

He, Q., Huang, C., and Liu, J. (2013). Preparation, Characterization and antibacterial activity of magnetic greigite and Fe_3S_4/Ag nanoparticles. *Nanosci. Nanotechnol. Lett.* 5, 1–8. doi: 10.1166/nnl.2014.1727

He, Y., Wilson, J., Su, C., and Wilkin, R. T. (2015). Review of abiotic degradation of chlorinated solvents by reactive iron minerals in aquifers. *Ground Water Monitoring Remediation* 35, 57–75. doi: 10.1111/gwmr.12111

Jin, A., Mi-Ju, K., Kug-Seung, L., Yu, S., and Sung, Y. (2019). Spindle-like Fe_7S_8/N-doped carbon nanohybrids for high-performance sodium ion battery anodes. *Nano Res.* 12, 695–700. doi: 10.1007/s12274-019-2278-y

Jin, J., Wu, W., Min, H., Wu, H., Wang, S., Ding, Y., et al. (2017). A glassy carbon electrode modified with FeS nanosheets as a highly sensitive amperometric sensor for hydrogen peroxide. *Microchim. Acta* 184, 1389–1396. doi: 10.1007/s00604-017-2105-7

Jin, Q., Liu, J., Zhu, W., Dong, Z., Liu, Z., and Cheng, L. (2018). Albumin-assisted synthesis of ultrasmall FeS_2 nanodots for imaging-guided photothermal enhanced photodynamic therapy. *ACS Appl. Mater. Interfaces* 10, 332–340. doi: 10.1021/acsami.7b16890

Kar, S., and Chaudhuri, S. (2004). Solvothermal synthesis of nanocrystalline FeS_2 with different morphologies. *Chem. Phys. Lett.* 398, 22–26. doi: 10.1016/j.cplett.2004.09.028

Kasting, J. (1993). Earth's early atmosphere. *Science* 259, 920–926. doi: 10.1126/science.11536547

Kavner, A., Duffy, T., and Shen, G. (2001). Phase stability and density of FeS at high pressures and temperatures: implications for the interior structure of Mars. *Earth Planet. Sci. Lett.* 185, 25–33. doi: 10.1016/S0012-821X(00)00356-3

Kim, E. J., and Batchelor, B. (2009). Synthesis and characterization of pyrite (FeS2) using microwave irradiation. *Mater. Res. Bull.* 44, 1553–1558. doi: 10.1016/j.materresbull.2009.02.006

Kong, X., Lou, T., and Li, Y. (2005). Fe_7S_8 nanorods and nanosheets. *J. Alloys Compd.* 390, 236–239. doi: 10.1016/j.jallcom.2004.07.054

Kuhn, S. J., Eskildsen, M. R., Debeer-Schmitt, L., Li, L., de La Cruz, C., and Sefat, A. S. (2016). Structure and magnetic interactions in FeS: a low-Tc superconductor. *Bull. Am. Phys. Soc.* 61, 2. Abstracts retrieved from APS March Meeting (Abstract ID: BAPS.2016.MAR.H11.12).

Kwon, K., Refson, K., Bone, S., Qiao, R., Yang, W., Liu, Z., et al. (2011). Magnetic ordering in tetragonal FeS: evidence for strong itinerant spin fluctuations. *Phys. Rev. B Cond. Matt.* 83, 064402.1–064402.7. doi: 10.1103/PhysRevB.83.064402

Lefèvre, C., Abreu, F., Lins, U., and Bazylinski, D. (2010). Nonmagnetotactic multicellular prokaryotes from low-saline, nonmarine aquatic environments and their unusual negative phototactic behavior. *Appl. Environ. Microbiol.* 76, 3220–3227. doi: 10.1128/AEM.00408-10

Li, M., Yao, Q., Zhou, G., Qu, X., Mu, C., and Fu, S. (2011). Microwave-assisted controlled synthesis of monodisperse pyrite microspherolites. *Cryst. Eng. Comm.* 13, 5936–5942. doi: 10.1039/c1ce05478c

Li, X., Xu, H., Chen, Z., Chen, Z., and Chen, G. (2011). Biosynthesis of nanoparticles by microorganisms and their applications. *J. Nanomater.* 2011, 1–16. doi: 10.1155/2011/270974

Li, Y., Pu, Q., Li, S., Zhang, H., Wang, X., Yao, H., et al. (2019). Machine learning methods for research highlight prediction in biomedical effects of nanomaterial application. *Patt. Recognit. Lett.* 117, 111–118. doi: 10.1016/j.patrec.2018.11.008

Liang, M., and Yan, X. (2019). Nanozymes: from new concepts, mechanisms, and standards to applications. *Acc. Chem. Res.* 52, 2190–2200. doi: 10.1021/acs.accounts.9b00140

Ma, J., Chang, L., Lian, J., Huang, Z., Duan, X., Liu, X., et al. (2010). Ionic liquid-modulated synthesis of ferrimagnetic Fe_3S_4 hierarchical superstructures. *Chem. Commun.* 46, 5006–5008. doi: 10.1039/c0cc00479k

Manafi, A., Hosseini, M., Fakhri, A., Gupta, V., and Agarwal, S. (2019). Investigation of photocatalytic process for iron disulfide-bismuth oxide nanocomposites by using response surface methodology: structural and antibacterial properties. *J. Mol. Liq.* 289:110950. doi: 10.1016/j.molliq.2019.110950

Mann, S., Sparks, N., Frankel, R., Bazylinski, D., and Jannasch, H. (1990). Biomineralization of ferrimagnetic greigite (Fe_3S_4) and iron pyrite (FeS_2) in a magnetotactic bacterium. *Nature* 343, 258–261. doi: 10.1038/343258a0

Mei, B., and Ma, Z. (2013). Study of anti-friction performance of spherical FeS nanoparticle. *Appl. Mechan. Mater.* 475-476, 1334–1339. doi: 10.4028/www.scientific.net/AMM.475-476.1334

Menyeh, A., and O'Reilly, W. (1997). Magnetic hysteresis properties of fine particles of monoclinic pyrrhotite Fe_7S_8. *J. Geomag. Geoelectr.* 49, 965–976. doi: 10.5636/jgg.49.965

Mofokeng, T., Mabena, G., Moloto, M. J., Shumbula, P. M., Mubiayi, P., and Nyamukamba, P. (2017). Temperature influence on the lactose capped metal sulphide nanoparticles. *Chalcogenide Lett.* 14, 347–355.

Mohindar, S., and Jagadeesh, M. (1979). Temperature-dependent magnetic susceptibility of marcasite (FeS_ {2}). *Phys. Rev. B* 20:3897. doi: 10.1103/PhysRevB.20.3897

Moore, J., Nienhuis, E., Ahmadzadeh, M., and Mccloy, J. (2019). Synthesis of greigite (Fe_3S_4) particles via a hydrothermal method. *AIP Adv.* 9:035012. doi: 10.1063/1.5079759

Niño, M., Flores, E., Sanchez, C., and Rojo, J. (2018). Reactivity of a FeS surface under room temperature exposure to nitrogen and H_2S. *J. Phys. Chem. B* 122, 705–712. doi: 10.1021/acs.jpcb.7b06309

Ono, S. (2007). Magnetic phase transition of FeS at high pressures. *Acta Crystallogr. Sect. A Found. Crystallogr.* 63:59. doi: 10.1107/S0108767307098716

Paolella, A., George, C., Povia, M., Zhang, Y., Krahne, R., Gich, M., et al. (2011). Charge transport and electrochemical properties of colloidal greigite (Fe_3S_4) nanoplatelets. *Chem. Mater.* 23, 3762–3768. doi: 10.1021/cm201531h

Powell, A. V., Vaqueiro, P., Knight, K. S., Chapon, L. C., and Sánchez, R. D. (2004). Structure and magnetism in synthetic pyrrhotite Fe_7S_8: a powder neutron-diffraction study. *Phys. Rev. B* 70, 014415. doi: 10.1103/PhysRevB.70.014415

Qi, W., and Cowan, J. (2011). Structural, mechanistic and coordination chemistry of relevance to the biosynthesis of iron–sulfur and related iron cofactors. *Coord. Chem. Rev.* 255, 688–699. doi: 10.1016/j.ccr.2010.10.016

Rawat, M., Nayan, R., Negi, B., Zaidi, M. G. H., and Arora, S. (2017). Physio-biochemical basis of iron-sulfide nanoparticle induced growth and seed yield enhancement in b. juncea. *Plant Physiol. Biochem.* 118, 274–284. doi: 10.1016/j.plaphy.2017.06.021

Rickard, D. (2006). The solubility of FeS. *Geochim. Cosmochim. Acta* 70, 5779–5789. doi: 10.1016/j.gca.2006.02.029

Rickard, D., and Luther, G. (2007). Chemistry of iron sulfides. *Chem. Rev.* 107, 514–562. doi: 10.1021/cr0503658

Roberts, A. (1995). Magnetic properties of sedimentary greigite (Fe_3S_4). *Earth Planetary Sci. Lett.* 134, 227–236. doi: 10.1016/0012-821X(95)00131-U

SantosCarballal, D., Roldan, A., Dzade, N., and de Leeuw, N. H. (2017). Reactivity of CO_2 on the surfaces of magnetite (Fe_3O_4), greigite (Fe_3S_4) and mackinawite (FeS). *Philos. Trans. R. Soc. A* 376:65. doi: 10.1098/rsta.2017.0065

Scaini, M., Bancroft, G., and Knipe, S. (1998). Reactions of aqueous Au^{1+} sulfide species with pyrite as a function of pH and temperature. *Am. Mineral.* 83, 316–322. doi: 10.2138/am-1998-3-415

Schoonen, M., Cohn, C., Roemer, E., Laffers, R., Simon, S., and O'Riordan, T. (2006). Mineral-induced formation of reactive oxygen species. *Med. Mineraol. Geochem.* 64, 179–221. doi: 10.2138/rmg.2006.64.7

Simeonidis, K., Liébana-Viñas, S., Wiedwald, U., Ma, Z., Li, Z.-A., Spasova, M., et al. (2016). A versatile large-scale and green process for synthesizing magnetic nanoparticles with tunable magnetic hyperthermia features. *RSC Adv.* 6, 53107–53117. doi: 10.1039/C6RA09362K

Snowball, I. (1991). Magnetic hysteresis properties of greigite (Fe_3S_4) and a new occurrence in holocene sediments from swedish lappland. *Phys. Earth Planetary Interiors* 68, 32–40. doi: 10.1016/0031-9201(91)90004-2

Srivastava, G., Das, A., Kusurkar, T., Roy, M., Airan, S., Sharma, R., et al. (2014a). Ironpyrite, a potential photovoltaic material, increases plant biomass upon seed pretreatment. *Mater. Express* 4, 23–31. doi: 10.1166/mex.2014.1139

Srivastava, G., Das, C. K., Das, A., Singh, S., Roy, M., Kim, H., et al. (2014b). Seed treatment with iron pyrite (FeS_2) nanoparticles increases the production of spinach. *RSC Adv.* 4, 58495–58504. doi: 10.1039/C4RA06861K

Usher, C., Paul, K., Narayansamy, J., Kubicki, J., Sparks, D., Schoonen, M., et al. (2005). Mechanistic aspects of pyrite oxidation in an oxidizing gaseous environment: an *in situ* HATR–IR isotope study. *Environ. Sci. Technol.* 39, 7576–7584. doi: 10.1021/es0506657

Vanitha, P., and O'Brien, P. (2008). Phase Control In The Synthesis Of Magnetic iron sulfide nanocrystals from a cubane-type Fe-S cluster. *J. Am. Chem. Soc.* 130, 17256–17257. doi: 10.1021/ja8078187

Wadia, C., Wu, Y., Gul, S., Volkman, S., Guo, J., and Paul Alivisatos, A. (2009). Surfactant-assisted hydrothermal synthesis of single phase pyrite FeS_2 nanocrystals. *Chem. Mater.* 21, 2568–2570. doi: 10.1021/cm901273v

Wang, X., Zhou, W., Zhou, Z., An, Y., and Wu, S. (2013). Shape-controlled synthesis of iron sulfide nanostructures by thermal decomposition of organometallic precursors. *Mater. Sci. Semicond. Proc.* 16, 530–536. doi: 10.1016/j.mssp.2012.10.002

Wang, Z., Hu, T., Liang, R., and Wei, M. (2020). Application of zero-dimensional nanomaterials in biosensing. *Front. Chem.* 8:320. doi: 10.3389/fchem.2020.00320

Watson, J., Cressey, B., Roberts, A., Ellwood, D. C., Charnock, J., and Soper, A. K. (2000). Structural and magnetic studies on heavy-metal-adsorbing iron sulphide nanoparticles produced by sulphate-reducing bacteria. *J. Magn. Magn. Mater.* 214, 13–30. doi: 10.1016/S0304-8853(00)00025-1

Watson, J., Ellwood, D., Deng, Q., Mikhalovsky, S., Hayter, C. E., and Evans, J. (1995). Heavy metal adsorption on bacterially produced FeS. *Minerals Eng.* 8, 1097–1108. doi: 10.1016/0892-6875(95)00075-2

Watson, J., Ellwood, D., Soper, A., and Charnock, J. (1999). Nanosized strongly-magnetic bacterially-produced iron sulfide materials. *J. Magnetism Magnetic Mater.* 203, 69–72. doi: 10.1016/S0304-8853(99)00191-2

Wei, H., and Wang, E. (2013). Nanomaterials with enzyme-like characteristics (nanozymes): next-generation artificial enzymes. *Chem. Soc. Rev.* 42, 6060–6093. doi: 10.1039/c3cs35486e

Xiao, S., Cheng, M., Zhong, H., Liu, Z., Liu, Y., Yang, X., et al. (2020). Iron-mediated activation of persulfate and peroxymonosulfate in both homogeneous and heterogeneous ways: a review. *Chem. Eng. J.* 384:123265. doi: 10.1016/j.cej.2019.123265

Xie, J., Zhang, X., Wang, H., Zheng, H., Huang, Y., and Xie, J. (2012). Analytical and environmental applications of nanoparticles as enzyme mimetics. *Trac Trends Analyt. Chemistry* 39, 114–129. doi: 10.1016/j.trac.2012.03.021

Xu, Z., Qiu, Z., Liu, Q., Huang, Y., Li, D., Shen, X., et al. (2018). Converting organosulfur compounds to inorganic polysulfides against resistant bacterial infections. *Nat. Commun.* 9:3713. doi: 10.1038/s41467-018-06164-7

Yang, K., Yang, G., Chen, L., Cheng, L., Wang, L., Ge, C., et al. (2015). FeS nanoplates as a multifunctional nano-theranostic for magnetic resonance imaging guided photothermal therapy. *Biomaterials* 38, 1–9. doi: 10.1016/j.biomaterials.2014.10.052

Yang, W., Xiang, C., Xu, Y., Chen, S., Zeng, W., Liu, K., et al. (2020). Albumin-constrained large-scale synthesis of renal clearable ferrous sulfide quantum dots for T1-Weighted MR imaging and phototheranostics of tumors. *Biomaterials* 255:120186. doi: 10.1016/j.biomaterials.2020.120186

Yao, W., Zhu, H., Li, W., Yao, H., Wu, Y., and Yu, S. (2013). Intrinsic peroxidase catalytic activity of Fe_7S_8 nanowires templated from $[Fe_{16}S_{20}]$/diethylenetriamine hybrid nanowires. *Chem. Plus Chem.* 78, 723–727. doi: 10.1002/cplu.201300075

Yosida, K. (1951). Note on the magnetic properties of the FeS_n system. *Progr. Theor. Phys.* 6, 356–365. doi: 10.1143/ptp/6.3.356

Zhang, L., and Webster, T. (2009). Nanotechnology and nanomaterials: promises for improved tissue regeneration. *Nano Today* 4, 66–80. doi: 10.1016/j.nantod.2008.10.014

Zhang, M., Cui, Z., and Jiang, H. (2018). Relative stability of FeS_2 polymorphs with the random phase approximation approach. *J. Mater. Chem. A* 6:6606. doi: 10.1039/C8TA00759D

Zhao, Q., Yi, X., Li, M., Zhong, X., Shi, Q., and Yang, K. (2016). High near-infrared absorbing Cu_5FeS_4 nanoparticles for dual-modal imaging and photothermal therapy. *Nanoscale* 8, 13368–13376. doi: 10.1039/C6NR04444A

Conflict of Interest: The authors declare that the research was conducted in the absence of any commercial or financial relationships that could be construed as a potential conflict of interest.

frontiers in Chemistry

MINI REVIEW
published: 10 September 2020
doi: 10.3389/fchem.2020.00680

Progress of Iron-Based Nanozymes for Antitumor Therapy

Linawati Sutrisno[1], Yan Hu[2], Yanhua Hou[3], Kaiyong Cai[2], Menghuan Li[1]* and Zhong Luo[1]*

[1] School of Life Science, Chongqing University, Chongqing, China, [2] Key Laboratory of Biorheological Science and Technology, Ministry of Education, College of Bioengineering, Chongqing University, Chongqing, China, [3] Chongqing Engineering Research Centre of Pharmaceutical Sciences, Chongqing Medical and Pharmaceutical College, Chongqing, China

Artificial nanoscale enzyme-mimics (nanozymes) are promising functional alternatives to natural enzymes and have aroused great interest due to their inherent *in vivo* stability, affordability, and high catalytic ability. Iron-based nanozymes are one of the most investigated synthetic nanomaterials with versatile enzyme-like catalytic properties and have demonstrated remarkable relevance to a variety of biomedical applications, especially biocatalytic therapy against tumor indications. Nevertheless, despite the recent advances in biology and nanotechnology, the therapeutic performance of iron-based nanozymes *in vivo* is still limited by technical issues such as low catalytic efficiency and lack of tumor specificity. In this mini review, we briefly summarized the representative studies of iron-based nanozymes, while special emphasis was placed on the current challenges and future direction regarding the therapeutic implementation of iron-based nanozymes for the development of advanced tumor therapies with improved availability and biosafety.

Keywords: iron-based nanozymes, biocatalysis, nanomedicine, tumor therapy, enzyme mimics

OPEN ACCESS

Edited by:
Kelong Fan,
Institute of Biophysics (CAS), China

Reviewed by:
Dawei Jiang,
Huazhong University of Science and Technology, China
Chengzhou Zhu,
Central China Normal University, China
Hui Wei,
Nanjing University, China

***Correspondence:**
Menghuan Li
menghuanli@cqu.edu.cn
Zhong Luo
luozhong918@cqu.edu.cn

Specialty section:
This article was submitted to Nanoscience,
a section of the journal Frontiers in Chemistry

Received: *12 May 2020*
Accepted: *30 June 2020*
Published: *10 September 2020*

Citation:
Sutrisno L, Hu Y, Hou Y, Cai K, Li M and Luo Z (2020) Progress of Iron-Based Nanozymes for Antitumor Therapy. Front. Chem. 8:680.
doi: 10.3389/fchem.2020.00680

INTRODUCTION

Enzymes are a class of powerful catalysts that are responsible for accelerating various chemical reactions in the human body and are required to promote numerous biological processes, such as metabolism, detoxification, and biosynthesis (DeBerardinis and Chandel, 2016; Huang et al., 2019; Leveson-Gower et al., 2019; Wu et al., 2019). Owing to their potential effect on catalyzing the chemical reaction, enzymes have been exploited to inhibit tumor proliferation. However, the clinical translation of the enzyme is limited by its susceptibility to environmental stress as well as manufacturing problems including difficult synthesis and high production costs. Thanks to the recent advances in nanotechnology and enzymology, artificial enzymes (nanozymes) have been developed for various biomedical applications due to their tunable catalytic activities, affordable cost, facile synthesis, and high structural stability (Gao and Yan, 2016). Iron-based nanozymes (INs) are one of the earliest inorganic nanomaterials with exploitable catalytic behaviors (Cramer and Kampe, 1965). Some representative examples are ferromagnetic nanoparticles and Prussian blue (PB) nanoparticles, which may provide critical benefits for tumor treatment including Fenton-augmented ROS stress and hypoxia amelioration. These promising features of iron-based nanozymes have thus inspired great scientific interest for therapeutic intervention against a variety of tumor indications.

Nevertheless, the clinical implementation of iron-based nanozymes has met with several challenges. Typically, these nanozymes are prone to aggregation and biofouling in the biological microenvironment, both of which could lead to reduced catalytic efficiency. Moreover, the mechanisms underlying the catalytic activity of INs are still elusive and their recycling and regeneration *in vivo* remain a major challenge. In this review, we will first provide a brief summary of the previous clinical exploitations of INs for cancer therapy and then special emphasis will be placed on those major impacting factors affecting their catalytic efficiency and therapeutic performance, as well as representative studies to overcome these limitations. A perspective on the possible breakthroughs in future nanozyme-mediated tumor therapies is also provided, which may offer indicative insight for research in related areas.

REACTION ROUTES UNDERLYING THE CATALYTIC ACTIVITY OF REPRESENTATIVE INs

As described above, iron-based nanomaterials are some of the most promising nanodrugs. They have been applied first to translational studies and several iron-containing nanoformulations have been approved by the FDA for clinical usage. Typically, INs have demonstrated many clinically favorable properties that are particularly relevant for tumor therapy. From a physiochemical perspective, previous study indicates that iron-based nanoparticles could remain stable even after being stored for 40 days at ambient temperature, and their catalytic efficiency is still maintained after multiple treatment sessions (Zhang et al., 2009; Woo et al., 2013). INs also have excellent biocompatibility, which contributes to both the efficacy and safety of the IN-mediated treatment. In addition, INs could efficiently be deposited into tumor tissues based on their controllable magnetic properties to increase the therapeutic index. Moreover, INs are more resistant to environmental stress such as basic/acidic environments and extreme temperatures compared to natural enzymes. Furthermore, INs have excellent morphological homogeneity and are easy to produce at an affordable price. Based on the advantages described above, INs contributed significantly to the advances of nanocatalytic cancer therapy.

Recent insights collectively demonstrated that the biocatalytic activity of iron-based nanozymes is strongly affected by the pH of the ambient environment. Specifically, under acidic pH some INs possess peroxidase-mimicking abilities where they could react with the excessive hydrogen peroxide (H_2O_2) in cancer cells to produce hydroxyl radicals via a Fenton reaction, which have higher reactivity than normal ROS and can amplify the cytotoxic damage to the tumor cells (Bokare and Choi, 2014; Ranji-Burachaloo et al., 2018). Alternatively, under the neutral pH in tumor cytosol, some INs could demonstrate catalase-like activity and decompose H_2O_2 into oxygen and water, which has particular relevance for the treatment of hypoxic tumors (Lee et al., 2011; Abdollah et al., 2018). The chemical reactions underlying these two enzyme-mimicking abilities are described below.

Peroxidase-mimicking abilities of INs under acidic condition (Li et al., 2020):

$$Fe^{2+} + H_2O_2 \rightarrow Fe^{3+} + HO^{\bullet} + OH^{-} \quad (1)$$

$$RH + HO^{\bullet} \rightarrow R^{\bullet} + H_2O \quad (2)$$

$$R^{\bullet} + Fe^{3+} \rightarrow Fe^{2+} + \text{non–radical product (termination)} \quad (3)$$

$$H_2O_2 + HO^{-} \rightarrow\ -HO_2 + H_2O \quad (4)$$

$$Fe^{2+} + HO^{\bullet} \rightarrow Fe^{3+} + HO^{-} \quad (5)$$

The peroxidase-like catalytic property of INs usually originates from the heme-like structures therein, although the detailed mechanism is still not clear. Heme is a prosthetic group that consists of an iron atom in the center of a large porphyrin ring, which is found in both peroxidase and catalase. In this reaction process, H_2O_2 is converted to hydroxyl radicals as the intermediate products, and then the hydroxyl radicals capture protons from the hydrogen donor, forming water and oxidized donor. To achieve the optimal peroxidase-mimicking activity of the INs, the temperature must be in the range of 37–40°C and the pH should be in the range of 3–6.5. Previous study also reported that both Fe_2O_3 and Fe_3O_4 could demonstrate peroxidase-mimetic activity, wherein the activity of the former is better (Chen et al., 2012). INs can also be stimulated by some reported activators, including adenosine triphosphate (ATP), adenosine diphosphate (ADP), and adenosine monophosphate (AMP). Notably, ATP can improve the peroxidase-mimicking activity under neutral pH by interfering with single electron transfer reactions (Gao et al., 2017).

Catalase-mimicking activities of INs under neutral or basic pH:

$$Fe^{3+} + H_2O_2 \rightarrow FeOOH^{2+} + H_2O \quad (6)$$

$$FeOOH^{2+} \rightarrow Fe^{2+} + HO_2^{\bullet} \quad (7)$$

$$Fe^{3+} + H_2O_2 \rightarrow Fe^{3+} + HO^{-} + OH^{\bullet} \quad (8)$$

$$HO_2^{\bullet} \rightarrow H^{+} + O_2^{-} \quad (9)$$

$$OH^{\bullet} + HO_2^{\bullet}/O_2^{-} \rightarrow H_2O + O_2 \quad (10)$$

As for catalase-mimicking properties, it is well-established that INs effectively catalyze the degradation of H_2O_2 into water and oxygen, which could be used to relieve the hypoxia condition in the tumor microenvironment (Li et al., 2020). Gu et al. first compared the catalase-mimicking biocatalytic properties between Fe_3O_4 and Fe_2O_3 and reported that Fe_3O_4 demonstrated a higher catalytic ability than Fe_2O_3 (Wei and Wang, 2008). Based on these underlying mechanisms, scientists have developed a plethora of iron-containing nanoformulations for tumor therapy, which will be briefly discussed below individually.

INs FOR NANOCATALYTIC CANCER THERAPY

As demonstrated by the mechanistic discussions above, INs could demonstrate multifaceted catalytic activities resembling various enzymes *in vivo*. This, in combination with the magnetic responsiveness, versatile surface chemistry, and excellent biocompatibility of iron-based nanomaterials, INs have been increasingly applied for the diagnosis and treatment of many tumor indications. For instance, Cai et al. demonstrated that the iron core in the ferrimagnetic H-ferritin nanoparticles had peroxidase-like catalytic activities and could be used for the immunohistochemical-like staining of the tumor tissues. The authors observed that xenografted tumor tissues incubated with the ferrimagnetic H-ferritin nanoparticles showed a brownish color due to the nanozyme-catalyzed oxidation of 3,3'-diaminobenzidine tetrahydrochloride substrates under the presence of excessive H_2O_2, while the normal tissues were stained purple by hematoxylin (Cai et al., 2015). Meanwhile, it has also been reported that catalase-like INs could decompose the tumor H_2O_2 to generate additional oxygen, which could be exploited to facilitate the ultrasound imaging of the tumor area (Wang et al., 2020). As for the therapeutic exploitation of the INs, current research mostly focuses on the application as Fenton nanocatalysts or oxygen generators, which will be discussed in the section below.

Nanocatalysts Based on Iron Oxide Nanostructures

Superparamagnetic iron oxide nanoparticles (SPIONs) are a class of biocompatible and degradable inorganic nanomaterials that have been widely explored for tumor diagnosis and therapy, which refers to small nanocrystals composed of iron oxide (usually in the form of magnetite Fe_3O_4 or maghemite γ-Fe_2O_3). After being internalized by cancer cells, SPIONs could demonstrate multifaceted catalytic functions for a variety of applications. For instance, SPIONs display peroxidase-mimetic properties via a Fenton reaction under an acidic microenvironment, while they are also capable of decomposing H_2O_2 under the neutral and basic pH conditions showing catalase-mimetic activity. Hence, the nanocatalytic effect of the SPIONs is dependent on their local pH, which could be exploited to modulate the therapeutic activities in biological environments (Chen et al., 2012).

Typically, it has been reported that ferumoxytol, an FDA-approved intravenous iron preparation based on SPIONs coated with lower molecular weight semi-synthetic carbohydrates, exhibits nanocatalytic therapeutic effects on leukemia cells with low ferroportin levels (Zanganeh et al., 2016). It was further revealed that ferumoxytol generates ROS at higher rates than free iron nanoparticles and the ROS production rate could remain at a steady level for a long time. Since the leukemic cells with low ferroportin expression levels are unable to efficiently export the ferumoxytol nanoformulations, the ROS generation cannot be stopped via normal antioxidation mechanisms, eventually leading to cell death. On the contrary, normal cells have high ferroportin expression, allowing the cells to export the exogenous iron species after ferumoxytol uptake and ameliorate the ferumoxytol-mediated Fenton-based cytotoxic damage (Trujillo-Alonso et al., 2019).

It's also possible to regulate the catalysis-based cancer therapy of SPION-based INs by combining them with other nanobiomaterials. For instance, Huang and coworkers fabricated a bubble-generating liposomal system for the delivery of iron oxide-based nanozymes, which was also loaded with ammonium bicarbonate to trigger the release of the INs in a responsive manner (Huang et al., 2016; **Figure 1**). After being internalized by cancer cells, ammonium bicarbonate would be hydrolyzed into CO_2 and NH_3 in the acidic environment of the endo/lysosomes, thus disrupting the liposomal membrane and releasing the INs, which would then react with the excessive H_2O_2 in the tumor cytosol and produce large amounts of cytotoxic hydroxyl radicals. The proposed controlling mechanism was also supported by the minimal toxicity of the nanosystem in early endosomes and the pronounced cytotoxic damage after reaching the cytoplasm. This study further confirmed the possibility of the acidity for controlling the Fenton reaction in the intracellular environment for amplifying the therapeutic efficacy.

Other Types of Iron-Containing Nanostructures With Catalytic Activity

Aside from the iron oxide nanostructure, some other iron-containing nanostructures have also been widely explored like a nanocatalytic therapeutic nanostructure used for cancer treatment. Prussian Blue ($Fe_4[Fe(CN)_6]_3$, PB) has been used in various biomedicine fields due to its multi-enzyme-like capabilities, including peroxidase, catalase, and superoxide dismutase. This phenomenon could be explained by the abundant redox potential of the various constituents of PB, which makes it an efficient electron transporter (Zhang et al., 2016). The enzyme-like catalytic mechanism of PB is distinctively different from conventional Fenton reactions, such as the capability of scavenging hydroxyl radicals due to their high affinity. The peroxidase-mimetic reaction routes of PB is demonstrated here below:

$$\begin{aligned}
&[\mathrm{Fe(III)Fe(II)(CN)_6}]-(\mathrm{PB})\\
&[\mathrm{Fe(II)Fe(II)(CN)_6}]^{2-}(\mathrm{PW})\\
&\mathrm{Fe(III)_3[Fe(III)(CN)_6]2[Fe(II)(CN)_6]}-\ (\mathrm{BG})\\
&[\mathrm{Fe(III)Fe(III)(CN_6}](\mathrm{PY})\\
&\mathrm{PB} + \mathrm{H}^+ + \bullet\mathrm{OH} \rightarrow \mathrm{PY} + \mathrm{H_2O}\\
&\mathrm{H_2O_2} \rightarrow \mathrm{O_2} + 2\mathrm{e}^- + 2\mathrm{H}^+\\
&\mathrm{H_2O_2} + 2\mathrm{e}^- + 2\mathrm{H}^+ \rightarrow 2\mathrm{H_2O}\\
&\mathrm{TMB} + \mathrm{H_2O_2} + 2\mathrm{H}\xrightarrow{\mathrm{PY}} \mathrm{TMB(oxidized)} + 2\mathrm{H_2O}
\end{aligned}$$

In neutral and basic microenvironment, PB could show catalase-mimetic activity, which effectively accelerates the decomposition of H_2O_2 into H_2O and O_2. The reaction mechanism is as follows:

$$\begin{aligned}
&\mathrm{PB} + \mathrm{e}^- \rightarrow \mathrm{PW}\\
&3\mathrm{PB} \rightarrow \mathrm{BG} + 2\mathrm{e}^-\\
&\mathrm{PB} \rightarrow \mathrm{PY} + \mathrm{e}^-\\
&3\mathrm{PB} + \mathrm{H_2O_2} \rightarrow \mathrm{BG} + 2\mathrm{OH}^-\\
&2\mathrm{BG} + \mathrm{H_2O_2} \rightarrow 6\mathrm{PY} + 2\mathrm{OH}^-
\end{aligned}$$

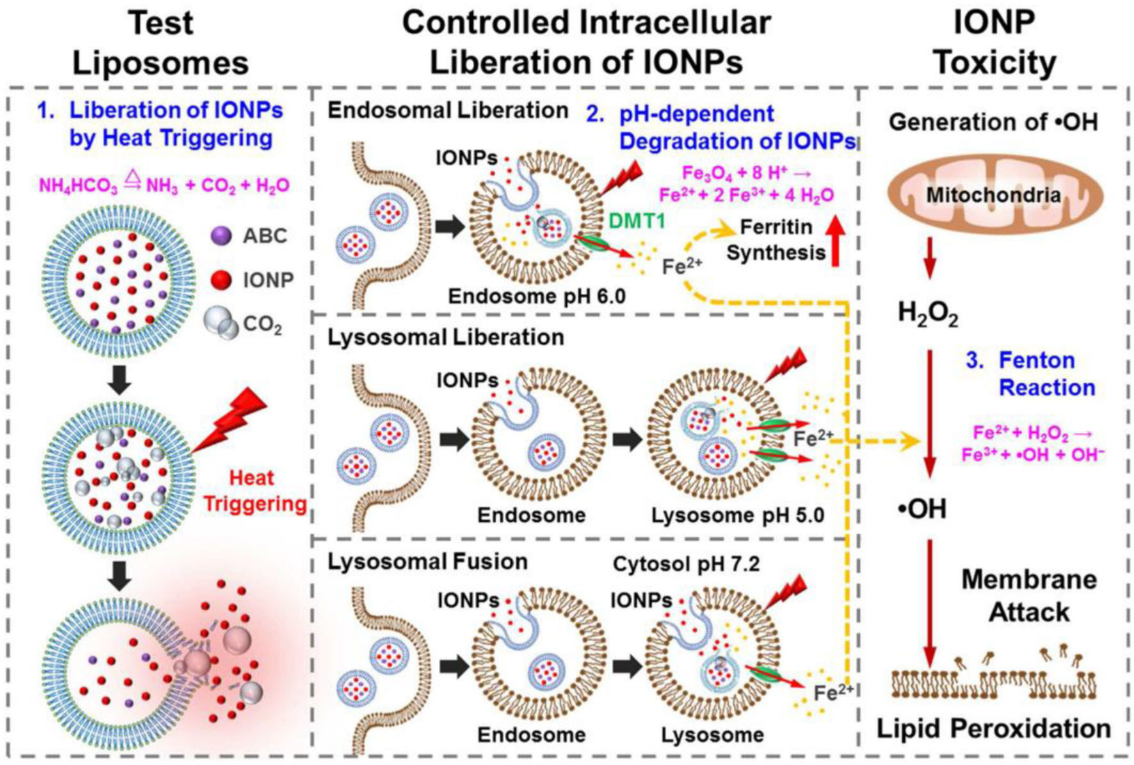

FIGURE 1 | Schematic illustrations of the structure of thermoresponsive bubble-generating liposomal system and its process of spatially precise versatile nanosystem-controlled intracellular liberation of IONPs in specific cellular organelles in various endocytic stages. The degradation of IONPs, release of iron ions, and subsequent reactive oxygen species (ROS) generation within cells are indicated. IONPs, iron oxide nanoparticles; ABC, ammonium bicarbonate; DMT1, divalent metal transporter-1. Reproduced with permission from Huang et al. (2016). Copyright © 2016, American Chemical Society.

$$6PY + H_2O_2 + 2OH^- \rightarrow 2BG + O_2 + 2H_2O$$

Generally, PB can be converted into Prussian White (PW) and oxidized into Berlin Green (BG) or Prussian Yellow (PY) at pH 3.0–8.0, which would then react with H_2O_2 to complete the redox cycle. When the electrode potential is below 0.7 V, high spin $Fe^{3+}/^{2+}$ plays the dominant role in the electron transfer process. Meanwhile, when the electrode potential is more than 0.9 V, $[Fe(CN)_6]^{3-}/^{4-}$ becomes the dominant species. At an acidic pH, the H_2O_2 exhibits strong oxidation capabilities and effectively oxidizes the PB into BG or PY, resulting in the peroxidase-mimetic activity. It's also worth mentioning that the catalytic activity of PB nanoparticles are very sensitive to environmental pH, as the oxidative capability of H_2O_2 would become weaker under basic pH, leading to reduced peroxidase-like activity while enhancing the catalase-mimetic activity.

In another study by Luo et al. the authors developed a DOX-Fe^{2+} complex and loaded it into tumor-responsive amorphous calcium carbonate (ACC) nanostructures, which was further functionalized with PAMAM dendrimer with folate or MMP2-sheddable PEG. The DOX-Fe^{2+} complex could not only enhance the *in vivo* stability of the catalytically active Fe^{2+} ions, but also elevated the production of H_2O_2 by activating the NAPDH pathways to sustain the catalytic activity of Fe^{2+} ions, thus efficiently inducing ferroptotic cell death in cancer cells (Xue et al., 2020).

The catalase-mimicking properties of INs have also been explored to reduce hypoxia-induced resistance to cancer therapy. The feasibility and potentially therapeutic advantages of this strategy were demonstrated in the previous study, in which a hybrid nanosphere containing Fe^{3+} was introduced to overcome tumor hypoxia through decomposing endogenous H_2O_2. The hybrid nanosphere was constructed through the coordination-driven assembly of ferric ions, TPEDXX, and sabutoclax. Experimental results showed that once the hybrid nanospheres were taken in by cancer cells, the intracellular H_2O_2 would decompose into oxygen and enhance the Fe^{3+-}catalyzed Fenton reaction. Meanwhile, sabutoclax could mitigate the PDT resistance through Bclx2 inhibition and enhance the ROS production under laser irritation (Shi et al., 2020).

It's also possible to synthesize iron-based nanocatalysts with tailored catalytic activities through the doping of other atoms. Typically, He and coworkers synthesized Fe-N-C artificial enzymes capable of activating oxygen for monooxygenation and dehydrogenation. The Fe-N_x center was an active site for O_2 activation by directly producing specific reactive oxygen species (ROS). The O_2 activation at the Fe-N site was caused by strong interactions between the N-doped carbon support and catalytic sites, which altered the electronic structure of Fe-N side. During the initiation of O_2, the Fe-N site may bound and stimulate $^3O_2$ to create $^1O_2$, and then was modified to $HO_2\bullet^-$ by receiving electrons and protons from other substances. Afterwards, the produced $HO_2\bullet^-$ was converted to HO_2- through the monooxygenation or dehydrogenation of organic substrates, which could effectively cause tumor cell death by elevating the ROS stress above the cytotoxic threshold. Interestingly, the N-doped nanomaterials also possessed high stability at extreme pH and are resistant to treatment with polar organic solutions (such as CH_2Cl_2, CH_3CN, and *n*-hexene), heating (up to 70°C), and air exposure, which may be attributed to the robust structure of Fe-N-C (Tan et al., 2018).

CRITICAL CONSIDERATIONS FOR THE IRON NANOZYME-MEDIATED BIOCATALYTIC TUMOR THERAPY

Despite the excellent therapeutic performance of iron nanozymes demonstrated *in vitro* and *in vivo*, it should be recognized that a tumor is a highly complex disease and the efficacy of IN-mediated biocatalytic tumor therapy may be affected by a variety of issues in the clinical context. These limiting factors and notable issues would be discussed in the section below.

Intratumoral H_2O_2 Level in Cancer Cells

As we have discussed in previous sections, most of the current iron nanozymes react with the endogenous H_2O_2 in the tumor cells to exert therapeutic effect. High local H_2O_2 level is a characteristic feature in many types of tumor indications due to the intense metabolism thereof. However, the endogenous H_2O_2 supply may also be exhausted or diminished due to various reasons and become a limiting factor for IN-mediated biocatalytic therapy (Huo et al., 2017). Therefore, it's sometimes necessary to incorporate supplementary measures to replenish the H_2O_2 in the tumor region to sustain the treatment (Ranji-Burachaloo et al., 2018).

In a recent study by Yeh et al. the authors encapsulated H_2O_2 into Fe_3O_4-PLGA polymersome to provide O_2 for echogenic reflectivity as well as to sustain the •OH production. The Fenton reaction could not be triggered without ultrasound treatment as the Fe_3O_4 and H_2O_2 components were separated by the polymeric contents in the system. The ultrasound treatment could disrupt the polymersomes and potentiates the reaction between H_2O_2 and Fe_3O_4 nanoparticles to generate •OH via Fenton reaction. Moreover, because of the Fe_3O_4 content, the H_2O_2/Fe_3O_4-PLGA polymersome also allows for the magnetic resonance imaging of the tumor tissues (Li et al., 2016). In another study by Huo et al., the authors incorporated Fe_3O_4 and GOx into biodegradable dendritic silica nanoplatforms with large pore size to construct an H_2O_2 self-replenishable Fenton nanocatalyst for tumor therapy. GOx will convert the glucose in the tumor cells in the presence of oxygen and water to gluconic acid and H_2O_2, which would then be catalyzed by the Fe_3O_4 nanoparticles into highly toxic hydroxyl radicals in a sequential manner and eventually lead to the cancer cell apoptosis (Huo et al., 2017; Jiang et al., 2019, **Figure 2**).

Tumor Specificity

Intravenous injection is one of the primary methods for the administration of antitumor nanoagents, during which the nanoformulations would circulate around the body and eventually accumulate at the desired site of action. Nevertheless, after the nanoformulations enter the blood circulation, they may be captured and eliminated by the mononuclear phagocyte system, which would severely compromise their bioavailability and increase the risk of the undesirable nanoparticle accumulation in healthy organs. An alternative approach to address this issue is to conjugate long-circulating and targeting moieties to the nanoparticle surface (Dai et al., 2016). Generally, there are two types of targeted drug delivery: active targeting and passive targeting. In passive targeting, the cancer-targeting efficiency is closely correlated to physical features of nanocarriers such as size, hydrophilicity, and surface charge. In active targeting, the constructed nanocarrier could interact with targeting tumor cells to enhance the specific retention and uptake, which depends on the specific association between targeting ligand conjugated on the nanocarrier's surface and the receptors on the diseased tissues/cells surface (Dai et al., 2016). At the current stage, the functionalization of targeting ligand to the surface of INs is still rarely explored, which warrants more research input in the future.

Optimization of the Catalytic Microenvironment

It's well-established that the catalytic functions of enzymes are highly susceptible to factors including pH, temperature, ionizable salts, and surfactants (Iyer and Ananthanarayan, 2008). Therefore, it's often necessary to optimize the reaction condition (acidity, temperature) of nanozymes in the biological environment to improve their efficacy. The optimal reaction pH for a Fenton reaction ranges from 2 to 4 due to the two major reasons: (i) it prevents the precipitation of iron ions under acidic environments and (ii) it inhibits degradation of the H_2O_2 under extremely low pH conditions. Meanwhile, the pH of tumor microenvironments range from 6.5 to 7.0, while the cancer cell endosomes have a pH of about 5.0 and lysosomes have a pH of ∼4.5. Therefore, the strategy to reduce the pH of tumor microenvironments or deliver the drugs to the lysosome can effectively facilitate the Fenton reaction (Tang et al., 2019). For example, Liu and coworkers constructed an amorphous iron oxide-based RNAi-incorporated nanoplatform, which could effectively escape from endosome through osmotic pressure and enter the tumor cytosol (Liu et al., 2018). Subsequently, the co-delivered siRNA could inhibit the MCT4-mediated lactate efflux routes to acidify the intracellular environment (**Figure 3**) and thus enhance the Fenton-based catalytic efficacy. Moreover, the small size of the nanoplatform enabled them to penetrate the tumor tissues and enhance tumor deposition via EPR effect.

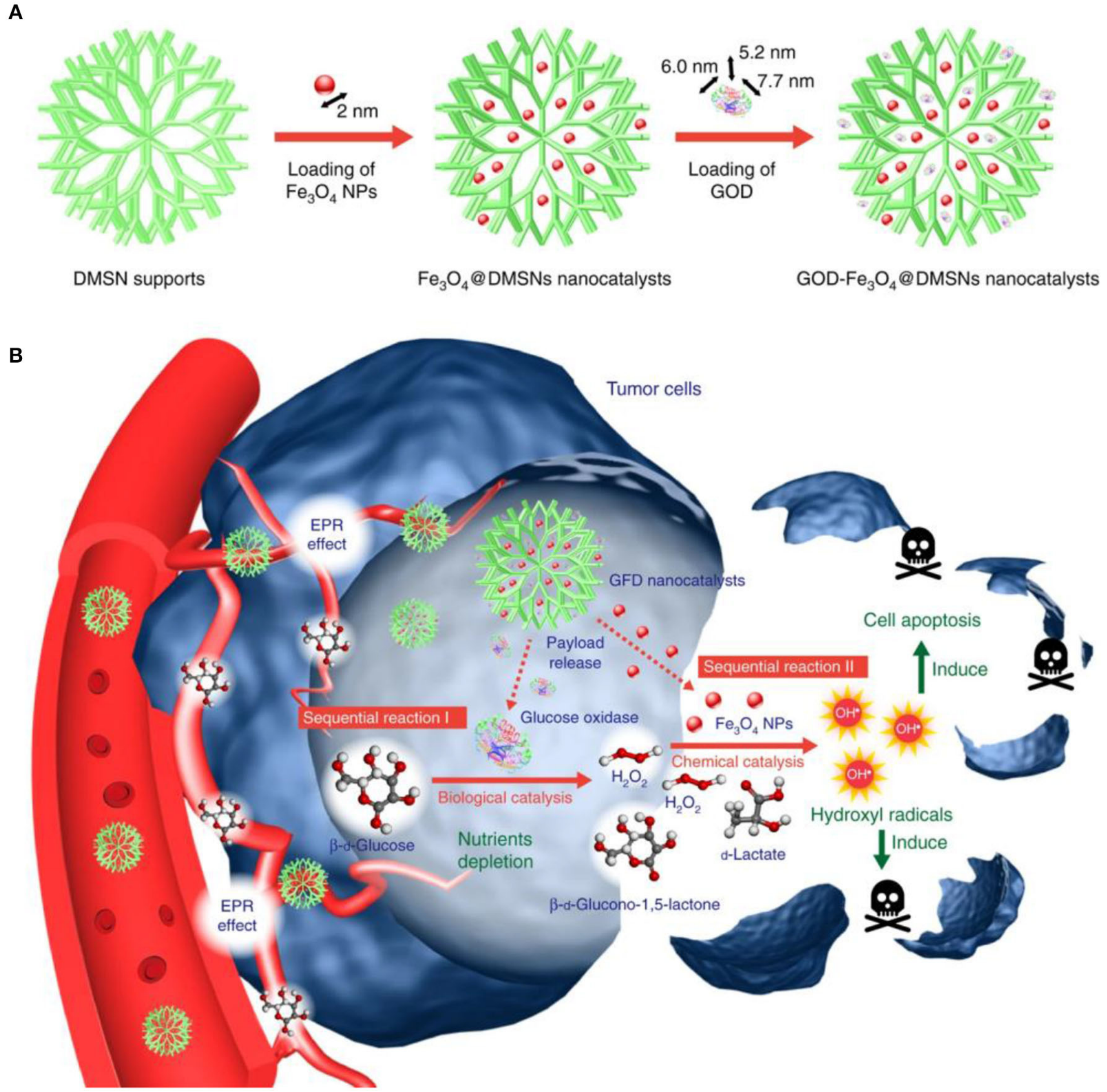

FIGURE 2 | The scheme of sequential catalytic-therapeutic mechanism of GFD NCs on the generation of hydroxyl radicals for cancer therapy. **(A)** Synthesis process of the GFD NCs. **(B)** *In vivo* action of the GFD NCs. Reproduced with permission from Huo et al. (2017). Copyright © 2017, Springer Nature.

Physicochemical Factors

It's well-known that the catalytic properties of nanozymes can be affected by their size, shape, concentration, structure, and chemical composition (Niu et al., 2010; Zhang et al., 2014). Therefore, there has been a growing interest in modulating the physicochemical properties of nanozymes to enhance their efficacy in a biological environment.

Particle size is one of the most important parameters that affects the catalytic activity of nanomaterials. It's widely accepted that nanozymes with smaller sizes usually have better catalytic activity than the larger counterparts, the size-induced changes in catalytic efficiency may be caused by the fact that small nanozymes have larger surface areas and a greater number of active sites (Könczöl et al., 2013; Li et al., 2015; Peng et al., 2015). In 2007, Yang et al. investigated the catalytic activity of Fe_3O_4 nanoparticles at different sizes (30, 150, and 300 nm). The experimental results indicated that 30 nm Fe_3O_4 nanoparticles exhibited the highest peroxidase-mimetic activity, while the 300 nm Fe_3O_4 nanoparticles showed the lowest catalytic ability (Gao et al., 2007). A similar trend has also been observed on Prussian blue nanoparticles, in which the researchers found that the catalytic efficiency of Prussian blue nanoparticles with an average diameter of 200 nm was 300 times higher than nanoparticles sized around 570 nm (Komkova et al., 2018).

Aside from nanoparticle size, shape and surface composition must also be considered when modulating the catalytic property of INs. Previous study revealed that between three Fe_3O_4 nanostructures, cluster spheres, octahedra, and triangular

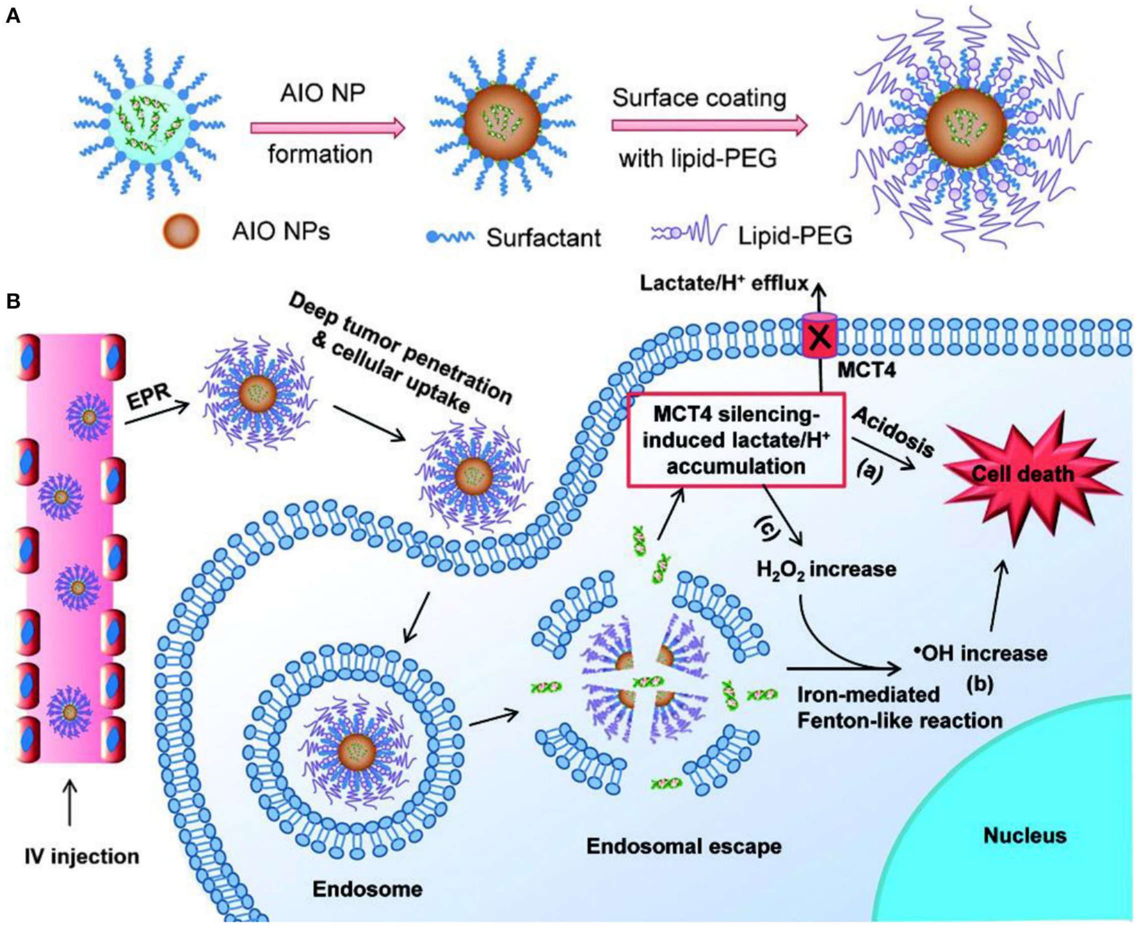

FIGURE 3 | Schematic illustration of the AIOI RNAi NPs **(A)** and the mechanism of action **(B)** in the tumor microenvironment. Reproduced from Liu et al. (2018). Copyright © 2018 The Authors. Published by Wiley-VCH Verlag GmbH & Co. KGaA.

plates displayed varied peroxidase-mimetic catalytic efficacy, of which the cluster spheres were highest while octahedra ones were lowest. This may be caused by the preferential exposure of catalytically-active Fe crystal planes or atoms (Liu et al., 2011). Typically, nanomaterials have many facets with varying surface energies. Consequently, the catalytic potential of different facets may change greatly from one to another. The high-energy (110) facet tends to have a higher catalytic activity, which may be attributed to the open surface structure and greater number of active sites (Jiang et al., 2010; Liu et al., 2011).

The activity of the INS also could be enhanced by doping or integrating them with other materials, such as Ag, Au, and Pt. The peroxidase-mimetic activity of Au@Fe_3O_4 was higher compare to Au or Fe_3O_4 alone, which may attribute to the special electronic structure at the interfaces between them and the polarization effects from Au to Fe_3O_4. Other metals, such as $Pt_{48}Pd_{52}$-Fe_3O_4, Fe_3O_4@Pt, and Fe_3O_4 coated Ag nanowire also displayed the enhanced activity with higher stability compared to INs alone (Lee et al., 2010; Ma et al., 2013; Sun et al., 2013; Wang et al., 2016).

Biosafety/Biocompatibility/Biodegradability

Aside from the promising antitumor efficacy of iron-based nanozymes, it's also necessary to investigate their potential impact on the health of the receiving host both in the short term and long term. Consequently, the INs should be non-toxic to the normal tissues and preferably be degraded in biological environments and eventually eliminated from the body after completing the therapeutic events. Biocompatibility and biosafety of both enzymes and nanozymes play the key role in ensuring their further clinical application. Nevertheless, INs are still a new technology in the early stage of development and most of their interaction patterns with the biological environment remain to be elucidated, which warrants continuous research input regarding their pharmacokinetics, absorption, distribution, metabolism, therapeutic sustainability, excretion, and toxicity at molecular, cellular, and systemic levels (Tibbitt et al., 2016).

Stimulation by External Irritation

The regeneration of Fe^{2+} species in cancer cells is also a limiting factor that affects the treatment-induced ROS stress. The photo-Fenton reaction is an emerging strategy to accelerate the regeneration of Fe^{2+} ions using external irradiation, which could significantly enhance the generation efficiency of hydroxyl radicals comparing to classical Fenton catalysts. From a mechanistic perspective, the Fe^{3+} species in the solution could undergo an efficient photoreaction under light illumination to generate Fe^{2+} and additional hydroxyl radicals, thus potentiating improved tumor inhibition effect. For example, the photo-Fenton strategy has been applied to enhance the catalytic efficiency of TAT peptide-conjugated Fe_3O_4 nanoparticles in tumor microenvironments. The results suggested that the combinational treatment of Fe_3O_4-TAT nanoparticles and 5 Gy radiation therapy effectively prevents tumor growth (Ranji-Burachaloo et al., 2018). These discoveries hold a great promise for improving the biocatalytic activity of INs against cancer for clinical translation.

FUTURE PERSPECTIVE AND CURRENT CHALLENGES

Although nanozymes have demonstrated great potential for tumor therapy, there are still some issues that need to be resolved for broad clinical implementation. First of all, unlike natural enzymes, most iron-based nanozymes have a low catalytic specificity and could respond to multiple substrates in the biological milieu, and this poor substrate selectivity may interfere with the endogenous enzyme-mediated catalytic pathways and increase the risk of undesirable side effects. Therefore, it's of high urgency and importance to investigate the overall impact of nanozymes on the catalytic landscape *in vivo* and improve their substrate selectivity. Secondly, the catalytic mechanisms of existing INs are still under investigation, and comprehensive mechanistic investigations are still needed, which could not only explain the correlation between the catalytic performance and the composition/structure of the nanozymes, but also provide indicative insight for the development of novel nanozyme-based therapeutics. Furthermore, as most of the iron-based nanozymes are intrinsically multifunctional and may offer other benefits such as cancer treatment, imaging and sensitization, it's important to balance their catalytic activity and other functions through rational structural design and surface modification. Finally, a thorough investigation is still needed to investigate the biosafety of these nanozymes in clinically relevant models, which may fill the blank in current nanozyme research and greatly facilitate their clinical translation.

CONCLUSION

To sum up, the intrinsic enzyme-mimetic activity of INs has been exploited for decades. As the new generation of artificial enzymes, the catalytic behaviors of INS have been systematically analyzed and improved by adjusting certain parameters, such as optimizing their physicochemical properties or modulating their local environment. Compared to natural enzymes, INs displayed higher stability and modification versatility, which opens up new avenues for nanocatalytic tumor therapy. However, several challenges still hinder its clinical application, which should be investigated in the future by both scientists and biomedical researchers.

AUTHOR CONTRIBUTIONS

ZL, ML, and YHo conceptualized this review. LS and ML wrote the paper and prepared the figures. All authors revised the manuscript.

FUNDING

This work was financially supported by the Natural Science Foundation of China (11832008 and 51773023), Fundamental Research Funds for the Central Universities (2020CDJQYA075 and 2019CDQYSW005), Central University's Basic Scientific Research Business Fee Medical Integration Project (2019CDYGYB004 and 2020CDJYGZL009), and Research Funds of the Chongqing Municipal Education Commission (KJQN201800109). The Natural Science Foundation of Chongqing Municipal Government (cstc2018jcyjAX0368), Chongqing Outstanding Young Talent Supporting Program (CQYC201905072), Chongqing Research Program of Basic Research and Frontier Technology (cstc2018jcyjAX0580), and Incentive Guidance for Chongqing Scientific Research Institutes Project (cstc2017jxjl130046).

REFERENCES

Abdollah, M. R. A., Carter, T. J., Jones, C., Kalber, T. L., Rajkumar, V., Tolner, B., et al. (2018). Fucoidan prolongs the circulation time of dextran-coated iron oxide nanoparticles. *ACS Nano* 12, 1156–1169. doi: 10.1021/acsnano.7b06734

Bokare, A. D., and Choi, W. (2014). Review of iron-free Fenton-like systems for activating H2O2 in advanced oxidation processes. *J. Hazard. Mater.* 275, 121–135. doi: 10.1016/j.jhazmat.2014.04.054

Cai, Y., Cao, C., He, X., Yang, C., Tian, L., Zhu, R., et al. (2015). Enhanced magnetic resonance imaging and staining of cancer cells using ferrimagnetic H-ferritin nanoparticles with increasing core size. *Int. J. Nanomed.* 10, 2619–2634. doi: 10.2147/IJN.S80025

Chen, Z., Yin, J.-J., Zhou, Y.-T., Zhang, Y., Song, L., Song, M., et al. (2012). Dual enzyme-like activities of iron oxide nanoparticles and their implication for diminishing cytotoxicity. *ACS Nano* 6, 4001–4012. doi: 10.1021/nn300291r

Cramer, F., and Kampe, W. (1965). Inclusion compounds. XVII.1 catalysis of decarboxylation by cyclodextrins. a model reaction for the mechanism of enzymes. *J. Am. Chem. Soc.* 87, 1115–1120. doi: 10.1021/ja01083a031

Dai, L., Liu, J., Luo, Z., Li, M., and Cai, K. (2016). Tumor therapy: targeted drug delivery systems. *J. Mater. Chem. B* 4, 6758–6772. doi: 10.1039/C6TB01743F

DeBerardinis, R. J., and Chandel, N. S. (2016). Fundamentals of cancer metabolism. *Sci. Adv.* 2:e1600200. doi: 10.1126/sciadv.1600200

Gao, L., Fan, K., and Yan, X. (2017). Iron oxide nanozyme: a multifunctional enzyme mimetic for biomedical applications. *Theranostics* 7, 3207–3227. doi: 10.7150/thno.19738

Gao, L., and Yan, X. (2016). Nanozymes: an emerging field bridging nanotechnology and biology. *Sci. China Life Sci.* 59, 400–402. doi: 10.1007/s11427-016-5044-3

Gao, L., Zhuang, J., Nie, L., Zhang, J., Zhang, Y., Gu, N., et al. (2007). Intrinsic peroxidase-like activity of ferromagnetic nanoparticles. *Nat. Nanotechnol.* 2:577. doi: 10.1038/nnano.2007.260

Huang, C.-C., Liao, Z.-X., Lu, H.-M., Pan, W.-Y., Wan, W.-L., Chen, C.-C., et al. (2016). Cellular organelle-dependent cytotoxicity of iron oxide nanoparticles and its implications for cancer diagnosis and treatment: a mechanistic investigation. *Chem. Mater.* 28, 9017–9025. doi: 10.1021/acs.chemmater.6b03905

Huang, Y., Ren, J., and Qu, X. (2019). Nanozymes: classification, catalytic mechanisms, activity regulation, and applications. *Chem. Rev.* 119, 4357–4412. doi: 10.1021/acs.chemrev.8b00672

Huo, M., Wang, L., Chen, Y., and Shi, J. (2017). Tumor-selective catalytic nanomedicine by nanocatalyst delivery. *Nat. Commun.* 8:357. doi: 10.1038/s41467-017-00424-8

Iyer, P. V., and Ananthanarayan, L. (2008). Enzyme stability and stabilization—Aqueous and non-aqueous environment. *Process Biochem.* 43, 1019–1032. doi: 10.1016/j.procbio.2008.06.004

Jiang, D., Ni, D., Rosenkrans, Z. T., Huang, P., Yan, X., and Cai, W. (2019). Nanozyme: new horizons for responsive biomedical applications. *Chem. Soc. Rev.* 48, 3683–3704. doi: 10.1039/C8CS00718G

Jiang, Z.-Y., Kuang, Q., Xie, Z.-X., and, Zheng, L.-S. (2010). Syntheses and properties of micro/nanostructured crystallites with high-energy surfaces. *Adv. Funct. Mater.* 20, 3634–3645. doi: 10.1002/adfm.201001243

Komkova, M. A., Karyakina, E. E., and Karyakin, A. A. (2018). Catalytically synthesized prussian blue nanoparticles defeating natural enzyme peroxidase. *J. Am. Chem. Soc.* 140, 11302–11307. doi: 10.1021/jacs.8b05223

Könczöl, M., Weiss, A., Stangenberg, E., Gminski, R., Garcia-Käufer, M., Gier,é, R., et al. (2013). Cell-cycle changes and oxidative stress response to magnetite in A549 human lung cells. *Chem. Res. Toxicol.* 26, 693–702. doi: 10.1021/tx300503q

Lee, J. H., Jang, J. T., Choi, J. S., Moon, S. H., Noh, S. H., Kim, J. W., et al. (2011). Exchange-coupled magnetic nanoparticles for efficient heat induction. *Nat. Nanotechnol.* 6, 418–422. doi: 10.1038/nnano.2011.95

Lee, Y., Garcia, M. A., Frey Huls, N. A., and Sun, S. (2010). Synthetic tuning of the catalytic properties of Au-Fe3O4 nanoparticles. *Angew. Chem. Int. Ed.* 49, 1271–1274. doi: 10.1002/anie.200906130

Leveson-Gower, R. B., Mayer, C., and Roelfes, G. (2019). The importance of catalytic promiscuity for enzyme design and evolution. *Nat. Rev. Chem.* 3, 687–705. doi: 10.1038/s41570-019-0143-x

Li, M., Zhang, H., Hou, Y., Wang, X., Xue, C., Li, W., et al. (2020). State-of-the-art iron-based nanozymes for biocatalytic tumor therapy. *Nanoscale Horiz.* 5, 202–217. doi: 10.1039/C9NH00577C

Li, P., Klet, R. C., S.-,Moon, Y., Wang, T. C., Deria, P., Peters, A. W., et al. (2015). Synthesis of nanocrystals of Zr-based metal–organic frameworks with csq-net: significant enhancement in the degradation of a nerve agent simulant. *Chem. Comm.* 51, 10925–10928. doi: 10.1039/C5CC03398E

Li, W.-P., Su, C.-H., Chang, Y.-C., Lin, Y.-J., and Yeh, C.-S. (2016). Ultrasound-induced reactive oxygen species mediated therapy and imaging using a fenton reaction activable polymersome. *ACS Nano* 10, 2017–2027. doi: 10.1021/acsnano.5b06175

Liu, S., Lu, F., Xing, R., and and, Zhu, J.-J. (2011). Structural effects of Fe3O4 nanocrystals on peroxidase-like activity. *Chem. Eur. J.* 17, 620–625. doi: 10.1002/chem.201001789

Liu, Y., Ji, X., W., Tong, W. L., Askhatova, D., Yang, T., Cheng, H., et al. (2018). Engineering multifunctional RNAi nanomedicine to concurrently target cancer hallmarks for combinatorial therapy. *Angew. Chem. Int. Ed.* 57, 1510–1513. doi: 10.1002/anie.201710144

Ma, M., Xie, J., Zhang, Y., Chen, Z., and Gu, N. (2013). Fe3O4@Pt nanoparticles with enhanced peroxidase-like catalytic activity. *Mater. Lett.* 105, 36–39. doi: 10.1016/j.matlet.2013.04.020

Niu, W., Zhang, L., and Xu, G. (2010). Shape-controlled synthesis of single-crystalline palladium nanocrystals. *ACS Nano* 4, 1987–1996. doi: 10.1021/nn100093y

Peng, Y., Wang, Z., Liu, W., Zhang, H., Zuo, W., Tang, H., et al. (2015). Size- and shape-dependent peroxidase-like catalytic activity of MnFe2O4 Nanoparticles and their applications in highly efficient colorimetric detection of target cancer cells. *Dalton Trans.* 44, 12871–12877. doi: 10.1039/C5DT01585E

Ranji-Burachaloo, H., Gurr, P. A., Dunstan, D. E., and Qiao, G. G. (2018). Cancer treatment through nanoparticle-facilitated fenton reaction. *ACS Nano* 12, 11819–11837. doi: 10.1021/acsnano.8b07635

Shi, L., Hu, F., Duan, Y., Wu, W., Dong, J., Meng, X., et al. (2020). Hybrid nanospheres to overcome hypoxia and intrinsic oxidative resistance for enhanced photodynamic therapy. *ACS Nano* 14, 2183–2190. doi: 10.1021/acsnano.9b09032

Sun, X., Guo, S., Chung, C.-S., Zhu, W., and Sun, S. (2013). A sensitive H2O2 assay based on dumbbell-like PtPd-Fe3O4 nanoparticles. *Adv. Mater.* 25, 132–136. doi: 10.1002/adma.201203218

Tan, H. Y., Eskandari, R., Shen, D., Zhu, Y. P., Liu, T. W., Willems, L. I., et al. (2018). Direct one-step fluorescent labeling of O-GlcNAc-modified proteins in live cells using metabolic intermediates. *J. Am. Chem. Soc.* 140, 15300–15308. doi: 10.1021/jacs.8b08260

Tang, Z., Liu, Y., He, M., and Bu, W. (2019). Chemodynamic therapy: tumour microenvironment-mediated fenton and fenton-like reactions. *Angew. Chem. Int. Ed.* 58, 946–956. doi: 10.1002/anie.201805664

Tibbitt, M. W., Dahlman, J. E., and Langer, R. (2016). Emerging frontiers in drug delivery. *J. Am. Chem. Soc.* 138, 704–717. doi: 10.1021/jacs.5b09974

Trujillo-Alonso, V., Pratt, E. C., Zong, H., Lara-Martinez, A., Kaittanis, C., Rabie, M. O., et al. (2019). FDA-approved ferumoxytol displays anti-leukaemia efficacy against cells with low ferroportin levels. *Nat. Nanotechnol.* 14, 616–622. doi: 10.1038/s41565-019-0406-1

Wang, C., Qian, J., Wang, K., Yang, X., Liu, Q., Hao, N., et al. (2016). Colorimetric aptasensing of ochratoxin A using Au@Fe3O4 nanoparticles as signal indicator and magnetic separator. *Biosens. Bioelectron.* 77, 1183–1191. doi: 10.1016/j.bios.2015.11.004

Wang, P., Wang, T., Hong, J., Yan, X., and Liang, M. (2020). Nanozymes: a new disease imaging strategy. *Front. Bioeng. Biotechnol.* 8, 15–15. doi: 10.3389/fbioe.2020.00015

Wei, H., and Wang, E. (2008). Fe3O4 magnetic nanoparticles as peroxidase mimetics and their applications in H2O2 and glucose detection. *Anal. Chem.* 80, 2250–2254. doi: 10.1021/ac702203f

Woo, M.-A., Kim, M. I., Jung, J. H., Park, K. S., Seo, T. S., and Park, H. G. (2013). A novel colorimetric immunoassay utilizing the peroxidase mimicking activity of magnetic nanoparticles. *Int. J. Mol. Sci.* 14, 9999–10014. doi: 10.3390/ijms14059999

Wu, J., Wang, X., Wang, Q., Lou, Z., Li, S., Zhu, Y., et al. (2019). Nanomaterials with enzyme-like characteristics (nanozymes): next-generation artificial enzymes (II). *Chem. Soc. Rev.* 48, 1004–1076. doi: 10.1039/C8CS00457A

Xue, C.-C., M.-,Li, H., Zhao, Y., Zhou, J., Hu, Y., K.-,Cai, Y., et al. (2020). Tumor microenvironment-activatable Fe-doxorubicin preloaded amorphous $CaCO_3$ nanoformulation triggers ferroptosis in target tumor cells. *Sci. Adv.* 6:eaax1346. doi: 10.1126/sciadv.aax1346

Zanganeh, S., Hutter, G., Spitler, R., Lenkov, O., Mahmoudi, M., Shaw, A., et al. (2016). Iron oxide nanoparticles inhibit tumour growth by inducing pro-inflammatory macrophage polarization in tumour tissues. *Nat. Nanotechnol.* 11, 986–994. doi: 10.1038/nnano.2016.168

Zhang, J., Feng, C., Deng, Y., Liu, L., Wu, Y., Shen, B., et al. (2014). Shape-controlled synthesis of palladium single-crystalline nanoparticles: the effect of HCl oxidative etching and facet-dependent catalytic properties. *Chem. Mater.* 26, 1213–1218. doi: 10.1021/cm403591g

Zhang, S., Zhao, X., Niu, H., Shi, Y., Cai, Y., and Jiang, G. (2009). Superparamagnetic Fe3O4 nanoparticles as catalysts for the catalytic oxidation of phenolic and aniline compounds. *J. Hazard. Mater.* 167, 560–566. doi: 10.1016/j.jhazmat.2009.01.024

Zhang, W., Hu, S., J.-,Yin, J., He, W., Lu, W., Ma, M., et al. (2016). Prussian blue nanoparticles as multienzyme mimetics and reactive oxygen species scavengers. *J. Am. Chem. Soc.* 138, 5860–5865. doi: 10.1021/jacs.5b12070

Conflict of Interest: The authors declare that the research was conducted in the absence of any commercial or financial relationships that could be construed as a potential conflict of interest.

frontiers
in Chemistry

ORIGINAL RESEARCH
published: 18 September 2020
doi: 10.3389/fchem.2020.00671

Colorimetric Detection of Salicylic Acid in Aspirin Using MIL-53(Fe) Nanozyme

Ling Liang, Yaojing Huang, Wenren Liu, Weiyuan Zuo, Fanggui Ye[*†] *and Shulin Zhao*

State Key Laboratory for the Chemistry and Molecular Engineering of Medicinal Resources, College of Chemistry and Pharmaceutical Science of Guangxi Normal University, Guilin, China

The impurity of salicylic acid (SA) in aspirin is a required inspection item for drug quality control. Since free SA is significantly toxic for humans, the content determination of free SA is absolutely necessary to ensure people's health. In this work, a facile colorimetric method was developed for the detection of SA in aspirin by utilizing the MIL-53(Fe) nanozyme. As MIL-53(Fe) possesses enzyme mimicking catalytic activity, 3,3,5,5-tetramethylbenzidine (TMB) can be easily oxidized to blue-oxidized TMB (oxTMB) with the existence of H_2O_2. Moreover, an inhibition effect on the catalytic activity of the MIL-53(Fe) nanozyme is induced due to the specific complexation between SA and Fe^{3+} in the center of MIL-53(Fe), which results in a lighter color in the oxTMB. The color change of oxTMB can be seen easily by the naked eye with the addition of different concentrations of SA. Thus, a simple colorimetric platform was established for effectively monitoring SA. A good linear relationship ($R^2 = 0.9990$) was obtained in the concentration range of 0.4–28 μmol L^{-1}, and the detection limit was 0.26 μmol L^{-1}. In particular, the rationally designed system has been well-applied to the detection of SA impurity in aspirin. Satisfyingly, the detection results are highly in accord with those of HPLC. This novel colorimetric platform broadens the application prospects of nanozymes in the field of pharmaceutical analysis.

Keywords: aspirin, complexation, colorimetric detection, MIL-53(Fe), nanozyme, salicylic acid

OPEN ACCESS

Edited by:
Fan Zhang,
Fudan University, China

Reviewed by:
Yong Fan,
Fudan University, China
Lidan Hu,
Xiamen University, China

***Correspondence:**
Fanggui Ye
fangguiye@163.com

[†]**ORCID:**
Fanggui Ye
orcid.org/0000-0002-2530-3695

Specialty section:
This article was submitted to Nanoscience,
a section of the journal
Frontiers in Chemistry

Received: *25 May 2020*
Accepted: *29 June 2020*
Published: *18 September 2020*

Citation:
Liang L, Huang Y, Liu W, Zuo W, Ye F and Zhao S (2020) Colorimetric Detection of Salicylic Acid in Aspirin Using MIL-53(Fe) Nanozyme. Front. Chem. 8:671. doi: 10.3389/fchem.2020.00671

INTRODUCTION

Salicylic acid (SA), as a major phytohormone, generally plays an important role in regulating diverse physiological processes such as defense responses, thermogenesis, and germination (Wang et al., 2010; Marques et al., 2020). SA is a promising material and it is commonly exploited in the manufacture of pharmaceutical products (Kopp and Ghosh, 1994). Additionally, SA is widely used in the cosmetics industry as an organic acid (Chanakul et al., 2016). Thus, SA has broadened application prospects in many fields. However, SA is one of the common pollutants in industrial wastewater (Collado et al., 2010). More importantly, SA may cause some toxic side effects on the human body. Because of its relatively strong acidity, SA can not only stimulate and damage the mouth, esophagus, and gastric membrane, but can also invoke adverse symptoms such as metabolic disorders, ototoxicity, fetal malformations, and central nervous system depression (Tian et al., 2009). Aspirin, as a widely used drug, has the effects of an antipyretic, analgesic and anti-inflammatory (Dahl and Kehlet, 1991; Parham and Rahbar, 2009). However, SA can be easily produced due to the incomplete acetylation in the production process of aspirin or hydrolysis during the refining process and storage. Besides, the phenolic hydroxyl group in the free SA is readily oxidized and consequently form a series of colored quinone compounds, leading to discoloration of aspirin. There have corresponding safety limits for free SA in aspirin in countries around the world. From the above consideration, the contents of SA need to be frequently determined to ensure people's health.

There have been many analytical strategies for the detection of SA so far. For instance, one common analysis method is the spectrophotometric Trinder test, which is based on the formation of a coordination complex between SA and Fe^{3+} (Shokrollahi et al., 2017). Beyond that, many chromatography-based methods like high-performance liquid chromatography (HPLC) (Aboul-Soud et al., 2004; Croubels et al., 2005), gas chromatography (GC) (Tanchev et al., 1980), HPLC-MS/MS (Uddin et al., 2014), GC-MS (Huang et al., 2015), and ultra-HPLC (UHPLC) coupled MS/MS spectrometry (Floková et al., 2014), have been previously reported for SA detection. Capillary electrophoresis (CE) is an alternative to HPLC-based methods by virtue of the high separation efficiency and low solvent consumption advantages. Lin's group designed an iron oxide-based solid phase extraction system coupled to CE-UV for analyzing SA (Chang et al., 2017). This method shows excellent sensitivity for SA detection. Furthermore, there was an electrochemical sensor developed for determination of SA recently, in order to improve the sensitivity and accuracy, the composite of multi-wall carbon nanotubes (MWNT) and carbon black (CB) was fabricated, and ferrocene (Fc) was exploited as the reference molecule to offer a built-in correction (Hu et al., 2020). In addition, a work from Wang and co-workers reported that a nanosensor had been prepared based on the structure-switching strategy, and the SA aptamer showed a good affinity to SA (Chen et al., 2019).

In comparison with other methods, the colorimetric method has garnered extensive attention due to its superior responsiveness, portability, and practicality with no need for expensive and cumbersome instruments (Yan et al., 2020). Additionally, the detection result is easy to read out with visual inspection (Hao et al., 2013; Fan et al., 2017). In some research, a colorimetric assay has been developed for the detection of SA using TiO_2 NPs. This nanomaterial shows good selectivity for SA, however, the sensitivity of detection is limited (Tseng et al., 2014). In another report, Yang's group developed two rhodamine-based fluorescent probes that could realize bioimaging of SA (Wang et al., 2019a). This colorimetric sensor not only possesses good selectivity and sensitivity toward SA but detection is also observable with the naked-eye. At the same time, it has some shortcomings. The method is time-consuming, involves fussy operation steps, and it is difficult to fabricate probes using it. Previous studies have made it clear that nanozymes can be used in the field of colorimetric sensing owing to the advantages of simple preparation, low cost, and high catalytic activity. In particular, based on the improvement of enzyme catalytic activity, many studies have been carried out to achieve the purpose of colorimetric detection (Zhang et al., 2018; Li et al., 2019). Besides, most studies have focused on the design of nanozymes with different activities for colorimetric sensing of biothiols (Xiong et al., 2015; Song et al., 2020), dopamine (Wang et al., 2019b), glutathione reductase (Zhang et al., 2019), and acid phosphatase (Lin et al., 2020). These sensors generally achieve the goal of detection by using reduced substances to interfere with the oxidation of chromogenic substrates or to reduce oxTMB. However, these methods are usually affected by substances with strong reducibility, and thus the samples generally need to be pretreated. In contrast, few reports have been devoted to designing a scheme for specifically inhibiting the activity of nanozymes to ensure the selectivity of colorimetric sensing.

Thus, herein, inspired by the specific complexation reaction between SA and Fe^{3+}, and considering that no efforts have been made toward colorimetric detection of SA in aspirin by utilizing a metal-organic framework (MOF) nanozyme. we select MIL-53(Fe) as the nanozyme serving to achieve colorimetric detection of SA (**Figure 1**). As a result, the as-prepared MIL-53(Fe) shows high peroxidase-like activity in catalyzing 3,3,5,5-tetramethylbenzidine (TMB) oxidation and thus makes it a blue color in the presence of H_2O_2. Interestingly, because of the complexation reaction of SA and Fe^{3+} in the center of MIL-53(Fe), the catalytic activity of MIL-53(Fe) is inhibited significantly with the addition of SA. Based on this, a simple colorimetric sensor was successfully developed to detect SA. The proposed system furnishes a cost-effective, highly selective, and sensitive strategy for the colorimetric detection of SA and broadens the application potential of MOF nanozymes in the field of pharmaceutical analysis.

EXPERIMENTAL

Materials

Acetic acid (HAc), H_2O_2 (30 wt%), *N,N'*-dimethylformamide (DMF), sodium acetate (NaAc), salicylic acid (SA), and 1,4-benzenedicarboxylic acid (H_2BDC) were acquired from Beijing HWRK Chem Co., LTD. (China). Iron chloride hexahydrate ($FeCl_3 \cdot 6H_2O$) and TMB were bought from Shanghai Macklin Biochemical Co., Ltd. (China). All the chemicals mentioned above were analytical grade and used as received. Aspirin was purchased from Shanghai Titan Scientific Co., Ltd. Ultra-pure water came from the Millipore purification system (18.2 MΩ).

Apparatus

The powder X-ray diffraction (XRD) pattern of MIL-53(Fe) was recorded with a D/max 2,550 VB/PC diffractometer (Rigaku, Japan) using Cu Kα radiation ($\lambda = 0.15418$ nm). Scanning electron microscopy (SEM) and transmission electron microscopy (TEM) pictures were taken using Quanta 200 FEG (Netherlands) and Tecnai G2 20 (PE, USA), respectively. A Fourier transform infrared (FTIR) spectra was obtained from spectrum-2000 (USA). Thermogravimetric analysis (TGA) was carried out by the LABSYS evo TG-DSC/DTA instrument (Setaram Instrumentation, France). The UV-Vis absorption spectrum was recorded on the Cary 60 spectrophotometer (Agilent, USA). And HPLC was performed on the liquid chromatography instrument (Shimadzu, Japan) with the LC-20AT pump and the SPD-20A UV-vis detector.

Preparation of MIL-53(Fe)

MIL-53(Fe) was synthesized with a solvothermal method referring to the literature with a minor modification (Millange et al., 2010). Typically, 1.0812 g $FeCl_3 \cdot 6H_2O$ was dissolved in 20 mL of DMF solution before adding 0.6646 g of H_2BDC. After 10 min of intense stirring, the solution was transferred to a 50 mL stainless-steel autoclave and then heated at 150°C for 48 h. After natural cooling, the yellow precipitate was

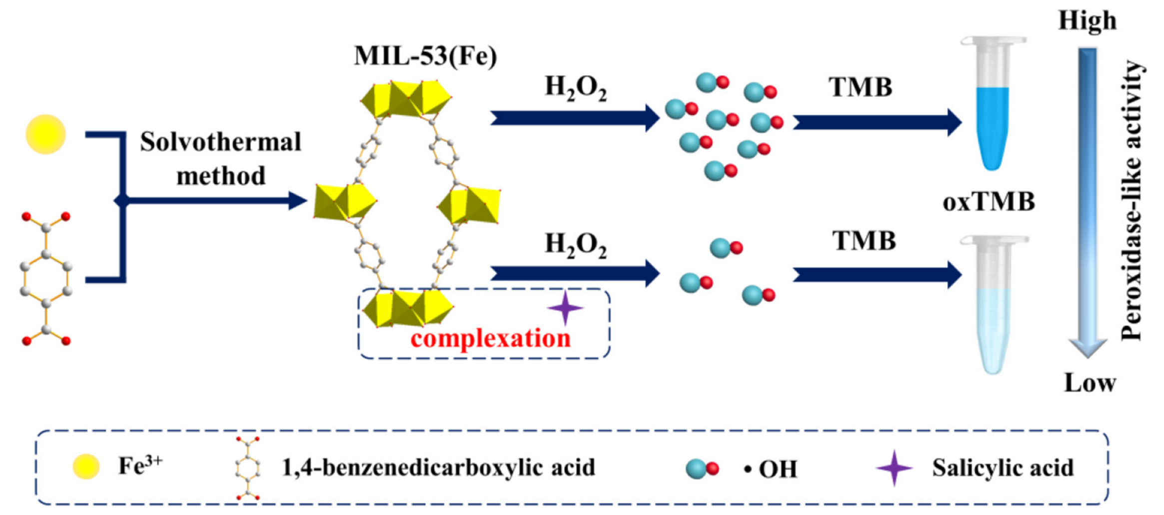

FIGURE 1 | Schematic illustration of MIL-53(Fe) synthesis and colorimetric detection of SA based on the MIL-53(Fe) nanozyme.

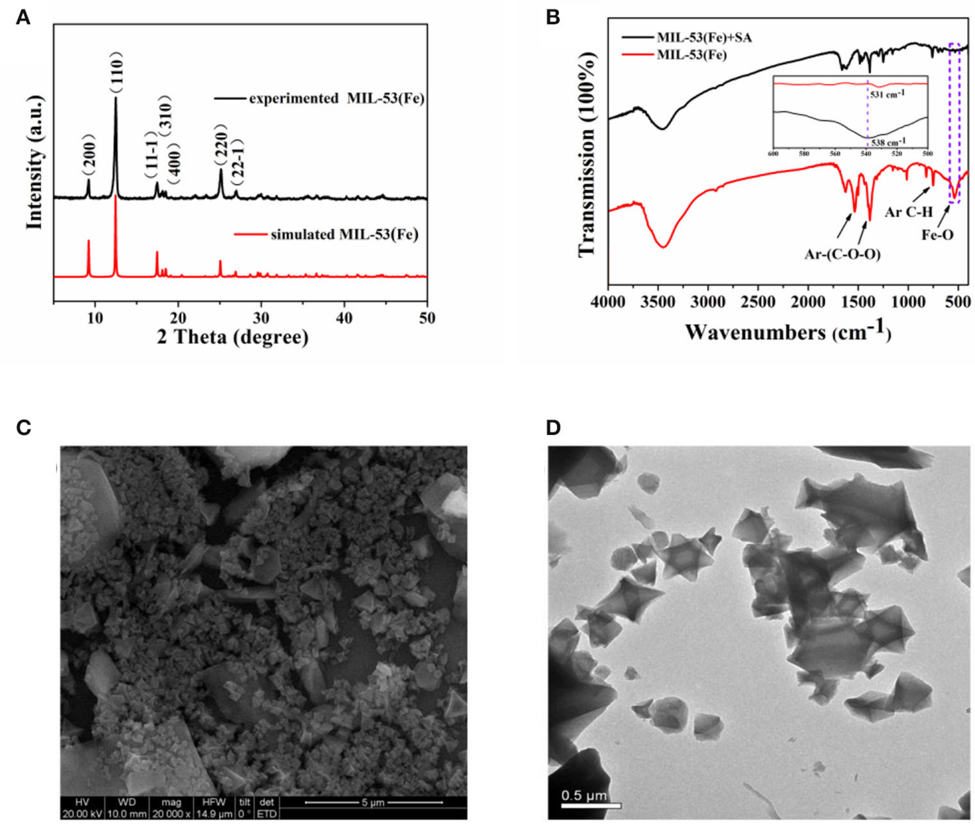

FIGURE 2 | (A) PXRD patterns of the as-prepared MIL-53(Fe) (black curve) and the simulated MIL-53(Fe) (red curve), **(B)** FTIR spectra of MIL-53(Fe) and MIL-53(Fe)+SA, **(C,D)** depicting the SEM and TEM images of MIL-53(Fe), respectively.

collected by centrifugation and washed with distilled water and ethanol. Finally, the yellow precipitate was dried in vacuum at 60°C overnight.

Detection of SA

To obtain a standard curve, SA detection was conducted as follows: 70 μL 1 mg/mL MIL-53(Fe) and 25 μL aliquots of SA solution of different concentrations were added to 875 μL 0.1 M pH 3.5 acetate buffers. After incubating for 4 min, 30 μL 4 mM TMB and 25 μL 0.1 M H_2O_2 were added to the above solution, and the solution was shaken and incubated at 37°C for 8 min. Finally, a Cary 60 spectrophotometer was used for analyzing the mixed solution.

Analysis of SA in Aspirin Sample

A standard addition method was applied for the determination of SA in aspirin. The sample was prepared as follows: 100 mg of aspirin powder was dissolved in 1% glacial acetic acid methanol solution (100 mL) and then filtered through a 0.45 μm filter paper. Next, the filtrate (100 μL) was placed in 0.1 M pH 3.5 acetate buffers. Subsequently, 70 μL 1 mg/mL of MIL-53(Fe) and different concentrations of SA were added. After incubating for 4 min, 30 μL 4 mM TMB and 25 μL 0.1 M H_2O_2 were added. At last, the mixture was incubated at 37°C for 8 min, the resulting solution was analyzed by the proposed colorimetric method, and the corresponding recoveries were obtained.

RESULTS AND DISCUSSION

Characterization of MIL-53(Fe)

The structure of MIL-53(Fe) was characterized first by XRD. As **Figure 2A** shows, particles of MIL-53(Fe) are highly crystalline, and the obvious sharp diffraction peaks correspond to the previously reported results as well as the simulated results (Lin et al., 2018). In addition, FTIR spectra was utilized for identifying the characteristic functional groups. As can be seen from **Figure 2B**, the spectrum clearly exhibits the typical asymmetrical and symmetrical vibration bands of carboxyl groups on the ligand, which indicates the existence of a dicarboxylate linker in MIL-53(Fe). Meanwhile, the C-H bending vibration of the benzene ring is observed and the stretching vibration of the Fe-O bond well-explains the formation of the metal-oxo cluster between Fe(III) and the carboxylic group of the organic linker. However, in the presence of SA, the absorption peak of the Fe-O bond shifted from 538 to 531 cm^{-1}, this result indicates that SA reacts with MIL-53(Fe) to form an iron salicylate complex. Furthermore, the morphology of MIL-53(Fe) was characterized by SEM and TEM. As shown by the images, the particles of MIL-53(Fe) have a very regular octahedron crystal structure (**Figures 2C,D**). Afterwards, the mass loss was explored via thermogravimetric analysis (TGA), it was ascertained that the first mass loss (∼39.27%) was due to the dehydration of MIL-53(Fe), and the subsequent mass loss (∼56.56%) corresponded to the collapse of MIL-53(Fe) into Fe_2O_3. The result from **Figure S1** is well-within the expected range according to the previous report (Millange et al., 2010). It could be concluded that MIL-53(Fe) was synthesized successfully with overall consideration in the characterization results above.

Detection Principle

In recent years, MIL-53(Fe) has been demonstrated exhibiting intrinsic peroxidase-mimicking catalytic activity and has been used for the colorimetric detection of ascorbic acid (AA) (Ai et al., 2013). In the presence of H_2O_2, the chromogenic substrates are oxidized with the catalytic effect of the MIL-53(Fe) nanozyme. As a result, the color of the solution is changed. In this work, a lighter color of oxTMB is created due to the inhibitory effect of SA on MIL-53(Fe) activity. Aiming at this phenomenon, a facile colorimetric platform was established to monitor SA (**Figure 1**). During the experiment, MIL-53(Fe) and

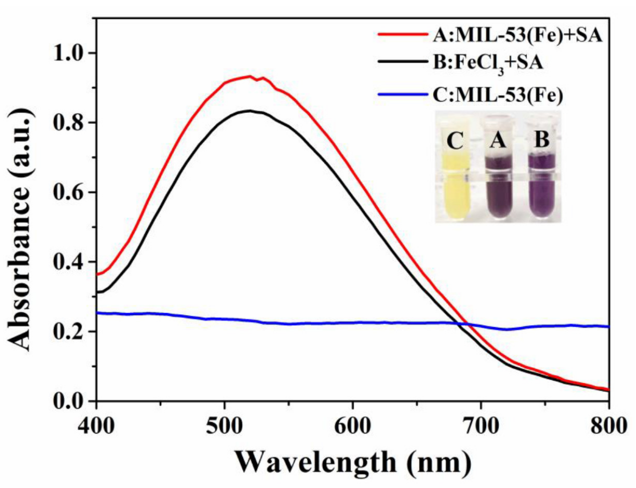

FIGURE 3 | The absorption peaks of SA-Fe(III) complex characterized by UV-Vis spectra: **(A)** MIL-53(Fe)+SA, **(B)** $FeCl_3$+SA, **(C)** MIL-53(Fe). Inset: the corresponding photograph of different systems.

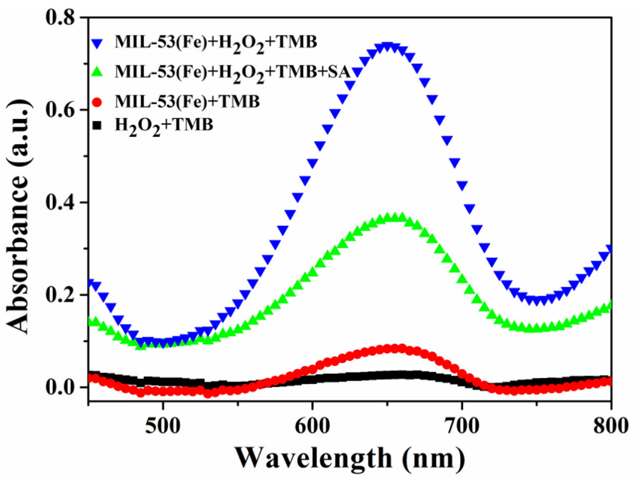

FIGURE 4 | UV-Vis absorbance spectra on the feasibility analysis for the detection of SA based on the MIL-53(Fe) nanozyme.

SA were incubated in an acetate buffer for 4 min, then TMB and H_2O_2 were added and the mixture was incubated at 37°C for 8 min. In the absence of SA, MIL-53(Fe) maintains its catalytic activity and a deep blue color for oxTMB emerges in the MIL-53(Fe)/TMB/H_2O_2 system. On the contrary, SA has strong complexation ability with Fe^{3+} in the center of MIL-53(Fe). After the addition of SA, the peroxidase-like activity of MIL-53(Fe) is significantly inhibited due to the reaction of SA and Fe^{3+} (**Figure 1**). Consequently, the catalytic oxidation of TMB begins to decelerate, enabling the blue color solution to lighten. The

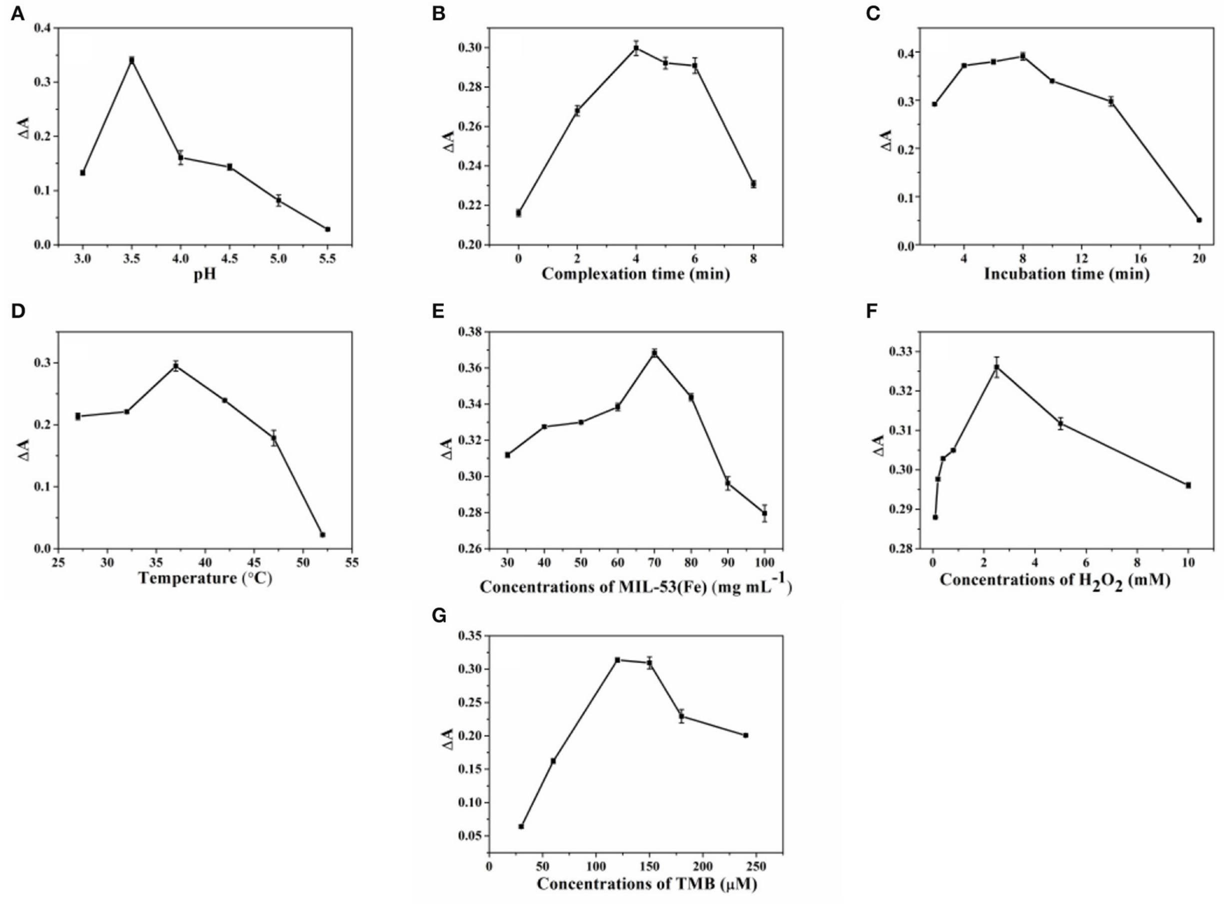

FIGURE 5 | The optimization of **(A)** pH, **(B)** complexation time, **(C)** incubation time, **(D)** temperature, and concentrations of **(E)** MIL-53(Fe), **(F)** H_2O_2, and **(G)** TMB for SA sensing. Error bars represent the standard deviation of the three trials.

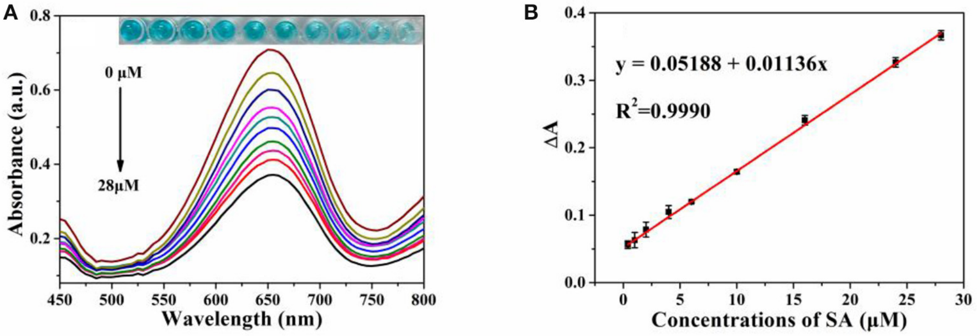

FIGURE 6 | (A) The vis absorption spectra of MIL-53(Fe)-TMB-H_2O_2 upon concentrations of SA (from 0 to 28 μmol L^{-1}). Inset: the corresponding photograph of the colored products; **(B)** The linear relationship between absorbance intensity (ΔA) and SA level. Error bars represent the standard deviation of three trials.

color change is easy to identify by the naked eye. The catalytic activity of MIL-53(Fe) and the absorption intensity of oxTMB at 652 nm are dependent on the SA concentration. Thus, the MIL-53(Fe)/TMB/H_2O_2 system is capable for the colorimetric detection of SA.

To illuminate the mechanism of inhibitory effects of SA on the MIL-53(Fe) activity, the purple complex of SA-Fe(III) was characterized by UV-Vis absorbance spectroscopy. As revealed by **Figure 3**, a conspicuous absorption peak at ∼520 nm appears when $FeCl_3$ is used as the standard sample to incubate with SA (Chang et al., 2017; Bodek et al., 2020), and the color of the solution changes to purple. Likewise, the same absorption peak at 520 nm occurs when MIL-53(Fe) and SA are incubated together. The solution of MIL-53(Fe) is yellow and has turned a dark purple color with the addition of SA. Obviously, no peak appears at 520 nm when there is only MIL-53(Fe) in the solution. What this suggests is that Fe(III) in the center of MIL-53(Fe) forms a purple complex with SA and results in the inhibited activity of MIL-53(Fe).

To further demonstrate the inhibitory effect of SA on the peroxidase-like activity of MIL-53(Fe), the production of hydroxyl radical (·OH) within the reaction was investigated. Electron spin resonance (ESR) spectroscopy was carried out with 5,5-dimethylpyrroline N-oxide (DMPO) as the ·OH trapping agent (Zhao et al., 2019). As depicted in **Figure S2**, it shows typical ·OH signals in the MIL-53(Fe)+H_2O_2 system. However, the signal intensity is obviously decreased with the addition of SA. To be specific, as Fe^{3+} ions in the center of MIL-53(Fe) are Fenton-like reagents, they can catalyze the decomposition of H_2O_2 into ·OH via a Fenton-type reaction (Yao et al., 2018). In the meantime, the redox cycle of Fe^{3+}/Fe^{2+} is decelerated due to the complexation of SA to Fe^{3+}. Consequently, the production of hydroxyl radical (·OH) in the reaction is decreased. This also proves that the catalytic activity of MIL-53(Fe) is inhibited by SA.

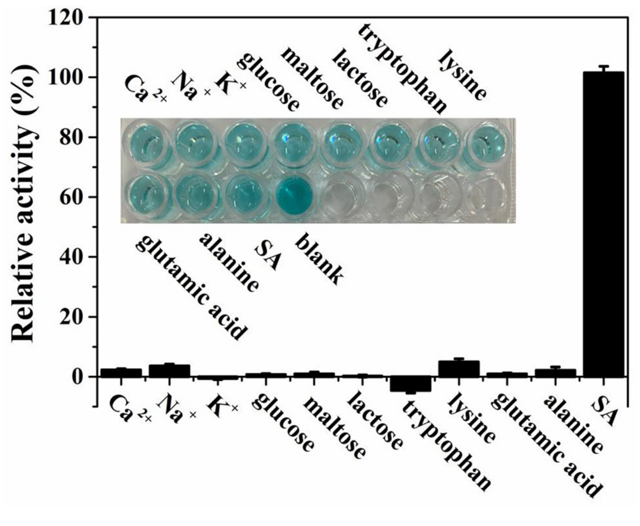

FIGURE 7 | Selectivity for SA detection with existence of several possible coexisting substances based on theMIL-53(Fe)-TMB-H_2O_2 system. The inset shows the corresponding photograph of the interference experiment.

Feasibility of SA Detection by MIL-53(Fe) Nanozyme

A feasibility test for SA detection was performed and the result is displayed in **Figure 4**. Obviously, the highest absorption peak occurs when MIL-53(Fe), H_2O_2, and TMB are mixed and incubated together, this is ascribed to the potential peroxidase-like activity of the as-prepared MIL-53(Fe). Additionally, no obvious absorption peak can be observed during either of the two groups (the group of H_2O_2+TMB or MIL-53(Fe)+TMB). What is interesting, however, is that while SA is added to the MIL-53(Fe)/TMB/H_2O_2 system, the absorption peak intensity is decreased significantly. As we know, SA has good strong complexation ability to Fe^{3+} ions, thereby forming iron salicylate complexes. That might be the reason why SA has an effective inhibitory effect on the catalytic activity of MIL-53(Fe). In brief, the proposed colorimetric method is built on the inhibitory effect of SA on the inherent activity of the MIL-53(Fe) nanozyme.

Optimization of Experimental Conditions

In realizing the best performance in SA detection, the influence of the experimental conditions, such as pH, complexation time, incubation time, temperature, and concentrations of MIL-53(Fe), H_2O_2, and TMB, were investigated. Since the activity of MIL-53(Fe) and the reaction of MIL-53(Fe) with SA are closely related to the pH value, therefore the effects of different pH values (3.0, 3.5, 4.0, 4.5, 5.0, and 5.5) were first studied. ΔA (A-A_0, A, and A_0 represent the absorbance of the system without or with SA, respectively), is used as the index to evaluate the best conditions for the detection of SA. As can be seen from **Figure 5A**, it is clear that the value of ΔA reaches a peak at pH 3.5. This can be explained by the fact that the activity of MIL-53(Fe) and the complexation ability of MIL-53(Fe) with SA is higher at pH 3.5. Consequently, 3.5 was chosen as the optimal pH value. **Figures 5B,C** clearly show that along with the increase of reaction time, the absorbance intensity (ΔA) starts to decrease after 4 and 8 min, indicating that 4 min was the most satisfactory time for MIL-53(Fe) to bind with SA and 8 min was the most suitable incubation time for the experiment. Moreover, the optimal temperature from 27 to 52°C was further discussed. As seen from **Figure 5D**, the value of ΔA declined dramatically as the temperature reached 37°C, hence, 37°C was considered as the optimal temperature for the reaction. Furthermore, the concentration of MIL-53(Fe) plays a key role in its catalytic activity. **Figure 5E** exhibits that with an increasing MIL-53(Fe) concentration, the ΔA value increased gradually

TABLE 1 | The recovery test of our assay for detecting SA in Pharmaceutical samples.

Sample	Original amount (μM)	Spiked (μM)	Found (μM)	Recovery (%)	RSD (%, *n* = 3)
Sample 1	1.55	12	10.92	91.0	4.2
		20	18.61	93.0	3.8
Sample 2	2.37	10	9.97	99.7	3.0
		14	13.7	98.0	4.0
Sample 3	3.83	8	8.11	101.4	2.0
		16	15.39	96.2	3.5

until 70 μg L^{-1}, showing that the concentrations of 70 μg L^{-1} of MIL-53(Fe) is sufficient for detecting SA. Additionally, **Figures 5F,G** depicted that TMB and H_2O_2 concentrations have an effect on the absorbance intensity. The value of ΔA reached the top as the concentrations of TMB and H_2O_2 increased to 120 μM and 2.5 mM, respectively. Overall, after optimization, 3.5, 4 min, 8 min, 37°C, 70 μg L^{-1}, 120 μM, and 2.5 mM are shown to be the optimal pH value, complexation time, incubation time, temperature, and concentrations of MIL-53(Fe), H_2O_2, and TMB.

Colorimetric Detection of SA

Since the addition of SA can significantly inhibit the peroxidase-like activity of MIL-53(Fe), a colorimetric assay for the determination of SA was developed. Under the optimal experimental conditions, different concentrations of the SA solution were added to the MIL-53(Fe)/TMB/H_2O_2 system. Meanwhile, the mixed solution was detected and the obtained absorption spectrum was analyzed. Eventually, the limit of detection (LOD) was calculated by using the signal-to-noise ratio (S/N = 3) (He et al., 2018). As revealed by **Figure 6A**, absorbance intensities at 652 nm decreased gradually as the concentrations of SA increased from 0 to 28 μmol L^{-1}, and the color change of oxTMB is visible to the naked eye. In the meantime, as depicted in **Figure 6B**, there was an excellent linear relationship between absorbance intensity (ΔA) and SA concentrations in the range of 0.4–28 μmol L^{-1} ($R^2 = 0.9990$), and the LOD was calculated to be 0.26 μmol L^{-1}. The Chinese Pharmacopeia (edition 2015), set a standard that the maximum limit of SA in aspirin is 0.3% (2.16 μmol L^{-1}). Hence, the value of LOD (0.26 μmol L^{-1}) was lower than the safety limits. Furthermore, the LOD value and linear ranges of our method are compared with those of other methods. As shown in **Table S1**, the sensitivity of our measurement was superior to most previously reported values, indicating that the established method was appropriate for SA detection.

Selectivity of the Colorimetric Biosensor

In order to study the selectivity of our assay toward SA detection, possible coexisting substances including some metal ions, amino acids, and carbohydrates were used for investigating under the optimal experimental conditions. As demonstrated in **Figure 7**, obviously, only the species SA can induce a significant absorption intensity when the concentrations of SA and possible coexisting substances are both 28 μmol L^{-1}. Additionally, as illustrated in the inset of **Figure 7**, there was no interference with the color change in the presence of other coexisting substances. All the results above show that the biosensor designed for colorimetric detection of SA was highly selective.

Detection of SA in Aspirin Samples

To confirm the reliability of the developed platform for colorimetric detection of SA, the original amount of SA in aspirin was first measured by using the HPLC method (**Figure S3**), and the detection results were compared with those obtained by colorimetry. As displayed in **Table 1**, the detected SA concentrations by the proposed strategy have shown satisfactory agreement in comparison with the measured data from HPLC, the relative error was within 5%. Meanwhile, to further investigate the precision and practicability of our assay, a spike recovery test was carried out. As demonstrated by **Table S2**, it shows that a meaningful recovery of 91.0–101.4% was obtained and the value of RSD ranged from 2.0 to 4.2%. In a word, the results proved the potential of this proposed method in practical applications.

CONCLUSIONS

In this study, we confirmed that the obtained MIL-53(Fe) possessed inherent peroxidase-mimicking activity, as they were equipped to catalyze the oxidation of chromogenic TMB in the presence of H_2O_2. Meanwhile, based on the strong complexing action between the Fe^{3+} in the center of MIL-53(Fe) and SA, the activity of MIL-53(Fe) can be effectively inhibited with the addition of SA, causing fewer hydroxyl radicals to be produced in the system to decelerate the oxidation of TMB. The experimental results clearly displayed that a lighter color for the oxTMB can be observed with naked eye. By combining the peroxidase-mimicking properties of MIL-53(Fe) and the inhibitory effect of SA on its activity, a colorimetric sensing platform for the detection of SA was established. The developed colorimetric method not only has excellent accuracy in detecting SA in aspirin compared with HPLC but also shows high selectivity and sensitivity to SA. In summary, the proposed method can be well-utilized for detecting SA in aspirin. Furthermore, the present work displays the great potential of using MOFs nanozymes for pharmaceutical analysis.

DATA AVAILABILITY STATEMENT

The raw data supporting the conclusions of this article will be made available by the authors, without undue reservation.

AUTHOR CONTRIBUTIONS

LL: conceptualization, methodology, data curation, investigation, and writing original draft. YH: conceptualization, methodology, data curation, and investigation. WL: data curation and investigation. WZ: investigation. FY: visualization, resources, funding acquisition, supervision, project administration, writing—review, and editing. SZ: funding acquisition and project administration. All authors contributed to the article and approved the submitted version.

FUNDING

This work was supported by the National Natural Science Foundations of China (21765002), Guangxi Natural Science Foundation of China (2017GXNSFDA198044), and the BAGUI Scholar Program.

SUPPLEMENTARY MATERIAL

The Supplementary Material for this article can be found online at: https://www.frontiersin.org/articles/10.3389/fchem.2020.00671/full#supplementary-material

REFERENCES

Aboul-Soud, M. A. M., Cook, K., and Loake, G. J. (2004). Measurement of salicylic acid by a high-performance liquid chromatography procedure based on ion-exchange. *Chromatographia* 59, 129–133. doi: 10.1365/s10337-003-0136-1

Ai, L. H., Li, L. L., Zhang, C. H., Fu, J., and Jiang, J. (2013). MIL-53(Fe): a metal-organic framework with intrinsic peroxidase-like catalytic activity for colorimetric biosensing. *Chem. Eur. J.* 19, 15105–15108. doi: 10.1002/chem.201303051

Bodek, M., Burch, M., Cannon, J., Finneran, D., Geveke, K., Sinkinson, H., et al. (2020). Revisiting the determination of percent aspirin lab: using a limiting reactant approach for students to also determine the amount of iron (III) chloride. *J. Chem. Educ.* 97, 574–577. doi: 10.1021/acs.jchemed.9b00154

Chanakul, A., Traiphol, R., and Traiphol, N. (2016). Colorimetric sensing of various organic acids by using polydiacetylene/zinc oxide nanocomposites: effects of polydiacetylene and acid structures. *Colloids Surf. A* 489, 9–18. doi: 10.1016/j.colsurfa.2015.09.068

Chang, Y. H., Huang, C. W., Fu, S. F., Wu, M. Y., Wu, T., and Lin, Y. W. (2017). Determination of salicylic acid using a magnetic iron oxide nanoparticle-based solid-phase extraction procedure followed by an online concentration technique through micellar electrokinetic capillary chromatography. *J. Chromatogr. A* 1479, 62–70. doi: 10.1016/j.chroma.2016.12.018

Chen, C., Feng, S., Zhou, M., Ji, C., Que, L., and Wang, W. (2019). Development of a structure-switching aptamer-based nanosensor for salicylic acid detection. *Biosens. Bioelectron* 140:111342. doi: 10.1016/j.bios.2019.111342

Collado, S., Garrido, L., Laca, A., and Diaz, M. (2010). Wet oxidation of salicylic acid solutions. *Environ. Sci. Technol.* 44, 8629–8635. doi: 10.1021/es1021944

Croubels, S., Maes, A., Baert, K., and De Backer, P. (2005). Quantitative determination of salicylic acid and metabolites in animal tissues by liquid chromatography–tandem mass spectrometry. *Anal. Chim. Acta* 529, 179–187. doi: 10.1016/j.aca.2004.08.020

Dahl, J. B., and Kehlet, H. (1991). Non-steroidal anti-inflammatory drugs: rationale for use in severe postoperative pain. *Br. J. Anaesth.* 66, 703–712. doi: 10.1093/bja/66.6.703

Fan, S., Zhao, M., Ding, L., Li, H., and Chen, S. (2017). Preparation of Co_3O_4/crumpled graphene microsphere as peroxidase mimetic for colorimetric assay of ascorbic acid. *Biosens. Bioelectron.* 89, 846–852. doi: 10.1016/j.bios.2016.09.108

Floková, K., Tarkowská, D., Miersch, O., Strnad, M., Wasternack, C., and Novák, O. (2014). UHPLC–MS/MS based target profiling of stress-induced phytohormones. *Phytochemistry* 105, 147–157. doi: 10.1016/j.phytochem.2014.05.015

Hao, Y., Xiong, D., Wang, L., Chen, W., Zhou, B., and Liu, Y. N. (2013). A reversible competition colorimetric assay for the detection of biothiols based on ruthenium-containing complex. *Talanta* 115, 253–257. doi: 10.1016/j.talanta.2013.04.076

He, Y. F., Li, X., Xu, X. C., Pan, J. M., and Niu, X. H. (2018). A cobalt-based polyoxometalate nanozyme with high peroxidase-mimicking activity at neutral pH for one-pot colorimetric analysis of glucose. *J. Mater. Chem. B* 6, 5750–5755. doi: 10.1039/C8TB01853G

Hu, Y., Wang, X., Wang, C., Hou, P., Dong, H., and Luo, B. (2020). A multifunctional ratiometric electrochemical sensor for combined determination of indole-3-acetic acid and salicylic acid. *RSC Adv.* 10, 3115–3121. doi: 10.1039/C9RA09951D

Huang, Z. H., Wang, Z. L., Shi, B. L., Wei, D., Chen, J. X., Wang, S. L., et al. (2015). Simultaneous determination of salicylic acid, jasmonic acid, methyl salicylate, and methyl jasmonate from ulmus pumila leaves by GC-MS. *Int. J. Anal. Chem.* 2015:698630. doi: 10.1155/2015/698630

Kopp, E., and Ghosh, S. (1994). Inhibition of NF-kappa B by sodium salicylate and aspirin. *Science* 265, 956–959. doi: 10.1126/science.8052854

Li, Z. M., Zhong, X. L., Wen, S. H., Zhang, L., Liang, R. P., and Qiu, J. D. (2019). Colorimetric detection of methyltransferase activity based on the enhancement of CoOOH nanozyme activity by ssDNA. *Sens. Actuators B* 281, 1073–1079. doi: 10.1016/j.snb.2018.11.085

Lin, T. R., Qin, Y. M., Huang, Y. L., Yang, R. T., Hou, L., Ye, F. G., et al. (2018). A label-free fluorescence assay for hydrogen peroxide and glucose based on the bifunctional MIL-53 (Fe) nanozyme, *Chem. Commun.* 54, 1762–1765. doi: 10.1039/C7CC09819G

Lin, Z., Zhang, X. M., Liu, S. J., Zheng, L. L., Bu, Y. M., Deng, H. H., et al. (2020). Colorimetric acid phosphatase sensor based on MoO_3 nanozyme. *Anal. Chim. Acta.* 1105, 162–168. doi: 10.1016/j.aca.2020.01.035

Marques, T. L., Moraes, L. M. B., and Rocha, F. R. P. (2020). Systematic evaluation of sample preparation for fractionation of phytohormone salicylic acid in fresh leaves. *Talanta* 208:120352. doi: 10.1016/j.talanta.2019.120352

Millange, F., Guillou, N., Medina, M. E., Férey, G., Carlin-Sinclair, A., Golden, K. M., et al. (2010). Selective sorption of organic molecules by the flexible porous hybrid metal-organic framework MIL-53(Fe) controlled by various host-guest interactions. *Chem. Mater.* 22, 4237–4245. doi: 10.1021/cm1008587

Parham, H., and Rahbar, N. (2009). Solid phase extraction-spectrophotometric determination of salicylic acid using magnetic iron oxide nanoparticles as extractor. *J. Pharm. Biomed. Anal.* 50, 58–63. doi: 10.1016/j.jpba.2009.03.037

Shokrollahi, A., Mohammadpour, Z., and Abbaspour, A. (2017). Colorimetric determination of free salicylic acid in aspirin and urine by scanometry as a new, reliable, inexpensive and simple method. *Pharm. Chem. J.* 51, 324–329. doi: 10.1007/s11094-017-1607-2

Song, C., Ding, W., Zhao, W., Liu, H. B., Wang, J., Yao, Y. W., et al. (2020). High peroxidase-like activity realized by facile synthesis of FeS_2 nanoparticles for sensitive colorimetric detection of H_2O_2 and glutathione. *Biosens. Bioelectron* 151:111983. doi: 10.1016/j.bios.2019.111983

Tanchev, S., Ioncheva, N., Genov, N., and Malchev, E. (1980). Gas chromatographic identification of phenolic acids found in sweet cherry and sour cherry juice. *Mol. Nutr. Food Res.* 24, 251–253. doi: 10.1002/food.19800240307

Tian, M., Adams, B., Wen, J., Asmussen, R. M., and Chen, A. (2009). Photoelectrochemical oxidation of salicylic acid and salicylaldehyde on titanium dioxide nanotube arrays. *Electrochim. Acta* 54, 3799–3805. doi: 10.1016/j.electacta.2009.01.077

Tseng, P. J., Wang, C. Y., Huang, T. Y., Chuang, Y. Y., Fu, S. F., and Lin, Y. W. (2014). A facile colorimetric assay for determination of salicylic acid in tobacco leaves using titanium dioxide nanoparticles. *Anal. Methods* 6, 1759–1765. doi: 10.1039/C3AY42209G

Uddin, N., Krieg, C., Stöggl, W., Stecher, G., Abel, G., Popp, M., et al. (2014). Quantitative analysis of salicylic acid and its derivatives in primulae radix by high performance liquid chromatography-diode array detection-electrospray ionization mass spectrometry (HPLC-DAD-ESI-MS) and simultaneous determination of total polyphenol content (TPC). *Curr. Anal. Chem.* 10, 271–279. doi: 10.2174/15734110113099990015

Wang, J., Hu, Y. Y., Zhou, Q., Hu, L. Z., Fu, W. S., and Wang, Y. (2019b). Peroxidase-like activity of metal-organic framework [Cu(PDA)(DMF)] and its application for colorimetric detection of dopamine. *ACS Appl. Mater. Interfaces* 11, 44466–44473. doi: 10.1021/acsami.9b17488

Wang, P. Y., Luo, X., Yang, L. L., Zhao, Y. C., Dong, R., Li, Z., et al. (2019a). A rhodamine-based highly specific fluorescent probe for the *in situ* and *in vivo* imaging of the biological signalling molecule salicylic acid. *Chem. Commun.* 55, 7691–7694. doi: 10.1039/C9CC03094H

Wang, Z., Ai, F., Xu, Q., Yang, Q., Yu, J. H., Huang, W. H., et al. (2010). Electrocatalytic activity of salicylic acid on the platinum nanoparticles modified electrode by electrochemical deposition. *Colloids Surf. B* 76, 370–374. doi: 10.1016/j.colsurfb.2009.10.038

Xiong, Y. H., Chen, S. H., Ye, F. G., Su, L. J., Zhang, C., Shen, S. F., et al. (2015). Synthesis of a mixed valence state Ce-MOF as an oxidase mimetic for the colorimetric detection of biothiols. *Chem. Commun.* 51, 4635–4638. doi: 10.1039/C4CC10346G

Yan, Z., Yuan, H., Zhao, Q., Xing, L., Zheng, X., Wang, W., et al. (2020). Recent developments of nanoenzyme-based colorimetric sensors for heavy metal detection and the interaction mechanism. *Analyst* 145, 3173–3187. doi: 10.1039/D0AN00339E

Yao, C., Wang, W. X., Wang, P. Y., Zhao, M. Y., Li, X. M., and Zhang, F. (2018). Near-infrared upconversion mesoporous cerium oxide hollow biophotocatalyst for concurrent pH-/H_2O_2-Responsive O_2-evolving synergetic cancer therapy. *Adv. Mater.* 30:1704833. doi: 10.1002/adma.201704833

Zhang, Y., Dai, C. L., Liu, W., Wang, Y. Y., Ding, F., Zou, P., et al. (2019). Ultrathin films of a metal-organic framework prepared from 2-methylimidazole, manganese(II) and cobalt(II) with strong oxidase-mimicking activity for colorimetric determination of glutathione and glutathione reductase activity. *Microchim. Acta* 186, 1–9. doi: 10.1007/s00604-019-3434-5

Zhang, Y., Zhang, W. T., Chen, K., Yang, Q. F., Hu, N., Suo, Y. R., et al. (2018). Highly sensitive and selective colorimetric detection of glutathione via enhanced fenton-like reaction of magnetic metal organic framework. *Sens. Actuators B* 262, 95–101. doi: 10.1016/j.snb.2018.01.221

Zhao, P. R., Tang, Z. M., Chen, X. Y., He, Z. Y., He, X. H., Zhang, M., et al. (2019). Ferrous-cysteine-phosphotungstate nanoagent with neutral pH fenton reaction activity for enhanced cancer chemodynamic therapy. *Mater. Horiz.* 6, 369–374. doi: 10.1039/C8MH01176A

Conflict of Interest: The authors declare that the research was conducted in the absence of any commercial or financial relationships that could be construed as a potential conflict of interest.

frontiers in Chemistry

MINI REVIEW
published: 29 September 2020
doi: 10.3389/fchem.2020.00764

The Role of Nanomaterials in Modulating the Structure and Function of Biomimetic Catalysts

Yanyan Huang[1], Deshuai Yu[2], Yibin Qiu[1], Lanlin Chu[1] and Youhui Lin[2]*

[1] *College of Light Industry and Food Engineering, Nanjing Forestry University, Nanjing, China,* [2] *Fujian Provincial Key Laboratory for Soft Functional Materials Research, Department of Physics, Research Institute for Biomimetics and Soft Matter, Xiamen University, Xiamen, China*

Nanomaterial-incorporated enzyme mimics have so far been examined in various cases, and their properties are governed by the properties of both catalysts and materials. This review summarizes recent efforts in understanding the role of inorganic nanomaterials for modulating biomimetic catalytic performance. Firstly, the importance of enzyme mimics, and the necessity for tuning their catalysis will be outlined. Based on structural characteristics, these catalysts are divided into two types: traditional artificial enzymes, and novel nanomaterial-based enzyme mimics. Secondly, the mechanisms on how nano-sized materials interact with these catalysts will be examined. Intriguingly, incorporating various nanomaterials into biomimetic catalysts may provide a convenient and highly efficient method for the modulation of activities as well as stabilities or introduce new and attractive features. Finally, the perspectives of the main challenges and future opportunities in the areas of nanomaterial-incorporated biomimetic catalysis will be discussed. In this regard, nanomaterials as a kind of promising scaffold for tuning catalysis will attract more and more attention and be practically applied in numerous fields.

Keywords: enzyme mimic, structure and function, catalysis, nanomaterial, natural enzyme

Edited by:
Zoe Pikramenou,
University of Birmingham,
United Kingdom

Reviewed by:
Xiaopeng Han,
Tianjin University, China
Guillermo Javier Copello,
Consejo Nacional de Investigaciones
Científicas y Técnicas
(CONICET), Argentina

***Correspondence:**
Youhui Lin
linyouhui@xmu.edu.cn

Specialty section:
This article was submitted to
Nanoscience,
a section of the journal
Frontiers in Chemistry

Received: *30 April 2020*
Accepted: *23 July 2020*
Published: *29 September 2020*

Citation:
Huang Y, Yu D, Qiu Y, Chu L and Lin Y (2020) The Role of Nanomaterials in Modulating the Structure and Function of Biomimetic Catalysts.
Front. Chem. 8:764.
doi: 10.3389/fchem.2020.00764

INTRODUCTION

Owing to their excellent catalytic efficiency, unique mechanistic pathways, and complicated structural features, natural enzymes have become a tremendous source of inspiration for chemists. Numerous studies have concentrated on the simulation of their structural characteristics and functions (Hooley, 2016). So far, a variety of synthetic structures, such as porphyrins, cyclodextrins, organoselenium, and metal complexes, have been widely explored to design and construct artificial enzymes through various approaches (Dong et al., 2012; Du et al., 2017; Elemans and Nolte, 2019). In recent years, with the development of nanotechnology, many functional nanomaterials have emerged. Carbon-based, silicon-based, and metal-based nanomaterials are often endowed with properties such as large specific surface areas, easy surface modification, and high recycling efficiency. The rapid development of nanotechnology and biology has provided new opportunities for the construction of different nano-scaled structures with enzyme-like catalytic properties (Jiang et al., 2019; Liang and Yan, 2019; Wu et al., 2019). With the assistance of nanomaterials, active molecules or nanoparticles can be well-dispersed. Furthermore, bi- or multi-active components can be assembled in one nano-scaled system successfully. As a new generation of artificial enzymes, such nanocatalysts, including Fe_3O_4 (MNPs) (Gao et al., 2007), CeO_2 (Xu and Qu, 2014), V_2O_5 (Ghosh et al., 2018), AuNPs

(Gao et al., 2015), MoS_2 nanosheets (Yin et al., 2016), graphene oxide (GO) and few-layer grapheme (Song et al., 2010), and other types of nanoparticles (Singh et al., 2017) are particularly impressive. Note: although the assembly of active components such as metal complexes and porphyrins on nanomaterial-based supports leads to the generation of nanocomposites (Wang et al., 2013; Huang Y. Y. et al., 2017), these examples treated in this review are categorized into traditional artificial enzymes, instead of nanomaterials-based artificial enzymes. The synthetic biocatalysts often possess the properties such as low cost, easy preparation, and anti-biodegradation as well as anti-denaturation when compared with natural enzymes (Huang et al., 2019). Although promising, the inherent limitations of the native forms hamper their practical applications. It is worth noting that these mimics often have relatively low catalytic performances. In this way, they can't match the high catalytic activities of natural enzymes. Furthermore, it is highly desirable that the generated enzyme mimics not only simply duplicate and mimic natural enzymes' inherent characteristics, but also may exhibit further novel properties for biological applications. Based on these unique and attractive features mentioned above, nanomaterials may also provide excellent scaffolds to the development of biomimetic catalysis for potential applications (Fan et al., 2018; Han et al., 2019, 2020).

Recently, numerous efforts have been devoted to exploring the behavior of nanomaterials in biomimetic systems (Wang et al., 2019). This review aims to provide an overview on recent developments in tuning biomimetic catalysis using nanoscale inorganic materials (**Figure 1**). The incorporation of nanomaterials into biomimetic catalysts provides a convenient and highly efficient method for the modulation of activities as well as the stabilities of catalysts. Alternatively, this can introduce unique and attractive features, which are not possessed by the catalysts themselves. The biomimetic catalysts discussed in this review can be roughly divided into two types according to their structural characteristics, which are traditional artificial enzymes and nanomaterials-based artificial enzymes. We hope this review may accelerate further progress in these promising areas.

TRADITIONAL ARTIFICIAL ENZYMES MODULATION

One challenge in chemistry has been the construction of synthetic systems that mimic the functions of natural enzymes. Until now, the artificial enzyme field has achieved remarkable progress. Furthermore, the incorporation of nanomaterials into these mimics have great potential for tailoring their catalytic activities and introducing other attractive features. This section will discuss nanomaterials when they interact with active molecules with enzyme-like properties.

Tuning Catalysis of Active Molecules

Nanomaterials for Minimizing Dimerization and Oxidative Degradation

Metal-organic-frameworks (MOFs) and their derivatives have served as outstanding supports for heterogeneous catalysis owing to their unique features such as large specific surface areas, excellent electron transfer ability as well as rich surface chemistry. Inspired by this, a study demonstrated that metalloporphyrins could be successfully assembled with secondary binding units of metal clusters to form 2D bimetallic MOF nanosheets (Wang et al., 2016). It is well-known that porphyrin molecules easily form dimers, which may affect their catalytic activity. After self-assembling, the obtained nanomaterials could efficiently disperse the metalloporphyrins and achieve an excellent biomimetic property to catalyze the co-oxidation reaction. Based on this work, Zhang et al. further designed Au-modified metalloporphyrinic MOF nanosheets. The obtained nanocomposites could efficiently disperse both Au nanoparticles and metalloporphyrin molecules. In this way, the nanocomposite could serve as a biomimetic catalyst for glucose-H_2O_2 cascade reaction (Huang Y. Y. et al., 2017).

Nanomaterials for Increasing Binding Affinity to Substrates

Natural enzymes have extraordinarily high catalytic efficiency. This is largely owing to their ability to bring corresponding substrates close to their active sites. Zhang et al. found that graphene oxide (GO) could dramatically increase the nuclease-like activity of the copper complexes-based DNA intercalators (Zheng et al., 2012). In their system, the copper complexes could be modified onto the surface of GO *via* π-π interaction. The nuclease activity of the resulting conjugates was significantly higher than that of the copper complexes alone. One reason for the DNA cleavage enhancement by GO is that the obtained conjugates have a much higher binding affinity to the DNA molecules. Furthermore, another reason may be related to the generation of reactive species by accelerating the reduction of the metal center (Zheng et al., 2014).

Nanomaterials for Constructing Multivalent Catalysts

A previous review on catalysis by colloid aggregates mentioned "…groups of molecules, properly assembled, can obviously accomplish much more than an equal number of molecules functioning separately" (Menger, 1991). As the evidence began to accumulate that a lot of biological systems function *via* the simultaneous effects of multiple interactions, this observation was becoming increasingly important. To date, significant progress in self-assembly of catalytic-active monolayers on multivalent scaffolds, such as micelles (Dong et al., 2012), liposomes, proteins (Hou et al., 2012), and nanoparticles, has been achieved.

For example, Liu et al. used poly(amido amine) dendrimers (PD5) and cricoid proteins (SP1) as the templates to bind with superoxide dismutase (SOD) and glutathione peroxidase (GPx) catalytic centers, respectively (**Figure 2A**). The obtained MnPD5 and SeSP1 were then self-assembled to form dual-enzyme cooperative nanowires. This nanocomposite could exhibit excellent SOD- and GPx-like properties to remove harmful reactive oxygen species (ROS) (Sun et al., 2015).

Introducing Additionally New and Attractive Features

By incorporating functional nanomaterial into enzyme mimics, such biomimetic catalysts cannot only mimic the functions of

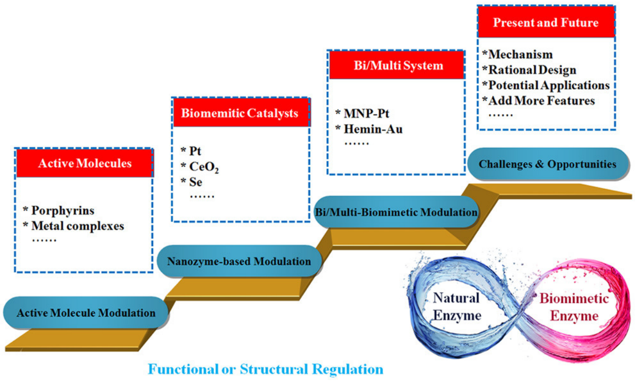

FIGURE 1 | Scheme describing the incorporation of nanomaterials into artificial enzymes for tuning catalysis.

natural enzymes, but also possess additionally advanced features in some cases.

Assembling an Electrode by Binding Active Sites to Nanomaterials

The interconversion of water and hydrogen in unitized regenerative fuel cells is considered as one important energy storage method to eliminate the temporal fluctuations of wind power and solar power. Nevertheless, to enable this technology to be economically viable, replacing current commercial platinum catalysts with cheaper and more abundant materials is highly desirable and challenging (Bashyam and Zelenay, 2006). A competitive alternative can be found in microorganisms which can metabolize molecular hydrogen using hydrogenases. Inspired by this, nanomaterials with a hydrogenase-like property can be modified on the electrodes for catalyzing this interconversion. Artero et al. prepared a noble metal-free catalytic nanomaterial through assembling a nickel bisdiphosphine-based complex and multiwalled carbon nanotubes (MWNTs). The obtained nanocomposites could serve as hydrogenase mimics. As a result, this hybrid could act as a highly specific surface area cathode material with outstanding catalytic performance even in the condition of strong acid solutions (Goff et al., 2009).

Near-Infrared Photothermal Control

Qu et al. demonstrated an approach to construct a $[Fe_2L_3]^{4+}$/GO-COOH-based peroxidase mimic. Since GO-COOH had strong absorption in near infrared regions, this peroxidase mimic had good sensitivity to NIR and high photothermal conversion efficiency (**Figure 2B**). Furthermore, the integration of this nanocomposite with glucose oxidase (GOx) could enable the creation of a catalytic ensemble for a cascade reaction. In addition, within a temperature range from 15 to 37°C, GOx and $[Fe_2L_3]^{4+}$-GO-COOH had a higher activity at an elevated temperature. In the presence of NIR laser irradiation, an obvious absorbance band at 417 nm was achieved, indicating that the oxidized 2,2′-azino-bis(3-ethylbenzothiazoline-6-sulfonic acid) ($ABTS^{\cdot +}$) was formed. Based on NIR photothermal effect and temperature-dependent activity, the activity of a GOx-$[Fe_2L_3]^{4+}$-GO-COOH cascade system could be controlled by near infrared (NIR) light (Xu et al., 2014). Taken together, based on the unique advantages of nanomaterials, they can serve as regulators to modulate the catalytic activities of active molecules with enzyme-like properties.

MODULATION OF NANOMATERIAL-BASED ARTIFICIAL ENZYMES

So far, a variety of nano-scaled materials have been discovered to have unique enzyme-like activities (Wu et al., 2019). Additionally, a few "small molecule" systems, such as deoxyribonucleic acid and ionic liquid, have shown the ability to modulate the activity of these novel enzyme mimics. In this section, as an alternative to small molecule inhibition, recent progress in nanomaterials provide a novel pathway to regulate the catalytic behaviors of nanomaterial-based artificial enzymes.

Regulation of Stability and Activity of Nanomaterials-Based Artificial Enzymes

The rapid advances in solid-supported catalysts prompt scientists to examine whether matrices can promote the catalytic behavior of these nano-sized enzyme mimics. Compared with bulk materials, materials filled in the nanochannels often exhibit superior performances such as enhanced catalytic activities and improved stabilities. Ling and Gao's group constructed combined Fe porphyrin and Zr^{4+} ions within MOFs. The obtained nanomaterials were noted as PMOF(Fe) and further assembled with ultrasmall Pt nanoparticles to generate Pt@PMOF(Fe). The MOFs could efficiently hinder the aggregation of the Pt component. In this way, the nanocomposite exhibited high peroxidase-like property and stability (Ling et al., 2020).

In addition, Qu et al. demonstrated one rational method for constructing CeO_2 NPs encapsulated on porous carbonaceous frameworks (**Figure 2C**). The porous carbonaceous frameworks could promote the formation of a high degree of very small, well-dispersed, and stable CeO_2 NPs. The obtained nanocomposites exhibited excellent oxidase-like ability compared with other types of CeO_2 NPs (Cao et al., 2018). Recently, they used GO as the template to assemble selenium nanoparticles. The formed GO-Se nanocomposites could serve as GPx mimics to eliminate harmful H_2O_2 with the assistance of glutathione. This enzyme mimic performed enhanced enzyme-like activities in comparison to their independent components and exhibited potential antioxidant effect for cytoprotection (Huang Y. Y. et al., 2017). Besides the mentioned materials, a carbon nanotube can also be used as a support for regulating the stability and activity of nanomaterial-based artificial enzymes.

Forming Hybrid Nanomaterials for Artificial Cascade Systems

In addition to regulating catalysis, nano-sized enzyme mimics can also be used for constructing artificial enzymatic cascade systems. For example, Qu et al. used polydopamine (pDA) as the bridge for assembling V_2O_5 nanowires and MnO_2

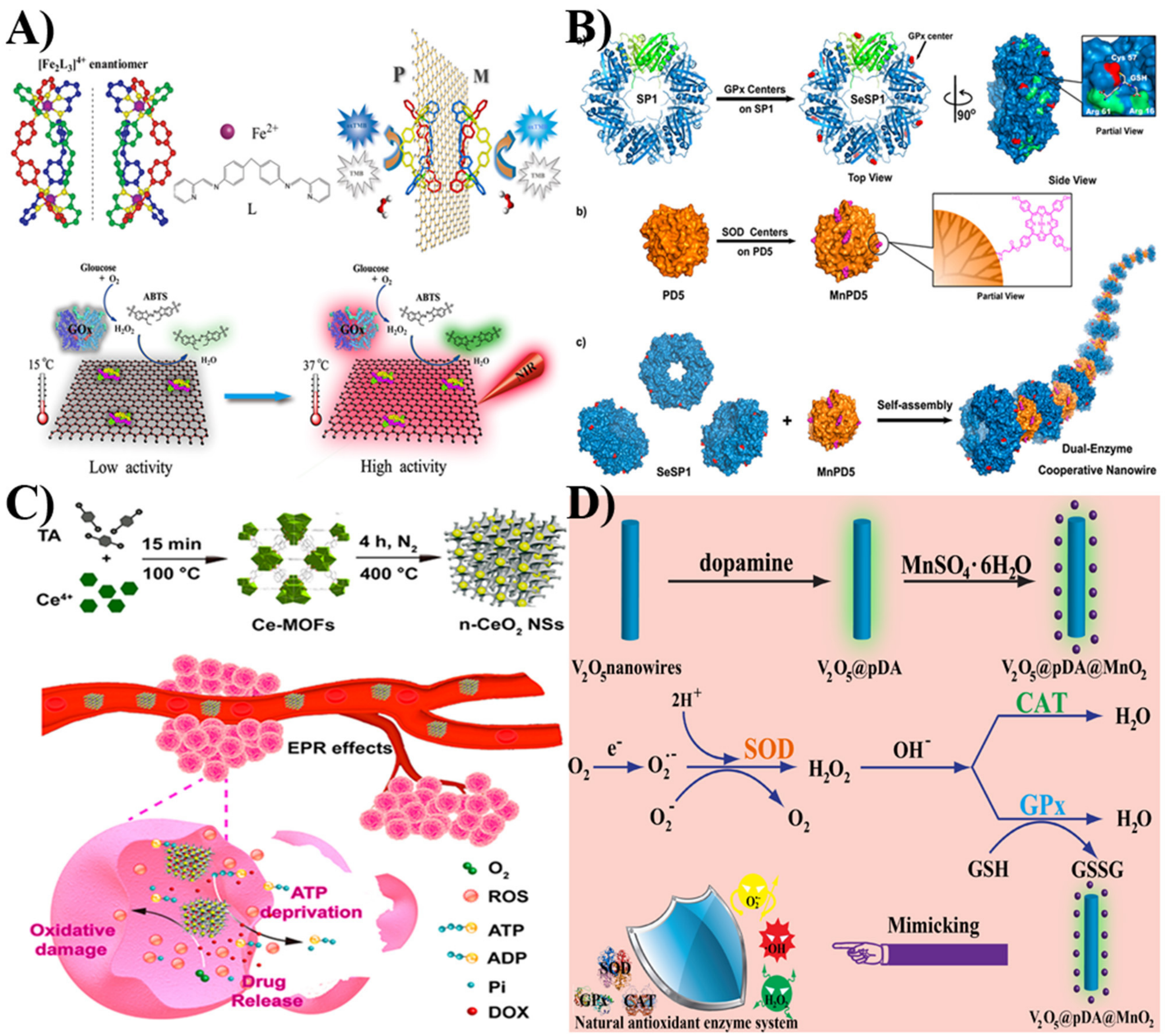

FIGURE 2 | (A) The peroxidase-like property of $[Fe_2L_3]^{4+}$/GO-COOH can be controlled by NIR. Reprinted with permission from Xu et al. Copyright (2014) Wiley-VCH. **(B)** The assembly of SeSP1 and MnPD5 to form dual-enzyme cooperative nanowire. Reprinted with permission from Sun et al. Copyright (2015) American Chemical Society. **(C)** The design of the CeO_2 NPs encapsulated-porous carbonaceous frameworks for cancer therapy. Reprinted with permission from Cao et al. Copyright (2018) American Chemical Society. **(D)** The assembly and the scheme of the V_2O_5@pDA@MnO_2 nanozyme for mimicking natural antioxidant enzyme system. Reprinted with permission from Huang et al. Copyright (2016) Wiley-VCH.

nanoparticles (**Figure 2D**). In their work, the MnO_2 component could serve as SOD mimics to transform a superoxide radical to H_2O_2 and O_2. With the inherent catalase-like property of MnO_2 and the GPx-like ability of the V_2O_5 component, the generated H_2O_2 would be scavenged as harmless products. With the antioxidant enzyme-like properties of nanozymes and the antioxidant ability of pDA, the nanocomposites could effectively scavenge overexpressed ROS and protect intracellular components against oxidative damage. This V_2O_5@pDA@MnO_2 nanozyme could mimic intracellular antioxidant enzyme-based defense systems for cytoprotection. Further animal inflammatory models illustrated that the nanocomposites could serve as potential nanoagents for ameliorating inflammation (Huang et al., 2016). Owing to their advantages of large specific surface area, easy surface modification, and excellent electron transfer ability, nanomaterials have been used as promising regulators to control the catalytic properties of artificial enzymes.

MODULATION OF MULTIPLE BIO- OR/AND BIOMIMETIC CATALYSTS

The attachment of different bio- or/and biomimetic catalysts on the same carbon nanomaterial provides a simple pathway for fabricating catalytic ensembles which possess synergic and complementary properties. Besides porous silica structures, mesoporous carbon can serve as a support for the construction of nanostructured multi-catalyst systems. For instance, combining MNPs with Pt nanoparticles in ordered mesoporous carbon has been prepared by Park et al. (Kim et al., 2014). As a result, this composite exhibited the enhanced peroxidase-like activity in comparison to independent MNPs, which could be due to the synergetic effect.

In addition to traditional graphene-based (Xue et al., 2014) and porous-based materials (He et al., 2013), graphene-mesoporous silica hybrid as a novel nanomaterial can be used for bio- or multi-artificial catalyst modulation. Very recently, Qu and Ren's group reported that hemin and AuNPs with complementary functions could be located in different regions in a graphene-mesoporous silica hybrid. Firstly, through weak π-π stacking interactions, hemin was tethered on the exposed surface of graphene. Since graphene could hinder the self-dimerization of hemin molecules, the as-prepared hemin-contained nanoconjugates can act as a highly efficient peroxidase mimic. Then, AuNPs, with glucose oxidase-mimicking activity, can be formed on the NH_2 groups functional silica surface by *in-situ* reduction. Consequently, these integrated catalysts exhibit glucose oxidase-like and peroxidase-like catalytic activities. More importantly, these nanocomplexes with multiple catalytic sites are able to catalyze artificial cascade reactions, without the addition of natural enzymes. This finding might pay the way to anchor multiple enzyme mimics on solid matrices for multicomponent cascade transformation or realizing artificial organelles in the future (Lin et al., 2015). In addition to regulating the activity of active molecules or biomimetic catalysts, nanomaterials can also be used for the regulation of multi-biomimetic systems.

CHALLENGES AND FUTURE OPPORTUNITIES

Although remarkable progress has been made, the development of nanomaterials incorporating enzymes and artificial enzymes is still in a relatively early stage. In order to carry out further research in these mentioned areas, the following challenges need to be addressed:

1) The mechanism leading to the change of catalytic performance. Obvious changes in activity, specificity, or selectivity of these catalysts may appear when combining artificial enzymes with various nanomaterials. However, in many cases, the mechanism on how nanoscale materials affect the properties of these catalysts is not properly understood and validated.
2) Rational design of surface functionalized nano-sized materials. It is important to take into account surface properties in the interactions of nanomaterials with bio- and biomimetic catalysts.
3) Apart from the surface properties, the size, morphology as well as composition of nanomaterials also play a crucial role. This point needs systematical examination in the future.
4) Constructing novel integrated catalysts which possess superior and often unique functions for their practical applications is still in its infancy. More attention should be devoted to the use of functional nanomaterials for constructing catalysts with new properties.
5) Although many enzymes and artificial enzymes have been combined with nanomaterials, it is indeed necessary to further investigate the potential applications of nanomaterials in tuning other biomimetic reactions.
6) It is important to further investigate their potential industrial applications.

CONCLUSIONS

Enzymes have attracted scientists' curiosity and attention for a long time. The concepts of enzyme-catalyzed transformations have been a tremendous source of inspiration for fabricating synthetic catalysts which possess the ability of mimicking the essential or general properties of natural enzymes. Particularly, recent developments in nanotechnology have enhanced the possibility for assembling engineered nanomaterials with biomimetic catalysts. This review systematically summarized the latest developing progress of nanomaterials especially inorganic nanomaterials in regulating biological and biomimetic catalysis. These works have exhibited great potential for applications ranging from the control and regulation of activity and biosensing to the separation and construction of hybrid nanoarchitectures. Evidentially, breakthroughs in biotechnology, nanotechnology as well as bionic technology may pave the way for constructing novel hybrid structures for broad applications by overcoming the unresolved issues and challenges.

AUTHOR CONTRIBUTIONS

YH, DY, YQ, LC, and YL conceived and wrote this paper. All the authors read and approved the final manuscript.

FUNDING

This work was financially supported by AcRF Tier 1(R-143–000–497–112), National Nature Science Foundation (Nos. 21271040, 51073031), and the Excellent Young Teachers Training.

REFERENCES

Bashyam, R., and Zelenay, P. (2006). A class of non-precious metal composite catalysts for fuel cells. *Nature* 443, 63–66. doi: 10.1038/nature05118

Cao, F. F., Zhang, Y., Sun, Y. H., Wang, Z. Z., Zhang, L., Huang, Y. Y., et al. (2018). Ultrasmall nanozymes isolated within porous carbonaceous frameworks for synergistic cancer therapy: enhanced oxidative damage and reduced energy supply. *Chem. Mater.* 30, 7831–7839. doi: 10.1021/acs.chemmater.8b03348

Dong, Z. Y., Luo, Q., and Liu, J. Q. (2012). Artificial enzymes based on supramolecular scaffolds. *Chem. Soc. Rev.* 41, 7890–7908. doi: 10.1039/c2cs35207a

Du, B. J., Li, D., Wang, J., and Wang, E. K. (2017). Designing metal-contained enzyme mimics for prodrug activation. *Adv. Drug Delivery Rev.*118, 78–93. doi: 10.1016/j.addr.2017.04.002

Elemans, J. A. A. W., and Nolte, R. J. M. (2019). Porphyrin cage compounds based on glycoluril-from enzyme mimics to functional molecular machines. *Chem. Commun.* 55, 9590–9605. doi: 10.1039/C9CC04372A

Fan, K. L., Xi, J. Q., Fan, L., Wang, P. X., Zhu, C. H., Tang, Y., et al. (2018). *In vivo* guiding nitrogen-doped carbon nanozyme for tumor catalytic therapy. *Nat. Common.* 9:1440. doi: 10.1038/s41467-018-03903-8

Gao, L., Liu, M. Q., Ma, G. F., Wang, Y. L., Zhao, L. N., Yuan, Q., et al. (2015). Peptide-Conjugated Gold Nanoprobe: Intrinsic Nanozyme-linked immunsorbant assay of integrin expression level on cell membrane. *ACS Nano* 9, 10979–10990. doi: 10.1021/acsnano.5b04261

Gao,. L. Z., Zhuang, J., Nie, L., Zhang, J. B., Zhang, Y., Gu, N., et al. (2007). Intrinsic peroxidase-like activity of ferromagnetic nanoparticles. *Nat. Nanotechnol.* 2, 577–583. doi: 10.1038/nnano.2007.260

Ghosh, S., Roy, P., Karmodak, N., Jemmis, E. D., and Mugesh, G. (2018). Nanoisozymes: crystal-facet-dependent enzyme-mimetic activity of V_2O_5 nanomaterials. *Angew. Chem. Int. Ed.* 57, 4510–4515. doi: 10.1002/anie.201800681

Goff, A. L., Artero, V., Jousselme, B., Tran, P. D., Guillet, N., Métayé, R., et al. (2009). From hydrogenases to noble metal-free catalytic nanomaterials for H_2 production and uptake. *Science* 326, 1384–1387.doi: 10.1126/science.1179773

Han, X. P., Ling, X. F., Wang, Y., Ma, T. Y., Zhong, C., Hu, W. B., et al. (2020). Generationof nanoparticle, atomic-cluster, and single-atom cobalt catalysts from zeolitic imidazole frameworks by spatial isolationand their use in zinc-air batteries. *Angew.Chem. Int. Ed.* 58, 5359–5364. doi: 10.1002/anie.201901109

Han, X. P., Ling, X. F., Yu, D. S., Xie, D. Y., Li, L. L., Peng, S. J., et al. (2019). Atomically dispersed binary Co-Nisites in nitrogen-doped hollow carbon nanocubes for reversible oxygen reduction and evolution. *Adv. Mater.* 31:1905622. doi: 10.1002/adma.201905622

He, X. L., Tan, L. F., Chen, D., Wu, X. L., Ren, X. L., Zhang, Y. Q., et al. (2013). Fe_3O_4-Au@mesoporous SiO_2 microspheres: an ideal artificial enzymatic cascade system. *Chem. Commun.* 49, 4643–4645. doi: 10.1039/c3cc40622a

Hooley, R. (2016). Biomimetic catalysis: taking on the turnover challenge. *Nat. Chem.* 8, 202–204. doi: 10.1038/nchem.2461

Hou, C. X., Luo, Q., Liu, J. L., Miao, L., Zhang, C. Q., Gao, Y. Z., et al. (2012). Construction of GPx active centers on natural protein nanodisk/nanotube: a new way to develop artificial nanoenzyme. *ACS Nano* 6, 8692–8701. doi: 10.1021/nn302270b

Huang, Y. Y., Liu, C. Q., Pu, F., Liu, Z., Ren, J. S., and Qu, X. G. (2017). AGO-Se nanocomposite as an antioxidant nanozyme for cytoprotection. *Chem. Commun.* 53, 3082–3085. doi: 10.1039/C7CC00045F

Huang, Y. Y., Liu, Z., Liu, C. Q., Ju, E. G., Zhang, Y., Ren, J. S., et al. (2016). Self-assembly of multi-nanozymes to mimic an intracellularantioxidant defense system. *Angew. Chem. Int. Ed.* 55, 6646–6650. doi: 10.1002/anie.201600868

Huang, Y. Y., Ren, J. S., and Qu, X. G. (2019). Nanozymes: classification, catalytic mechanisms, activity regulation, and applications. *Chem. Rev.* 119, 4357–4412. doi: 10.1021/acs.chemrev.8b00672

Jiang, D. W., Ni, D. L., Rosenkrans, Z. T., Huang, P., Yan, X. Y., and Cai, W. B. (2019). Nanozyme: new horizons for responsive biomedical applications. *Chem. Soc. Rev.* 48, 3683–3704. doi: 10.1039/C8CS00718G

Kim, M. I., Ye, Y., Woo, M. A., Lee, J., and Park, H. G. (2014). A highly efficient colorimetric immunoassay using a nanocomposite entrapping magnetic and platinum nanoparticles in ordered mesoporous carbon. *Adv. Healthc. Mater.* 3, 36–41. doi: 10.1002/adhm.201300100

Liang, M. M., and Yan, X. Y. (2019). Nanozymes: from new concepts, mechanisms, and standards to applications. *Acc. Chem. Res.* 52, 2190–2200. doi: 10.1021/acs.accounts.9b00140

Lin, Y. H., Wu, L., Huang, Y. Y., Ren, J. S., and Qu, X. G. (2015). Positional assembly of hemin and gold nanoparticles in graphene-mesoporous silica nanohybrids for tandem catalysis. *Chem. Sci.* 6, 1272–1276. doi: 10.1039/C4SC02714K

Ling, P. H., Cheng, S., Chen, N., Qian, C. H., and Gao, F. (2020). Nanozyme-modified metal-organic frameworks with multienzymes activity as biomimetic catalysts and electrocatalytic interfaces. *ACS Appl. Mater. Interfaces* 12, 17185–17192. doi: 10.1021/acsami.9b23147

Menger, F. M. (1991). Groups of organic molecules that operate collectively. *Angew. Chem. Int. Ed.* 30, 1086–1099. doi: 10.1002/anie.199110861

Singh, N., Savanur, M. A., Srivastava, S., D'Silva, P., and Mugesh, G. (2017). A redox modulatory Mn_3O_4 nanozyme with multi-enzyme activity provides efficient cytoprotection to human cells in a Parkinson's disease model. *Angew. Chem. Int. Ed.* 56, 14267–14271. doi: 10.1002/anie.201708573

Song, Y. J., Qu, K. G., Zhao, C., Ren, J. S., and Qu, X. G. (2010). Graphene oxide: intrinsic peroxidase catalytic activity and its application to glucose detection. *Adv. Mater.* 22, 2206–2210. doi: 10.1002/adma.200903783

Sun, H. C., Miao, L., Li, J. X., Fu, S., An, G., Si, C. Y., et al. (2015). Self-assembly of cricoid proteins induced by "soft nanoparticles": an approach to design multienzyme cooperative antioxidative systems. *ACS Nano* 9, 5461–5469. doi: 10.1021/acsnano.5b01311

Wang, H., Wan, K. W., and Shi, X. H. (2019). Recent advances in nanozyme research. *Adv. Mater.* 31, 1805368. doi: 10.1002/adma.201805368

Wang, Q. B., Lei, J. P., Deng, S. Y., Zhang, L., and Ju, H. X. (2013). Graphene-supported ferric porphyrin as a peroxidase mimic for electrochemical DNA biosensing. *Chem. Commun.* 49, 916–918. doi: 10.1039/C2CC37664D

Wang, Y. X., Zhao, M. T., Ping, J. F., Chen, B., Cao, X. H., and Huang, Y., et al. (2016). Bioinspired design of ultrathin 2D bimetallic metal-organic-framework nanosheets used as biomimeticenzymes. *Adv. Mater.* 28, 4149–4155. doi: 10.1002/adma.201600108

Wu, J. J., Wang, X. Y., Wang, Q., Lou, Z. P., Li, S. R., Zhu, Y. Y., et al. (2019). Nanomaterials with enzyme-like characteristics (nanozymes): next-generation artificial enzymes (II). *Chem. Soc. Rev.* 48, 1004–1076. doi: 10.1039/c8cs00457a

Xu, C., and Qu, X. G. (2014). Cerium oxide nanoparticle: a remarkably versatile rare earth nanomaterial for biological applications. *NPG Asia Mater.* 6:e90. doi: 10.1038/am.2013.88

Xu, C., Zhao, C. Q., Li, M., Wu, L., Ren, J. S., and Qu, X. G. (2014). Artificial evolution of graphene oxide chemzyme with enantioselectivity and near-infrared photothermal effect for cascade biocatalysis reactions. *Small* 10, 1841–1847. doi: 10.1002/smll.201302750

Xue, T., Peng, B., Xue, M., Zhong, X., Chiu, C. Y., Yang, S., et al. (2014). Integration of molecular and enzymatic catalysts on graphene for biomimetic generation of antithrombotic species. *Nat. Commun.* 5, 3200–3205. doi: 10.1038/ncomms4200

Yin, W. Y., Yu, J., Lv, F. T., Yan, L., Zheng, L. R., Gu, Z. J., et al. (2016). Functionalized nano-MoS_2 with peroxidase catalytic and near-infrared photothermal activities for safe and synergetic wound antibacterial applications. *ACS Nano* 10, 11000–11011. doi: 10.1021/acsnano.6b05810

Zheng, B., Wang, C., Wu, C. Y., Zhou, X. J., Lin, M., Wu, X. C., et al. (2012). Nuclease activity and cytotoxicity enhancement of the DNA intercalators via graphene oxide. *J. Phys. Chem. C* 116, 15839–15846. doi: 10.1021/jp3050324

Zheng, B., Wang, C., Xin, X. Z., Liu, F., Zhou, X. J., Zhang, J. Y., et al. (2014). Electron transfer from graphene quantum dots to the copper complex enhances its nuclease activity. *J. Phys. Chem. C* 118, 7637–7642. doi: 10.1021/jp411348f

Conflict of Interest: The authors declare that the research was conducted in the absence of any commercial or financial relationships that could be construed as a potential conflict of interest.

frontiers in Chemistry

ORIGINAL RESEARCH
published: 21 October 2020
doi: 10.3389/fchem.2020.564968

Construct of Carbon Nanotube-Supported Fe_2O_3 Hybrid Nanozyme by Atomic Layer Deposition for Highly Efficient Dopamine Sensing

Yingchun Yang†, Tao Li†, Yong Qin, Lianbing Zhang and Yao Chen*

School of Life Sciences, Northwestern Polytechnical University, Xi'an, China

The Fe_2O_3 nanozyme has been identified as the most promising alternative for the Fe_3O_4 nanozyme due to its relatively low toxic risk and good chemical stability. However, its enzyme-like activity is relatively low enough to meet specific application requirements. Furthermore, previous synthesis approaches have difficulties in fabricating ultra-small Fe_2O_3 nanoparticles with tunable size and suffer from agglomeration problems. In this study, atomic layer deposition (ALD) was used to deposit Fe_2O_3 on surfaces of carbon nanotubes to form hybrid nanozymes (Fe_2O_3/CNTs). ALD enables the preparation of ultrafine Fe_2O_3 nanoparticles with precise size control <1 nm, while CNTs could be served as promising support for good dispersibility and as an effective activity activator. Hence, the formed Fe_2O_3/CNTs exhibit excellent peroxidase-like activity with a specific peroxidase activity of 24.5 U mg^{-1}. A colorimetric method for sensing dopamine (DA) was established and presented good sensitivity with a limit of detection (LOD) as low as 0.11 μM. These results demonstrated that, in virtue of meticulous engineering methods like ALD, carbon nanomaterial-based hybrids can be developed as talented enzyme mimetic, thus paving a way for nanozyme design with desired activity and broadening their applications in biosensing and other fields.

Keywords: atomic layer deposition, hybrid nanozymes, ultrafine Fe_2O_3 nanoparticles, peroxidase activity, biosensing

Edited by:
Youhui Lin,
Xiamen University, China

Reviewed by:
Mingzai Wu,
Anhui University, China
Khaled Mohammad Saoud,
Virginia Commonwealth University School of the Arts, Qatar

***Correspondence:**
Yao Chen
chenyao@nwpu.edu.cn

† These authors have contributed equally to this work

Specialty section:
This article was submitted to Nanoscience, a section of the journal Frontiers in Chemistry

Received: *23 May 2020*
Accepted: *24 August 2020*
Published: *21 October 2020*

Citation:
Yang Y, Li T, Qin Y, Zhang L and Chen Y (2020) Construct of Carbon Nanotube-Supported Fe_2O_3 Hybrid Nanozyme by Atomic Layer Deposition for Highly Efficient Dopamine Sensing. Front. Chem. 8:564968. doi: 10.3389/fchem.2020.564968

INTRODUCTION

It is well-known that nanozymes have been developed as the most promising alternative for natural enzymes, owing to their good stability, simple and large-scale preparation, and cost effectiveness (Gao et al., 2007; Lin et al., 2014; Wang et al., 2019). In the past 10 years, over 300 kinds of nanomaterials, including metals, metal oxides, and carbon nanomaterials, have been demonstrated to mimic the activities of oxidase, peroxidase, catalase, and superoxide dismutase, which connects an important bridge between nanotechnology and biological science (Natalio et al., 2012; Wei and Wang, 2013; Liu and Liu, 2017; Li et al., 2018; Wu et al., 2019).

As the most studied nanozymes, iron oxide nanozymes (IONzymes) have attracted great interest since the first exciting discovery that ferromagnetic oxide possesses an intrinsic peroxidase activity (Gao et al., 2007), and they show great application potential in fields of biosensing, magnetic resonance imaging, anti-biofouling, and cancer therapy (Cheng et al., 2017; Jiang et al., 2019; Li et al., 2019; Wang et al., 2019; Šálek et al., 2020). Between the two main IONzymes Fe_3O_4 and Fe_2O_3, most attention was paid on Fe_3O_4 due to the relatively higher saturation magnetization and simpler synthesis procedures. However, the ferrous ions of Fe_3O_4 may raise its toxic risk and make it chemically unstable (Chen et al., 2012). Therefore, Fe_2O_3 nanozymes should be better candidates for applications. However, their enzyme-mimicking activities are relatively low enough to meet a variety of specific application requirements (e.g., biosensing, antimicrobial therapy). Furthermore, it remains a great challenge to synthesize ultrafine Fe_2O_3 nanoparticles with both controllable and uniform sizes, as well as to eliminate nanoparticle aggregation, which could inevitably affect their enzyme-like activity during catalytic reaction.

Among the huge family of nanozymes, great attention was also paid on carbon nanomaterials due to their excellent nanozymatic activities, diverse structures, and good biocompatibility (Sun et al., 2017; Wang et al., 2018). Especially, their structural merits such as large surface area and good mechanical properties make them an ideal support for anchoring metal/metal oxide nanozymes to form hybrid nanozymes and to inhibit the possible agglomeration of nanoparticles (Tao et al., 2013). Wang Q. et al. (2017) reported that Fe_3O_4 nanoparticles loaded on 3D porous graphene exhibited good dispersibility as well as stability. Moreover, their high electrical conductivity could facilitate electron transfer in many redox reactions, displaying a synergistic effect on the catalytic properties of metal/metal oxide (Yang et al., 2014). Such promotion effect was also applicable for upregulating enzyme-mimicking activities of metal/metal oxide nanozymes, thus leading to greatly enhanced activities compared to their single component. For instance, the peroxidase-like activity of Pt and Fe_3O_4 was remarkably increased when hybridized with carbon nanodots or C_3N_4 nanoflakes (Fan et al., 2018; Wang et al., 2018).

Recently, atomic layer deposition (ALD), as a gas-phase film deposition technology, has been demonstrated to be an advanced avenue in the preparation of ultrafine nanoparticles (Marichy and Pinna, 2013; Zhang and Qin, 2018). Owing to its self-limiting characteristic, it is capable of synthesizing nanoparticles with accurate size control at the atomic level. Zhang et al. reported that a series of Pt species, including single Pt atoms, Pt clusters, and Pt nanoparticles, could be easily fabricated by use of ALD (Sun et al., 2013). Furthermore, ALD can be served as a powerful approach to prepare hybrid nanomaterials due to its good step coverage over substrates with a complicated structure (Marichy and Pinna, 2013). Our previous study found that carbon nanotubes and graphene-supported nanoparticles with adjustable size and good distribution can be achieved by ALD (Zhang et al., 2015, 2016, 2018), which cannot be fulfilled by traditional method and confirms again the superiority of ALD. Furthermore, it has been demonstrated that the interface structure of nanozymes could also be precisely engineered by ALD to tune their enzyme-mimicking activities (Chen et al., 2020). However, until now there is no report on fabricating carbon-based IONzymes by ALD.

Hence, in this study, CNT-supported Fe_2O_3 nanozymes (Fe_2O_3/CNTs) were fabricated to solve the problems of aggregation and relatively low activity of the Fe_2O_3 nanozyme. ALD was adopted, for the first time, to precisely synthesize CNT-supported Fe_2O_3 nanoparticles with good uniformity and dispersibility. With the adjustment of cycle numbers, ultrasmall Fe_2O_3 nanoparticles with size down to 1 nm could be accurately achieved. The uniform and ultrafine Fe_2O_3 nanoparticles, as well as the synergistic effect of CNTs, contributed to an excellent enzyme-mimicking activity of the Fe_2O_3/CNT hybrid nanozyme, which made it an efficient peroxidase mimic for the catalytic conversion of a chromogenic substrate of 3,3′,5,5′-tetramethylbenzidine (TMB) and for colorimetric probe in dopamine (DA) sensing.

MATERIALS AND METHODS

Materials

Carbon nanotubes (CNTs) with diameter of 20–30 nm and length of 0.5–2 μm were purchased from Shenzhen Nanotech Port Co., Ltd. (China). Raw CNTs were treated in HNO_3 (68 wt %) at 140°C for 4 h to remove possible catalyst residues and provide nuclear sites for subsequent ALD processes. Ferrocene, dimethyl sulfoxide (DMSO), hydrogen peroxide (H_2O_2), dopamine, and 3,3′,5,5′-tetramethylbenzidine (TMB) were obtained from J&K Scientific. All of the chemicals were used as received.

Synthesis of Fe_2O_3/CNTs by ALD

Firstly, treated CNTs were dispersed in ethanol under ultrasonic agitation and dropped onto quartz wafers. Then, the wafers were placed into an ALD chamber and the ALD process was carried out in a homemade and self-heating system. For Fe_2O_3 ALD, both ferrocene and O_3 were used as precursors and ferrocene was heated to 75°C to obtain optimal vapor pressure. To ensure successful Fe_2O_3 deposition, the chamber was maintained at 260°C. The pulse, exposure, and purge time for ferrocene and O_3 were 1.5/20/30 and 0.2/15/30 (s), respectively. The particle size of Fe_2O_3 was adjusted by ALD cycles and the samples with different ALD cycle numbers (n) were noted as nFe_2O_3/CNTs in this study. After deposition, the samples were collected for further use.

Characterization

Transmission electron microscopy (TEM) and high-resolution TEM (HRTEM) were measured on a FEI Tecnai F20 instrument. High-angle annular dark-field scanning-TEM (HAADF-STEM) images were also collected on this equipment operated at 200 kV. X-ray photoelectron spectroscopy (XPS) data were collected with a Thermo ESCALAB 250 xi with an Al-Ka line as the radiation source. X-ray diffraction (XRD) data were recorded on a MAXima XRD-7000 diffractometer with Cu Kα radiation. Inductively coupled plasma optical emission spectrometry (ICP-OES; Thermo iCAP 6300) was used to determine the content of the metal in the hybrid nanozyme.

Peroxidase-Mimicking Activity Assay

A colorimetric method was adopted to estimate the peroxidase activity of Fe_2O_3/CNT samples by using TMB as the chromogenic substrate. Typically, the catalytic reaction was processed by adding 20 μL of Fe_2O_3/CNT nanozyme (0.5

mg/mL), 80 μL of TMB (2.5 mM), and 100 μL of H_2O_2 (10 mM) into a 2 mL tube. The final volume was adjusted to 1 mL by adding 800 μL NaAc buffer (0.2 M, pH 3.6). The mixed solutions were incubated at 37°C for 10 min. Then, the UV-vis absorbance of oxidized TMB (TMB_{ox}) at a wavelength of 652 nm was immediately recorded. Furthermore, the enzyme-like property was evaluated according to Yan's protocol (Jiang et al., 2018). The experiments were carried out at 37°C in NaAc-HAc buffer (0.2 M, pH 4.0) containing TMB (4 μL of 10 mg mL^{-1}) and H_2O_2 (1 M). The time-dependent absorbance curves were immediately recorded at a 10 s interval within 400 s, and the nanozyme activity expressed in units (U) was calculated according to the following equation:

$$b_{\text{nanozyme}} = \frac{V}{\varepsilon l} \times \frac{\Delta A}{\Delta t} \tag{1}$$

where b_{nanozyme} is the nanozyme activity (U), V is the total volume of reaction solution (μL), ε is the molar absorption coefficient of the TMB substrate (39,000 M^{-1} cm^{-1} at 652 nm), l is the optical path length through reaction solution (cm), and $\Delta A/\Delta t$ is the initial rate of the absorbance change (per minute). The specific activity of the nanozyme was determined using the following equation:

$$a_{\text{nanozyme}} = \frac{b_{\text{nanozyme}}}{m} \tag{2}$$

where a_{nanozyme} is the specific activity of the nanozyme (U mg^{-1}) and m is the nanozyme amount for each assay (mg).

Steady-State Kinetic Analysis

Kinetic experiments were carried out in a 2 mL cuvette with 1 mL NaAc buffer (0.2 M, pH 3.6) containing 10 μg $10Fe_2O_3$/CNTs. Both TMB and H_2O_2 were also added and tested in a time-course model at 37°C. TMB_{ox} at 652 nm was recorded every 30 s in the range of 0–10 min, and the initial rates of two different substrates were determined. The kinetic assay with TMB as substrate was conducted by varying concentrations of TMB with the concentration of H_2O_2 fixed at 0.1 nM, and vice versa. The key kinetic parameters, such as Michaelis–Menten constant (K_m), catalytic efficiency (K_{cat}), and specific activity were calculated by fitting the initial velocity data to the Michaelis–Menten equation: $1/V = K_m/V_m\ (1/[S] + 1/K_m)$, where V represents the initial rate, V_m is the maximal rate of the enzyme-like reaction, K_m corresponds to the Michaelis–Menten constant, and $[S]$ is the substrate concentration.

Colorimetric Sensing of DA

Colorimetric sensing of DA was evaluated using the $10Fe_2O_3$/CNTs hybrid nanozyme under the optimized conditions. The experiments were carried out as follows: 80 μL of TMB (0.2 mM in DMSO), 100 μL of H_2O_2 (0.1 mM), and 5 μL of $10Fe_2O_3$/CNTs (0.5 mg/mL) were

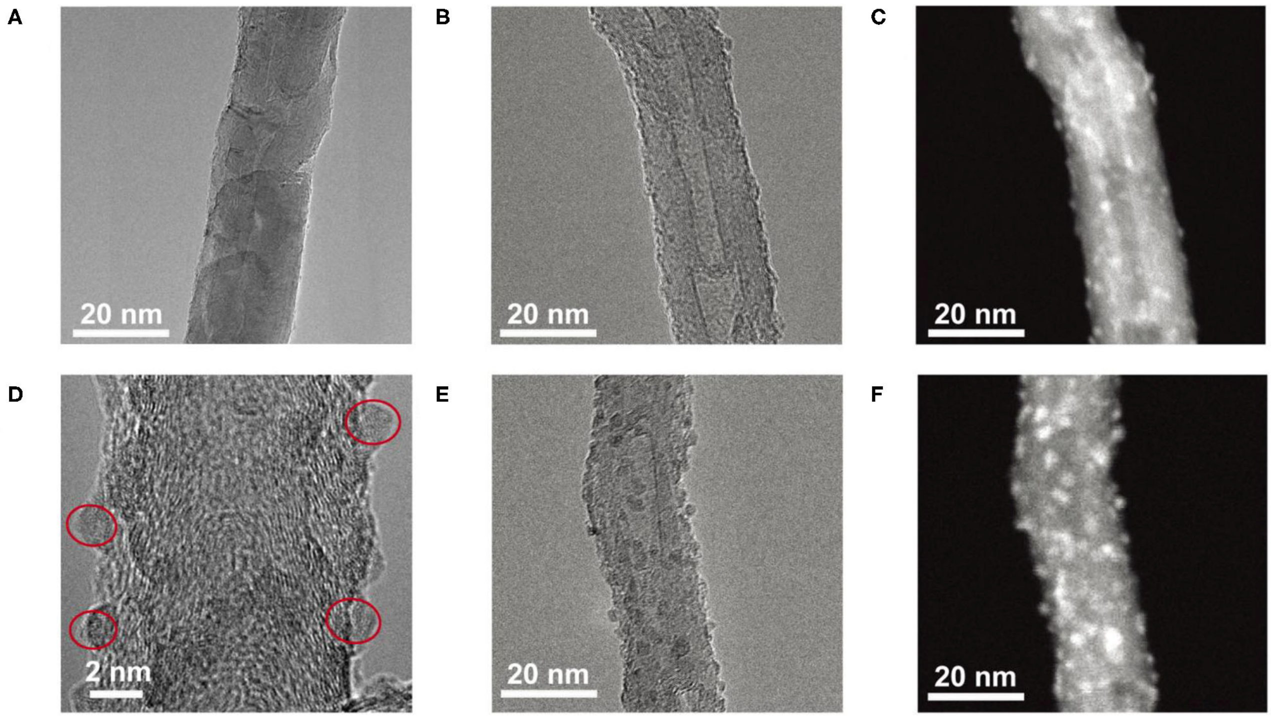

FIGURE 1 | TEM images of $5Fe_2O_3$/CNTs **(A)**, TEM image **(B)**, HAADF image **(C)**, HRTEM image of $10Fe_2O_3$/CNTs **(D)**, HRTEM image **(E)**, and HAADF image **(F)** of $15Fe_2O_3$/CNTs.

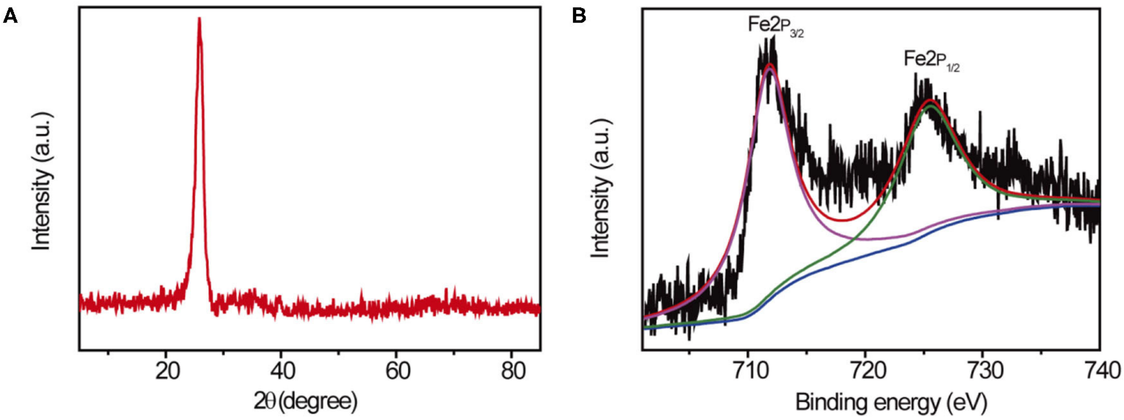

FIGURE 2 | (A) XRD spectra of Fe_2O_3/CNTs and **(B)** the XPS core level of Fe2p.

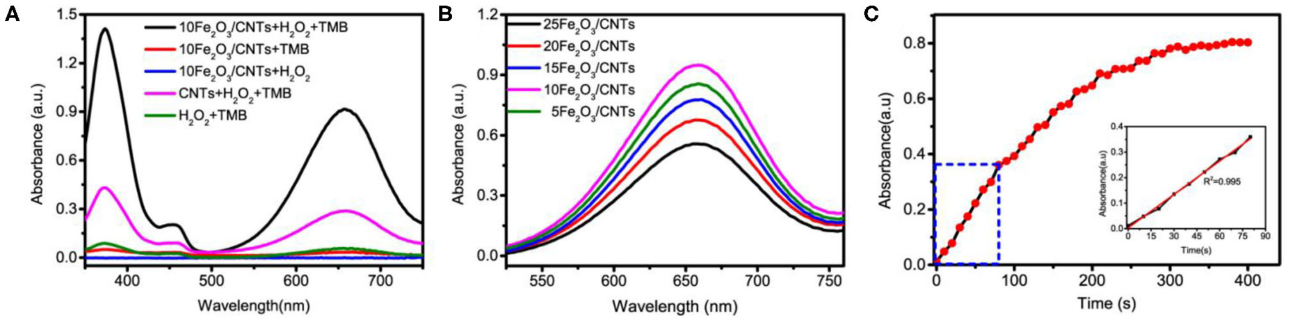

FIGURE 3 | (A) UV-vis spectra of monitoring oxidized TMB catalyzed by different systems. **(B)** Peroxidase-like activities of Fe_2O_3/CNTs with different Fe_2O_3 cycles. **(C)** The absorbance-time curves of the TMB chromogenic reaction catalyzed by the $10Fe_2O_3$/CNTs.

successively added to 750 μL of NaAc buffer (0.2 M, pH 3.6). Then, 50 μL of DA with different concentration was added and the mixture was incubated at 37°C for 10 min, followed by monitoring of the UV-vis absorbance of TMB_{ox} at 652 nm.

RESULTS AND DISCUSSION

In order to characterize the morphology of the as-deposited Fe_2O_3/CNT samples, TEM measurements were conducted; the results are depicted in **Figure 1**. For the sample of $5Fe_2O_3$/CNTs, almost no Fe_2O_3 nanoparticle can be distinguished from surfaces of CNTs due to its low loading content (**Figure 1A**). With increasing ALD cycles, it remained difficult to identify the existence of Fe_2O_3 in the TEM image of $10Fe_2O_3$/CNTs (**Figure 1B**), but the HAADF image (**Figure 1C**) recorded at the same region reveals visibly the successful deposition of Fe_2O_3 nanoparticles on CNTs. This can be clearly distinguished from the HRTEM image as depicted in **Figure 1D**. It is obvious that these nanoparticles are uniformly distributed with diameter of around 1 nm. In addition, it is worth noting that the as-synthesized Fe_2O_3 by ALD is amorphous with no visible crystalline structure found in HRTEM images. When 15 cycles of Fe_2O_3 were applied, a higher density of nanoparticles with larger size of around 2 nm on CNTs was observed both in HRTEM (**Figure 1E**) and HAADF (**Figure 1F**) images. These results fully demonstrate that ALD can be served as a novel avenue to synthesize Fe_2O_3 nanoparticles with ultrasmall and adjustable size, which cannot be fulfilled by traditional method and fully reveals the superiority of ALD.

Further studies were conducted in characterization of the chemical structure of $10Fe_2O_3$/CNTs by XRD measurement, and the spectra of $10Fe_2O_3$/CNTs are presented in **Figure 2A**. The main diffraction peak located at $2\theta = 23.8°$ belongs to typical XRD spectra of CNTs. However, no characteristic peak of iron oxide could be found in the spectra, which matches well with the abovementioned TEM results. As revealed by ICP analysis, the content of Fe_2O_3 in $10Fe_2O_3$/CNTs was as low as 2.1 wt% (results not provided). Actually, similar results have been achieved in our previous study (Zhang et al., 2015) and the unobservable XRD signal of Fe_2O_3 was ascribed to its poor crystallinity and low content, when few cycles of ALD were conducted. In addition, XPS test was also performed to investigate the surface elemental composition of $10Fe_2O_3$/CNTs. Deconvolution of Fe2p core-level spectra shown in **Figure 2B** reveals that there are two main peaks located at 712.6 and 726.1 eV, which can be ascribed to

Fe2p 3/2 and Fe2p 1/2, respectively. These results demonstrated the 3+ valence state of Fe species in $10Fe_2O_3$/CNTs. Meanwhile, the existence of an associate satellite peak located at 718.9 eV could correspond to the characteristic XPS spectra of Fe_2O_3. The combined results of TEM, XRD, and XPS strongly support that Fe_2O_3 was successfully deposited on CNTs by ALD.

The Peroxidase-Mimicking Activity of Fe_2O_3/CNTs

With assistance of the ALD method, it is expected that the as-synthesized Fe_2O_3/CNT samples with ultrafine particle size and good dispersibility possess excellent enzyme-mimicking activities. The peroxidase-like activities of Fe_2O_3/CNT samples were manifested through TMB oxidation in the presence of H_2O_2 into a charge transfer product (TMB_{ox}). Several control experiments were carried out to confirm the catalytic nature. It can be seen in **Figure 3A** that neither H_2O_2 nor TMB alone was capable of inducing catalytic reaction and no significant absorbance peak was generated. When both substrates were presented, the catalytic oxidation rate was accelerated by $10Fe_2O_3$/CNTs in comparison to bare CNTs, as revealed by a great enhancement in the absorbance at 652 nm. It can be concluded that the hybridization of CNTs with uniform and ultra-small Fe_2O_3 nanoparticles contributes to great enhancement in peroxidase-like activity.

Since ALD has a unique advantage of flexible control over cycles, it enables the optimization of the peroxidase-mimicking activity by adjusting the particle size of Fe_2O_3. The peroxidase-like activity of Fe_2O_3/CNT samples with different cycles was also tested, and the results are shown in **Figure 3B**. It is obvious that the activity was enhanced with increase in ALD cycle ($n < 10$) but showed an opposite trend when more than 10 cycles of Fe_2O_3 ALD were conducted. Among them, $10Fe_2O_3$/CNTs presented the highest activity, which might be due to the hybridization of CNTs with Fe_2O_3, as well as the ultrafine nanoparticles with good distribution. The relative low activity of $5Fe_2O_3$/CNTs might be attributed to the low loading content of Fe_2O_3 in the hybrid nanozyme, while the nanoparticle stacking as well as the blocking access to active sites resulted in the low activity of samples with more than 10 cycles. As depicted in **Figure 3C**, the specific activity determined according to the protocol of Yan's group (Jiang et al., 2018) shows that the absorbance is linear to reaction time in the first minutes. By choosing 80 s as the initial

TABLE 1 | Typical specific peroxidase-like activity of $10Fe_2O_3$/CNTs and its comparison with other nanozymes.

Nanozymes	Specific peroxidase activity (U mg^{-1})	References
Fe_3O_4 NPs	5.143	Jiang et al., 2018
IONPs	8.5	Šálek et al., 2020
Carbon NPs	3.302	Jiang et al., 2018
Fe–N–C	57.76	Niu et al., 2019
Fe–N–C	25.33	Jiao et al., 2020
This work	24.5	–

TABLE 2 | Typical Michaelis–Menten constant and maximum velocity for H_2O_2 and TMB substrates and their comparison with HRP.

Catalyst	Substrate	K_m [mM]	V_{max} [10^{-8} Ms^{-1}]
$10Fe_2O_3$/CNTs	TMB	0.515	14.61
$10Fe_2O_3$/CNTs	H_2O_2	0.704	17.43
HRP (Gao et al., 2007)	TMB	0.43	10
HRP (Gao et al., 2007)	H_2O_2	3.7	8.71

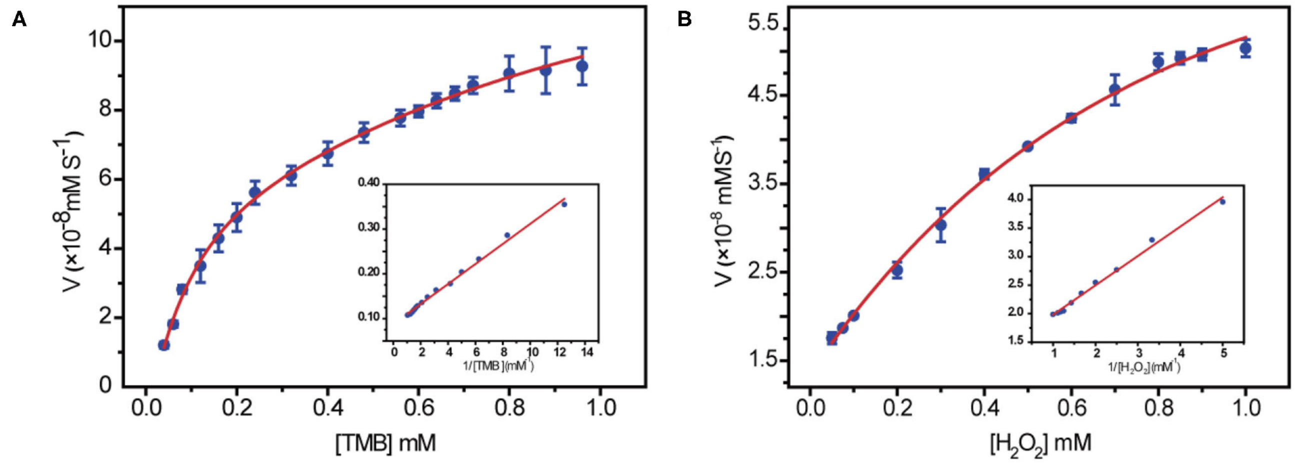

FIGURE 4 | Steady-state kinetic assays by using 10 µg/mL $10Fe_2O_3$/CNTs in 0.2 M NaAc (pH 3.6) at 37°C for 10 min. **(A)** The concentration of H_2O_2 was 0.5 mM, and the TMB concentration was varied. **(B)** The concentration of TMB was 0.4 mM, and the H_2O_2 concentration was varied. Insets are the Lineweaver–Burk plots of the double reciprocal of the Michaelis–Menten equation, with the concentration of one substrate fixed and the other varied. Error bars shown represent the standard error derived from three repeated measurements.

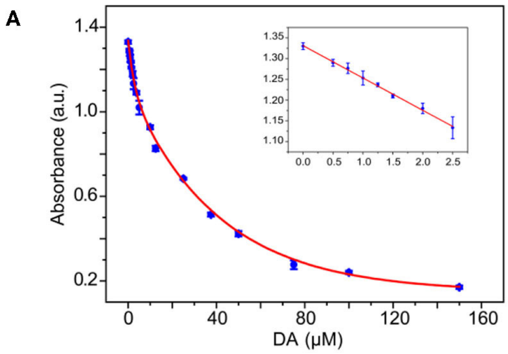

B

Nanozymes	LOD (μM)	Linear range (μM)	Contents of nanozyme (μg)	Ref
this work	0.11	10-80	2.5	
AuMS	0.012	0.5-25	10	(Ray et al. 2020)
h-CuS NCs	1.67	2-150	20	(Zhu et al. 2019)
CuS-rGO	0.48	2-100	10	(Dutta et al. 2015)
Pt/hBNNS	0.76	2-50	7	(Ivanova et al. 2019)

FIGURE 5 | (A) The absorbance of oxidized TMB in the DA detection system in the presence of DA. (Insets) The linear calibration plot and the optical image for DA detection using $10Fe_2O_3$/CNTs. The error bars indicate the standard deviation of three repeated measurements. **(B)** Comparison of the sensing properties of typical nanozymes (Dutta et al., 2015; Ivanova et al., 2019; Zhu et al., 2019; Ray et al., 2020).

rate period, the calculated peroxidase activity of $10Fe_2O_3$/CNTs was 24.5 U mg^{-1} (the inset in **Figure 3C**). It is obvious that this value is higher than that of reported IONzymes and carbon-based nanozymes (**Table 1**) and very close to the highest specific activity of the Fe–N–C single atom nanozyme, demonstrating the excellent performance of $10Fe_2O_3$/CNTs fabricated by ALD.

Steady-State Kinetic Theory of $10Fe_2O_3$/CNTs

In order to get a clear understanding of the intrinsic mechanism for peroxidase activity enhancement of $10Fe_2O_3$/CNT samples, the kinetic was exploited by altering the concentration of one substrate while keeping constant of the other. A set of concentrations for each substrate was recorded in a time-course mode, and the initial rate of TMB and H_2O_2, which is the slope of ΔA652 per unit time (min), was obtained by applying the Beer–Lambert law. The collected data were fitted based on the Michaelis–Menten equation, and the nanozymatic parameters were calculated with the typical Lineweaver–Burk double reciprocal plots as depicted in **Figure 4**.

The key parameters of K_m and V_{max} are listed in **Table 2**. Since K_m is identified as the indicator of the affinity of enzyme to substrates, achieving low K_m and high V_{max} is important to ensure better catalytic performance. It is obvious that the $10Fe_2O_3$/CNTs displayed smaller K_m values for H_2O_2, indicating a better affinity to H_2O_2 and a relatively low concentration of H_2O_2 needed for achieving a high response of $10Fe_2O_3$/CNTs in catalytic reaction. This result is consistent with the report that in the reaction of TMB oxidation with H_2O_2, decomposition of H_2O_2 is the rate-determining step (Zhao et al., 2008), whereby the K_m for TMB is close to the natural HRP enzyme, suggesting its good binding affinity for TMB.

Sensitivity of $10Fe_2O_3$/CNTs for Detection of DA

A variety of biosensors have been established based on the excellent enzyme-mimicking activities of nanozymes. As an essential neurotransmitter, dopamine (DA) is critically involved in a variety of motor and non-motor information transmission and affecting human emotions and perceptions (Paval, 2017; Sgambato-Faure and Tremblay, 2018). DA disorder will cause a series of diseases (Ashok et al., 2017; Sgambato-Faure and Tremblay, 2018). For instance, if too much dopamine is secreted, it can lead to neurological dysfunction. Hence, it is necessary to develop a simple and sensitive approach to detect the DA level. Inspired by the behavior that the existence DA in catalytic reaction solution will inhibit peroxidase-mimicking activity of the $10Fe_2O_3$/CNTs, a colorimetric method was employed to determination of DA. **Figure 5A** shows the absorbance response of TMB_{ox} in the system when different concentrations of DA were added. A typical linear calibration plot was obtained in the 0–25 μM concentration range with a limit of detection (LOD) of 0.11 μM. The LOD was calculated by using the typical formula LOD = $3\sigma/k$, where σ is the standard deviation for the target-blank sample and k stands for the slope of the calibration curve. This approach provides a convenient and sensitive method for sensing of DA. As shown in **Figure 5B**, the LOD of our system is not the lowest by comparing with typical Au nanoparticles, hollow CuS nanocubes, and Pt nanoparticles. However, it is worth noting that the concentration of the nanozyme used in our approach is the lowest, which demonstrates that the $10Fe_2O_3$/CNT hybrids fabricated by ALD are a promising candidate for DA biosensing applications.

CONCLUSIONS

To sum up, CNT-loaded Fe_2O_3 nanoparticles with uniform distribution and precise size control can be easily prepared by ALD. The CNTs not only serve as the support to inhibit possible aggregation of Fe_2O_3 nanoparticles but also act as activity enhancer for Fe_2O_3, which endows Fe_2O_3/CNT hybrids with an excellent peroxidase activity. In our approach, the peroxidase activity could be optimized by adjusting the cycle number of Fe_2O_3 ALD and the highest activity was achieved by $10Fe_2O_3$/CNTs, due to the well-distributed and ultrafine Fe_2O_3

nanoparticles on the surface of CNTs. The steady kinetic assay demonstrated that $10Fe_2O_3$/CNTs show good binding affinity to both TMB and H_2O_2. In addition, a colorimetric method for sensing of DA was established based on the excellent activity of $10Fe_2O_3$/CNTs, which presented a good sensitivity with LOD as low as 0.11 μM. Based on the abovementioned results, the unique advantage of ALD by precise and controllable nanomaterial fabrication enables a novel avenue for nanozyme synthesis with finely tunable activities, which can be convenient for in-depth investigation and understanding of the catalytic mechanism of nanozymes and broaden also their application in biosensing and other areas.

DATA AVAILABILITY STATEMENT

All datasets generated for this study are included in the article/supplementary material.

AUTHOR CONTRIBUTIONS

YY, TL, LZ, YQ, and YC conceived and carried out experiments, analyzed data, and wrote the paper. All authors read and approved the final manuscript.

FUNDING

This work was financially supported by the National Natural Science Foundation of China (31971315), the Natural Science Basic Research Plan in Shaanxi Province of China (2018JQ2038), the Innovation Capability Support Program of Shaanxi (2020TD-042), the Fundamental Research Funds for the Central Universities (3102017OQD048, 3102017OQD049), the China Postdoctoral Science Foundation (2018M633566), and the Postdoctoral Science Foundation of Shaanxi (2018BSHQYXMZZ35).

REFERENCES

Ashok, A. H., Marques, T. R., Jauhar, S., Nour, M. M., Goodwin, G. M., Young, A. H., et al. (2017). The dopamine hypothesis of bipolar affective disorder: the state of the art and implications for treatment. *Mol. Psychiatry* 22, 666–679. doi: 10.1038/mp.2017.16

Chen, Y., Yuchi, Q., Li, T., Yang, G., Miao, J., Huang, C., et al. (2020). Precise engineering of ultra-thin Fe2O3 decorated Pt-based nanozymes via atomic layer deposition to switch off undesired activity for enhanced sensing performance. *Sens. Actuat. B* 305:127436. doi: 10.1016/j.snb.2019.127436

Chen, Z., Yin, J. J., Zhou, Y. T., Zhang, Y., Song, L., Song, M., et al. (2012). Dual enzyme-like activities of iron oxide nanoparticles and their implication for diminishing cytotoxicity. *ACS Nano* 6, 4001–4012. doi: 10.1021/nn300291r

Cheng, N., Song, Y., Zeinhom, M. M. A., Chang, Y. C., Sheng, L., Li, H., et al. (2017). Nanozyme-mediated dual immunoassay integrated with smartphone for use in simultaneous detection of pathogens. *ACS Appl. Mater. Interfaces* 9, 40671–40680. doi: 10.1021/acsami.7b12734

Dutta, S., Ray, C., Mallick, S., Sarkar, S., Sahoo, R., Negishi, Y., et al. (2015). A gel-based approach to design hierarchical CuS decorated reduced graphene oxide nanosheets for enhanced peroxidase-like activity leading to colorimetric detection of dopamine. *J. Phys. Chem. C* 119, 23790–23800. doi: 10.1021/acs.jpcc.5b08421

Fan, L., Xu, X., Zhu, C., Han, J., Gao, L., Xi, J., et al. (2018). Tumor catalytic-photothermal therapy with yolk-shell Gold@Carbon nanozymes. *ACS Appl. Mater. Interfaces* 10, 4502–4511. doi: 10.1021/acsami.7b17916

Gao, L., Zhuang, J., Nie, L., Zhang, J., Zhang, Y., Gu, N., et al. (2007). Intrinsic peroxidase-like activity of ferromagnetic nanoparticles. *Nat. Nanotechnol.* 2, 577–583. doi: 10.1038/nnano.2007.260

Ivanova, M. N., Grayfer, E. D., Plotnikova, E. E., Kibis, L. S., Darabdhara, G., Boruah, P. K., et al. (2019). Pt-decorated boron nitride nanosheets as artificial nanozyme for detection of dopamine. *ACS Appl. Mater. Interfaces* 11, 22102–22112. doi: 10.1021/acsami.9b04144

Jiang, B., Duan, D., Gao, L., Zhou, M., Fan, K., Tang, Y., et al. (2018). Standardized assays for determining the catalytic activity and kinetics of peroxidase-like nanozymes. *Nat. Protoc.* 13, 1506–1520. doi: 10.1038/s41596-018-0001-1

Jiang, D., Ni, D., Rosenkrans, Z. T., Huang, P., Yan, X., and Cai, W. (2019). Nanozyme: new horizons for responsive biomedical applications. *Chem. Soc. Rev*. 48, 3683–3704. doi: 10.1039/C8CS00718G

Jiao, L., Wu, J., Zhong, H., Zhang, Y., Xu, W., Wu, Y., et al. (2020). Densely isolated FeN4 sites for peroxidase mimicking. *ACS Catal.* 10, 6422–6429. doi: 10.1021/acscatal.0c01647

Li, S., Liu, X., Chai, H., and Huang, Y. (2018). Recent advances in the construction and analytical applications of metal-organic frameworks-based nanozymes. *TrAC Trends Anal. Chem.* 105, 391–403. doi: 10.1016/j.trac.2018.06.001

Li, W., Fan, G. C., Gao, F., Cui, Y., Wang, W., and Luo, X. (2019). High-activity Fe3O4 nanozyme as signal amplifier: a simple, low-cost but efficient strategy for ultrasensitive photoelectrochemical immunoassay. *Biosens. Bioelectron*. 127, 64–71. doi: 10.1016/j.bios.2018.11.043

Lin, Y., Ren, J., and Qu, X. (2014). Catalytically active nanomaterials: a promising candidate for artificial enzymes. *Acc. Chem. Res.* 47, 1097–1105. doi: 10.1021/ar400250z

Liu, B., and Liu, J. (2017). Surface modification of nanozymes. *Nano Res*. 10, 1125–1148. doi: 10.1007/s12274-017-1426-5

Marichy, C., and Pinna, N. (2013). Carbon-nanostructures coated/decorated by atomic layer deposition: growth and applications. *Coord. Chem. Rev*. 257, 3232–3253. doi: 10.1016/j.ccr.2013.08.007

Natalio, F., Andre, R., Hartog, A. F., Stoll, B., Jochum, K. P., Wever, R., et al. (2012). Vanadium pentoxide nanoparticles mimic vanadium haloperoxidases and thwart biofilm formation. *Nat. Nanotechnol*. 7, 530–535. doi: 10.1038/nnano.2012.91

Niu, X., Shi, Q., Zhu, W., Liu, D., Tian, H., Fu, S., et al. (2019). Unprecedented peroxidase-mimicking activity of single-atom nanozyme with atomically dispersed Fe-Nx moieties hosted by MOF derived porous carbon. *Biosens. Bioelectron*. 142:111495. doi: 10.1016/j.bios.2019.111495

Paval, D. (2017). A dopamine hypothesis of autism spectrum disorder. *Dev. Neurosci*. 39, 355–360. doi: 10.1159/000478725

Ray, S., Biswas, R., Banerjee, R., and Biswas, P. (2020). Gold nanoparticle intercalated mesoporous silica based nanozyme for selective colorimetric detection of dopamine. *Nanoscale Adv.* 734–745. doi: 10.1039/C9NA00508K

Šálek, P., Golunova, A., Dvoráková, J., Pavlova, E., Macková, H., and Proks, V. (2020). Iron oxide nanozyme as catalyst of nanogelation. *Mater. Lett*. 269:127610. doi: 10.1016/j.matlet.2020.127610

Sgambato-Faure, V., and Tremblay, L. (2018). Dopamine and serotonin modulation of motor and non-motor functions of the non-human primate striato-pallidal circuits in normal and pathological states. *J. Neural. Transm. 125*, 485–500. doi: 10.1007/s00702-017-1693-z

Sun, A., Mu, L., and Hu, X. (2017). Graphene oxide quantum dots as novel nanozymes for alcohol intoxication. *ACS Appl. Mater. Interfaces* 9, 12241–12252. doi: 10.1021/acsami.7b00306

Sun, S., Zhang, G., Gauquelin, N., Chen, N., Zhou, J., Yang, S., et al. (2013). Single-atom catalysis using Pt/graphene achieved through atomic layer deposition. *Sci. Rep*. 3:1775. doi: 10.1038/srep01775

Tao, Y., Lin, Y., Huang, Z., Ren, J., and Qu, X. (2013). Incorporating graphene oxide and gold nanoclusters: a synergistic catalyst with surprisingly high peroxidase-like activity over a broad pH range and its application for cancer cell detection. *Adv. Mater*. 25, 2594–2599. doi: 10.1002/adma.201204419

Wang, H., Li, P., Yu, D., Zhang, Y., Wang, Z., Liu, C., et al. (2018). Unraveling the enzymatic activity of oxygenated carbon nanotubes and their application in the treatment of bacterial infections. *Nano Lett*. 18, 3344–3351. doi: 10.1021/acs.nanolett.7b05095

Wang, H., Wan, K., and Shi, X. (2019). Recent advances in nanozyme research. *Adv. Mater*. 31:e1805368. doi: 10.1002/adma.201805368

Wang, Q., Zhang, X., Huang, L., Zhang, Z., and Dong, S. (2017). One-pot synthesis of Fe3O4 nanoparticle loaded 3D porous Ggraphene nanocomposites with enhanced nanozyme activity for glucose detection. *ACS Appl. Mater. Interfaces* 9, 7465–7471. doi: 10.1021/acsami.6b16034

Wei, H., and Wang, E. (2013). Nanomaterials with enzyme-like characteristics (nanozymes): next-generation artificial enzymes. *Chem. Soc. Rev*. 42, 6060–6093. doi: 10.1039/c3cs35486e

Wu, J., Wang, X., Wang, Q., Lou, Z., Li, S., Zhu, Y., et al. (2019). Nanomaterials with enzyme-like characteristics (nanozymes): next-generation artificial enzymes (II). *Chem. Soc. Rev*. 48, 1004–1076. doi: 10.1039/C8CS00457A

Yang, Z., Zhou, X., Jin, Z., Liu, Z., Nie, H., Chen, X., et al. (2014). A facile and general approach for the direct fabrication of 3D, vertically aligned carbon nanotube array/transition metal oxide composites as non-Pt catalysts for oxygen reduction reactions. *Adv. Mater*. 26, 3156–3161. doi: 10.1002/adma.201305513

Zhang, B., Chen, Y., Li, J., Pippel, E., Yang, H., Gao, Z., et al. (2015). High efficiency Cu-ZnO hydrogenation catalyst: the tailoring of Cu-ZnO interface sites by molecular layer deposition. *ACS Catal*. 5, 5567–5573. doi: 10.1021/acscatal.5b01266

Zhang, B., and Qin, Y. (2018). Interface tailoring of heterogeneous catalysts by atomic layer deposition. *ACS Catal*. 8, 10064–10081. doi: 10.1021/acscatal.8b02659

Zhang, J., Chen, C., Yan, W., Duan, F., Zhang, B., Gao, Z., et al. (2016). Ni nanoparticles supported on CNTs with excellent activity produced by atomic layer deposition for hydrogen generation from the hydrolysis of ammonia borane. *Catal. Sci. Technol*. 6, 2112–2119. doi: 10.1039/C5CY01497B

Zhang, J., Chen, W., Ge, H., Chen, C., Yan, W., Gao, Z., et al. (2018). Synergistic effects in atomic-layer-deposited PtCox/CNTs catalysts enhancing hydrolytic dehydrogenation of ammonia borane. *Appl. Catal. B* 235, 256–263. doi: 10.1016/j.apcatb.2018.04.070

Zhao, X., Cheng, K., Hao, J., and Liu, D. (2008). Preparation of peracetic acid from hydrogen peroxide, part II: Kinetics for spontaneous decomposition of peracetic acid in the liquid phase. *J. Mol. Catal. A Chem*. 284, 58–68. doi: 10.1016/j.molcata.2008.01.003

Zhu, J., Peng, X., Nie, W., Wang, Y., Gao, J., Wen, W., et al. (2019). Hollow copper sulfide nanocubes as multifunctional nanozymes for colorimetric detection of dopamine and electrochemical detection of glucose. *Biosens. Bioelectron*. 141:111450. doi: 10.1016/j.bios.2019.111450

Conflict of Interest: The authors declare that the research was conducted in the absence of any commercial or financial relationships that could be construed as a potential conflict of interest.

frontiers in Chemistry

MINI REVIEW
published: 27 November 2020
doi: 10.3389/fchem.2020.565940

Two-Dimensional Nanomaterials With Enzyme-Like Properties for Biomedical Applications

Shuangfei Cai[1] **and Rong Yang**[1,2]*

[1] Chinese Academy of Sciences Key Laboratory for Biomedical Effects of Nanomaterials and Nanosafety, Center of Materials Science and Optoelectronics Engineering, Chinese Academy of Sciences Center for Excellence in Nanoscience, National Center for Nanoscience and Technology, University of Chinese Academy of Sciences, Beijing, China, [2] Sino-Danish Center for Education and Research, Sino-Danish College, University of Chinese Academy of Sciences, Beijing, China

Recently, remarkable progress has been made in nanozyme research due to the rapid development of nanomaterials. Two-dimensional nanomaterials such as metal nanosheets, graphene-based materials, transition metal oxides/dichalcogenides, etc., provide enhanced physical and chemical functionality owing to their ultrathin structures, high surface-to-volume ratios, and surface charges. They have also been found to have high catalytic activities in terms of natural enzymes such as peroxidase, oxidase, catalase, and superoxide dismutase. This review provides an overview of the recent progress of nanozymes based on two-dimensional nanomaterials, with an emphasis on their synthetic strategies, hybridization, catalytic properties, and biomedical applications. Finally, the future challenges and prospects for this research are discussed.

Keywords: two-dimensional, nanomaterials, nanozyme, catalysis, biomedical

Edited by:
Kelong Fan,
Institute of Biophysics (CAS), China

Reviewed by:
Sanjay Singh,
Ahmedabad University, India
Moon Il Kim,
Gachon University, South Korea
Wei Chen,
Fujian Medical University, China

***Correspondence:**
Rong Yang
yangr@nanoctr.cn

Specialty section:
This article was submitted to
Nanoscience,
a section of the journal
Frontiers in Chemistry

Received: 26 May 2020
Accepted: 28 October 2020
Published: 27 November 2020

Citation:
Cai S and Yang R (2020)
Two-Dimensional Nanomaterials With
Enzyme-Like Properties for Biomedical
Applications. Front. Chem. 8:565940.
doi: 10.3389/fchem.2020.565940

INTRODUCTION

Enzymes are catalysts that speed up almost all biochemical reactions in cells. They have some inherent defects that make them unfavorable in large-scale applications. Since the fascinating discovery of enzymatically active Fe_3O_4 nanoparticles (NPs) for immunoassay (Gao et al., 2007), the last decade has witnessed great advances in nanozyme research (Wei and Wang, 2013; Huang et al., 2019; Jiang D. W. et al., 2019), deriving from the growth of nanoscience and developments in technology. Various types of catalytic nanomaterials (NMs), primarily zero-dimensional (0D) NPs based on metals [e.g., Pt (Ju and Kim, 2015)], bimetallic compounds [e.g., AuPt (He et al., 2010)], metal oxides [e.g., Co_3O_4 (Mu et al., 2013)], and metal chalcogenides [e.g., CuS (He et al., 2012)], have been extensively explored to mimic peroxidases (PODs), oxidases (ODs), catalases (CATs), and superoxide dismutases (SODs) for biomedical applications. Despite much progress in the structural design of 0D nanozymes, there are still several obvious drawbacks. Firstly, most metal-based NPs are often used in a disposable manner, which inevitably causes either economic concerns for the precious metals used or environmental issues due to the pollution and toxicity of these heavy metals (Zhang T. et al., 2014). Secondly, it is known that NPs tend to agglomerate because of huge surface energy, which decreases catalytically active sites, impairing catalytic performance (Yang et al., 2004). Lastly, the inherently imperfect surface accessibility of 0D nanostructures is unfavorable and it is difficult to fully exert the biocatalytic capacity to mimic enzymes (Maromeze et al., 2016). Therefore, researchers should develop nanozymes with novel types of structures and functionalities, a significant research frontier in the nanozyme area.

Two-dimensional (2D) NMs within general sheet-like structures are a newly emerging but very important class of materials. Their lateral dimensions are generally one or several orders of magnitude larger than the thickness, with typical morphologies of nanosheets (NSs), nanoribbons, nanoplates, and nanowalls (Zhang, 2015). Different from their 0D counterparts, 2D NMs with these unique shapes could render large specific surface and distinctive physicochemical attributes, especially in terms of extraordinary surface chemistry, due to the exposure of most of the atoms in 2D NMs on their surface. Initial work about layered materials focused on MoS_2, dating back nearly half a century (Gan et al., 2017). A surge of interest and studies on 2D NMs started after the discovery of graphene in 2004 (Novoselov et al., 2004). Since then, a host of 2D NMs, including layered double hydroxides (LDHs) (Harvey et al., 2016), transition metal dichalcogenides (TMDs) (Zhu et al., 2013), ultrathin metal NMs (Huang et al., 2011), transition metal oxides (TMOs) (Zhou et al., 2017), Xenes (e.g., black phosphorus) (Khan et al., 2020), metal carbides/nitrides (MXenes) (Jiang C. M. et al., 2019), graphitic carbon nitride (g-C_3N_4) (Yang et al., 2013), hexagonal boron nitride (*h*-BN) (Chen M. M. et al., 2017), and metal-organic frameworks (MOFs) (Ding et al., 2017), have attracted considerable attention in numerous research fields, such as sensing, catalysis/electrocatalysis, batteries, electronics/optoelectronics, supercapacitors, and biomedical areas.

In terms of mechanical, chemical, and optical attributes, the potential biocompatibility and degradability, 2D NMs have been enthusiastically researched in various biomedical fields including biosensing (Oudeng et al., 2018), antibacterial agents (Lu et al., 2017), bioimaging (Ma D. T. et al., 2020), and cancer therapy (Kong et al., 2017). Also, with a single-atom layer or several-atoms-thick layers, 2D NMs possess the highest specific surface areas among all known materials, thus they have large reservoirs and abundant anchoring sites to load and deliver therapeutic agents (Qian et al., 2017). Moreover, the planar structure endows them with unusual properties including light/ultrasonic/magnetic responses and biological behaviors (e.g., endocytosis, biodistribution, biodegradation, and excretory pathways), which evokes the broad interest in developing 2D NMs as biomaterials (Chimene et al., 2015).

The rapid development of 2D NMs as versatile biomaterials has benefited from significant research progress in graphene, especially its bulk-quantity production and surface functionalization to improve its water solubility (Li et al., 2008; Sun et al., 2008), which paved the way for graphene to be potentially utilized for biomedical purposes. Meanwhile, it should be pointed out that, the success of 0D nanozymes in biomedical applications has promoted the exploration of the enzymatic properties of other nanostructures. As the first example of the employment of 2D NMs to mimic enzymes, the carboxyl-modified graphene oxide (GO) NSs were found to be able to mimic horseradish peroxidase (HRP), which were further developed as a glucose biosensor based on POD-like activity (Song et al., 2010). Later, a large number of 2D NMs with enzymatic activities have been successively reported and become a new type of enzyme-mimic, hereafter referred to as 2D nanozymes.

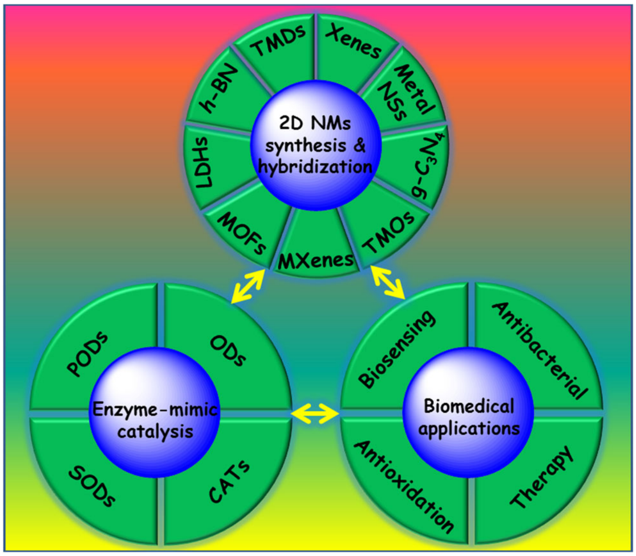

FIGURE 1 | Two-dimensional NMs with enzyme-like activities for biomedical applications.

To our knowledge, despite many reviews (Huang et al., 2016; Agarwal and Chatterjee, 2018; Chen Y. et al., 2018; Dong et al., 2018; Merlo et al., 2018; Tao et al., 2019; Yan et al., 2019; Zhang X. L. et al., 2019; Ren et al., 2020) on the outstanding biomedical performance of 2D NMs, few of them have emphasized enzymatic properties, which are of significant importance to the development of 2D NMs. In this mini-review, we aim to highlight recent progress in 2D NMs with enzymatic properties for biomedical applications. Firstly, we briefly introduce crystal structures, synthesis, and hybridization strategies for 2D NMs. Then, we discuss the enzyme-like activities of 2D NMs. In the following, we summarize the recent advances of 2D nanozymes in diversified biomedical applications, ranging from biosensors, antibacterial agents, and antioxidants to therapeutics (**Figure 1**). Finally, we share our insights into the development prospects and challenges of 2D nanozymes.

CRYSTAL STRUCTURES, SYNTHESIS, AND HYBRIDIZATION STRATEGIES OF 2D NMs

Crystal Structures of 2D NMs

In essence, the unusual physicochemical attributes of 2D NMs largely depends on their atomic arrangements, which have been clarified in detail elsewhere (Butler et al., 2013; Zhang, 2015; Tan et al., 2017). Despite multifarious composition and structural differences, 2D NMs can be generally categorized as layered and non-layered (Hu et al., 2019). For the former, each in-plane atom connects to the neighboring ones through strong chemical bonding in every layer. The layers, however, stack together via weak van der Waals (VDW) interaction (Bhimanapati et al., 2015). A typical layered compound is graphite, in which each atom covalently bonds to three adjacent atoms in planes by σ-bond but weak VDW interaction exists between layers (Allen et al., 2010). LDHs, TMDs, g-C_3N_4, h-BN, Xenes, MXenes, and MOFs, also have a graphite-like crystallite structure. By contrast, the non-layered NMs crystallize in three dimensions by atomic/chemical bonds to form bulk crystals, which typically include 2D metals, metal oxides/chalcogenides, and others (Tan and Zhang, 2015). Relying on the specific arrangement of atoms, coordination modes between atoms, or stacking order between layers, these non-layered NMs can crystallize into different crystal phases, which greatly affect their attributes and functionalities (Tan et al., 2017).

Synthetic Approaches of 2D NMs

The top-down and bottom-up methodologies, as two types of commonly used approaches to the synthesis of 2D NMs, are well-summarized in the literature (Chen et al., 2015; Tan et al., 2017). The former is based on direct cleavage of bulk precursors, aiming to break weak VDW interaction between layers in 2D NMs by various driving forces, typically mechanical/liquid-phase/ion-intercalation and exfoliation (Zeng et al., 2011; Huo et al., 2015; Yi and Shen, 2015). Notably, these methods are only suitable for layered materials. They are relatively simple but suffer from certain disadvantages and limitations. Take synthesis of MoS_2 NSs for example, mechanic exfoliation (Novoselov et al., 2005) is limited by low throughput, thereby making it unsuitable for most biomedical applications: Li-intercalation process not only requires a long time (e.g., 3 days) and high temperature (e.g., 100°C) but results in semiconducting-to-metallic phase-transition of MoS_2 bulk (Yuwen et al., 2016); liquid exfoliation proposes difficulties in removing high-boiling organic solvents (Coleman et al., 2011).

Contrarily, the bottom-up methods usually begin with small organic or inorganic molecules/atoms, employing crystal growth/assembly into a 2D ordered structure, which includes classical chemical vapor deposition (CVD) (Shi et al., 2010) and wet-chemical synthesis (hydro-/solvo-thermal (Duan et al., 2014; Huang et al., 2014) and the self-assembly (Wu et al., 2015) of crystals, etc.). Since the bottom-up methods are based on the chemical reactions of certain precursors in given synthetic systems, they are more versatile than the top-down methods in enabling access to all types of 2D NMs. Despite the above protocols, it is still challenging to develop an appropriate strategy to synthesize 2D NMs with controlled and desirable structural parameters so as to satisfy the specific requirements.

Hybridization of 2D NMs

It is known that the hybridization of 2D NMs with functionalized species is an effective strategy to extend and expand their functionalities, which could potentially make them suitable for practical applications. Numerous functionalized species (e.g., atoms, ions, molecules, polymers, and nanostructures), have been modified onto/into 2D NMs by various methods such as doping, adsorption, electrodeposition, covalent functionalization, chemical reduction, and self-assembly (Guan and Han, 2019). For example, to improve water dispersibility and the stability of pristine MXenes NSs in a physiological solution for biomedical applications, Shi's group reported modification of Ti_3C_2 NSs with soybean phospholipid by adsorption (Lin et al., 2017). The functionalized materials were found to possess enhanced permeability, stable circulation, and retention ability. In a similar study by Geng's group, titanium carbide NSs terminated with $Al(OH)_4^-$, obtained by intercalation of Ti_3AlC_2 bulk with tetramethylammonium (TMAOH) were modified with polyethylene glycol (PEG) molecules. The functionalized NSs demonstrated excellent stability in various physiological solutions, which were further developed as promising photothermal therapeutic agents (Xuan et al., 2016).

A variety of 0D metal NPs-functionalized 2D NSs have also been reported by different groups, including 0D/2D nanostructured Au/GO (Tao et al., 2013), Au/MOF (Huang et al., 2017a), and Pt/black phosphorus (Ouyang et al., 2018). In recent studies, the *in-situ* growth method was also adopted by different groups for the synthesis of Pt/h-BN (Ivanova et al., 2019) and "naked" Au NPs on g-C_3N_4 NSs (Wu et al., 2019), via the reduction of metal precursors on NSs with various reducing agents like $NaBH_4$, ascorbic acid, etc. Our group also constructed a variety of 0D/2D heterostructures, including PtAg NPs-decorated MoS_2 NSs through the hydrothermal process (Cai et al., 2016), Pt NPs-covered CuO NSs by $NaBH_4$ reduction (Wang X. H. et al., 2017), and IrO_2 NPs-modified GO (Sun et al., 2020) and reduced GO (rGO) (Liu X. L. et al., 2019) NSs by electrostatic adsorption/hydrothermal treatment. The modification of NPs onto 2D NMs could not only prevent NPs from aggregation but inhibit the restacking of NSs, which could facilitate practical applications. However, to access these nanocomposites, a multi-step procedure was generally required for synthesis. In a recent study, our group reported a one-pot fabrication of PtRh NPs-modified Rh NSs (Cai et al., 2019). During the synthesis, Pt atoms/clusters as seeds were first formed by reduction of Pt precursors ($H_2PtCl_6{\cdot}6H_2O$), which promoted the reduction of Rh precursors ($Rh(acac)_3$) to form PtRh NPs and directed formation of Rh NSs around PtRh NPs. In another work, our group demonstrated the one-pot synthesis of Pd NPs-modified $NiCl_2$ NSs, by using a three-step process of "*in situ* reduction-oxidation-assembly" (Cai et al., 2018a). Notably, the pre-preparation and/or functionalization of NSs as well as immobilization of NPs on NSs, generally involved in conventional synthetic protocols, were unnecessary in the above studies.

ENZYMATIC PROPERTIES OF 2D NANOZYMES

POD- and OD-Like Properties

PODs and ODs are a class of known oxidative enzymes in biosystems, which activate H_2O_2 and O_2 to catalyze the oxidation of respective substrates under mild conditions (Wei and Wang, 2013; Huang et al., 2019; Jiang D. W. et al., 2019). To evaluate the POD-/OD-like activity of 2D NMs, catalytic oxidations of enzymatic chromogenic substrates like 3,3',5,5'-tetramethylbenzidine (TMB), which are often carried out in acidic media and produce colored products (**Equation 1**), are chosen as a probe reaction by most researchers (Gao et al., 2007; Song et al., 2010; Tao et al., 2013; Cai et al., 2016, 2018a, 2019; Huang et al., 2017a; Wang X. H. et al., 2017; Ouyang et al., 2018; Ivanova et al., 2019; Liu X. L. et al., 2019; Wu et al., 2019; Sun et al., 2020). The reaction process is tracked by UV-Vis spectroscopy and the color variation of the reaction solution can be easily observed by naked eyes.

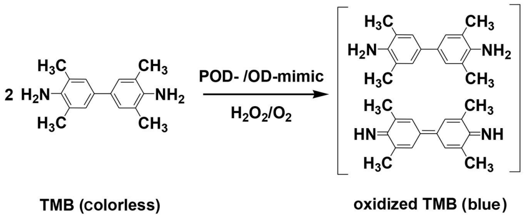

(1)

Since the first report of GO NSs as a 2D POD-mimic by Qu's group (Song et al., 2010), similar observations were obtained from other types of 2D NMs, which also exhibited typical Michaelis-Menten kinetics during POD-catalysis. The apparent kinetic constant (K_m) and maximum reaction rate (V_{max}), as two important parameters related to enzyme-catalysis, could be determined from the Linewearver-Burk plot. The constant K_m characterizes the binding affinity of a substrate to the enzyme, in which a lower K_m value means the higher affinity. **Table 1** lists the kinetic parameters of typical 2D NMs as POD-mimics based on GO (Zhang L. N. et al., 2014; Sun et al., 2020) or rGO (Liu X. L. et al., 2019), TMDs (Lin et al., 2014a,b; Chen T. M. et al., 2017; Huang et al., 2018; Wu et al., 2018; Feng et al., 2020), LDHs (Zhan et al., 2018; Yang et al., 2020), *g*-C_3N_4 (Darabdhara et al., 2019), MOF NSs (Chen J. Y. et al., 2018), *h*-BN (Ivanova et al., 2019), metal oxides (Wang X. H. et al., 2017; Li et al., 2019), and metallic NSs (Wei et al., 2015; Cai et al., 2018b, 2020).

In an earlier study on the POD-like properties of TMDs, Guo's group reported that the commercially obtained MoS_2 NSs by solution-based exfoliation gave a K_m value of 0.0116 mM with H_2O_2 as substrate, far lower than those of HRP (3.7 mM) (Gao et al., 2007) and Fe_3O_4 NPs (154 mM) (Gao et al., 2007), suggesting good affinity of as-obtained materials toward H_2O_2 (Lin et al., 2014a). The authors also found the POD-catalysis of MoS_2 NSs was efficient over a broad pH range (2.0–7.5), wider than those of GO NSs and several 0D NPs [e.g., Fe_3O_4 (Gao et al., 2007), Co_3O_4 (Mu et al., 2012), and $ZnFe_2O_4$ (Su et al., 2012)]. In a recent study, Wang's group synthesized MoS_2 NSs using a hydrothermal method, followed by the treatment of N_2 plasma, producing N-doped MoS_2 NSs (Feng et al., 2020). With H_2O_2 as a substrate, the as-obtained materials not only gave a much lower K_m value (0.4459 mM) compared to that of the undoped ones (2.0828 mM), but presented a larger V_{max} value (4.348×10^{-8} M s^{-1}) than that of undoped NSs (1.346×10^{-8} M s^{-1}), suggesting enhanced affinity and the activity of NSs by N-doping. The N_2 plasma treatment efficiently increased the surface wettability and affinity of pristine NSs, thus improving the access of the electrons and substrates of catalytic reactions. In another study, Das's group synthesized a series of metal NPs (e.g., Au, Ni, and AuNi NPs) decorated *g*-C_3N_4 NSs by a solvothermal method (Darabdhara et al., 2019). With a substrate of either TMB or H_2O_2, the bimetallic nanocomposites gave both lower K_m values and larger V_{max} values (**Table 1**) than those of monometallic ones, indicating better affinity and POD-like activity by introducing bimetallic NPs into *g*-C_3N_4 NSs. Similar observations were obtained by Pt/CuO (Wang X. H. et al., 2017), IrO_2/rGO (Liu X. L. et al., 2019), Pd/$NiCl_2$ (Cai et al., 2018a), and PtM/MoS_2 (M = Ag, Cu, and Au) (Cai et al., 2016, 2017; Qi et al., 2016) as reported by our group.

Compared to the layered NM-based POD-mimics, non-layered examples are few. In a study by our group, the Pd NSs were prepared in CH_3COOH by bubbling of CO gas, followed by Galvanic replacement of Au^{3+} ions to obtain Au NPs decorated Pd NSs (Cai et al., 2020). When TMB and H_2O_2 respectively acted as a substrate, the as-obtained nanocomposites afforded two large V_{max} values (19.65×10^{-8} and 8.19×10^{-8} M S^{-1}), an ~2-fold enhancement in those of Pd NSs (7.01×10^{-8} and 4.02×10^{-8} M S^{-1}). In another study, Zheng's group synthesized ultrathin Pd NSs with a thickness below 10 atomic layers in the presence of PVP and a halide salt, followed by coating Pt nanodots onto the Pd NSs by reduction of $Pt(acac)_2$ with hydrazine hydrate in DMF solution (Wei et al., 2015). As listed in **Table 1**, compared to Pd NSs, the as-prepared nanocomposites gave lower K_m values and larger V_{max} values, demonstrating superior affinity and activity. To further make a meaningful comparison of catalytic efficiency between Pd NSs and the nanocomposites, the catalytic rate constant (K_{cat}) was introduced by the authors, which was calculated from the equation $K_{cat} = V_{max}/E$, where E is the concentration of the catalyst. With either TMB or H_2O_2 as a substrate, the obtained K_{cat} value for the nanocomposites was appropriately two times larger than those of Pd NSs. However, compared to several NPs such as Fe_3O_4 NPs (Gao et al., 2007), the catalytic efficiency of the nanocomposites is not high enough. In an interesting study, our group presented superior POD-catalysis of single-layer Rh NSs synthesized via the solvothermal method (Cai et al., 2018b). The obtained K_m values for Rh NSs that were comparable to those of HRP (Gao et al., 2007), while the V_{max} value for Rh with H_2O_2 as the substrate was exceptionally larger than those of HRP (Gao et al., 2007), Rh NPs (Choleva et al., 2018), and layered NMs based on GO (Gao et al., 2007), and TMD-based NSs (Lin et al., 2014a,b; Chen T. M. et al., 2017; Wu et al., 2018). Moreover, the obtained K_{cat} value for Rh NSs to H_2O_2 was 128 times, 323 times, and 34 times larger than those of HRP (Gao et al., 2007), Rh NPs (Choleva et al., 2018), and few-layer Pd NSs (Wei et al., 2015), respectively. This high activity could be attributed to the large number of exposed active Rh atoms that were coordinately unsaturated, which facilitated efficient interaction with reactants during catalysis. The Rh NSs also demonstrated satisfactory chemical/thermal stability.

Previous studies revealed that POD-catalysis generally involves two types of pathways: (1) the generation of reactive oxygen species (ROS) including hydroxyl radicals (·OH) (Song et al., 2010; Lin et al., 2014a; Wei et al., 2015; Wang X. H. et al., 2017; Cai et al., 2018a), and (2) electron-transfer (ET) process (Cai et al., 2018b, 2020). The former is believed to undergo a radical chain mechanism, in which the O-O bonds

TABLE 1 | The kinetics parameters of HRP, Fe_3O_4 NPs, and typical 2D POD-mimics^a.

Catalyst	[E] (10^{-12} M)	Substrate	K_m (mM)	V_{max} (10^{-8} M S^{-1})	K_{cat} (10^4 s^{-1})	References
HRP	25	TMB	0.434	10	0.4	Gao et al., 2007
		H_2O_2	3.7	8.71	0.348	
Fe_3O_4 NPs	1.14	TMB	0.098	3.44	3.02	Gao et al., 2007
		H_2O_2	154	9.78	8.58	
GO	NA	TMB	0.0237 ± 0.001	3.45 ± 0.31	NA	Song et al., 2010
		H_2O_2	3.99 ± 0.67	3.85 ± 0.22		
Pt/GO	NA	TMB	0.1864	10.2	NA	Zhang et al., 2014
		H_2O_2	221.4	12.45		
IrO_2/GO	NA	TMB	0.56	32.8	NA	Sun et al., 2020
		H_2O_2	5.19	20.8		
IrO_2/rGO	NA	TMB	0.276	42.7	NA	Liu X. L. et al., 2019
		H_2O_2	229	372.9		
MoS_2	NA	TMB	0.525	5.16	NA	Lin et al., 2014a
		H_2O_2	0.0116	4.29		
WS_2	NA	TMB	1.83	4.31	NA	Lin et al., 2014b
		H_2O_2	0.24	4.52		
$MoSe_2$	NA	TMB	0.014	0.56	NA	Wu et al., 2018
		H_2O_2	0.155	0.99		
WSe_2	NA	TMB	0.0433	1.43	NA	Chen T. M. et al., 2017
		H_2O_2	19.53	2.22		
VS_2	NA	TMB	0.28	41.6	NA	Huang et al., 2018
		H_2O_2	3.49	55.7		
PtAg/MoS_2	NA	TMB	25.71	7.29	NA	Cai et al., 2016
		H_2O_2	0.386	3.22		
N-doped MoS_2	NA	TMB	0.7916	1.796	NA	Feng et al., 2020
		H_2O_2	0.4459	4.348		
NiFe LDHs	NA	TMB	0.5 ± 0.05	NA	NA	Zhan et al., 2018
		H_2O_2	2.4 ± 0.1			
CeO_2/CoFe LDHs	NA	TMB	0.419	NA	NA	Yang et al., 2020
		H_2O_2	10.82			
AuNi/*g*-C_3N_4	NA	TMB	0.16	2.34	NA	Darabdhara et al., 2019
		H_2O_2	4.47	6.16		
Au/*g*-C_3N_4	NA	TMB	0.27	1.27	NA	Darabdhara et al., 2019
		H_2O_2	11.13	3.44		
Ni/*g*-C_3N_4	NA	TMB	0.49	0.75	NA	Darabdhara et al., 2019
		H_2O_2	19.91	1.38		
MOF	NA	TMB	0.365	6.53	NA	Chen J. Y. et al., 2018
		H_2O_2	2.49	130		
h-BN	NA	TMB	0.42	NA	NA	Ivanova et al., 2019
		H_2O_2	12.2			
Pt/*h*-BN	NA	TMB	0.21	NA	NA	Ivanova et al., 2019
		H_2O_2	9.2			
WO_3	NA	TMB	10.6	1.53	NA	Li et al., 2019
		H_2O_2	1260	3		
Pt/CuO	NA	TMB	0.413	14.6	NA	Wang X. H. et al., 2017
		H_2O_2	2.887	8.85		
Pd	NA	TMB	0.21	7.01	NA	Cai et al., 2020
		H_2O_2	4.44	4.02		
Pd	5.06	TMB	0.1098	5.82	1.2	Wei et al., 2015
		H_2O_2	4.398	6.51	1.3	

(Continued)

TABLE 1 | Continued

Catalyst	[E] (10^{-12} M)	Substrate	K_m (mM)	V_{max} (10^{-8} M S^{-1})	K_{cat} (10^4 s^{-1})	References
Au/Pd	NA	TMB	0.295	19.65	NA	Cai et al., 2020
		H_2O_2	5.89	8.19		
Pt/Pd	1.9	TMB	0.0865	6.228	3.1	Wei et al., 2015
		H_2O_2	2.231	5	2.5	
Rh	1.53	TMB	0.264	12.56	8.2	Cai et al., 2018b
		H_2O_2	4.51	68.09	44.5	

[a] $K_{cat} = V_{max}/E$, where E is the concentration of the catalyst.
Not available, NA.

of H_2O_2 molecules are broken to generate ·OH radicals, which subsequently oxidize the substrates. In a representative example, Yang's group found that after the coverage of Au NPs onto the g-C_3N_4 NSs (Wu et al., 2019), the generation of ·OH radicals remarkably increased during catalysis, evidenced by electron spin resonance (ESR). The increase in ·OH radicals could be attributed to the synergistic effect of Au NPs and g-C_3N_4 NSs, which enhanced the POD-catalysis. By contrast, for the latter, the 2D NMs mediate ET between the substrates and H_2O_2 molecules, instead of ROS generation. Take the Au NPs coated Pd NSs reported by our group (Cai et al., 2020) for example, with the introduction of Au atoms, the electronic structure of Pd NSs was modified, which subsequently caused a change in the catalytic pathway of Pd NSs (i.e., from ·OH generation to rapid ET process).

Different from PODs, ODs catalyze oxidations with O_2 as the oxygen source (generally in the open air), instead of unstable H_2O_2. The potential oxidative damage of biological species by H_2O_2 could also be avoided by the use of O_2. The metal oxide NSs like MnO_2 NSs (Liu et al., 2017; Yan et al., 2017; Ge et al., 2019) were found to exhibit OD-like activities, with the merits of operational simplicity and fine compatibility. Besides, good stability of MnO_2 NSs as OD-mimics was also found by several research groups. For example, Dyson's group synthesized the MnO_2 NSs by exfoliation of bulk δ-MnO_2 in BSA aqueous solution (Liu et al., 2017). After storage for 3 months, no significant loss in the activity of NSs was observed. Similar findings were obtained from Rh NSs (Cai et al., 2018b) and PtRh/Rh nanocomposites (Cai et al., 2019). In some studies, the OD-catalysis was believed to go through the generation of ROS such as superoxide ions ($O_2^{\cdot-}$), via cleavage of O-O bonds in O_2 molecules (Cai et al., 2019; Ge et al., 2019).

Notably, besides temperature and substrate concentration, the POD/OD-like activities of 2D nanozymes greatly depend on system pH (often around 4 is efficient), which is similar to the 0D examples and enzymes. Thus, to facilitate their application in biosystems, it is highly desirable to develop 2D nanozymes with a wide range of pH, especially at neutral pH. In an early study, Qu's group synthesized the lysozyme-stabilized Au clusters on GO NSs (Au/GO), which exhibited good catalytic activity over a broad pH range, even in physiological pH (Tao et al., 2013). Compared to that at pH 3.0, the POD-like activity of Au/GO remained about 82 % at pH 7.0. In a recent study, Kim's group reported the rosette-shaped C_3N_4 by the polymerization reaction between cyanuric acid and melamine, followed by calcination (Heo et al., 2020). Due to larger surface area and higher porosity, the activity of as-prepared materials was appropriately 10-fold higher than that of conventional bulk-C_3N_4. Interestingly, the maximal activity was shown at pH 8.0, and over 80% of the activity relative to the maximum activity remained across a pH range of 6.0–9.0.

Although numerous 2D nanozymes exhibited high activity, the catalysis is also lacking selectivity, similar to the 0D ones. To this end, Lee's group synthesized the N- and B-codoped rGO NSs, which showed high efficiency in POD-catalysis, nearly 1000-fold higher than that of undoped rGO (Kim et al., 2019). More importantly, no OD-like activity was observed for the as-prepared materials, suggesting high selectivity. The same group also provided another valuable example, in which the Fe-N_4 single site, resembled the heme cofactor present in HRP, was embedded in graphene to obtain the Fe-N-rGO nanocomposites (Kim et al., 2020). Intriguingly, the nanocomposites not only showed a remarkable enhancement in catalytic efficiency, up to appropriately 700-fold higher than that of undoped rGO but had excellent selectivity toward H_2O_2. The single-atom nanozymes (SAzymes), as a very new concept in the nanozyme field (Jiao et al., 2019), could open a window to develop a new type of highly active and selective 2D hybrid nanozymes at the atomic scale.

SOD- and CAT-Like Properties

Contrary to oxidative biocatalysts, SODs and CATs are a type of antioxidant enzyme, which plays an essential part in maintaining redox balance in living organisms by scavenging excess ROS (Liu Y. et al., 2014). There are three forms of human SODs [i.e., cytosolic CuZn SOD, mitochondrial Mn SOD, and extracellular SOD, of which the first is the most studied (Korschelt et al., 2017)]. In a typical cycle of CuZn SOD (Yu et al., 2014; Korschelt et al., 2017), the metal Cu center shuttles between the Cu^{2+}/Cu^{+} redox states (**Equations 2, 3**), catalyzing the disproportionation of $O_2^{\cdot-}$ into O_2 and H_2O_2 under neutral conditions (**Equation 4**).

$$O_2^{\cdot-} + \mathrm{Cu(II)} \rightarrow O_2 + \mathrm{Cu(I)} \tag{2}$$

$$O_2^{\cdot-} + \mathrm{Cu(I)} + 2H^+ \rightarrow H_2O_2 + \mathrm{Cu(II)} \tag{3}$$

$$2O_2^{\cdot-} + 2H^+ \rightarrow H_2O_2 + O_2 \tag{4}$$

Following a similar mechanism to that described above, several NMs based on V_2O_5 nanowires (Vernekar et al., 2014) and CeO_2 NPs (Korsvik et al., 2007) have displayed intrinsic SOD-like activities. The polyvinylpyrrolidone (PVP)-modified Nb_2C NSs obtained by liquid-phase exfoliation (Ren et al., 2019) also provide an interesting example of SOD-mimics. By density functional theory (DFT) calculations together with the characterization of active intermediates via X-ray photoelectron spectroscopy (XPS) and X-ray diffraction (XRD) analysis, the authors discovered the SOD-like activity of Nb_2C NSs originated from the surface oxidation process, in which Nb_2O_5 formed as catalytically active species.

CATs accelerate the dismutation of H_2O_2 into O_2 and H_2O, often in the reaction solutions at a high pH (Wei and Wang, 2013; Huang et al., 2019; Jiang D. W. et al., 2019). Previous studies have revealed that the CAT-like activities of 0D metal oxide NPs originated from ion pairs (catalytic sites in two different oxidation states), such as Co^{2+}/Co^{3+} (Mu et al., 2013), Fe^{2+}/Fe^{3+} (Lin and Gurol, 1998), and Mn^{3+}/Mn^{4+} (Hasan et al., 1999). Take Co_3O_4 NPs (Mu et al., 2013) for example, the catalytic mechanism can be described as follows. Under alkaline conditions, it is believed that there is a larger concentration of perhydroxyl anions (OOH^-) in the reaction system (**Equation 5**) (Mu et al., 2013). Since OOH^- radicals are more nucleophilic than H_2O_2 molecules, they could readily interact with Co(III) centers (**Equation 6**) to generate Co(II) species and release ·OOH radicals (**Equation 7**), while H_2O_2 molecules were activated by Co(II) center to produce ·OH radicals (**Equation 8**). The coupling reaction of the generated ·OH and ·OOH radicals gave water and oxygen as final products (**Equation 9**).

$$H_2O_2 + OH^- \rightarrow OOH^- + H_2O \tag{5}$$

$$\mathrm{Co(III)} + OOH^- \rightarrow \mathrm{Co(II)} \cdot OOH \tag{6}$$

$$\mathrm{Co(II)} \cdot OOH \rightarrow \mathrm{Co(II)} + \cdot OOH \tag{7}$$

$$\mathrm{Co(II)} + H_2O_2 \rightarrow \mathrm{Co(III)} + \cdot OH + OH^- \tag{8}$$

$$\cdot OH + \cdot OOH \rightarrow H_2O + O_2 \tag{9}$$

The above mechanism could also apply to 2D counterparts. For example, Jiang's group prepared MnFe LDHs by simple co-precipitation, which exhibited intrinsic CAT-like activities (Ruan et al., 2018). The authors explained that both the $Mn^{3+/4+}$ and Fe^{3+} species exhibited catalytic activity toward H_2O_2, which could be used for H_2O_2 decomposition to generate oxygen in cancer tissues, to enhance the effect of oxygen-dependent photodynamic therapy (PDT). In another study, besides the metal center shuttling during catalysis, Zheng's group demonstrated the role of ligands in the CAT-like activity of MOF NSs. The Cu MOF NSs were synthesized based on the coordination reaction between the Cu^{2+} ions and isophthalic acids as ligands, with different substituent groups (e.g., $-CH_3$, $-NO_2$, -OH, and $–NH_2$) at 5-position (Wang et al., 2019). The authors found that the CAT-like activity of as-obtained materials was related to the charge density around Cu atoms in the NSs, in which the nitro-functionalized NSs exhibited the highest activity. Since the nitro group is an electron-drawing group while other groups are electron-donating ones, the positive charge density around Cu atoms for the nitro-modified NSs was the highest, which was favorable for the binding of H_2O_2 as an electron donor.

It is also of note that several 2D NMs were found to have multiple enzymatic activities. For example, Yang's group found that the few-layer MoS_2 NSs prepared by liquid-exfoliation exhibited ternary activities (POD-, OD-, and CAT-like activities) (Chen T. M. et al., 2018). As discussed above, these enzymatic activities could be closely associated with specific reaction conditions especially system pH, in which the acidic conditions are usually favorable for POD/OD-mimic catalysis (Qi et al., 2016; Cai et al., 2017; Darabdhara et al., 2019; Feng et al., 2020), while a high pH is beneficial to CAT-catalysis (Liu Y. et al., 2014; Ruan et al., 2018; Wang et al., 2019). Due to the use of various 2D NMs in biomedical fields, for a meaningful discussion of enzyme-like activity, the reaction parameters, nature of materials (e.g., morphology, structure, composition, and size), capping agents, and surface charge, are believed to be taken into account (Cai and Yang, 2020).

BIOMEDICAL APPLICATIONS OF 2D NANOZYMES

Toxicology of 2D NMs

To access the full potential of 2D NMs for practical applications, it is necessary to know their toxicity, including *in vitro* cellular uptake, location, toxicity, *in vivo* biodistribution, degradation, and excretion. However, to date, few studies have highlighted biocompatibility.

The *in vitro* biocompatibility of graphene-based materials, as the oldest and most studied 2D examples, was found to be highly related to their structural/compositional parameters and physicochemical properties, such as morphology, size, layer numbers, hydrophobicity/hydrophilicity, dispersion, and concentration (Ghosal and Sarkar, 2018). For example, hydrophobic and large-size graphene had higher cytotoxicity than hydrophilic and nanosized counterparts (Sukumar et al., 2020). Cui's group found that the cytotoxicity of GO was affected by their concentration, in which the presence of GO with a low concentration (<10 μg mL^{-1}) slightly decreased the viability of human fibroblast cells (<20% when exposed for 4 days), but high concentrations of graphene (>50μg mL^{-1}) showed obvious cytotoxicity even after only 1 day of exposure (>20%) (Wang et al., 2011). This was caused by the agglomerates of the physiological medium formed between GO layers *via* π - π interactions. Since the aggregated macroparticles could not enter into the cells, they became entrapped on the cell membrane and gave rise to cytoskeleton disruption, membrane deformation, and an increase in intercellular stress, ultimately resulting in cell death. In addition, Koyakutty's group observed that the cytotoxicity of pristine graphene could be improved by carboxyl functionalization (Sasidharan et al., 2011). As the concentration of pristine graphene increased from 0 to 300 μg mL^{-1}, the viability of Vero cells decreased remarkably. A lower concentration of pristine graphene (100 μg mL^{-1}) resulted in the death of appropriately 50% of cells, which further increased to about 60% at 300 μg mL^{-1}. Contrarily, the functionalized graphene showed negligible effects on the viability, even at the highest concentration studied. In another study by the same group, functionalized hydrophilic graphene was found to be favorable for macrophage cell (RAW 264.7) uptake (Sasidharan et al., 2012), distinct from the hydrophobic pristine graphene. The pristine graphene was primarily accommodated at the cell surface and induced ROS-mediated apoptosis when the concentration was above 50 μg mL^{-1}, which has not been found for functionalized graphene at a higher concentration of 75 μg mL^{-1}. Despite enhanced cytocompatibility by surface functionalization, all forms of graphene-based materials could lead to ROS generation in mammalian cells, which should be carefully taken into account for biomedical applications (Liao et al., 2011; Gollavelli and Ling, 2012).

In an earlier study on the *in vivo* biodegradability of graphene, Koyakutty's group revealed that time-bound spectral alternations using confocal Raman imaging, such as the formation of the defective D$^{'}$ band, widening of D and G bands, and increase in I_D/I_G ratio of pristine graphene, embedded in different organs (e.g., lung, liver, kidney, and spleen of mice) over a time of 8–90 days (Girish et al., 2013). These observations arose from the increase in structural disorders in graphene phagocytosed by macrophages. The most enhanced amount of disorder, which was observed for the spleen bound samples, caused complete amorphization after 90 days of intravenous injection. In another study, after intravenous GO administration, the accumulation of GO was increased largely in the lung and liver for a longer time (Liu et al., 2012). GO NSs accumulated because of the possible instability and nonspecific binding of GO with different proteins. Since the blood initially flowed to the lung, more GO NSs were accumulated in the lung than other organs. Dash's group investigated the effect of GO and rGO on blood platelet functions (Singh et al., 2011). In this study, the GO sheets were found to cause strong aggregatory responses in platelets by activating a family of Src kinases, which further led to the release of calcium from intercellular compartments. Moreover, this study revealed that, due to charge distribution on the surface of GO NSs, the intravenous administration of GO in mice could trigger pulmonary thromboembolism. By contrast, rGO was unable to effectively activate platelets because of reduced charge density on the graphene surface.

The exploration of TMDs in biomedical areas began in 2013–2014. Similar to graphene-based materials, after surface modification, several members of TMDs also showed good *in vitro* biocompatibility. A relevant example is the WS_2 NSs prepared by Liu's group using the Li ions insertion method (Cheng et al., 2014). Without surface modification, the authors found that the WS_2 NSs exhibited obvious toxicity toward 4T1 (murine breast cancer cells), HeLa (human epithelial carcinoma cells), and 293T (human embryo kidney cells) after incubation for 24 h. At a high concentration of 0.1 mg mL^{-1} of WS_2 NSs, only about 50% of cells were alive; however, after modification with PEG, the as-obtained NSs demonstrated no significant cytotoxicity under the same conditions. Contrarily, without surface functionalization, Zhao's group prepared the WS_2 NSs by H_2SO_4 intercalation and exfoliation in an aqueous solution, which showed low toxicity toward HeLa cells (Yong et al., 2014). The cell viability remained high (above 85%) even at a high concentration (0.2 mg mL^{-1}). The authors outlined that the biocompatibility of unmodified WS_2 NSs could be attributed to a mild aqueous phase in synthesis, in which the toxic organic solvents/chemicals were unnecessary. Using a similar method, Zhao's group prepared MoS_2 NSs, followed by coating with chitosan (Yin et al., 2014). Even at a high concentration up to 0.4 mg mL^{-1}, the as-obtained NSs demonstrated low cytotoxicity against KB (human epithelial carcinoma cell line) and Panc-1 (pancreatic carcinoma, epithelial-like cell line). The functionalized NSs also showed negligible hemolysis of red blood cells (RBCs), suggesting good blood compatibility. The above studies revealed that the *in vitro* toxicity of TMDs could be affected by synthetic methodology, surface chemistry, and specific cells. For the investigations on *in vivo* biocompatibility, Liu's group evaluated the toxicity of PEGylated WS_2 NSs (Cheng et al., 2014) toward Balb/c mice, by hematoxylin and eosin (H&E) assay, serum biochemistry assay, and complete blood panel test. In their study, no obvious abnormal behavior of mice at the dose of 20 mg kg^{-1} was observed during the assay (45 days after photothermal therapy). In a similar study by the same group, the PEGylated MoS_2 NSs also demonstrated no obvious toxicity against Balb/c mice, at a relatively lower dose of 3.4 mg kg^{-1} (Liu T. et al., 2014). However, to fully understand their potential toxicity/metabolism in longer terms, more studies are needed.

Compared to graphene-based materials and TMDs, the biocompatibility/biosafety of other 2D NMs especially Xenes, MXenes, and ultrathin metallic NSs, is less explored. Considering these structural and compositional differences, their solubility, biodegradation, and biocompatibility could be different from each other. Presently, the evaluations of *in vitro*/*vivo* biocompatibility of these materials are in progress (Wang S. G. et al., 2020). Despite the low toxicities of several types of 2D NMs [e.g., MnO_2 (Gao et al., 2020), *g*-C_3N_4 (Liang et al., 2017), and *h*-BN (Mateti et al., 2018)] exhibited in preliminary investigations, it is too soon to confirm the biosafety of 2D NMs at this stage. Thus, careful systematic tests on their toxicity are required before practical applications can be developed.

Biomedical Applications of 2D Nanozymes

Biosensors

The accurate determination of biologically important analytes is of significance for clinical diagnosis. The colorimetric method, as an appealing one for point-of-care (POC) applications with many merits (e.g., low cost, simplicity, and practicality), has attracted considerable interest in biosensing (Song et al., 2011).

With good stability and adjustable catalytic activities, 2D NMs provide useful platforms for *in vitro* colorimetric detection. Recently, the assays for various bioanalytes like small molecules, cancer cells, and ions, have been proposed based on POD-like activities of 2D NMs (**Table 2**). As a typical example, the colorimetric assays for glucose have been largely developed based

TABLE 2 | Summary of several typical 2D nanozymes for colorimetric detection of various target analytes.

Analyte	**Materials**	**Activity**	**LDR**	**LOD**	**References**
Glucose	GO	POD	1–20 μM	1 μM	Song et al., 2010
Glucose	FePd/rGO	POD	1–200 μM	1.76 μM	Yang et al., 2019
Glucose	MoS_2	POD	5–150 μM	1.2 μM	Lin et al., 2014a
Glucose	WS_2	POD	5–300 μM	2.9 μM	Lin et al., 2014b
Glucose	WSe_2	POD	10–60 μM	10 μM	Chen T. M. et al., 2017
Glucose	VS_2	POD	5–250 μM	1.5 μM	Huang et al., 2018
Glucose	PtAg/MoS_2	POD	1–10 μM	0.8 μM	Cai et al., 2016
Glucose	NiFe LDHs	POD	0.05–2.0 mM	23 ± 2 μM	Zhan et al., 2018
Glucose	CeO_2/CoFe	POD	0.05–2.0 mM	15 μM	Yang et al., 2020
Glucose	g-C_3N_4	POD	5–100 μM	1.0 μM	Lin et al., 2014c
Glucose	Au/g-C_3N_4	POD	5–100 μM	1.2 μM	Wu et al., 2019
Glucose	Pd/g-C_3N_4	POD	50–2,000 μM	50 μM	Zhang W. C. et al., 2019
Glucose	Fe/g-C_3N_4	POD	0.5–10 μM	0.5 μM	Tian et al., 2013
Glucose	AuNi/g-C_3N_4	POD	0.5–30 μM	1.7 μM	Darabdhara et al., 2019
Glucose	Au/Pd	POD	5–400 μM	0.85 μM	Cai et al., 2020
Glucose	Pt/Pd	POD	0.1–0.5 mM	NA	Wei et al., 2015
Glucose	Au/MOF	GOx, POD	10–300 μM	8.5 μM	Huang et al., 2017a
AA	Pt/CuO	POD	1 μM–0.6 mM	0.796 μM	Wang X. H. et al., 2017
AA	IrO_2/GO	POD	5–70 μM	324 nM	Sun et al., 2020
GSH	MnO_2	OD	NA	300 nM	Liu et al., 2017
GSH	MnO_2	OD	10 nM–5 μM	5.6 nM	Ge et al., 2019
GSH	IrO_2/rGO	POD	0.1–50 μM	83 nM	Liu X. L. et al., 2019
Cysteine	IrO_2/rGO	POD	0.1–50 μM	40 nM	Liu X. L. et al., 2019
Homocysteine	IrO_2/rGO	POD	0.1–50 μM	57 nM	Liu X. L. et al., 2019
Xanthine	Rh	POD	2–80 μM	0.73 μM	Cai et al., 2018b
Xanthine	WO_3	POD	25–200 μM	1.24 μM	Li et al., 2019
Xanthine	$MoSe_2$	POD	0.01–0.32 mM	1.964 μM	Wu et al., 2018
Dopamine	Pt/BN	POD	2–55 μM	0.76 μM	Ivanova et al., 2019
Dopamine	CuS/rGO	POD	2–100 μM	0.48 μM	Dutta et al., 2015
Cholesterol	CuS/BN	POD	10–100 μM	2.9 μM	Zhang et al., 2017
AChe	MnO_2	OD	0.1–15 mU mL^{-1}	35 μU mL^{-1}	Yan et al., 2017
MCF-7 cells	Au/GO	POD	NA	1,000	Tao et al., 2013
MCF-7 cells	PtCu/MoS_2	OD	NA	300	Qi et al., 2016
MCF-7 cells	Pt/GO	POD	NA	125	Zhang L. N. et al., 2014
S^{2-} ions	MoS_2/g-C_3N_4	POD	0.1-10 μM	37 nM	Liu et al., 2020
Fe^{2+} ions	MoS_2	POD	0.01–0.8 μM	7 nM	Wang et al., 2016
Pb^{2+} ions	WS_2	POD	5–80 μg L^{-1}	4 μg L^{-1}	Tang et al., 2020

[a] *Acetylcholinesterase.*

AChe, Linear detection range; LDR, Limit of detection, LOD.

on a host of 2D NMs and their hybrids, including graphene derivatives [e.g., GO (Song et al., 2010), FePd/rGO (Yang et al., 2019)], TMDs [e.g., MoS_2 (Lin et al., 2014a), WS_2 (Lin et al., 2014b), WSe_2 (Chen T. M. et al., 2017), VS_2 (Huang et al., 2018)] and their hybrids [e.g., PtAg/MoS_2 (Cai et al., 2016)], LDHs [e.g., NiFe (Zhan et al., 2018)], and their hybrids [e.g., CeO_2/CoFe (Yang et al., 2020)], g-C_3N_4 (Lin et al., 2014c) and its hybrids [e.g., Au/g-C_3N_4 (Wu et al., 2019), Pd/g-C_3N_4 (Zhang W. C. et al., 2019), Fe/g-C_3N_4 (Tian et al., 2013), and AuNi/g-C_3N_4 (Darabdhara et al., 2019)], and metallic NSs-based hybrids [e.g., Au/Pd (Cai et al., 2020) and Pt/Pd (Wei et al., 2015)]. Some of them showed excellent analytic performance (e.g., wide linear detection range, high sensitivity, and selectivity) for glucose detection and demonstrated practicality and superiority for real samples. However, it is noteworthy that these materials could only be employed to mimic PODs and that glucose oxidase (GOx) was required for detection, since it catalyzed the aerobic oxidation of glucose to generate H_2O_2. Intriguingly, Zhang's group proposed a non-enzyme colorimetric assay for glucose based on GOx- and the POD-like activities of Au/MOF, which catalyzed cascade reactions for detection (Huang et al., 2017a). The multifunctional enzymatic properties of hybridized 2D NMs provide valuable opportunities to develop advanced biosensors.

By taking advantage of POD-/OD-like activity of 2D NMs, the colorimetric assays for other analytes like AA (Wang X. H. et al., 2017; Sun et al., 2020), biothiols [e.g., GSH (Liu et al., 2017; Ge et al., 2019; Liu X. L. et al., 2019), cysteine (Liu X. L. et al., 2019), and homocysteine (Liu X. L. et al., 2019)], xanthine (Cai et al., 2018b; Wu et al., 2018; Li et al., 2019), dopamine (Dutta et al., 2015; Ivanova et al., 2019), cholesterol (Zhang et al., 2017), acetylcholinesterase (Yan et al., 2017), cancer cells (Tao et al., 2013; Zhang L. N. et al., 2014; Qi et al., 2016), ions [e.g., S^{2-} (Liu et al., 2020), Fe^{2+} (Wang et al., 2016), and Pb^{2+} (Tang et al., 2020)], have also been established by different groups. The colorimetric biosensing based on 2D nanozymes continues to be a rapidly growing field.

Antibacterial Agents

The POD-like activities of 2D NMs have gained ever-increasing interest in antibacterial applications. For example, Yang's group prepared $MoSe_2$ NSs by exfoliation of bulk $MoSe_2$ powder in the aqueous solution of carboxyl-modified silk fibroin under sonication conditions (Huang X.-W. et al., 2017). In their study, a high concentration of H_2O_2 (100 mM) alone was required to eliminate most Gram-negative bacteria *E. Coli*, while only 100 μM H_2O_2 could display excellent antibacterial activity in the presence of $MoSe_2$ NSs (50 μg mL^{-1}). The effectiveness of a combination of $MoSe_2$ NSs and H_2O_2 was further verified for disinfection and healing of Kunming mice with infected skin wounds. The study provided a type of TMD-based antibacterial agents with the usage of low-dose H_2O_2, which potentially avoid the harmful side effects of high-dose H_2O_2 in traditional medical therapy. Similarly, Yin's group (Ma D. Q. et al., 2020) and Gu's group (Wang T. et al., 2020) respectively reported good antibacterial efficacy of lysozyme-modified MoS_2 NSs and N-doped MoS_2 or WS_2 NSs, against *E. Coli* and Gram-positive *Bacillus subtilis*. The POD-mimics catalyzed H_2O_2 decomposition to generate ·OH radicals, which promoted bacteria-infected wound healing. Several 2D hybrid NMs like Au/*g*-C_3N_4 (Wang Z. Z. et al., 2017) also showed potential in antibacterial agents.

Recently, Qu's group constructed a self-activated cascade reagent based on GOx-adsorbed 2D Cu-TCPP(Fe) MOF NSs (**Figure 2A**), which was used together with glucose in the antibacterial system (Liu X. P. et al., 2019). The authors also created the wound model on the back of Kunming mice and prepared a MOF/GOx-band-aid for the *in vivo* bacterial study (**Figure 2B**). The principle was based on the consecutive reactions, in which GOx firstly catalyzed the oxidation of glucose to gluconic acid and H_2O_2, which was further catalytically decomposed into ·OH radicals by MOF NSs as a POD-mimic, thus leading to an antibacterial effect and ultimately, wound healing (**Figure 2C**). In the *in vitro* antibacterial investigation, the group (glucose + MOF/GOx) led to high bacteria inactivation rates, up to 88% and 90 % for *E. Coli* and *S. aureus*, respectively. By contrast, for the control groups including (1) PBS, (2) glucose, (3) glucose + MOF, and (4) MOF/GOx, the viabilities remained above 50% for the two bacteria. In the *in vivo* antibacterial study, the bacteria for the group (glucose + MOF/GOx-band-aid) were decreased to 9.1%; however, the bacteria for the control group (glucose + GOx-band-aid) were only decreased to 56.5%. These results showed high antibacterial activity of MOF/GOx. More interestingly, since H_2O_2 is an oxidant that was continuously produced by oxidation of glucose in the cascade catalysis, the study provided a benign antibacterial system to avoid the direct introduction of highly concentrated H_2O_2.

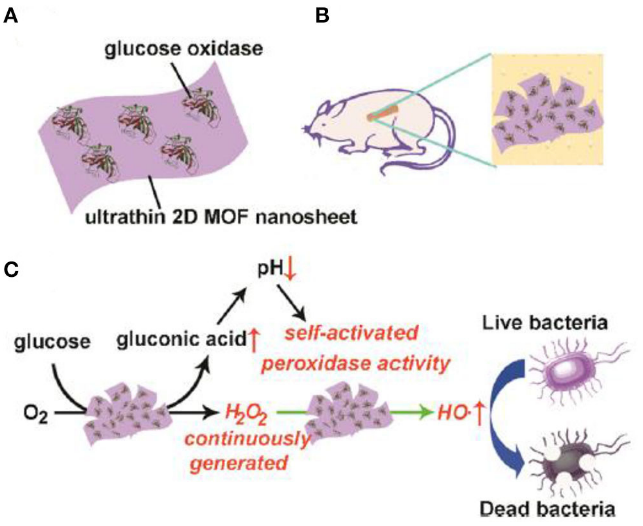

FIGURE 2 | Illustration of **(A)** composition, **(B)** use for wound healing of mice, and **(C)** antibacterial mechanism of 2D MOF/GOx hybrid nanozyme. Reproduced with permission from Liu X. P. et al. (2019). Copyright 2019 American Chemical Society.

Antioxidants

2D NMs had important applications in antioxidants. **Table 3** shows a summary of 2D nanozymes as antioxidants. Typical examples include GO NSs (Halim et al., 2019), Se NPs *in situ* grown on GO NSs (Huang et al., 2017b), and MoS_2 NSs prepared by sonication-assisted exfoliation (Chen T. M. et al., 2018). In another example, the different TMDs (WS_2, $MoSe_2$, and WSe_2) were functionalized with an amphiphilic poly(ε-caprolactone)-*b*-PEG (PCL-*b*-PEG) diblock copolymer, which efficiently captured mitochondrial and intracellular ROS and reaction nitrogen species (RNS) like ·NO radicals, of which the WS_2 NSs displayed the best performance (Yim et al., 2020). With effective scavenging of ROS and RNS as well as suppression of inflammatory cytokines of WS_2 NSs, the survival rate of the septic mice remarkably increased to 90%.

Chen's group found that the PVP-functionalized Nb_2C NSs could greatly reduce ROS generation caused by ionizing radiation, thereby providing a kind of antioxidant based on 2D nanozymes for radioprotective applications (Ren et al., 2019). Wang's group also demonstrated the potential of Se-modified *g*-C_3N_4 NSs against oxidative stress (Cao X. N. et al., 2020).

Therapeutics

A new hotspot in nanozyme research is the integration of enzymatic properties for therapy. Using an *in situ* growth strategy, Liu's group fabricated Pt NPs decorated on the surface

TABLE 3 | Summary of representative 2D nanozymes as antioxidants.

2D NMs	Enzymatic activity	Applications	References
GO NSs	SOD, CAT	Protecting mesenchymal stem cells from ROS accumulation	Halim et al., 2019
Se/GO	Glutathione Peroxidase	protecting RAW264.7 cells from oxidative stress by catalyzing H_2O_2 decomposition to H_2O	Huang et al., 2017
MoS_2 NSs	SOD, CAT	Protecting *Escherichia coli* (*E. coli*), *Staphylococcus aureus* (*S. aureus*) and A549 cells from H_2O_2-induced oxidative stress	Chen T. M. et al., 2018
WS_2, $MoSe_2$ and WSe_2 NSs coated with PCL-b-PEG	SOD, CAT	Scavenging mitochondrial and intracellular ROS and RNS in lipopolysaccharide (LPS)- or bacteria-induced inflammatory cells	Yim et al., 2020
PVP-modified Nb_2C NSs	SOD	Scavenging ROS against ionizing radiation	Ren et al., 2019
Se-modified *g*-C_3N_4 NSs	CAT	Protecting A549 cells from ROS-induced damage	Cao X. N. et al., 2020

of black phosphorus (BP) NSs, obtained by the liquid exfoliation method (**Figure 3A**) (Ouyang et al., 2018). The as-obtained BP NSs were freestanding with several hundred nanometers (**Figure 3B**), while the Pt NPs had an average size of appropriately 4.2 nm (**Figure 3C**), with the crystal lattice fringe of 0.223 nm of (111) plane. The element distribution was further obtained from high-angle annular dark-field scanning TEM (HAADF-STEM) image (**Figure 3D**) and element maps (**Figures 3E,F**). The as-obtained Pt/BP nanocomposites integrated CAT-like activity of Pt NPs and photodynamic therapy (PDT) activity of BP NSs, in which the Pt NPs catalytically decomposed the accumulated H_2O_2 in tumors to relieve tumor hypoxia (**Figure 3A**). In the *in vitro* antitumor experiment, the BP NSs alone only reduced 26% of cell viability under near infrared (NIR) light irradiation, while about 65% of tumor cells were dead after the treatment of the Pt/BP. The result showed that the elevated O_2 level caused by CAT-catalysis of Pt NPs remarkably improved the PDT efficiency of BP NSs. Moreover, as a result of the Pt/BP treatment, the overexpression of hypoxia-inducible factor-1α (HIF-1α), which is associated with therapy resistance in tumor cells, was significantly down-regulated, since the intensity of fluorescence appeared on the tumor slices of mice was decreased by 64% in the immunohistochemical staining experiment. The down-regulation of HIF-1α by the Pt/BP decreased the tumor apoptotic resistance, which ultimately enhanced the therapeutic effect in the *in vivo* antitumor experiment, in which the growth of the tumor was completely regressed by the treatment of Pt/BP, while the treatment of BP NSs alone only led to a decline in about 47% of average tumor size.

By using a similar *in situ* growth method, Sun's group synthesized Pt NPs coated 2D MOF, that is, Sm-modified tetrakis(4-carboxyphenyl)porphyrin (Sm-TCPP), which afforded a multifunctional nanozyme with excellent tumor specificity for enhanced PDT efficiency (Cao Z. G. et al., 2020). In their study, the Pt NPs acted as a CAT-mimic, catalyzing over-expressed H_2O_2 in a tumor microenvironment (TME) into O_2. The generated O_2 was further catalytically transformed to $^1O_2$ by Sm-TCPP, owing to its high ROS generation capacity under light irradiation.

PROSPECT AND CHALLENGES

This review has undertaken a summary of recent progress in developing 2D NMs with enzyme-like activities for diversified biomedical applications. The continuous advancement of nanoscience and nanotechnology in relation to 2D NMs will offer great opportunities to develop new types of nanozymes with varied functionalities in the future. Meanwhile, the exploration of new biocatalytic properties and integration of enzymatic activities of 2D NMs with other nanostructures like 0D NPs have potentially limitless applications in biomedical areas, and more fundamental technological breakthroughs in 2D nanozymes are expected in the near future.

Despite the many achievements that have been made in research on 2D nanozymes, studies on this field are still in the initial stages and future studies must address some challenges. Firstly, compared to 0D NPs with easy preparation, it is challenging to achieve the controlled synthesis of 2D NMs with uniform thickness, desirable size, and colloidal stability. Despite great success in creating layered materials by the top-down methods, there are still some obvious shortcomings. A typical example is the synthesis of TMDs for biomedical applications, in which the liquid exfoliation and chemical intercalation methods were adopted in most studies. Although the former had a high yield with simple operations, the morphologies of the obtained products had a lack of uniformity, often involving a mixture of single and few-layer sheets with different lateral dimensions (Agarwal and Chatterjee, 2018). Despite the more uniform single-layer NSs created by the latter, it both brought structural and electronic deformations and involved toxic reagents. The chemical intercalation process was highly sensitive to the environment and time-consuming. Therefore, it is still desirable to develop an efficient method to prepare TMDs. Another example is the metallic NSs. Bearing lots of unsaturated atoms, the ultrathin metallic nanostructures are difficult to stabilize, because metal atoms readily form 3D close-packed crystals. Despite tremendous efforts in the synthesis of metallic NSs by bottom-up protocols, the formation mechanism in most reports was proposed based on a simple correlation between a few synthetic parameters and the final shape, in which several characterization techniques (e.g., TEM, XRD, etc.) were employed to identify reaction intermediates, were formed either at certain time intervals or in the control experiments (Chen Y. et al., 2018). However, there is not enough evidence relating to authentic reactive species during synthesis. Therefore, to better understand the formation process (e.g., nucleation, growth, and assembly) of metallic NSs for synthesis, it is essential to carry out

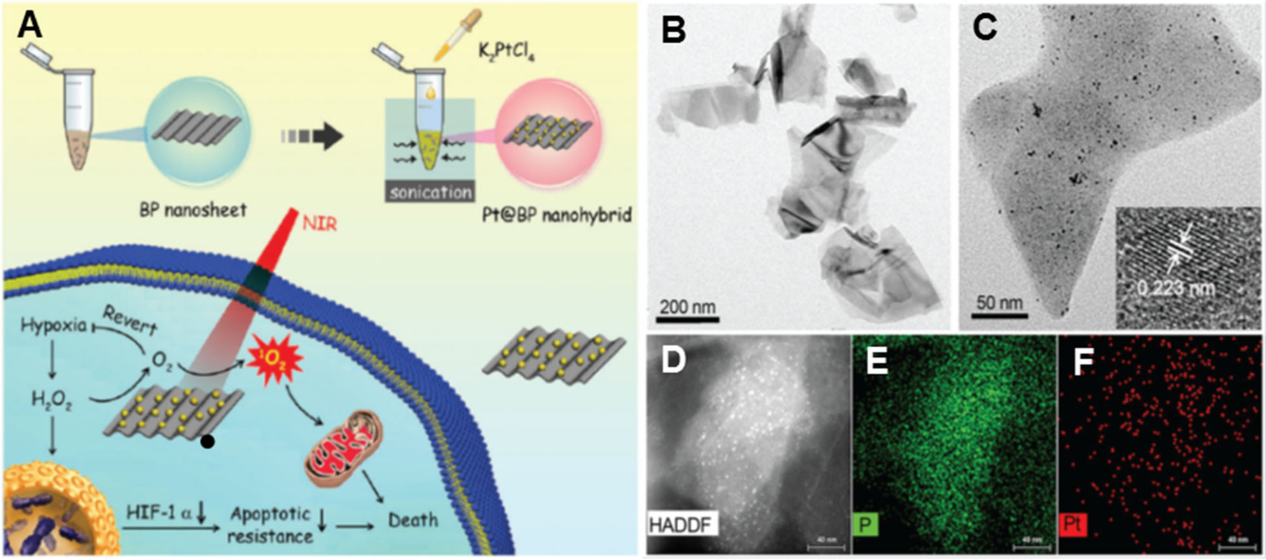

FIGURE 3 | (A) Illustration of synthesis and antitumor process of Pt/BP nanocomposites as well as their characterization: **(B)** TEM image of BP NSs and **(C)** Pt/BP nanocomposites (inset shows the high-resolution TEM image of a Pt NP), **(D)** high-angle annular dark-field scanning TEM (HAADF-STEM) image of Pt/BP, elemental maps of **(E)** P, and **(F)** Pt. Adapted with permission from Ouyang et al. (2018). Copyright 2018 Royal Society of Chemistry.

more *in situ* studies on the morphological evolution toward the 2D structure.

Secondly, despite the fascinating enzymatic properties of numerous 2D NMs, few studies on the in-depth catalytic mechanism are available. At present, it is still difficult to predict the nanozyme activity of 2D NMs for a specific structure. It is also difficult to achieve the best performance (e.g., activity and selectivity) for a specific application in biomedical areas, and hard to design the desired 2D nanozymes with optimal structures. Fundamentally, the missing link of structure-property relationship is largely because the enzyme-catalysis mechanism of 2D NMs remains unclear. For example, we must ask what the true active sites of 2D NMs and catalytically active intermediates during enzyme-catalysis are. In this regard, a deeper understanding of the catalytic mechanism of 2D nanozymes could benefit from *in situ* experimental studies and theoretical calculation by establishing appropriate models for catalysis, which are beneficial to the structural design of 2D nanozymes.

Thirdly, unlike 0D nanosystems, the biocompatibility and environmental stability of 2D NMs remains largely unknown, to date. Despite numerous studies on the biocompatibility of graphene-based NMs and TMDSs, evaluations of the toxicity of other types of 2D NMs are urgently required. The solubility, biodegradation, and biocompatibility of 2D NMs could be different from each other due to differences in their structure, composition, the methodology of synthesis and functionalization, and the cells studied. Therefore, it is hard to speculate whether a specific 2D NM is toxic or not. Their toxicity (both short-term and long-term), cellular-uptake mechanism, and the metabolic pathways of 2D NMs should be systematically tested for clinical trials.

Finally, it is acknowledged that many of the current applications of 2D nanozymes that display an outstanding performance are just proof-of-concept and have only been performed in laboratories. A number of reports fail to examine processability, scale-up possibility, and cost. The long-term stability and durability of 2D nanozymes are also less explored by researchers. Accordingly, there is still a long way to go before 2D nanozymes can be implemented in practical applications, which ultimately require interdisciplinary collaboration from chemistry, materials science, and biology.

AUTHOR CONTRIBUTIONS

RY: design the work. SC: drafting the manuscript. All authors contributed to the article and approved the submitted version.

FUNDING

This work was supported by the Strategic Priority Research Program of the Chinese Academy of Sciences (XDB36000000), the National key research and development program from the Ministry of Science and Technology of China (2016YFC0207102), and the National Natural Science Foundation of China (21503053).

REFERENCES

Agarwal, V., and Chatterjee, K. (2018). Recent advances in the field of transition metal dichalcogenides for biomedical applications. *Nanoscale* 10, 16365–16397. doi: 10.1039/C8NR04284E

Allen, M. J., Tung, V. C., and Kaner, R. B. (2010). Honeycomb carbon: a review of graphene. *Chem. Rev*. 110, 132–145. doi: 10.1021/cr900070d

Bhimanapati, G. R., Lin, Z., Meunier, V., Jung, Y., Cha, J., Das, S., et al. (2015). Recent advances in two-dimensional materials beyond graphene. *ACS Nano*. 9, 11509–11539. doi: 10.1021/acsnano.5b05556

Butler, S. Z., Hollen, S. M., Cao, L. Y., Cui, Y., Gupta, J. A., Gutiérrez, H. R., et al. (2013). Progress, challenges, and opportunities in two-dimensional materials beyond graphene. *ACS Nano*. 7, 2898–2926. doi: 10.1021/nn400280c

Cai, S. F., Fu, Z., Xiao, W., Xiong, Y. L., Wang, C., and Yang, R. (2020). Zero-dimensional/two-dimensional Au_xPd_{100-x} nanocomposites with enhanced nanozyme catalysis for sensitive glucose detection. *ACS Appl. Mater. Interfaces*. 12, 11616–11624. doi: 10.1021/acsami.9b21621

Cai, S. F., Han, Q. S., Qi, C., Lian, Z., Jia, X. H., Yang, R., et al. (2016). $Pt_{74}Ag_{26}$ nanoparticle-decorated ultrathin mos_2 nanosheets as novel peroxidase mimics for highly selective colorimetric detection of H_2O_2 and glucose. *Nanoscale* 8, 3685–3693. doi: 10.1039/C5NR08038J

Cai, S. F., Han, Q. S., Qi, C., Wang, X. H., Wang, T., Jia, X. H., et al. (2017). MoS_2-Pt_3Au_1 nanocomposites with enhanced peroxidase-like activities for selective colorimetric detection of phenol. *Chin. J. Chem*. 35, 605–612. doi: 10.1002/cjoc.201600694

Cai, S. F., Lian, C., Duan, H. H., Xiao, W., Han, Q. S., Qi, C., et al. (2019). Facile strategy to prepare Rh nanosheet-supported PtRh nanoparticles with synergistically enhanced catalysis in oxidation. *Chem. Mater*. 31, 808–818. doi: 10.1021/acs.chemmater.8b03889

Cai, S. F., Liu, X. L., Han, Q. S., Qi, C., Yang, R., and Wang, C. (2018a). A novel strategy to construct supported Pd nanocomposites with synergistically enhanced catalytic performances. *Nano Res*. 11, 3272–3281. doi: 10.1007/s12274-017-1868-9

Cai, S. F., Xiao, W., Duan, H. H., Liang, X. X., Wang, C., Yang, R., et al. (2018b). Single-layer Rh nanosheets with ultrahigh peroxidase-like activity for colorimetric biosensing. *Nano Res*. 11, 6304–6315. doi: 10.1007/s12274-018-2154-1

Cai, S. F., and Yang, R. (2020). Noble Metal-Based Nanozymes. in: *Nanozymology. Nanostructure Science and Technology*, eds X. Y. Yan (Singapore: Springer), 331–365. doi: 10.1007/978-981-15-1490-6_10

Cao, X. N., Lian, S., Tong, Y. W., Lin, W., Jia, L., Fang, Y. X., et al. (2020). Fluorescent Se-modified carbon nitride nanosheets as biomimetic catalases for free-radical scavenging. *Chem. Commun*. 56, 916–919. doi: 10.1039/C9CC08665J

Cao, Z. G., Li, Y. J., Zhang, Y., Cheng, K. W., An, P. J., Chen, F. H., et al. (2020). Biomimetic platinum nanozyme immobilized on 2D metal-organic frameworks for mitochondrion-targeting and oxygen self-supply photodynamic therapy. *ACS Appl. Mater. Interfaces* 12, 1963–1972. doi: 10.1021/acsami.9b14958

Chen, J. Y., Shu, Y., Li, H. L., Xu, Q., and Hu, X. Y. (2018). Nickel metal-organic framework 2D nanosheets with enhanced peroxidase nanozyme activity for colorimetric detection of H_2O_2. *Talanta* 189, 254–261. doi: 10.1016/j.talanta.2018.06.075

Chen, M. M., Wei, D., Chu, W., Wang, T., and Tong, D. G. (2017). One-pot synthesis of O-doped BN nanosheets as a capacitive deionization electrode for efficient removal of heavy metal ions from water. *J. Mater. Chem. A* 5, 17029–17039. doi: 10.1039/C7TA05459A

Chen, T. M., Wu, X. J., Wang, J. X., and Yang, G. W. (2017). WSe_2 few layers with enzyme mimic activity of high-sensitive and high-selective visual detection of glucose. *Nanoscale* 9, 11806–11813. doi: 10.1039/C7NR03179C

Chen, T. M., Zou, H., Wu, X. J., Liu, C. C., Situ, B., Zheng, L., et al. (2018). Nanozymatic antioxidant system based on MoS_2 nanosheets. *ACS Appl. Mater. Interfaces*. 10, 12453–12462. doi: 10.1021/acsami.8b01245

Chen, Y., Fan, Z. X., Zhang, Z. C., Niu, W. X., Li, C. L., Yang, N. L., et al. (2018). Two-dimensional metal nanomaterials: synthesis, properties, and applications. *Chem. Rev*. 118, 6409–6455. doi: 10.1021/acs.chemrev.7b00727

Chen, Y., Tan, C. L., Zhang, H., and Wang, L. Z. (2015). Two-dimensional graphene analogues for biomedical applications. *Chem. Soc. Rev*. 44, 2681–2701. doi: 10.1039/C4CS00300D

Cheng, L., Liu, J. J., Gu, X., Gong, H., Shi, X. Z., Liu, T., et al. (2014). PEGylated WS_2 nanosheets as a multifunctional theranostic agent for *in vivo* dual-modal CT/photoacoustic imaging guided photothermal therapy. *Adv. Mater*. 26, 1886–1893. doi: 10.1002/adma.201304497

Chimene, D., Alge, D. L., and Gaharwar, A. K. (2015). Two-dimensional nanomaterials for biomedical applications: emerging trends and future prospects. *Adv. Mater*. 27, 7261–7284. doi: 10.1002/adma.201502422

Choleva, T. G., Gatselou, V. A., Tsogas, G. Z., and Giokas, D. L. (2018). Intrinsic peroxidase-like activity of rhodium nanoparticles, and their application to the colorimetric determination of hydrogen peroxide and glucose. *Microchim. Acta*. 185, 22–30. doi: 10.1007/s00604-017-2582-8

Coleman, J. N., Lotya, M., O'Neill, A., Bergin, S. D., King, P. J., Khan, U., et al. (2011). Two-dimensional nanosheets produced by liquid exfoliation of layered materials. *Science* 331, 568–571. doi: 10.1126/science.1194975

Darabdhara, G., Bordoloi, J., Manna, P., and Das, M. R. (2019). Biocompatible bimetallic Au-Ni doped graphitic carbon nitride sheets: a novel peroxidase-mimicking artificial enzyme for rapid and highly sensitive colorimetric detection of glucose. *Sens. Actuat. B* 285, 277–290. doi: 10.1016/j.snb.2019.01.048

Ding, Y. J., Chen, Y. P., Zhang, X. L., Chen, L., Dong, Z. H., Jiang, H. L., et al. (2017). Controlled intercalation and chemical exfoliation of layered metal-organic frameworks using a chemically labile intercalating agent. *J. Am. Chem. Soc*. 139, 9136–9139. doi: 10.1021/jacs.7b04829

Dong, Y. Q., Wang, Q., Wu, H. S., Chen, Y. M., Lu, C.-H., Chi, Y. W., et al. (2018). Graphitic carbon nitride materials: sensing, imaging and therapy. *Biomater. Sci*. 6, 2298–2311. doi: 10.1002/smll.201602056

Duan, H. H., Yan, N., Yu, R., Chang, C. R., Zhou, G., Hu, H. S., et al. (2014). Ultrathin rhodium nanosheets. *Nat. Commun*. 5:3093. doi: 10.1038/ncomms4093

Dutta, S., Ray, C., Mallick, S., Sarkar, S., Sahoo, R., Negishi, Y., et al. (2015). A gel-based approach to design hierarchical CuS decorated reduced graphene oxide nanosheets for enhanced peroxidase-like activity leading to colorimetric detection of dopamine. *J. Phys. Chem. C*. 119, 23790–23800. doi: 10.1021/acs.jpcc.5b08421

Feng, L. P., Zhang, L. X., Zhang, S., Chen, X., Li, P., Gao, Y., et al. (2020). Plasma-assisted controllable doping of nitrogen into MoS_2 nanosheets as efficient nanozymes with enhanced peroxidase-like catalysis activity. *ACS Appl. Mater. Interfaces* 12, 17547–17556. doi: 10.1021/acsami.0c01789

Gan, X. R., Zhao, H. M., and Quan, X. (2017). Two-dimensional MoS_2: a promising building block for biosensors. *Biosens. Bioelectron*. 89, 56–71. doi: 10.1016/j.bios.2016.03.042

Gao, F., Yang, X., Luo, X. P., Xue, X. L., Qian, C. G., and Sun, M. J. (2020). Photoactivated nanosheets accelerate nucleus access of cisplatin for drug-resistant cancer therapy. *Adv. Funct. Mater*. 2001546. doi: 10.1002/adfm.202001546

Gao, L. Z., Zhuang, J., Nie, L., Zhang, J. B., Zhang, Y., Gu, N., et al. (2007). Intrinsic peroxidase-like activity of ferromagnetic nanoparticles. *Nat. Nanotechnol*. 2, 577–583. doi: 10.1038/nnano.2007.260

Ge, J., Cai, R., Chen, X. G., Wu, Q., Zhang, L. L., Jiang, Y., et al. (2019). Facile approach to prepare HSA-templated MnO_2 nanosheets as oxidase mimic for colorimetric detection of glutathione. *Talanta* 195, 40–45. doi: 10.1016/j.talanta.2018.11.024

Ghosal, K., and Sarkar, K. (2018). Biomedical applications of graphene nanomaterials and beyond. *ACS Biomater. Sci. Eng*. 4, 2653–2703. doi: 10.1021/acsbiomaterials.8b00376

Girish, C. M., Sasidharan, A., Gowd, G. S., Nair, S., and Koyakutty, M. (2013). Confocal Raman imaging study showing macrophage mediated biodegradation of graphene *in vivo*. *Adv. Healthcare Mater*. 2, 1489–1500. doi: 10.1002/adhm.201200489

Gollavelli, G., and Ling, Y.-C. (2012). Multi-functional graphene as an *in vitro* and *in vivo* imaging probe. *Biomaterials* 33, 2532–2545. doi: 10.1016/j.biomaterials.2011.12.010

Guan, G. J., and Han, M.-Y. (2019). Functionalized hybridization of 2D nanomaterials. *Adv. Sci*. 6:1901837. doi: 10.1002/advs.201901837

Halim, A., Liu, L., Ariyanti, A. D., Ju, Y., Luo, Q., and Song, G. B. (2019). Low-dose suspended graphene oxide nanosheets induce antioxidant response and osteogenic differentiation of bone marrow-derived mesenchymal stem cells via JNK-dependent FoxO1 activation. *J. Mater. Chem. B*. 7, 5998–6009. doi: 10.1039/C9TB01413F

Harvey, A., He, X. Y., Godwin, I. J., Backes, C., McAteer, D., Berner, N. C., et al. (2016). Production of $Ni(OH)_2$ nanosheets by liquid phase exfoliation: from optical properties to electrochemical applications. *J. Mater. Chem. A* 4, 11046–11059. doi: 10.1039/C6TA02811J

Hasan, M. A., Zaki, M. I., Pasupulety, L., and Kumari, K. (1999). Promotion of the hydrogen peroxide decomposition activity of manganese oxide catalysts. *Appl. Catal. A* 181:171. doi: 10.1016/S0926-860X(98)00430-X

He, W., Jia, H., Li, X., Lei, Y., Li, J., Zhao, H., et al. (2012). Understanding the formation of CuS concave superstructures with peroxidase-like activity. *Nanoscale* 4, 3501–3506. doi: 10.1039/c2nr30310h

He, W. W., Wu, X. C., Liu, J. B., Hu, X. N., Zhang, K., Hou, S., et al. (2010). Design of AgM bimetallic alloy nanostructures (M = Au, Pd, Pt) with tunable morphology and peroxidase-like activity. *Chem. Mater*. 22, 2988–2994. doi: 10.1021/cm100393v

Heo, N. S., Song, H. P., Lee, S. M., Cho, H. J., Kim, H. J., Huh, Y. S., et al. (2020). Rosette-shaped graphitic carbon nitride acts as a peroxidase mimic in a wide pH range for fluorescence-based determination of glucose with glucose oxidase. *Microchim. Acta*. 187:286. doi: 10.1007/s00604-020-04249-z

Hu, T. T., Mei, X., Wang, Y. J., Weng, X. S., Liang, R. Z., and Wei, M. (2019). Two-dimensional nanomaterials: fascinating materials in biomedical field. *Sci. Bull*. 64, 1707–1727. doi: 10.1016/j.scib.2019.09.021

Huang, J. K., Zhang, J. Z., Shi, G.-W., and Wei; Liu, Y. M. (2014). Hydrothermal synthesis of molybdenum disulfide nanosheets as supercapacitors electrode material. *Electrochim. Acta*. 132, 397–403. doi: 10.1016/j.electacta.2014.04.007

Huang, K., Li, Z. J., Lin, J., Han, G., and Huang, P. (2016). Two-dimensional transition metal carbides and nitrides (MXenes) for biomedical applications. *Chem. Soc. Rev*. 47, 5109–5124. *Small* 12, 5376–5393. doi: 10.1039/C7CS00838D

Huang, L. J., Zhu, W. X., Zhang, W. T., Chen, K., Wang, J., Wang, R., et al. (2018). Layered Vanadium(IV) disulfide nanosheets as a peroxidase-like nanozyme for colorimetric detection of glucose. *Microchim. Acta*. 185, 7–15. doi: 10.1007/s00604-017-2552-1

Huang, X.-W., Wei, J. J., Liu, T., Zhang, X. L., Bai, S. M., and Yang, H. H. (2017). Silk fibroin-assisted exfoliation and functionalization of transition metal dichalcogenide nanosheets for antibacterial wound dressings. *Nanoscale* 9, 17193–17198. doi: 10.1039/C7NR06807G

Huang, X. Q., Tang, S. H., Mu, X. L., Dai, Y., Chen, G. X., Zhou, Z. Y., et al. (2011). Freestanding palladium nanosheets with plasmonic and catalytic properties. *Nat. Nanotechnol*. 6, 28–32. doi: 10.1038/nnano.2010.235

Huang, Y., Liu, C. Q., Pu, F., Liu, Z., Ren, J. S., and Qu, X. G. (2017b). A Go-Se nanocomposites as an antioxidant nanozyme for cytoprotection. *Chem. Commun*. 53, 3082–3085. doi: 10.1039/C7CC00045F

Huang, Y., Zhao, M. T., Han, S. K., Lai, Z. C., Yang, J., Tan, C. L., et al. (2017a). Growth of Au nanoparticles on 2D metalloporphyrinic metal-organic framework nanosheets used as biomimetic catalysts for cascade reactions. *Adv. Mater*. 29:1700102. doi: 10.1002/adma.201700102

Huang, Y. Y., Ren, J. S., and Qu, X. G. (2019). Nanozymes: classification, catalytic mechanisms, activity regulation, and applications. *Chem. Rev*. 119, 4357–4412. doi: 10.1021/acs.chemrev.8b00672

Huo, C., Yan, Z., and Song, X. (2015). 2D materials via liquid exfoliation: a review on fabrication and applications. *Sci. Bull*. 60, 1994–2008. doi: 10.1007/s11434-015-0936-3

Ivanova, M. N., Grayfer, E. D., Plotnikova, E. E., Kibis, L. S., Darabdhara, G., Boruah, P. K., et al. (2019). Pt-decorated boron nitride nanosheets as artificial nanozyme for detection of dopamine. *ACS Appl. Mater. Interfaces* 11, 22102–22112. doi: 10.1021/acsami.9b04144

Jiang, C. M., Wu, C., Li, X. J., Yao, Y., Lan, L. Y., Zhao, F. N., et al. (2019). All-electrospun flexible triboelectric nanogenerator based on metallic MXene nanosheet. *Nano Energy*. 59, 268–276. doi: 10.1016/j.nanoen.2019.02.052

Jiang, D. W., Ni, D. L., Rosenkrans, Z. T., Huang, P., Yan, X. Y., and Cai, W. B. (2019). Nanozyme: new horizons for responsive biomedical applications. *Chem. Soc. Rev*. 48, 3683–3704. doi: 10.1039/C8CS00718G

Jiao, L., Yan, H. Y., Wu, Y., Gu, W. L., Zhu, C. Z., Du, D., et al. (2019). When nanozymes meet single-atom catalysis. *Angew. Chem. Int. Ed*. 59, 2565–2576. doi: 10.1002/anie.201905645

Ju, Y., and Kim, J. (2015). Dendrimer-encapsulated Pt nanoparticles with peroxidase-mimetic activity as biocatalytic labels for sensitive colorimetric analyses. *Chem. Commun*. 51, 13752–13755. doi: 10.1039/C5CC06055A

Khan, K., Tareen, A. K., Aslam, M., Wang, R. H., Zhang, Y. P., Mahmood, A., et al. (2020). Recent developments in emerging two-dimensional materials and their applications. *J. Mater. Chem. C*. 8, 387–440. doi: 10.1039/C9TC04187G

Kim, M. S., Cho, S., Joo, S. H., Lee, J., Kwak, S. K., Kim, M. I., et al. (2019). N- and B-codoped graphene: a strong candidate to replace natural peroxidase in sensitive and selective bioassays. *ACS Nano*. 13, 4312–4321. doi: 10.1021/acsnano.8b09519

Kim, M. S., Lee, J., Kim, H. S., Cho, A., Shim, K. H., Le, T. N., et al. (2020). Heme cofactor-resembling Fe-N single site embedded graphene as nanozymes to selectively detect H_2O_2 with high sensitivity. *Adv. Funct. Mater*. 30:1905410. doi: 10.1002/adfm.201905410

Kong, L., Xing, L., Zhou, B., Du, L., and Shi, X. (2017). Dendrimer-modified MoS_2 nanoflakes as a platform for combinational gene silencing and photothermal therapy of tumors. *ACS Appl. Mater. Interfaces* 9, 15995–16005. doi: 10.1021/acsami.7b03371

Korschelt, K., Ragg, R., Metzger, C. S., Kluenker, M., Oster, M., Barton, B., et al. (2017). Glycine-functionalized copper(II) hydroxide nanoparticles with high intrinsic superoxide dismutase activity. *Nanoscale* 9, 3952–3960. doi: 10.1039/C6NR09810J

Korsvik, C., Patil, S., Seal, S., and Self, W. T. (2007). Superoxide dismutase mimetic properties exhibited by vacancy engineered ceria nanoparticles. *Chem. Commun*. 1056–1058. doi: 10.1039/b615134e

Li, D., Muller, M. B., Gilje, S., Kaner, R. B., and Wallace, G. G. (2008). Processable aqueous dispersions of graphene nanosheets. *Nat. Nanotechnol*. 3, 101–105. doi: 10.1038/nnano.2007.451

Li, Z. H., Liu, X. Y., Liang, X. H., Zhong, J. H., Guo, L. Q., and Fu, F. F. (2019). Colorimetric determination of xanthine in urine based on peroxidase-like activity of WO_3 nanosheets. *Talanta* 204, 278–284. doi: 10.1016/j.talanta.2019.06.003

Liang, Q. H., Li, Z., Bai, Y., Huang, Z.-H., Kang, F. Y., and Yang, Q.-H. (2017). Reduced-sized monolayer carbon nitride nanosheets for highly improved photoresponse for cell imaging and photocatalysis. *Sci. China Mater*. 60, 109–118. doi: 10.1007/s40843-016-5131-9

Liao, K.-H., Lin, Y.-S., Macosko, C. W., and Haynes, C. L. (2011). Cytotoxicity of graphene oxide and graphene in human erythrocytes and Skin Fibroblasts. *ACS Appl. Mater. Interfaces* 3, 2607–2615. doi: 10.1021/am200428v

Lin, H., Wang, X. G., Yu, L. D., Chen, Y., and Shi, J. L. (2017). Two-dimensional ultrathin MXene ceramic nanosheets for photothermal conversion. *Nano Lett*. 17, 384–391. doi: 10.1021/acs.nanolett.6b04339

Lin, S. S., and Gurol, M. D. (1998). Catalytic decomposition of hydrogen peroxide on iron oxide: kinetics, mechanism, and implication. *Environ. Sci. Technol*. 32, 1417–1423. doi: 10.1021/es970648k

Lin, T. R., Zhong, L. S., Guo, L. Q., Fu, F. F., and Chen, G. N. (2014a). Seeing diabetes: visual detection of glucose based on the intrinsic peroxidase-like activity of MoS_2 nanosheets. *Nanoscale* 6, 11856–11862. doi: 10.1039/C4NR03393K

Lin, T. R., Zhong, L. S., Song, Z. P., Guo, L. Q., Wu, H. Y., Guo, Q. Q., et al. (2014b). Visual detection of blood glucose based on peroxidase-like activity of WS_2 nanosheets. *Biosens. Bioelectron*. 62, 302–307. doi: 10.1016/j.bios.2014.07.001

Lin, T. R., Zhong, L. S., Wang, J., Guo, L. Q., Wu, H. Y., Guo, Q. Q., et al. (2014c). Graphite-like carbon nitrides as peroxidase mimetics and their applications to glucose detection. *Biosens. Bioelectron*. 59, 89–93. doi: 10.1016/j.bios.2014.03.023

Liu, J., Meng, L. J., Fei, Z. F., Dyson, P. J., Jing, X. N., and Liu, X. (2017). MnO_2 nanosheets as an artificial enzyme to mimic oxidase for rapid and sensitive detection of glutathione. *Biosens. Bioelectron*. 90, 69–74. doi: 10.1016/j.bios.2016.11.046

Liu, J.-H., Yang, S.-T., Wang, H., Chang, Y., Cao, A., and Liu, Y. (2012). Effect of size and dose on the biodistribution of graphene oxide in mice. *Nanomedicine* 7, 1801–1812. doi: 10.2217/nnm.12.60

Liu, T., Wang, C., Gu, X., Gong, H., Cheng, L., Shi, X. Z., et al. (2014). Drug delivery with PEGylated MoS_2 nano-sheets for combined photothermal and chemotherapy of cancer. *Adv. Mater*. 26, 3433–3440. doi: 10.1002/adma.201305256

Liu, X. L., Wang, X. H., Han, Q. S., Qi, C., Wang, C., and Yang, R. (2019). Facile synthesis of IrO_2/rGO nanocomposites with high peroxidase-like activity for sensitive colorimetric detection of low weight biothiols. *Talanta* 203, 227–234. doi: 10.1016/j.talanta.2019.05.070

Liu, X. N., Huang, L. J., Wang, Y. P., Sun, J., Yue, T. L., Zhang, W. T., et al. (2020). One-pot bottom-up fabrication of a 2D/2D heterojuncted nanozyme towards optimized peroxidase-like activity for sulfide ions sensing. *Sens. Actuat. B* 306:127565. doi: 10.1016/j.snb.2019.127565

Liu, X. P., Yan, Z. Q., Zhang, Y., Liu, Z. W., Sun, Y. H., Ren, J. S., et al. (2019). Two-dimensional metal-organic framework/enzyme hybrid nanocatalyst as a benign and self-activated cascade reagent for *in vivo* wound healing. *ACS Nano*. 13, 5222–5230. doi: 10.1021/acsnano.8b09501

Liu, Y., Wu, H. H., Li, M., Yin, J.-J., and Nie, Z. H. (2014). pH dependent catalytic activities of platinum nanoparticles with respect to the decomposition of hydrogen peroxide and scavenging of superoxide and singlet oxygen. *Nanoscale* 6, 11904–11910. doi: 10.1039/C4NR03848G

Lu, X. L., Feng, X. D., Werber, J. R., Chu, C. H., Zucker, I., Kim, J. H., et al. (2017). Enhanced antibacterial activity through the controlled alignment of graphene oxide nanosheets. *Proc. Natl. Acad. Sci. U. S. A*. 114, E9793–E9801. doi: 10.1073/pnas.1710996114

Ma, D. Q., Xie, C. J., Wang, T., Mei, L. Q., Zhang, X., Guo, Z., et al. (2020). Liquid-phase exfoliation and functionalization of MoS_2 nanosheets for effective antibacterial application. *ChemBioChem*. 21, 2373–2380. doi: 10.1002/cbic.202000195

Ma, D. T., Zhao, J. L., Xie, J. L., Zhang, F., Wang, R., Wu, L. M., et al. (2020). Ultrathin boron nanosheets as an emerging two-dimensional photoluminescence material for bioimaging. *Nanoscale Horiz*. 5, 705–713. doi: 10.1039/C9NH00698B

Maromeze, C. M., Dos Santos, G. P., De Moraes, V. B., Da, C. L., and Kubota, L. T. (2016). Multifunctional catalytic platform for peroxidase mimicking, enzyme immobilization and biosensing. *Biosens. Bioelectron*. 77, 746–751. doi: 10.1016/j.bios.2015.10.042

Mateti, S., Wong, C. S., Liu, Z., Yang, W. R., Li, Y. C., Li, L. H., et al. (2018). Biocompatibility of boron nitride nanosheets. *Nano Res*. 11, 334–342. doi: 10.1007/s12274-017-1635-y

Merlo, A., Mokkapati, V. R. S. S., Pandit, S., and Mijakovic, I. (2018). Boron nitride nanomaterials: biocompatibility and bio-applications. *Biomater. Sci*. 6, 2298–2311. doi: 10.1039/C8BM00516H

Mu, J. S., Wang, Y., Zhao, M., and Zhang, L. (2012). Intrinsic peroxidase-like activity and catalase-like activity of Co_3O_4 nanoparticles. *Chem. Commun*. 48, 2540–2542. doi: 10.1039/c2cc17013b

Mu, J. S., Zhang, L., Zhao, M., and Wang, Y. (2013). Co_3O_4 nanoparticles as an efficient catalase mimic: properties, mechanism and its electrocatalytic sensing application for hydrogen peroxidase. *J. Mol. Catal. A Chem*. 378, 30–37. doi: 10.1016/j.molcata.2013.05.016

Novoselov, K. S., Geim, A. K., Morozov, S. V., Jiang, D., Zhang, Y., Dubonos, S. V., et al. (2004). Electric field effect in atomically thin carbon films. *Science* 306, 666–669. doi: 10.1126/science.1102896

Novoselov, K. S., Jiang, D., Schedin, F., Booth, T. J., Khotkevich, V. V., Morozov, S. V., et al. (2005). Two-dimensional atomic crystals. *Proc. Natl. Acad. Sci. U. S. A*. 102, 10451–10453. doi: 10.1073/pnas.0502848102

Oudeng, G., Au, M., Shi, J., Wen, C., and Yang, M. (2018). One-step *in situ* detection of MiRNA-21 expression in single cancer cells based on biofunctionalized MoS_2 nanosheets. *ACS Appl. Mater. Interfaces* 10, 350–360. doi: 10.1021/acsami.7b18102

Ouyang, J., Deng, Y. Y., Chen, W. S., Xu, Q. F., Wang, L. Q., Liu, Z. J., et al. (2018). Marriage of artificial catalase and black phosphorous nanosheets for reinforced photodynamic antitumor therapy. *J. Mater. Chem. B* 6, 2057–2064. doi: 10.1039/C8TB00371H

Qi, C., Cai, S. F., Wang, X. H., Li, J. Y., Lian, Z., Sun, S. S., et al. (2016). Enhanced oxidase/peroxidase-like activities of aptamer conjugated MoS_2/PtCu nanocomposites and their biosensing application. *RSC Adv*. 6, 54949–54955. doi: 10.1039/C6RA03507H

Qian, X., Gu, Z., and Chen, Y. (2017). Two-dimensional black phosphorus nanosheets for theranostic nanomedicine. *Mater. Horiz*. 4, 800–816. doi: 10.1039/C7MH00305F

Ren, B. Y., Wang, Y. C., and Ou, J. Z. (2020). Engineering two-dimensional metal oxides via surface functionalization for biological applications. *J. Mater. Chem. B* 8, 1108–1127. doi: 10.1039/C9TB02423A

Ren, X. Y., Huo, M. F., Wang, M. M., Lin, H., Zhang, X. X., Yin, J., et al. (2019). Highly catalytic niobium carbide (MXene) promotes hematopoietic recovery after radiation by free radical scavenging. *ACS Nano*. 13, 6438–6454. doi: 10.1021/acsnano.8b09327

Ruan, Y. D., Jia, X. D., Wang, C., Zhen, W. Y., and Jiang, X. E. (2018). Mn-Fe layered double hydroxide nanosheets: a new photothermal nanocarrier for O_2-evolving phototherapy. *Chem. Commun*. 54, 11729–11732. doi: 10.1039/C8CC06033A

Sasidharan, A., Panchakarla, L., Chandran, P., Menon, D., Nair, S., Rao, C., et al. (2011). Differential nano-bio interactions and toxicity effects of pristine versus functionalized graphene. *Nanoscale* 3, 2461–2464. doi: 10.1039/c1nr10172b

Sasidharan, A., Panchakarla, L. S., Sadanandan, A. R., Ashokan, A., Chandran, P., Girish, C. M., et al. (2012). Hemocompatibility and macrophage response of pristine and functionalized graphene. *Small* 8, 1251–1263. doi: 10.1002/smll.201102393

Shi, Y., Hamsen, C., Jia, X., Kim, K. K., Reina, A., Hofmann, M., et al. (2010). Synthesis of few- layer hexagonal boron nitride thin film by chemical vapor deposition. *Nano Lett*. 10, 4134–4139. doi: 10.1021/nl1023707

Singh, S. K., Singh, M. K., Nayak, M. K., Kumari, S., Shrivastava, S., Grácio, J. J., et al. (2011). Thrombus inducing property of atomically thin graphene oxide sheets. *ACS Nano*. 5, 4987–4996. doi: 10.1021/nn201092p

Song, Y. J., Qu, K. G., Zhao, C., Ren, J. S., and Qu, X. G. (2010). Graphene oxide: intrinsic peroxidase catalytic activity and its application to glucose detection. *Adv. Mater*. 22, 2206–2210. doi: 10.1002/adma.200903783

Song, Y. J., Wei, W. L., and Qu, X. G. (2011). Colorimetric biosensing using smart materials. *Adv. Mater*. 23, 4215–4236. doi: 10.1002/adma.201101853

Su, L., Feng, J., Zhou, X. M., Ren, C. L., Li, H. H., and Chen, X. G. (2012). Colorimetric detection of urine glucose based $ZnFe_2O_4$ magnetic-nanoparticles. *Anal. Chem*. 84, 5753–5758. doi: 10.1021/ac300939z

Sukumar, T., Varghese, J., Suja Bhargavan, K. S., Jayasree, P., Suvekbala, V., Alaganandam, K., et al. (2020). Cytotoxicity of formulated graphene and its natural rubber nanocomposite thin film in human vaginal epithelial cells: an influence of noncovalent interaction. *ACS Biomater. Sci. Eng*. 6, 2007–2019. doi: 10.1021/acsbiomaterials.9b01897

Sun, H. Y., Liu, X. L., Wang, X. H., Han, Q. S., Qi, C., Li, Y. M., et al. (2020). Colorimetric determination of ascorbic acid using a polyallylamine-stabilized IrO_2/graphene oxide nanozyme as a peroxidase mimic. *Microchim. Acta* 187:110. doi: 10.1007/s00604-019-3897-4

Sun, X. M., Liu, Z., Welsher, K., Robinson, J. T., Goodwin, A., Zaric, S., et al. (2008). Nano-graphene oxide for cellular imaging and drug delivery. *Nano Res*. 1, 203–212. doi: 10.1007/s12274-008-8021-8

Tan, C. L., Cao, X. H., Wu, X. J., He, Q. Y., Yang, J., Zhang, X., et al. (2017). Recent advances in ultrathin two-dimensional nanomaterials. *Chem. Rev*. 117, 6225–6331. doi: 10.1021/acs.chemrev.6b00558

Tan, C. L., and Zhang, H. (2015). Wet-chemical synthesis and applications of non-layer structured two-dimensional nanomaterials. *Nat. Commun*. 6:7873. doi: 10.1038/ncomms8873

Tang, Y., Hu, Y., Yang, Y. X., Liu, B. Y., and Wu, Y. G. (2020). A facile colorimetric sensor for ultrasensitive and selective detection of lead(II) in environmental and biological samples based on intrinsic peroxidase-mimic activity of WS_2 nanosheets. *Anal. Chim. Acta* 1106, 115–125. doi: 10.1016/j.aca.2020.01.043

Tao, W., Kong, N., Ji, X. Y., Zhang, Y. P., Sharma, A., Ouyang, J., et al. (2019). Emerging two-dimensional monoelemental materials (Xenes) for biomedical applications. *Chem. Soc. Rev*. 48, 2891–2912. doi: 10.1039/C8CS00823J

Tao, Y., Lin, Y. H., Huang, Z. Z., Ren, J. S., and Qu, X. G. (2013). Incorporating graphene oxide and gold nanoclusters: a synergistic catalyst with surprisingly high peroxidase-like activity over a broad pH range and its application for cancer cell detection. *Adv. Mater*. 25, 2594–2599. doi: 10.1002/adma.201204419

Tian, J. Q., Liu, Q., Asiri, A. M., Qusti, A. H., Al-Youbi, A. O., and Sun, X. P. (2013). Ultrathin graphitic carbon nitride nanosheets: a novel peroxidase mimetic, Fe doping-mediated catalytic performance enhancement and application to rapid, highly sensitive optical detection of glucose. *Nanoscale* 5, 11604–11609. doi: 10.1039/c3nr03693f

Vernekar, A. A., Sinha, D., Srivastava, S., Paramasivam, P. U., D'Silva, P., and Mugesh, G. (2014). An antioxidant nanozyme that uncovers the cytoprotective potential of Vanadia nanowires. *Nat. Commun*. 5, 5301–5314. doi: 10.1038/ncomms6301

Wang, J. Y., Li, W. Y., and Zheng, Y.-Q. (2019). Nitro-functionalized metal-organic frameworks with catalase mimic properties for glutathione detection. *Analyst* 144, 6041–6047. doi: 10.1039/C9AN00813F

Wang, K., Ruan, J., Song, H., Zhang, J., Wo, Y., Guo, S., et al. (2011). Biocompatibility of graphene oxide. *Nanoscale Res. Lett*. 6:8. doi: 10.1007/s11671-010-9751-6

Wang, S. G., Yang, X. Q., Zhou, L. L., Li, J. F., and Chen, H. R. (2020). 2D nanostructures beyond graphene: preparation, biocompatibility and biodegradation behaviors. *J. Mater. Chem. B* 8, 2974–2989. doi: 10.1039/C9TB02845E

Wang, T., Zhang, X., Mei, L. Q., Ma, D. Q., Liao, Y., Zu, Y., et al. (2020). A two-step gas/liquid strategy for the production of N-doped defect-rich transition metal dichalcogenide nanosheets and their antibacterial applications. *Nanoscale* 12, 8415–8424. doi: 10.1039/D0NR00192A

Wang, X. H., Han, Q. S., Cai, S. F., Wang, T., Yang, R., and Wang, C. (2017). Excellent peroxidase mimicking property of CuO/Pt nanocomposites and their application as an ascorbic acid sensor. *Analyst* 142, 2500–2506. doi: 10.1039/C7AN00589J

Wang, Y., Hu, J., Zhuang, Q. F., and Ni, Y. N. (2016). Enhancing sensitivity and selectivity in a label-free colorimetric sensor for detection of iron(II) ions with luminescent molybdenum disulfide nanosheet-based peroxidase mimetics. *Biosens. Bioelectron*. 80, 111–117. doi: 10.1016/j.bios.2016.01.037

Wang, Z. Z., Dong, K., Liu, Z., Zhang, Y., Chen, Z. W., Sun, H. J., et al. (2017). Activation of biologically relevant levels of reactive oxygen species by Au/*g*-C_3N_4 hybrid nanozyme for bacteria killing and wound disinfection. *Biomaterials* 113, 145–157. doi: 10.1016/j.biomaterials.2016.10.041

Wei, H., and Wang, E. K. (2013). Nanomaterials with enzyme-like characteristics (nanozymes): next-generation artificial enzymes. *Chem. Rev*. 42, 6060–6093. doi: 10.1039/c3cs35486e

Wei, J. P., Chen, X. N., Shi, S. G., Mo, S. G., and Zheng, N. F. (2015). An investigation of the mimetic enzyme activity of two-dimensional Pd-based nanostructures. *Nanoscale* 7, 19018–19026. doi: 10.1039/C5NR05675F

Wu, N., Wang, Y. T., Wang, X. N., Guo, F. N., Wen, H., and Yang, T. (2019). Enhanced peroxidase-like activity of Au NPs loaded graphitic carbon nitride nanosheets for colorimetric biosensing. *Anal. Chim. Acta* 1091, 69–75. doi: 10.1016/j.aca.2019.09.072

Wu, X. J., Chen, T. M., Wang, J. X., and Yang, G. W. (2018). Few-layered $MoSe_2$ nanosheets as an efficient peroxidase nanozyme for highly sensitive colorimetric detection of H_2O_2 and xanthine. *J. Mater. Chem. B* 6, 105–111. doi: 10.1039/C7TB02434G

Wu, Z. N., Liu, J. L., Li, Y. C., Cheng, Z. Y., Li, T. T., Zhang, H., et al. (2015). Self-assembly of nanoclusters into mono-, few-, and multilayered sheets via dipole-induced asymmetric van der Waals attraction. *ACS Nano*. 9, 6315–6323. doi: 10.1021/acsnano.5b01823

Xuan, J. N., Wang, Z. Q., Chen, Y. Y., Liang, D. J., Cheng, L., Yang, X. J., et al. (2016). Organic-based-driven intercalation and delamination for the production of functionalized titanium carbide nanosheets with superior photothermal therapeutic performance. *Angew. Chem. Int. Ed*. 55, 14569–14574. doi: 10.1002/anie.201606643

Yan, L., Gonca, S., Zhu, G. Y., Zhang, W. J., and Chen, X. F. (2019). Layered double hydroxide nanostructures and nanocomposites for biomedical applications. *J. Mater. Chem. B*. 7, 5583–5601. doi: 10.1039/C9TB01312A

Yan, X., Song, Y., Wu, X. L., Zhu, C. Z., Su, X. G., Du, D., et al. (2017). Oxidase-mimicking activity of ultrathin MnO_2 nanosheets in colorimetric assay of acetylcholinesterase activity. *Nanoscale* 9, 2317–2323. doi: 10.1039/C6NR08473G

Yang, C., Feng, W. J., Li, Y., Tian, X. K., Zhou, Z. X., Lu, L. Q., et al. (2019). A promising method for diabetes early diagnosis via sensitive detection of urine glucose by Fe-Pd/rGO. *Dyes Pigments* 164, 20–26. doi: 10.1016/j.dyepig.2018.12.061

Yang, H., Zhang, X., Tang, A., and Qiu, G. (2004). Gobalt ferrite nanoparticles prepared by coprecipitation/mechanochemical treatment. *Chem. Lett*. 33, 826–827. doi: 10.1246/cl.2004.826

Yang, S. B., Gong, Y. J., Zhang, J. S., Zhan, L., Ma, L. L., Fang, Z. Y., et al. (2013). Exfoliated graphitic carbon nitride nanosheets as efficient catalysts for hydrogen evolution under visible light. *Adv. Mater*. 25, 2452–2456. doi: 10.1002/adma.201204453

Yang, W. N., Li, J., Yang, J., Liu, Y., Xu, Z. P., Sun, X. F., et al. (2020). Biomass-derived hierarchically porous CoFe-LDH/CeO_2 hybrid with peroxidase-like activity for colorimetric sensing of H_2O_2 and glucose. *J. Alloy Compound* 815:152276. doi: 10.1016/j.jallcom.2019.152276

Yi, M., and Shen, Z. (2015). A review on mechanical exfoliation for the scalable production of graphene. *J. Mater. Chem. A* 3, 11700–11715. doi: 10.1039/C5TA00252D

Yim, D. B., Lee, D.-E., So, Y., Choi, C., Son, W., Jang, K., et al. (2020). Sustainable nanosheet antioxidants for sepsis therapy via scavenging intracellular reactive oxygen and nitrogen species. *ACS Nano*. 14, 10324–10336. doi: 10.1021/acsnano.0c03807

Yin, W. Y., Yan, L., Yu, J., Tian, G., Zhou, L. J., Zheng, X. P., et al. (2014). High-throughput synthesis of single-layer MoS_2 nanosheets as a near-infrared photothermal-triggered drug delivery for effective cancer therapy. *ACS Nano*. 8, 6922–6933. doi: 10.1021/nn501647j

Yong, Y., Zhou, L. J., Gu, Z. J., Yan, L., Tian, G., Zheng, X. P., et al. (2014). WS_2 nanosheet as a new photosensitizer carrier for combined photodynamic and photothermal therapy of cancer cells. *Nanoscale* 6, 10394–10403. doi: 10.1039/C4NR02453B

Yu, F. T., Cangelosi, V. M., Zastrow, M. L., Tegoni, M., Plegaria, J. S., Tebo, A. G., Mocny, C. S., et al. (2014). Protein design: toward functional metalloenzymes. *Chem. Rev*. 114, 3495–3578. doi: 10.1021/cr400458x

Yuwen, L., Yu, H., Yang, X., Zhou, J., Zhang, Q., Zhang, Y., et al. (2016). Rapid preparation of single-layer transition metal dichalcogenide nanosheets via ultrasonication enhanced lithium intercalation. *Chem. Commun*. 52, 529–532. doi: 10.1039/C5CC07301D

Zeng, Z. Y., Yin, Z. Y., Huang, X., Li, H., He, Q. Y., Lu, G., et al. (2011). Single-layer semiconducting nanosheets: high-yield preparation and device fabrication. *Angew. Chem. Int. Ed*. 50, 11093–11097. doi: 10.1002/anie.201106004

Zhan, T. R., Kang, J. X., Li, X. J., Pan, L., Li, G. J., and Hou, W. G. (2018). NiFe layered double hydroxide nanosheets as an efficiently mimic enzyme for colorimetric determination of glucose and H_2O_2. *Sens. Actuat. B* 255, 2635–2642. doi: 10.1016/j.snb.2017.09.074

Zhang, H. (2015). Ultrathin two-dimensional nanomaterials. *ACS Nano*. 9, 9451–9469. doi: 10.1021/acsnano.5b05040

Zhang, L. N., Deng, H. H., Lin, F. L., Xu, X. W., Weng, S. H., Liu, A. L., et al. (2014). *In situ* growth of porous platinum nanoparticles on graphene oxide for colorimetric detection of cancer cells. *Anal. Chem*. 86, 2711–2718. doi: 10.1021/ac404104j

Zhang, T., Lu, Y., Luo, G. (2014). Synthesis of hierarchical iron hydrogen phosphate crystal as a robust peroxidase mimic for stable H_2O2 detection. *ACS Appl. Mater. Interfaces* 6, 14433–14438. doi: 10.1021/am503708a

Zhang, W. C., Li, X., Xu, X. C., He, Y. F., Qiu, F. X., Pan, J. M., et al. (2019). Pd nanoparticle-decorated graphitic C_3N_4 nanosheets with bifunctional peroxidase mimicking and ON-OFF fluorescence enable naked-eye and fluorescent dual-readout sensing of glucose. *J. Mater. Chem. B* 7, 233–239. doi: 10.1039/C8TB02110D

Zhang, X. L., Li, G. L., Wu, D., Li, X. L., Hu, N., Chen, J., et al. (2019). Recent progress in the design fabrication of metal-organic frameworks-based nanozymes and their applications to sensing and cancer therapy. *Biosens. Bioelectron*. 137, 178–198. doi: 10.1016/j.bios.2019.04.061

Zhang, Y., Wang, Y. N., Sun, X. T., Chen, L., and Xu, Z. R. (2017). Boron nitride nanosheet/CuS nanocomposites as mimetic peroxidase for sensitive colorimetric detection of cholesterol. *Sens. Actuat. B* 246, 118–126. doi: 10.1016/j.snb.2017.02.059

Zhou, X. F., Zheng, X. L., Yan, B., Xu, T., and Xu, Q. (2017). Defect engineering of two-dimensional WO_3 nanosheets for enhanced electrochromism and photoeletrochemical performance. *Appl. Surf. Sci*. 400, 57–63. doi: 10.1016/j.apsusc.2016.12.072

Zhu, C. F., Zeng, Z. Y., Li, H., Li, F., Fan, C. H., and Zhang, H. (2013). Single-layer MoS_2-based nanoprobes for homogeneous detection of biomolecules. *J. Am. Chem. Soc*. 135, 5998–6001. doi: 10.1021/ja4019572

Conflict of Interest: The authors declare that the research was conducted in the absence of any commercial or financial relationships that could be construed as a potential conflict of interest.

The handling Editor declared a shared affiliation, though no other collaboration, with one of the authors SC and RY.

frontiers
in Chemistry

REVIEW
published: 11 February 2021
doi: 10.3389/fchem.2020.00831

Rational Design and Biological Application of Antioxidant Nanozymes

Ruizhen Tian[1], **Jiayun Xu**[1,2], **Quan Luo**[1], **Chunxi Hou**[1] **and Junqiu Liu**[1]*

[1] State Key Laboratory of Supramolecular Structure and Materials, College of Chemistry, Jilin University, Changchun, China,
[2] College of Material, Chemistry and Chemical Engineering, Hangzhou Normal University, Hangzhou, China

Nanozyme is a type of nanostructured material with intrinsic enzyme mimicking activity, which has been increasingly studied in the biological field. Compared with natural enzymes, nanozymes have many advantages, such as higher stability, higher design flexibility, and more economical production costs. Nanozymes can be used to mimic natural antioxidant enzymes to treat diseases caused by oxidative stress through reasonable design and modification. Oxidative stress is caused by imbalances in the production and elimination of reactive oxygen species (ROS) and reactive nitrogen species (RNS). This continuous oxidative stress can cause damage to some biomolecules and significant destruction to cell structure and function, leading to many physiological diseases. In this paper, the methods to improve the antioxidant properties of nanozymes were reviewed, and the applications of nanozyme antioxidant in the fields of anti-aging, cell protection, anti-inflammation, wound repair, cancer, traumatic brain injury, and nervous system diseases were introduced. Finally, the future challenges and prospects of nanozyme as an ideal antioxidant were discussed.

Keywords: antioxidants, nanozyme, oxidative stress, rational design, biological application

OPEN ACCESS

Edited by:
Kelong Fan,
Institute of Biophysics (CAS), China

Reviewed by:
Sanjay Singh,
Ahmedabad University, India
Moon Il Kim,
Gachon University, South Korea
Yu Zhang,
Southeast University, China

****Correspondence:***
Junqiu Liu
junqiuliu@jlu.edu.cn

Specialty section:
This article was submitted to
Nanoscience,
a section of the journal
Frontiers in Chemistry

Received: *13 June 2020*
Accepted: *07 August 2020*
Published: *11 February 2021*

Citation:
Tian R, Xu J, Luo Q, Hou C and Liu J (2021) Rational Design and Biological Application of Antioxidant Nanozymes. Front. Chem. 8:831. doi: 10.3389/fchem.2020.00831

INTRODUCTION

Reactive oxygen species (ROS) are produced in the normal physiological activities of aerobic organisms. Oxygen (O_2) undergoes a series of electron transport in biological metabolism, which results in the formation of ROS, such as superoxide anion radical ($O_2^{\bullet-}$), hydrogen peroxide (H_2O_2), hydroxyl radicals ($^{\bullet}OH$) (Winterbourn, 2008; Dickinson and Chang, 2011; Nathan and Cunningham-Bussel, 2013). Appropriate amounts of ROS participate in a variety of signal pathways in response to changes in external conditions and play an essential role as a second messenger in signal transduction, immune response, and cell function regulation (Gechev et al., 2006; D'Autréaux and Toledano, 2007; Finkel, 2011; Sena and Chandel, 2012; Schieber and Chandel, 2014). There is an antioxidant system composed of non-enzymatic antioxidant molecules and natural antioxidant enzymes in the organism to maintain the balance of ROS. Some non-enzymatic antioxidants, such as ascorbic acid (AA), reductive glutathione (GSH), vitamin E (VE), and melanin, are effective in scavenging free radicals (Niki and Noguchi, 2004; Liu Y. L. et al., 2012; Kakaroubas et al., 2019). The natural synergistic antioxidant system mainly includes superoxide dismutase (SOD), glutathione peroxidase (GPx), catalase (CAT) (Morry et al., 2016). Nevertheless, too much ROS consumes a lot of antioxidant molecules and attacks antioxidant enzymes, which can cause oxidative stress when the redox homeostasis is disturbed (Griendling and FitzGerald, 2003; Reuter et al., 2010). This continuous oxidative stress can cause severe damage to some biomolecules,

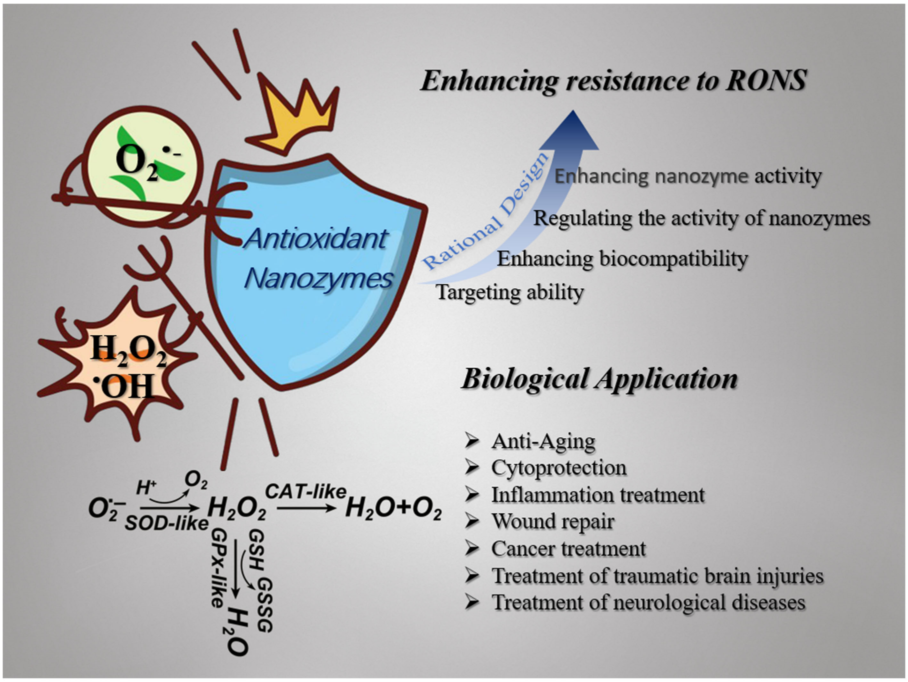

SCHEME 1 | Schematic illustration of nanozymes with multienzyme-like activity (SOD-like, GPx-like, CAT-like, et al.) against ROS ($O_2^{\bullet-}$, H_2O_2, •OH, et al.). Nanozymes are broadly used in the field of biomedicine as antioxidants and their antioxidant capacity can be enhanced by rational design.

such as DNA, lipids, proteins, and significant destruction of cell structure and function (Ray et al., 2000; Valko et al., 2004; Dalle-Donne et al., 2006). Severe cell damage and tissue inflammation can also induce many physiological diseases (Nechifor et al., 2009) such as diabetes (Baynes, 1991), sepsis (Macdonald et al., 2003), atherosclerosis (Harrison et al., 2003), arthritis (Tak et al., 2000), aging (Vitale et al., 2013), kidney disease (Forbes et al., 2008), cardiovascular diseases (Cai and Harrison, 2000), nervous system diseases (Barnham et al., 2004), and lung diseases (Ceccarelli et al., 2008).

Although a wide range of antioxidants has been widely used to inhibit and fight oxidative stress-related pathological diseases, there are still some severe limitations. For example, natural enzyme antioxidants lack stability and are readily inactivated under non-physiological conditions. Some non-enzymatic antioxidants cannot pass through the blood-brain barrier (Gilgun-Sherki et al., 2001) and have low bioavailability (Heim et al., 2002). Compared with traditional antioxidants, nanozyme antioxidant is a kind of enzyme mimetics based on nanomaterials, which has the characteristics of flexible operation, excellent stability, low cost, mass production, and easy treatment (Wu et al., 2019). In recent years, many different inorganic nanomaterials have been developed as antioxidant nanozymes, such as noble metals (Liu X. P. et al., 2016), metal oxides (Soh et al., 2017), carbon-based nanomaterials (Mu et al., 2019a), and other substrates (Zhao et al., 2018). The ability of nanozymes to scavenge ROS mainly originates from intrinsic SOD, CAT, GPx, NAC mimicking activities, or peroxidase (POD) mimicking activity without producing hydroxyl radicals, and •OH-, •DPPH-, or •NO-scavenging activity (Akhtar et al., 2015b; Chen et al., 2018; Hao et al., 2019; Yan et al., 2019). Nanozymes are often accompanied by a variety of enzyme mimetic activities that can efficiently scavenge ROS, but there are also some inherent shortcomings. The toxicity of nanoparticles is the first consideration in biological applications. It has been shown that some inorganic nanoparticles can interact with lipid, proteins, and DNA, thereby impairing the integrity of biofilms and the function of enzymes (Cedervall et al., 2007; Wang et al., 2008; Pelka et al., 2009). The significant disadvantages of nanozymes are insufficient targeting and lacking the ability to bind to substrates specifically, which affect the effectiveness of the treatment of the disease. Some nanozymes have an antagonistic effect, which can catalyze the generation and elimination of ROS, which is not conducive to biological applications. The size and morphology of nanoparticles have a significant influence on the activity and function of mimetic enzymes. Therefore, it is necessary to rationally design the nanozyme to improve the biocompatibility, targeting, adjust, and enhance the activity of the nanozyme, reduce the dosage, and get a better application in the biological field. This review focuses on rationally designing nanozymes to enhance their antioxidant capacity and their application in biomedical field (**Scheme 1**).

ANTIOXIDANT ENZYME ACTIVITIES OF NANOZYMES

In this section, we introduce the antioxidant properties of nanozymes, which have been developed as antioxidants in recent years (**Table 1**).

TABLE 1 | Summary of the applications of nanozymes as antioxidant in recent years.

Nanozymes	Enzyme mimic activity	Biological application	Reference
Porous CuxO NPs	SOD, CAT, and GPx-like	Parkinson's Disease	Hao et al., 2019
Porous platinum NPs	CAT-like	Enhance radiation efficacy	Li et al., 2019
Carbogenic nanozyme	SOD, CAT-like $^{\bullet}$NO and $ONOO^-$scavenging activities	Traumatic brain injury	Mu et al., 2019a
Pt/CeO_2	POD, SOD, CAT, GPx-like, and $^{\bullet}$OH and $ONOO^-$ scavenging activities	Brain trauma	Yan et al., 2019
CuTA nanosheets	SOD-like, CAT-like, and $^{\bullet}$OH scavenging activity	Smoking-induced lung destruction	Lin et al., 2019
A single-atom Fe–N_4 catalytic site	SOD-like, CAT-like	Cytoprotection	Ma et al., 2019
PtPdMo trim	POD, CAT-like $^{\bullet}$OH, $^1O_2$, and $^{\bullet}$NO scavenging activities	Brain injury	Mu et al., 2019b
Fe_3O_4 NPs	CAT-like	Anti-Aging Experimental cerebral malaria	Zhang et al., 2015 Zhao et al., 2019
MoS_2 NPs	SOD, CAT-like	Osteoarthritis	Chen et al., 2019
CeO_2 NPs	SOD-like, CAT-like	Parkinson's disease Neuroprotective effect, Regenerative wound healing	Kwon et al., 2018 Zeng et al., 2018 Wu et al., 2018
Prussian blue NPs	POD, CAT, and SOD-like	Reduce colitis in mice	Zhao et al., 2018
Silver-gold-apoferritin nanozyme	POD, CAT, and SOD-like	Suppress oxidative stress during cryopreservation	Dashtestani et al., 2018
MoS_2 nanosheets	SOD, CAT, POD-like, and $^{\bullet}$OH-, $^{\bullet}$DPPH-, and $^{\bullet}$NO- scavenging activity	Cytoprotection	Chen et al., 2018
Se@Pda	GPx	Anti-inflammation	Huang et al., 2018
Mn_3O_4 NPs	SOD, CAT, GPx-like, and $^{\bullet}$OH scavenging activity	Anti-inflammation Parkinson's disease	Singh et al., 2017 Yao et al., 2018
$Ce_{0.7}Zr_{0.3}O_2$ NPs	SOD, CAT-like, and $^{\bullet}$OH scavenging activity	Anti-inflammation	Soh et al., 2017
GO-Se nanocomposite	GPx-like	Cytoprotection	Huang et al., 2017
Se-CQDs	$^{\bullet}$OH scavenging activity	Cytoprotection	Li F. et al., 2017
Melanin NPs	SOD-like	Ischemic stroke	Liu et al., 2017
ZnO/CeOx HMS	SOD-like, CAT-like	UV-induced epidermal hypertrophy	Ju et al., 2017
Multicomponent nanoreactor	Photosynthesizing H_2 gas	Anti-inflammation	Wan et al., 2017
Ceria/POMs hybrid NPs	Proteolytic and SOD-like	Treatment of neurotoxicity of amyloid-β peptide	Guan et al., 2016
Pt NPs	SOD, CAT, POD-like	Human Cerebral Cavernous Malformation (CCM) disease	Moglianetti et al., 2016
MnO_2 NPs	SOD, CAT-like	Overcome tumor hypoxia, Cytoprotection	Song et al., 2016 Li W. et al., 2017
V_2O_5@pDA@MnO_2 nanocomposite	SOD, CAT, and GPx-like	Anti-inflammation	Huang et al., 2016
PVP-IrNPs	CAT, POD-like	Cytoprotection	Su et al., 2015
Molybdenum NPs (Mo NPs)	NAC-like	Human breast and fibrosarcoma cells	Akhtar et al., 2015a

Prussian blue nanoparticles have also been found to have a variety of antioxidant enzyme activities, including peroxidase activity, catalase activity, and superoxide dismutase activity, which can effectively scavenge ROS (**Figure 1A**). Chen's group reported a polyvinylpyrrolidone (PVP)-modified Prussian blue nanoparticle (PPB) with good biological safety and physiological stability. The prepared PPBs have the abilities of scavenging ROS and inhibiting proinflammatory cytokines. The intravenous administration of PPBs can significantly reduce colitis without obvious side effects. A hydroxyl radical-generating TiO_2/UV system was used to investigate the ROS scavenging ability of PPBs. As the concentration of PPBs increases from 0 to 10 μg/mL, the signal intensity of BMPO/$^\bullet$OH displays a steep decline, indicating the excellent scavenging capability of PPBs against $^\bullet$OH. The effect of PPBs on $^\bullet$OH can be represented in reactions:

$$K_xFe(III)_y[Fe(II)(CN)_6]_z(PB)$$
$$K_xFe(III)_y[Fe(III)(CN)_6]_n[Fe(II)(CN)_6]_{z-n}(BG)$$
$$K_xFe(III)_y[Fe(III)(CN)_6]_z(PY)$$

$$PB \rightarrow BG + e^- \tag{1}$$
$$BG \rightarrow PY + (z-n)e^- \tag{2}$$
$$PB + H^+ + \mathit{HO} \rightarrow PY + H_2O \tag{3}$$

The addition of H_2O_2 into the PPB solution generated a number of observable bubbles, catalyzing the decomposition of H_2O_2 to produce oxygen. The CAT-like activity of PPBs can be shown in the following reactions

$$PB + H_2O_2 \rightarrow BG + OH^- \tag{4}$$
$$BG + H_2O_2 \rightarrow PY + OH^- \tag{5}$$
$$PY + H_2O_2 + OH^- \rightarrow BG + O_2 + H_2O \tag{6}$$
$$BG + H_2O_2 + OH^- \rightarrow PB + O_2 + nH_2O$$

(7), Zhao et al. (2018).

In addition, the commonly used natural POD substrates 3,5,3,5-tetramethylbenzidine (TMB) were also determined to study the POD activity of PPBs. The absorbance increased after the addition of PPBs, indicative of POD-like activity.

$$TMB + H_2O_2 + H^+ \overset{PY}{\rightarrow} TMB_{(oxidized)} + H_2O \tag{8}$$

The authors used the xanthine/xanthine oxidase system to investigate the effects of PPBs on superoxide radicals ($^\bullet$OOH). With the increase of PPBs concentration, the signal intensity of BMPO/$^\bullet$OOH decreased significantly, indicating that PPBs could be used as SOD-like nanozyme to scavenge $^\bullet$OOH.

$$^\bullet OOHSOD/PB \overset{SOD/PB}{\rightarrow} H_2O_2 + O_2 \tag{9}$$

In conclusion, the PPBs can be used as artificial nanozymes to effectively convert harmful ROS to H_2O and O_2 and to avoid lipid peroxidation, protein oxidation and DNA damage (Zhao et al., 2018).

Li's group demonstrated that single-atom catalysts can be used as single-atom nanozymes (SAzymes) with multiple antioxidant activities (**Figure 1B**). Atom-dispersed Fe-N_4 active sites can mimic SOD and CAT activities, effectively removing H_2O_2 and O_2. To compare the efficiency of Fe-SAs/NC with other reported nanozymes, the authors calculated the TOF (turnover frequency) values per active site of Fe-SAs/NC-based enzyme and nanozymes. The TOF of Fe-SAs/NC was estimated to be 1809.34 min^{-1}, which is much higher than other nanozymes such as Pd octahedrons (1.51 min^{-1}) (Ge et al., 2016) and Mn_3O_4 nanoflowers (111.86 min^{-1}) (Singh et al., 2017) reported previously (Ma et al., 2019).

Melanin nanoparticles modified PEG can provide more effective and safer antioxidant therapy. The authors speculated the mechanism of melanin scavenging $O_2^{\bullet-}$, as follows:

$$melanin^\bullet + O_2{}^{\bullet-} \rightarrow melanin^- + O_2$$
$$melanin^- + O_2{}^{\bullet-} + 2H_2O \rightarrow melanin^\bullet + H_2O_2 + 2OH^-$$

When $O_2^{\bullet-}$ was added, a large number of bubbles appeared in the PEG-MeNPs solution (**Figure 1C**). PEG-MeNPs could also scavenge $^\bullet$OH and ONOO–, which are the most toxic secondary electrons produced in diseases and can cause lipid peroxidation, protein oxidation, and nucleic acid damage, and maintain high stability. Moreover, they found that the PEG-MeNPs blocked the formation of $^\bullet$OH, possibly because melanin had a strong chelating ability with transition metal ions, which impeded the Fenton reaction (Liu et al., 2017).

CeO_2 NPs are well-known as a superoxide dismutase (SOD) mimetic due to the redox cycle between Ce^{3+} and Ce^{4+}, Ce^{4+} sites are responsible for the decomposition of hydrogen peroxide through the CAT-like activity (Korsvik et al., 2007; Pirmohamed et al., 2010). Mn_3O_4 NPs have been demonstrated to possess remarkable SOD-like activity (**Figure 1D**), due to the mixed valance states of Mn^{2+} and Mn^{3+}. Besides, Mn_3O_4 has CAT-like activity (**Figure 1E**) and $^\bullet$OH scavenging activity (**Figure 1F**). Compared with CeO_2 NPs, Mn_3O_4 nanoparticles exhibit higher ROS scavenging capability (**Figures 1D–F**) (Yao et al., 2018). Mugesh's group demonstrated for the first time that Mn_3O_4 nanoparticles with flower-like morphology (Mnf) could mimic the activity of three antioxidant enzymes, including SOD, CAT, and GPx. The multienzyme activity of Mnf may be due to the existence of two oxidation states of manganese (Mn^{2+}/Mn^{3+}), large surface area, and abnormal large pore size. To understand the relative influence of the two different oxidation states on the activity of Mnf, the author treated Mnf with an oxidizing agent ($NaIO_4$) and a reducing agent ($NaBH_4$) to obtain the oxidized (O-Mnf) and reduced (R-Mnf) forms with different ratios of Mn^{3+}/Mn^{2+}. Interestingly, O-Mnf, with a higher Mn^{3+}/Mn^{2+} ratio, exhibited enhanced CAT and GPx-like activities compared with Mnf. In contrast, the SOD activity of O-Mnf and R-Mnf was slightly higher than that of Mnf, suggesting that the oxidation states of both played a crucial role in enzyme mimetic activity. In the experimental model of Parkinson's disease, Mnf could be effectively internalized into human cells, inhibited apoptosis caused by the neurotoxin, and played an influential role in cytoprotection (Singh et al., 2017). Few-layer MoS_2 nanosheets possessed intrinsic activity of mimicking SOD, CAT, and POD under physiological conditions (pH 7.4, 25°C). The POD-like activity originated from their ability to transfer electrons without producing hydroxyl radicals (Chen et al., 2018). Fullerene-Like MoS_2 (F-MoS_2) nanoparticles are effective lubricants and antioxidants for artificial synovial fluid due to their unique structures and intrinsic dual-enzyme-like (SOD- and CAT-like) activity (Chen et al., 2019).

Mugesh's group confirmed that V_2O_5 nanowires (Vn) have GPx-like activity and biocompatibility and proposed a

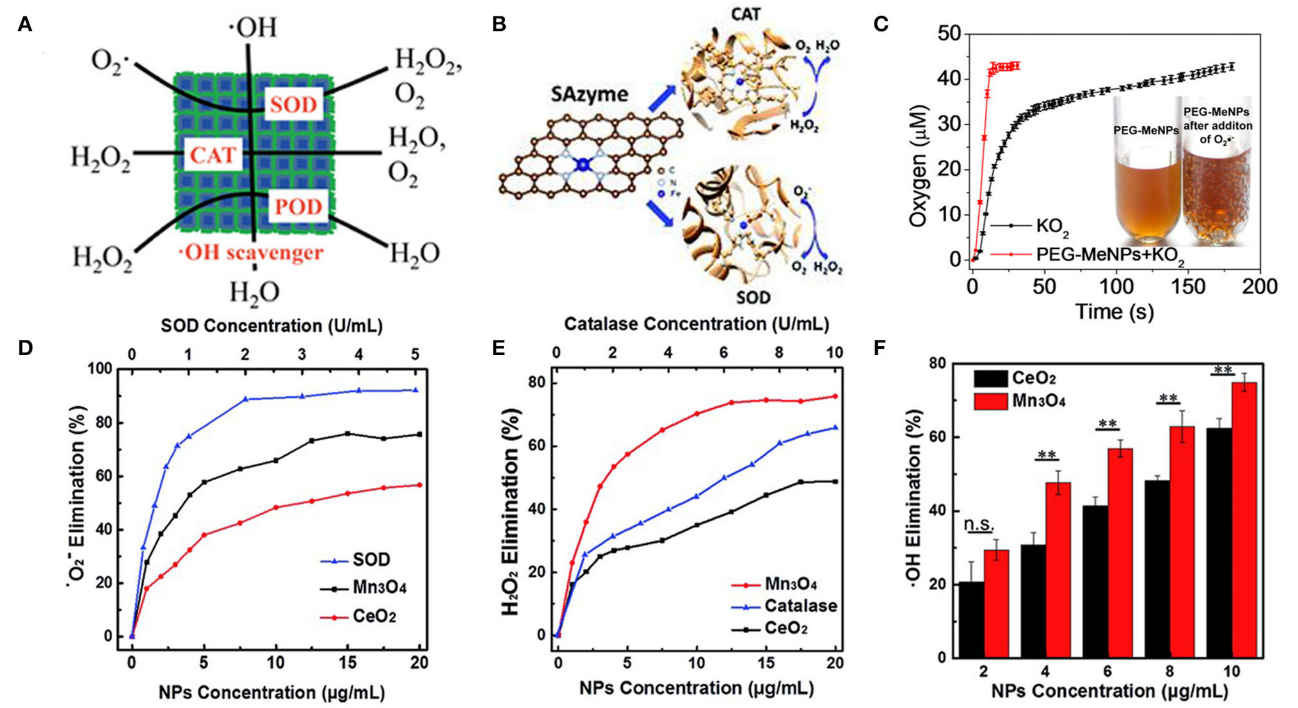

FIGURE 1 | Antioxidant activity of nanozymes. **(A)** The PPBs could act as an artificial enzyme, effectively scavenging ROS including •OH, H_2O_2, and •OOH via POD, CAT, and SOD activity [reproduced from Zhao et al. (2018) with permission from the American Chemical Society]. **(B)** Atomically dispersed Fe–N_4 sites anchored on N-doped porous carbon materials [reproduced from Ma et al. (2019) with permission from the Royal Society of Chemistry (RSC)]. **(C)** O_2 production from the KO_2 solution (100 μM) with vs. without PEG-MeNPs. The insert is the digital picture of the PEG-MeNPs solution before vs. after addition of KO_2 [reproduced from Liu et al. (2017) with permission from the American Chemical Society]. **(D)** Dependence between the elimination of $^{\bullet}O_2^-$ and concentrations of Mn_3O_4 NPs, CeO_2 NPs, and natural SOD. **(E)** Dependence between the elimination of H_2O_2 and concentrations of Mn_3O_4 NPs, CeO_2 NPs, and natural catalase. **(F)** Dependence between the elimination of •OH and concentration of Mn_3O_4 NPs and CeO_2 NPs (mean ± S.D., $^{**}p < 0.05$; n.s., not significant) [reproduced from Yao et al. (2018) with permission from the Royal Society of Chemistry (RSC)].

corresponding catalytic mechanism (Vernekar et al., 2014). In the nanostructure, the surface of Vn serves as a template for GSH reduction of H_2O_2. The functional groups on the surface of Vn changed to form vanadium peroxide species 1. The GS^- nucleophilically attacks the peroxide bond in complex 1, resulting in the formation of unstable sulfinate binding intermediate 2, which is hydrolyzed to produce glutathione sulfonic acid (3, GSOH) and dihydroxy intermediate 4. The hydrolysis of 2 to generate GSOH may be similar to the removal of HOBr from V-OBr intermediate in vanadium haloperoxidase (Natalio et al., 2012). Then, 4 reacts with H_2O_2 to produce peroxide compound 1. This is similar to one of the steps proposed in the mechanism of vanadium chloroperoxidase (Ligtenbarg et al., 2003). GSOH reacts with GSH to produce GSSG. GR/NADPH can reduce GSSG to GSH. It is worth noting that GSOH (3) is further oxidized to the corresponding sulfinic acid (5, GSO_2H) under the condition of higher H_2O_2 concentration. In addition to GSH, other small thiol-containing molecules such as cysteine, cysteamine, and mercaptoethanol can also be used as thiol cofactors. In the presence of thiols, Vn showed notable thiol peroxidase activity through catalytic reduction of H_2O_2(**Figure 2**).

In the presence of peroxides, nanocarbon materials (CNMs) can catalyze the oxidation of organic substrates such as TMB (Shi et al., 2011; Zhang et al., 2013; Sun et al., 2015). Qu's group explored the dynamics of CO-COOH catalytic oxidation of TMB in the presence of H_2O_2. Based on the Michaelis Menten model, the kinetic parameters of GO-COOH, V_{max}, and K_m, were estimated and compared by using Lineweaver–Burk plots. At high H_2O_2 concentrations, the reaction catalyzed by GO-COOH was inhibited and followed ping-pong mechanism, which was similar to the reaction catalyzed by HRP. The UV spectra of GO-COOH showed that the addition of 88.2 mM H_2O_2 resulted in a red shift of about 19 nm, indicating the electron transfer from the top of the graphene valence band to the lowest unoccupied molecular orbital (LUMO) of H_2O_2 (Song et al., 2010).

ENHANCE THE ANTIOXIDANT EFFECT OF NANOZYMES

An ideal nano-antioxidant should have at least the following characteristics: (i) valid clearance of multiple primary and secondary reactive oxygen and nitrogen species (RONS); (ii) highly stable antioxidant activity against oxidative damage; (iii)

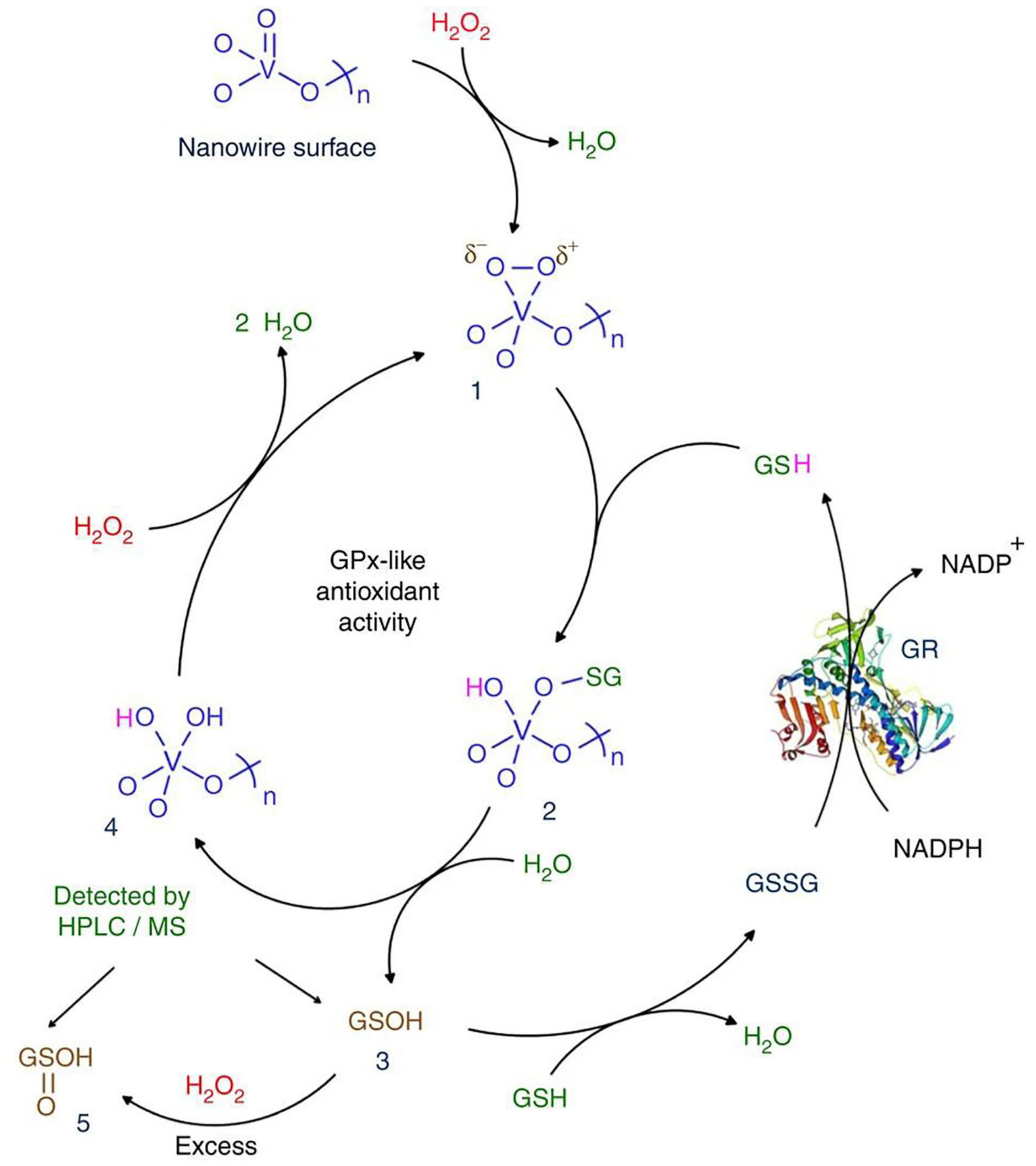

FIGURE 2 | Mechanism of GPx activity of Vn [reproduced from Vernekar et al. (2014) with permission from the Springer Nature].

the ability to prevent the activation of inflammation triggered by RONS; and (iv) excellent biocompatibility (Liu et al., 2017). Therefore, it is crucial to design the nanozyme reasonably to make it become an ideal antioxidant and widely used.

Enhancing Nanozyme Activity

At present, the ROS scavenging capability of most nanozymes is moderate. Therefore, numerous strategies have been proposed to design more active nanozymes. One possible strategy is ion doping adding. For example, doping ions (such as Zr^{4+}) into ceria NPs to modulate the ratio of Ce^{3+}/Ce^{4+}. The superoxide scavenging activity of ceria NPs could also be enhanced through an electron transfer strategy. Co-catalysis of various nanozymes can also improve catalytic activity.

Ion Doping Strategy

Ceria nanoparticles (CeO_2 NPs) are well-known as a superoxide dismutase (SOD) mimetic due to the redox cycle between Ce^{3+} and Ce^{4+}. The surface Ce^{3+} to Ce^{4+} ratio is important because the capacity of removing $O_2^{\bullet-}$ and $^{\bullet}OH$ is largely determined by

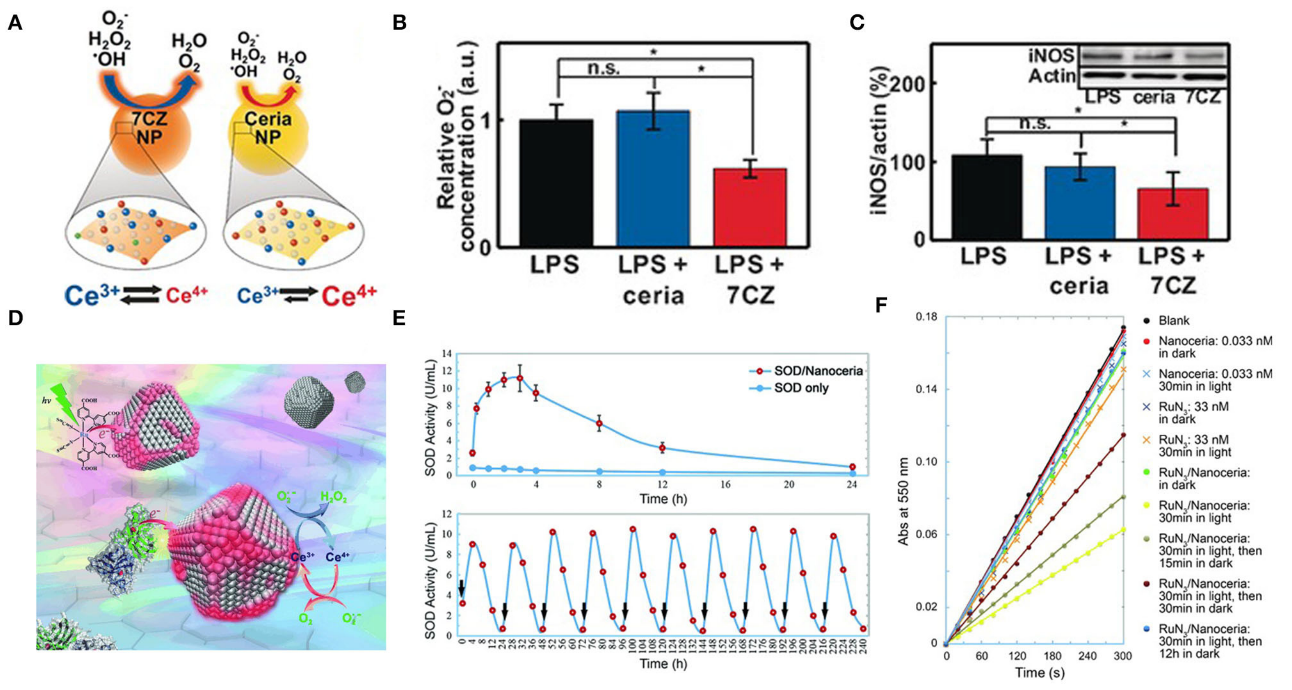

FIGURE 3 | Ion-doping and electron transfer strategies enhance antioxidant enzyme activity. **(A)** Representing the different catalytic activities of ceria NPs and ceria-zirconia (CZ) NPs. **(B)** *in vitro* O_2-assay: luminescence intensities of U937 cells were measured and expressed as relative O_2-concentration, determined by measured values relative to those for the LPS-treated control; $n = 4$. **(C)** *in vitro* western blot analysis for iNOS: the blots were quantified using relative optical densities of iNOS and β-actin; $n = 4$ [reproduced from Soh et al. (2017) with permission from the John Wiley and Sons]. **(D)** Nanoceria acquire superoxide-scavenging ability after electron transfer. **(E)** The SOD mimetic activity of the CuZn-SOD/nanoceria mixture. **(F)** Effect of RuN_3/nanoceria on superoxide anions from hypoxanthine/xanthine oxidase system as determined by a ferricytochrome C assay [reproduced from Li et al. (2014) with permission from the John Wiley and Sons].

the fractions of Ce^{3+}(Baldim et al., 2018). Therefore, increasing the Ce^{3+}/Ce^{4+} ratio is an effective strategy to improve the ability of nano-cerium to remove ROS. Seal's group doped the CeO_2 NPs lattice with trivalent dopants (La, Sm, and Er) to significantly increase the surface Ce^{3+} ion concentration and produce a good SOD-like activity, as expected. Among the three dopants, Sm doped CeO_2 NPs had the highest SOD activity, followed by La and Er doped CeO_2 NPs. This ordering was due to the association energy of dopant atoms O-vacancies and the high concentration of Ce^{3+} on the surface. CeO_2 NPs with higher content of Ce^{3+} were effective scavengers of intracellular ROS (Gupta et al., 2016). Hyeon's group reported ceria–zirconia nanoparticles [$Ce_{0.7}Zr_{0.3}O_2$(7CZ)] in which the Zr^{4+} is used to modulate the ratio of Ce^{3+}/Ce^{4+} (Soh et al., 2017). They demonstrated that the rate of Ce^{4+} to Ce^{3+} reduction is strongly increased throughout the Zr^{4+}-containing NPs (**Figure 3A**). This finding may be due to the fact that the ionic radius of Zr^{4+} ion (0.084nm) is smaller than that of Ce^{4+} ion and Ce^{3+} ion (0.097 nm and 0.114 nm, respectively), which can reduce the lattice strain caused by the increase of the ionic radius of Ce^{4+} ion to Ce^{3+} ion. In *in vitro* lipopolysaccharide (LPS)-induced inflammation model, 7CZ NPs is more effective in scavenging O_2^- compared to the ceria NPs (**Figure 3B**). In the inflammatory process, iNOS gene expression is upregulated and induced NO production (Grisham et al., 1999). Excessive NO can lead to vasodilation and hypotension, and eventually septic shock (Crawford et al., 2004). In LPS-stimulated macrophages, 7CZ NPs reduced NO and iNOS proteins, while ceria NPs did not show any effect (**Figure 3C**). Through the determination of extracellular lactate dehydrogenase content, 7CZ NPs could better inhibit the LPS-induced release of LDH, suggesting that it could provide better cell protection. These *in vitro* data indicated that compared to ceria NPs, 7CZ NPs are more effective in blocking the abnormal inflammatory response of macrophages by clearing the ROS/reactive nitrogen species (RNS) and other effects on the inflammatory pathway. Huang's group doped Mo into Pt_3Ni nanocrystals to obtain highly active nanozymes, which are ∼80 times the commercial catalyst activity (Huang et al., 2015). Zhang's group reported that a trimetallic (triM) nanozyme was obtained by doping transition metal molybdenum in platinum-palladium nanoparticles, which significantly improved the antioxidant activity (Mu et al., 2019b). The density functional theory (DFT) simulation results showed that the Mo atom has a strong attraction compared to the Pt and Pd atoms, which helps to separate the small unit into two atoms that are further apart and are independent of the free radical unit. Further analysis of the electrostatic potential (ESP) and the electron localization function (ELF) showed that Mo atoms are more attractive to small units and decrease the binding ability of adjacent Pt atoms. When small units are attached to triM nanozyme, there is a higher chance that they will be stretched by Mo and other atoms. Therefore, Mo doping can improve the catalytic efficiency of nanozymes.

Electronic Transfer Strategy

Another method to accelerate the induced reduction of Ce^{4+} to Ce^{3+} is the electron transfer strategy (**Figure 3D**). Zhang's group found that one of their ceria nanoparticles, which is (5.1 ± 0.4) nm in size, had an inappreciable Ce^{3+}/Ce^{4+} ratio and weak SOD mimetic activity. But when co-incubated with CuZn-SOD in a PBS solution, the activity of ceria NPs was activated within a few minutes (**Figure 3E**). In the process of scavenging superoxide free radicals, there is a certain possibility that electrons are transferred from the Cu-Zn SOD to ceria NPs accompanied by the reduction of copper ions. Ceria NPs acts as an electronic sponge that can store electrons and regenerate active sites that scavenge superoxide radicals. Mixing $[Ru\ (dcbpy)_2\ (NCS)_2]$ with ceria NPs into PBS, they also found that the activity of SOD mimetic in the mixture increased significantly under visible light (**Figure 3F**), and gradually disappeared after the removal of light. These results suggested that the activity of ceria NPs could be excited after interfacial electron transfer (Li et al., 2014). Similarly, the bioconjugation of ceria NPs with apoferritin exhibited an excellent ROS scavenging activity due to charge transfer at the interface between protein corona and ceria NPs, resulting in a change in the valence of the oxide and increasing the fraction of Ce^{3+} (Liu X. Y. et al., 2012). Qu's group reported a graphene oxide (GO)-Se nanozyme that exhibited higher GPx-like activity than SeNPs, possibly due to the large surface area and strong electron transfer ability of GO (Huang et al., 2017). Singh's group found that Fe_3O_4 NPs exhibited increased peroxidase-like activity in ATP presence over a wide range of pH values and temperatures. In terms of mechanism, it was found that ATP participated in the single-electron transfer reaction by complexing with Fe_3O_4 NPs, leading to the generation of hydroxyl radicals, which enhanced the activity of peroxidase-like at physiological pH (Vallabani et al., 2017).

Confinement Space

Nanoreactors provide a confining space in which reactive molecules and catalysts are encapsulated to enhance the activity of the reaction. The Au @ SiO2 yolk/shell structured nanoreactor framework was used for catalytic reduction of p-nitrophenol (Lee et al., 2008). Another nanoreactor composed of Pd @ meso-SiO_2 showed excellent activity in the Suzuki coupling reaction (Chen et al., 2010). Amphiphilic networks have also been used as nanoreactors to stabilize and enhance enzyme catalytic activity in organic solvents (Bruns and Tiller, 2005). Nickel nanoparticles encapsulated by nitrogen-doped hollow carbon nanocapsules showed superior activity in oxygen reduction reaction. The low catalytic activity of the catalyst was compensated by increasing the collision rate in the nanocapsules. Defects in the graphene nano-shell allowed oxygen and hydroxyl to diffuse easily (Li B. et al., 2017). The CeO_X nanoparticles, encapsulated in hollow microspheres, can remove ROS more efficiently in a limited space (Ju et al., 2017). Sung's group encapsulated chlorophyll a, l-ascorbic acid, and gold nanoparticles in a liposome system to construct a multicomponent nanoreactor for efficient photo-driven hydrogen (H_2) production (**Figure 4A**). The results of gas chromatography analysis showed that the cumulated H_2 concentrations from the nanoreactors consistently surpassed those from bulk solution (**Figure 4B**) (Wan et al., 2017). This confinement space may raise the local concentration of the reaction, increase the probability of molecular collision, and thus improve the efficiency of the catalytic reaction.

Single Atom Catalysis

Single atom catalysis can be used as an essential tool to enhance catalytic activity. For example, Lee's group synthesized heme cofactor-resembling $Fe–N_4$ single-site-embedded graphene in which the activity of each iron ion was 5 million times higher than that of Fe_3O_4 NPs (Kim et al., 2019b). Atom-dispersed metal centers can maximize the utilization efficiency of atoms and the density of active sites. Dong's group prepared the single-atom nanozymes of carbon nanoframe–confined axial N-coordinated single-atom Fe (FeN_5 SA/CNF). The active sites of FeN_5 SA/CNF were comparable to those of axially coordinated heme of natural redox enzyme. Taking oxidase catalysis as a model reaction, the theoretical calculations and experimental studies clearly showed that the highest oxidase-like of FeN_5 SA/CNF is due to the synergistic effect and electron donation mechanism. It is worth noting that the oxidase-like activity of FeN_5 SA/CNF was 17 times and 70 times higher than that of the square planar FeN_4 catalyst and commercial Pt/C with normalized metal content, respectively (Huang et al., 2019). Ming's group anchored single-atom Pt on ultrasmall CeO_2 nanoclusters, and the scavenging activity of RONS increased by 2–10 times compared with CeO_2 clusters (Yan et al., 2019). The higher Ce^{3+}/Ce^{4+} ratio in Pt/CeO_2 and the catalytically active sites provided by single-atom Pt with oxygen vacancies are the two main reasons for improving the catalytic activity. Pt single atoms tend to be stabilized at CeO_2 (111) and have a strong attraction, reducing the energy of units of free radicals bound to the surface of Pt/CeO_2 (111) (**Figure 4C**), thereby enhancing the RONS scavenging ability. Zhao's group used $Mn_3[Co(CN)_6]_2$ MOF as supporting material to frame a single atom of Ru with a load-weight ratio of up to 2.23 wt%. Ru partly replaced Co as a single atom catalytic site for endogenous oxygen production. Since the ligand terminal carbon had a stronger coordination ability with Ru than Co, partial substitution of Co was realized. The high catalase-like activity of this nanozyme should be attributed to six unsaturated $Ru–C_6$ coordination sites, resulting in the rapid decomposition of H_2O_2 into O_2 to overcome the tumor hypoxia (Wang et al., 2020). In addition, Lee's group developed N-and B-doped reduced graphene (NB-rGO) as a carbon nanomaterial mimicking peroxidase, whose catalytic activity was much higher than that of traditional carbon-based peroxidase-like nanozymes, even comparable to horseradish peroxidase (HRP). N- and B-codoping converts inert pyridine N atoms into catalytically active centers while retaining the peroxidase-like activity of a single B atom. Synergistic effect of N- and B-codoping further enhanced peroxidase activity over the undoped or single doped graphene (N or B) (Kim et al., 2019a).

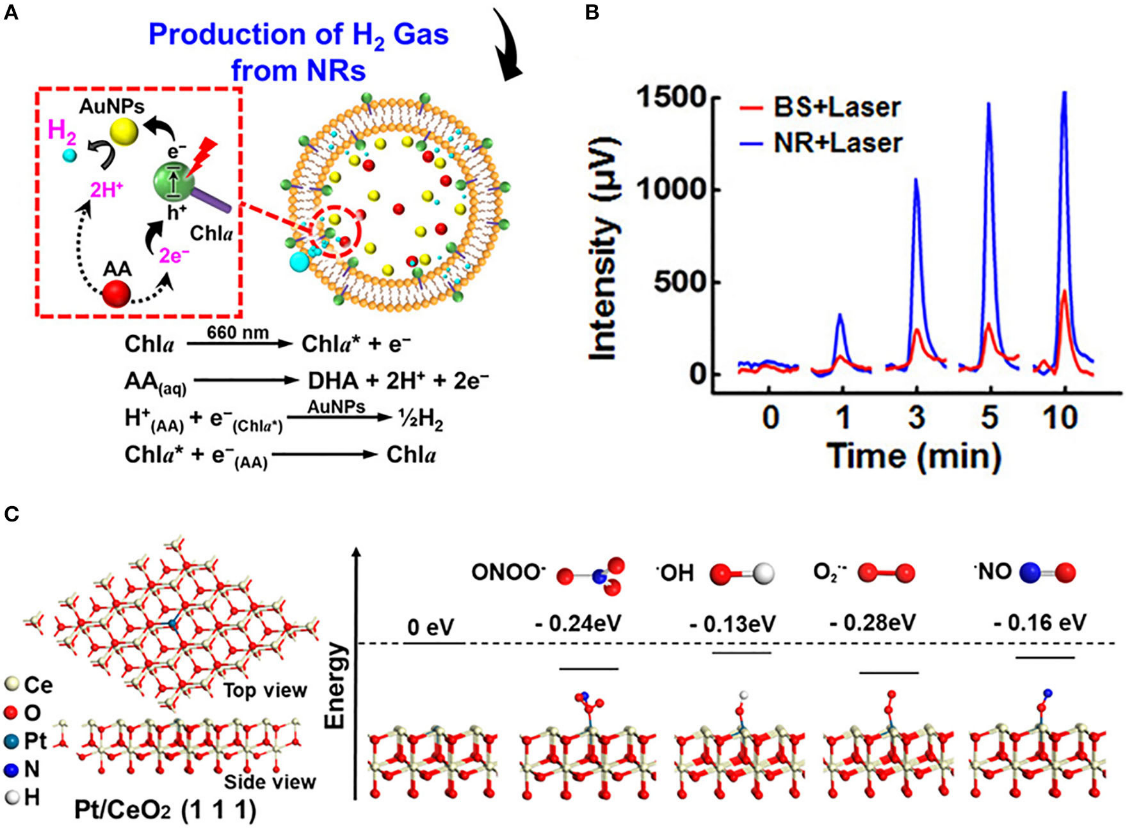

FIGURE 4 | Introducing confinement space and single atom catalysis to enhance antioxidant activity. **(A)** Composition/structure of photodriven NR and mechanisms of its photosynthesis of H_2 gas *in situ*. **(B)** Cumulative H_2 concentrations generated in BS and NR following laser irradiation [reproduced from Wan et al. (2017) with permission from the American Chemical Society]. **(C)** Atomic structure of Pt/CeO$_2$ along (111) facets and energy feature of the segment model with different radical units [reproduced from Yan et al. (2019) with permission from the American Chemical Society].

Molecular Imprinting

Nanozymes are nanomaterials that mimic the activity of natural enzymes, and but most of them lack substrate specificity. The molecular imprinting technology of nanoenzymes provides a simple solution to this problem, but also improves the catalytic activity. Molecularly imprinted polymers (MIPs) are polymerized from monomers around template molecules (Schirhagl, 2014). The selected monomers are usually complementary to the properties of the template to form pre-polymer-bound complexes (Chen et al., 2011). During polymerization, the template is imprinted by the crosslinked polymer matrix. After removing the template, a cavity is generated for rebinding the template (Mahajan et al., 2019). The combination of PtPd nanoparticles with molecular imprinting enhanced peroxidase-like activity (Fan et al., 2017). Shen's group developed an efficient strategy for co-catalyzing peptide disulfide bond formation by molecularly imprinted polymer microzymes and inorganic magnetic nanozymes (Chen et al., 2017). Liu's group added acrylamide and nisopropylacrylamide (NIPAAm) as monomers and N, N′-methylenebis(acrylamide) (MBAAm) as a cross-linker to the Fe_3O_4 NPs and TMB (or ABTS) mixture. After adding the initiators into the system, the nanogels were obtained by precipitation polymerization. The substrate templates were then rinsed off to create binding pockets. The TMB and ABTS imprinted gels are named T-MIP and A-MIP, respectively. The authors next measured the rates of the nanozymes at various substrate concentrations to obtain enzyme parameters. The k_{cat} of T-MIP nanogel (15.0 s^{-1}) is more than twice that of free Fe_3O_4 NPs and A-MIP when oxidizing TMB. For oxidizing ABTS, the A-MIP gel has the highest activity and affinity. T-MIP has 2.8-fold higher k_{cat}/K_m ($6.8 \times 10^{-2}\ s^{-1}\ \mu M^{-1}$) than that of bare Fe_3O_4 ($2.4 \times 10^{-2}\ s^{-1}\ \mu M^{-1}$). When oxidizing ABTS, the same gel showed ~3 times lower k_{cat}/K_m than bare Fe_3O_4. Similarly, the AMIP has 4-fold higher specificity than bare Fe_3O_4 for oxidizing ABTS but 1.5-fold lower for oxidizing TMB. Since TMB has a positive charge and ABTS has a negative charge, the imprinting was further improved by incorporating charged monomers. The TMB imprinted nanogels are named T-MIPneg if containing anionic AMPS and named T-MIPpos if containing cationic DMPA. The T-MIPneg has the best catalytic efficiency, 15-fold higher than that of the bare Fe_3O_4 NPs, much better than the 3-fold improvement for the T-MIP gel without the negative AMPS monomer. In the best case, the selectivity for TMB over ABTS using the T-MIPneg nanogel is 98-fold, while the selectivity for ABTS over TMB using the A-MIPpos is 33-fold (Zhang et al., 2017). Liu's group used surface science to understand the enhancement of activity by dissecting enzyme reactions to substrate adsorption, reaction, and product release. The enrichment of local substrate concentration induced by imprinting was about eight times, and the increase of substrate concentration could promote the improvement of the activity. The diffusion of the substrate on the imprinted gel layer was studied by pre-culture experiment, and the difference between the imprinted and non-imprinted gel layer was also highlighted. The activation energy of substrate imprinting sample was the lowest, 13.8 kJ/mol. The isothermal droplet calorimetry using the substrate and product samples imprinted separately showed that the product release rate was also improved after imprinting (Zhang et al., 2019).

Others

Choosing appropriate structure-oriented agents to synthesize nanoparticles may be an effective strategy to improve nanoparticles' catalytic activity. Kuang' group prepared a Cu_XO-Ph nanocluster with phenylalanine (Phe) as a structure-directing agent with good biocompatibility and the properties of multiple antioxidants enzyme-like (Hao et al., 2019). The authors found that the selection of different molecular structure-oriented agents resulted in nanoclusters' different shapes and activity. The authors synthesized five other nanoclusters using five other amino acids as structure-directing agents, among which Cu_XO -Ph showed the highest catalytic activity. Through the nitrogen adsorption test, it is found that the total volume and pore size of Cu_XO-Phe are larger than those of other materials except Cu_XO-Tyr. Although the size and surface area of CuXO-Phe (65 nm) is smaller than that of Cu_XO-Tyr (186 nm), the catalytic activity of CuXO-Phe is much higher than that of Cu_XO-Tyr, possibly because the ligand of the material plays an essential role in regulating its activity.

Single nanoparticle enzymes sometimes cannot achieve the desired antioxidant effect. The combined use of multiple nanoparticle enzymes can co-catalyze the elimination of ROS and perform a better scavenging effect. Qu's group assembled V_2O_5 and manganese dioxide (MnO_2) nanoparticles through dopamine to construct a synergistic antioxidant system with multiple enzyme mimicking activities. V_2O_5 nanowires have GPx-like activity, and MnO_2 nanoparticles are used to mimic SOD and CAT. The *in vitro* and *in vivo* experimental data showed that their biocompatible multi-nanozymes system had excellent intracellular ROS removal capacity, which protected intracellular components from oxidative damage, indicating its potential application in anti-inflammatory (Huang et al., 2016).

The activity can be activated by increasing the water solubility of the inorganic nanoparticles. Bulk $Cu(OH)_2$ is highly water-insoluble ($KL = 5.6{\cdot}10^{-20}$ $mol^3{\cdot}L^{-3}$) and does not exhibit any catalytic activity. However, after surface modification with glycine, it is easy to disperse in an aqueous medium, showing SOD-like activity that exceeds the activity of the natural CuZn enzyme (Korschelt et al., 2017).

Regulating the Activity of Nanozymes

Some nanozymes have been found to have antagonistic peroxidase-like and catalase-like activities, such as Fe_3O_4 NPs, platinum NPs, and gold NPs. They were able to decompose H_2O_2 into toxic hydroxyl radicals ($^{\bullet}OH$) which are highly active and harmful to cells by the activity of peroxidase-like. In contrast, hydrogen peroxide could be broken down into H_2O and O_2 by the activity of catalase-like. The size, morphology, and surface catalytic sites of nanozymes have essential effects on their activity. Therefore, it is necessary to exert the antioxidant activity of nanozymes through reasonable regulation.

PH Regulation

The activities of various nanozymes have been found to have pH-adjustable properties, and exploring their intrinsic mechanism is of great significance for us to precisely regulate the activities of nanozymes. Yan's group reported that Fe_3O_4 magnetic nanoparticles (NPs) had an intrinsic peroxidase-like activity with a pH of 3.5 (Gao et al., 2007), and Gu's group reported that these particles had catalase-like activity under neutral pH conditions (Chen et al., 2012). Yin's group reported that Ag and Au NPs could catalyze the rapid decomposition of H_2O_2. At lower pH, the breakdown of H_2O_2 was accompanied by the production of $^{\bullet}OH$, and at higher pH, by the production of O_2. These particles also exhibited SOD-like activity when the $pH = 7.4$ (He et al., 2012, 2013). Gao's group studied the mechanism of PH-adjustable peroxidase and catalase-like activities of gold, silver, platinum, and palladium nanomaterials (**Figure 5A**) by calculation and experiment. The peroxidase-like activity of these metals at low pH is due to the basic-like decomposition of H_2O_2 on the metal surfaces. In contrast, the catalase-like activity at high pH is thought to be due to the acid-like decomposition of H_2O_2 on the metal surfaces (**Figure 5B**). They also proved that the activity of the enzyme is an inherent property of metals and has nothing to do with the environment. The relative enzymatic activity of metals with similar surface morphology can be predicted by the relative adsorption energy between H_2O_2 and metals (Li et al., 2015). The results are instructive for the design, synthesis, and application of metal-based artificial enzymes.

Surface Modification

Since the surface atoms are the critical catalytic sites, the antioxidant capacity of these nanoparticles can be fully exerted by choosing appropriate coating molecules to modify nanoparticles to block peroxidase-like activity and preserving catalase-like activity. Lin's group accidentally discovered that gold nanoparticles surface modified with amine-terminated PAMAM dendrimers lost peroxidase-like activity while still retained catalase-like activity under different pH conditions related to the biological microenvironment (**Figure 5C**). The authors proposed a possible mechanism that polymeric 3°-amines that are abundant on the surface of AuNCs-NH_2 can be oxidized by hydroxyl radicals, which was confirmed by ^1H NMR measurements. AuNCs-NH_2 thus acquired the ability to scavenge $^{\bullet}OH$ and inhibit peroxidase-like activity (Liu C.-P. et al., 2016). However, with the gradual oxidation of tertiary amines, the peroxidase activity of nanoparticles is gradually restored,

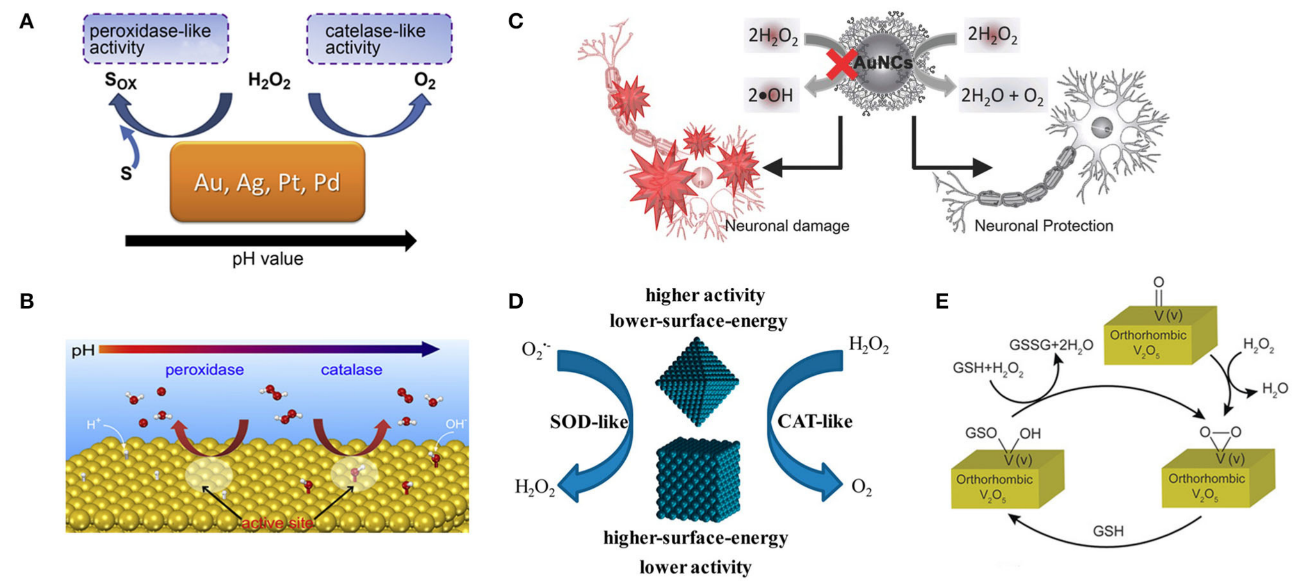

FIGURE 5 | Various methods for regulating the activity of nanozymes include PH regulation, surface modification, and the effect of surface energy. **(A)** The pH-switchable peroxidase-like and catalase-like activities of Au, Ag, Pt, and Pd metals. **(B)** The predicted mechanisms for the pH-switchable peroxidase-like and catalase-like activities of the metals [reproduced from Li et al. (2015) with permission from the Elsevier]. **(C)** A schematic diagram shows the dendrimer-encapsulated AuNCs with the catalase-like activity to detoxify H_2O_2 for primary neuronal protection against oxidative damage [reproduced from Liu C.-P. et al. (2016) with permission from the John Wiley and Sons]. **(D)** Lower surface energy {111}-faceted Pd octahedrons have greater intrinsic antioxidant enzyme-like activity than higher surface energy {100}-faceted Pd nanocubes [reproduced from Ge et al. (2016) with permission from the American Chemical Society]. **(E)** Schematic representation of the reaction of H_2O_2 and GSH on the surface of orthorhombic V_2O_5 crystal [reproduced from Ghosh et al. (2018) with permission from the John Wiley and Sons].

which may be detrimental to the long-term use of nanoparticles and broader application. Karakoti's group demonstrated that modifying the surface of CeO_2 NPs with suitable ligands, especially triethyl phosphite (TEP) and tris(2,4,6 trimethoxyphenyl)phosphine (TTMPP), could alter their redox properties and reverse the oxidation state. It was evident from XPS and PL studies that both TEP and TTMPP could electron-couple with the surface cerium ions of cerium CeO_2 NPs. TEP can be used as a reductant to reduce the surface Ce^{4+} ion on CeO_2 NPs, thus promoting the SOD activity of CeO_2 NPs. It can be speculated that TTMPP is a large molecule, which can block the active surface sites of CeO_{2-x} NPs and make them lose SOD activity, but this does not explain how it activates their catalase activity. Therefore, a more comprehensive understanding of ligands' role in the regulation of enzyme-like activity of NPs is needed (Patel et al., 2018). Yan's group attached histidine to Fe_3O_4 NPs increasing its peroxidase-like activity by 20-fold (Fan et al., 2017). Liu's group adsorbed fluoride on nanoceria increasing its oxidase-like turnover by nearly 100-fold (Liu X. P. et al., 2016). Li's group prepared MIP around TiO_2 photocatalyst also showing enhanced activity (Shen et al., 2009).

Control of Surface Energy

There is a tight correlation between the catalytic activity of metal-based nanomaterials and their surfaces. Different crystal forms of the same nanomaterial have different surface energies and may exhibit different catalytic activities. Yin's group found that the lower-surface-energy Pd octahedron {111} had higher antioxidant enzyme activity than the higher-surface-energy Pd nanoparticle {100} (**Figure 5D**). Their theoretical calculations showed that Pd octahedron with lower surface energy exhibits higher catalytic activity by lowering the reaction energy of scavenging reactive oxygen species, consistent with experimental observations. This study also provides a new perspective on the design of highly active antioxidant nanozymes (Ge et al., 2016). Mugesh's group synthesized four orthogonal V_2O_5 nanozymes with different morphologies [nanowires (VNw), nanosheets (VSh), nanoflowers (VNf), and nanospheres (VSp)] and found that their activity was independent of surface area. The differences in their GPX-like activity are due to differences in surface v-peroxide speciation rates (**Figure 5E**). In the same crystal system, the exposed crystal facets can adjust the H_2O_2 reduction capacity of V_2O_5 nanozyme. These results suggest that we can fine-tune the redox properties of nanomaterials by designing their surfaces (Ghosh et al., 2018).

Enhancing Biocompatibility

It has been shown that some inorganic nanoparticles can interact with lipid, proteins, and DNA, thereby impairing the integrity of biofilms and the function of enzymes (Cedervall et al., 2007; Wang et al., 2008; Pelka et al., 2009), so improving the biocompatibility of nanoparticles is essential for their more extensive biological application.

Nanoparticles encapsulated in proteins can improve the biocompatibility of nanoparticles. Yeung group fixed BSA onto Au-Pt nanocomposites through electrostatic interaction, and the modified nanoparticles still maintained high antioxidant activity (Xiong et al., 2014). Knez's group encapsulated Pt NPs and PtAu NPs in apoferritin (Zhang et al., 2010, 2011), respectively, and Najaf's group reported apoferritin-encapsulated silver-gold nanoparticles (Dashtestani et al., 2018). The obtained nanoparticles not only have excellent biocompatibility but also can effectively remove $O_2^{\bullet-}$ and H_2O_2. Apoferritin is a globular protein with an outer diameter of 12 nm and an inner cavity diameter of 7.6 nm. 14 small channels, 3–4 Å in diameter, run through the protein shell, providing size selection for ions and small molecules (Ford et al., 1984). These nanoparticles could safely enter human intestinal Caco-2 cells capable of expressing ferritin receptors constitutively without showing any toxicity to the cells. The protein shell of apoferritin can also avoid the aggregation of noble metal nanoparticles in solution and improve the stability of nanoparticles, which is beneficial to its long-term application in biological systems. The biocompatibility of nanoparticles can be improved by changing the surface stabilizer of nanoparticles. Erlichman's group reported that citrate/EDTA stabilized ceria NPs were well-tolerated and absorbed by the liver and spleen far less than previous nanoceria formulations when given intravenously to mice (Heckman et al., 2013). Pompa's group demonstrated that their citrate -capped Pt NPs did not exhibit significant cytotoxicity to cells *in vitro* (Moglianetti et al., 2016). PVP (Su et al., 2015) and PEG (Liu et al., 2017) are generally used polymer stabilizer because of their low cost, good water solubility, outstanding biocompatibility, and commercial availability.

Magnetite nanoparticles (Fe_3O_4 NPs) are proved to be biocompatible nanomaterials and have broad prospects in various biomedical applications (Lee et al., 2015). Fan's team found that the catalytic activity of Fe_3O_4 NP has a novel biocompatibility mechanism significantly different from that of conventional inert NP (Wang et al., 2018). The authors found that both nanoparticles induced response to oxidative stress by comparing the cellular effects of two ferric oxide nanoparticles (Fe_3O_4 and α-Fe_2O_3). Nevertheless, Fe_3O_4 NPs significantly delayed the production of toxic reactive oxygen species (ROS) and reduced autophagy and programmed cell death due to their antagonism of inherent catalase-like activity. The dynamic equilibrium mechanism proposed in this work inspires us to improve nanomaterials' biocompatibility by introducing antioxidant properties.

Others

Enhancing the endogenous antioxidant ability of cells is an effective way to improve the ability of cells to resist oxidative stress. Interestingly, Alrokayan's group found that ceria NPs and Mo NPs could significantly increase in intracellular level of antioxidant molecule glutathione (GSH) in cells [human breast (MCF-7) and human fibrosarcoma (HT-1080)] challenged with oxidants (Akhtar et al., 2015a,b). This discovery can provide us a new perspective to explore the antioxidant mechanism of nanozyme, not only considering the antioxidant properties of nanozyme itself, but also taking the impact of nanozyme on biological environment into account.

The targeting properties of nanoparticles can be changed by surface modification of targeting agents or changing the size of nanoparticles. As the only biological barrier, the blood-brain barrier protects the brain from potentially harmful compounds in the blood, so, unfortunately, it prevents the build-up of nanoparticles in the brain (Hawkins and Thomas, 2005). During cerebral ischemia, the blood-brain barrier is damaged, leading to an increase in permeability (Kim et al., 2012; Jiang X. et al., 2018). Some nanoparticles can pass through the damaged part of the blood-brain barrier into the damaged part of the brain. However, the accumulation of nanoparticles in the brain is limited, which also limits the treatment of nanoparticles. Shi's group modified Angiopep-2 (ANG) onto CeO_2 nanoparticles to create a BBB-targeted nanoplatform (Bao et al., 2018). ANG binds specifically to the over-expressed LDLR protein (LRP) in the cells that make up the BBB, significantly increasing the accumulation of nanoparticles in the brain through receptor-mediated endocytosis. Excess ROS, present in mitochondria, both intracellular and extracellular, plays a special role in disease (Kwon et al., 2018). Hyeon's group prepared three kinds of ceria NPs by changing the size and surface modification, which can selectively eliminate these three kinds of ROS. Small-sized nano-cerium is easily absorbed by cells, eliminating ROS from the cytoplasm. Triphenylphosphonium-modified nano-cerium can enter mitochondria and remove ROS in mitochondria. Because the endocytosis of large nanoparticles is suppressed, the 300 nm-sized cluster-ceria NPs remain outside the cell and eliminate the extracellular ROS (Kwon et al., 2018).

BIOLOGICAL APPLICATION OF ANTIOXIDANT NANOZYMES

Anti-aging

As animals age, oxidative damage accumulates in their bodies, which is closely related to aging, behavioral decline, geriatric disease, and lifespan (Finkel and Holbrook., 2000). Dugan's group administered carboxy fullerenes SOD mimetics to non-transgenic, and non-senescence accelerated mice starting at middle age. The authors found that this chronic treatment reduced age-related oxidative stress and the production of mitochondrial free radicals, significantly prolonged lifespan, and improved the performance of mice in Morris water maze learning and memory tasks (Quick et al., 2008). A mixture of Pd and Pt nanoparticles has been reported to reduce age-related skin atrophy in mice. Drosophila melanogaster has been widely used to study and explain the mechanism of some complex biological processes, including development, metabolism, and aging (Shibuya et al., 2014). Song's group found that dietary Fe_3O_4 NPs significantly reduced ROS levels in aged drosophilae, boosting their ability to climb and prolonging their lifespan (Zhang et al., 2015).

Cytoprotection

Excessive production of intracellular ROS and inefficiency of the endogenous antioxidant system can cause oxidative stress, which leads to cell component damage and cell apoptosis. Nanozymes with antioxidant capacity can protect cells from oxidative stress. For example, Mn_3O_4 NPs can mimic three major antioxidant enzymes, including SOD, GPx, and CAT (Singh et al., 2017). Mugesh's group explored specific ways in which Mn_3O_4 NPs protect cells from oxidative damage, and demonstrated that the NPs do not interfere with the endogenous antioxidant mechanisms of cells (Singh et al., 2019). Their experimental data proved that this nanozyme could prevent ROS from damaging proteins (**Figure 6A**), breaking DNA double-strand (**Figure 6B**), and lipid peroxidation in cells (**Figure 6C**). This work also ascertained that under conditions of oxidative stress, this nanozyme would not affect the expression of Nrf2 protein (**Figure 6D**), which is a crucial regulator of the expression of antioxidant proteins in cells. This study demonstrated the remarkable ability of nanoenzymes to regulate cellular oxidation-reduction homeostasis without interfering with intracellular antioxidant proteins/enzymes.

Qu's group proposed a novel cell protection strategy, which uses manganese dioxide (MnO_2) nanozyme as a smart shell to encapsulate a single living cell to achieve long-term protection and operation (Li W. et al., 2017). The authors encapsulated the yeast cells in the MnO_2 shell through the process of biomineralization (**Figure 6E**), which enhanced the cell's tolerance to severe physical stress, such as dehydration and lyase, and improved the survival time of the cells under high levels of toxic chemicals (**Figure 6F**). What is more, once the shell is removed by stimulation with pure biomolecule glutathione (GSH), these encapsulated cells can fully restore growth and function (**Figures 6G,H**). Stabler's group prepared a ceria NPs-alginate composite hydrogel, which could play a useful role in protecting the encapsulated cells (Weaver and Stabler, 2015).

Inflammation Treatment

Excessive ROS induces microglia polarization, from the anti-inflammatory M2 phenotype to the pro-inflammatory M1 phenotype (Zhang et al., 2016). This phenotypic change usually aggravates neuronal damage and M1-activated microglia produce more ROS through up-regulated anaerobic glycolysis (Orihuela et al., 2016). Li's group demonstrated that CeNP-PEG effectively protected neurons by blocking the inflammatory signaling pathway triggered by ROS, allowing the phenotype of microglia to switch from proinflammatory M1 to anti-inflammatory M2 (Zeng et al., 2018). A large amount of toxic reactive active oxygen (ROS) in cigarette smoke (such as superoxide radicals, hydrogen peroxide, hydroxyl radicals) will increase the oxidative stress in the lungs of cigarette smokers, causing severe pulmonary inflammation, and leading to serious lung diseases (Stämpfli and Anderson, 2009). Effective removal of ROS from cigarette smoke is very important to prevent smoking-induced inflammatory lung diseases. Nagai's group reported a Platinum nanoparticle stabilized with polyacrylate (Pt-PAA) which can efficiently quench ROS. In *in vitro* and *in vivo* experiments, the results suggested that the PT-PAA inhibited cell death and pulmonary inflammation in smoking mice (Onizawa et al., 2009).

Wei's group reported a CuTA nanozyme by the coordination of Cu^{2+} and tannic acid, which was utilized to mimic antioxidative enzymes including SOD-like activity, catalase-like and $^{\bullet}OH$ elimination capacity. These characteristics endued CuTA nanozyme with an excellent ROS scavenging ability. The nanozyme was further applied in cigarette filter modification to reduce the damage caused by ROS in cigarette smoke to mouse models (Lin et al., 2019). Their group also reported another Mn_3O_4 nanozyme which was synthesized via a hydrothermal method (Yao et al., 2018). They demonstrated that the nanozyme possessed extraordinary SOD mimicking activities due to the mixed oxidation valence states of Mn^{2+} and Mn^{3+}. In addition, the Mn_3O_4 nanozyme also possessed CAT mimicking activity and hydroxyl radical scavenging activity. Fluorescence images and corresponding fluorescent intensity indicated that the dose-dependent intracellular ROS scavenging activities of Mn_3O_4 NPs by using Hela cell line as a model. In an ear inflammation mouse model, experiment data showed that the Mn_3O_4 NPs possessed efficient ROS scavenging capacity and negligible toxicity toward live tissues (**Figure 7A**).

Sung's group reported a multicomponent nanoreactor (NR) that comprises chlorophyll a (Chla), l-ascorbic acid (AA), and gold nanoparticles that are encapsulated in a liposomal (Lip) system that can produce H_2 gas *in situ* upon photon absorption to mitigate inflammatory responses (Wan et al., 2017). Chla, a photosensitizer, is excited (Chla*) by absorbing light with wavelengths of 660 nm and an electron-hole pair is thus generated. The hole in the excited Chla* can accept a new electron from AA which as an electron donor, returning to its ground state. Colloidal AuNPs, a catalyst, can promote conversion of the electrons from the excited Chal* and the protons from the oxidized AA to H_2 gas. H_2 can selectively reduce $^{\bullet}OH$ to H_2O while retaining other required ROS for normal signal regulation. In LPS-induced mouse paw inflammation model, the ROS, ir-6, and IL-1β levels in the inflammatory tissues irradiated with NR laser were lower (**Figure 7B**). The multicomponent system had excellent anti-inflammation effects and great potential in mitigating tissue inflammation. Selenium-based nanozymes have also been reported to remove ROS because of the special electronegativity of selenium, which gives it unique chemical properties, such as redox reactivity (Li F. et al., 2017). Xu's group reported selenium-doped carbon quantum dots, which had redox-dependent reversible fluorescence property, were effective in protecting cells from oxidative stress (Li F. et al., 2017). Qu's group reported a Se@pDA nanocomposite, in which selenium possessed excellent GPx-like activity, and dopamine had reducibility, which could synergistically remove harmful ROS from cell components (Huang et al., 2018). In the LPS-induced pneumonia model in mice, this nanocomposite could significantly alleviate the inflammatory response, including nuclear contraction, inflammatory cell infiltration, thickening of the alveolar wall, and protect life systems from oxidative damage (**Figure 7C**). Melanin nanoparticles have been reported to have multiple antioxidant and anti-inflammatory properties *in vitro* (Liu et al., 2017). In a rat model of ischemic stroke, the authors evaluated the *in vivo* efficacy of the nanozyme by pre-injection into the lateral ventricle. Compared with the saline control group, the PEG-MeNPs pre-treated rats had smaller infarct areas, significantly reduced sensitivity to ischemia, and significantly inhibited the formation of $O_2^{\bullet-}$. The evaluation

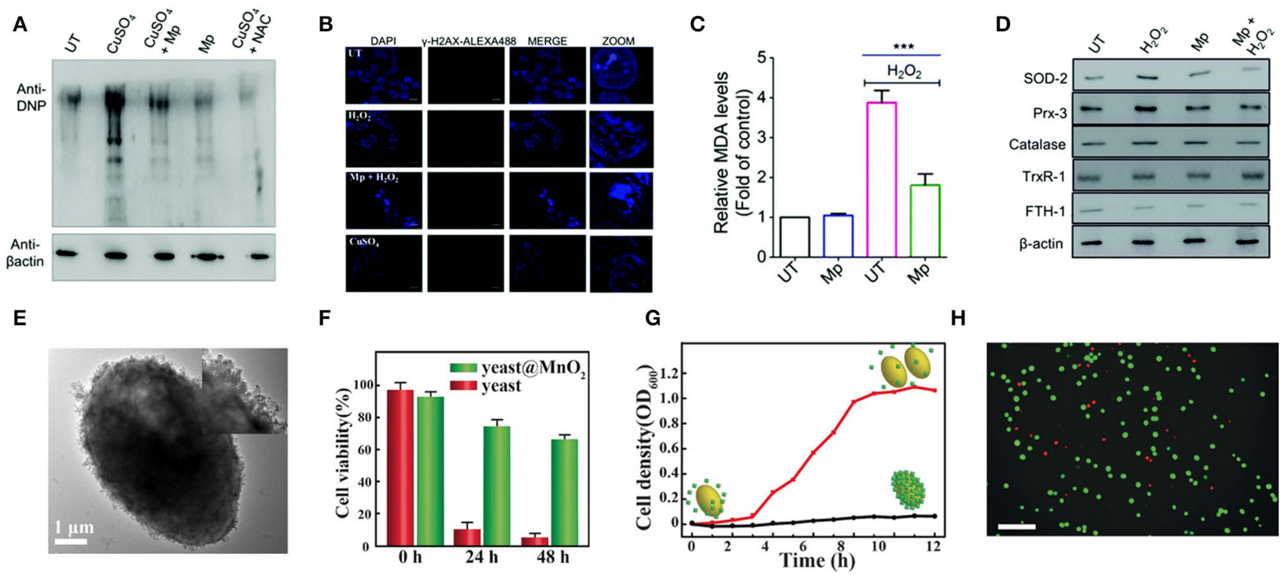

FIGURE 6 | Cellular protection of nanozymes. **(A)** HEK293T cells subjected to treatment were lysed and derivatized using 2,4-DNPH (2,4-dinitrophenylhydrazine) before SDS-PAGE. Immunoblot analysis was performed using anti-DNP antibodies. N-Acetyl cysteine treated cells (NAC) (100 mM) were used as the positive control. **(B)** Immunofluorescence microscopy was carried out to analyze the amount of DNA double-strand break by detecting the formation of γH2AX foci formed through phosphorylation. **(C)** The level of MDA formed in the cell lysate was quantified to determine the extent of lipid peroxidation using the TBARS assay. **(D)** The expression of Nrf2 responsive genes and antioxidant machinery was investigated in the presence of Mp by western blotting using specific antibodies for various stress-markers and antioxidant enzymes [reproduced from Singh et al. (2019) with permission from the Royal Society of Chemistry (RSC)]. **(E)** TEM image of yeast@MnO_2. Inset: HR-TEM image. **(F)** Cell viability of native yeast and yeast@MnO_2 after incubation with H_2O_2 for different time. **(G)** Growth curve of yeast@MnO2 with (red line) and without (black line) glutathione (GSH) stimuli. **(H)** Live/dead stained cells after removal of MnO_2 shells. Scale bar: 50 μm. [reproduced from Li W. et al. (2017) with permission from the John Wiley and Sons].

results of *in vivo* toxicity indicated that nanozymes did not induce systemic cytokine responses in mice and showed excellent blood compatibility. These results all suggested the great potential of PEG-MeNPs to prevent oxidative damage to the ischemic brain. Zhang's group reported that the PtPdMo triM nanozymes could exhibit the best antioxidant activity under a neutral environment, effectively scavenging ROS and RNS (Mu et al., 2019b). *In vitro* experiments showed that the nanoparticles protected the H_2O_2 -and LPS- treated neutral cells from oxidative damage. All *in vivo* toxicity evaluation results showed that triM nanozymes did not produce severe inflammation and immune reactions in the body and were a relatively safe antioxidant. Besides, the elimination of overproduced free radicals after treatment with nanoenzymes reduced neuroinflammation and significantly improved survival rate and reference memory in mice.

Wound Repair

The recovery of tissue integrity and tissue function of injured skin is crucial to wound repair and regeneration, but the synergistic effect of both is still challenging to achieve (Wu et al., 2018). At present, most wound healing treatment focuses on the process of structural restoration (Ghobril and Grinstaff, 2015). However, little work has been done on the microenvironment regulation of the injured site by the intrinsic regeneration ability of the host (Forbes and Rosenthal, 2014). Due to the increased production of ROS in the injured area, which may induce a series of harmful effects such as cell senescence (Finkel and Holbrook, 2000), fibrosis scar (Pellicoro et al., 2014), and inflammatory reaction (Mittal et al., 2014), it is suggested that the reduction of oxidative stress in the microenvironment of the injured area will help to promote the healing of regenerated wounds. Water-soluble CeO_2 nanoparticles can penetrate wound tissue, reduce oxidative damage to cell membrane and protein, and accelerate the healing of full-thickness dermal wounds (Chigurupati et al., 2013). However, the hydrophilic coating may weaken their tissue adhesion properties and affect the effect of wound repair. Ling's group fixed ultrasmall CeO_2 nanocrystals on the surface of uniform mesoporous silica nanoparticles (MSN) and prepared a multipurpose ROS-scavenging tissue adhesive nanocomposite (Wu et al., 2018). CeO_2 nanocrystals loaded with MSN not only have muscular tissue adhesion strength but also much limit the damage mediated by ROS, which effectively accelerates wound healing. More importantly, the wound area manifested an unexpected regenerative healing characteristic, marked by skin attachment morphogenesis and the formation of limited scarring. This strategy is also suitable for the repair of wounds that have a great need for the removal of ROS and tissue adhesion.

Cancer Treatment

Radiotherapy (RT) is one of the primary methods of cancer treatment. However, inadequate intratumoral radiation energy deposition and hypoxia-related radiation resistance are still

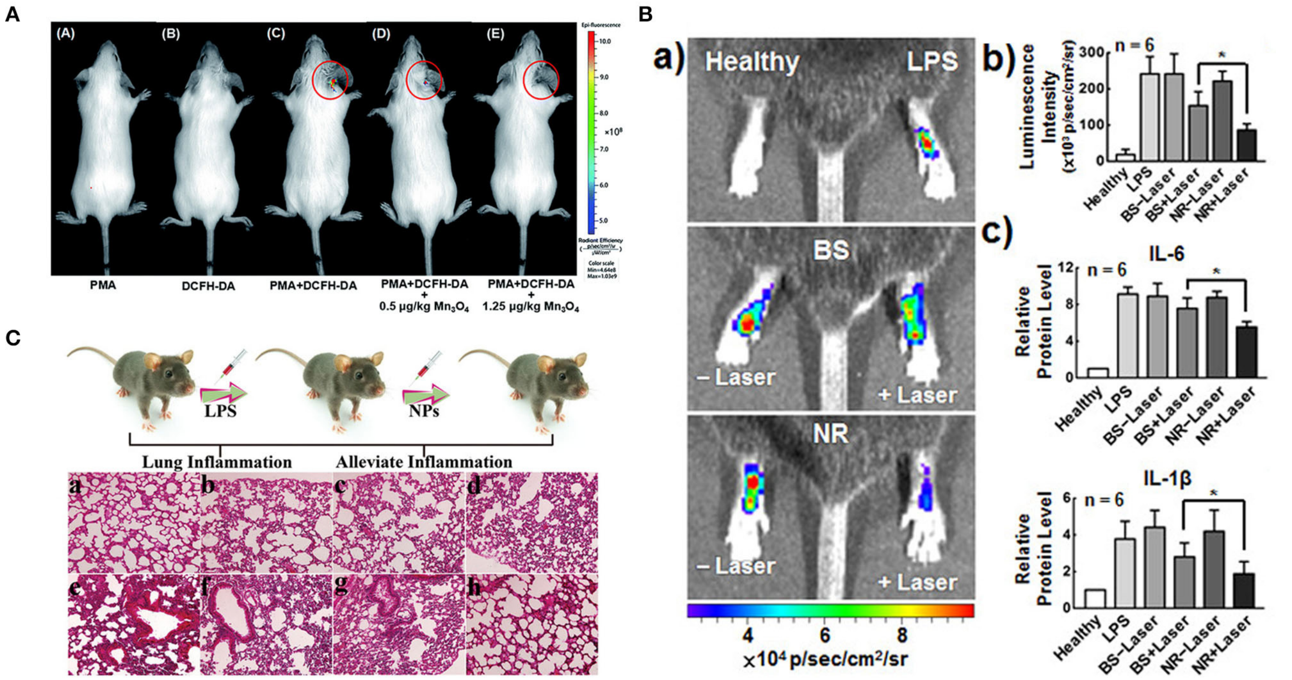

FIGURE 7 | Therapeutic effects of nanozymes on different inflammatory models. **(A)** *in vivo* fluorescence imaging of mice with PMA-induced ear inflammation [reproduced from Yao et al. (2018) with permission from the Royal Society of Chemistry (RSC)]. **(B)** (a) IVIS images and (b) corresponding L-012 luminescence intensities of ROS in LPS-induced inflamed paws following treatment with BS and NR without/with laser irradiation. (c) Levels of inflammatory cytokines IL-6 and IL-1β [reproduced from Wan et al. (2017) with permission from the American Chemical Society]. **(C)** Schematic illustration of lung inflammation model, and histological images of mouse lung tissue with different treatments: (a) untreated; (b) pDA; (c) Se; (d) Se@pDA; (e) LPS; (f) pDA and LPS; (g) Se and LPS; (h) Se@pDA and LPS [reproduced from Huang et al. (2018) with permission from the John Wiley and Sons].

the biggest obstacles to RT. Manganese dioxide (MnO_2) nanoparticles, which can decompose hydrogen peroxide into oxygen due to their inherent CAT-like activity, have been used to enhance RT *in vivo* (Song et al., 2016). However, after the interaction of MnO_2 NPs and x-rays, the radiation dose cannot be increased by effectively emitting electron radiation. Choi's group used porous platinum nanoparticles as a new nanomedical platform to solve two obstacles that restrict the efficacy of RT. *In vivo* experiments showed that high atom-number platinum interacted with tumor X-rays could emit electron radiation effectively, maximally enhance the radiation dose of tumor cells, and the porous PtNPs could rapidly convert H_2O_2 to O_2, overcoming the microenvironment of tumor hypoxia by utilizing its high porosity and large surface area (Li et al., 2019).

Treatment of Traumatic Brain Injuries

Traumatic brain injury (TBIs) causes many complications, the most prominent of which is nerve inflammation (Russo and McGavern, 2016). Reactive oxygen species (ROS) and reactive nitrogen species (RNS), especially RNS caused by inflammation can cause continuous damage to TBI, which can lead to severe tissue necrosis and apoptosis (Russo and McGavern, 2016).The RNS after TBI is highly active and toxic and difficult to remove (Simon et al., 2017). Hu's group reported a carbogenic nanozyme which was prepared by simple microwave heating with lysine and ascorbic acid and exhibited an ultrahigh ROS (including $O_2^{\bullet-}$, H_2O_2, and $^{\bullet}OH$) and RNS (such as $^{\bullet}NO$ and $ONOO^-$) scavenging efficiency (∼16 times higher than AA) (Hao et al., 2019). After the LPS- and H_2O_2-damaged neuron cells were treated with carbogenic nanozyme, the cell viability was significantly improved by eliminating various RONS. After the nanozyme was injected intravenously into the TBI mouse model, as the injection time increased, the BBB permeability and the MMP-9 expression level gradually decreased, indicating that the nanozyme could effectively repair the BBB destruction and subsequent brain edema. Furthermore, the spatial learning and memory capabilities of TBI mice could be effectively restored by the nanozyme treatment (Hao et al., 2019). This work confirmed the enormous potential of carbogenic nanozyme in the treatment of acute TBI. Ming's group used single-atom Pt/CeO_2 bandage for local non-invasive treatment of TBI. Throughout the 30 days of treatment, the nanozyme bandages showed good stability and catalytic activity without any significant decline. After the nanozyme-based bandages were applied to the injured brain area of mice with TBI, the size and area of wounds were significantly reduced to normal levels. At the same time, the untreated group recovered only partially (∼50%) (Yan et al., 2019).

Treatment of Neurological Diseases

The Cu_XO nanoparticle clusters can effectively inhibit the neurotoxicity of Parkinson's disease cell model and repair

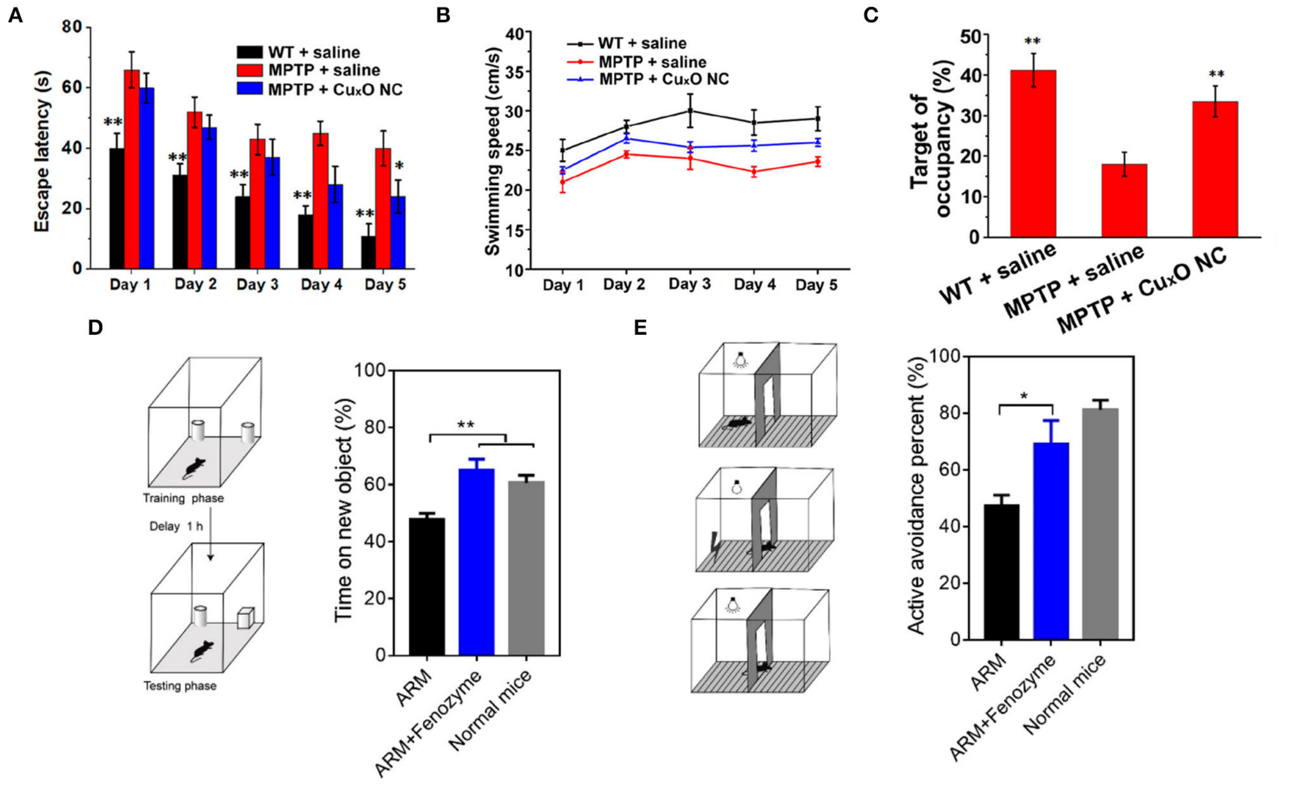

FIGURE 8 | Treatment of nervous system diseases with nanozymes **(A)** Escape latency. **(B)** swimming speed. **(C)** relative time spent on the target quadrant where the escape platform used to be located [reproduced from Hao et al. (2019) with permission from the American Chemical Society]. **(D)** Time spent on the new object by ARM- and ARM + Fenozyme-treated ECM mice (*n* = 5). **(E)** Active avoidance percent by ARM- and ARM + Fenozyme-treated ECM mice in the last 30 times after 500 times of training (*n* = 5). Normal mice without infection were also used as a control [reproduced from Zhao et al. (2019) with permission from the American Chemical Society].

memory loss in Parkinson's disease mice (Hao et al., 2019). The PD group had less time in the target quadrant than the other group, and the motion paths were random, which reflected the memory impairment caused by MPTP. The mice treated with Cu_XO -NCs showed spatially oriented swimming behavior and stayed in the target quadrant for a long time (**Figures 8A–C**), and the motor pathways were mainly concentrated in the target quadrant, suggesting that the Cu_XO-NCs treatment repaired memory loss in PD mice.

Cerebral malaria is a deadly complication of malaria infection accompanied by severe central nervous system dysfunction. Traditional combined antimalarial therapy can not treat it effectively (Zhao et al., 2019). In experiments based on brain malaria mouse models, it was found that when encephalopathy occurs, microvascular endothelial cells are often damaged, and the blood-brain barrier is destroyed (Coban et al., 2018). Studies have shown that the rupture of an infected parasite releases free hemoglobin, which may lead to excessive production of ROS, damaging endothelial cells, and the blood-brain barrier (Pamplona et al., 2007). Therefore, ROS might be an essential regulator of damage to the blood-brain barrier during the occurrence of cerebral malaria. Based on the pathogenesis of malignant cerebral malaria, fan's group developed a ferritin nanozyme (Fenozyme), which consisted of recombinant human ferritin (HFn) protein shell that specifically targeted the BBB endothelial cells and the core of the Fe_3O_4 nanozyme, which had ROS scavenging activity. In the experimental cerebral malaria (ECM) mouse model, by injecting fenozyme, the damage of blood-brain barrier induced by parasites was well-inhibited, the survival rate of infected mice was improved, and the macrophages in the liver were polarized into M1 phenotype, and the clearance of malaria parasites in blood was promoted. Besides, fenozyme significantly reduced encephalitis and memory impairment in ECM mice treated with artemether (**Figures 8D,E**). These results indicated that ROS played an essential role in the development of cerebral malaria and that fenozyme combined with antimalarial drugs was a very effective treatment strategy (Zhao et al., 2019).

Amyloid-β peptide (Aβ) agglomeration plays an essential role in the pathogenesis of Alzheimer's disease (AD) (Hamley, 2012), accompanied by excessive ROS production (Cimini et al., 2012). CeO_2 nanoparticles combined with enzymes or molecules resisting Aβ-aggregation have been used in the treatment of AD, showing a good therapeutic effect (Li et al., 2013; Guan et al., 2016). However, these nanoparticles lack a certain degree of targeting. Qu's group combined Aβ-target peptide KLVFF and C_{60} with up-conversion nanoparticles to construct a nano-platform for the treatment of AD (Du et al., 2018). In near-infrared light, Aβ-targeting nano-platform produced ROS that caused photooxidation of Aβ, which inhibited Aβ-aggregation and attenuated subsequent cytotoxicity. In the dark, the nanocomposite relieved oxidative stress by eliminating the overproduction of ROS.

Others

Nanozymes can be used as an adjuvant to endow some nanostructures with antioxidant properties, thus arousing the potential of nanoparticles in biological applications. Komatsu's team reported an artificial O_2 carrier with antioxidant activity, which is formed by combining hemoglobin-albumin clusters with Pt nanoparticles [Hb-HSA$_3$(PtNP)]. The resulting nanocluster has a robust ability to bind oxygen and avoids damage from $O_2^{\bullet -}$ and H_2O_2. In many clinical cases involving ischemia-reperfusion injury, such nanoclusters have high medical value and can be used as a substitute for red blood cells for blood transfusion (Hosaka et al., 2014). Qu's group developed a novel artificial metalloenzyme-based enzyme replacement therapy for the treatment of hyperuricemia. Uric acid enzyme (UA) and platinum nanoparticles (PtNPs) were tightly packed in the pores of mesoporous silica nanoparticles to form a tandem catalysis system. PtNPs could effectively eliminate H_2O_2 produced by UA, which enhanced the mammalian cell viability and had a significant therapeutic effect on hyperuricemia mice (Liu X. P. et al., 2016). CeO_X nanoparticles can effectively remove the ROS generated by ZnO during ultraviolet irradiation, thus providing broad-spectrum ultraviolet protection (Ju et al., 2017). Qin's group introduced PtNPs into the single-channel volumetric bar-chart chip (V-Chip) to detect biomarkers quantitatively (Song et al., 2014). To detect lung cancer biomarker CYFRA 21-1, they used a typical three-component sandwich ELISA method in which PtNPs were combined with probe antibodies and reacted with hydrogen peroxide to generate oxygen. At the same time, V-Chip can quantitatively measure the volume of oxygen generated. They used the PtV-Chip to assess the expression levels of HER2 in three breast cancer cell lines, suggesting that the PtV-Chip chip could be used to analyze biomarkers. Ceria NPs were introduced into bioabsorbable electronic stents to remove ROS produced in the perfusion by percutaneous coronary intervention and reduce inflammation that can cause thrombosis in the stent (Son et al., 2015).

CONCLUSION AND OUTLOOK

In this article, we have gathered recent research on the design and development of novel antioxidants based on nanozymes. We summarized several approaches to enhance the antioxidant activity of these enzymes, including enhancing catalytic activity, regulating the exertion of catalytic activity, improving biocompatibility, and targeting, and stimulating intracellular antioxidant activity. Nanozymes are broadly used in the field of biomedicine as an antioxidant, such as anti-aging, cell protection, anti-inflammatory, wound repair, cancer treatment, traumatic brain injury, and neurological diseases.

Although considerable progress has been made, there are still some obstacles to be overcome. (1) Compared with natural enzymes, nanozymes have poorer selectivity for substrates and have no specific structure to bind to substrates. Although it can be improved by surface modification, shape modification, etc., it will also affect the activity of the nanozyme. Moreover, under some conditions, nanozymes will combine with various substrates, and some side reactions will occur, which is not conducive to application in the biological field. Therefore, it is very important to improve the ability of nanozymes to specifically bind to substrates. (2) Many of the catalytic mechanisms of nanozymes lack detailed theoretical research. A further understanding of the catalytic mechanism can help us better comprehend the relationship between the structure of nanozymes and catalytic performance, thereby better regulating catalytic efficiency and substrate selectivity. Eventually, the research of nanozymes will be transferred from empirical science to substantial and basic theoretical science. (3) Different synthesis methods and conditions will also affect the antioxidant properties of nanozymes. Therefore, more uncomplicated, programmable strategies for synthesis and fabrication are required, which may be beneficial for future research on nanozymes. (4) Evaluation of the toxicity of nanozymes is still at a short-term level, and accurate data on the distribution, metabolism, clearance, and antioxidant activity of nanozymes in organisms are lacking. Most biological applications remain at the stage of mouse studies, making it difficult to transition to clinical studies and actual production. Thus, more detailed biological data, such as the long-term toxicity, pharmacodynamics, pharmacokinetics, immunogenicity, and catalytic activity of nanozymes *in vivo*, are needed to reduce the distance from basic research to clinical application. (5) There is no uniform standard to analyze the antioxidant activity of nanoparticles. It will be beneficial to the research and development of this field to establish a unified standardized analysis method.

In short, nanozymes may play a vital role in the biomedical field as an ideal antioxidant in the foreseeable future. (1) The influence of the structure of nanozyme on its catalytic mechanism will be more apparent in the future. In this regard, optimal synthesis methods should be designed and developed through experimental and computational approaches to achieve the highest possible effect. (2) The types of nanozymes will further increase, for example, analogs of active centers can be created in natural enzymes and then incorporated into MOFs or other nanomaterials to mimic catalytic activity. (3) Standard methods for the determination of catalytic activity and kinetics of peroxidase-like nanozymes have been reported (Jiang B. et al., 2018). Uniform standards for analyzing the antioxidant activity of nanoparticles will soon be established, which will lead to more reliable results and significantly promote research in this field. (4) In addition to catalysis, nanomaterials also endow nanozymes with more functions, including magnetic, optical, and thermal properties. This multi-functional antioxidant nanozyme will enhance antioxidant activity and broaden its application fields. (5) With the further development of pathology, the pathogenesis of various diseases will be more explicit, which will be more conducive to the broader application of nanozymes.

AUTHOR CONTRIBUTIONS

RT wrote the first draft. JX, QL, CH, and JL modified the manuscript content and format. All authors contributed to the article and approved the submitted version.

FUNDING

This work was supported by National Key R&D Program of China (Grant No. 2018YFA0901600).

REFERENCES

Akhtar, M. J., Ahamed, M., Alhadlaq, H., Khan, M. A. M., and Alrokayan, S. A. (2015a). Glutathione replenishing potential of CeO_2 nanoparticles in human breast and fibrosarcoma cells. *J. Colloid. Interf. Sci.* 453, 21–27. doi: 10.1016/j.jcis.2015.04.049

Akhtar, M. J., Ahameda, M., Alhadlaqa, H. A., Alshamsana,. A., Khana, M. A. M., and Alrokayan, S. A. (2015b). Antioxidative and cytoprotective response elicited by molybdenum nanoparticles in human cells. *J. Colloid. Interf. Sci.* 457, 370–377. doi: 10.1016/j.jcis.2015.07.034

Baldim, V., Bedioui, F., Mignet, N., Margaillc, I., and Berret, J. F. (2018). The enzyme-like catalytic activity of cerium oxide nanoparticles and its dependency on $Ce3^+$ surface area concentration. *Nanoscale* 10, 6971–6980. doi: 10.1039/C8NR00325D

Bao, Q. Q., Hu, P., Xu, Y. Y., Cheng, T. S., Wei, C. Y., Pan, L., et al. (2018). Simultaneous blood-brain barrier crossing and protection for stroke treatment based on edaravone-loaded ceria nanoparticles. *ACS Nano* 12, 6794–6805. doi: 10.1021/acsnano.8b01994

Barnham, K. J., Masters, C. L., and Bush, A. I. (2004). Neurodegenerative diseases and oxidative stress. *Nat. Rev. Drug Discov.* 3, 205–214. doi: 10.1038/nrd1330

Baynes, J. W. (1991). Role of oxidative stress in development of complications in diabetes. *Diabetes*. 40, 405–412. doi: 10.2337/diab.40.4.405

Bruns, N., and Tiller, J. C. (2005). Amphiphilic Network as nanoreactor for enzymes in organic solvents. *Nano Lett.* 5, 45–48. doi: 10.1021/nl048413b

Cai, H., and Harrison, D. G. (2000). Endothelial dysfunction in cardiovascular diseases: the role of oxidant stress. *Circ. Res.* 87, 840–844. doi: 10.1161/01.RES.87.10.840

Ceccarelli, J., Delfino, L., Zappia, E., Castellani, P., Borghi, M., Ferrini, S., et al. (2008). The redox state of the lung cancer microenvironment depends on the levels of thioredoxin expressed by tumor cells and affects tumor progression and response to prooxidants. *Int. J. Cancer* 123, 1770–1778. doi: 10.1002/ijc.23709

Cedervall, T., Lynch, I., Lindman, S., Berggard, T., Thulin, E., Nilsson, H., et al. (2007). Understanding the nanoparticle-protein corona using methods to quantify exchange rates and affinities of proteins for nanoparticles. *Proc. Natl. Acad. Sci. U.S.A.* 104, 2050–2055. doi: 10.1073/pnas.0608582104

Chen, L. X., Xu, S. F., and Li, J. H. (2011). Recent advances in molecular imprinting technology: current status, challenges and highlighted applications. *Chem. Soc. Rev.* 40, 2922–2942. doi: 10.1039/c0cs00084a

Chen, T. M., Zou, H., Wu, X. J., Chen, Y., Situ, B., Zheng, L., et al. (2019). Fullerene-like mos2 nanoparticles as cascade catalysts improving lubricant and antioxidant abilities of artificial synovial fluid. *ACS Biomater. Sci. Eng.* 5, 3079–3088. doi: 10.1021/acsbiomaterials.9b00372

Chen, T. M., Zou, H., Wu, X. J., Liu, C. C., Situ, B., Zheng, L., et al. (2018). A nanozymatic antioxidant system based on MoS_2 nanosheets. *ACS Appl. Mater. Inter.* 10, 12453–12462. doi: 10.1021/acsami.8b01245

Chen, Z., Cui, Z. M., Niu, F., Jiang, L., and Song, W. J. (2010). Pd nanoparticles in silica hollow spheres with mesoporous walls: a nanoreactor with extremely high activity. *Chem. Commun.* 46, 6524–6526. doi: 10.1039/c0cc01786h

Chen, Z., Yin, J.-J., Zhou, Y.-T., Zhang, Y., Song, L., Song, M., et al. (2012). Dual enzyme-like activities of iron oxide nanoparticles and their implication for diminishing cytotoxicity. *ACS Nano* 6, 4001–4012. doi: 10.1021/nn300291r

Chen, Z. L., Sellergren, B., and Shen, X. T. (2017). Synergistic catalysis by "Polymeric microzymes and inorganic nanozymes": the 1+1>2 effect for intramolecular cyclization of peptides. *Front. Chem.* 5:60. doi: 10.3389/fchem.2017.00060

Chigurupati, S., Mughal, M. R., Okun, E., Das, S., Kumar, A., McCaffery, M., et al. (2013). Effects of cerium oxide nanoparticles on the growth of keratinocytes, fibroblasts.and vascular endothelial cells in cutaneous wound healing. *Biomaterials* 34, 2194–2201. doi: 10.1016/j.biomaterials.2012.11.061

Cimini, A., D'Angelo, B., Das, S., Gentile, R., Benedetti, E., Singh, V., et al. (2012). Antibodyconjugated PEGylated cerium oxide nanoparticles for specific targeting of Abeta aggregates modulate neuronal survival pathways. *Acta Biomater.* 8, 2056–2067. doi: 10.1016/j.actbio.2012.01.035

Coban, C., Lee, M. S. J., and Ishii, K. J. (2018). Tissue-specific immunopathology during malaria infection. *Nat. Rev. Immunol.* 18, 266–278. doi: 10.1038/nri.2017.138

Crawford, J. H., Chacko, B. K., Pruitt, H. M., Piknova, H. B. N., and Patel, R. P. (2004). Transduction of NO-bioactivity by the red blood cell in sepsis: novel mechanisms of vasodilation during acute inflammatory disease. *Blood* 104, 1375–1382. doi: 10.1182/blood-2004-03-0880

Dalle-Donne, I., Aldini, G., Carini, M., Colombo, R., Rossi, R., and Milzani, A. (2006). Protein carbonylation, cellular dysfunction, and disease progression. *J. Cell. Mol. Med.* 10, 389–406. doi: 10.1111/j.1582-4934.2006.tb00407.x

Dashtestani, F., Ghourchiana, H., and Najafi, A. (2018). Silver-gold-apoferritin nanozyme for suppressing oxidative stress during cryopreservation. *Mat. Sci. Eng. C* 94, 831–840. doi: 10.1016/j.msec.2018.10.008

D'Autréaux, B., and Toledano, M. B. (2007). ROS as signalling molecules: mechanisms that Generate specificity in ROS homeostasis. *Nat. Rev. Mol. Cell Biol.* 8, 813–824. doi: 10.1038/nrm2256

Dickinson, B. C., and Chang, C. J. (2011). Chemistry and biology of reactive oxygen species in signaling or stress responses. *Nat. Chem. Biol.* 7, 504–511. doi: 10.1038/nchembio.607

Du, Z., Gao, N., Wang, X. H., Ren, J. S., and Qu, X. G. (2018). Near-infrared switchable fullerene-based synergy therapy for Alzheimer's disease. *Small.* 14:1801852. doi: 10.1002/smll.201801852

Fan, K., Wang, H., Xi, J., Liu, Q., Meng, X., Duan, D., et al. (2017). Optimization of Fe_3O_4 nanozyme activity via single amino acid modification mimicking an enzyme active site. *Chem. Commun.* 53, 424–427. doi: 10.1039/C6CC08542C

Finkel, T. (2011). Signal yransduction by reactive oxygen species. *J. Cell Biol.* 194, 7–15. doi: 10.1083/jcb.201102095

Finkel, T., and Holbrook, N. J. (2000). Oxidants, oxidative stress and the biology of ageing. *Nature* 408, 239–247. doi: 10.1038/35041687

Forbes, J. M., Coughlan, M. T., and Cooper, M. E. (2008). Oxidative stress as a major culprit in kidney disease in diabetes. *Diabetes* 57, 1446–1454. doi: 10.2337/db08-0057

Forbes, S. J., and Rosenthal, N. (2014). Preparing the ground for tissue regeneration: from mechanism to therapy. *Nat. Med.* 20, 857–869. doi: 10.1038/nm.3653

Ford, G. C., Harrison, P. M., Rice, D. W., Smith, J. M., Treffry, A., White, J. L., et al. (1984). Ferritin: design and formation of an iron-storage molecule. *Philos. Trans. R. Soc. B* 304, 551–565. doi: 10.1098/rstb.1984.0046

Gao, L., Zhuang, J., Nie, L., Zhang, J., Zhang, Y., Gu, N., et al. (2007). Intrinsic peroxidase-like activity of ferromagnetic nanoparticles. *Nat. Nanotechnol.* 2, 577–583. doi: 10.1038/nnano.2007.260

Ge, C., Fang, G., Shen, X. M., Chong, Y., Wamer, W. G., Gao, X. F., et al. (2016). Facet energy versus enzyme-like activities: the unexpected protection of palladium nanocrystals against oxidative damage. *ACS Nano* 10, 10436–10445. doi: 10.1021/acsnano.6b06297

Gechev, T. S., Breusegem, F. V., Stone, J. M., Denev, I., and Laloi, C. (2006). Reactive oxygen species as signals that modulate plant stress responses and programmed cell death. *Bioessays* 28, 1091–1101. doi: 10.1002/bies.20493

Ghobril, C., and Grinstaff, M. W. (2015). The chemistry and engineering of polymeric hydrogel adhesives for wound closure: a tutorial. *Chem. Soc. Rev.* 44, 1820–1835. doi: 10.1039/C4CS00332B

Ghosh, S., Roy, P., Karmodak, N., Jemmis, E. D., and Mugesh, G. (2018). Nanoisozymes: crystal-facet-dependent enzyme-mimetic activity of V_2O_5 nanomaterials. *Angew. Chem. Int. Ed.* 57, 4510–4515. doi: 10.1002/anie.201800681

Gilgun-Sherki, Y., Melamed, E., and Offen, D. (2001). Oxidative stress induced-neurodegenerative diseases: the need for antioxidants that penetrate the blood brain barrier. *Neuropharmacology* 40, 959–975. doi: 10.1016/S0028-3908(01)00019-3

Griendling, K. K., and FitzGerald, G. A. (2003). Oxidative stress and cardiovascular injury: part I: basic Mechanisms and *in vivo* monitoring of ROS. *Circulation* 108, 1912–1916. doi: 10.1161/01.CIR.0000093660.86242.BB

Grisham, M. B., Jourd'Heuil, D., and Wink, D. A. (1999). Nitric oxide. I. Physiological chemistry of nitric oxide and its metabolites:implications in inflammation. *Am. J. Physiol.* 276, 315–321. doi: 10.1152/ajpgi.1999.276.2.G315

Guan, Y. J., Li, M., Dong, K., Gao, N., Ren, J. S., Zheng, Y. C., et al. (2016). Ceria/POMs hybrid nanoparticles as a mimicking metallopeptidase for treatment of neurotoxicity of amyloid-b peptide. *Biomaterials* 98, 92–102. doi: 10.1016/j.biomaterials.2016.05.005

Gupta, A., Das, S., Neal, C. J., and Seal, S. (2016). Controlling the surface chemistry of cerium oxide nanoparticles for biological applications. *J. Mater. Chem. B* 4, 3195–3202. doi: 10.1039/C6TB00396F

Hamley, I. W. (2012). The amyloid beta peptide: a chemist's perspective. Role in Alzheimer's and fibrillization. *Chem. Rev.* 112, 5147–5192. doi: 10.1021/cr3000994

Hao, C. L., Qu, A., Xu, L. G., Sun, M. Z., Zhang, H. Y., and Xu, C. L. (2019). Chiral molecule-mediated porous CuXO nanoparticle clusters with antioxidation activity for ameliorating parkinson's disease. *J. Am. Chem. Soc.* 141, 1091–1099. doi: 10.1021/jacs.8b11856

Harrison, D. G., Griendling, K. K., Landmesser, U., Hornig, B., and Drexler, H. (2003). Role of oxidative stress in atherosclerosis. *Am. J. Cardiol.* 91, 7–11. doi: 10.1016/S0002-9149(02)03144-2

Hawkins, B. T., and Thomas, P. D. (2005). The blood-brain barrier/neurovascular unit in health and disease. *Pharmacol. Rev.* 57, 173–185. doi: 10.1124/pr.57.2.4

He, W., Zhou, Y. T., Wamer, W. G., Boudreau, M. D., and Yin, J. J. (2012). Mechanisms of the pH dependent generation of hydroxyl radicals and oxygen induced by Ag nanoparticles. *Biomaterials* 33, 7547–7555. doi: 10.1016/j.biomaterials.2012.06.076

He, W., Zhou, Y. T., Wamer, W. G., Hu, X., Wu, X., Zheng, Z., et al. (2013). Intrinsic catalytic activity of Au nanoparticles with respect to hydrogen peroxide decomposition and superoxide scavenging. *Biomaterials* 34, 765–773. doi: 10.1016/j.biomaterials.2012.10.010

Heckman, K. L., DeCoteau, W., Estevez, A., Reed, K. J., Costanzo, W., et al. (2013). Custom cerium oxide nanoparticles protect against a free radical mediated autoimmune degenerative disease in the brain. *ACS Nano* 7, 10582–10596. doi: 10.1021/nn403743b

Heim, K. E., Tagliaferro, A. R., and Bobilya, D. J. (2002). Flavonoid antioxidants: chemistry, metabolism and structure-activity relationships. *J. Nutr. Biochem.* 13, 572–584. doi: 10.1016/S0955-2863(02)00208-5

Hosaka, H., Haruki, R., Yamada, K., Bottcher, C., and Komatsu, T. (2014). Hemoglobin–albumin cluster incorporating a Pt nanoparticle: artificial O_2 carrier with antioxidant activities. *PLoS ONE*. 9:e110541. doi: 10.1371/journal.pone.0110541

Huang, L., Chen, J. X., Gan, L. F., Wang, J., and Dong, S. J. (2019). Single-atom nanozymes. *Sci. Adv.* 5:eaav5490. doi: 10.1126/sciadv.aav5490

Huang, X., Zhao, Z., Cao, L., Chen, Y., Zhu, E., Lin, Z., et al. (2015). High-performance transition metal-doped Pt3Ni octahedra for oxygen reduction reaction. *Science* 348, 1230–1234. doi: 10.1126/science.aaa8765

Huang, Y. Y., Liu, C. Q., Fang, P., Liu, Z., Ren, J. S., and Qu, X. G. (2017). GO-Se nanocomposite as an antioxidant nanozyme for cytoprotection. *Chem. Commun.* 53, 3082–3085. doi: 10.1039/C7CC00045F

Huang, Y. Y., Liu, Z., Liu, C. Q., Ju, E. G., Zhang, Y., Ren, J. S., et al. (2016). Self-assembly of multi-nanozymes to mimic an intracellular antioxidant defense system. *Angew. Chem. Int. Ed.* 55, 6646–6650. doi: 10.1002/anie.201600868

Huang, Y. Y., Liu, Z., Liu, C. Q., Zhang, Y., Ren, J. S., and Qu, X. G. (2018). Selenium-based nanozyme as a biomimetic antioxidant machinery. *Chem. Eur. J.* 24, 10224–10230. doi: 10.1002/chem.201801725

Jiang, B., Duan, D., Gao, L., Zhou, M., Fan, K., Tang, Y., et al. (2018). Standardized assays for determining the catalytic activity and kinetics of peroxidase-like nanozymes. *Nat. Protoc.* 13, 1506–1520. doi: 10.1038/s41596-018-0001-1

Jiang, X., Andjelkovic, A. V., Zhu, L., Yang, T., Bennett, M. V., Chen, J., et al. (2018). Blood-brain barrier dysfunction and recovery after ischemic stroke. *Prog. Neurobiol.* 163, 144–171. doi: 10.1016/j.pneurobio.2017.10.001

Ju, E. G., Dong, K., Wang, Z. Z., Zhang, Y., Cao, F. F., Chen, Z. W., et al. (2017). Confinement of reactive oxygen species in an artificial-enzyme based hollow structure to eliminate adverse effects of photocatalysis on UV filters. *Chem. Eur. J.* 23, 13518–13524. doi: 10.1002/chem.201703005

Kakaroubas, N., Brennan, S., Keon, M., and Saksena, N. K. (2019). Pathomechanisms of blood-brain barrier disruption in ALS. *Neurosci J.* 2019:2537698. doi: 10.1155/2019/2537698

Kim, C. K., Kim, T., Choi, I. Y., Soh, M., Kim, D., Kim, Y. J., et al. (2012). Ceria nanoparticles that can protect against ischemic stroke. *Angew. Chem. Int. Ed.* 124, 11201–11205. doi: 10.1002/ange.201203780

Kim, M. S., Cho, S., Joo, H. S., Lee, J., Kwak, S. K., Kim, M. I., et al. (2019a). N- and B-codoped graphene: a strong candidate to replace natural peroxidase in sensitive and selective bioassays. *ACS Nano* 13, 4312–4321. doi: 10.1021/acsnano.8b09519

Kim, M. S., Lee, J., Kim, H. S., Cho, A., Shim, K. H., Le, T. N., et al. (2019b). Heme cofactor-resembling Fe–N single site embedded graphene as nanozymes to selectively detect H_2O_2 with high sensitivity. *Adv. Funct. Mater.* 30:1905410. doi: 10.1002/adfm.201905410

Korschelt, K., Ragg, R., Metzger, C. S., Kluenker, M., Oster, M., Bar-ton, B., et al. (2017). Glycine-functionalized copper(II) hydroxide nanoparticles with high intrinsic superoxide dismutase activity. *Nanoscale* 9, 3952–3960. doi: 10.1039/C6NR09810J

Korsvik, C., Patil, S., Sealb, S., and Self, W. T. (2007). Superoxide dismutase mimetic properties exhibited by vacancy engineered ceria nanoparticles. *Chem. Commun.* 10, 1056–1058. doi: 10.1039/b615134e

Kwon, H. J., Kim, D., Seo, K., Kim, Y. G., Han, S. I., Kang,T., et al. (2018). Ceria nanoparticle systems for selective scavenging of mitochondrial, intracellular, and extracellular reactive oxygen species in parkinson's disease. *Angew. Chem. Int. Ed.* 57, 9408–9412. doi: 10.1002/anie.201805052

Lee, J., Park, J. C., and Song, H. (2008). A nanoreactor framework of a Au@SiO2 yolk/shell structure for catalytic reduction of p-nitrophenol. *Adv. Mater.* 20, 1523–1528. doi: 10.1002/adma.200702338

Lee, N., Yoo, D., Ling, D. S., Cho, M. H., Hyeon, T., and Cheon, J. (2015). Iron oxide based nanoparticles for multimodal imaging and magnetoresponsive therapy. *Chem. Rev.* 115, 10637–10689. doi: 10.1021/acs.chemrev.5b00112

Li, B., Nam, H. G., Zhao, J., Chang, J., Lingappan, N., Yao, F., et al. (2017). Nanoreactor of nickel-containing carbon–shells as oxygen reduction catalyst. *Adv. Mater.* 29:1605083. doi: 10.1002/adma.201605083

Li, F., Li, T. Y., Sun, C. X., Xia, J. H., Jiao, Y., and Xu, H. P. (2017). Selenium-doped carbon quantum dots (Se-CQDs) for free radical scavenging. *Angew. Chem. Int. Ed.* 56, 9910–9914. doi: 10.1002/anie.201705989

Li, J. N., Liu, W. Q., Wu, X. C., and Gao, X. F. (2015). Mechanism of pH-switchable peroxidase and catalase-like activities of gold, silver, platinum and palladium. *Biomaterials* 48, 37–44. doi: 10.1016/j.biomaterials.2015.01.012

Li, M., Shi, P., Xu, C., Ren, J. S., and Qu, X. G. (2013). Cerium oxide caged metal chelator: anti-aggregation and anti-oxidation integrated H_2O_2-responsive controlled drug release for potential Alzheimer's disease treatment. *Chem. Sci.* 4, 2536–2542. doi: 10.1039/c3sc50697e

Li, W., Liu, Z., Liu, C. Q., Guan, Y. J., Ren, J. S., and Qu, X. G. (2017). Manganese dioxide nanozymes as intelligent cytoprotective shells for individual living cell encapsulation. *Angew. Chem. Int. Ed.* 56, 13661–13665. doi: 10.1002/anie.201706910

Li, Y., Yuna, K.-H., Leea, H., Gohb, S.-H., Suhc, Y.-G., and Choi, Y. (2019). Porous platinum nanoparticles as a high-Z and oxygen generating nanozyme for enhanced radiotherapy *in vivo*. *Biomaterials* 197, 12–19. doi: 10.1016/j.biomaterials.2019.01.004

Li, Y. Y., He, X., Yin, J. J., Ma, Y. H., Zhang, P., Li, J. Y., et al. (2014). Acquired superoxide-scavenging ability of ceria nanoparticles. *Angew. Chem. Int. Ed.* 127, 1852–1855. doi: 10.1002/ange.201410398

Ligtenbarg, A. G. J., Hage, R., and Feringa, B. L. (2003). Catalytic oxidations by vanadium complexes. *Coord. Chem. Rev.* 237, 89–101. doi: 10.1016/S0010-8545(02)00308-9

Lin, S. C., Cheng, Y., Zhang, H., Wang, X. Y., Zhang, Y. Y., and Zhang, Y. J. (2019). Copper tannic acid coordination nanosheet: a potent nanozyme for scavenging ROS from cigarette smoke. *Small* 16:1902123. doi: 10.1002/smll.201902123

Liu, C.-P., Wu, T.-H., Lin, Y.-L., Liu, C.-Y., Wang, S., and Lin, S.-Y. (2016). Tailoring enzyme-like activities of gold nanoclusters by polymeric tertiary amines for protecting neurons against oxidative stress. *Small* 12, 4127–4135. doi: 10.1002/smll.201503919

Liu, X. P., Zhang, Z. J., Zhang, Y., Guan, Y. J., Liu, Z., Ren, J. S., et al. (2016). Artificial metalloenzyme-based enzyme replacement therapy for the treatment of hyperuricemia. *Adv. Funct. Mater.* 26, 7921–7928. doi: 10.1002/adfm.201602932

Liu, X. Y., Wei, W., Yuan, Q., Zhang, X., Li, N., Du, Y. G., et al. (2012). Apoferritin–CeO_2 nano-truffle that has excellent artificial redox enzyme activity. *Chem. Commun.* 48, 3155–3157. doi: 10.1039/C1CC15815E

Liu, Y. L., Ai, K. L., Ji, X. Y., Askhatova, D., Du, R., Lu, L. H., et al. (2017). Comprehensive insights into the multi-antioxidative mechanisms of melanin nanoparticles and their application to protect brain from injury in ischemic stroke. *J. Am. Chem. Soc.* 139, 856–862. doi: 10.1021/jacs.6b11013

Liu, Y. L., Ai, K. L., Liu, J. H., Deng, M., He, Y. Y., and Lu, L. H. (2012). Dopamine-melanin colloidal nanospheres: an efficient near-infrared photothermal therapeutic agent for *in vivo* cancer therapy. *Adv. Mater.* 25, 1353–1359. doi: 10.1002/adma.201204683

Ma, W. J., Mao, J. J., Yang, X. T., Pan, C., Chen, W. X., Wang, M., et al. (2019). A single-atom Fe–N_4 catalytic site mimicking bifunctional antioxidative enzymes for oxidative stress cytoprotection. *Chem. Commun.* 55, 159–162. doi: 10.1039/C8CC08116F

Macdonald, J., Galley, H. F., and Webster, N. R. (2003). Oxidative stress and gene expression in sepsis. *Br. J. Anaesth.* 90, 221–232. doi: 10.1093/bja/aeg034

Mahajan, R., Rouhi, M., Shinde, S., Bedwell, T., Incel, A., Mavliutova, L., et al. (2019). Highly efficient synthesis and assay of protein-imprinted nanogels by using magnetic templates. *Angew. Chem. Int. Ed.* 58, 727–730. doi: 10.1002/anie.201805772

Mittal, M., Siddiqui, M. R., Tran, K., Reddy, S. P., and Malik, A. B. (2014). Reactive oxygen species in inflammation and tissue injury. *Antioxid. Redox Sign.* 20, 1126–1167. doi: 10.1089/ars.2012.5149

Moglianetti, M., Luca, E. D., Pedone, D., Marotta, R., Catelani, T., Sartori, B., et al. (2016). Platinum nanozymes recover cellular ROS homeostasis in an oxidative stress-mediated disease model. *Nanoscale* 8:3739. doi: 10.1039/C5NR08358C

Morry, J., Ngamcherdtrakul, W., and Yantasee, W. (2016). Oxidative stress in cancer and fibrosis: opportunity for therapeutic intervention with antioxidant compounds, enzymes, and nanoparticles. *Redox. Bio.* 11, 240–253. doi: 10.1016/j.redox.2016.12.011

Mu, X. Y., He, H., Wang, J. Y., Long, W., Li, Q. F., and Liu, H. L. (2019a). Carbogenic nanozyme with ultrahigh reactive nitrogen species selectivity for traumatic brain injury. *Nano Lett.* 19, 4527–4534. doi: 10.1021/acs.nanolett.9b01333

Mu, X. Y., Wang, J. Y., Li, Y. H., Xu, F. J., Long, W., Ouyang, L. F., et al. (2019b). Redox trimetallic nanozyme with neutral environment preference for brain injury. *ACS Nano* 13, 1870–1884. doi: 10.1021/acsnano.8b08045

Natalio, F., Andre, R., Hartog, A. F., Stoll, B., Jochum, K. P., Wever, R., et al. (2012). Vanadium pentoxide nanoparticles mimic vanadium haloperoxidases and thwart biofilm formation. *Nat. Nanotechnol.* 7, 530–535 doi: 10.1038/nnano.2012.91

Nathan, C., and Cunningham-Bussel, A. (2013). Beyond oxidative stress: an immunologist's guide to reactive oxygen species. *Nat. Rev. Immunol.* 13, 349–361. doi: 10.1038/nri3423

Nechifor, M. T., Neagu, T. M., and Manda, G. (2009). Reactive oxygen species, cancer and anti- cancer therapies. *Curr. Chem. Biol.* 3, 22–46. doi: 10.2174/2212796810903010022

Niki, E., and Noguchi, N. (2004). Dynamics of antioxidant action of vitamin E. *Acc. Chem. Res.* 37, 45–51. doi: 10.1021/ar030069m

Onizawa, S., Aoshiba, K., Kajita, M., Miyamoto, Y., and Nagai, A. (2009). Platinum nanoparticle antioxidants inhibit pulmonary inflammation in mice exposed to cigarette smoke. *Pulm. Pharmacol. Ther.* 22, 340–349. doi: 10.1016/j.pupt.2008.12.015

Orihuela, R., McPherson, C. A., and Harry, G. J. (2016). Microglial M1/M2 polarization and metabolic states. *Br. J. Pharmacol.* 173, 649–665. doi: 10.1111/bph.13139

Pamplona, A., Ferreira, A., Balla, J., Jeney, V., Balla, G., Epiphanio, S., et al. (2007). Heme oxygenase-1 and carbon monoxide suppress the pathogenesis of experimental cerebral malaria. *Nat. Med.* 13, 703–710. doi: 10.1038/nm1586

Patel, V., Singh, M., Mayes, E. L. H., Martinez, A., Shutthanandan, V., Bansal, V., et al. (2018). Ligand-mediated reversal of the oxidation state dependent ROS scavenging and enzyme mimicking activity of ceria nanoparticles. *Chem. Commun.* 54, 13973–13976. doi: 10.1039/C8CC08355J

Pelka, J., Gehrke, H., Esselen, M., Turk, M., Crone, M., Brase, S., et al. (2009). Cellular uptake of platinum nanoparticles in human colon carcinoma cells and their impact on cellular redox systems and DNA integrity. *Chem. Res. Toxicol.* 22, 649–659. doi: 10.1021/tx800354g

Pellicoro, A., Ramachandran, P., Iredale, J. P., and Fallowfield, J. A. (2014). Liver fibrosis and repair: immune regulation of wound healing in a solid organ. *Nat. Rev. Immunol.* 14, 181–194. doi: 10.1038/nri3623

Pirmohamed, T., Dowding, J. M., Singh, S., Wasserman, B., Heckert, E. A., and Karakoti, S. (2010). Nanoceria exhibit redox state-dependent catalase mimetic activity. *Chem. Commun.* 46, 2736–2738. doi: 10.1039/b922024k

Quick, K. L., Ali, S. S., Arch, R., Xiong, C. J., Wozniak, D., and Dugan, L. L. (2008). A carboxyfullerene SOD mimetic improves cognition and extends the lifespan of mice. *Neurobiol. Aging.* 29, 117–128. doi: 10.1016/j.neurobiolaging.2006.09.014

Ray, G., Batra, S., Shukla, N. K., Deo, S., Raina, V., Ashok, S., et al. (2000). Lipid peroxidation, free radical production and antioxidant status in breast cancer. *Breast Cancer Res. Treat.* 59, 163–170. doi: 10.1023/A:1006357330486

Reuter, S., Gupta, S. C., Chaturvedi, M. M., and Aggarwal, B. B. (2010). Oxidative stress, inflammation, and cancer: how are they linked? *Free Radic. Biol. Med.* 49, 1603–1616. doi: 10.1016/j.freeradbiomed.2010.09.006

Russo, M. V., and McGavern, D. B. (2016). Inflammatory neuroprotection following traumatic brain injury. *Science* 353, 783–785. doi: 10.1126/science.aaf6260

Schieber, M., and Chandel, N. S. (2014). ROS function in redox signaling and oxidative stress. *Curr. Biol.* 24, 453–462. doi: 10.1016/j.cub.2014.03.034

Schirhagl, R. (2014). Bioapplications for molecularly imprinted polymers. *Anal. Chem.* 86, 250–261. doi: 10.1021/ac401251j

Sena, L. A., and Chandel, N. S. (2012). Physiological roles of mitochondrial reactive oxygen species. *Mol. Cell.* 48, 158–167. doi: 10.1016/j.molcel.2012.09.025

Shen, X., Zhu, L., Liu, G., Tang, H., Liu, S., and Li, W. (2009). Photocatalytic removal of pentachlorophenol by means of an enzyme-like molecular imprinted photocatalyst and inhibition of the generation of highly toxic intermediates. *New J. Chem.* 33, 2278–2285. doi: 10.1039/b9nj00255c

Shi, W. B., Wang, Q. L., Long, Y. J., Cheng, Z. L., Chen, S. H., Zheng, H. Z., et al. (2011). Carbon nanodots as peroxidase mimetics and their applications to glucose detection. *Chem. Commun.* 47, 6695–6697. doi: 10.1039/c1cc11943e

Shibuya, S., Ozawa, Y., Yokote, K., and Shimizu, T. (2014). Palladium and platinum nanoparticles attenuate aging-like skin atrophy via antioxidant activity. *Free Radic. Biol. Med.* 76:315. doi: 10.1016/j.freeradbiomed.2014.10.315

Simon, D. W., McGeachy, M. J., Bayir, H., Clark, R. S., Loane, D. J., and Kochanek, P. M. (2017). The far-reaching scope of neuroinflammation after traumatic brain injury. *Nat. Rev. Neurol.* 13, 171–191. doi: 10.1038/nrneurol.2017.13

Singh, N., Savanur, M. A., Srivastava, S., D'Silva, P., and Mugesh, G. (2017). A redox modulatory Mn_3O_4 nanozyme with multi-enzyme activity provides efficient cytoprotection to human cells in a parkinson's disease model. *Angew. Chem. Int. Ed.* 56, 14267–14271. doi: 10.1002/anie.201708573

Singh, N., Savanur, M. A., Srivastava, S., D'Silva, P., and Mugesh, G. (2019). A manganese oxide nanozyme prevents oxidative damage of biomolecules without affecting the endogenous antioxidant system. *Nanoscale* 11, 3855–3863. doi: 10.1039/C8NR09397K

Soh, M., Kang, D. W., Jeong, H. G., Kim, D., Kim, D. Y., Yang, W., et al. (2017). Ceria–zirconia nanoparticles as enhanced multi-antioxidant for sepsis treatment. *Angew. Chem. Int. Ed*. 56, 11399–11403. doi: 10.1002/anie.201704904

Son, D., Lee, J., Lee, D. J., Ghaffari, R., Yun, S., Kim, S. J., et al. (2015). Bioresorbable electronic stent integrated with therapeutic nanoparticles for endovascular diseases. *ACS Nano* 9, 5937–5946. doi: 10.1021/acsnano.5b00651

Song, M., Liu, T., Shi, C., Zhang, X., and Chen, X. (2016). Bioconjugated manganese dioxide nanoparticles enhance chemotherapy response by priming tumor-associated macrophages toward M1-like phenotype and attenuating tumor hypoxia. *ACS Nano* 10, 633–647. doi: 10.1021/acsnano.5b06779

Song, Y. J., Qu, K. G., Zhao, C., Ren, J. S., and Qu, X. G. (2010). Graphene oxide: intrinsic peroxidase catalytic activityand its application to glucose detection. *Adv. Mater*. 22, 2206–2210. doi: 10.1002/adma.200903783

Song, Y. J., Xia, X. F., Wu, X. F., Wang, P., and Qin, L. D. (2014). Integration of platinum nanoparticles with a volumetric bar-chart chip for biomarker assays. *Angew. Chem. Int. Ed*. 53, 12451–12455. doi: 10.1002/anie.201404349

Stämpfli, M. R., and Anderson, G. P. (2009). How cigarette smoke skews immune responses to promote infection, lung disease and cancer. *Nat. Rev. Immunol*. 9, 377–384. doi: 10.1038/nri2530

Su, H., Liu, D. D., Zhao, M., Hu, W. L., Xue, S. S., Cao, Q., et al. (2015). Dual-enzyme characteristics of polyvinylpyrrolidone-capped iridium nanoparticles and their cellular protective effect against H_2O_2-induced oxidative damage. *ACS Appl. Mater. Inter*. 7, 8233–8242. doi: 10.1021/acsami.5b01271

Sun, H., Zhao, A., Gao, N., Li, K., Ren, J., and Qu, X. (2015). Deciphering a nanocarbon-based artificial peroxidase: chemical identification of the catalytically active and substrate-binding sites on graphene quantum dots. *Angew. Chem. Int. Ed*. 54, 7176–7180. doi: 10.1002/anie.201500626

Tak, P. P., Zvaifler, N. J., Green, D. R., and Firestein, G. S. (2000). Rheumatoid arthritis and p53: how oxidative stress might alter the course of inflammatory diseases. *Immunol. Today* 21, 78–82. doi: 10.1016/S0167-5699(99)01552-2

Valko, M., Izakovic, M., Mazur, M., Rhodes, C. J., and Telser, J. (2004). Role of oxygen radicals in DNA damage and cancer incidence. *Mol. Cell. Biochem*. 266, 37–56. doi: 10.1023/B:MCBI.0000049134.69131.89

Vallabani, N. V. S., Karakoti, A. S., and Singh, S. (2017). ATP-mediated intrinsic peroxidase-like activity of Fe_3O_4-based nanozyme: one step detection of blood glucose at physiological pH. *Colloid. Surface B* 153, 52–60. doi: 10.1016/j.colsurfb.2017.02.004

Vernekar, A. A., Sinha, D., Srivastava, S., Paramasivam, P. U., D'Silva,. P., and Mugesh, G. (2014). An antioxidant nanozyme that uncovers the cytoprotective potential of vanadia nanowires. *Nat. Commun*. 5:5301. doi: 10.1038/ncomms6301

Vitale, G., Salvioli, S., and Franceschi, C. (2013). Oxidative stress and the ageing endocrine system. *Nat. Rev. Endocrinol.* 9, 228–240. doi: 10.1038/nrendo.2013.29

Wan, W. L., Lin, Y. J., Chen, H. L., Huang, C. C., Shih, P. C., Bow, Y. R., et al. (2017). *In situ* nanoreactor for photosynthesizing H_2 gas to mitigate oxidative stress in tissue inflammation. *J. Am. Chem. Soc.* 139, 12923–12926. doi: 10.1021/jacs.7b07492

Wang, B., Zhang, L., Bae, S. C., and Granick, S. (2008). Nanoparticle-induced surface reconstruction of phospholipid membranes. *Proc. Natl. Acad. Sci. U.S.A.* 105, 18171–18175. doi: 10.1073/pnas.0807296105

Wang, D. D., Wu, H. H., Phua, S. Z. F., Yang, G., B., Lim, W. Q., et al. (2020). Self-assembled single-atom nanozyme for enhanced photodynamic therapy treatment of tumor. *Nat. Commun.* 11:357. doi: 10.1038/s41467-019-14199-7

Wang, L., Wang, Z. J., Li, X. M., Zhang, Y., Yin, M., and Li, J. (2018). Deciphering active biocompatibility of iron oxide nanoparticles from their intrinsic antagonism. *Nano Res.* 11, 2746–2755. doi: 10.1007/s12274-017-1905-8

Weaver, J. D., and Stabler, C. L. (2015). Antioxidant cerium oxide nanoparticle hydrogels for cellular encapsulation. *Acta Biomater.* 16, 136–144. doi: 10.1016/j.actbio.2015.01.017

Winterbourn, C. C. (2008). Reconciling the chemistry and biology of reactive oxygen species. *Nat. Chem. Biol.* 4, 278–286. doi: 10.1038/nchembio.85

Wu, H. B., Li, F. Y., Wang, S. F., Lu, J. X., Li, J. Q., Du, Y., et al. (2018). Ceria nanocrystals decorated mesoporous silica nanoparticle based ROS-scavenging tissue adhesive for highly efficient regenerative wound healing. *Biomaterials* 151, 66–77. doi: 10.1016/j.biomaterials.2017.10.018

Wu, J. J. X., Wang, X. Y., Wang, Q., Lou, Z. P., Li, S., Zhu, Y. Y., et al. (2019). Nanomaterials with enzyme-like characteristics (nanozymes): next-generation artificial enzymes (II). *Chem. Soc. Rev*. 48, 1004–1076. doi: 10.1039/C8CS00457A

Xiong, B.in., Xu, R. L., Zhou, R., He, Y., and Yeung, E. (2014). Preventing UV induced cell damage by scavenging reactive oxygen species with enzyme-mimic Au–Pt nanocomposites. *Talanta* 120, 262–267. doi: 10.1016/j.talanta.2013.12.020

Yan, R. J., Sun, S., Yang, J., Long, W., Wang, J. Y., Mu, X. Y., et al. (2019). A nanozyme-based bandage with single-atom catalysis for brain trauma. *ACS Nano* 13, 11552–11560. doi: 10.1021/acsnano.9b05075

Yao, J., Cheng, Y., Zhou, M., Zhao, S., Lin, S. C., Wang. X., et al. (2018). ROS scavenging Mn_3O_4 nanozymes for *in vivo* anti-inflammation. *Chem. Sci*. 9, 2927–2933. doi: 10.1039/C7SC05476A

Zeng, F., Wu, Y. W., Li, X. W., Ge, X. J., Guo, Q. H., Lou, X. B., et al. (2018). Custom-made ceria nanoparticles show a neuroprotective effect by modulating phenotypic polarization of the microglia. *Angew. Chem. Int. Ed*. 57, 5808–5812. doi: 10.1002/anie.201802309

Zhang, B., Bailey, W. M., McVicar, A. L., and Gensel, J. C. (2016). Age increases reactive oxygen species production in macrophages and potentiates oxidative damage after spinal cord injury. *Nuerobiol. Aging* 47, 157–167. doi: 10.1016/j.neurobiolaging.2016.07.029

Zhang, L. B., Fischer, W., Pippel, E., Hause, G., Brandsch, M., and Knez, M. (2011). Receptor-mediated cellular uptake of nanoparticles: a switchable delivery system. *Small* 7, 1538–1541. doi: 10.1002/smll.201100238

Zhang, L. B., Laug, L. D., Munchgesang, W., Pippel, E., Gosele, U., Brandsch, M., et al. (2010). Reducing stress on cells with apoferritin-encapsulated platinum nanoparticles. *Nano Lett*. 10, 219–223. doi: 10.1021/nl903313r

Zhang, Y., Wang, Z. Y., Li, X. J., Wang, L., Yin, M., Wang, L. H., et al. (2015). Dietary iron oxide nanoparticles delay aging and ameliorate neurodegeneration in drosophila. *Adv. Mater.* 28, 1387–1393. doi: 10.1002/adma.201503893

Zhang, Y., Wu, C. Y., Zhou, X. J., Wu, X. C., Yang, Y. Q., Wu, H. X., et al. (2013). Graphene quantum dots/gold electrode and its application in living cell H_2O_2 detection. *Nanoscale* 5, 1816–1819. doi: 10.1039/c3nr33954h

Zhang, Z., Zhang, X. H., Liu, B. W., and Liu, J. W. (2017). Molecular imprinting on inorganic nanozymes for hundred-fold enzyme specificity. *J. Am. Chem. Soc.* 139, 5412–5419. doi: 10.1021/jacs.7b00601

Zhang, Z. J., Li, Y. Q., Zhang, X. H., and Liu, J. W. (2019). Molecularly imprinted nanozymes with faster catalytic activity and better specificity. *Nanoscale* 11, 4854–4863. doi: 10.1039/C8NR09816F

Zhao, J. L., Cai, X. J., Gao, W., Zhang, L. L., Zou, D. W., Zheng, Y. Y., et al. (2018). Prussian blue nanozyme with multi-enzyme activity reduces colitis in mice. *ACS. Appl. Mater. Inter*. 10, 26108–26117. doi: 10.1021/acsami.8b10345

Zhao, S., Duan, H. X., Yang, Y. L., Yan, X. Y., and Fan, K. L. (2019). Fenozyme protects the integrity of blood brain barrier against experimental cerebral malaria. *Nano Lett*. 19, 8887–8895. doi: 10.1021/acs.nanolett.9b03774

Conflict of Interest: The authors declare that the research was conducted in the absence of any commercial or financial relationships that could be construed as a potential conflict of interest.

Advantages of publishing in Frontiers

OPEN ACCESS
Articles are free to read
for greatest visibility
and readership

FAST PUBLICATION
Around 90 days
from submission
to decision

HIGH QUALITY PEER-REVIEW
Rigorous, collaborative,
and constructive
peer-review

TRANSPARENT PEER-REVIEW
Editors and reviewers
acknowledged by name
on published articles

Frontiers
Avenue du Tribunal-Fédéral 34
1005 Lausanne | Switzerland

Visit us: www.frontiersin.org
Contact us: frontiersin.org/about/contact

REPRODUCIBILITY OF RESEARCH
Support open data
and methods to enhance
research reproducibility

DIGITAL PUBLISHING
Articles designed
for optimal readership
across devices

FOLLOW US
@frontiersin

IMPACT METRICS
Advanced article metrics
track visibility across
digital media

EXTENSIVE PROMOTION
Marketing
and promotion
of impactful research

LOOP RESEARCH NETWORK
Our network
increases your
article's readership